

ST&B

U 393

.S7

AMP

v. 1

Copy 1

CONFIDENTIAL

Return To
SCIENCE AND TECHNOLOGY DIVISION
Library of Congress

LC REGULATION: BEFORE SERVICING
OR REPRODUCING ANY PART OF THIS
DOCUMENT, ALL CLASSIFICATION
MARKINGS MUST BE CANCELLED.

Return To
SCIENCE AND TECHNOLOGY DIVISION
Library of Congress

15119

SUMMARY TECHNICAL REPORT
OF THE
NATIONAL DEFENSE RESEARCH COMMITTEE

**LC REGULATION: BEFORE SERVICING
OR REPRODUCING ANY PART OF THIS
DOCUMENT, ALL CLASSIFICATION
MARKINGS MUST BE CANCELLED.**

DECLASSIFIED

By authority Secretary of

OCT 13 1960

Defense memo 2 August 1960

LIBRARY OF CONGRESS

This document contains information affecting the national defense of the United States within the meaning of the Espionage Act, 50 U. S. C., 31 and 32, as amended. Its transmission or the revelation of its contents in any manner to an unauthorized person is prohibited by law.

This volume is classified **TOP SECRET** in accordance with security regulations of the War and Navy Departments because certain chapters contain material which was **TOP SECRET** at the time of printing. Other chapters may have had a lower classification. The reader is advised to consult the War and Navy agencies listed on the reverse of this page for the current classification of any material.

TOP SECRET

Manuscript and illustrations for this volume were prepared for publication by the Summary Reports Groups of the Columbia University Division of War Research under contract OEMsr-1131 with the Office of Scientific Research and Development. This volume was printed and bound by the Columbia University Press.

Distribution of the Summary Technical Report of NDRC has been made by the War and Navy Departments. Inquiries concerning the availability and distribution of the Summary Technical Report volumes and microfilmed and other reference material should be addressed to the War Department Library, Room 1A-522, The Pentagon, Washington 25, D. C., or to the Office of Naval Research, Navy Department, Attention: Reports and Documents Section, Washington 25, D. C.

Copy No.

238

This volume, like the seventy others of the Summary Technical Report of NDRC, has been written, edited, and printed under great pressure. Inevitably there are errors which have slipped past Division readers and proofreaders. There may be errors of fact not known at time of printing. The author has not been able to follow through his writing to the final page proof.

Please report errors to:

JOINT RESEARCH AND DEVELOPMENT BOARD
PROGRAMS DIVISION (STR ERRATA)
WASHINGTON 25, D. C.

A master errata sheet will be compiled from these reports and sent to recipients of the volume. Your help will make this book more useful to other readers and will be of great value in preparing any revisions.

CONFIDENTIAL

SUMMARY TECHNICAL REPORT OF THE
APPLIED MATHEMATICS PANEL, NDRC

VOLUME 1

MATHEMATICAL STUDIES
RELATING TO MILITARY
PHYSICAL RESEARCH

DECLASSIFIED
By authority Secretary of

OCT 13 1960

Defense memo 2 August 1960

LIBRARY OF CONGRESS

OFFICE OF SCIENTIFIC RESEARCH AND DEVELOPMENT
VANNEVAR BUSH, DIRECTOR

NATIONAL DEFENSE RESEARCH COMMITTEE
JAMES B. CONANT, CHAIRMAN

APPLIED MATHEMATICS PANEL
WARREN WEAVER, CHIEF

WASHINGTON, D. C., 1946

CONFIDENTIAL

NATIONAL DEFENSE RESEARCH COMMITTEE

James B. Conant, *Chairman*

Richard C. Tolman, *Vice Chairman*

Roger Adams Army Representative¹

Frank B. Jewett Navy Representative²

Karl T. Compton Commissioner of Patents³

Irvin Stewart, *Executive Secretary*

¹Army representatives in order of service:

Maj. Gen. G. V. Strong	Col. L. A. Denson
Maj. Gen. R. C. Moore	Col. P. R. Faymonville
Maj. Gen. C. C. Williams	Brig. Gen. E. A. Regnier
Brig. Gen. W. A. Wood, Jr.	Col. M. M. Irvine
Col. E. A. Routheau	

²Navy representatives in order of service:

Rear Adm. H. G. Bowen	Rear Adm. J. A. Furer
Capt. Lybrand P. Smith	Rear Adm. A. H. Van Keuren
Commodore H. A. Schade	

³Commissioners of Patents in order of service:

Conway P. Coe	Casper W. Ooms
---------------	----------------

NOTES ON THE ORGANIZATION OF NDRC

The duties of the National Defense Research Committee were (1) to recommend to the Director of OSRD suitable projects and research programs on the instrumentalities of warfare, together with contract facilities for carrying out these projects and programs, and (2) to administer the technical and scientific work of the contracts. More specifically, NDRC functioned by initiating research projects on requests from the Army or the Navy, or on requests from an allied government transmitted through the Liaison Office of OSRD, or on its own considered initiative as a result of the experience of its members. Proposals prepared by the Division, Panel, or Committee for research contracts for performance of the work involved in such projects were first reviewed by NDRC, and if approved, recommended to the Director of OSRD. Upon approval of a proposal by the Director, a contract permitting maximum flexibility of scientific effort was arranged. The business aspects of the contract, including such matters as materials, clearances, vouchers, patents, priorities, legal matters, and administration of patent matters were handled by the Executive Secretary of OSRD.

Originally NDRC administered its work through five divisions, each headed by one of the NDRC members. These were:

- Division A — Armor and Ordnance
- Division B — Bombs, Fuels, Gases, & Chemical Problems
- Division C — Communication and Transportation
- Division D — Detection, Controls, and Instruments
- Division E — Patents and Inventions

In a reorganization in the fall of 1942, twenty-three administrative divisions, panels, or committees were created, each with a chief selected on the basis of his outstanding work in the particular field. The NDRC members then became a reviewing and advisory group to the Director of OSRD. The final organization was as follows:

- Division 1 — Ballistic Research
- Division 2 — Effects of Impact and Explosion
- Division 3 — Rocket Ordnance
- Division 4 — Ordnance Accessories
- Division 5 — New Missiles
- Division 6 — Sub-Surface Warfare
- Division 7 — Fire Control
- Division 8 — Explosives
- Division 9 — Chemistry
- Division 10 — Absorbents and Aerosols
- Division 11 — Chemical Engineering
- Division 12 — Transportation
- Division 13 — Electrical Communication
- Division 14 — Radar
- Division 15 — Radio Coordination
- Division 16 — Optics and Camouflage
- Division 17 — Physics
- Division 18 — War Metallurgy
- Division 19 — Miscellaneous
- Applied Mathematics Panel
- Applied Psychology Panel
- Committee on Propagation
- Tropical Deterioration Administrative Committee

NDRC FOREWORD

AS EVENTS of the years preceding 1940 revealed more and more clearly the seriousness of the world situation, many scientists in this country came to realize the need of organizing scientific research for service in a national emergency. Recommendations which they made to the White House were given careful and sympathetic attention, and as a result the National Defense Research Committee [NDRC] was formed by Executive Order of the President in the summer of 1940. The members of NDRC, appointed by the President, were instructed to supplement the work of the Army and the Navy in the development of the instrumentalities of war. A year later, upon the establishment of the Office of Scientific Research and Development [OSRD], NDRC became one of its units.

The Summary Technical Report of NDRC is a conscientious effort on the part of NDRC to summarize and evaluate its work and to present it in a useful and permanent form. It comprises some seventy volumes broken into groups corresponding to the NDRC Divisions, Panels, and Committees.

The Summary Technical Report of each Division, Panel, or Committee is an integral survey of the work of that group. The first volume of each group's report contains a summary of the report, stating the problems presented and the philosophy of attacking them, and summarizing the results of the research, development, and training activities undertaken. Some volumes may be "state of the art" treatises covering subjects to which various research groups have contributed information. Others may contain descriptions of devices developed in the laboratories. A master index of all these divisional, panel, and committee reports which together constitute the Summary Technical Report of NDRC is contained in a separate volume, which also includes the index of a microfilm record of pertinent technical laboratory reports and reference material.

Some of the NDRC-sponsored researches which had been declassified by the end of 1945 were of sufficient popular interest that it was found desirable to report them in the form of monographs, such as the series on radar by Division 14 and the monograph on sampling inspection by the Applied Mathematics Panel. Since the material treated in them is not dupli-

cated in the Summary Technical Report of NDRC, the monographs are an important part of the story of these aspects of NDRC research.

In contrast to the information on radar, which is of widespread interest and much of which is released to the public, the research on subsurface warfare is largely classified and is of general interest to a more restricted group. As a consequence, the report of Division 6 is found almost entirely in its Summary Technical Report, which runs to over twenty volumes. The extent of the work of a division cannot therefore be judged solely by the number of volumes devoted to it in the Summary Technical Report of NDRC: account must be taken of the monographs and available reports published elsewhere.

Perhaps the highest tribute which could have been paid to the role of mathematicians in World War II was the complete lack of astonishment which greeted their contributions. To the Applied Mathematics Panel of NDRC came urgent, varied, and formidable requests from every other group in NDRC and every military service. As expected, these requests were met; and, also as expected, the results were found invaluable in every phase of warfare from defense against enemy attack to the design of new weapons, recommendations for their use, predictions of their usefulness, and analysis of their effects.

To meet such obligations, the Applied Mathematics Panel under the leadership of Warren Weaver, together with members of its staff and of its contractors' staffs, made available the services of a group of men who were not merely able, competent mathematicians but also loyal, devoted Americans cooperating unselfishly in the defense of their country. The Summary Technical Report of the Applied Mathematics Panel, prepared under the direction of the Panel Chief and authorized by him for publication, is a record of their accomplishments and a testimonial to their scientific integrity. They deserve the grateful appreciation of the Nation.

VANNEVAR BUSH, Director
Office of Scientific Research and Development

J. B. CONANT, Chairman
National Defense Research Committee

FOREWORD

WHEN THE National Defense Research Committee was reorganized at the end of 1942, it was decided to set up a new organization, called the Applied Mathematics Panel [AMP], in order to bring mathematicians as a group more effectively into the work being carried on by scientists in support of the Nation's war effort. At the time of the original appointment of the National Defense Research Committee by President Roosevelt, no mathematicians were included on the Committee, and it was not until the NDRC had been operating for more than a year that the need of a separate division devoted to applied mathematics was recognized. Although many of the operating Divisions of NDRC had set up mathematical groups to handle their own analytical problems, it was intended that the new Applied Mathematics Panel should supplement such groups and should furnish mathematical advice and service to all Divisions of the NDRC, carrying out requested mathematical analyses and remaining available as consultants after the original analyses had been completed. The Panel was organized too late to make possible a fully definitive trial of the success of this type of organization. That mathematics has a fundamental role to play in the science of warfare, I am sure; I have set forth some of the considerations which seem to be relevant and important in the last chapter of Volume 2 of the AMP Summary Technical Report.

The actual development of wartime scientific work proved to be such that the Applied Mathematics Panel has not only been called upon for assistance by NDRC Divisions but has also directly assisted many branches of the Army and Navy. Indeed, at the conclusion of hostilities, when approximately two hundred studies had been undertaken by the Panel, roughly one-half of these represented direct requests from the Armed Services. Furthermore, the consulting activities, growing out of studies originally undertaken to answer specific questions, turned out to be considerably more extensive and significant than was originally anticipated. I think that the importance of this phase of the work cannot be too strongly emphasized. But no account of such general consulting activities is given here, this report being restricted to the formally constituted studies.

The analytical work under AMP studies was carried on by mathematicians associated in groups at various universities and operating under OSRD contracts administered by the Panel. To the men who served as technical representatives of the universities

under these contracts, and to the technical aides who assisted the Chief in the administration of the Panel's scientific work, the Panel owes a large measure of whatever success it achieved. These men combined outstanding scientific competence with energy, resourcefulness, and a selfless willingness to devote their own efforts, as well as the efforts of their staffs, to the solution of other people's problems. The general plans for the Panel's activities were based upon the counsel of a group of eminent mathematicians, formally labeled the *Committee Advisory to the Scientific Officer*. This group, meeting every week, and consisting of R. Courant, G. C. Evans, T. C. Fry, L. M. Graves, H. M. Morse, O. Veblen, and S. S. Wilks, had responsibility for the preliminary examination of requests which reached the Panel and for decisions on overall policy. The Chief relied heavily on their advice which, to a large extent, determined the effectiveness of the Panel's activities.

As the work of NDRC developed, the Panel was called upon for assistance by all of NDRC's nineteen Divisions. It is not, therefore, surprising that the scope of the Panel's activities covers a wide range, falling into four broad, though somewhat overlapping, categories:

1. *Mathematical studies based upon certain classical fields* of applied mathematics, such as classical mechanics and the dynamics of rigid bodies, the theory of elasticity and plasticity, fluid dynamics, electrodynamics, and thermodynamics.

2. *Analytical studies in aerial warfare*, including assessment of the performance of sights and anti-aircraft fire control equipment; studies relating to the vulnerability of aircraft to plane-to-plane and to anti-aircraft fire and the optimal defense of the airplane against these; and analyses of problems arising from the use of rockets in air warfare.

3. *Probability and statistical studies* concerned with the effectiveness of bombing; various aspects of naval warfare, including fire effect analysis and the performance of torpedoes; the design of experiments; sampling inspection; and analyses of many types of data collected by the Armed Services.

4. *Computational services* concerned with the evaluation of integrals; the construction of tables and charts; the development of techniques adapted to the solution of special problems; the nature and capabilities of computing equipment.

The work of the Panel in the first two of these cate-

gories is summarized in Volumes 1 and 2 of the AMP Summary Technical Report. Volume 3, together with two monographs^a which the Panel has prepared dealing with sampling inspection and techniques of statistical analysis, provides a summary of the work in the third category. The fourth class of activities has been reported in AMP Note 25, *Description of Mathematical Tables Computed under the auspices of the Applied Mathematics Panel, NDRC*; in AMP Note 26, *Report on Numerical Methods Employed by the Mathematical Tables Project*; and in the reports published by the Panel under AMP Study 171, *Survey of Computing Machines*. No attempt has been made to report on work which will shortly be published as articles in scientific journals or on results which are deemed too special to be of continuing interest.

^a *Sampling Inspection and Techniques of Statistical Analysis*, published by the McGraw Hill Book Co., Inc.

The preparation of this Summary Technical Report was undertaken after the end of World War II, at a time when the members of the Panel's staff and of the contract groups were eager to return to their peacetime careers. Thus the preparation of these three volumes, solely for the purpose of recording for the Services, in easily accessible form, the scientific results of the Panel's activities, was achieved at real personal sacrifice. I am greatly indebted to the authors of the several parts of these volumes and to the Editorial Committee, consisting of Mina Rees, I. S. Sokolnikoff, and S. S. Wilks, for the admirable job they have done in bringing together, under high pressure, a summary of the principal scientific accomplishments of the Panel.

WARREN WEAVER
Chief, Applied Mathematics Panel

PREFACE

THIS VOLUME presents a summary which reflects typical activities of the Applied Mathematics Panel, NDRC, in a domain which can be loosely defined as classical applied mathematics. It comprises studies utilizing methods of classical mechanics and the dynamics of rigid bodies, the theories of elasticity and plasticity, fluid dynamics, and electrodynamics.

The first portion of the volume (Part I, "Fluid Dynamics and Related Problems") reviews work done largely by the Applied Mathematics Group at New York University, headed by Richard Courant. Prior to the organization of the Applied Mathematics Panel, Courant and K. O. Friedrichs were consultants on certain acoustical problems of interest to the Navy. Courant was also a consultant for Division 8 of the NDRC on shock wave interactions and for the David Taylor Model Basin of the Bureau of Ships on problems connected with underwater explosions. In 1943, these activities were organized, together with related work, under the Applied Mathematics Panel. Certain of the gas-dynamical problems were integrated into a more comprehensive and general study of nonlinear wave motion. As a consequence, the New York University Group found it useful to organize fundamental known results and certain basic new material into a reference work, *Supersonic Flow and Shock Waves*, issued as AMP Report 38.2R, OSRD 4266. This book is reviewed in Part I, partly for completeness and partly to supply background material for a reader without previous specialized knowledge of the subject. The New York University Group also made significant advances in the hydrodynamical study of underwater explosions and in the study of certain limited aspects of the entry of missiles from air into water. The latter topic is closely related to the work of the Harvard Group reported in Part IV. The acoustical research was conducted largely under the leadership of J. K. L. MacDonald; J. J. Stoker led in the research on water waves and underwater jet propulsion.

Some of the acoustical work done at New York University is summarized in Part II, which also contains two chapters reporting on the work of Leon Brillouin in the field of wave theory and electronics. In general, Applied Mathematics Panel studies in wave propagation and electrodynamics were conducted by Brillouin under an AMP contract with Columbia University. His researches on the plane and cylindrical magnetron are not reported here, since it is planned to publish them in a scientific journal.

Problems in classical dynamics and in the mechanics of deformable media were customarily assigned by the Panel to the Applied Mathematics Group at Brown University, where scientific work was carried on under the scientific direction of W. Prager and G. E. Hay and the general administrative leadership of R. G. D. Richardson. A review of their activities forms Part III of this volume.

The fourth and final part of the volume differs from the others in being a survey of an entire field of research, namely, underwater ballistics. An analytical study of the behavior of projectiles entering water was started, without funds in 1942, at the request of the Bureau of Ordnance under the auspices of the National Academy of Sciences. The original committee consisted of George D. Birkhoff and Garrett Birkhoff. After a preliminary study indicated that the application of simple mathematical techniques gave results which agreed roughly with observed facts, it was decided to ask the National Defense Research Committee to support the study. The desired support was offered in 1943 through the Applied Mathematics Panel, and intensive work was carried on by the original committee and Turner L. Smith.

The study entered into a new and expanded phase in 1944, when a contract with Harvard University was set up to provide for a study of the principles which determine the dynamic behavior of a projectile entering water. In addition, the services of the Alden Hydraulic Laboratory (Worcester Polytechnic Institute) were contracted for, while close, cordial, and effective liaison was maintained with the other groups working on underwater ballistics in this country and in England.

The project suffered a tremendous loss when the death of George D. Birkhoff in November 1944 deprived the committee of its most distinguished and experienced member. His warm inspiration is cherished by all who had the privilege of being associated with him.

Acknowledgment has been made in the text of Part IV, where possible, to the achievements of other groups. Especial mention is due to the David Taylor Model Basin, the Naval Ordnance Laboratory, and the groups working at the California Institute of Technology. The investigation of the fundamental laws of underwater ballistics was carried out in close cooperation with these establishments, which also permitted the reproduction of some of their photographs.

It has been the aim of the authors of this volume to present the material in such a way that no prior knowledge of specific technical matters is presupposed on the part of the reader. The reader is expected to have a background in mathematics and physics ordinarily possessed by an individual with a bachelor's degree in engineering.

Considering the mass of material which the authors had to examine, assimilate, and abstract in the short

time available to them, and considering the intrinsic difficulty of their assignment, they have produced a remarkably coherent volume, for which they deserve great credit. In comparison with their work, the tasks performed by the editor are truly negligible.

I. S. SOKOLNIKOFF
Editor

CONTENTS

CHAPTER

PAGE

Summary by <i>Warren Weaver</i>	1
---	---

PART I

FLUID DYNAMICS AND RELATED PROBLEMS

By Stewart S. Cairns

1 Gas Dynamics — Shock Wave Theory	9
2 Underwater Explosions and Hydrodynamic Investigations	53

PART II

WAVE PROPAGATION AND ELECTRONICS

3 Wave Transmission Through Metal Shells by <i>Stewart S. Cairns</i>	71
4 The Scattering Cross Section of Spheres for Electromagnetic Waves by <i>Leon Brillouin</i>	80
5 Coils Yielding a Single Dipole Moment by <i>Leon Brillouin</i>	96

PART III

MECHANICS

By G. E. Hay

6 Mechanics of Particles and Rigid Bodies	109
7 Mechanics of a Continuum	128

PART IV

UNDERWATER BALLISTICS

By Garrett Birkhoff

(with Norman Levinson and Lynn Loomis)

8 Descriptive Summary	141
9 Impact Forces	159
10 The Cavity	168
11 Underwater Trajectories	184
12 Modeling and Scale Effects	195

CHAPTER	PAGE
APPENDIX	
I Antibroach Devices	203
II Impact Forces	208
III Theory of Entry Whip	211
IV Steady-State Cavity Theory	213
V Transient Cavity Theory	218
VI Mathematical Classification of Types of Motion	222
VII Differential Equation Theory of Virtual Mass	226
VIII Remarks on Modeling	229
Glossary	233
Bibliography	237
OSRD Appointees	246
Contract Numbers	247
Service Project Numbers	249
Index	251

SUMMARY ^a

IN THIS Summary Technical Report of the Applied Mathematics Panel, a résumé is given of the principal scientific accomplishments of the Panel from its beginning in 1943 until the conclusion of hostilities. The activities here reported cover a wide range, dealing as they do with studies undertaken at the request of each of the nineteen Divisions of NDRC and of many branches of the Army and Navy. For the purpose of this report, that portion of the Panel's work which deals with specific military problems has been divided into three parts: Volume 1, *Mathematical Studies Relating to Military Physical Research*; Volume 2, *Analytical Studies in Aerial Warfare*; and Volume 3, *Probability and Statistical Studies in Warfare Analysis*. In addition to reporting on specific military problems, Volume 1 also indicates directions in which certain of the theories of fluid dynamics have been extended under AMP auspices as an aid in the planning and interpretation of military experiments, and in understanding the operation of enemy weapons. These three volumes contain no account of the new developments in statistical methods which have already been partially reported in a published article ¹ and a published book ² on sequential analysis, nor of certain important new applications of statistical theory which grew out of the Panel's attempt to solve problems presented to it by the Services. These latter are reported in two published monographs, *Sampling Inspection* and *Techniques of Statistical Analysis* (published by McGraw-Hill), which have been prepared under Panel auspices and which form part of the Panel's report of its technical activities.

Most AMP studies were concerned with the improvement of the theoretical accuracy of equipment by suitable changes in design; or with the development of basic theory, particularly in the field of fluid dynamics; or with the best use of existing equipment, particularly in fields like bombing and the barrage use of rockets. Two studies carried out under AMP auspices come closer to having general tactical or strategic scope than do most of the other work. I have myself given an account of these two studies in Part IV of Volume 2, where I have also set forth some incomplete and preliminary ideas of what a general analytical theory of air warfare could and should comprise and some arguments for and against attempting to construct and use such a theory. I have there indicated how certain activities of the Applied Mathematics Panel and of other agencies relate to a

scheme for a broad approach to the problems of air warfare and of warfare in general, and I have pointed out some of the contributions which mathematics can make to the field of national defense.

That part of the Panel's work which may be roughly described as classical applied mathematics is presented in Volume 1. Certain phases of this subject were developed under Panel auspices and adapted to problems of military interest, the principal emphasis being on problems of primary concern to the Navy.

In the early stages of the war, certain acoustic equipment employed in submarine detection by echo ranging used a "dome" — a streamlined convex shell filled with water or other liquid, such as oil. The presence of these domes caused interference with the directional pattern sent out from the projector, and in some of the equipment the disturbance was extremely serious. The Panel was asked to study the situation and to suggest changes in the domes which would minimize the disturbances. Practical conclusions were reached regarding desirable materials and design. It was found desirable for practical reasons to use thin shells reinforced by stiffening elements such as ribs and rods rather than to achieve strength by general thickness. Difficulties arising in direction finding due to annoying reflections were also analyzed, and suggestions were made for improving conditions, for example, by corrugations on the inner surface of the side walls of the domes. This dome study was one aspect of the work in wave propagation with which the Panel was concerned. There were others. For example, an investigation was made of the scattering of electromagnetic waves by spherical objects to assist in the analysis of smokes and fogs. A study of somewhat similar mathematical character (but dealing with electromagnetic disturbances rather than actual mechanical waves in a liquid) was undertaken at the request of the Fire Control Division (Division 7, NDRC), which had under development a predictor, the T-28, intended for use with the 40-mm gun. The computing mechanism used by this predictor included a sphere on which were placed electrical windings in such a way that the resulting field was one which corresponded to one simple dipole at the center of the sphere. Although the theoretical way in which the winding should be distributed on the surface of this sphere was well known, it was necessary as a practical matter to

^a By Warren Weaver.

substitute a winding in which the turns were located in grooves on the sphere. The formulas resulting from the Panel's study of this problem form a basis for practical applications which include ammeters, galvanometers, and direction finders. This mathematical study was of critical importance for the fire control instrument in question, for without it, it was impossible to obtain useful accuracy in the spherical "electromagnetic resolver" which carried out the essential steps in the target predicting process.

The Panel's work in gas dynamics, mechanics, and underwater ballistics is also reported in this first volume. The Panel's work in *gas dynamics* was principally concerned with the theory of explosions in the air and under water, and with certain aspects of jet and rocket theory. New developments were made in the study of shock fronts, associated with violent disturbances of the sort which result from explosions. An interesting and significant aspect of the work was concerned with Mach phenomena which frequently play a practical role in determining the destructive effects of shocks. For example, the advantages of air-bursting large blast bombs were suggested by a consideration of Mach waves. A request from the Bureau of Aeronautics for assistance in the design of nozzles for jet motors to be used for assisted take-off gave rise to an extended study of gas flow in nozzles and supersonic gas jets. As a result, suggestions were made not only for the design of nozzles for jet-assisted take-off, but also for "perfect" exhaust nozzles and compressors (of use in supersonic wind tunnels) and for various instruments to aid in rocket development and experimentation. The jet propulsion studies were related to Army and Navy interest in intermittent jet motors of the V-1 type. Jet propulsion under water was also studied, with results which should prove useful as a guide to experiment in this field where experimentation has thus far not reached the stage where the theoretical results can be fully put to test.

The problems in *mechanics* fall under two general headings: (1) those involving the mechanics of particles and rigid bodies and (2) those involving the mechanics of a continuum. For example, a study in the second category sought possible explanations of the break-up in cylindrical powder grains in the 4½-in. rocket to explain difficulties which were being encountered at the Allegheny Ballistics Laboratory, and an experimental program was outlined for the testing of the most probable theories. One of the most interesting of the mechanical studies concerned the so-called spring hammer box used by the U. S. Navy

in acoustic mine warfare. The dependence of the operation of this device on various physical parameters (for example, the mass of the hammer) was analyzed with the aid of a simple mechanical model, and of an electrical analog. Another problem of this type studied the dynamics of the gun equilibrator, or balancing system, when an Army gun was mounted on board a ship. The pitching and rolling of the ship naturally introduced special difficulties.

In the section on underwater ballistics, the problems involved are classified according to the various phases in the motion of the projectile: the impact phase, the development of the cavity, and the underwater trajectory. During the impact phase, forces act which are important partly because of their possible effects on the nose structure and mechanism of the projectile, partly because of their influence in determining the projectile's subsequent motion. It is during the impact phase that the greatest deceleration occurs. The theoretical analysis involves, among many other considerations, the direction of entry (vertical or oblique), and the shape of the projectile. Save when the speed of a missile is slow, its entry is accompanied by the formation of a cavity which becomes sealed behind the projectile and accompanies it to a greater or less extent during its underwater motion, influencing that motion in an important way. The underwater trajectory itself presents problems of great complexity. Frequently, slight changes in values of the parameters which determine the motion will cause a complete change in the type of motion. A mathematical discrimination among the several types of motion is made, part of the distinction depending on such things as the position of the center of gravity of the missile, the ratio of its length to its diameter, its density, its radius of gyration, and the manner of its entry. Throughout this treatment, an attempt has been made to integrate into a single report the results which have been obtained by the many agencies concerned with the several phases of the problem and thus to assist the theoretical and experimental studies which must be carried forward in future attempts to understand this difficult array of problems.

Many of the studies reported in Volume 2, as well as those contained in Volume 3, involve probability considerations, a field which is notoriously tricky and within which "common sense" is often quite helpless. For example, what is the optimum mixture of armor-piercing and incendiary ammunition for the rear guns of a bomber? Specifications often designate such

mixtures as five AP to two incendiary (we are neglecting tracers here). Why? The somewhat striking, and by no means obvious, fact is that, given any fixed type of target, it is better to have either *all* AP or *all* incendiary, depending on the nature of the target. The justification for any other intermediate mixture should be based on knowledge of the relative probability of encountering different targets, certain of which would be more vulnerable to AP and others more vulnerable to incendiary. This conclusion was reached as an incidental result of a study which was concerned with alternative fighter-plane armament and which arose out of the enthusiasm of a few persons associated with the Panel for two papers attributable to L. B. C. Cunningham, Chief of the Air Warfare Analysis Section in England, and his associates. Another study concerned with the practical effectiveness of equipment grew out of a request to NDRC from Headquarters, AAF, asking for collaboration with the AAF "in determining the most effective tactical application of the B-29 airplane." The results of this study, obtained on the basis of large-scale experiments in New Mexico and small-scale optical experiments by the Mt. Wilson Observatory staff at Pasadena, were concerned principally with the defensive strength of single B-29's and of squadrons of B-29's against fighter attack, and the effectiveness of fighters against B-29's. One indirect result of the optical studies was a set of moving pictures showing the fire power variation of formations as a fighter circles about them. Concerning such pictures the President of the Army Air Forces Board remarked that he "believed these motion pictures gave the best idea to airmen as to the relative effect of fire power about a formation yet presented." Certain of these pictures were flown to the Marianas and viewed by General Le May and by many gunnery officers at the front.

These two studies are reported in the last part of Volume 2. The first three parts of this volume report on special and detailed problems which arise when shots are fired against targets moving in the air or on the ground. The problem of shooting from an aircraft in motion against an enemy aircraft or against a ground target in motion and the problem of shooting from the ground or from a naval craft against an enemy aircraft all involve a number of considerations.

1. Whenever the target is in motion, its position at the instant of firing is different from its position at impact, if impact occurs. For an effective shot, the motion of the target during the time of flight of the

bullet or rocket or shell must therefore be predicted, at least approximately. The special character of this problem for the special cases which have come under the Panel's study are discussed for air-to-air warfare in Part I, for rocket fire from the air in Part II, and for ground or ship based antiaircraft fire in Part III.

2. When one's own ship is in motion, the apparent motion of the target is affected.

3. There are oscillations in aim as the gunner attempts to point continuously at the target. These oscillations are greater in air-to-air and in ship-to-air than in ground-to-air gunnery because of the vibrations, rotations, and bumpy motions of one's own ship.

4. There is the effect of gravity on the bullet. In air-to-air gunnery, for the short ranges used in World War II, this was of minor importance, but for rocket fire it introduced very considerable complications.

5. The resistance of the air varies with the altitude. Thus, at 22,000 feet above sea level the air is half as dense as it is at sea level. This will affect the average speed of a bullet, hence its time of flight, and hence the prediction referred to above.

A large part of Volume 2 is devoted to problems connected with so-called flexible gunnery, i.e., with the aiming of those guns, carried on aircraft, which can be pointed in various directions with respect to the aircraft (as contrasted with fixed guns in the wings or nose, which are aimed only by movement of the aircraft). In January 1944, Brigadier General Robert W. Harper, AC/AS (Training), wrote in a letter to Dr. Vannevar Bush, Director of OSRD, that "the problems connected with flexible gunnery are probably the most critical being faced by the Air Forces to-day. It would be difficult to overstate the importance of this work or the urgency of the need; the defense of our bomber formations against fighter interception is a matter which demands increasing coordinated expert attention." This situation arose because of the inadequate training and inadequate deflection rules given to the gunners who had to handle ring sights in bombers. The "relative speed" and "apparent motion" rules currently taught were not thoroughly learned by the gunners and in many cases were by no means adequate when they were properly applied. There were well authenticated cases of gunners who "led" the attacking fighters in a direction exactly opposite to that of the true lead!

The immediate proposal contained in General Harper's letter was that the Applied Mathematics

Panel should recruit and train competent mathematicians who had the "versatility, practicality, and personal adaptability requisite for successful service in the field;" it was planned that these men, after two months' training in this country, would be assigned to the Operations Research Sections in the various theaters to devote their attention to aerial flexible gunnery problems. The Panel was in a position to carry out this program because it had already been drawn into studies of rules for flexible gunnery training and because it had access to many of the ablest young mathematicians in the country. The assignment was completed promptly, and, as a partial result of this undertaking, the Panel found itself even more closely in touch with the Operations Analysis Division of the AAF (with which it had already established cordial working relations) and with the AAF Central School for Flexible Gunnery. Around this interest and the interest of the Army, the Navy, Division 7, and Division 14 in the improvement in the effectiveness of guns as well as gunnery, grew up a very considerable body of knowledge and experience which is reported in Part I of Volume 2. Here an attempt is made to bring together into a single account the state of the art of air-to-air gunnery, not only as that has been affected by the work of the Applied Mathematics Panel, but as it has reflected the activities of agencies in this country and abroad. The topics discussed are:

1. The motion of a projectile from an airborne gun, constituting that branch of exterior ballistics which is called *aeroballistics*.

2. A mathematical *theory of deflection shooting* considered first for the case of a target moving at constant speed on a straight line which lies in a plane with the gun-mount velocity vector; second, for a target which moves in a curved path; and third, for the case where mount and target move in arbitrary space paths.

3. *Pursuit curve theory*. Pursuit curves were important in World War II, since the standard fighter employed a heavy battery of guns so fixed in the aircraft as to fire sensibly in the direction of flight. Thus it was necessary to fly on such a correctly banked turn that a correct and changing aiming allowance was continuously made. This pursuit curve theory is also of importance in the study of guided missiles which continuously change direction under radio, acoustic, or optical guidance unwillingly supplied by the target.

4. The design and characteristics of *own-speed sights* which were introduced as devices designed for use against the special case of pursuit curve attack on a defending bomber. Simple charts which might be used in the air are given, based on optimum rules for determining deflection against an aerodynamic pursuit curve.

5. *Lead computing sights* which do not assume that the fighter is coming in on a pursuit curve but which basically assume that the target's track relative to the gun mount is essentially straight over the time of flight of the bullet. The mechanical sights of the Sperry series are considered in some detail.

6. The basic theory of a *central station fire control system*.

7. The analytical aspects of experimental programs for *testing airborne fire control equipment*. It is recognized that field tests, laboratory tests, and theoretical analyses all have an important place in such a program. Instrumentation for tests, reduction of data, measures of effectiveness, and optimum dispersion are discussed.

8. *New developments*, such as stabilization and the use of radar.

The second part of Volume 2 is devoted largely to a presentation of the results obtained by the Panel in a study intended to determine what sighting methods are feasible for airborne rockets. The essential problems involved in this question have to do with ballistic formulas, attack angle and skid, the effect of wind and target motion, how these various factors affect each proposed sighting method, and how tracking affects and is affected by them.

In Part III of Volume 2 certain special studies of antiaircraft equipment which were made under AMP auspices are discussed, and a report is given of the *flak analysis* and other *fragmentation and damage studies* carried on by the Panel. This report is concerned with some mathematical problems which arise in attempts to estimate the probability of damage to an aircraft or group of aircraft from one or many shots from heavy antiaircraft guns. Related problems arise in air-to-air bombing and in air-to-air or ground-to-air rocket fire, but the major part of the mathematical analysis so far performed has been devoted to problems of flak risk. The emphasis in the discussion is on the description of a method for treating problems of risk, since specific numerical conclusions are likely to become obsolete before further need for them arises, while the techniques by which

the results were obtained will be useful as long as weapons which destroy by means of flying fragments are in use. The original experimental information on which the Panel computations were based came from a variety of sources, principally Army, Navy, OSRD, and British reports. The Panel's chief contribution was the development of computational techniques which could be carried through before the project became obsolete, the selection of pertinent examples, and the applications of the computational techniques to the selected examples. Certain applications of the underlying theory to time-fuzed and proximity-fuzed shells and to proximity-fuzed rockets are here reported.

Another major field of effort in the work of the Panel is that of *mathematical statistics*, reported in Volume 3. A remarkably wide variety of probability and statistical investigations was carried out by the Panel. These investigations ranged from the development of sampling inspection plans in connection with procurement of military matériel to extensive statistical analyses of combat data. Of the Panel's 194 studies, 53 related to problems in probability and statistical analysis.

The work of the Panel in mathematical statistics can be grouped into the following major categories:

1. *Bombing accuracy* research.
2. *Development of statistical methods* in inspection, research, and development work.
3. Development of new *fire effect tables* and diagrams for the Navy.
4. *Miscellaneous studies* relating to spread angles for torpedo salvos, lead angles for aerial torpedo attacks against maneuvering ships, land mine clearance, performance of heat-homing devices, search problems, verification of weather forecasting for military purposes, procedures for testing sensitivity of explosives, distribution of Japanese balloon landings, etc.

Of these four main categories of work, category 1 required by far the greatest amount of energy. This activity had its beginning in a fairly small study undertaken for the Armament Laboratory, Wright Field, on the design of a computer for determining the optimum spacing of bombs in a train of bombs dropped from a bomber in attacking a given target under specified conditions. The study was started in 1942 under Division 7, NDRC, and was transferred to the Panel when the Panel was organized. In pursuing this study the group working on it came in contact with individuals in more than a dozen Army,

Navy, and NDRC groups interested in bombing accuracy problems. As the war progressed, an increasing number of requests came from these groups for studies of all kinds of accuracy and coverage problems arising in train bombing, area bombing, pattern bombing, guided-missile bombing, incendiary bombing, and so on. By the end of the war the work in this field had grown to the point where the major effort of three Panel research groups was being spent on nineteen studies dealing with probability and statistical aspects of bombing problems.

The methods and results developed in category 2 are of much broader interest than that associated with their wartime applications. During the war, it was recognized by the Services that the statistical techniques which were developed by the Panel for Army and Navy use, on the basis of the new theory of sequential analysis, if made generally available to industry, would improve the quality of products produced for the Services. In March 1945, the Quartermaster General wrote to the War Department liaison officer for NDRC a letter containing the following statement:

"By making this information available to Quartermaster contractors on an unclassified basis, the material can be widely used by these contractors in their own process control and the more process quality control contractors use, the higher quality the Quartermaster Corps can be assured of obtaining from its contractors. For, by and large, the basic cause of poor quality is the inability of the manufacturer to realize when his process is falling down until he has made a considerable quantity of defective items. . . . With thousands of contractors producing approximately billions of dollars worth of equipment each year, even a 1% reduction in defective merchandise would result in a great saving to the Government. Based on our experience with sequential sampling in the past year, it is the considered opinion of this office that savings of this magnitude can be made through wide dissemination of sequential sampling procedures."

On the basis of this and similar requests, the Panel's work on sequential analysis was declassified, and the reports mentioned above were published. The Quartermaster Corps reported in October 1945 that at least 6,000 separate installations of sequential sampling plans had been made and that in the few months prior to the end of the war new installations were being made at the rate of 500 per month. The maximum number of plans in operation simultaneously was nearly 4,000.

Thus extensive use was made by the Army of sequential analysis as a basis for sampling inspection. It was at the request of several Navy bureaus that

the Panel undertook to assemble a manual setting forth procedures to be used not only with sequential sampling but also with single and double sampling plans. As an extension and expansion of this manual, the Panel undertook the preparation of its monograph, *Sampling Inspection*. The monograph, *Techniques of Statistical Analysis*, presents a variety of statistical methods which have been developed, or adapted from more general methods, for dealing with various statistical problems which have arisen in connection with research and development work.

The work done in category 3 was of highly specialized long-range interest to the Office of the Commander in Chief of the U. S. Fleet. After the work had been carried forward under the direction of the Panel for nearly two years, arrangements were made to transfer and continue the work under a contract, effective June 1, 1945, between the Navy and Princeton University. During the time this work was under the Panel's direction, a series of nine basic reports was submitted to the Navy. None of this work, which was only partially completed under the direction of the Panel, is reported upon in the Panel's Summary Technical Report.

Certain of the studies in category 4 are of such limited interest that it has been considered neither appropriate nor worth while to report upon them here. Accounts are given of the work which relates to torpedoes, land mine clearance, and the performance of heat-homing devices.

An important adjunct of the probability and statistical work of the Panel was a statistical consulting service for various Army, Navy, and NDRC agencies. Although some of this consulting was done in connection with formal AMP studies and projects in such a way that the results are adequately reported in original Panel reports or the Panel's Summary Technical Report, a large fraction of it was informal and the results of it are to be found in reports and memoranda of many agencies, particularly Divisions

2, 5, 8, and 11 of NDRC; Joint Army-Navy Target Group, Army Air Forces Board; Proving Ground Command, Eglin Field, AAF; Operational Analysis Division, Twentieth Air Force, AAF; Combat Analysis Unit, Statistical Control, AAF; Office of the Quartermaster General; Navy Air Intelligence Group; Navy Operational Research Group; and the Guided Missile Committee of the Joint Chiefs of Staff.

Men from several of the Panel's research groups acted as consultants to these various agencies for periods ranging from two months to two years. In my opinion some of the most useful service which the Panel was able to render came about through the work of these men in their capacities as consultants; the effectiveness of this work increased constantly until the end of the war. The work of these men varied widely: assistance in setting up sampling inspection plans for procurement of matériel, helping in the introduction of a quality control system in rocket production, working on designs of experiments for toxic gas bombing, testing controlled missiles, cooperation in the preparation of an incendiary manual, and dozens of other projects.

I cannot leave the topic of mathematical statistics without emphasizing the powerful yet severely practical role which this relatively young branch of applied mathematics has played in the work of the Panel. The tools of the probabilist and statistician have been applied to an almost unbelievably wide array of problems. Probability analysis played a fundamental part in a priori investigation of various kinds of weapons and tactics studied by the Panel. As the war progressed and these weapons and tactics were tested at the proving ground and tried out in combat, the analysis of the observational data became primarily statistical. The work of the Panel surely indicates that the Army and Navy will do well in their research, development, and testing of weapons and tactics to see to it that the tools of the mathematical statistician are not overlooked.

PART I

FLUID DYNAMICS AND RELATED PROBLEMS

CONFIDENTIAL

Chapter 1

GAS DYNAMICS — SHOCK WAVE THEORY

1.1 INTRODUCTION

THE TERM *fluid dynamics* is here used to include problems of both hydrodynamics and gas dynamics. A large part of the work is concerned with the theory of explosions, both in air and under water. In the gas-dynamical portion of the research, a basic role is played by the properties of shock waves, rarefaction waves, and so-called contact discontinuities. These phenomena and the events arising from their interactions and reflection are fundamental, not only in the study of explosions but also in the closely related theories of detonation and deflagration, which are required in rocket and jet propulsion investigations. In the study of underwater explosions an important theory of a pulsating migrating bubble was developed. The problem of the entry of a solid from air into water led to a new application of Sommerfeld's method for boundary-value problems. Studies of jet propulsion in air, together with certain hydrodynamical investigations, contributed to researches in underwater jet propulsion. In the practical engineering aspects of rocket development, questions of heat flow are intimately bound up with gas-dynamical considerations, and it was therefore natural for the same personnel to treat both topics.

1.2 MATHEMATICAL THEORY OF NONLINEAR WAVE MOTION

1.2.1 Introduction

A unified, general theory (necessarily incomplete in the present-day stage of the subject) of nonlinear wave motion was found to be an essential prerequisite to any important practical contributions to gas flow problems. A conspicuous aspect of the incompleteness of this theory is to be observed in three-dimensional applications, where only special cases have yielded to analysis. Another fundamental lack is the

absence of a uniqueness theorem for the differential systems which formulate the problems. The existence of alternative mathematical solutions in certain problems is clearly a source of possible discrepancies between theoretical and experimental results.

Fundamental classical knowledge, supplemented by new developments made under direction of the Applied Mathematics Panel, was organized into a report ¹ to be used as a source of basic information by research workers on problems involving nonlinear differential equations. The parts of the report needed in this review are summarized in this section. In general, analytic details are omitted. For such details, and for references to more elementary sources of general information, see the complete report.

The mathematical analysis of acoustic, optical, and electromagnetic phenomena is governed by systems of linear differential equations. Such systems imply the validity of the familiar laws of superposition, reflection, and refraction. On the other hand, violent disturbances of the sort which result from explosions, jet flow from rockets, and supersonic flight of projectiles lead to certain types of nonlinear differential systems. The acoustic principles of superposition, reflection, and refraction became invalid, and a number of striking features appear. Among the most conspicuous of these are the so-called *shock fronts*, discontinuities across which sudden and significant increases in pressure and temperature frequently occur. Shock discontinuities can arise from initially continuous motions and, conversely, can be smoothed out into continuous phenomena.

In linear wave motion, local disturbances are transmitted with a definite speed (that of light or sound). In nonlinear motion, certain small disturbances (wavelets) are similarly propagated with *sonic speed*, but shock fronts, or shock waves advance at supersonic speeds. These discontinuities are represented by singularities of the solutions of the corresponding nonlinear mathematical problem. Solutions of nonlinear problems, unlike those of linear systems, fre-

quently cannot be extended continuously throughout domains where the original equations are regular. The interaction and reflection of nonlinear waves can lead to enormous increases in pressure, by contrast with the, at most, additive properties of pressures in interfering sound waves.

For the most part, in investigations of the motion of compressible fluids or gases, heat conduction and viscosity are neglected. In continuous motions, the particles of the medium are assumed to undergo only adiabatic changes of state (constant entropy along the path of any particle). The state of any medium in which wave propagation or particle motion is investigated is taken to be characterized by such quantities as the density ρ (or specific volume $\tau = 1/\rho$), the pressure p , the entropy η per unit mass, internal energy e per unit mass, and the temperature T . All these quantities may vary in space and time; in other words, they may depend on rectangular space coordinates (x, y, z) and on the time t .

Of the parameters (ρ, p, T, η) , only two are independent, and the specific thermodynamical nature of the medium is characterized by (1) a function defining T in terms of ρ and η , and (2) the so-called *equation of state*:

$$p = f(\rho, \eta) \quad \text{or} \quad p = g(\tau, \eta). \quad (1)$$

For most gases, including the polytropic gases, this equation has the form

$$p = A\rho^\gamma \quad \text{or} \quad \frac{p}{p_0} = \left(\frac{\rho}{\rho_0}\right)^\gamma \quad (2)$$

in which case γ is called the *adiabatic exponent* ($\gamma = 1.4$ for air, and $\gamma > 1$ for all polytropic gases).

A mathematical system governing a specific gas-dynamical phenomenon is afforded by (1) differential equations expressing Newton's law of motion and the principle of conservation of mass, (2) the equation of state of the medium, and (3) appropriate initial and boundary conditions.

In the important case of *steady motion*, the flow velocity, pressure, and density vary with position but not with time at any fixed point P . Hence all particles passing through P follow the same path, called the *streamline through P* .

The flow in a medium usually is assumed to be *isentropic*. In other words, the entropy is assumed to have, initially, the same value throughout the medium. Hence, in view of the adiabatic assumptions, it retains this constant value. Then η can be sup-

pressed as a variable in equation (1), giving the simpler equation of state

$$p = f(\rho) \quad \text{or} \quad p = g(\tau). \quad (3)$$

In place of the energy, the *enthalpy* or *heat content*, i , given by

$$i = e + \tau p \quad (4)$$

is frequently useful. Let \mathbf{q} (boldface type indicates vectors), with components (u, v, w) , be the particle velocity in a medium. The differential equations for steady isentropic flow then imply that, on each streamline,

$$\frac{1}{2}q^2 + i = \frac{1}{2}(u^2 + v^2 + w^2) + i = \frac{1}{2}\hat{q}^2 \quad (5)$$

where \hat{q} , constant on any particular streamline, is referred to as the ultimate or limit speed for the streamline in question. Equation (5) expresses *Bernoulli's law* in the *weak form*, by contrast with the same law in the *strong form*. The latter is said to hold in case \hat{q} is the same for all streamlines; and it is also said to hold for flows, not necessarily steady, which are both irrotational and isentropic. For an irrotational flow, there exists a *velocity potential*, that is, a function $\phi(x, y, z, t)$ such that

$$\mathbf{q} = \text{grad } \phi \quad \text{or} \quad u = \phi_x, v = \phi_y, w = \phi_z \quad (6)$$

where subscripts indicate differentiation. Bernoulli's law in the *strong form*, expressed in terms of ϕ , is

$$\begin{aligned} \frac{1}{2}(\phi_x^2 + \phi_y^2 + \phi_z^2) + \phi_t + i \\ = \frac{1}{2}q^2 + \phi_t + i = \frac{1}{2}\hat{q}^2. \end{aligned} \quad (7)$$

The limit speed \hat{q} , possibly dependent on the time, is the same throughout the fluid, whether or not the flow is steady.

In the case of an isentropic flow, the *sound speed* c is defined as

$$c = \sqrt{f'(\rho)} \quad (8)$$

where (3) is the equation of state. Somewhere between 0 and \hat{q} there exists the so-called *critical speed* c_* (sometimes denoted by q_*). It has the property that (1) for $q = c_*$, flow speed agrees with sound speed, that is, $q = c = c_*$; (2) for $q > c_*$, the flow is *supersonic* ($q > c$); and (3) for $q < c_*$, the flow is *subsonic* ($q < c$). For a polytropic gas with equation of state (2) the critical speed for any streamline is given in terms of the q for that streamline by

$$c_* = \mu \hat{q} \quad (9)$$

where

$$\mu = \sqrt{\frac{\gamma - 1}{\gamma + 1}}. \quad (10)$$

1.2.2 Isentropic Flows Depending on Two Independent Variables

Three-dimensional non-steady flow has thus far proved to be much too involved for analytic treatment. Practically all the cases which can be treated are those in which only *two* independent variables occur and in which the flow is isentropic. For these, a theory of the corresponding types of partial differential equations has been developed. Practical situations covered by this theory include the following:

(a) One-dimensional fluid motion, that is, motion in which the state depends only on the time t and on one space coordinate x ; for example, gas in a cylindrical tube along the x axis, the independent variables being the distance x and the time t .

(b₁) Axially symmetric two-dimensional motion, where the state depends only on the time t and on the distance x from a fixed axis normal to the plane of motion.

(b₂) Three-dimensional flow with spherical symmetry about the origin, the independent variables being x and t , where x is now the radial distance from the origin.

(c) Steady flow in the x, y plane.

(d) Steady flow in space with symmetry about the x axis, the independent variables being x and the distance y from the x axis.

All these cases lead to systems of differential equations of similar mathematical structure. The independent and dependent variables in the problems just classified have different physical interpretations. For the present, they will, however, be denoted by (x, y) and (u, v) respectively. The equations of motion are then, in each case, of the following form

$$\begin{aligned} A_1 u_x + B_1 u_y + C_1 v_x + D_1 v_y + E_1 &= 0 \\ A_2 u_x + B_2 u_y + C_2 v_x + D_2 v_y + E_2 &= 0 \end{aligned} \quad (11)$$

where the A, B, C, D, E are known functions of (x, y, u, v) .

The theory depends on transforming the system (11) to a *normal* form or *characteristic* form by the introduction of two suitable new independent variables α, β (so-called *characteristic parameters*) in place of x and y . This results in replacing the two equations (11) by four equations for the four quantities (u, v, x, y) as dependent variables and the two parameters α, β as independent variables. It is convenient to express the resulting equations in terms of the following new notation. Brackets $[]$ will be used for a determinant, as follows:

$$[XY] = \begin{vmatrix} X_1 Y_1 \\ X_2 Y_2 \end{vmatrix}. \quad (12)$$

The following functions are introduced:

$$R = \frac{[AC]}{[AB]}, S = \frac{[BC]}{[AB]}, K = \frac{[AE]}{[AB]}, H = \frac{[BE]}{[AB]} \quad (13)$$

and also the quadratic equation

$$[AC] \epsilon^2 - ([AD] + [BC]) \epsilon + [BD] = 0. \quad (14)$$

The roots of this quadratic are denoted by ϵ_+ and ϵ_- . It is supposed that the system (11) is hyperbolic, that is, that

$$([AD] + [BC])^2 - 4[AC][BD] > 0 \quad (15)$$

and that $[AB], [CD], [AC]$, and $[BD]$ are different from zero. Condition (15) is satisfied for all the problems in question with the qualification that for steady flow, the velocity is supersonic. Under the hypotheses just stated, the characteristic differential equations equivalent to (11) are as follows:

$$\begin{aligned} \text{(I+)} \quad y_\alpha - \epsilon_+ x_\alpha &= 0 \\ \text{(I-)} \quad y_\beta - \epsilon_- x_\beta &= 0 \\ \text{(II+)} \quad u_\alpha + (R\epsilon_+ - S)v_\alpha + (K\epsilon_+ - H)x_\alpha &= 0 \\ \text{(II-)} \quad u_\beta + (R\epsilon_- - S)v_\beta + (K\epsilon_- - H)x_\beta &= 0. \end{aligned} \quad (16)$$

It is noteworthy that in two of these equations only differentiations with respect to α , and in the other two only differentiations with respect to β , occur; also that the independent variables α, β do not occur explicitly. The systems (11) and (16) are equivalent in the sense that any solution of either yields a solution of the other.

Given a specific solution of the system, the equations $\alpha = \text{constant}$ and $\beta = \text{constant}$ determine two families of lines in the x, y plane and their images in the u, v plane. The lines in the x, y plane are called the *characteristics* C and their images in the u, v plane are called the characteristics Γ , with the following further modification:

$$\begin{aligned} C_+, \Gamma_+ : \quad \beta &= \text{constant} \\ C_-, \Gamma_- : \quad \alpha &= \text{constant}. \end{aligned} \quad (17)$$

The characteristics, aside from constituting a mathematical tool for simplifying the form of the differential equations, play an important physical role as lines of propagation of disturbances, or *Mach lines*. This role can best be indicated with the aid of the basic problem of hyperbolic differential equations, namely, the *initial value problem*. In terms of the system (11), this problem involves a given curve L in the x, y plane which is nowhere characteristic or

tangent to a characteristic, and certain initial values u, v defined as functions of position on L . The problem then is to find a solution (u, v) of (11) which assumes these given initial values on L . It turns out that the values of u and v at a point P in the x, y plane do not depend on the totality of initial values on L but only on the initial values on the section of L intercepted by the two characteristics through P . This intercepted section is called the *domain of dependence* of the point P (see Figure 1). Correspondingly, the

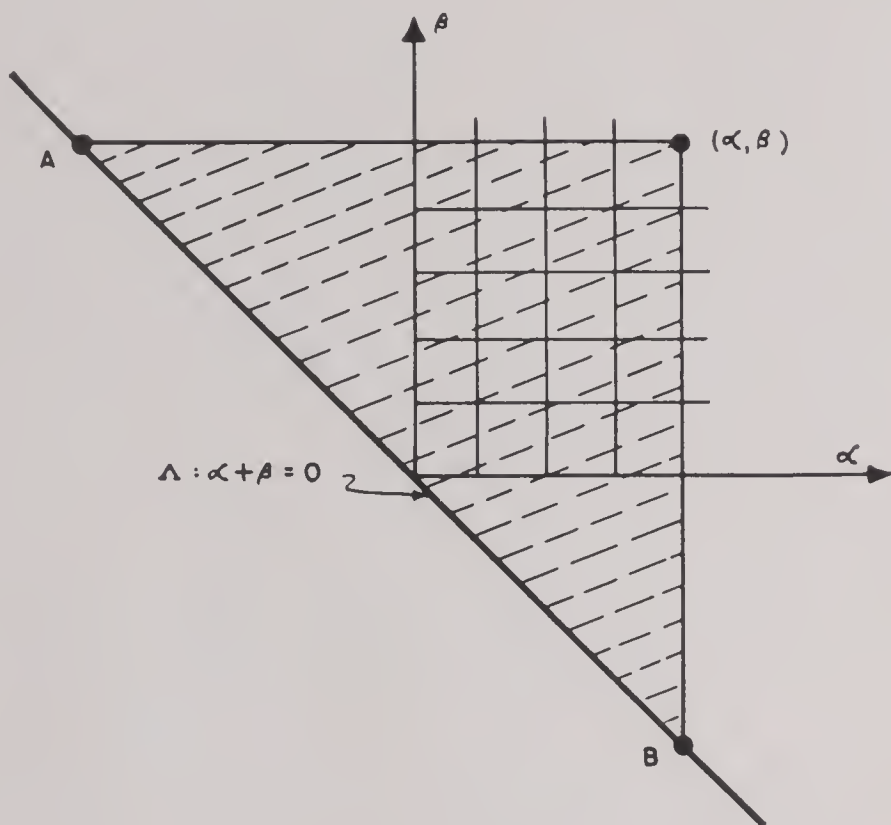


FIGURE 1. Domain of dependence of a point.

range of influence of a point Q on L ; in other words, the totality of points influenced by the initial data at Q is the angular region between the two characteristics drawn through Q . The existence of such domains of dependence and ranges of influence characterizes phenomena of *wave propagation* in contrast to states of equilibrium. In the latter, the differential equations are elliptic. Their solutions are then analytic functions, entirely determined by their values in any domain, however small. But the solutions of wave propagation problems are not necessarily analytic. Such expressions as “the medium at a point P does not know of the state at a point Q ” are used to mean that P does not belong to the range of influence of Q .

Initial values of u and v along L are assumed to be continuous. However, these initial values may have discontinuities in their first or higher derivatives along L . The solutions u, v of the problem will have continuous first and higher derivatives at points P whose domains of dependence do not contain the

discontinuity points of the derivatives of the initial data. Discontinuities of derivatives of u and v occur only along characteristics through the discontinuity points on the initial curve L , unless new ones appear because of the vanishing of the Jacobian $x_\alpha y_\beta - x_\beta y_\alpha$.

Furthermore, if there is a discontinuity at a point A in some derivatives of the initial data on L , then this discontinuity will be propagated along the two characteristics through A . It can never disappear. If the variable y is identified with the time t , then any discontinuity will spread through the one-dimensional x region with the velocities dx/dt given by the slopes of the two characteristics through the corresponding point of discontinuity in the x, t plane. In two-dimensional steady flow, characteristics issuing from the boundary of the flow will indicate small disturbances caused by slight roughness of the boundary which reach out into the medium. Such characteristics, or Mach lines, are often actually visible in flows between slightly roughened walls.

The following remark is of basic importance. *Whenever the flow in two adjacent regions is described by analytically different expressions, for example, when one is a region of rest or constant state and the other is not of constant state, then the two regions are separated by a characteristic.*

For an important class of flows, a flow pattern (II) adjacent to a zone of constant state (I) has a simple description. These cases are characterized by homogeneous equations (11) with coefficients which do not contain x and y explicitly. They arise in cases (a) and (c) above, for one-dimensional flow and steady isentropic irrotational two-dimensional flow, respectively. The conditions imply that the characteristics Γ are fixed families of curves which can be represented in the form $\beta(u, v) = \text{constant}$ and $\alpha(u, v) = \text{constant}$. In this sense, *fixed characteristics* will be assumed for the present. The flow (II) is then of a peculiar pattern, called a *simple wave*. Before defining it further, note that in a zone of constant state, the characteristics C_+ and C_- are straight lines, since constant values of u and v imply constant values of β and α . For flows with fixed characteristics, a simple wave is a zone with the following property: *One of the two sets of characteristics C , say the family of curves C_+ , consists of straight lines along each of which the values of u, v, p, ρ remain constant, although they vary from one characteristic C_+ to another.* Simple waves play an important role as zones which necessarily neighbor zones of constant state in a flow with fixed characteristics Γ .

1.2.3 Motion in One Dimension

INTRODUCTION

One-dimensional motion occurs when the state of the medium depends only on the time t and a single space coordinate x . As a model, consider the flow of a gas in a long tube extending along the x axis, where the tube may be open at both ends or closed at one or both ends by either pistons or walls. Assume an initial state of uniform velocity, pressure, and density, (u_0, p_0, ρ_0) , and let any motion be caused by action of pistons. The resulting phenomena can be represented in an x, t plane.

The simplest type of continuous motion is a *rarefaction* or *expansion wave*, caused by a receding piston. Suppose the piston recedes with a never-decreasing speed from a gas at rest. The result is an expansion wave of particles moving toward the piston. At the head, or front, of the wave, which moves into the gas at sound speed, the velocity of the gas is zero. Throughout the wave, the gas is accelerated. If the piston speed w is a constant less than a certain speed q_e , known as the escape speed for the gas, then the gas expands until it reaches the speed w of the piston, after which it continues with constant velocity, density, and pressure. If w exceeds q_e , expansion becomes complete, and the wave ends in a zone of cavitation between the tail and the piston. In any case, the wave moves into the quiet gas, while the gas particles move at increasing speed from the wave front to the tail, that is, from zones of higher pressure and density to zones of lower pressure and density.

This qualitative summary outlines the fairly exhaustive mathematical treatment which is feasible in the one-dimensional case. The differential equations reduce to relatively simple systems for which a complete integration in terms of arbitrary functions is possible. To obtain the reduction, replace y and v by t and ρ (standing for time and density, respectively) in the differential equations of the form (11). A straightforward application of the procedure described in Section 1.2.2, with $c^2 = p'(\rho)$ leads to $\epsilon_+ = 1/(u + c)$ and $\epsilon_- = 1/(u - c)$. Accordingly, the characteristic form of the differential equations (with the characteristic parameters α, β as independent variables) is

$$\begin{aligned} \text{(I+)} \quad x_\alpha &= (u + c)t_\alpha & \text{(II+)} \quad u_\alpha &= -\frac{c}{\rho} \rho_\alpha \\ \text{(I-)} \quad x_\beta &= (u - c)t_\beta & \text{(II-)} \quad u_\beta &= \frac{c}{\rho} \rho_\beta \end{aligned} \quad (18)$$

CONTINUOUS MOTION — SIMPLE WAVES

In the x, t plane, the motion of the piston is represented by a so-called piston curve L , which can be taken as starting at the origin, for a suitable choice of axes.

The wave caused by the motion of a receding piston always is continuous, though this is not true for a piston moving into a gas. As long as one deals with continuous motions satisfying the differential equations, a complete determination is always possible with the aid of the simple wave theory defined at the end of Section 1.2.2. In the x, t representation, the undisturbed gas corresponds to a zone of rest I adjacent to the x axis and, as long as the disturbance proceeds at sound speed, bounded by a characteristic C_+ : $x = c_0 t$, terminating the range of influence of the piston curve L . The general theory of Section 1.2.2

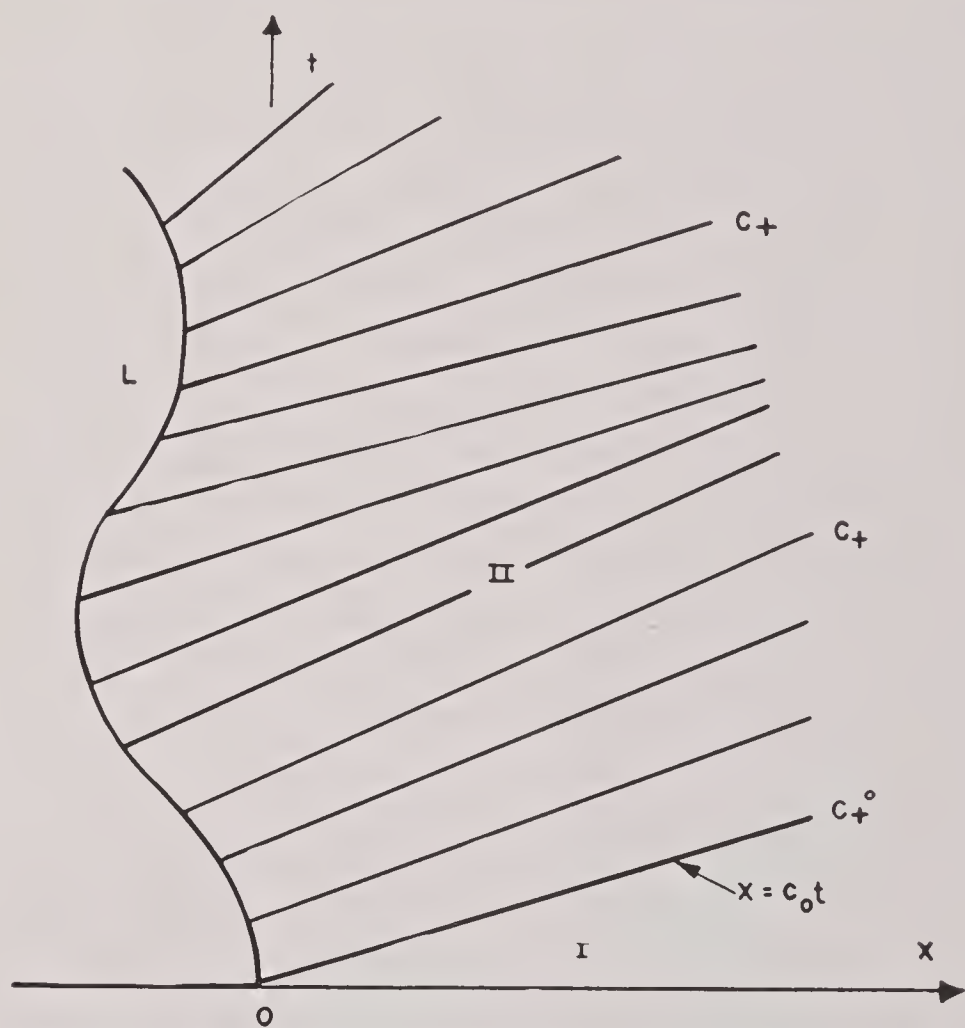


FIGURE 2. Simple wave (II) adjacent to zone of constant state (I).

implies that the zone I of rest is followed beyond the line $x = c_0 t$ by a simple wave II generated by a family of straight characteristics C_+ (see Figure 2).

Of particular interest is a *centered rarefaction wave*, corresponding to an idealized piston motion where the piston is thought of as starting suddenly from rest with its constant terminal velocity. The family of characteristics C_+ forming the simple wave then degenerates into a pencil of lines through the origin (see Figure 3). At the origin, the quantities u, ρ, p (velocity, density, pressure) are discontinuous func-

tions of x and t , but the discontinuity is immediately smoothed out in the subsequent motion. This is typical of an initial discontinuity immediately resolved into continuous motion.

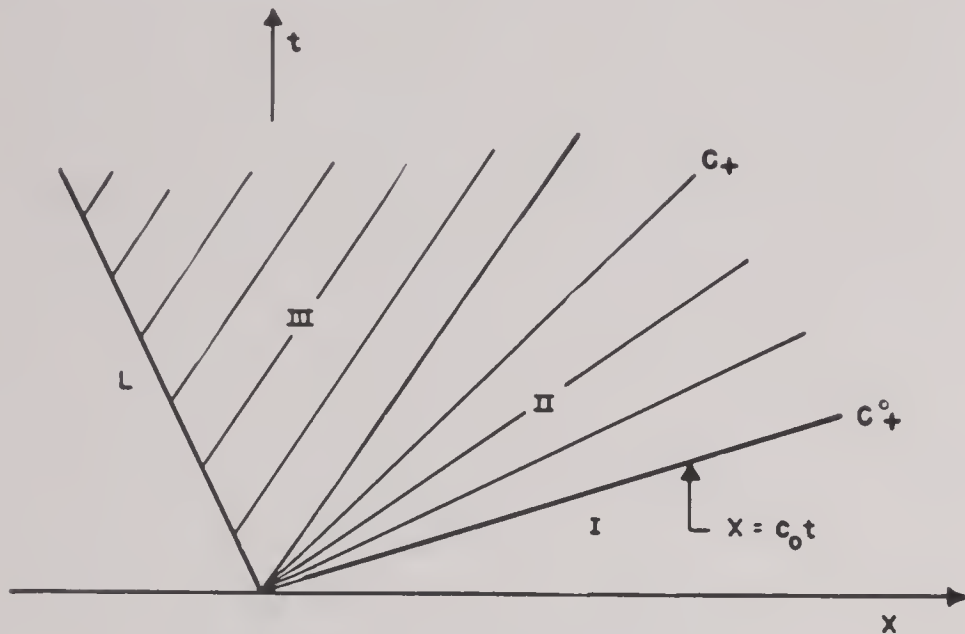


FIGURE 3. Centered rarefaction wave.

Suppose now that a piston is moved *into* a gas-filled tube with a speed which never decreases, or that a receding piston is slowed down or stopped; then a *contraction wave* originates at the piston. The forward characteristics C_+ converge and have an envelope if extended sufficiently. The simple contraction wave cannot extend beyond this envelope. Various inconsistencies readily follow from the assumption that the motion remains continuous. Hence all compressive motion is seen to lead to discontinuities, which must occur before or on the envelope. This fact was apparently first noticed by Stokes in 1848.

SHOCK FRONTS

For a mathematical description of motions caused by impinging pistons and of many other motions as well, the mathematical framework thus far employed must be supplemented. In connection with the present phenomena, the original description is oversimplified, and a closer approximation to reality must be sought by taking into account physical facts neglected in the original differential equations. Accordingly, viscosity and heat conduction are introduced, represented by additional (linear) terms of the second order in the differential equations. When such terms are included, the differential equations have continuous solutions, no matter how small the coefficients of heat conduction and viscosity may be. If, however, in the completed differential equations, these coefficients tend to zero, the continuous solutions converge to solutions of the original first-order differential equations, save that certain surfaces

emerge across which these solutions have discontinuities in the velocity u , density ρ , pressure p , sound speed c , and temperature T . The values of these quantities at both sides of such discontinuity surfaces are restricted by certain *jump conditions*. The effect of viscosity and heat conduction is mathematically represented by these jump conditions, the original differential equations being otherwise retained.

Two types of discontinuity surfaces are distinguished: contact surfaces and shock fronts. The former separate two parts of the medium without flow of substance through the surface, the latter are *crossed by the flow of gas*. If the shock front moves in time it is called a shock wave. The side of the shock front against which the flow is directed is called the *front*, the other the *back*. Observed from the front, the shock front always moves with supersonic speed. In the present section, concerned with one-dimensional motion, the discontinuity surfaces are assumed to be planes perpendicular to the x axis and are represented on the x axis by points or in the x, t plane by lines S known as shock lines or contact lines whichever they may be.

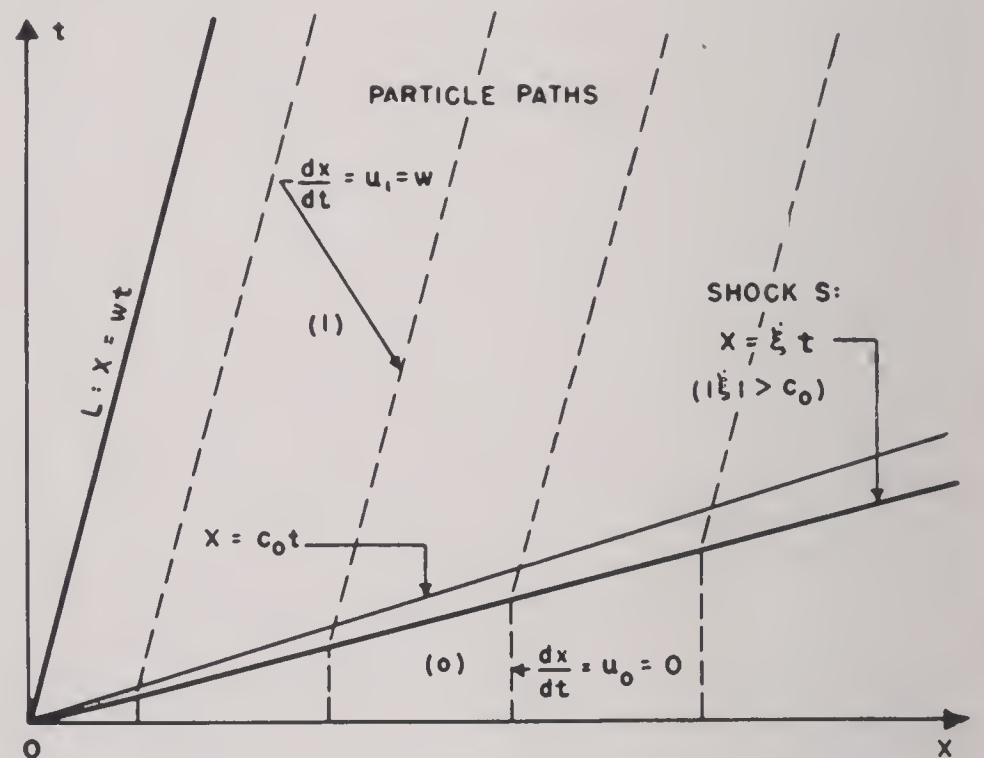


FIGURE 4. Shock resulting from piston moving into gas with constant velocity.

The simplest case of a motion involving a shock wave is that caused by a piston starting from rest and suddenly moving with constant speed w into a quiet gas. However small w may be, there will immediately appear a shock front moving away from the piston with a constant supersonic speed ξ , uniquely determined by the density and sound speed in the quiet gas and by the piston speed w . The gas is at rest in front of the shock, while behind the shock it moves with constant velocity w . This very simple motion is

represented in Figure 4. If decreasing values of w are considered, the shock line S approaches the characteristic $x = c_0 t$ and the jump of velocity, pressure, and density across the shock approaches zero. The shock becomes *weak* and approaches a sonic disturbance.

Application of the laws of conservation of mass and momentum lead to the first two jump conditions for shock. A third shock condition, expressing the principle of conservation of energy, takes account of discontinuous changes of entropy across a shock. It is known as the Rankine-Hugoniot discontinuity condition and replaces the assumption of adiabatic changes made for continuous motion. If $v_j = u_j - \dot{\xi}$ ($j = 0, 1$) is the flow velocity of the gas relative to the discontinuity surface ($j = 0$ referring to the front of the shock front and $j = 1$ to the back), then the three conditions can be expressed in the forms

$$(i) \quad \rho_1 v_1 - \rho_0 v_0 = 0 \quad \text{or} \quad \rho_0 v_0 = \rho_1 v_1 = m,$$

where m is the mass flux through the surface,

$$(ii) \quad \rho_0 v_0^2 + p_0 = \rho_1 v_1^2 + p_1 = p$$

$$(iii) \quad \frac{1}{2} v_0^2 + i_0 = \frac{1}{2} v_1^2 + i_1 = \frac{1}{2} \hat{q}^2$$

where \hat{q} is the ultimate or limit speed for the flow of the fluid in question (see Section 1.2.1). From various forms of the above conditions, the shock relations

$$(iii_*) \quad \frac{1}{2} v_0^2 + e_0 + \frac{p_0}{\rho_0} = \frac{1}{2} v_1^2 + e_1 + \frac{p_1}{\rho_1}$$

and

$$(iii_{**}) \quad (\tau_0 - \tau_1) \frac{p_1 + p_0}{2} = e_1 - e_0 \quad \left(\tau = \frac{1}{\rho} \right)$$

can be deduced. This latter equation can be interpreted to mean that the increase in internal energy across the shock front is due to the work done by the mean pressure in performing the compression. It is equivalent to

$$(iii_{***}) \quad (\tau_0 + \tau_1) \frac{p_1 - p_0}{2} = i_1 - i_0.$$

Since e or i is a known function of ρ and p depending on physical properties of the gas, we have three relations among seven quantities: p_j , ρ_j , u_j , $\dot{\xi}$. Hence, if three of the quantities are fixed, there is still possible a one-parameter family of shocks.

Under wide conditions, including the case of polytropic gases, the following theorems hold.

1. *The state (0) on the front of the shock front and the shock velocity $\dot{\xi}$ determine the state (1) on the back of the shock front.*

2. *The state (0) and the pressure p_1 (or density ρ_1 or velocity u_1) determine the complete state (1).*

Although extremely difficult boundary value problems for the differential equations are encountered, many important cases can be analytically treated, for example, ones in which simple piecewise solutions can be fitted together across straight shock lines.

Since mathematical uniqueness proofs have not been given for any solutions involving shock fronts, it is most important that the physical significance of the mathematical solutions be experimentally verified. Mathematical theory in gas dynamics is largely a means of finding qualitative and quantitative patterns which can serve to interpret experimental data.

If, in (i), we have $m = 0$, so that no substance crosses the surface of discontinuity, then $v_0 = v_1 = 0$, $u_0 = u_1 = \dot{\xi}$, and $p_0 = p_1$ and the form

$$(iii') \quad \rho_1 \left(\frac{1}{2} u_1^2 + e_1 \right) v_1 - \rho_0 \left(\frac{1}{2} u_0^2 + e_0 \right) v_0 = p_0 u_0 - p_1 u_1$$

of the conservation of energy principle is automatically satisfied. This discontinuity surface is then a contact surface. It moves with the gas and separates two zones of different densities and temperatures. The pressures and flow velocities on both sides are equal. In flows in more than one dimension, the tangential component of flow velocity can have a discontinuity while the normal component relative to the surface is zero.

Pressure and density are always greater behind a shock than in front of it. The degree of the increase can be used in various ways to measure the intensity of a shock. The direction in which a shock wave moves, given by the sign of $\dot{\xi}$, is independent of the direction toward which it *faces*, that is, the distinction between the front and back of the shock, which depends only on the relative velocity v .

If a shock is stationary ($\dot{\xi} = 0$), then the corresponding discontinuity conditions can be found, in the following form, by putting $v_j = u_j$ in (i), (ii) and (iii):

$$(i'') \quad \rho_0 u_0 = \rho_1 u_1 = m$$

$$(ii'') \quad \rho_0 u_0^2 + p_0 = \rho_1 u_1^2 + p_1 = P$$

$$(iii'') \quad \frac{1}{2} u_0^2 + i_0 = \frac{1}{2} u_1^2 + i_1 = \frac{1}{2} \hat{q}^2.$$

The first two shock conditions are called the mechanical conditions, since they do not explicitly involve the thermodynamical nature of the substance. The latter is represented in the third condition by the energy e or the enthalpy i as a known function of p and ρ . In certain cases of great practical importance, the first two conditions above, together with the pres-

sure density relation (equation of state) suffice to determine the shock phenomenon. This applies to flow in substances where the pressure depends on the density alone and not, or not noticeably, on the entropy.

For polytropic gases, the relation between the relative velocities v_0 , v_1 on either side of the shock can be put in the form

$$(iii_P) \quad v_0 v_1 = c_*^2$$

referred to as Prandtl's relation, which is equivalent to

$$(iii'_P) \quad \frac{c_*}{v_1} + \frac{v_1}{c_*} = \frac{c_*}{v_0} + \frac{v_0}{c_*}.$$

Prandtl's relation exhibits the fact that a weak shock (v_0 approximately equal to v_1) is approximately a sonic disturbance. *It also follows that the speed of the gas relative to the shock front is supersonic on the front, subsonic on the back of the shock front.*

The *strength* of a shock might be measured by any of the following:

$$\text{Excess pressure ratio} = \frac{p_1 - p_0}{p_0},$$

$$\text{Condensation} = \frac{\rho_1 - \rho_0}{\rho_0},$$

$$\text{Parameter} = M_0^2 - 1,$$

where $M_0 = v_0/c_0$ is the Mach number of the incoming flow relative to the shock front.

From the second law of thermodynamics, which stipulates that entropy increases from the front to the back of a shock front, it follows that a polytropic gas acquires higher pressure, temperature, density, and entropy on crossing the shock front. It is important that the change in entropy across a shock front is only of the third order in the shock strength, that is, in any of the above three measures of shock strength. For weak shocks, the jump in entropy is therefore very small and usually may be neglected. A weak shock may thus be treated as an adiabatic change, in which case only the first two shock conditions are needed.

A problem of great importance presents itself in the reflection of a shock. Suppose that an oncoming column of gas of constant velocity w behind a shock front impinges on a zone of quiet bounded by a rigid wall. The ensuing physical phenomenon can be described as a reflection of the shock wave at the wall and can be represented mathematically by piecewise constant solutions of the differential equations, satis-

fying the shock conditions across the *incident* shock wave and the *reflected* shock wave. Under the impact of the incident shock wave, the zone (0) of quiet next to the wall will shrink to zero, say at $t = 0$; then a reflected shock will start in the opposite direction and in turn will leave a growing zone of quiet between itself and the wall. Figure 5 illustrates the situation.

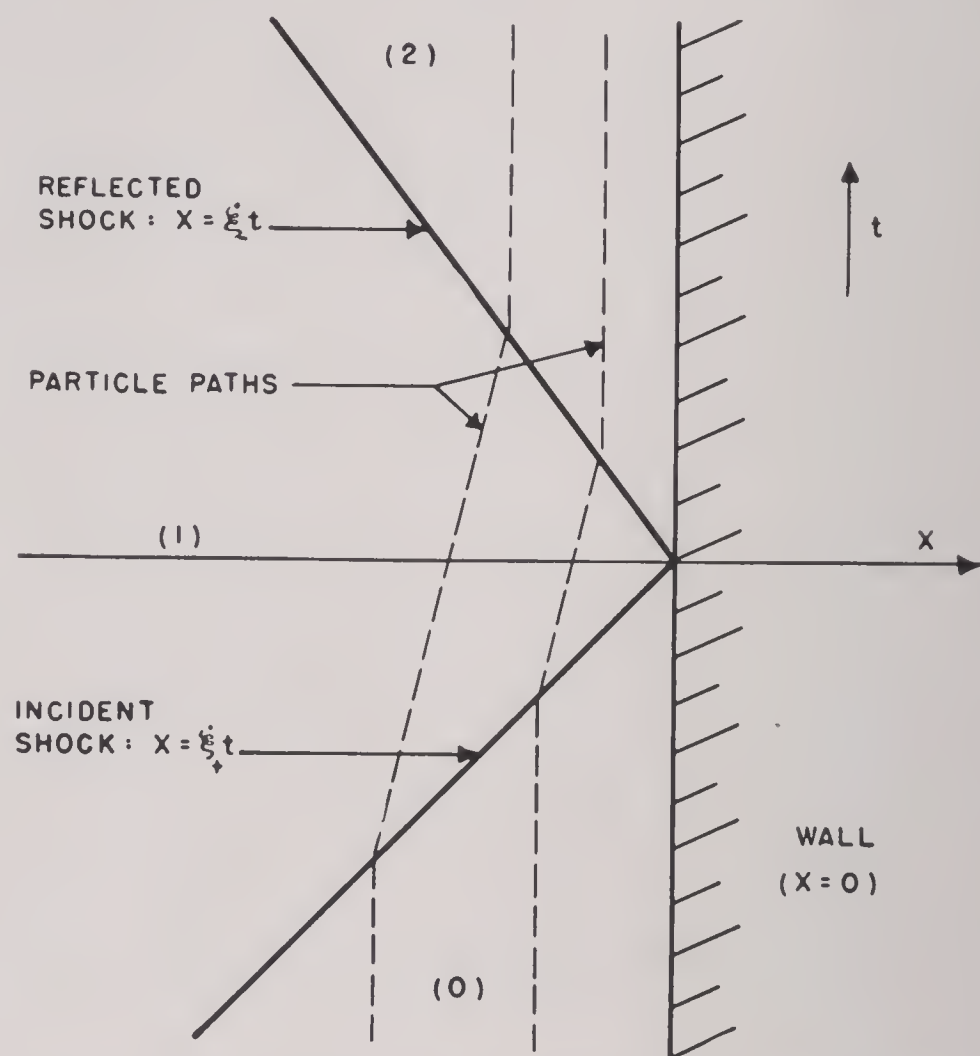


FIGURE 5. Reflection of shock wave on a rigid wall.

State (0) is characterized by the quantities $u_0 = 0$, ρ_0 , p_0 , c_0 . In the state (1) following the incident shock, we have $u_1 = w$. State (2) is characterized by $u_2 = 0$ and new values ρ_2 , p_2 , c_2 . The problem is to determine (2) from the data (ρ_0, p_0, w) . In terms of the notation of equation (10) the excess reflected pressure ratio has the value

$$\frac{p_2}{p_1} - 1 = \frac{1 + \mu^2}{1 + \mu^2 \left(\frac{p_1}{p_0} \right)} \left(\frac{p_1}{p_0} - 1 \right). \quad (19)$$

Equation (19) is the basic relation for reflection. To see the contrast with the mere doubling of excess pressure after reflection, suppose p_1/p_0 is large. Then

$$\frac{p_2}{p_1} \sim 2 + \frac{1}{\mu^2} = \begin{cases} 8 & \text{for } \gamma = 1.4 \\ 13 & \text{for } \gamma = 1.2 \text{ (air)} \\ 23 & \text{for } \gamma = 1.1 \end{cases} \quad (20)$$

The reflection of strong shocks thus results in a considerable increase of pressure at the wall. The situ-

ation just described was greatly simplified by the assumption that the shock establishes the transition from one *constant* state to another, implying a constant speed and strength of the shock wave. Such a shock wave in the x,t plane is represented by a straight shock line whose slope relative to the t axis is the shock velocity ξ . Frequently, the states on the two sides of the shock front cannot both be considered constant but are described by more complicated solutions of the differential equations. Moreover, the shock wave will not have a constant velocity, that is, the shock line in the x,t plane will be *curved*. For such shocks, the entropy change will in general also vary. Hence, even if the state in front of the shock is of uniform entropy, the gas, after passing the shock front, will no longer have the same entropy throughout. This forces us back to the use of the more general differential equations, a mathematical complication which has thus far precluded any complete theory, though calculations in specific instances are feasible. In many cases of practical importance, neglect of changes in entropy is justifiable, and a numerical treatment of the problem is thus facilitated; the simpler differential equations can be used, assuming an adiabatic process, and one can then operate solely with the first two shock conditions. The third condition is used only to determine thermodynamical quantities after the solution is complete.

INTERACTIONS

The topics thus far discussed pertain primarily to immediate developments following on simple expansion, compression and shock waves originating from a state of rest. However, when shock waves are reflected, collide, or overtake one another, more general states of motion result as a consequence of various interactions in which no principle of superposition is valid. The generation of excessively high pressures by reflection of shocks is only an example of phenomena altogether different from those of linear motion.

The so-called *elementary* interactions consist of interactions of waves meeting contact discontinuities or of waves facing each other and colliding or of one wave overtaking another. As an ultimate outcome of such interactions, two waves can be expected, moving away in opposite directions from the spot of interaction.

It is to be noted that if any two waves, other than two rarefaction waves, face in the same direction, then one will ultimately overtake the other. This

fact follows from the relations of the wave speeds to sound speeds both in front and in back of a wave.

Interactions have very different effects according to whether the waves clash head-on or one of them overtakes the other. The reflection of a shock wave on a rigid wall is equivalent to a special case of the *head-on collision of two shock waves*, namely, two symmetrical equal shock waves. In general, when two shock waves of different intensities collide, a more complex situation results. After the two shock waves have penetrated and thereby weakened and retarded each other, they leave behind an expanding zone of constant pressure and flow velocity as in the case of symmetry. The density in this zone is, however, not uniform. Instead, a certain point (contact discontinuity) moving with the flow velocity of the zone separates two regions of different (uniform) density (and temperature). This fact indicates the necessity of considering contact surfaces in the interaction problem along with shock and rarefaction waves. A fuller discussion of interactions in one dimension is in Section 1.3.

1.2.4 Isentropic Irrotational Steady Plane Flow

The mathematical theory of the type of flow involved in the study of oblique shock fronts and shock reflection was developed along lines similar to those used for one dimension.

CONTINUOUS MOTION — SIMPLE WAVES

The transformation to characteristic parameters is possible only for supersonic flow ($u^2 + v^2 = q^2 > c^2$), a condition hereafter to be assumed. This is required if the solutions of the differential equations are to be interpreted in terms of wave propagation, implying the occurrence of definite ranges of influence and domains of dependence.

The steady character of a flow is dependent on the choice of a coordinate system. Observed from a coordinate system moving at constant velocity relative to the original one, a flow in general does not remain steady. When necessary, it is possible to reduce non-steady flow to steady by changing to a suitable moving coordinate system.

The characteristics C_+ and C_- in the x,y plane depend on the specific flow under consideration. If $M = q/c$ denotes the Mach number of a flow and if $\sin \alpha = 1/M$, then the characteristics C are the two sets of lines in the x,y plane which intersect the

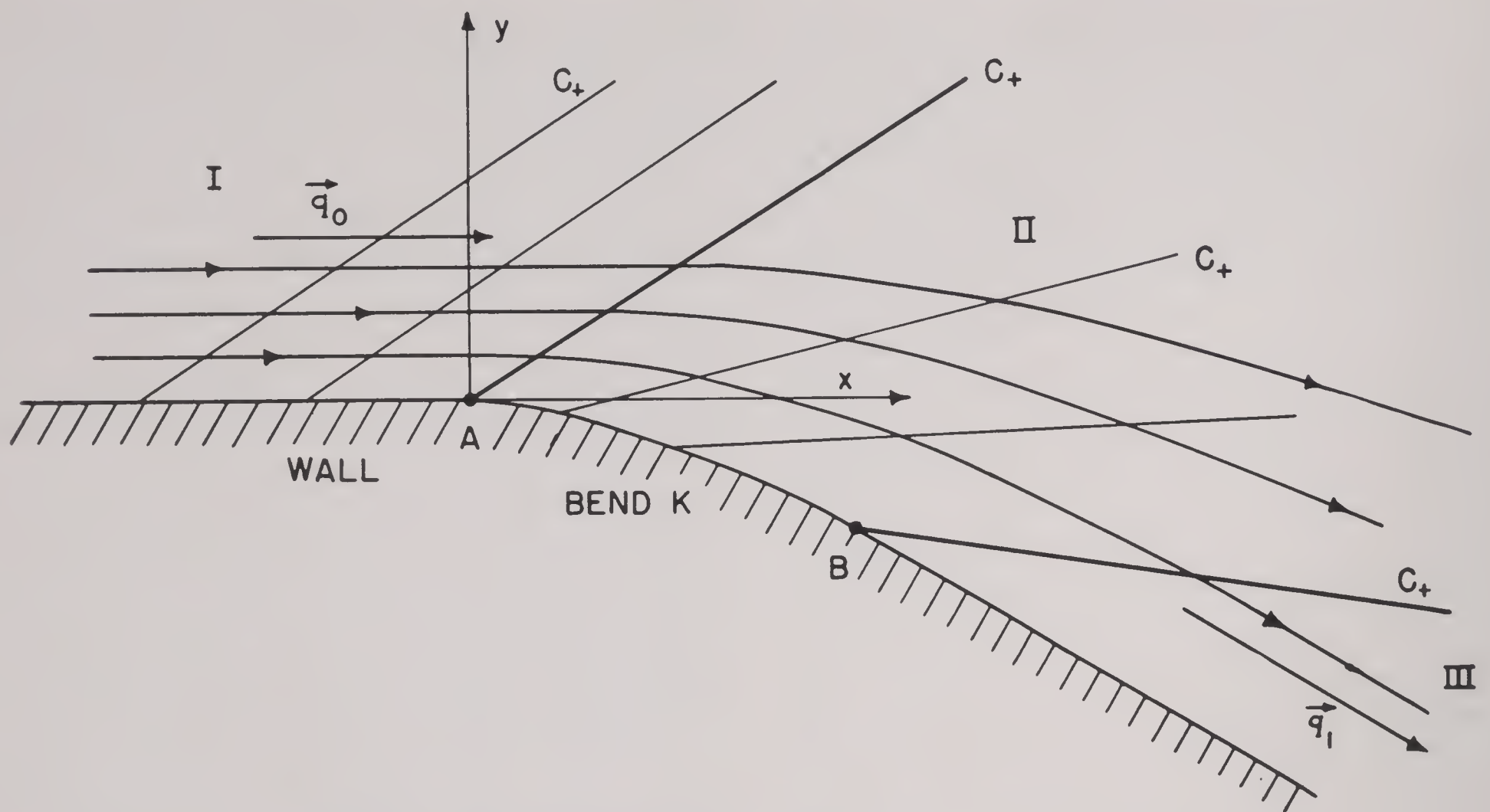


FIGURE 6. Flow around corner effected by a simple expansion wave.

streamlines at the Mach angle α . Characteristics in steady flows are sometimes called Mach lines. In steady two-dimensional supersonic flow, the component of the flow velocity normal to the Mach lines is equal to the local sound speed c .

If a subsonic flow were under consideration, no characteristics could exist. Also, there could be no subregion of exactly constant state, for the analyticity of the solution would then imply a constant state throughout. For supersonic flow, a constant state in some parts is, however, compatible with non-constant states in other parts, the different zones being separated by characteristics C .

An exceedingly important problem in simple waves is presented by supersonic flow around a bend or sharp corner. Suppose the flow arrives with a constant velocity q_0 along a wall which is straight up to a point A (see Figure 6), then curves along a smooth bend K from A to B , and continues straight beyond the point B . Assume that, in a region adjacent to the straight part of the wall before A , the oncoming flow is of constant state. The problem is how the flow turns the corner or how it continues along the bend K and along the straight wall beyond K . The solution can be obtained by piecing together various domains of the flow having essentially different analytic character, namely, the zone I of constant state of the oncoming flow, a simple wave II which necessarily follows, and through which the flow effects its turn, and

finally a zone III, also of constant state, which may be either a zone of flow parallel to the straight wall beyond B , if the simple wave effects the complete turn described by the bend, or a zone of cavitation, if the flow has expanded to zero density before the full turn around the bend has been achieved.

The results just indicated and the corresponding treatment hold just as well for the idealized case where the gradual bend is replaced by a sharp corner K . Then the flow arrives along the wall before K and suddenly turns at K in a new direction. The turn, discontinuous at K , is smoothed out into a continuous turn. It is effected by a centered simple wave, swept by a set of characteristics C , all of which come from the center K .

The above remarks relate to expansion waves in which density and pressure decrease while flow speed increases along the streamlines. Since the flows under consideration are reversible, however, it is immediately seen that compression waves are equally possible in flow around a bend or corner.

Material on jets, relevant to the present discussion, is contained in Section 1.8.

OBLIQUE SHOCK FRONTS

Thus far, velocity, pressure, and density are assumed, in the flows, to be continuous functions of x and y , though discontinuities in the derivatives may occur across characteristics or Mach lines. How-

ever, it often happens that conditions are not compatible with a continuous flow and that discontinuities are therefore bound to occur. As in the one-dimensional case the simplest mathematical assumption, that of shock fronts, is fortunately in agreement with experimental evidence, and the situation is similar to that in which a simple shove was seen to result in a shock, if it entailed a contraction rather than a rarefaction, and when the straight characteristics accordingly had an envelope inside the x, t domain of flow. Throughout the present analysis, the contrast between flow *around* a corner and flow *in* a corner plays a role corresponding to that of the contrast between expansive and compressive motion in the one-dimensional case. Although a continuous flow around a corner is possible in an expansion wave (also, under special conditions, in a contraction wave), a new situation arises if a parallel supersonic flow arriving along a straight wall is forced to bend in a concave corner K (see Figure 7). In principle,

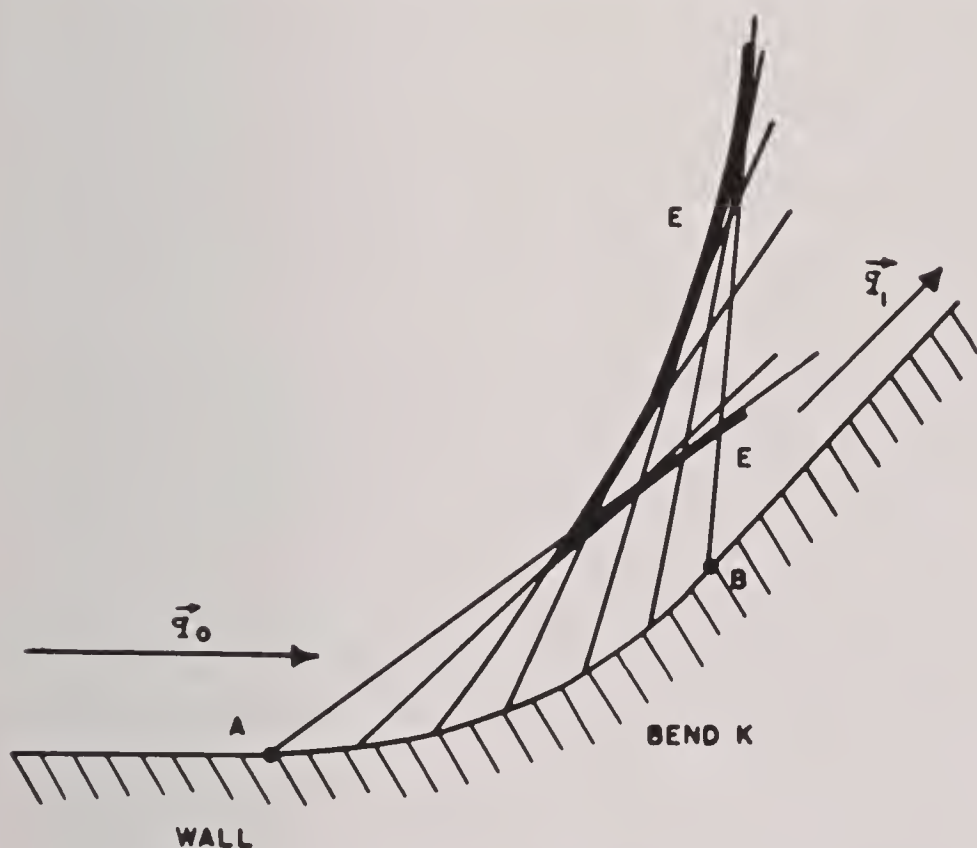


FIGURE 7. Envelope E of straight characteristics issuing from bend K .

the previous construction of a simple wave remains valid *near* the wall. In the x, y plane, the constant flow I passes into a simple wave along a characteristic (Mach line) through A . But, in contrast to the flow around a bend, the subsequent straight characteristics of the simple wave will now turn so that an envelope originates inside the flow. The ambiguous state (mathematically) behind the envelope, where u, v would not be uniquely defined, is physically impossible. As observations indicate, it is avoided by a shock discontinuity, that is, a line S of discontinuity for the quantities u, v, ρ, p, τ , and η . The shock line

starts with zero strength at the cusp of the envelope and runs between its two branches. Conditions are such that the flow ceases to be isentropic, and particles crossing the shock front S from a zone of constant entropy in general suffer entropy changes. Consideration of nonconstant entropy behind a shock front is unavoidable. However, in many important cases, the only ones which lend themselves to relatively simple analysis, the variation in entropy is either absent or negligible, so that the simple differential equations of isentropic flow remain valid on both sides of the line S .

This condition is surely satisfied when the shock line S is straight and the state is constant on either side of S . Typical for this situation and of basic intrinsic importance is the ideal limiting case where the bend is concentrated in a sharp corner K and where the flow arrives with constant supersonic speed at K , parallel to one leg of the angle, and then turns discontinuously into the direction of the other leg, again at constant velocity. The sudden transition of direction and speed of the flow is effected across a straight shock line S extending from K into the fluid obliquely to the direction of the flow. Here the *oblique shock front* merely connects two zones I and II of constant state. Not only is there no complication from variations in entropy but the algebraic character of the problem also obviates the necessity of any concern with even the differential equations. For a qualitative representation of the situation, see Figure 8. The

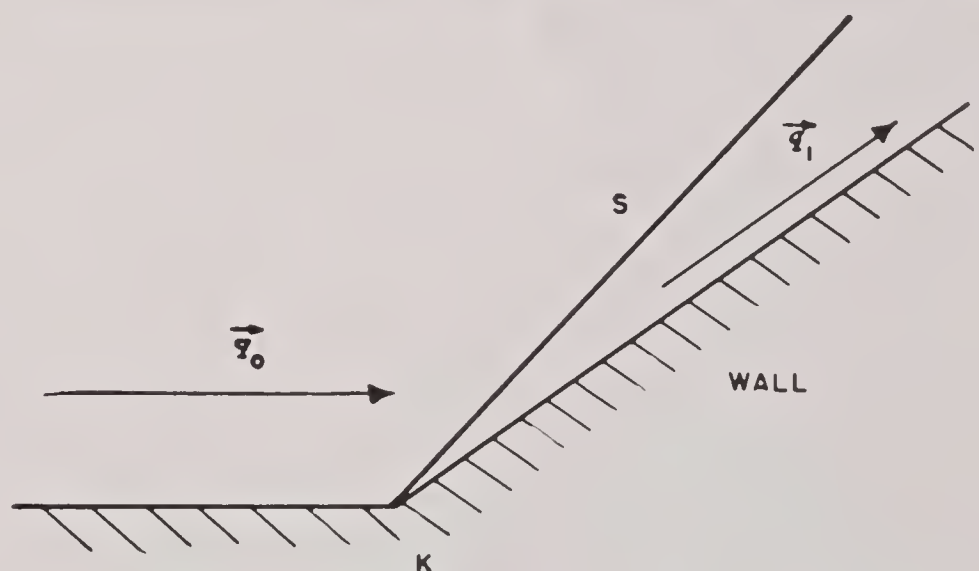


FIGURE 8. Straight shock line resulting from flow in sharp corner K .

above remarks apply to two-dimensional supersonic flow against a wedge, which can be regarded as an idealized projectile.

For shocks in two dimensions, and also in three, not restricted to steady isentropic flow, the discontinuity conditions are obtained from the principles of conservation of mass, of momentum, and of energy

in exactly the same way as for one-dimensional flow. An alternative method for obtaining the shock relations is to consider the flow from a moving coordinate system with respect to which the shock front is not oblique but normal, so that the conditions used in the one-dimensional case can immediately be applied. In order to accomplish this, it is assumed, as a locally approximate condition, that (1) the discontinuity surface S is plane; (2) the speed $\dot{\xi}$ of S in the direction of its normal is constant; and (3) the states (0) and (1) on the two sides of S are constant.

Since shock conditions are invariant if referred to a coordinate system moving with a constant velocity relative to the original one, it follows that these conditions can be obtained by using the shock line S as one coordinate axis, in other words, by regarding the shock front as stationary, regardless of whether the flow under consideration is steady. Since the origin of the coordinate system can be permitted to move at constant speed along S , it is permissible to assume that the velocity component of the flow parallel to S is zero and thus to visualize the flow as one of constant speed meeting a stationary discontinuity surface S at a right angle. If speed is not zero, that is, if mass is transported through S , the law of conservation of momentum requires that, in state (1) behind the shock, the velocity likewise be perpendicular to S . In other words, observed from a suitable coordinate system, an oblique shock front is always equivalent to a stationary one-dimensional shock front.

The shock conditions can be formulated as follows in terms of the normal and tangential components, N and L respectively, of the flow vector \mathbf{q} .

$$(i') \quad \rho_0(N_0 - \dot{\xi}) = \rho_1(N_1 - \dot{\xi}) = m \quad (\text{Conservation of mass})$$

$$(ii'_N) \quad \rho_0 N_0(N_0 - \dot{\xi}) + p_0 = \rho_1 N_1(N_1 - \dot{\xi}) + p_1 \quad (\text{Conservation of momentum})$$

$$(ii'_L) \quad L_0 - L_1 = 0 \quad (\text{Continuity of tangential component})$$

$$(iii') \quad \frac{1}{2}\rho_0(N_0 - \dot{\xi})q_0^2 + \rho_0(N_0 - \dot{\xi})e_0 + N_0p_0 = \frac{1}{2}\rho_1(N_1 - \dot{\xi})q_1^2 + \rho_1(N_1 - \dot{\xi})e_1 + N_1p_1,$$

where

$$q^2 = L^2 + N^2 \quad (\text{Conservation of energy})$$

For a stationary shock front, these become

$$(i) \quad N_0\rho_0 = N_1\rho_1 = m$$

$$(ii_N) \quad \rho_0 N_0^2 + p_0 = \rho_1 N_1^2 + p_1 = P$$

$$(ii_L) \quad L_0 = L_1$$

$$(iii) \quad \frac{1}{2}q_0^2 + i_0 = \frac{1}{2}q_1^2 + i_1 = \frac{1}{2}\hat{q}^2$$

where q^2 is the square of the flow speed and \hat{q} is the limit speed of the flow.

If there is a contact discontinuity with $m = 0$, then (i), (ii_N), and (iii) hold. It follows that $p_0 = p_1$ and $N_0 = N_1$. However, L_1 and L_0 can be different and so can ρ_0 and ρ_1 . Unless explicitly stated otherwise, it will be assumed that $m \neq 0$ and $L_0 = L_1$.

A more symmetric way of writing the first two conditions for stationary shocks, expressing the conservation of the mechanical quantities mass and momentum, is

$$(ii_0^*) \quad \frac{p_1 - p_0}{\rho_0} = \mathbf{q}_0(\mathbf{q}_0 - \mathbf{q}_1)$$

$$(ii_1^*) \quad \frac{p_0 - p_1}{\rho_1} = \mathbf{q}_1(\mathbf{q}_1 - \mathbf{q}_0)$$

from which

$$(ii^*) \quad (p_1 - p_0)(\tau_0 - \tau_1) = (\mathbf{q}_0 - \mathbf{q}_1)^2.$$

Conditions (ii_L), (ii₀^{*}) and (ii₁^{*}) together are equivalent to (i), (ii_L) and (ii_N).

As in the case of one-dimensional shocks, conditions (i), (ii_N), (ii_L), (ii₀^{*}) and (ii₁^{*}) are valid on the basis of mechanics alone. Only through condition (iii) do the thermodynamical characteristics of the medium intervene. In many instances, it is possible to disregard the thermodynamical shock condition, thus greatly facilitating the solution of a flow problem.

Of great importance in studying shocks for gases is the generalization of Prandtl's relation $q_0 q_1 = c_*^2$, mentioned above for normal shocks. This generalization,

$$(iii_P) \quad N_0 N_1 = c_*^2 - \mu^2 L$$

can be used instead of preceding forms of the thermodynamical shock condition.

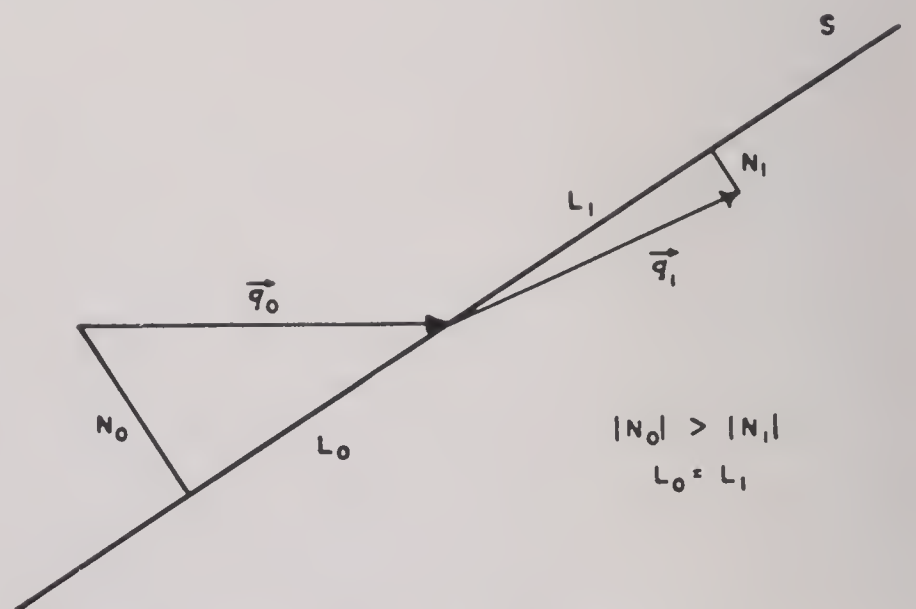


FIGURE 9. Showing how flow is turned toward the shock line.

It can be concluded, as in earlier cases, that the speed of the flow on the front of a shock (observed

from the shock front) is supersonic. However, the speed on the back can be either subsonic or supersonic.

Furthermore, an oblique shock in a gas always turns the flow towards the shock line S (see Figure 9).

It is important to note the relative positions of Mach lines and flow vectors. In the case of a normal shock line S facing towards (0), the supersonic zone (0) contains two directions of Mach lines, C_+ and C_- , and the Mach angle α_0 is defined by $\sin \alpha = c_0/q_0$. In zone (I), the flow is subsonic, so there exist no Mach lines behind a normal shock front (see Figure 10). For an oblique shock, this latter statement

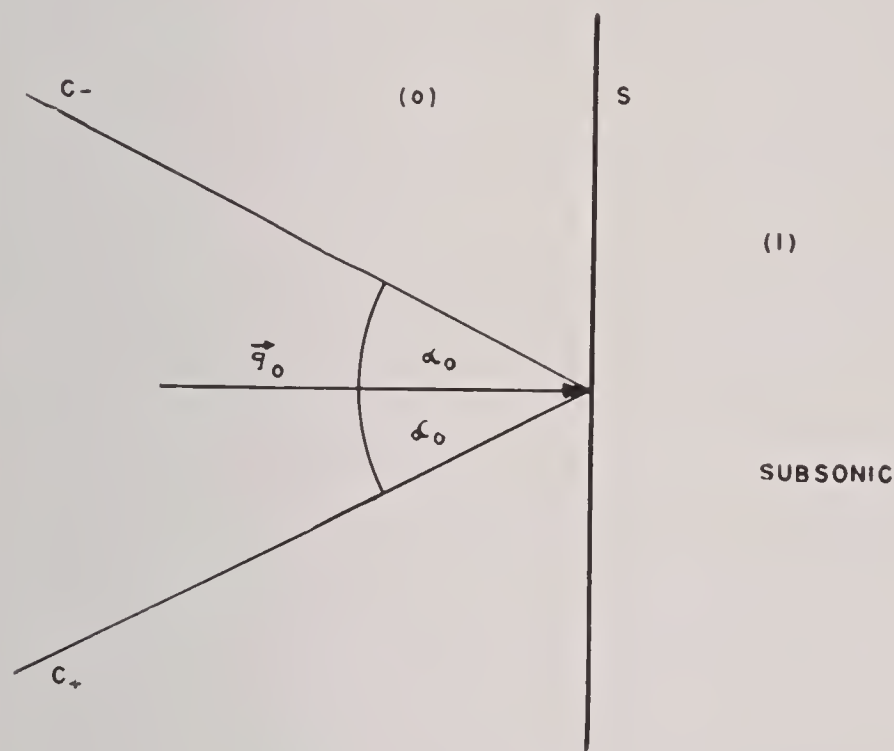


FIGURE 10. Characteristics C exist only in front of a normal shock line.

remains true as long as $q_1 < c_*$, that is, as long as the state (1) is subsonic. If $q_1 = c_*$, a Mach line appears perpendicular to the flow velocity in (1). If $q_1 > c_*$, there are two different Mach line directions in (1), and it is important to realize that their positions are as indicated in Figure 11. In other words, the two Mach directions, if they exist, form behind the shock front the same angle α_1 with the flow direction and lie in the obtuse angle between S and the direction of the flow vector q_1 .

A weak shock, for which the difference $q_1 - q_0$ (or $\rho_1 - \rho_0$ or $p_1 - p_0$) is small, differs little from a sonic disturbance; and the direction of the shock line S is almost a Mach or characteristic direction.

CONFIGURATIONS WITH SEVERAL OBLIQUE SHOCK FRONTS

Problems in *shock reflection* occur in connection with physical situations of the following type. Suppose an approximately plane shock front moving

through space hits a rigid wall obliquely. This effect is produced, for example, by an explosion or by a fast-flying projectile, provided the wall is sufficiently far from the source of disturbance so that the shock fronts can be considered plane. Observations reveal that a flow pattern may result which exhibits an incident and a reflected shock front (see Figure 12).

For very weak stationary shocks, the shock lines are approximately Mach lines and therefore form a Mach angle with the wall, which is a streamline. Thus a stationary flow pattern containing a weak incident and reflected shock will almost agree with the law of reflection of geometrical optics, that is,

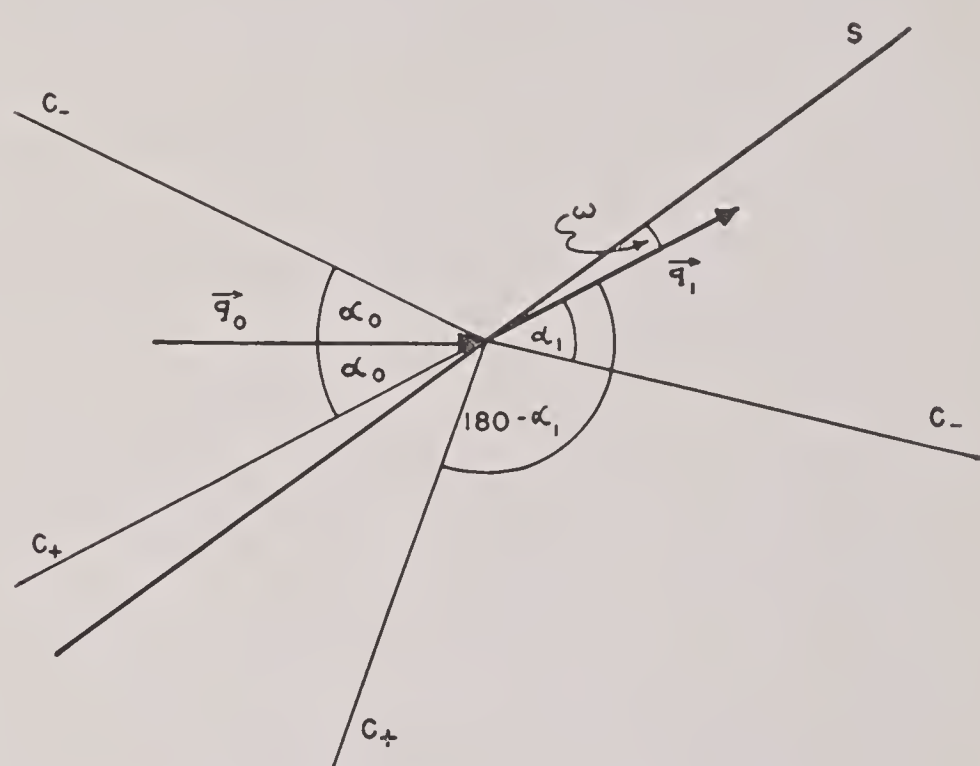


FIGURE 11. Positions of characteristics C in front and in back of an oblique shock line.

both shock lines form approximately the same angle with the wall. However, when the incident or reflected shock (or both) has sufficient strength, observations show definite deviations of the flow pattern from that of sonic waves. One speaks of regular reflection when the resulting flow resembles qualitatively that of the sonic case, that is, when it can be described solely in terms of incident and reflected waves. Even in regular reflection, the angles between incident and reflected waves are in general not equal.

The peculiar character of the reflection of shock waves can be derived and analyzed theoretically. Such a theoretical discussion consists in finding a mathematically possible flow pattern which (1) is compatible with the observed qualitative and quantitative features of the phenomena and (2) yields quantitatively correct predictions of flows not yet observed.

As a preliminary step, it is important to note that although the phenomenon, as presented to the ob-

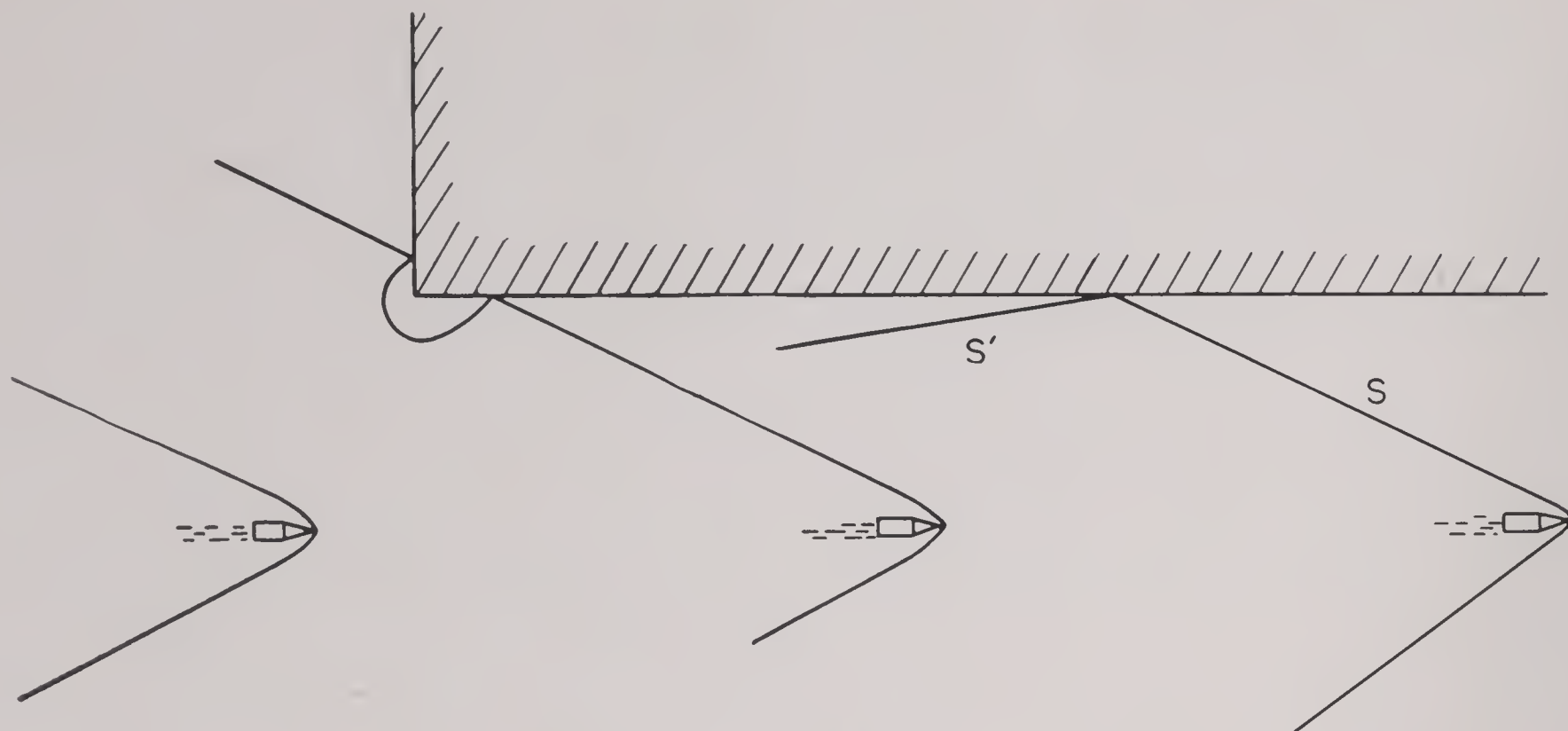


FIGURE 12. Regular reflection of shock wave produced by projectile.

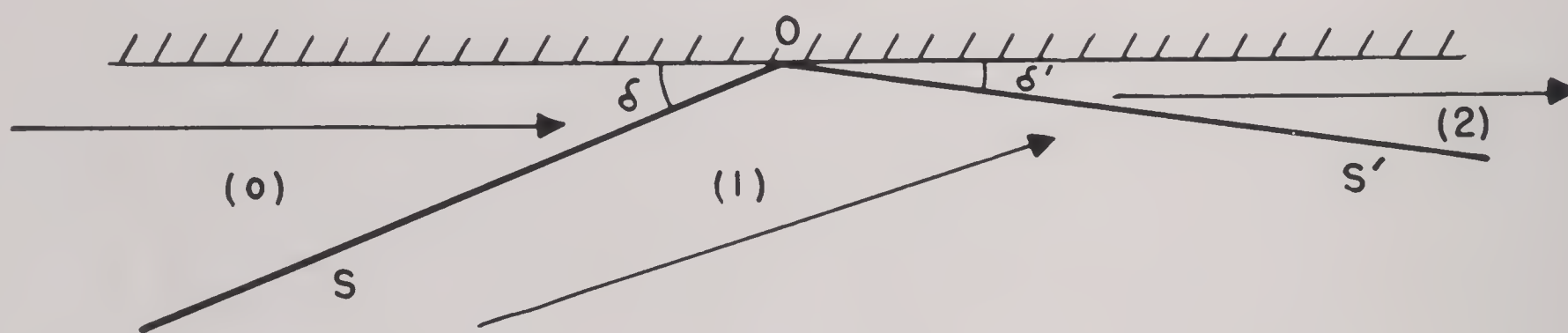


FIGURE 13. Regular weak reflection of shock fronts on a rigid wall.

server, need not be stationary, it can be reduced to one of steady flow by subtracting from all velocities the velocity vector, parallel to the wall, of the point O at which reflection takes place, in other words, by referring the flow to a coordinate system moving with the point O . The problem then becomes one of finding a steady flow in the x, y plane for $y \leq 0$ such that the lower half-plane $y < 0$ is divided, as in Figure 13, into three regions (0), (1), and (2), each of constant state, separated by two stationary shock lines S and S' ; and such that in the regions (0) and (2) the flow is parallel to the wall $y = 0$; that is, $v_0 = v_2 = 0$. The configuration then consists of the succession of two oblique shocks, the incident shock S and the reflected shock S' . In accordance with the above discussion, the incident flow with the velocity \mathbf{q}_0 is turned, on passing the incident shock front, toward the wall into a flow which is still supersonic with the velocity \mathbf{q}_1 . On crossing the reflected shock, this flow (1) is turned into a flow with velocity \mathbf{q}_2 parallel to the wall, and supersonic or subsonic as the case may be. In this problem, a considerable rise in pressure is to be expected behind the reflected shock front.

It is noteworthy that regular reflection, however weak or strong, can occur only under very restrictive conditions. In particular, such reflection is impossible when the incoming wave is very strong (for given q_0/c_*) or when a shock impinges on a quiet medium so that the angle $\beta_{01} = \delta$ between the incoming shock and the wall is rather large.

Long ago in experiments and papers by E. Mach, innumerable phenomena of wave interaction were studied under conditions which do not produce regular reflection. Only recently, however, various authors developed a mathematical theory with a view to applications and to the understanding and control of phenomena involving the considerable increases in pressure which occur in the oblique collision of shocks. When regular shock reflection does not occur, configurations of three shocks through one point arise. It is most important to note that three shocks separating three zones of different continuous density and pressure are impossible. A contrary assumption leads to the conclusion that two of the adjacent states are identical. Hence, reflection patterns must allow for an additional discontinuity, and the simplest assumption, which is fortunately in

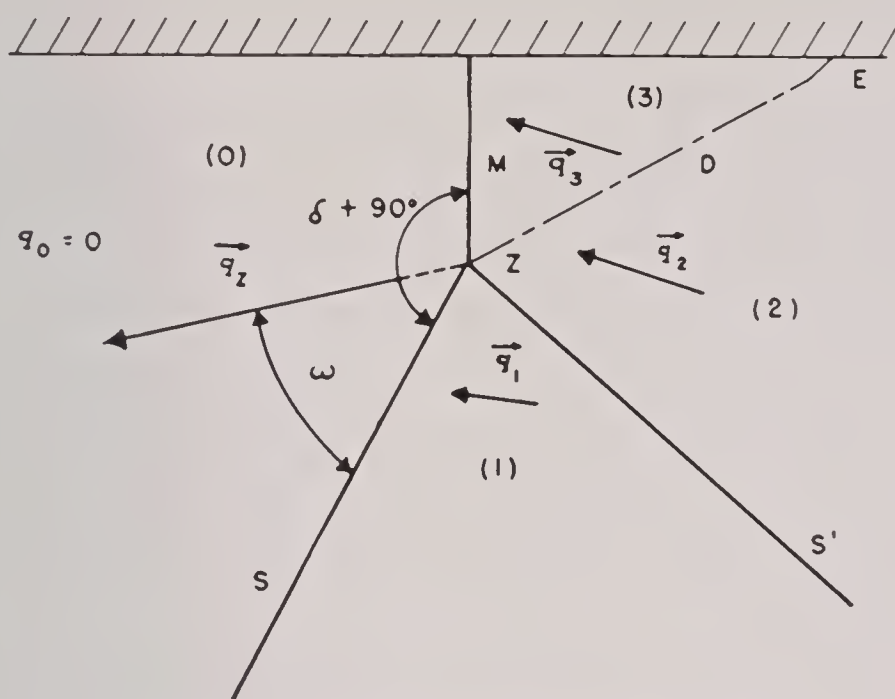


FIGURE 14. Direct Mach configuration.

into a zone of rest and reflected at a wall, the situation can be characterized by parameters which depend solely on the state (0) of rest and on the incident shock wave. As such parameters, one can use (1) the ratio p_0/p_1 of the pressure in front of the incident wave to the pressure behind the wave, characterizing the strength of the shock, and (2) the angle δ between the incident shock front and the wall. For Mach reflection as well as for regular reflection, much of the interest is focused on the resulting pressure. Consider the ratio p_2/p_1 of the pressure behind and in front of the reflected shock front S' . The reflected pressure ratio varies when the angle δ of incidence varies from 0° to 90° while the strength of the incident shock $(p_1 - p_0)/p_0$ is kept fixed.

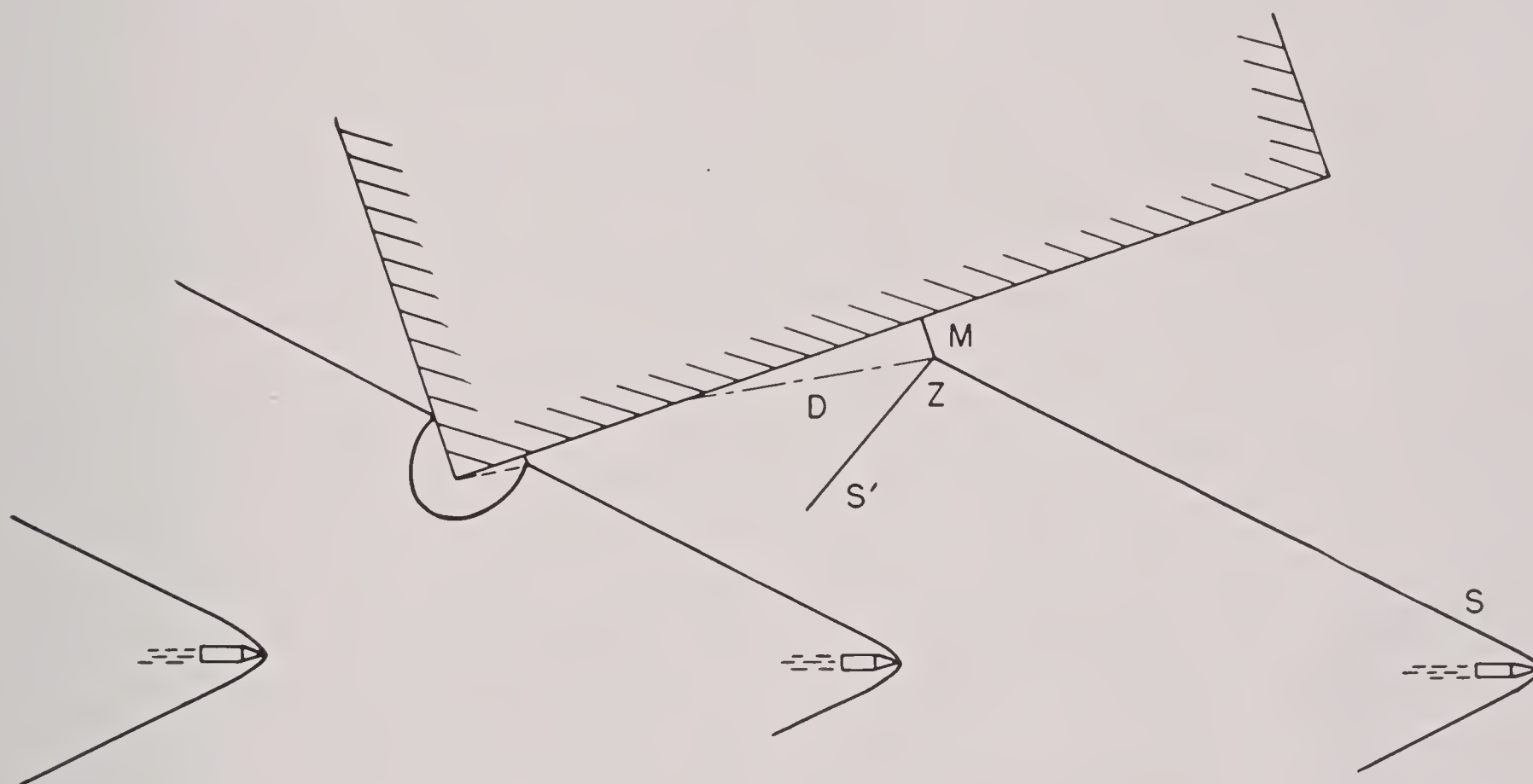


FIGURE 15. Mach reflection of shock wave caused by projectile.

agreement with many observations, is that of a contact discontinuity line. The Mach reflection can be described as a configuration consisting of three shock fronts through one point and, in addition, a line of contact discontinuity D through the same point (compare Figures 14 and 15). The incident shock S is followed by a reflected shock S' (S facing left in Figure 14). In this case, the reflection takes place, not at the wall but at a branch point Z moving obliquely away from the wall. The point Z is connected with the wall by a perpendicular shock through which the flow is normal. Finally, there is a discontinuity line or vortex line D from Z toward the wall. Figure 15 shows a possible genesis of a Mach reflection as frequently observed.

In the case of an incident shock wave penetrating

Although the simple mathematical pattern of the three-shock configuration fits many phenomena surprisingly well, there exists much experimental material clearly in disagreement with theoretically determined Mach configurations. No theory thus far developed accounts for all the available experimental evidence, but some of the more elusive phenomena can be adequately explained by the hypothesis of additional simple waves with center in the branch point.

1.2.5 Flow in Three Dimensions

The discussion of three-dimensional flow cannot at present be systematic since only very restricted cases have thus far been attacked with a reasonable degree of success. Three types of such flow will be

briefly considered: flow through nozzles and jets, flow against a conical obstacle, and flow with spherical symmetry. The first two flows are essentially steady in character whereas the third is not. A simple but satisfactory approximate analysis for nozzle and jet flows is treated in Section 1.5.

CONICAL FLOW

Conical flow admits of a fairly extensive analysis on the basis of the differential equations. The analysis is concerned with steady, isentropic, irrotational flow with symmetry about the axis. The condition that the flow be conical means that the quantities u , ρ , p , and q retain constant values on cones (considered infinite) with a common vertex, the origin. Such a flow may occur, for example, at the conical tip of a projectile opposed to a supersonic stream of air.

If the cone angle is not too large, the deflection of the flow is achieved by a shock front beginning at the tip of the cone and having the shape of a straight cone (see Figure 16A). If, however, the cone angle exceeds a certain extreme value (Figure 16B) no

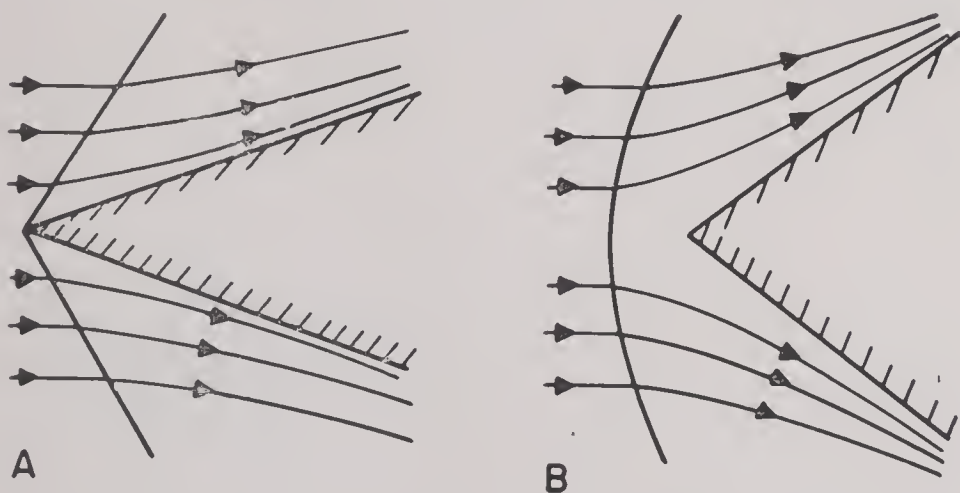


FIGURE 16. A. Conical shock front and conical flow resulting from supersonic flow against a cone with a sufficiently small angle. B. Curved shock front in supersonic flow against a cone with a large angle.

such conical shock is possible. Instead, a curved shock front stands ahead of the cone. Discussion is confined to the first case, since it alone can be handled on the assumption that the flow is conical.

Actual projectiles have a conical tip and then taper off, for example, into a cylindrical shape of finite length. Thus, farther back, the wave from the conical tip interacts with such other waves as expansion waves coming from the bend of the projectile. When a shock wave stands ahead of a projectile, the distance, under otherwise equal conditions, is the greater the farther the cone extends before tapering off. There is a shock front which begins near the rim of the end surface of a bullet, and there is also the

wake which begins at the end surface and whose cross section decreases, eventually approaching a constant area.

In the idealized case of a strictly conical flow, the situation answers the following qualitative description. Ahead of the shock front, the air is in a constant state, flowing in the direction of the axis with constant velocity. Behind the shock front, the state is also constant and the flow isentropic, since the shock front is a straight cone making everywhere the same angle with the incident flow. The state of the air beyond the shock cone will be constant on coaxial cones.

For transition through a conical shock, the relations are the same as for the plane oblique shock, and the curvature of the shock is not involved. When the shock cone is straight, the jumps of μ , v , p , and of the entropy are constant along each ray, provided the assumption of conical flow is satisfied on one side. As a consequence, this assumption is satisfied on the other side, and the flow can continue as a conical flow with constant entropy after crossing the shock.

SPHERICAL WAVES

Spherical wave motion is of basic importance for the study of explosion waves in water, air and other media. In spherical motion, the velocity is radial. Its magnitude, as well as that of density, pressure, temperature, and entropy, depends only on the distance r from the origin and on the time t . Such motion might be considered analogous to one-dimensional motion in a tube under the influence of a piston. The role of the piston is then played by an expanding or contracting sphere which impresses a motion on the medium inside or outside. It should be noted that in three-dimensional space an energy supply at an increasing rate would be required to maintain constant speed of a spherical "piston."

Better agreement with actual situations is afforded by the assumption that the total energy available for the motion is fixed. This is true for spherical blast waves caused by the explosion of a given mass of explosive.

The models just suggested differ from each other essentially in the following important respect. When a spherical piston moves at a constant radial rate, the shock wave ahead of the piston has constant speed, so that the shock conditions are compatible with the assumption of isentropic flow on both sides of the discontinuity. In blast waves, the strength of the shock, and hence the change of entropy, rapidly de-

creases, so that behind the shock front the flow is no longer isentropic. Moreover, in blast waves, the air or water, after having crossed the shock front and having thereby undergone compression, will rapidly expand again to a pressure in general even below that in front of the shock wave. This *suction phase* is an important feature of motion caused by explosions.

1.2.6 Detonation and Deflagration Waves in Gases

While an explosion is in progress, a fast-moving discontinuity surface separates the unexploded part of the explosive from the products of the explosion. This so-called *detonation wave* is closely related to shock waves, even though the equation of state of the medium is different on the two sides of the front. The two mechanical discontinuity conditions still obtain. However, the thermodynamic condition requires essential modification, for the law of conservation of energy demands an additional term in the energy balance to represent the energy set free by the chemical reaction. This liberated chemical energy per unit mass is a quantity f , characteristic of the explosive material. If (0) indicates the unexploded substance and (1) the burnt gases, then the thermodynamic discontinuity condition, analogous to (iii) in Section 1.2.3, becomes

$$\frac{1}{2}v_0^2 + i_0 = \frac{1}{2}v_1^2 + i_1 + f. \quad (21)$$

Another form obtained by eliminating v_0^2 and v_1^2 with the aid of the mechanical shock conditions is

$$\frac{1}{2}(p_1 - p_0)(\tau_1 + \tau_0) - i_1 + i_0 = f. \quad (22)$$

The two mechanical conditions, together with equation (21) or (22) constitute the *detonation conditions*.

For a shock wave, some externally acting agent, as a piston, is needed as a source of energy. A detonation, on the other hand, maintains itself by means of the liberated chemical energy.

In addition to the detonation conditions, a plausible hypothesis in good agreement with experiments serves to single out the two particular possible transitions between state (0) and state (1). This hypothesis, discovered in several different forms, can be expressed by the statement (Jouguet's hypothesis) that the *flow of the exploded gases immediately behind the front is exactly sonic* ($v_1 = c_1$). The two possible transitions which this hypothesis serves to single out are (1) the *detonation* in the proper sense, and (2) a process customarily identified with *deflagration*. In the former, pressure and density are increased beyond

the front. The latter leads to lower pressure and density. The second type of transition would correspond to expansive shocks with decrease in pressure, and it is doubtful whether such transitions should be excluded on the basis of the second law of thermodynamics.

In both detonation and deflagration combustion, a *reaction front* sweeps over the combustible substance, which is assumed to be a gas, and separates the explosive from the burnt gases. The term reaction front will be used indiscriminately for the transition front due to detonation or deflagration. Conditions additional to those usually employed in gas flows are needed to determine the motion, and the degree of indeterminacy, relative to the usual equations, is greater for deflagration or combustion than for detonation fronts. The mathematical problems inherent in the situation are (1) to discover the extent to which reaction waves are left undetermined by the laws of conservation, and (2) to find appropriate additional conditions sufficient to determine the reaction front.

A mathematical investigation² was based on the theory of characteristics and, in particular, the concept of domain of dependence, described in Section 1.2.2. The particular case treated was that of a gas filling a tube along the x axis. It was first supposed that at time $t = 0$ the explosive is at rest in the half-infinite tube $x \geq 0$, at $t = 0$ a reaction begins at the closed end $x = 0$, and the closed end is operated as a piston moving with the prescribed velocity U .

The mathematical determinacy of flows involving reaction fronts depends essentially on the geometrical relationships among (1) the characteristics of the system of differential equations expressing the laws of conservation, (2) the line W representing the reaction front in the x, t plane, and (3) the line π representing the moving piston at the closed end of the tube.

For isentropic flow, only the mechanical conditions are needed. For any flow, there exist two sets of characteristics C_- , C_+ in the x, t plane, defined by

$$\begin{aligned} C_+: dx &= (u + c)dt \quad (\text{along } C_+, dp + \rho c du = 0) \\ C_-: dx &= (u - c)dt \quad (\text{along } C_-, dp - \rho c du = 0). \end{aligned} \quad (23)$$

For nonisentropic flow, the third family, C_0 , of characteristics, the streamlines, must be considered.

$$C_0: dx = u dt. \quad (24)$$

With the situation analogous in the general case, attention is primarily restricted to isentropic flow. In general, the flow in front of and behind the reaction front is thought of as consisting of zones of constant flow and simple waves, so that either both sets C_- and C_+ are straight or at least one of them is.

The domains of greatest interest in the x, t plane are (1) that between the x axis and the reaction line W , representing the front, and (2) that between W and the piston curve $\pi: x = Ut$. Four cases (denoted in an obvious manner by AA, AB, BA, BB) are considered, according to whether the flow relative to W is (A) supersonic or (B) subsonic before or behind the front, that is, AB means supersonic in front of W and subsonic behind, and so on. These four cases are analyzed² with regard to the respective degrees of indeterminacy they present.

The higher degree of indeterminacy of flows involving detonation or deflagration fronts as compared with those involving merely shock discontinuities occurs because all cases AA, AB, BA, and BB may occur in reaction processes, whereas all shocks belong to the case AB.

Detonations and deflagrations are distinguished as weak or strong by comparison of the resulting gas velocities with those which would satisfy the so-called *Chapman-Jouguet condition*. This condition can be expressed in a number of useful forms, one of which, for example, is that the propagation speed $|v|$ of the front observed from the burnt gas is sonic ($|v| = c$).

A weak detonation corresponds to the case AA. The state of flow in front of W is determined by the initial conditions and the state immediately behind W by the transition conditions. An analysis is then needed on the way in which the flow velocity behind the front is adjusted to the piston velocity for various values of the parameter u . The nature of the adjustment depends on whether or not the piston speed U exceeds that gas velocity u_D behind the detonation front which would satisfy the Chapman-Jouguet conditions.

If $U < u_D$ and u is between U and u_D , the transition from the flow with velocity u behind the front to a flow with velocity U at the piston is effected by a *centered rarefaction* wave. If $u = u_D$, the rarefaction wave immediately follows the detonation wave and if $u = U$, the rarefaction wave drops out. If $U < u_D$ and if $0 < u < U$, then the adjustment is effected by a shock.

If $U > u_D$, then, as in the preceding case, a

variety of weak detonations is possible; however, the adjustment is always effected by a shock. Let the parameter u be thought of as assuming positive values, commencing with zero (constant volume detonation). A value $u^* < u_D$ exists for which the velocity $v_0 = (p - p_0)/\rho_0 u^*$ of the weak detonation equals that of the shock which accelerates the gas to the piston speed $U > u_D$. Weak detonations with $u < u^*$ are possible, followed by a slower shock adjusting the particle velocity to the piston speed U . If the particle velocity u behind the weak detonation front equals u^* , then the detonation front and the subsequent shock coalesce into a single discontinuity front W , across which the laws of conservation are fulfilled and the pressure raised. Thus W is a detonation front. It is a strong detonation front appearing as a weak detonation immediately followed by a shock.

Deflagration processes differ from detonation processes in many important respects. If a weak deflagration wave begins at $x = 0$ and moves into the interior, $x > 0$ of the tube, then the velocity u of the burnt gas behind the deflagration front comes out negative, $u < 0$. Hence the piston, under the conditions of the problem, must move out with a speed at least equal to u . Otherwise a deflagration front cannot move into the explosive gas. According to actual observations, however, a precompression wave is sent out into the explosive, pushing it ahead just fast enough to insure that it can come to rest when it is swept over by the deflagration wave. It has been observed that the deflagration wave moves with gradually increasing velocity and sends out a continuous compression wave into the explosive. For theoretical treatment, it can, however, be assumed that a single constant shock wave is sent out into the explosive, and that the deflagration wave follows with a constant velocity. (Compare Figures 17 and 18.) For each assumed precompression shock, there exists a great variety of possible adjustments by either a uniquely determined weak deflagration wave or by a strong deflagration wave, arbitrarily chosen from a one-parameter family and followed by a rarefaction or a shock wave. The velocity of each wave is, of course, less than that of the preceding wave.

If the shock wave following a strong deflagration wave coalesces with it, the result is equivalent to a weak deflagration wave. A *deflagration wave, however, coalescing with its precompression wave is equivalent to a detonation wave*. Thus, by increasing the strength

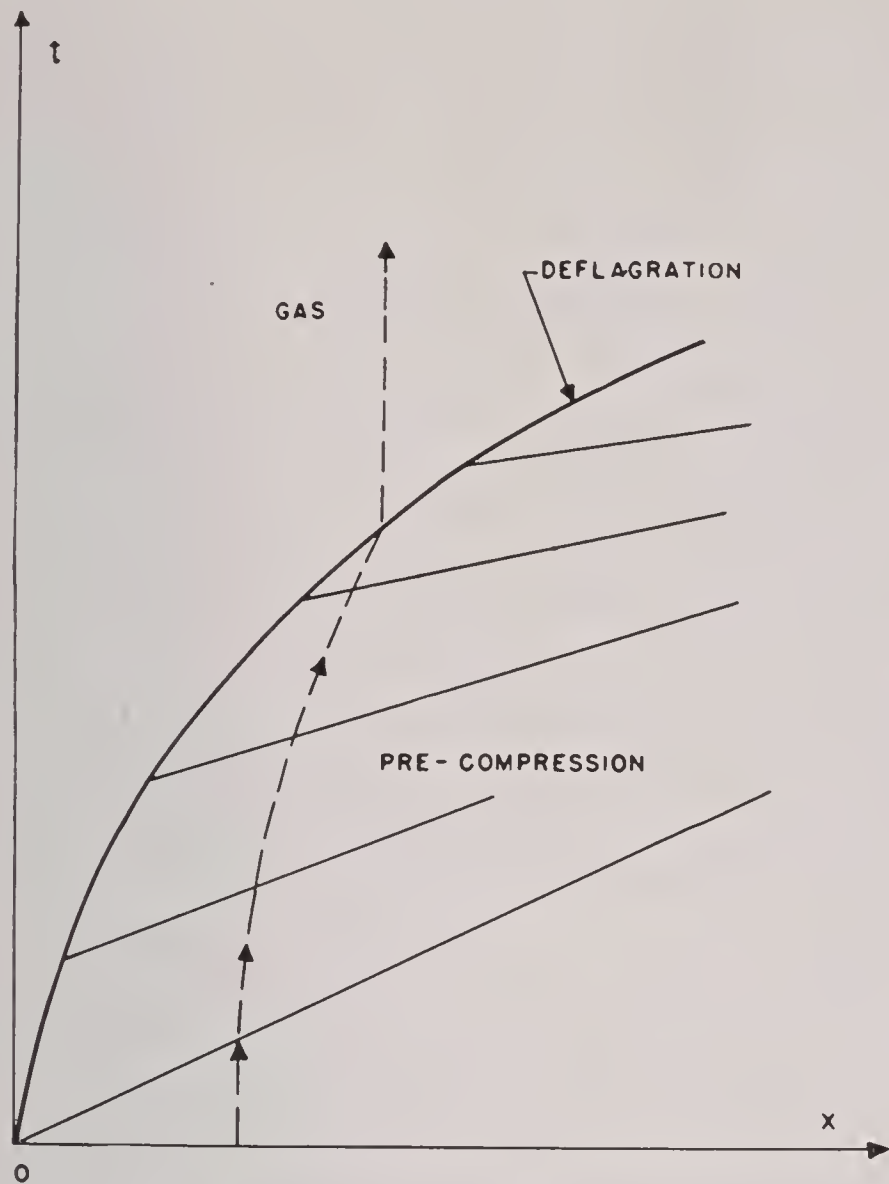


FIGURE 17. Actual deflagration with continuous pre-compression, $U = 0$.

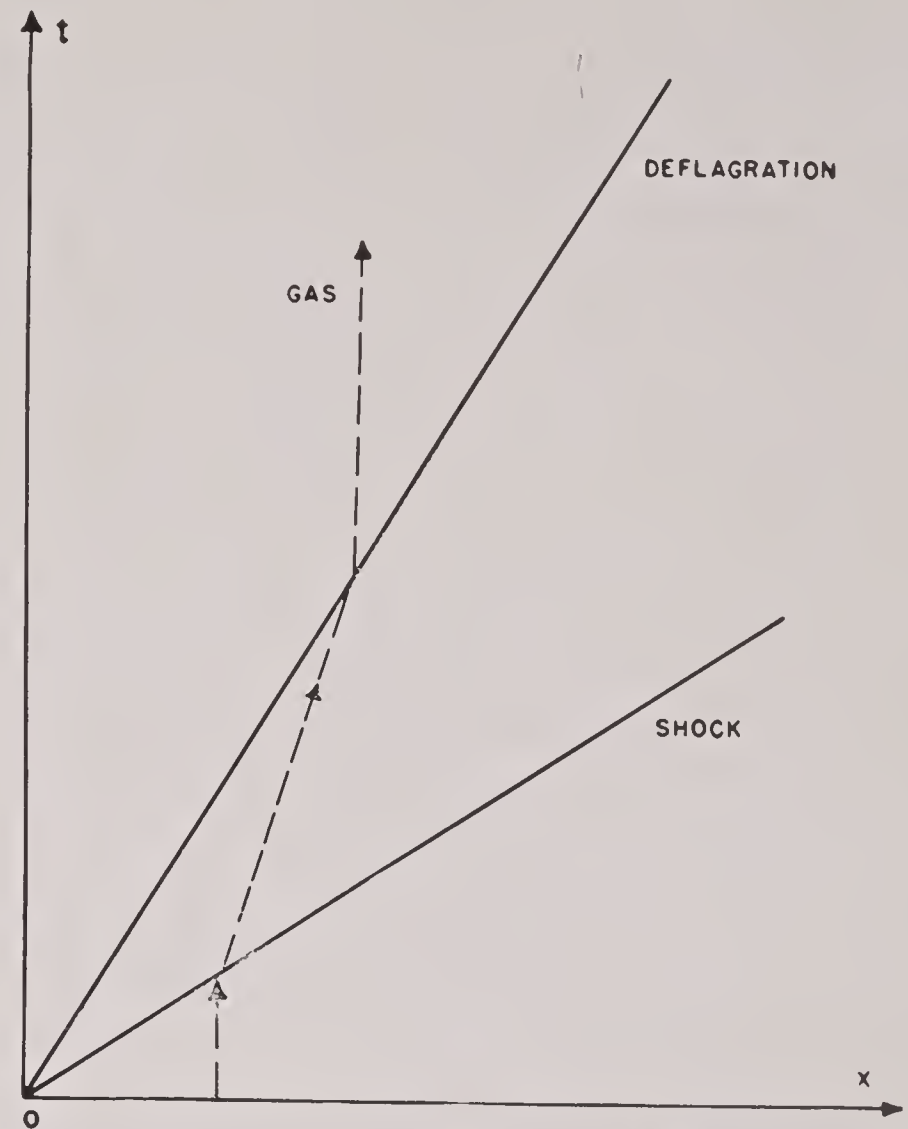


FIGURE 18. Deflagration with shock precompression, $U = 0$.

of the precompression wave so much that its speed equals that of a possible detonation, one may envision a continuous transition from deflagration to detonation processes.

In view of the greater indeterminacy of deflagration processes in comparison to those of detonation, new physical conditions are required to determine the former.

1.3 INTERACTIONS IN ONE DIMENSION

1.3.1 Description of the Problem

The reflection of a straight shock wave on a rigid wall, the head-on collision of two straight shocks and the overtaking of one shock by another, were investigated mathematically⁵ under Division 2 of the NDRC. From such collisions, not only shocks but also rarefaction waves and contact discontinuities can result. To obtain a complete understanding of possible phenomena involving discontinuities in a linear motion of a compressible gas, it was therefore appropriate, in the analysis^{1,3} by the Applied Mathematics Panel to consider shocks, rarefaction waves, and contact discontinuities on an equal basis, in other words, to study the results of the interaction of any two or more of them.

Riemann²⁹ in a classical paper discussed a problem closely related to the present one. Consider an infinite linear column of gas along the x axis, divided at time $t = 0$, by the point $x = 0$ into two constant states l and r (left and right). It is required to determine the subsequent state of the gas. Riemann concluded that the initial discontinuity may resolve into either two shocks moving apart or two centered rarefaction waves or one shock and one rarefaction wave. However, Riemann's theory was incomplete in that no contact surfaces were postulated. This occurred because only two shock conditions were used which could be satisfied without further assumptions.

The basic situation in the interactions problem, as here discussed, is the following. Three constant states l , m , r are given, separated by two waves R (rarefaction), S (shock), or by a contact surface T . These separating phenomena move so as to intersect, destroying m . It is assumed that (after a period of penetration) a terminal state l, m_*, r results, where l and r are the same as before, and where m_* is the new middle zone of constant pressure p_* and velocity u_* , while the density ρ_* is permitted to vary discontinuously or continuously in m_* . It is further assumed that m_* is separated from l by a backward wave (moving from right to left) and from r by a

CONFIDENTIAL

forward wave. The problem solved³ was the determination of m_* and of the two waves connecting m_* with l and r . In certain cases, the intermediate state m_* may fail to exist. When it does exist, and when one of the two resulting waves is a shock, then two different values, ρ_{l*} and ρ_{r*} , can be found for the density in m_* , according as this density is determined by a transition from the left or from the right. These two values can be reconciled by the presence in m_* of a contact discontinuity whose motion or direction in the (x,t) plane is given by the velocity u_* .

The initial situation can be characterized by five independent quantities. If the three states are separated by shock or rarefaction waves, the pressures p_l , p_m , p_r and the values of (u,ρ) for one of the three states are used. The other quantities u and ρ are determined by certain transition conditions described below. Also, the velocities of the separating shocks or the velocities of both ends of any resulting rarefaction waves are determined. The only restriction on the five initial quantities is that they lead to a collision, that is, that m must shrink to zero. (For a discontinuity, not p but ρ is to be prescribed on either side.)

The terminal middle state is determined from the states l and r and the condition that the transition l_{m*} be backward and r_{m*} be forward. The state m_* is determined uniquely, and the type of the resulting new waves depends, as in Riemann's problem, on

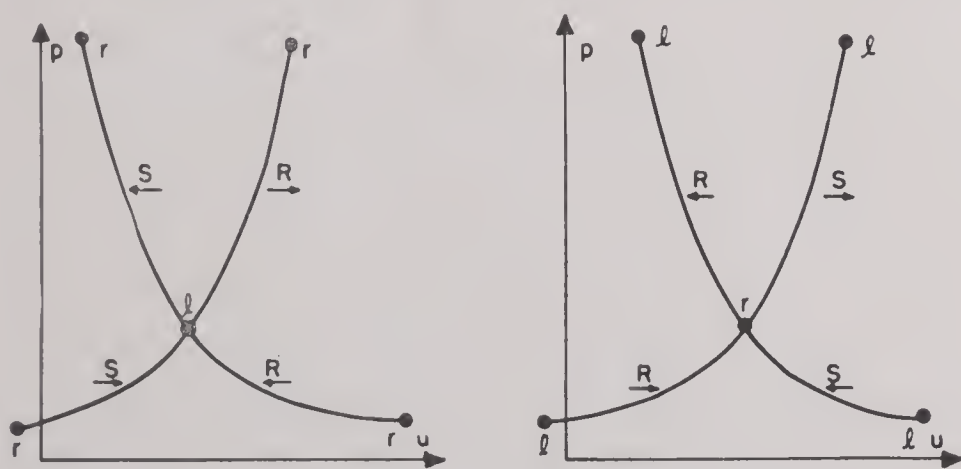


FIGURE 19. The states on the left and right sides of shock and rarefaction waves.

ρ_l , ρ_r , and the relative positions of the points $l : (u_l, p_l)$ and $r : (u_r, p_r)$ in the (u,p) diagram. The general analysis can be characterized as an algebraic discussion of the transition relation for shock fronts and rarefaction waves, guided by a graphical representation. Most of the graphical work is accomplished with the aid of representation in a (p,u) plane. Figure 19 illustrates the method, explained in

Section 1.3.2, of representing two constant states between which shock and rarefaction waves take place.

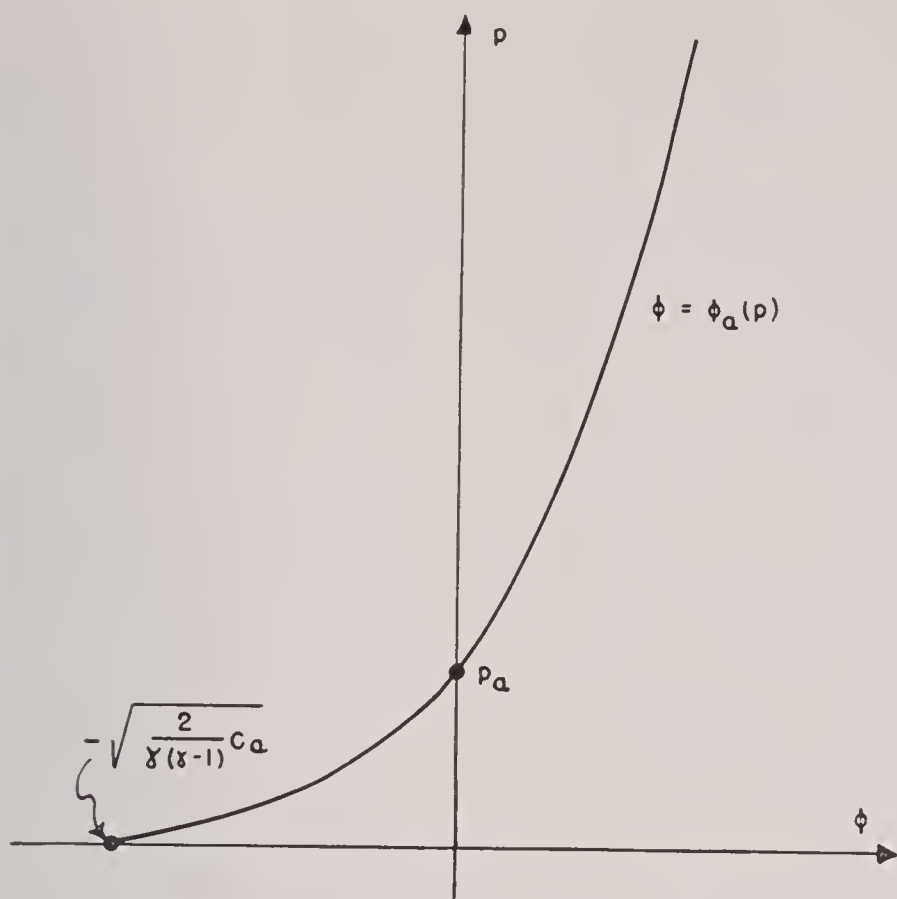
1.3.2

Penetration

When rarefaction waves are involved in interactions, a process of penetration occurs before two waves emerge and move apart. When a shock and a rarefaction wave collide, the shock enters the zone of rarefaction and continuously changes velocity and intensity until it reaches the constant terminal state. During the penetration process, the particles which cross the shock suffer different changes in density and entropy. They thus form a *contact zone*, that is, a zone in which density varies continuously instead of undergoing a discontinuous change across a contact surface. The assumption of a constant pressure and velocity in the terminal state implies that all particles in the contact zone move with the same velocity, a situation compatible with the equations of motion of gas dynamics if account be taken of the possibility of a nonconstant entropy.

The decision whether or not such a terminal state with a stationary contact zone can actually result from the penetration process should be based on a complete analysis of the gas-dynamical differential equations of the process. Such a complete analysis has not, as yet, been carried through. It has been proved, for a weak incoming rarefaction wave, that the ensuing contact zone is actually stationary in the first approximation. In the second approximation, however, it widens like a rarefaction zone.

In general, the penetration problem would require solution of nontrivial boundary value problems for the differential equations of flow, in fact, the more general differential system is needed in which non-uniform shocks and variable entropy are involved. The only case on which mathematical work has been done is that of two colliding rarefaction waves. The problem depends on a simpler system of equations for which the solution goes back to Riemann's work. To effect a numerical solution of the initial value problem methods of finite differences can be employed. In the studies here reviewed,^{1,3} the assumption of a simple terminal state, as described in the Section 1.3.1, obviates the necessity of analyzing the process of penetration, which is the integration of relevant differential equations of gas dynamics.

FIGURE 20. Graph of the function $\phi_a(p)$.

1.3.3 Transition Relations in the (u, p) Diagram for S , R , and T

A shock or rarefaction wave is referred to as forward or backward, according as particles cross it from right to left, that is, in the negative x direction, or left to right, respectively.

The following notation is employed:

$\underline{R}, \underline{R}$ Forward and backward rarefaction waves.

$\underline{S}, \underline{S}$ Forward and backward shocks.

It may be noted that, when algebraic signs are considered, $u_r < u_l$ for shocks and $u_r > u_l$ for rarefaction waves, regardless of the direction in which these waves face; also that the quotient $(p_r - p_l)/(u_r - u_l)$ is always positive for forward waves and negative for backward waves.

Contact surfaces are denoted by T and are distinguished as follows according to which side of the discontinuity has the greater density.

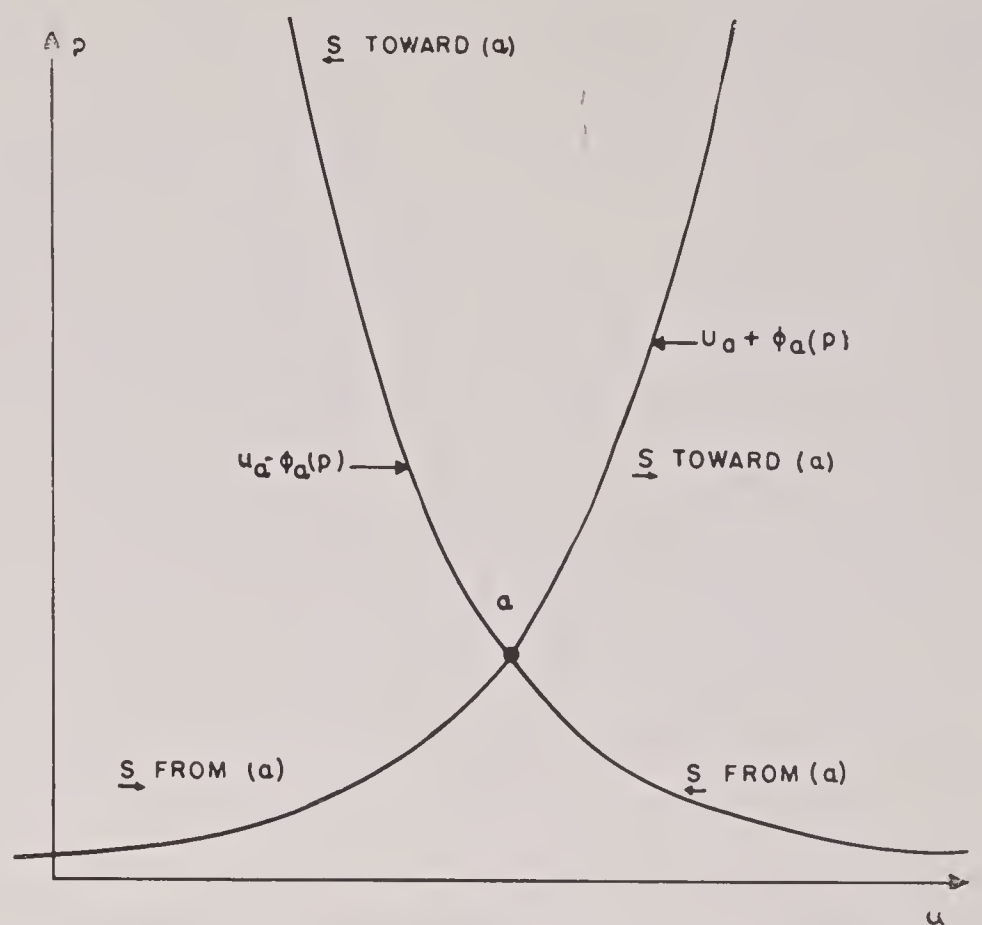
$$T_{<} \quad \text{if} \quad \rho_l < \rho_r$$

$$T_{>} \quad \text{if} \quad \rho_l > \rho_r.$$

These density inequalities imply the following relationships among absolute temperatures Θ , entropy η , and speed of sound c , all of which depend jointly on pressure and density:

$$\begin{aligned} (T_{<}) \quad c_l &> c_r, \quad \Theta_l > \Theta_r, \quad \eta_l > \eta_r \\ (T_{>}) \quad c_l &< c_r, \quad \Theta_l < \Theta_r, \quad \eta_l < \eta_r \end{aligned} \quad (25)$$

An ideal gas is assumed with the adiabatic exponent γ such that $pp^{-\gamma} = p_0\rho_0^{-\gamma}$ is the equation of state for adiabatic changes. If a state (a) of the gas,

FIGURE 21. Locus of all states which can be connected with a given state (a) through shock waves \underline{S} and \underline{S} facing toward and away from a .

characterized by values u_a , p_a , and $\rho_a = 1/\tau_a$, is connected by transition through a shock with a state (b) , characterized by $(u_b, p_b, \rho_b = 1/\tau_b)$ then the following relations can be readily deduced from relations (i), (ii), and (iii**) of Section 1.2.3, along with the definition of μ in equation (10).

$$\frac{p_b - p_a}{u_b - u_a} = m = \pm \sqrt{\frac{p_b - p_a}{\tau_a - \tau_b}} = \pm \sqrt{\frac{p_b + \mu^2 p_a}{(1 - \mu^2)\tau_a}}$$

where

$$\mu^2 = \frac{\gamma - 1}{\gamma + 1}.$$

Hence

$$u_b = u_a \pm \phi_a(p_b) \quad (26)$$

where

$$\phi_a(p) = (p - p_a) \sqrt{\frac{(1 - \mu^2)\tau_a}{p + \mu^2 p_a}}. \quad (27)$$

The plus sign in (26) is used for shock fronts \underline{S} and the minus sign for \underline{S} . The function ϕ_a depends on the parameters p_a and τ_a (or ρ_a) assigned to the state (a) . It represents the difference of the normal particle velocities across a shock line as a function of the pressure p on one side of the line when p and ρ are given on the other side. Therefore,

$$\phi_a(p_b) = -\phi_b(p_a). \quad (28)$$

It may be noted that $\phi_a(p)$ increases monotonically, becoming infinite with p ; also that the derivative,

$\phi_a'(p)$ approaches zero as p becomes infinite. The graph of ϕ_a (Figure 20) touches the ϕ axis at

$$\phi_a(0) = -\left(\frac{2}{\gamma(\gamma-1)}\right)^{\frac{1}{2}} c_a \quad (29)$$

where c_a is the sound speed in region a .

The curves (26) are shown graphically in Figure 21. They will be referred to as the \underline{S} and the \underline{S} curves through a . In a diagram, the \underline{S} and \underline{S} curves are distinguishable as having positive and negative slopes, respectively. It may be verified that the indications in Figure 21 show correctly the various branches of the curves corresponding to shock waves facing toward or away from (a) by considering that $u_r < u_l$ and that the pressure behind a shock wave exceeds that in front.

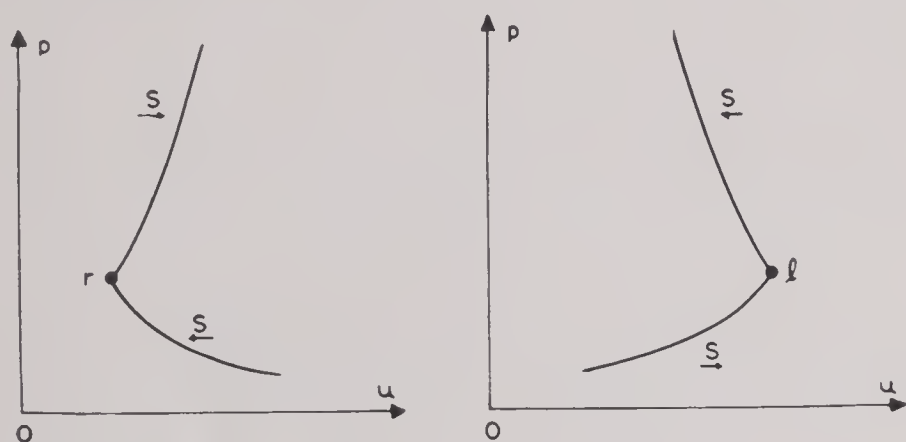


FIGURE 22. Left. Locus of possible states l on left of a shock wave if state r on right is prescribed. Right. Locus of possible states r on right of a shock wave if state l on left is prescribed.

In Figure 22 the loci of all states which can be connected by shock waves \underline{S} and \underline{S} with a given state (r) to the right or (l) to the left are indicated.

Finally, the shock velocity U_{rl} is given by

$$U_{rl} = u_r + \tau_r \frac{[p]}{[u]} = u_l + \tau_l \frac{[p]}{[u]} \quad (30)$$

where

$$[p] = p_l - p_r, \quad [u] = u_l - u_r.$$

Thus, if $S = \underline{S}$, then $[p]/[u] > 0$ and hence $U_{rl} > u_l > u_r$. On the other hand, if $S = \underline{S}$, then $U_{rl} < u_l < u_r$, since $[p]/[u] < 0$.

For particles moving across a rarefaction wave, there are adiabatic changes of state and hence

$$\frac{\rho_a}{\rho_b} = \left(\frac{p_a}{p_b}\right)^{1/\gamma}. \quad (31)$$

For rarefaction waves, an analog of (26) follows by integration of the differential equations of motion. With the notation $\eta = \frac{1}{2}(1 - \gamma^{-1}) = (\gamma - 1)/2\gamma$, the following equation holds.

$$u_b = u_a \pm \psi_a(p_b) \quad (32)$$

where

$$\psi_a(p) = \frac{\sqrt{1 - \mu^4}}{\mu^2} \tau_a^{\frac{1}{2}} p_a^{1/2\gamma} (p^\eta - p_a^\eta) \quad (33)$$

the plus sign in (34) being used for forward rarefaction waves \underline{R} and the minus sign for backward ones \underline{R} . The function ψ_a depends on the parameters p_a and $\tau_a^{\frac{1}{2}} p_a^{1/2\gamma}$ (essentially the entropy). By analogy with (30),

$$\psi_a(p_b) = -\psi_b(p_a). \quad (34)$$

It may be noted that $\psi_a(p)$ and $\psi_a'(p)$ are monotonic, and that $\psi_a(p)$ becomes infinite with p , while

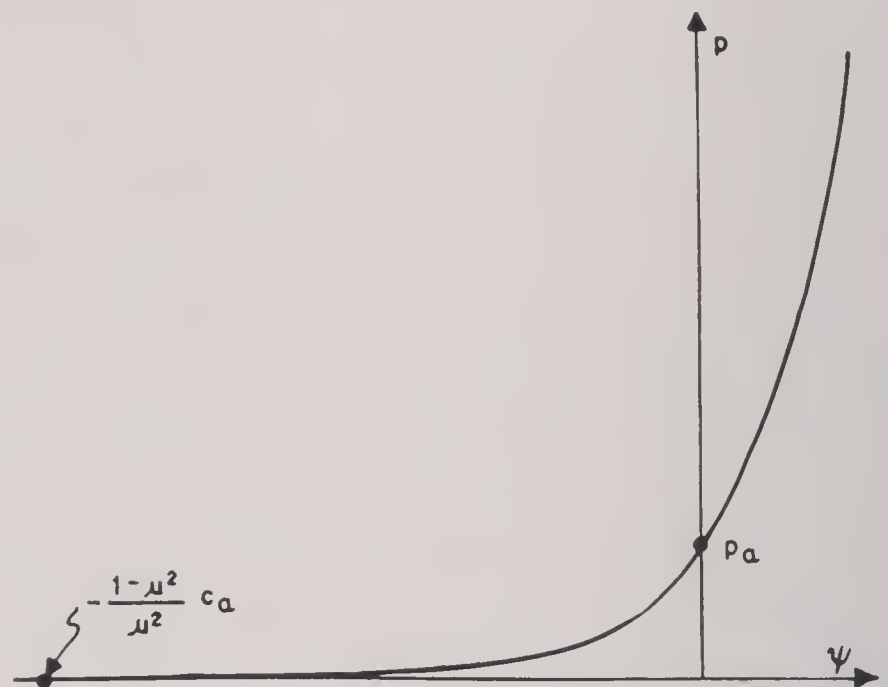


FIGURE 23. Graph of the function $\psi_a(p)$.

$\psi_a'(p)$ approaches zero as p becomes infinite. The graph of ψ_a (Figure 23) touches the ψ axis tangentially at

$$\psi_a(0) = -\frac{\sqrt{1 - \mu^4}}{\mu^2} \sqrt{\tau_a p_a} = -\frac{1 - \mu^2}{\mu^2} c_a. \quad (35)$$

The curves of equation (32) are shown graphically in Figure 24. They will be referred to as the \underline{R} and the \underline{R} curves through (a) . In a figure, \underline{R} and \underline{R} are distinguishable from one another as having positive and negative slopes respectively. This figure, analogous to Figure 21, shows the possible states (b) which can be connected with (a) by rarefaction waves facing toward or away from (a) .

Figure 25 analogous to Figure 22, shows the loci of all states which can be connected with a given state (l) or (r) , on the left or right of the wave, respectively, by rarefaction waves \underline{R} or \underline{R} . For a contact discontinuity, transition relations in the (u, p) plane between the values of velocity and pressure are trivial, since across such a discontinuity, these quantities remain continuous, while only the density or entropy suffers the discontinuity.

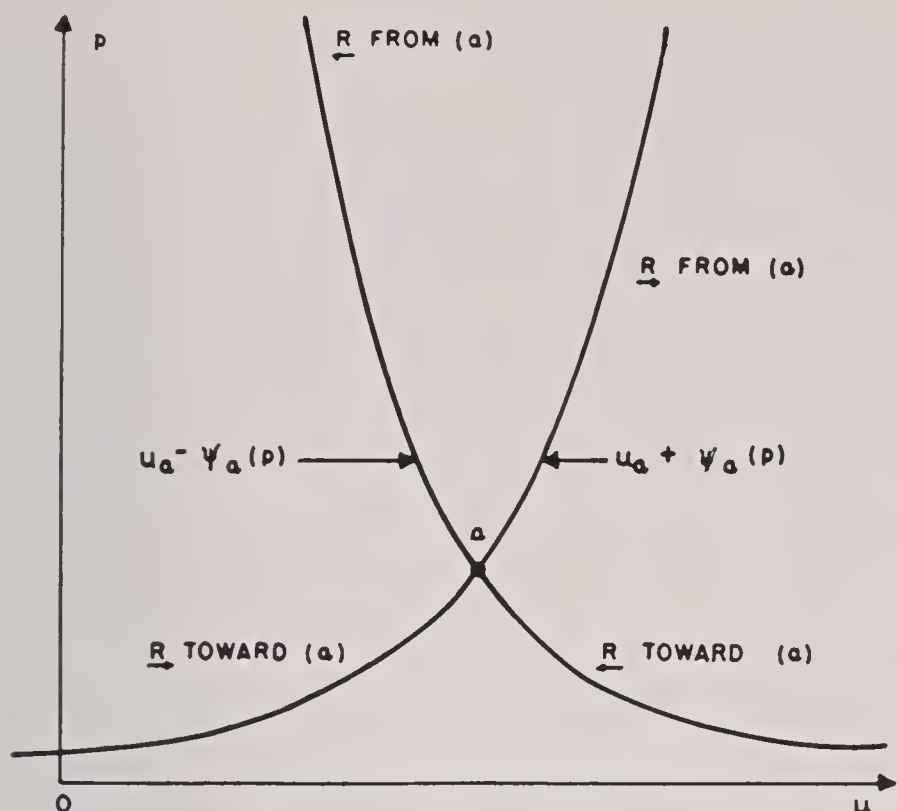


FIGURE 24. Locus of all states which can be connected with a given state (a) through rarefaction waves \underline{R} and \overline{R} facing toward and away from a .

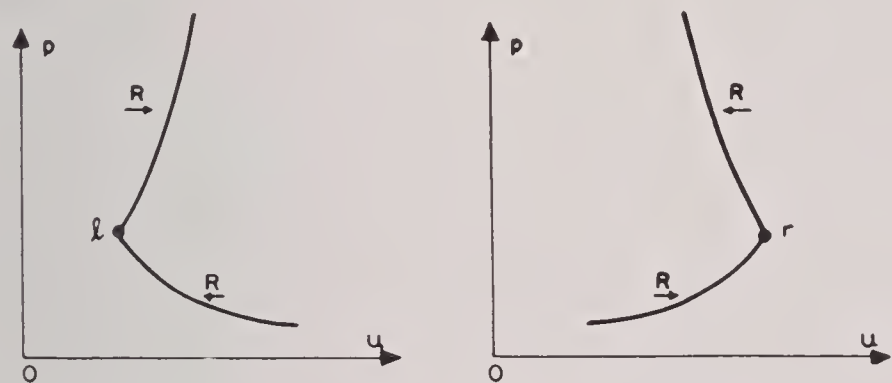


FIGURE 25. Left. Locus of possible states r on right of a rarefaction wave if state l on left is prescribed. Right. Locus of possible states l on left of a rarefaction wave if state r on right is prescribed.

1.3.4 A Diagrammatic Method

All states attainable from a given state (r) by a forward wave are represented in the (p, u) plane by the curve Γ_r as follows (Figure 26).

$$\Gamma_r \begin{cases} u = u_r + \phi_r(p), & p > p_r, \underline{S} \\ u = u_r + \psi_r(p), & p < p_r, \overline{R}. \end{cases} \quad (36)$$

Similarly all points representing states connected with (l) by a backward wave are on a curve (Figure 26).

$$\Gamma_l \begin{cases} u = u_l - \phi_l(p), & p > p_l, \underline{S} \\ u = u_l - \psi_l(p), & p < p_l, \overline{R}. \end{cases} \quad (37)$$

If (l) and (r) are known, let the two Γ curves be drawn through them. Their intersection determines (m_*) and the waves from (m_*) to (l) and (r). Such a graphical construction needs to be supplemented by calculations, if greater precision is needed.

The curves Γ_l and Γ_r are referred to as *left* and *right transition curves*, respectively. Γ_l consists of an upper branch of an \underline{S} curve joined at (l) with a lower branch of an \overline{R} curve, and an analogous de-

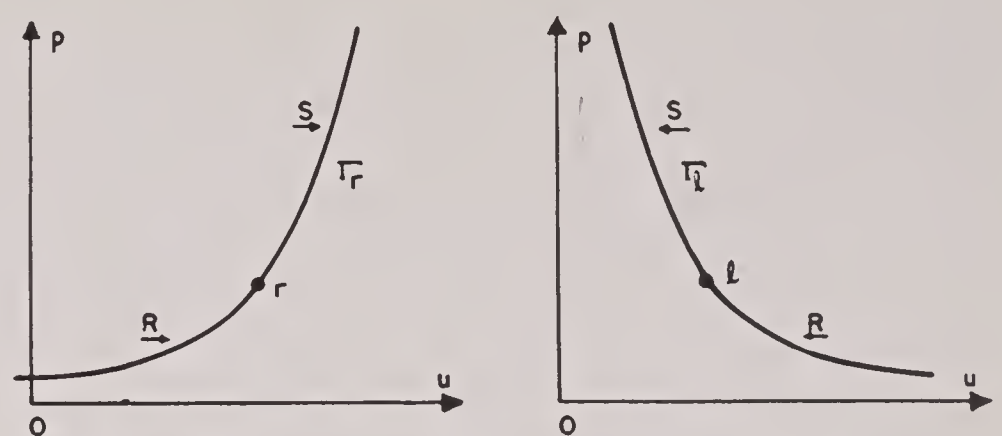


FIGURE 26. Left. Curve Γ_r representing all states which can be reached from a given state r on the right of forward waves \underline{S} or \overline{R} . Right. Curve Γ_l representing all states which can be reached from a given state l on the left of backward waves \underline{S} or \overline{R} .

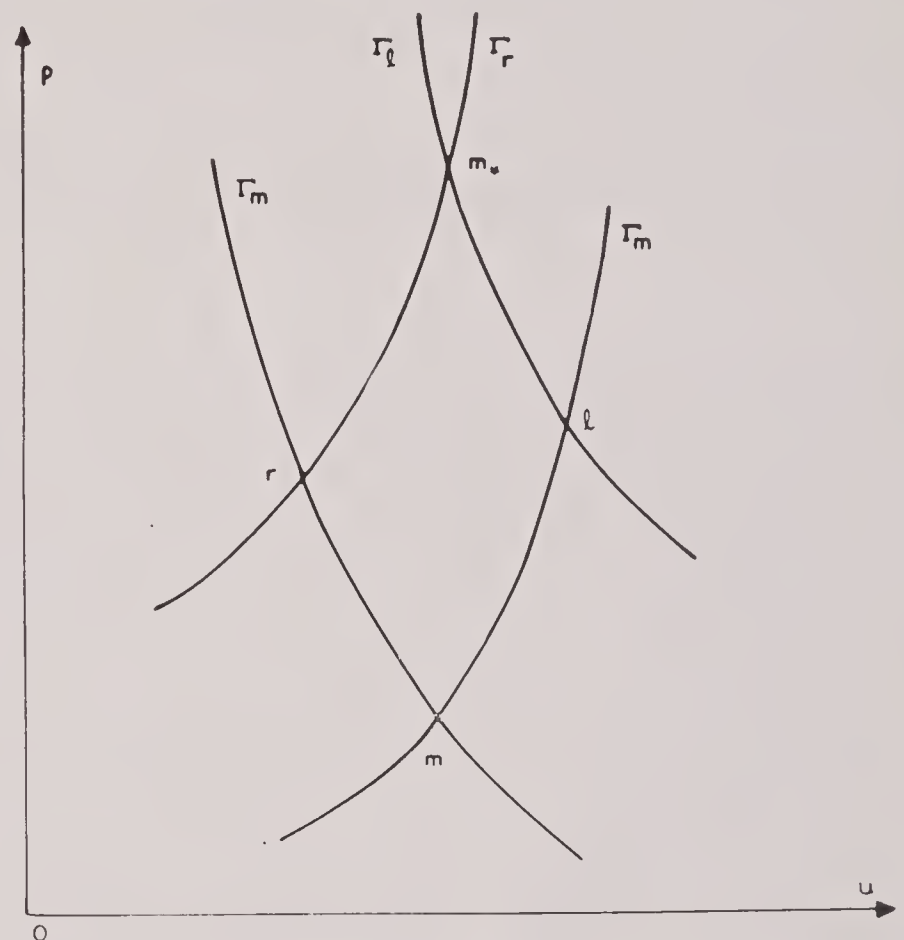


FIGURE 27. Graphical analysis of head-on collision of two shock waves.

scription holds for Γ_r . The smoothness with which these branches fit together is indicated by

$$\phi_a'(p_a) = \psi_a'(p_a) \quad (38)$$

and

$$\phi_a''(p_a) = \psi_a''(p_a). \quad (39)$$

The diagrammatic method described above always yields a result, in other words, the transition curves always have a unique intersection (m_*) save when

$$u_r - \left(\frac{1 - \mu^2}{\mu^2} \right) c_r > u_l + \left(\frac{1 - \mu^2}{\mu^2} \right) c_l, \quad (40)$$

in which case Γ_l and Γ_r reach the u axis without intersecting. In this exceptional case, no intermediate state (m_*) results and penetration continues indefinitely. When there is a regular intersection, two

different values, ρ_{l*} and ρ_{r*} are found for ρ_* in m_* . This is explained, as stated above, by the presence of a contact discontinuity, whose motion, or direction in the (x,t) plane, is given by the velocity u_* . One advantage of considering p and u as independent variables is that such contact discontinuities are obtained as a by-product and need not be introduced from the outset.

1.3.5 Illustration of the Method

Assume an S from l and an S from r move toward each other. Then

$$p_m < p_l \quad \text{and} \quad p_m < p_r. \quad (41)$$

For two shocks moving toward one another, this is the only restriction on the initial data. In Figure 27, the relative positions of the states l, m, r are depicted. It will be assumed that

$$p_l > p_r. \quad (42)$$

The assumption involves no essential loss of generality, since a contrary case would involve only the interchange of l and r . The transition curves, Γ_l and Γ_r , through l and r intersect in their upper branches, from which it follows that the two new transitions are shocks. Symbolically,

$$\underline{S} \underline{S} \longrightarrow \underline{S} T \underline{S}, \quad (43)$$

where T stands for a contact discontinuity in the middle region, m_* .

After u_* , p_* are determined (Figure 29), the shock velocities U_{l*} and U_{r*} can be obtained, and also the two densities, ρ_* and ρ_{r*} . The following inequality holds:

$$u_* > u_m \quad \text{if} \quad p_l > p_r. \quad (44)$$

That is, the stronger shock (from the left) will impart to the middle zone a velocity in its own direction. Other relations imply that shocks, after penetrating one another, have weakened one another, and that in the middle region, the shock reverses the relative magnitudes of the densities; that is

$$\rho_{l*} < \rho_{r*} \quad \text{if} \quad p_l > p_r. \quad (45)$$

Hence there is always a contact discontinuity in m_* save when the two exterior states are equal — when the initial situation is symmetrical.

1.3.6 Summary of Results

The method just illustrated was applied^{1,3} to obtain results as indicated below, using the same sort of symbolism as in equation (43).

Collision of Two Shocks: $\underline{S} \underline{S} \longrightarrow \underline{S} T \underline{S}$ (see Section 1.3.5).

Collision of Two R Waves: $\underline{R} \underline{R} \longrightarrow \underline{R} \underline{R}$ In this case, if the cavitation condition equation (40) holds, penetration continues indefinitely.

Collision of an S and an R: $\underline{S} \underline{R} \longrightarrow \underline{R} (TT) \underline{S}$, where (TT) signifies an intervening contact zone.

Interaction of S with Contact Surface:

$$\underline{S} T_{<} \longrightarrow \underline{S} T_{<} \underline{S} \quad \text{and} \quad \underline{S} T_{>} \longrightarrow \underline{R} T_{>} \underline{S}$$

Interaction of R with Contact Surface:

$$\underline{R} T_{<} \longrightarrow \underline{R} T_{<} \underline{R}$$

The case $\underline{R} T_{>}$ gives rise to complications³ which preclude a simple statement of results.

Overtaking of Shock by Shock: $\underline{S} \underline{S} \longrightarrow \underline{S} T \underline{S}$ if $\gamma \leq 5/3$; if $\gamma > 5/3$, then either $\underline{S} \underline{S} \longrightarrow \underline{R} T \underline{S}$ or $\underline{S} \underline{S} \longrightarrow \underline{S} T \underline{S}$ depending on initial pressure ratio.

Overtaking of Rarefaction by Shock: If oncoming shock \underline{S} is strong, then $\underline{S} \underline{R} \longrightarrow \underline{S} (TT) \underline{S}$; if \underline{S} is weak, $\underline{S} \underline{R} \longrightarrow \underline{S} (TT) \underline{R}$; and, in an intermediate case, $\underline{S} \underline{R} \longrightarrow \underline{S} (TT)$.

Overtaking of Shock by Rarefaction: All four combinations of forward and backward waves can result.

Overtaking of Rarefaction by Rarefaction: This cannot occur since two rarefaction waves moving in the same direction remain separated by a zone of constant length.

1.4 GEOMETRIC REPRESENTATIONS FOR STATIONARY SHOCK TRANSITIONS

Considerable progress can be made in the analysis and understanding of shocks, both linear and two-dimensional, by the following type of geometric interpretation. The work of the Panel^{1,6} in this connection consisted in further development of methods already in the literature. These geometric devices apply to the algebraic relations connecting the states adjacent to the two sides of a shock discontinuity. Applications are made to regular and Mach reflections.

1.4.1 The One-Dimensional Case

The basic diagrams are in the (u,p) plane and represent curves of the form $p = p(u)$, where u is selected as the independent variable. The physical situation is that of a fluid in a steady state filling a straight tube along the x axis. The limit speed \hat{q} [see equation (5)] is kept fixed throughout the entire discussion, but the entropy η is permitted to vary as a parameter. This does not imply that the

hypothesis of isentropy is abandoned, but rather that various isentropic situations will be considered distinguished from one another by the assigned values of η . To emphasize the role played by η , the equations for p in terms of u can be written as follows

$$p = p(u) = p(u, \eta) \quad (46)$$

where it is to be understood that each individual curve is obtained by assigning a particular value to η . Figure 28 represents the resulting family of curves.

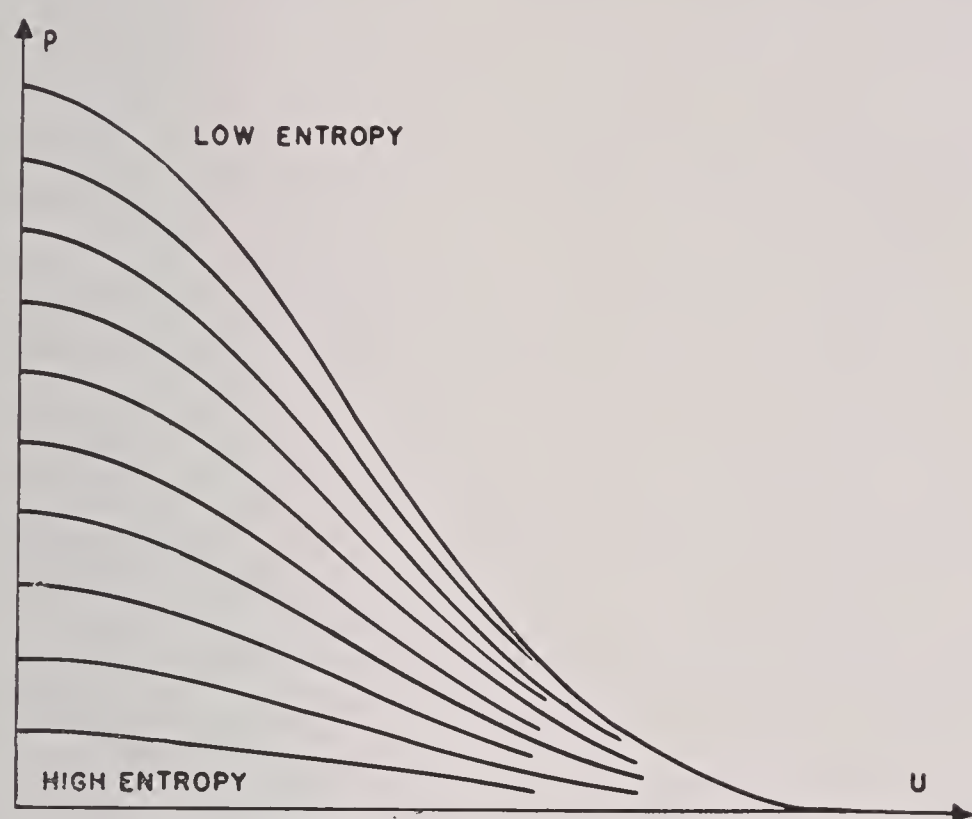


FIGURE 28. Pressure as a function of flow velocity u for the same limit speed and various constant values of the entropy.

In these curves, the critical velocity c_* of equation (9) plays a significant part, for when the velocity is subsonic, that is when u is between $-c_*$ and $+c_*$, all the curves are concave down. On the other hand, for supersonic velocities, they are concave up. Hence each has a point of inflection where $u = \pm c_*$. The value c_* is thus seen to be independent of the entropy. It depends, as revealed in equation (9) and (10), only on the adiabatic constant γ of the gas and on the value of \hat{q} (or of the Bernoulli constant $i = \frac{1}{2}\hat{q}^2 = \frac{1}{2}q^2 + i$).

It can be shown that $\partial p / \partial u = -\rho u$. Geometrically, this means that negative slope of the curve $p = p(u)$ represents the mass crossing a unit cross section per unit time. The intercept on the p axis of the tangent line at a point of the curve $p = p(u)$ has the value $p + \rho u^2$ (the sum of the pressure and momentum crossing a unit area per unit time) a quantity entering into the second shock condition, equation (ii) of Section 1.2.3 (see Figure 29). The functions $p = p(u)$ for different entropies differ only by a constant factor. As η decreases from the idealized

value $\eta = \text{infinity}$, corresponding to $p = 0$, to low values of entropy, the curves sweep out a region of the (u, p) plane. No two curves intersect. To represent a shock transition graphically, suppose the shock front faces the left side (indicated by subscript

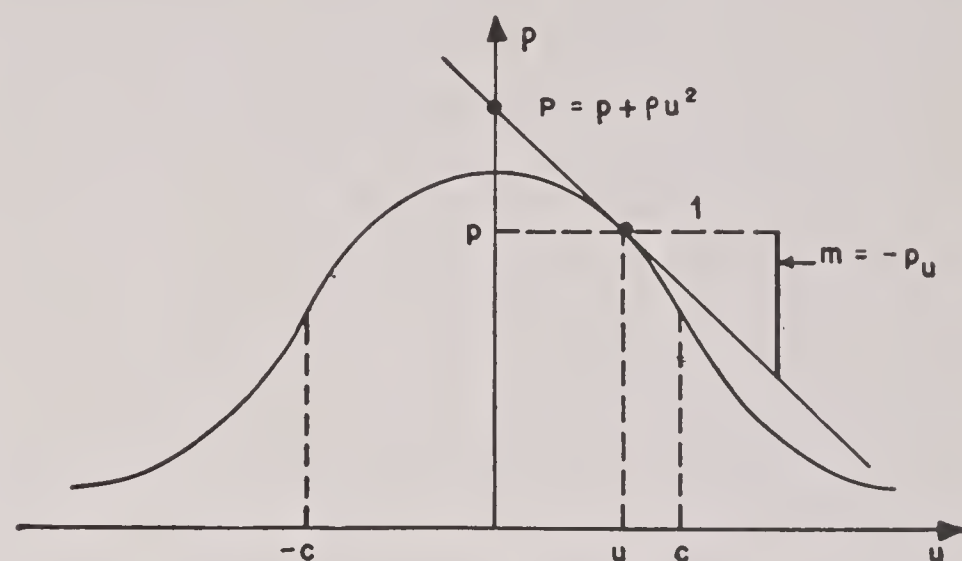


FIGURE 29. Graphical representation of $m = \rho u = -p_u$ and $P = p + \rho u^2$.

0), so that $u_0 > 0$. The two points in the (p, u) plane representing the two sides of the shock can be located on two curves $p = p(u)$ having the same value of c_* but differing in density. The relationship $u_0 \rho_0 = u_1 \rho_1$, where the subscript 1 goes with the right side, signifies geometrically that the tangent lines to the two $p = p(u)$ curves at the points 0 and 1 are parallel. The shock relation $p_0 + \rho_0 u_0^2 = p_1 + \rho_1 u_1^2$ means that these lines have the same intercepts on the p

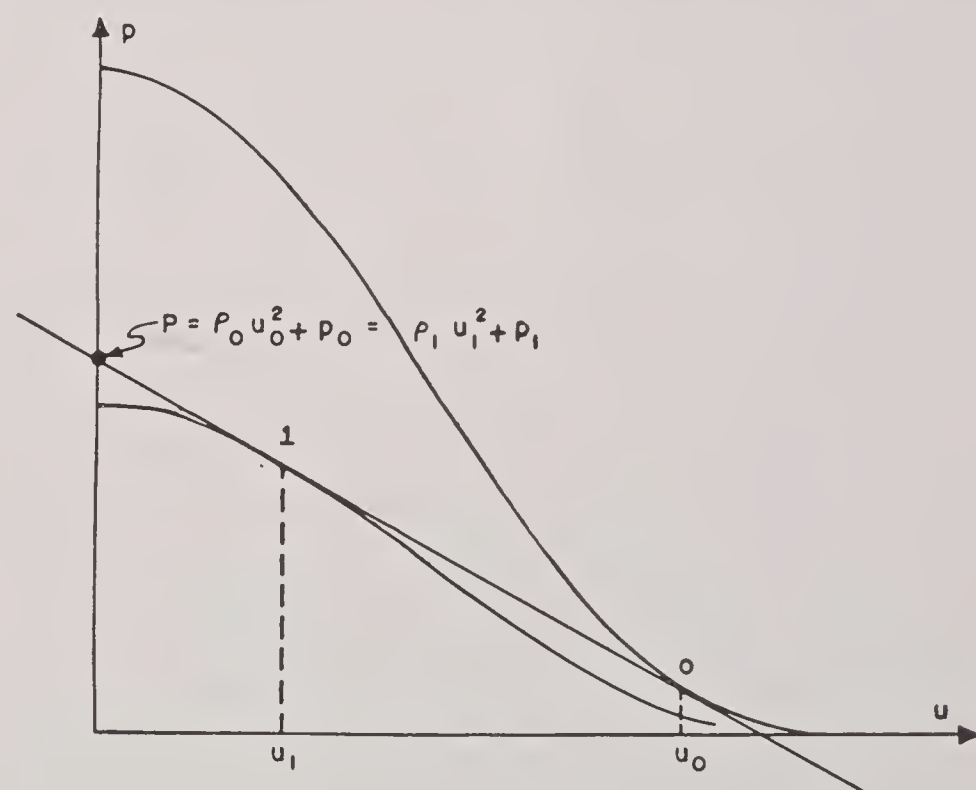


FIGURE 30. Representation of shock transition in (p, u) diagram.

axis. Hence the two lines coincide. But this is readily seen to imply a situation like that illustrated in Figure 30. Thus, $u_0 > c_*$ and $u_1 < c_*$; $p_1(u) > p_0(u)$, and $\eta_1 < \eta_0$. For ideal gases, $u_0 u_1 = c_*$ as brought out in equation (iii)_P of Section 1.2.3.

1.4.2 The Two-Dimensional Case

PRESSURE SURFACES

Two-dimensional oblique shocks can be similarly interpreted graphically. This requires a three-dimensional (p, u, v) space, where (u, v) are velocity components. A pressure surface, $p = p(u, v)$ is utilized, representing states corresponding to prescribed values of the entropy and the Bernoulli constant $i_0 = \frac{1}{2}\hat{q}^2 = i + \frac{1}{2}q^2$, where $q^2 = u^2 + v^2$. Thus surface is a surface of revolution generated by one of the curves $p = p(u)$ of the preceding section (Figure 30) revolved about the p axis. Hence the subsonic states fill the interior, $q < c_*$, of a circle of radius c_* , and the supersonic states are outside this circle, $c_*^2 < q^2 < \hat{q}^2$ (see Figure 31). Curvature is positive

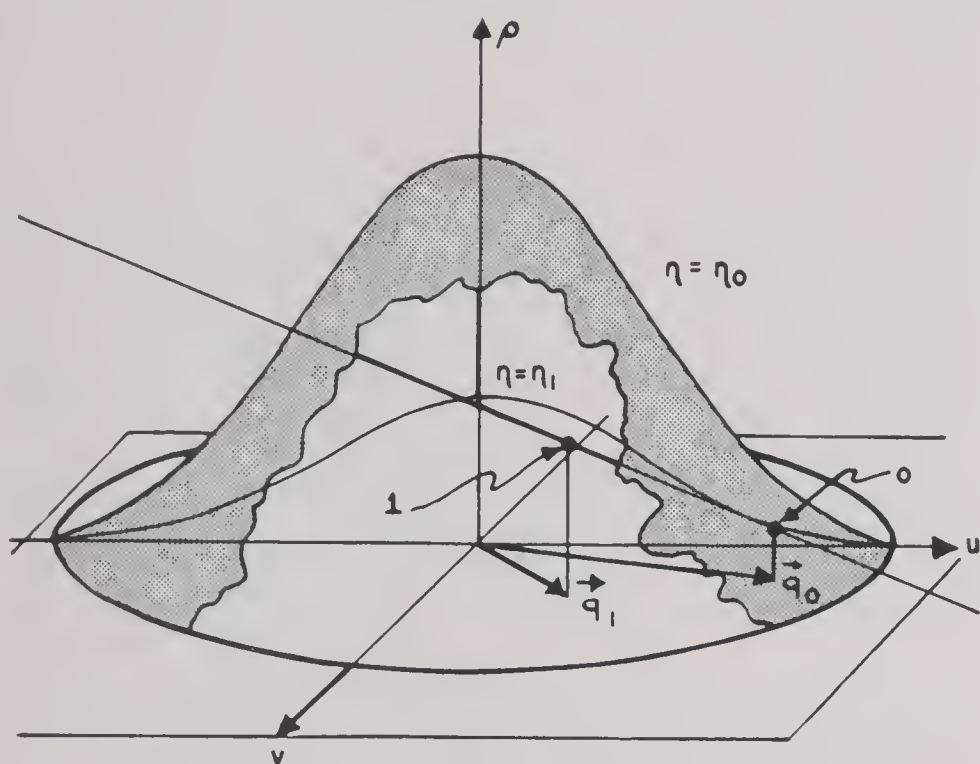


FIGURE 31. Representation of shock transition by (u, v, p) surfaces.

for subsonic and negative for supersonic velocities. The subsonic and supersonic parts of the surface may be called the *dome* and *rim*, respectively, of the surface. As η decreases from the idealized value infinity to low values of entropy, the corresponding pressure surface rises steadily from coincidence with the (u, v) plane and sweeps out a region of (u, v, p) space.

If two states 0 and 1 are separated by an oblique shock, the corresponding points in (p, u, v) space will be on different pressure surfaces with the same c_* but different entropies. In a manner analogous to the one-dimensional case, it can be seen that the straight line through these two points is a common tangent line to the two pressure surfaces (see Figure 31).

The general problem of characterizing all states which can be connected with a given state 0 by an

oblique shock has the following geometric interpretation. All the desired states lie on the tangent plane T_0 to $p = p(u, v)$ at the point 0. Consider a surface $p = p(u, v)$ of any given entropy. If this surface intersects T_0 in a curve which has two tangent lines through 0, then the points of tangency of these lines represent the desired states 1 of the given entropy which can be connected with 0 by a shock.

An investigation of the locus of all such states 1, as the entropy varies, is of obvious interest and importance. Assume, first, that state 0 is supersonic, and let the pressure surfaces be considered for decreasing entropy η , commencing with the case where η is infinite and the pressure surface coincides with the (u, v) plane.

As η decreases, the dome of the corresponding pressure surface rises, touches, and crosses the fixed tangent plane T_0 . The state for which the dome of the varying pressure surface just touches T_0 corresponds to a *normal shock*. After the dome has crossed T_0 , the intersection is an oval, and there are two tangent lines, yielding two states 1 which correspond to *two possible oblique shocks*. This condition obtains until the decreasing entropy reaches the value, η_0 , corresponding to the given state 0. The two points 1 then move into coincidence with 0. Up to this point, the state 0 is on the front side and the state 1 on the back side of the shock. As η passes through the value η_0 , the situation is reversed. The state 1 then acquires greater speed than the state 0. As η decreases still farther, the speed of state 1 approaches the limit \hat{q} .

If 0 now be assumed subsonic, a similar discussion can be carried out, in which the state 0 is, of course, always on the back of the shock.

THE SHOCK POLAR

Let the locus in (p, u, v) space of all points 1 which can be connected with a given state 0 by a shock be projected vertically onto the (u, v) plane. The resulting locus is called a *shock polar*.

A shock polar can also be directly derived from the analytical shock conditions instead of by the projection just described. The locus (Figure 32) is a folium of Descartes (sometimes called a *strophoid* in the literature). In obtaining it, oblique stationary shocks are considered in an (x, y) plane with a straight shock line S separating two constant states 0 and 1. The gas is assumed polytropic. The shock direction can be characterized by the angle between the shock line S and the direction of the oncoming flow.

The shock polar has a double or isolated point corresponding to the velocity of state 0 and has an asymptote lying outside the limit circle $u^2 + v^2 = \hat{q}^2$. Only that part of the shock polar in the limit circle ($u^2 + v^2 = \hat{q}^2$) has physical significance as representing those states 1 which can be connected with the fixed state 0 by shock.

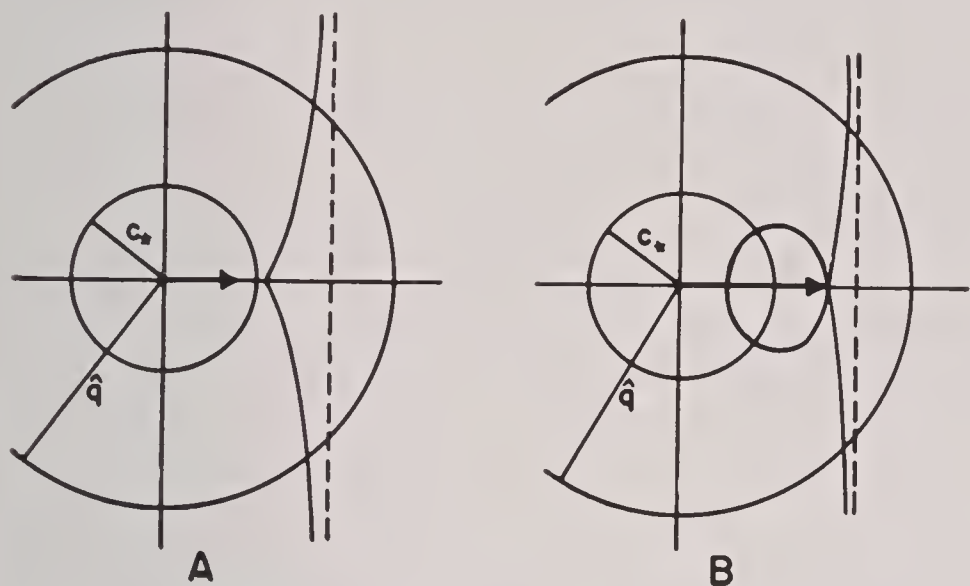


FIGURE 32. A. Shock polar for $q_0 < c_*$. B. Shock polar for $q_0 > c_*$.

DISCUSSION OF OBLIQUE SHOCKS BY MEANS OF THE SHOCK POLAR

The shock polar, dependent on q_0 and c_* as parameters, can be used to construct oblique shocks. In Figure 33 is shown a shock polar with double point

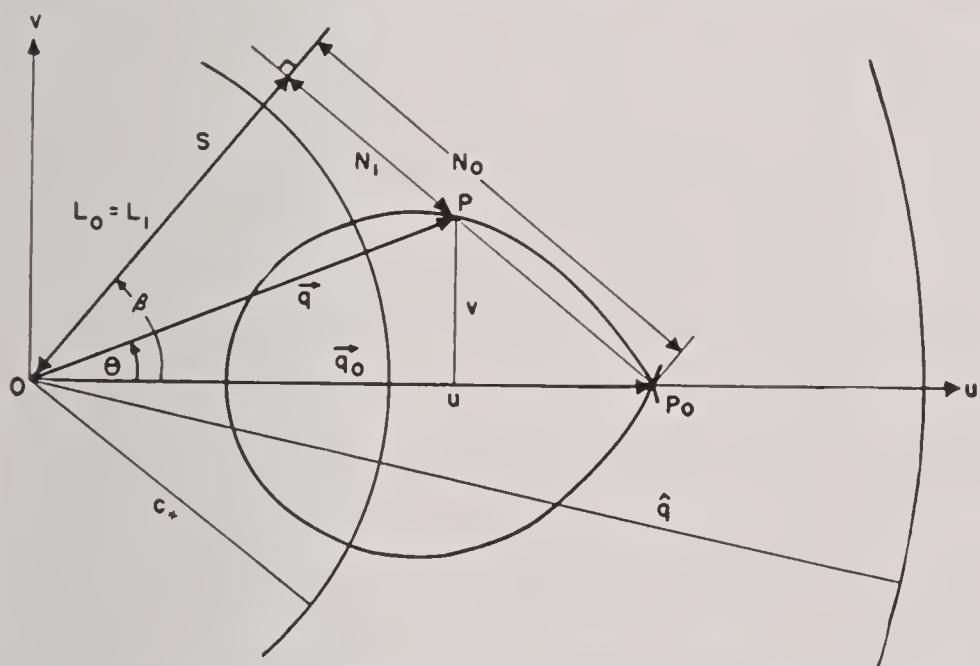


FIGURE 33. Construction of shock with shock polar in (u, v) plane.

at P_0 , the end point of the vector \mathbf{q}_0 . If P is on the shock polar, the vector \mathbf{OP} represents the velocity behind the shock front. The angle between OP and the u axis is the angle through which the shock turns the incoming flow. The direction of the shock line S , making the angle β with the incoming flow, is perpendicular to the line connecting the double point P_0 with the point P . The components $L_0 = L_1$, N_0 , N_1

of \mathbf{q}_0 and \mathbf{q} with respect to the shock line can be read from the diagram as indicated.

A point P with coordinates u, v near the double point q_0 on the loop of the strophoid represents a weak shock with little change in velocity and pressure. As P tends to the double point, the shock becomes sonic, the vector $\mathbf{q} - \mathbf{q}_0$ becomes tangential and the shock line S tends to a Mach line. Consequently, the two tangents to the loop at the double point give the normals to the Mach lines in the double point, since they are orthogonal to these limiting shock lines.

Further details of the development include: computation of the pressure and the density behind the shock front, various limiting cases, and the strophoid for a subsonic state 0.

SHOCK REFLECTION

Regular reflection can be discussed with the aid of shock polars in the (u, v) plane, applied to the shocks S and S' joining the states 0 to 1 and 1 to 2 respectively (Figure 13). Geometrically, both a regular weak and a regular strong reflection are possible in some cases; but, in other cases, regular reflection (weak or strong) is revealed to be impossible.

In the discussion of Mach reflection, it is useful to transform the shock polar to a (θ, p) plane, where θ is the angle through which the oncoming flow is turned by the shock. The search for Mach configurations is then replaced by a discussion of shock polar loops and their intersections.

1.5 SHOCK WAVES IN ARBITRARY FLUIDS

1.5.1 Introduction

Some effort was directed toward clarifying the general hydrodynamical and thermodynamical foundations of the shock phenomenon; for example, by a study⁷ of the conditions for the equation of state of a fluid under which shocks can be produced and by an investigation of the physical structure of a shock layer of infinitesimal width, provided heat conductivity and viscosity are similarly small. The differential equations of the shock layer have the initial and final states as singular points and are of a nature which suggests that the problem may have a unique solution. In connection with these studies, a reflection problem of great practical importance was treated, and the algebra of the shock problem was brought into a relatively satisfactory mathematical form.

More general equations of state for the gas were admitted than in Sections 1.2 through 1.5. In shock waves, the temperatures run so high that the assumption of constant specific heat is only a rough approximation. As an alternative, a more general study⁸ was based on the hypothesis of an empirically given function f expressing the energy U per mol in terms of temperature. This necessitated the expression of all variables concerned in terms of the temperature. The result was a system of algebraic equations adaptable to purposes of computation, once the energy function $U = f(t)$ is known. This particular study⁸ applied a single scheme of algebraic attack to ideal gases and to fluids obeying Tammann's equation of state. It deals with the one-dimensional case and also, in two dimensions, with the reflection of a shock wave. In the two-dimensional problem, conditions were developed for the existence of a solution corresponding to three given temperatures in the regions into which the half-plane containing the phenomena is divided by the incident and reflected shock (coordinates being such that these shock fronts are at rest and meet on the reflecting wall). In some cases, a single solution was shown to exist; in other cases, either no solutions or two solutions. The criteria depend on various inequalities involving functions of the temperature. This general analysis led to fairly simple criteria for head-on collision and for grazing waves. A grazing wave or a nearly grazing wave was shown^{7,8} to be impossible (see Section 1.5.4) under the assumption of a certain reasonable hypothesis.

1.5.2 General Comments on the Shock Phenomenon

Consider a fluid in a three-dimensional space, in which (x, y, z) are rectangular Cartesian coordinates. At any time and place, the fluid is in a definite thermodynamical state Z and a definite state of motion characterized by the components (u, v, w) of the velocity q . The possible thermodynamical states form a two-dimensional manifold \mathcal{Z} ; that is, only two variables are independent among the quantities (see Section 1.2.1) and have definite values in any particular thermodynamical state. On \mathcal{Z} , the fundamental thermodynamical equation

$$de = Td\eta - pd\tau$$

holds. It is assumed that the thermodynamical state Z and the velocity q depend on position only, not on the time, in other words, that the state is stationary.

In the limiting case, as viscosity and heat conductivity are permitted to vanish, *discontinuities* are possible of the following sort: (Z, q) might have constant values (Z_0, q_0) , for example, in the region $x < 0$, and other constant values (Z_1, q_1) for $x > 0$. The symbols $[0]$ and $[1]$, used frequently as subscripts, will refer to the two regions $x < 0$ and $x > 0$, respectively, divided by the shock front $x = 0$. The laws of conservation of mass, momentum, and energy lead to the following relation between the two thermodynamical states Z_0 and Z_1 [compare (iii**) and (iii***) in Section 1.2.3].

$$\begin{aligned} i_1 - i_0 &= \frac{1}{2}m^2(\tau_0 - \tau_1)(\tau_0 + \tau_1) \\ &= \frac{1}{2}(p_1 - p_0)(\tau_0 + \tau_1) \end{aligned} \quad (47)$$

or

$$e_1 - e_0 = \frac{1}{2}(p_1 + p_0)(\tau_0 - \tau_1)$$

where m is the mass flux across the shock front. The study of shocks is thus reduced to a study of the following relation between two states (Hugoniot equation).

$$\begin{aligned} H &\equiv H(Z_1, Z_0) \\ &\equiv (e_1 - e_0) - \frac{1}{2}(p_1 + p_0)(\tau_0 - \tau_1) = 0 \end{aligned} \quad (48)$$

The value of m turns out to be of the order of ρc , where c is the acoustic velocity. This implies that the phenomenon of shock and that of contact surface (or *slip stream*) must arise from quite different circumstances. In other words, the case $m = 0$ cannot be considered as the limiting case of a nonvanishing m , since m , if different from zero, is of the order ρc . These two phenomena can, however, be compared by first taking viscosity and heat conductivity into account and then letting them tend to zero. In the limiting process, there is found an explanation of the nonconservative nature of a shock with respect to entropy, although it conserves energy.

1.5.3 Thermodynamical Assumptions

The following assumptions are made:

I Infinitesimal adiabatic increase of pressure effects compression:

$$\left(\frac{d\tau}{dp}\right)_{\text{ad}} < 0.$$

II The rate of compression $\left(\frac{-d\tau}{dp}\right)$ diminishes in the process:

$$\left(\frac{d^2\tau}{dp^2}\right)_{\text{ad}} > 0.$$

III In the continuous process of adiabatic compression one can run pressure arbitrarily high.

IV The state Z is uniquely specified by pressure and specific volume, and the points (p, τ) representing the possible states Z in a (p, τ) diagram form a convex region.

Since, in view of IV, η is a single-valued function of p and τ , the adiabatic process of compression is defined by

$$\frac{\partial \eta}{\partial p} dp + \frac{\partial \eta}{\partial \tau} d\tau = 0. \quad (49)$$

This equation, with hypothesis I, implies that $\partial \eta / \partial p$ and $\partial \eta / \partial \tau$ are of like sign, either both positive or both negative, and, since they cannot vanish simultaneously, they have these same signs everywhere on \mathcal{Z} . Without essential loss of generality, it is assumed that

$$\frac{\partial \eta}{\partial p} > 0, \quad \frac{\partial \eta}{\partial \tau} > 0 \quad \text{everywhere on } \mathcal{Z}. \quad (50)$$

A formulation for infinitesimal adiabatic compression leads to analytic expressions equivalent to hypotheses I and II. Various analytic consequences can then be drawn from the first three hypotheses, with the aid of geometric methods in the (p, τ) plane and on \mathcal{Z} . For example, the derivatives $\eta' = d\eta/dt$ and $d\eta'/dt$ were studied on a line $p = p_0 + at$, $\tau = \tau_0 + bt$, on \mathcal{Z} , and it was found that η increases (decreases) along the whole line provided $a \geq 0$, $b \geq 0$ ($a \leq 0$, $b \leq 0$); also that if $\eta' = 0$ for a value of t , then $d\eta'/dt < 0$ for that value; and that if $\eta' \leq 0$ for $t = 0$, then $\eta' < 0$ for $t > 0$.

From $Z_0: (p_0, \tau_0)$, let an adiabatic be followed, raising p continually. By III, p can be indefinitely increased. Consideration of slopes reveals that just one point of the upper branch $p > p_0$ of the adiabatic lies on the ray from (p_0, τ_0) in a given direction $s = (p - p_0)/(\tau_0 - \tau)$, provided s lies between m_0 and ∞ .

In order to establish a basic inequality for a direction Z_0Z_1 , it was shown that $dH = Td\eta$ along any ray. If Z_0Z_1 satisfy equation (48) then it follows that $H(Z_1, Z_0) = \int_{Z_0}^{Z_1} Td\eta = 0$.

A. From this fact one can deduce that

$$N^* \equiv (p_1 - p_0)(\tau_0 - \tau_1) > 0 \quad (51)$$

$$\begin{aligned} (p_1 - p_0) + m_0(\tau_1 - \tau_0) &> 0 \\ (p_1 - p_0) + m_1(\tau_1 - \tau_0) &> 0 \end{aligned} \quad (52)$$

Physically, equation (52) implies that the flow

relative to the shock front in $[0]$ is supersonic, in $[1]$ subsonic.

The proof⁸ of equations (51) and (52) reveals that as Z traverses the ray Z_0Z_1 from Z_0 , H is positive until Z_1 , and thereafter negative, so that Z_1 is the only point on the ray such that $H(Z_0, Z_1) = 0$.

The inequalities $(p_1 > p_0, \tau_0 > \tau_1)$ are expressed by $Z_1 > Z_0$; and $(p_1 < p_0, \tau_0 < \tau_1)$ by $Z_1 < Z_0$.

B. It is then shown that if $H(Z_1, Z_0) = 0$, then $\eta > \eta_0$ or $\eta < \eta_0$ according as $Z_1 > Z_0$ or $Z_1 < Z_0$ [by equation (51) one of these must hold].

C. The locus of Z_1 , for given Z_0 , $H(Z_1, Z_0) = 0$ and $Z_1 > Z_0$ is shown to be a simple curve, starting from Z_0 on which s and η increase monotonically. This locus is called the *Hugoniot line* ζ . (s increases from m_0 to $+\infty$, η from η_0 to an unknown value. The variable s is a convenient parameter on ζ .)

At this point a fifth hypothesis is introduced.

Hypothesis V, that if (p_0, τ_0) is in Z (of IV) then so is the entire vertical ray $\tau = \tau_0$, $p_0 < p < \infty$, means physically that when the unit quantum of fluid in state (p_0, τ_0) is sealed in a vessel of volume τ_0 and heated, its pressure can be raised arbitrarily high.

D. Under this hypothesis, the function $p(s)$, representing pressure as a function of s along the Hugoniot line, becomes infinite with s .

For an idealized gas, the conditions I, II, III, IV and the additional hypothesis V are all verified. Attention is called to the fact that parameterizing the adiabatic line through Z with T in place of s makes the Hugoniot equation (48) solvable by a simple extraction of square roots.

1.5.4 Reflection of a Shock Wave

Consider a two-dimensional fluid covering the half-plane $y, 0$, which is assumed to be bounded by a wall along the x axis. Suppose two oblique shock fronts meet at the origin. See Figure 34 for notation. Direction cosines of the normals in the directions $[1] \rightarrow [0]$ and $[0] \rightarrow [2]$ are denoted by (α_1, β_1) and (α_2, β_2) respectively. Velocity components are denoted by $(u_1, 0)$, (u_0, v_0) and $(u_2, 0)$. The law of increasing entropy, with result B of Section 1.5.3, shows that $Z_1 < Z_0 < Z_2$, that is

$$p_1 < p_0 < p_2 \quad \text{and} \quad \tau_1 > \tau_0 > \tau_2. \quad (53)$$

For three states Z_1, Z_0, Z_2 so restricted, algebraic equations were developed⁷ and put into a simple form to determine the normals (α_1, β_1) and (α_2, β_2) of the shock fronts.

E. On the basis of such equations, together with Hugoniot relations and hypotheses I–IV, it was shown that glancing incidence is impossible.

The result depends on the separation of the two normal components ($u_0^{(1)}$, $u_0^{(2)}$) in the region [0] by the acoustic or sonic velocity. The stationary flow in [0] is subsonic as far as $u_0^{(1)}$ is concerned, but supersonic with respect to $u_c^{(2)}$.

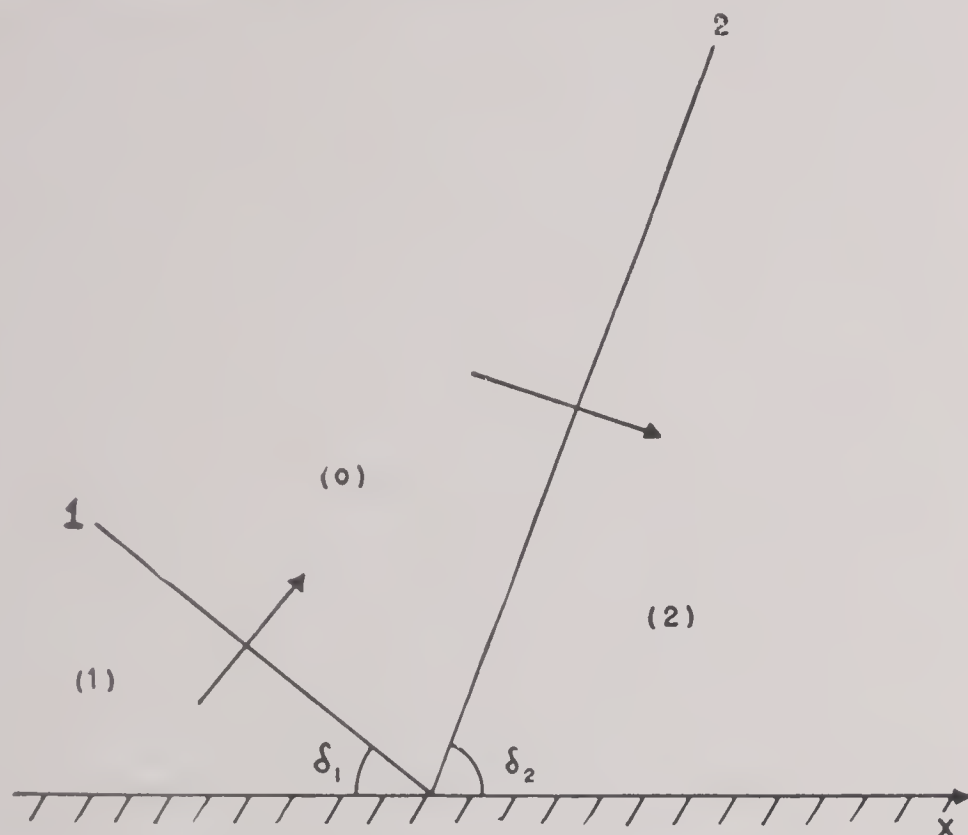


FIGURE 34. Shock wave reflection.

E'. Glancing incidence, under hypothesis V, is impossible even in the limit for $s \rightarrow \infty$, in the sense that $\sigma = -\tau_0\alpha_1\alpha_2/\beta_1\beta_2$ stays bounded while $s \rightarrow \infty$.

As soon as s exceeds a certain limit, simple reflection gives way to the more complicated Mach phenomenon, not yet analyzed even for an ideal gas with constant specific heat. (See Section 1.7.)

1.5.5 Problem of the Shock Layer

In addition to the thermodynamical assumptions I–IV, let the following be assumed:

Ia. Heating a quantum of fluid at constant volume raises its pressure and temperature.

The five equations expressing the laws of conservation take heat conductivity and viscosity into account through quantities involving coefficients λ, ν, ν' . A shock layer is obtained as a limit when $\epsilon\chi, \epsilon\lambda, \epsilon\nu, \epsilon\nu'$ replace χ, λ, ν, ν' and ϵ shrinks to zero. A slip layer (contact surface) is similarly obtained, letting $\epsilon\chi, \epsilon\mu, \epsilon^2\lambda, \epsilon^2\nu, \epsilon^2\nu'$ replace $\chi, \mu, \lambda, \nu, \nu'$. It is thus a question of orders of infinitesimals in the manner in which heat conductivity and viscosity drop out. Analytic reasons were advanced to show that it is misleading

to link the alternatives $m \neq 0$, $m = 0$, where m is mass flux across the discontinuity, to the discrimination of shock and slip layers. The argument depends on a discussion of singular points of a differential system. The case of transition through a shock layer from a state Z_0 to a state Z_1 is associated with special behavior of solutions to a differential system in the neighborhood of singular points corresponding to Z_0 and Z_1 . The behavior in question is such as to suggest the existence of a unique solution of the shock layer problem. Other types of behavior would lead one to expect either no solution or an infinity of solutions.

1.6 A PROPOSED NUMERICAL METHOD

The hypotheses of isentropy and that of all shocks being "straight" are generally not fulfilled. When they are abandoned, however, any exact mathematical analysis becomes quite intractable, by any methods thus far employed save in exceptional cases. Consequently, considerable importance attaches to a computational treatment, developed⁹ under the Applied Mathematics Panel, which ignores shocks but which appears to produce arbitrarily good approximations to a rigorous theory allowing for shocks. The treatment depends on a much simplified quasimolecular model in place of the continuous theory. Experimental punch-card solutions produced satisfactory results with respect to precision and duration of the computations. Physical considerations, for example propagation of sound and conservation of energy, serve as a means of finding errors. Possible extension of the method to spherically symmetric and to multi-dimensional problems was discussed.⁹

The considerations apply to any gas or liquid in which compressibility is taken into account, but viscosity and heat conduction are neglected. The substance is characterized by its *caloric equation of state*, giving the internal energy e as a function

$$e = e(\tau, \eta) \quad (54)$$

of the specific volume τ and the specific entropy η . Shocks appear as discontinuities (rapid changes of specific volume and of velocity) in the solutions of differential equations expressing conservation of momentum and energy.

With the aid of the Rankine-Hugoniot equations and the second law of thermodynamics, the nature of the change in entropy on crossing a shock is re-

vealed. It is the addition of the shock conditions which leads to extreme mathematical complications of the nature of unknown boundaries for regions in which the differential equations of the continuous case are valid. The boundary conditions of the system pertain to a free boundary, and the very coefficients of the differential equations depend on this unknown boundary. In view of the lack of any general theory of such problems and of any practicable numerical procedures, a new method was presented⁹ for dealing with the continuous case in a manner to approximate satisfactorily the discontinuous situation.

In carrying out these numerical approximations, the continuous independent variables of the differential equation are replaced by discrete ones. The elementary volumes of the substance, for which the label a is used, are essentially discrete; whereas the (one-dimensional) space coordinate x and the time t are naturally continuous. The actual number of molecules in a gram-mol of a real substance is about $6 \cdot 10^{23}$. For practical computational purposes, it was necessary that a much smaller number, perhaps $N < 100$, be assumed. A corresponding scaling up of intramolecular forces was introduced to simulate the correct hydrodynamical forces.

The differential equations with (x,t) continuous and the label a discrete conserve the total kinetic plus potential energy but apparently take no account of the thermic energy, which plays a basic role in shock theory. However, it is pointed out that in the quasimolecular model under consideration, the thermic energy necessarily appears as part of the kinetic energy. It is surmised, in view of this consideration, that the quasimolecular kinetic solution converges to the hydrodynamic solution of the shock problem, in the sense, not that the $x_a(t)$ of the discrete case approximate the $x(a,t)$ of the continuous, but that the average of the former over a suitable time interval approximates the latter. In the absence of a mathematical proof of this surmise, the latter was experimentally tested⁹ in the case of problems which involve shocks and for which a rigorous hydrodynamics solution is known.

An effective computational scheme requires that the variable t be also made discrete. The differential system is then replaced by a system of difference equations well suited to mechanization and, indeed, to solution with punch-card equipment.

For the differential equation, influences are propagated in a definite manner, namely, along char-

acteristic lines, a property which must in some way be represented in the computational process. The propagation by the computation involves a sort of false signal, which is very weak and can be made arbitrarily weak by the use of a sufficiently small grain size.

In the computational process, a molecule a will develop an oscillation after crossing the equivalent of a shock. This oscillation represents thermic agitation caused by the degradation of energy through the shock.

Aside from fulfilling the propagation criteria, the computational process should, and does, approximately conserve the equivalent of the total energy.

In one of the experimental problems whereby the Ballistic Research Laboratory at Aberdeen tested the computational method, the relation $p = 1 - \tau + \frac{1}{4}\tau^2$ was used in the interval $0 < \tau < 2$, $1 > p > 0$; and the normal initial state of the substance was taken as $\tau - \tau_1 = 1$, $p = p_1 = 0.25$. The sound velocity is then $c = \tau\sqrt{1 - \frac{1}{2}\tau}$, with the initial value $c_1 = \sqrt{0.5} = 0.707$. Boundary conditions correspond to collision of the substance with a wall. In the mathematical model, rigid walls are assumed at the two ends $x_0 = 0$ and $x_{a_0} = a_0$ of a finite sequence $a = 0, 1, 2, \dots, a_0$ of particles. Initially, the substance has normal specific volume $\tau = 1$ and uniform motion $d\chi_a/dt = x - \alpha$ to the left. The first and last molecules represent the walls. The others $(1, \dots, a_0 - 1)$ represent the substance. A compression wave originates at the wall $a = 0$ and an expansion wave at the wall $a = a_0$. The former is a shock, the latter a Riemann rarefaction wave. Comparison with the normal sound velocity $c_1 = \sqrt{0.5}$ gives $\mu = \alpha/c = \sqrt{2\alpha}$, the Mach number of the initial motion. The problems considered correspond to the choices $\alpha = 0.2$ and $\alpha = 0.4$, or $\mu = 0.283$ and $\mu = 0.566$. In the first case, $N = 14$ molecules was used, with two separate basic time intervals $t^* = 0.5$ and $t^* = 0.25$, and computations were carried until $t = 31$, $t^* = 15.5$ and $t = 51$, $t^* = 12.75$, respectively. In the case $\alpha = 0.4$, $N = 29$ molecules was used, and the calculation extended over 61 intervals $t^* = 0.5$, that is, until $t = 30.5$. The entire punch-card process (setting up, etc.) for these three problems took less than ten days, and the actual computations on each problem required 6 to 12 working hours net. The results show, on graphs, a very satisfactory relation between the paths of the molecules in the computational solution and

the shock lines and rarefaction waves of the rigorous hydrodynamical solution. All the criteria for a good computational approximation are fulfilled. The shocks are followed by more lasting oscillations than those accompanying the rarefaction. Quantitatively, there is excellent agreement between the specific volumes behind the shock and rarefactions on the one hand and the compression and expansion revealed by the numerical method on the other. The numerical rate of degradation of energy checks well with the oscillations and the trends of the approximate energy.

An interesting feature of the numerical results is a location of the course of the shock across the rarefaction, a result not obtainable by classical methods in the rigorous, hydrodynamical theory of the collision of a shock and a rarefaction.

It is noteworthy that $N = 14$ or 29 molecules was adequate to describe even the finer nuances of hydrodynamic motion.

The punch-card equipment can also quite simply and efficiently handle cases involving nonpolynomial equations as, for example, the adiabatic

$$p = \tau^{-\gamma}.$$

For spherically symmetric motion, the hydrodynamical partial differential equation is quite similar to that of the one-dimensional case, and approximate, numerical procedures can be similarly applied.

In truly multi-dimensional problems, the number of molecules required for a similar approximating method is expected to increase exponentially with the dimensionality so that the numbers may exceed the capacity of present machines.

1.7 REGULAR REFLECTIONS AND MACH REFLECTIONS

For other material bearing on the present topic, see Sections 1.2.4 and 1.4.2. The description in the former section of the basic relevant phenomena can be regarded as an introduction to the present discussion. It may be noted that Mach reflections have important practical significance, for example, in the airbursting of large blast bombs, where, under appropriate conditions, the Mach wave gives an enhanced destructive effect.

Many important unsolved problems are associated with the phenomenon of Mach waves. In an Applied Mathematics Panel Memorandum¹⁰ an ap-

proach was made to the unsolved question of a continuous transition from regular to Mach reflection. In a later report¹¹ discussed in Section 1.7.1, the hydrodynamical equations were utilized in an approximate treatment of the Mach effect. As in the problem of Section 1.6, extremely great mathematical difficulties are encountered in any attempt at an exact treatment. Even an approximate treatment presents difficulty for Mach reflections as contrasted with regular reflections because the latter can be satisfactorily treated when both the incident and reflected waves are assumed to be plane. The curvatures of these waves cannot, however, be so readily neglected in the study of the Mach effect.

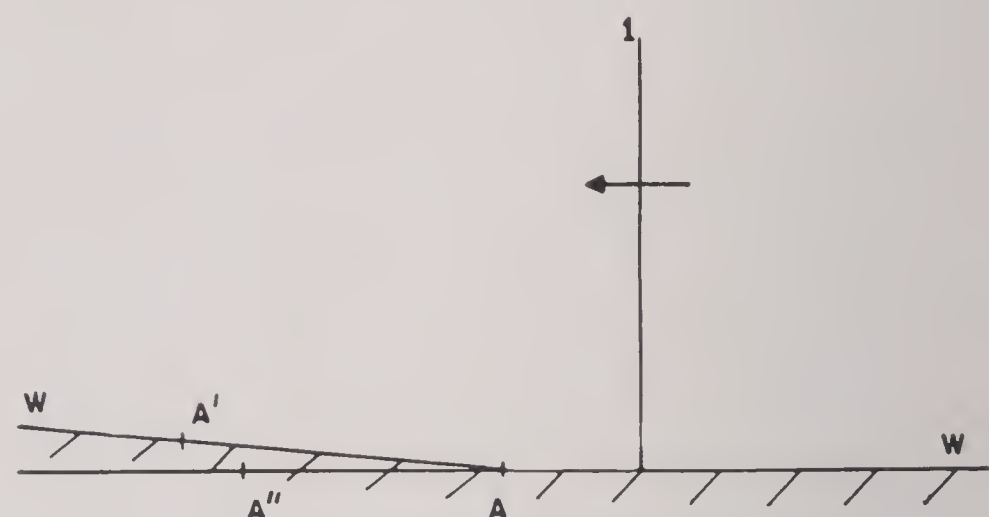


FIGURE 35. Shock running into a corner.

1.7.1 Nearly Glancing Reflection of Shocks

Regular reflection of a plane shock wave from a rigid wall occurs as long as the angle α of incidence is smaller than a critical angle depending on the strength of the incident shock. For larger values of α , Mach reflections occur.

The discussion¹¹ here reviewed treats a limiting case in which an approximate form of the differential equations can be used, the position of the shocks is known in the 0th approximation, and vorticity and anisentropy (associated with curved shocks) can be neglected.

A shock I , traveling with a constant velocity D parallel to a wall WW (see Figure 35) hits a flat corner A , the angle $A''AA'$ being very small. Ahead of I , the air is at rest. After the shock passes the corner, a disturbance R spreads from A (Figure 36). The disturbance R is centered in a point O moving with the velocity U of the air behind the shock. The shock front is distorted; for it keeps its original direction far from the wall but must also be orthogonal to

path of each particle, it is constant throughout C . For similar reasons, vorticity is shown to be negligible in C . Hence the assumptions of a potential flow and of isentropy in C are justified.

In solving the boundary value problem for the velocity potential, a suitable system of new independent variables is introduced. These new variables permit an easy derivation of the potential function from a harmonic function. The velocity potential Ω is first replaced by the more convenient function

$$\omega = \frac{\pi}{U}\Omega \quad (58)$$

whose derivatives are denoted by $\omega_i = \partial\omega/\partial y_i$ ($i = 1, 2$).

Then the flow in C_0 (the approximation to C bounded, in Figure 36, by PAQ_0T and the indicated arc of the unit circle) is shown to be determined by $\omega = \omega - \epsilon y_i \omega_i$ together with the derivatives ω_i ; while the boundary values of ω and $\partial\omega/\partial r$ define the positions of the Mach shock and the reflected wave R .

In fact, the flow in C_0 is given by

$$u_1 = -\epsilon \frac{U}{\pi} \omega_1 \quad u_2 = -\epsilon \frac{U}{\pi} \omega_2 \quad (59)$$

relative to the (y_1, y_2) reference system. Pressure, density, and sound velocity are determined by

$$p = \frac{1}{\gamma} + \epsilon \frac{U}{\pi} \hat{\omega}, \quad p = 1 + \epsilon \frac{U}{\pi} \hat{\omega}, \quad c^2 = 1 + \epsilon(\dot{\gamma} - 1) \cdot \frac{U}{\pi} \hat{\omega} \quad (60)$$

The position of the Mach shock is given by

$$y_1 = -\sigma - \epsilon \mu(y_2), \quad (61)$$

where $\mu = \omega/\pi$, figured for $y_1 = -\sigma$ and the position of the reflected wave R is given by

$$r = 1 + \epsilon \lambda(d), \quad (62)$$

where $\lambda = [- (\dot{\gamma} + 1)/4](U/\pi)(\partial\omega/\partial r)$ and $\partial\omega/\partial r$ is taken along the arc $R^\circ = TP$ of unit circle (Figure 36).

It turns out that the ω_i as well as $\hat{\omega}$ are harmonic in certain variables

$$k_i = \frac{y_i}{1 + \sqrt{1 - r^2}} \quad (63)$$

suggested by consideration of a variational principle with an appropriate Lagrangian. The differential equation with boundary conditions for ω in terms of k_1, k_2 is first solved in a simplified form and then

solved explicitly in general by a combination of two of the simplified solutions.

In the solution, it appears that $\partial\omega/\partial r$ is zero when $r = 1$. Hence in the approximation involving only first order terms in ϵ , the boundary R coincides with R° . Furthermore, since the pressure in B is $p_0 = 1/\gamma$, and since $\hat{\omega}$ is found to be zero when $r = 1$, it follows from equation (60) that the pressure is continuous across R , as is the density. Thus r is not a shock at all in the first approximation. However, the pressure (or density) gradient becomes infinite at R .

In the second approximation, where terms in ϵ^2 are considered, there is still neither vorticity nor anisentropy. But R is now found to deviate from R° , and both p and ρ suffer discontinuities. R turns out to be a shock of variable strength, infinitesimal at the triple point.

In the first approximation, pressure and density in C_0 increase monotonically towards the wall along any vertical. At the triple point, the pressure is $p_0 = 1/\gamma$. At the foot Q of the Mach shock, the pressure is $p_0 + \epsilon(U/\pi) \hat{\omega} \sqrt{1 - \sigma^2}$.

Certain phenomena, related to the pressure gradient along the shock front, calculated on the basis of the above approximation are in agreement with experiments carried out at Princeton, though other calculated properties of this gradient have not thus been verified.

The Mach front, determined by equation (61), has vertical tangent and zero curvature at the triple point, a property apparently confirmed by experimental evidence.

1.7.2 Reflection of Conical Shocks

In a plane shock at a plane wall, regular reflection can occur only for sufficiently small angles of incidence. For larger angles, up to 90° , a Mach reflection occurs. An investigation was made¹² of the question of whether the situation is similar for axially symmetric shocks. Regular reflection at an axis would involve an incident and reflected conical shock, having their tips in common. The following basic assumption is natural.

Assumption: Along each straight ray through the tip, pressure, density, and even velocity are constant.

It was demonstrated that, under the basic assumption, no regular reflection of conical shocks is possible. No attempt was made definitely to settle the question whether Mach reflection takes place instead of regu-

lar reflection even for small angles of incidence or whether the basic assumption should be abandoned. It was, however, remarked that experimental evidence seems to point to the second alternative.

1.8 GAS-DYNAMICAL THEORY OF NOZZLES AND JETS

1.8.1 Introduction

The jet research under the direction of the Applied Mathematics Panel was initiated by a request from the Bureau of Aeronautics of the Navy for help in the design of nozzles for jet motors to be used in assisted takeoffs. This request led directly to investigations of gas flow in nozzles and in supersonic jets from nozzles and orifices. Various other jet problems soon came under consideration, partly associated with rocket development and partly with the development of intermittent jet motors of the V-I type. Close cooperation was maintained with the Bureau of Aeronautics in connection with their program, carried on at their Engineering Station in Annapolis, to improve such motors, and work along these lines is still in progress under Navy auspices. Consultation was provided to various organizations engaged in the development of jet-propelled missiles.

Problems of detonation and deflagration were naturally encountered (compare Section 1.2.6). Special investigations were concerned with the efficiency of various modes of burning in an intermittent jet motor. Causes of irregular burning of tubular propellants in rockets were studied; and in this connection current theories of gas flow inside rockets were re-examined.

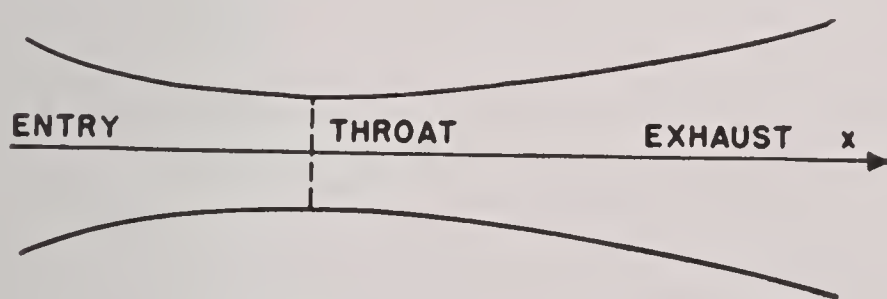


FIGURE 38. De Laval nozzle.

The initial jet research problem mentioned above involved the designing of unconventional nozzles for rocket motors, combining shortness with high efficiency. This necessitated improvements in the classical (hydraulic) theory of the de Laval nozzle. Methods and results were developed¹³ of potential interest in other problems such as in the design of kinetic compressors, a sort of reverse of exhaust nozzles

intended to receive a parallel flow of gas at high supersonic speed in order to compress and arrest the incoming gas.

A treatment was presented¹³ for three-dimensional flow through nozzles as a refinement of the customary one-dimensional theory under the assumptions that: the fluid is ideal and homogeneous, the flow is isentropic, steady, and irrotational; viscosity and heat conduction are negligible; shocks and jet detachment do not occur in the nozzle. Conditions for the fulfillment of the last assumption were analyzed.

A formula for thrust was derived and applied to various contours, especially for widely divergent short nozzles. One of the problems is to determine the shortest nozzle among families of nozzles yielding the same thrust.

A discussion was given¹³ of so-called perfect exhaust nozzles, which yield maximum thrust and a parallel exhaust flow for a prescribed expansion ratio. Perfection, although of slight importance for exhaust flow, is essential to reverse nozzle or compressor flow, also in supersonic wind tunnels. In compressor flow, it was shown that shocks must be admitted to avoid instability of the phenomena under slight variations of velocities and pressures. Conditions were analyzed for the possibility of a supersonic stream of air entering a compressor without interference of shocks, and limitations of the rim angle were given for a compressor carried in the nose part of a projectile.

For nozzles of customary design, refinements in construction cannot produce much increase in rocket propulsion efficiency, since such nozzles have already been found to yield thrusts between 90 and 100 per cent of the theoretical values.

In the classical hydraulic theory, the thrust produced by the flow through a nozzle depends only on the expansion ratio: (exit area)/(throat cross-section area). The refined theory makes distinctions which depend on the length of nozzle. It is revealed that only very long nozzles can produce optimal thrust, but that much shorter nozzles can be so designed as to come within a few per cent thereof. The perfect nozzle, which yields optimal thrust, has an end section which bends gently inward as to produce a completely axial flow with constant velocity.

1.8.2 Flow in Nozzles and Jets

The usual description¹ of phenomena in a jet is based on interaction of simple waves. A jet is formed by gas flowing with supersonic speed from an orifice

into the atmosphere (Figure 37). In accordance with a somewhat oversimplified analysis, it is supposed that the jet of escaping gas is separated from the quiet air at atmospheric pressure by a boundary wall consisting of a vortex layer (which becomes thicker along the jet and may ultimately consume it). The phenomenon is assumed to be two-dimensional, steady and isentropic, taking place, say, between two plane plates. It is assumed that the pressure p_0 in the oncoming gas flow exceeds atmospheric pressure p_A . Then, at the corners of the orifice, the compressed gas expands to atmospheric pressure in two symmetrical centered waves. These two simple waves interact and emerge again as simple waves from their zone of penetration. From the boundary layer which forms the wall of the jet, they are reflected again as simple waves, which penetrate each other and again continue as simple waves. The pattern is assumed to repeat itself periodically, save for the influence of the boundary layer, which gradually leads to a disintegration of the phenomena. Although strictly speaking such a flow should be considered as steady, isentropic, irrotational flow with symmetry about the x axis, it is possible to give an approximate treatment of great practical value without entering into difficult manipulations with the differential equations.

The so-called de Laval nozzle plays a decisive role in the operation of turbines, wind tunnels, and rockets. It consists of a converging entry section and a diverging exhaust section (see Figure 38). Two possibilities arise when a gas at rest in a container or chamber under high pressure escapes through such a nozzle. In the first place, the flow may be expanded in the entry section and it then remains subsonic throughout. This occurs when the ratio of chamber pressure to outside pressure remains below a certain critical value. In the second place, when the critical value is exceeded, the flow becomes supersonic on passing the throat and is expanded from there on.

The important fact that subsonic flow is contracted and supersonic flow expanded in a diverging section can best be recognized by considering flow in a cone. Assume the flow to be steady, isentropic, and radially directed. Assume also that speed q , density ρ , and pressure p depend only on the distance r from the tip. If a denotes the area intercepted by the cone on the sphere $r = \text{constant}$ and if G is the rate of mass crossing this area per unit time, then

$$A\rho q = G. \quad (64)$$

This, with the adiabatic relation

$$p\rho^{-\gamma} = \text{constant} \quad (65)$$

and Bernoulli's law

$$\mu^2 q^2 + (1 - \mu^2)c^2 = c_*^2 \quad \text{with} \quad c^2 = \frac{\gamma p}{\rho} \quad (66)$$

suffice to determine the flow. On the basis of these equations, it can be shown that for increasing area A , the speed q increases when $q > c$ and decreases when $q < c$. Since increasing speed corresponds to decreasing density, it follows that, in the direction of increasing area A , the flow is expanded when supersonic and contracted when subsonic.

Another important consequence of the above equations is that no transition from subsonic to supersonic flow is possible in a cone.

The treatment of conical flow is useful to describe approximately the flow through a de Laval nozzle, although its components are not necessarily conical. The resulting approximate treatment is referred to as the hydraulic nozzle theory and is a modification of the work of O. Reynolds.³⁰ The hydraulic theory, though very simple, accounts for a variety of peculiar types of nozzle flow arising under various conditions. In adapting the conical treatment to the de Laval nozzle, a set of surfaces is introduced which intersect the nozzle wall perpendicularly. The flow is assumed to be orthogonal to these surfaces, and on them all relevant quantities are assumed to be constant. By a cross-section area A is meant the area on one of these surfaces intercepted by the nozzle wall (see Figure 39). The same formulas are then applied as

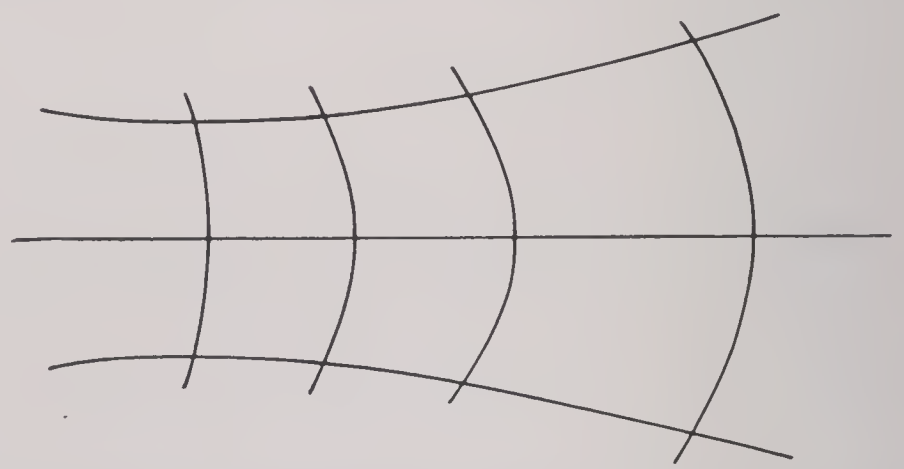


FIGURE 39. Surface across nozzle on which q, p, ρ are assumed constant.

in the case of the conical flow. The pressure on A is denoted by p . Let $A = A_t = A_*$ denote the minimum value of A , which is the value at the throat. Then, if the flow changes at all from a subsonic to a supersonic state, it must become sonic at the throat, that is, $q = q_* = c_*$ when $A = A_t = A_*$. (Note that

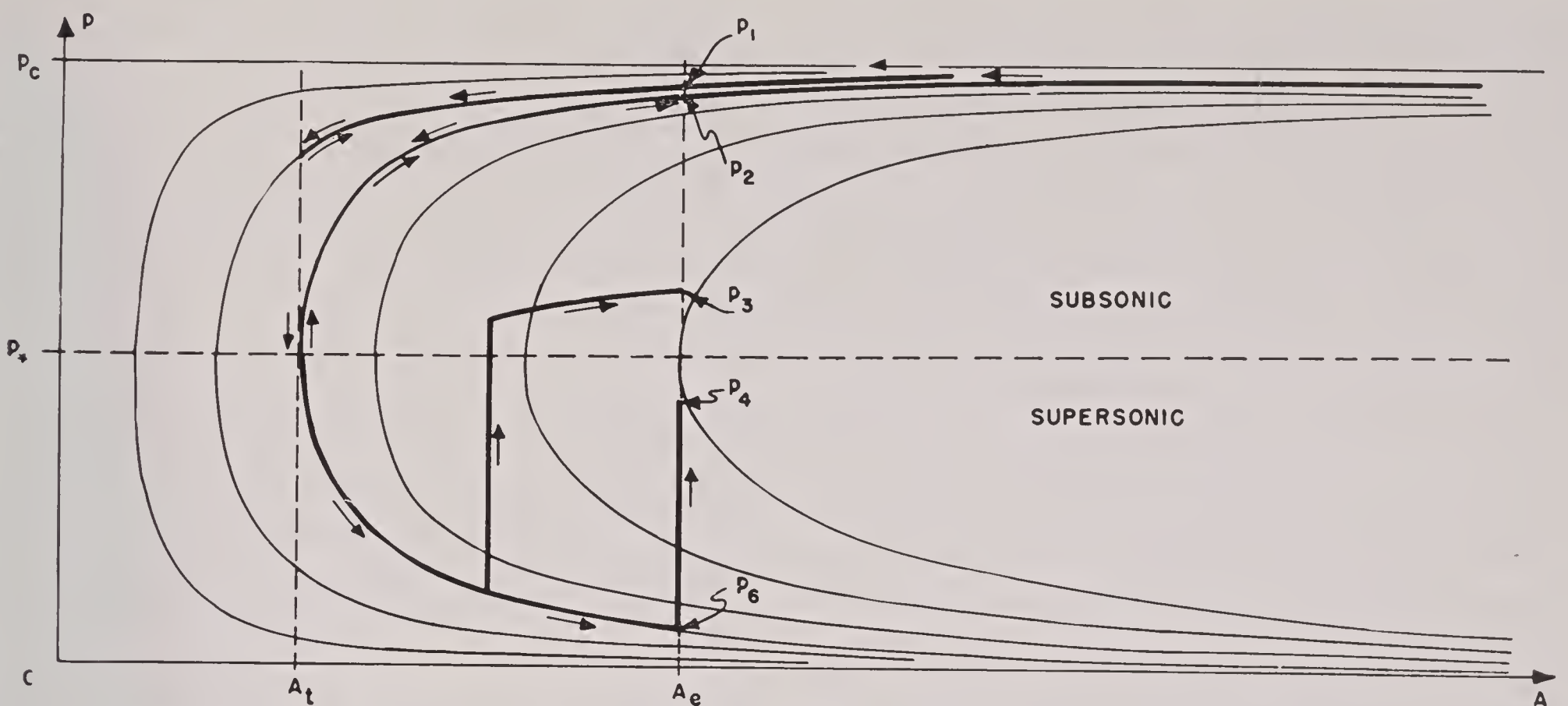


FIGURE 40. Relation between pressure and cross-section area for the various nozzle flows resulting from various receiver pressures.

$c_* = q_*$ is considered a fixed parameter, and that the critical values p_* and q_* of pressure and density are also fixed.) The ratio A/A_* is then a well-defined function of p/p_* . In developing an understanding of the variety of flows compatible with a given fixed state in the chamber, graphs (Figure 40) of the functions

$$A = A_* \cdot f(p/p_*)$$

for various values of the parameter A_* are useful. The curves have the lines $p = 0$ and $p = p_c$ as asymptotes. Of the two values of p corresponding to a given value of A , the greater refers to a subsonic and the smaller to a supersonic state. Suppose, for a given nozzle, the value of A as a function of the abscissa x along the axis is inserted in $A = A_* f(p/p_*)$. Then p is determined as a function of x . The situation is depicted in Figure 41 in which the relation between pressures and areas along any flow in the nozzle from chamber to receiver is represented by arcs of the graphs.

The exhaust flow is thought of as being discharged into a large receiver vessel in which an arbitrary pressure p_r can be maintained. The chamber or container pressure p_c is thought of as fixed, whereas p_r is varied. When $p_r = p_c$, there is no flow. If p_r is slightly less than p_c , a flow with low speed results. This case corresponds to the situation indicated in Figures 40 and 41 by the value $p_r = p_1$. The situation corresponding to $p_r = p_2$ is one where the receiver pressure has been lowered to just such a value that $A_t = A_*$, the critical area associated with the curve

in Figure 40 through the point (A_e, p_r) in which A_e is the exit cross-section area of the nozzle. Then the flow just becomes sonic at the throat but remains subsonic elsewhere. Corresponding to $p_r = p_3$, a value somewhat lower than p_2 , is an entirely different type of motion, as indicated in Figures 40 and 41.

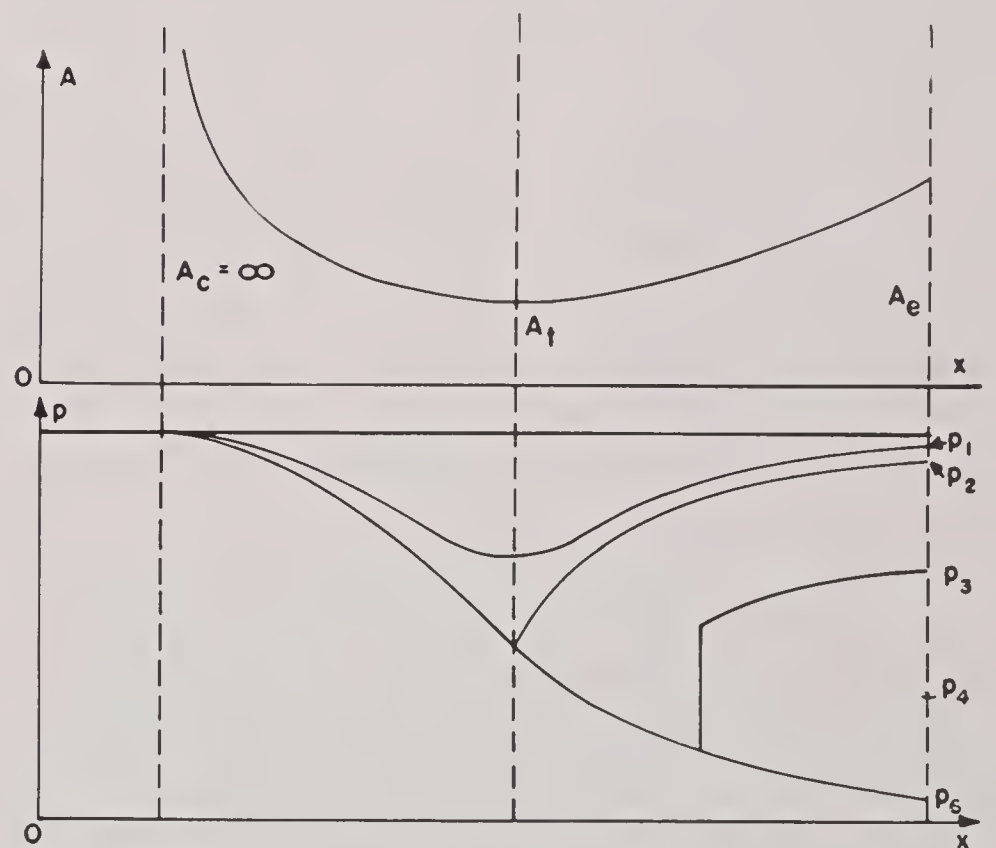


FIGURE 41. Pressure as a function of position along the axis of a nozzle for various flows resulting from various receiver pressures.

From the chamber to the throat, the flow is subsonic and represented by the upper arc of the curve coming from $A = \infty$ and belonging to $A_* = A_t$. This part of the flow is determined solely by A_t and p_* (or p_c) and is thus independent of the receiver pressure.

After passing the throat, the flow becomes supersonic and is represented by the lower branch of the same curve $A = A_t \cdot f(p/p_*)$, which intersects the line $A = A_e$ at a definite point, where $p = p_6$. Note that p_6 is determined by $A_e = A_t \cdot f(p_r/p_*)$.

If the receiver pressure is exactly $p_r = p_6$, we have what is considered the ideal flow through the nozzle. The design of a nozzle for given pressures p_c and p_r usually means the selection of A_t and A_e so that in the present notation $p_6 = p_r$, that is, $A_e/A_t = f(p/p_*)$.

When p_r is gradually lowered below the value p_2 , the flow attains supersonic speed behind the throat. It continues as indicated by the lower branch of the specific curve $A = A_t \cdot f(p/p_*)$. At a certain place in the diverging part of the nozzle, a shock front occurs, the gas is compressed and is slowed down to subsonic speed. From there on, the gas is further compressed and slowed down. The relation between pressure and area is represented by the upper branch of the curve $A = A_* \cdot f(p/p_*)$ passing through A_e and p_r with an appropriate smaller value of p_* . The position and strength of the shock front is automatically adjusted so that the end pressure at the exit becomes p_r . In the diagram, the place corresponding to the shock front indicates a jump from the supersonic branch of the curve with $A_* = A_t$ to the upper branch of the curve through (A_e, p_r) .

When p_r is decreased below p_2 , the shock front moves from the throat toward the exit. It reaches the exit for a value $p_r = p_4 > p_6$ (see Figure 40). For still lower values of p_r , no adjustment of the flow to the receiver pressure is possible by a shock in the nozzle. Accordingly, a new type of flow pattern must be found to describe what happens under the condition $p_r < p_4$.

In the nozzle, the flow will be the same as that in the ideal case where $p_r = p_6$; that is, the subsonic branch of the corresponding curve $A = A_t f(p/p_*)$, defined by $A_t < A < \infty$, and also the supersonic branch $A_t < A < A_e$ indicate the flow in the nozzle. It is in the jet outside the nozzle that the adjustment to the outside pressure p_r takes place. There are two types of phenomenon according as $p_4 > p_r > p_6$ or $p_r < p_6$; the intermediate case, $p_r = p_6$ is the ideally adjusted continuous flow considered above. These phenomena were discussed¹ in some detail.

If a divergent exhaust flow results from a given nozzle, it is possible by rerouting only a section

thereof to make the flow perfect; that is, to guide it so that it eventually acquires constant axial velocity. Every streamline of a perfect flow yields a perfect nozzle. Furthermore, a perfect nozzle can be constructed so as to produce any desired exhaust velocity, that is, the Mach number of the exhaust flow or, what is equivalent, the ratio of chamber to exhaust pressure can be prescribed.

1.8.3 Outline of the Mathematical Theory

Underlying the refinements of the hydraulic treatment are the basic partial differential equations for an irrotational isentropic flow. These can be expressed in terms of the coordinate x along the axis in the exhaust direction, the distance y from the axis, the angle θ of the flow direction with respect to the x axis, the velocity potential function ϕ , and the stream function ψ , so normed that $\pi\psi^2$ is the rate of mass flow per unit time carried by the stream tube $\psi \leq \text{constant}$. The basic equations for the four dependent variables ϕ , ψ , θ and the velocity q are

$$\begin{aligned}\frac{\partial \phi}{\partial x} &= q \cos \theta \\ \frac{\partial \phi}{\partial y} &= q \sin \theta \\ \psi \frac{\partial \psi}{\partial x} &= -\rho q y \sin \theta \\ \psi \frac{\partial \psi}{\partial y} &= \rho q y \cos \theta\end{aligned}\quad (67)$$

where ρ can be expressed in terms of q in the usual way.

The straightforward procedure of prescribing nozzle contour and state in the chamber and asking for the resulting flow leads to a boundary value problem for equations (67). A simpler, reverse procedure consists in prescribing the velocity distribution, $q = q_0(x)$ for $y = 0$ along the axis and then seeking possible nozzle contours from the resulting stream surfaces. It was found expedient in carrying out the work to use ϕ and ψ as independent variables and x , y , θ , and q as dependent variables to be developed in powers of ψ .

Using $q_* = c_*$ for the critical speed, which is the flow speed when it coincides with local sound speed, and using ρ_* for the associated density, let the dimensionless quantity

$$h = \frac{\rho_* q_*}{\rho q}\quad (68)$$

be introduced. It is a function of q , since ρ is a function of q . On the axis, by virtue of $q = q_0(x)$, h is a function of x , denoted by $h = h_0(x)$. The origin ($x = 0, y = 0$) is so placed that $q_0(0) = q_*$. Then two new parameters, ξ and η are introduced, instead of ϕ and ψ , as follows:

$$\phi = \int_0^\xi q_0(x) dx \quad (69)$$

$$\psi = \sqrt{\rho_* q_*} \eta. \quad (70)$$

The surfaces $\xi = \text{constant}$ and $\eta = \text{constant}$ are the potential and stream surfaces, respectively. The basic differential system of this problem has the following solutions,¹³ using expansions through the second degree terms in ξ and η , where h_0, h_0', h_0'' stand for $h_0(\xi), h_0'(\xi), h_0''(\xi)$.

$$x = \xi - \frac{1}{2} h_0 h_0' \eta^2 \quad (71)$$

$$y = h_0 \eta \left\{ 1 + \frac{1}{8} [(M_0^2 - 1) h_0 h_0'' - (h_0')^2] \eta^2 \right\} \quad (72)$$

$$q = q_0 (1 + \frac{1}{2} h_0 h_0'' \eta^2) \quad (73)$$

$$\theta = h_0' \eta \quad (74)$$

$$h = h_0 \left[1 + \frac{1}{4} (M_0^2 - 1) h_0 h_0'' \eta^2 \right] \quad (75)$$

$$p = p_0 \left[1 - \frac{\gamma}{2} M_0^2 h_0 h_0'' \eta^2 \right]. \quad (76)$$

Equations (71) and (72) are parametric representations of the potential and stream surfaces respectively. Each stream surface can serve as a nozzle contour.

1.8.4 Qualitative Conclusions and Comments

If only the first degree approximation is used in the above solution, the results of the hydraulic theory are obtained; so that equations (68) through (76) can properly be regarded as a refinement of the hydraulic theory. In particular, equation (71) reveals a deviation from the constancy of speed on potential surfaces assumed in the hydraulic theory. This deviation has a simple expression in terms of the ratio of the width of the nozzle to the radius of curvature of the nozzle contour.

Unless the end section of the nozzle curves inward, as would be true for $h_0''(\xi) < 0$, the speed increases, and thus the pressure decreases, along potential surfaces, as one recedes from the axis. Hence, the pressure along the nozzle wall is found to assume values less than those calculated from the hydraulic theory. This result agrees with the physical consideration that a widely divergent opening gives the gas an opportunity for quick expansion.

The somewhat unnatural procedure, underlying the present analysis, of prescribing such a quantity as $q_0(x)$ is justifiable as long as $q_0(x)$ is smooth and analytic. This property is then shared by the streamlines in the neighborhood of the axis. Thus the method of solving the underlying differential equations is applicable if the desired nozzle contour is represented by a smooth and analytic curve; but it should not be expected to apply to nonanalytic cases in general. However, it appears likely that the approximations employed may remain valid if the curvature of the nozzle contour is continuous.

The neglect of viscosity and of possible jet detachment becomes dubious, on physical grounds, for nozzles of relatively wide divergence. Jet detachment appears to be a likely explanation of certain experimentally observed phenomena at variance with theoretically established results. Such detachment has been observed when the chamber pressure is so low that the exit pressure which would result from undisturbed expansion is noticeably less than the outside pressure. When the jet breaks away from the wall, it generally changes direction, the change being accomplished through an oblique shock front beginning at the point of detachment (Figure 42). Beyond the detached jet, experiments indicate back flow and a pressure rise.

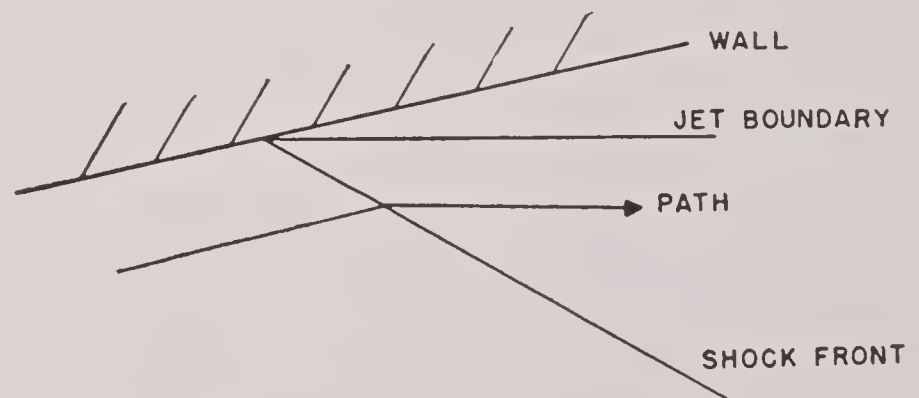


FIGURE 42. Jet detachment.

It appears that a jet will not detach from the wall before it has decreased at least to outside pressure. Jet detachment could thus be avoided by making the nozzle so short that the pressure at the nozzle wall remains above outside pressure. Another advantage of this plan is in the production of a larger thrust. Sometimes for a widely diverging nozzle, the hydraulic theory predicts a value of exit pressure above atmospheric pressure, and the more refined treatment¹³ just outlined indicates expansion below atmospheric pressure with the resulting possibility of jet detachment.

One product of the improved theory¹³ was an approximate formula, simpler and more exact than

that of the hydraulic theory, for determining the reactive thrust produced by a flow through a nozzle. The formula is, indeed, an exact one for purely radial flow through a conical nozzle. If F denotes the resultant internal thrust from the pressure against the walls of the chamber and of the nozzle, and if F_i denotes the external counterthrust which would result if atmospheric pressure were acting against the outer surface of the body within which the nozzle is imbedded, then the total thrust is customarily defined as

$$F = F_i - F_a.$$

Deviations of external pressure from atmospheric pressure contribute to the total force, but such contributions are considered part of the drag, not a modification of the thrust. The dimensionless thrust ratios

$$\begin{aligned} K_i &= \frac{F_i}{A_* p_*}, \\ K &= \frac{F_a}{A_* p_*}, \\ K &= K_i - K_a \end{aligned}$$

are employed, where A_* is the throat cross-sectional area in the hydraulic approximation. A theoretical maximum, K_{\max} is easily found for the thrust coefficient K , and the ratio K/K_{\max} then serves to measure the efficiency of an exhaust nozzle.

The problem of maximum thrust, that is, the problem of designing a rocket exhaust nozzle so as to achieve as large a thrust as possible, can be approached in two ways: an indefinitely long nozzle contour is to be cut off at that endpoint for which the maximum thrust will result, and a perfect nozzle contour is to be found whose maximum thrust is as large as possible. In the first of these problems the thrust attains its maximum when the contour is cut off at the point where the gas pressure has just been reduced to outside pressure. This is found to hold quite generally and not merely for the hydraulic case, for which it was well known. As for the second approach, an earlier discussion¹⁴ led to the fairly obvious condition that the flow direction be axial on a surface of constant flow speed passing through the rim of the nozzle mouth, provided the pressure on this surface equals the outside pressure.

As already remarked, it is only for unconventional, widely divergent nozzles that the problem of design acquires practical importance. Although even the refined thrust theory does not lead readily to specific

conclusions, the following rather general properties were suggested by the investigations:

1. The maximum thrust of a contour is smaller the more divergent the contour.
2. The maximum thrust from the short optimal section of a widely divergent contour is larger than the thrust obtained from an equally short section of a less divergent contour.

This second statement implies that if one desires to cut off a section of nozzle at the sacrifice of a small part of the thrust, he could obtain the same thrust by making the nozzle still shorter but more divergent. However, it should be emphasized that it is doubtful that the various assumptions underlying the work remain justifiable for the more divergent nozzles here considered.

Examples of particular types of contours were considered:¹³ (1) contours C_1 , more or less hyperbolic in form, approximately symmetrical with respect to the throat; to a first approximation, the streamlines and potential lines are confocal hyperbolas and ellipses; (2) more or less circular contours C_2 , whose potential lines, to a first approximation, are circles through a pair of fixed points on the axis and whose streamlines, also to a first approximation, are the orthogonal set of circles. It is observed, first, that the maximum thrust attainable is smaller for the more curved contour C_2 than for the more conventional contour C_1 ; and second, that the thrusts attainable for the more curved C_2 are obtained from shorter sections than the same thrusts for the contour C_1 .

Relatively little importance attaches to the fact that the above nozzle contours C_1 and C_2 are approximately symmetric in the throat section, whereas the entry section of actual nozzles is usually much more curved than the exhaust section. Computations point to the conclusion that the entry section of a nozzle has no great influence on the flow past the throat.

The theoretical investigations were correlated¹⁵ with British experimental observations in the form of a series of remarkable shadow photographs of jets issuing at high speed from exhaust nozzles. In the period between 1940 and 1941 when the photographs were made, and the time of the panel study in 1944, sufficient progress had occurred in the theoretical understanding of possible patterns of shock and expansion waves to permit practical contributions to the interpretation and analysis of Fraser's work. The photographs reveal the boundary of jets, after leaving the nozzles, as contact surfaces, the density in the jets being greater than that in the outside

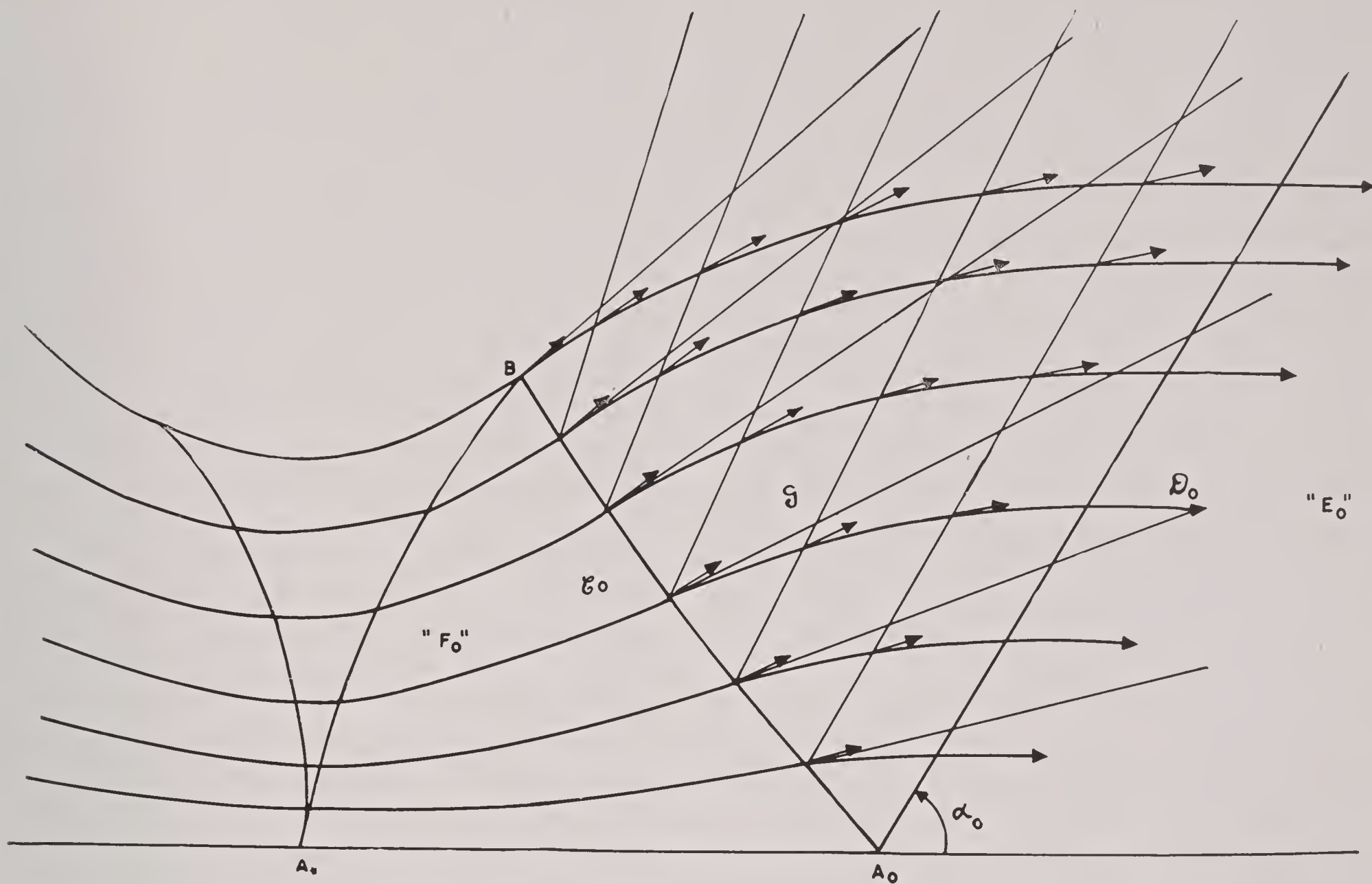


FIGURE 43. Perfect exhaust flow.

atmosphere. They also reveal the discontinuity at the jet boundary developing into a gradually disintegrating boundary layer, with accompanying vortices and agitated flow. According to conditions, rarefaction waves and shock fronts, observable in the photographs, are in agreement with theoretical considerations.

From the present viewpoint the most interesting of Fraser's observations concerned certain pressure measurements, obtained by drilling a hole through the nozzle wall and measuring the pressure of the air stream at the wall. The ratio of chamber pressure to test point pressure was nearly constant for chamber pressure from 1,100 to 500 psi, but the test point pressure increased rapidly for smaller chamber pressures, a phenomenon taken to indicate jet detachment before the jet reached the test point. The nozzles tested involved a sudden change of direction at the throat and a consequent shock front development (observable in some photographs), which also influenced the test point pressures. The observations do not yield conclusive information regarding the performance of smooth nozzles with wide divergence.

1.8.5 Perfect Exhaust Nozzles and Compressors

Perfect nozzles can be constructed to produce any desired exhaust velocity. In dimensionless terms, the Mach number of the exhaust flow, or what is equivalent, the ratio of chamber to exhaust pressure can be prescribed. In carrying out the construction, the methods outlined in Section 1.8.4 can be employed to secure a flow which at least has the desired exhaust velocity. A simple rerouting process can then be used. The method of achieving the rerouting was described¹³ for a two-dimensional exhaust flow. The accompanying diagram (Figure 43) is merely suggestive of the process. In the figure, A_0 is the point on the axis where the basic flow F_0 attains the desired exhaust velocity q_0 ; C_0 is the backward Mach line determined by the flow F_0 , and D_0 is the forward Mach line of a flow with constant parallel velocity q_0 . Up to the line C_0 , the flow F_0 is retained. In the angle between C_0 and D_0 it is altered into the flow with constant parallel velocity q_0 . The straight lines in the sector between C_0 and D_0 are Mach lines.

CONFIDENTIAL

With their aid, a field of directions is determined, the integration of which gives the streamlines of the new flow F . A special property of the Mach lines is employed to make a natural selection of that modified streamline (through B in the figure), which is to serve as nozzle contour. The Mach lines in the sector increase in their inclination to the axis for a time, but thereafter decrease. The point B is chosen as the place where the inclination is a maximum.

By a similar less simple process, a perfect three-dimensional flow and a perfect three-dimensional nozzle can be constructed. For this, the flow is determined from the basic differential equations in the region bounded by the fronts analogous to C_0 and D_0 . Because of the particular type of initial condition involved in the problem, a numerical procedure can be readily applied¹³ to solve these differential equations. The construction of perfect nozzles was discussed a number of years ago by Prandtl and Busemann.

Because in principle isentropic flow is reversible, it follows that a nozzle so designed as to permit a shockless exhaust flow should also permit the reversed flow from exit into chamber. It thus appears possible to compress a supersonic stream of air or gas so that it comes to rest, by guiding it through a reversed exhaust nozzle or compressor. Only in a perfect exhaust flow is the reversal of any immediate practical interest, because all the applications thus far involve flows entering the compressor with constant velocity in the axial direction.

In the compressor problem, the flow speed, pressure, and density are prescribed at the entrance. Through Bernoulli's law and the adiabatic relation, these quantities determined the stagnation pressure p_{st} , which corresponds to vanishing speed. In order for the flow to be isentropic, this stagnation pressure must be maintained in the chamber $p_c = p_{st}$. Hence the design of the compressor is determined by the ratio of stagnation pressure to entrance pressure.

The actual operation of a compressor precisely in accordance with the theory here outlined depends essentially on the extent to which viscosity and heat conduction are negligible. It is especially to be noted that the action of viscosity is not reversible and therefore enters into the compressor problem differently from the way in which it enters the problem of exhaust flow. Since the flow is directed against a pressure rise, there is danger that the boundary layer may detach itself from the wall somewhere in the

diverging section between the throat and the chamber. This danger is probably avoidable by restrictions on the divergence of that section.

Further investigations of the influence of the boundary layer on the main stream in compressor flow are needed.

Viscosity enters into the formation of shock fronts. When a compressive flow curves inward too strongly, it cannot continue isentropically, and a shock front then develops in the stream. As long as the influence of the boundary layer does not interfere, however, the perfect design of the nozzle guarantees the existence of an isentropic continuation of the flow.

For a compressive flow, in contrast to an exhaust flow, a decrease, not an increase, of chamber pressure will cause a shock front to develop, because the stagnation pressure decreases when entropy increases. In order to avoid instability in the flow, it is necessary to operate the compressor with a chamber pressure less than the ideal one for which the nozzle was designed.

A qualitative discussion¹³ of the stability of compressor flow involves the expected effects of altering the entering speed q_e of the gas and altering the pressure chamber p_c . With the hydraulic theory as a basis for approximations, it was noted that when q_e is increased above the ideal entering speed, the flow may pass the throat in a supersonic state and thus be a supersonic expansive flow in a short interval. A shock front may then occur between throat and chamber to reduce the flow speed to zero in the chamber. The position of the shock front depends on p_c , an increase in p_c causing the shock to recede toward the throat. If \bar{p}_c is the chamber pressure which causes the shock just to stand in the throat, then the result of increasing p_c above \bar{p}_c is a matter for speculation. The flow is surely unstable when $p_c = \bar{p}_c$, and pulsation might occur if $p_c > \bar{p}_c$.

If, now, q_e is reduced below the ideal value, then no steady flow can result, regardless of chamber pressure. An oscillatory flow is a probability.

As a general conclusion, ideal flow is unstable, because increase of chamber pressure above \bar{p}_c or decrease of entrance speed will cause pulsations or some other complete change of flow. Stable operation of the compressor requires an entrance speed q_e greater than the ideal speed for which the compressor was designed and a chamber pressure less than the maximum value $\bar{p}_c(q_e)$ corresponding to the entrance speed q_e . It is thus necessary to admit a shock in the operation of the compressor, but the shock strength

can be kept small, and its position can be confined to the neighborhood of the throat.

Particular interest attaches to projectiles or missiles of similar shape carrying a compressor bored into the nose. When a missile is opposed to a supersonic stream of air, the air has the opportunity of entering the compressor and arriving in the chamber isentropically compressed. Although a rigorous mathematical analysis was not feasible, there was a discussion¹³ of whether or not the phenomenon just described will actually take place, and also a discussion of the question of drag resulting from the outer surface of the projectile. One possible disturbing influence is the rim of the compressor, which may interfere with the air entering the bore with constant axial velocity. Another is the shock front, standing ahead of or commencing at the foremost part of a missile moving with supersonic velocity. The position and shape of the shock front depend in part on the Mach number M_0 of the air flow relative to the missile and are influenced quite generally by the shape of the missile.

If an object carries a compressor of the type under consideration, the exterior flow does not change much except at the rim. Near the rim, the flow is locally the same as a two-dimensional flow deflected by a wedge. Hence the condition that the shock front begin at the rim and not stand ahead of it is the same as for a two-dimensional flow with reference to a wedge, namely, that the wedge angle be less than a certain extreme wedge angle depending on the Mach number M_0 . In general, this extreme wedge angle is roughly half the corresponding extreme angle for a cone.

When the rim angle exceeds the corresponding extreme wedge angle, a shock front either stands entirely ahead of the missile or stands ahead of the rim and is drawn into the missile. Various more or less complicated patterns of shock front and flow are possible, depending on the diameter of the compressor opening in relation to the distance the shock front stands ahead of the rim. An entrance shock is, however, entirely avoided by a rim angle less than the extreme, for example, 21 degrees when M_0 is 1.91, provided the compressor entrance is cylindric with axial direction, as in a perfect compressor. Hence the following condition:

The supersonic stream enters a perfect compressor with constant velocity without shock interference if the rim angle is less than the corresponding extreme angle for a wedge.

If a missile with conical nose is opposed to a supersonic stream of air of such strength that a shock front begins at the tip of the nose, existing theory permits surprisingly accurate calculation of the pressure drag on the nose. When a compressor is bored out of the missile, however, only rough estimates for the pressure drag become feasible.

In a supplement¹⁶ to the first report on nozzles, a detailed description was given of the construction of a perfect nozzle, and further light was thrown on the theoretical background of the construction. Between the appearance of these two reports, the method in question had been applied in a simple case. As a check on its accuracy, terms of third and fourth order were taken into account, and a more detailed derivation of the underlying differential equation was given.

In the actual design of a compressor duct, viscosity and heat conduction are not strictly negligible so that the design presented¹⁶ is only an approximation, although apparently a good one. Another respect in which it is merely an approximation is that shocks must, in reality, be admitted in the flow in order to avoid instability.

1.8.6 Related Heat Flow and Instrumentation Problems

The general program of rocket development involves problems not directly concerned with gas dynamics but closely associated therewith such as the problem of damage to airplanes by blast from rockets fired from beneath their wings. For many of the problems, there is need for considerable experimentation for which proper measuring instruments have not yet been devised. A program was consequently initiated and is still being carried out for the design and analysis of various instruments for measuring transient pressures, temperatures, and velocities in blast phenomena.

Another important line of research in rocket development is concerned with heat flow, especially heat flow in the walls of rockets, and the effects of thermal stresses caused by large temperature gradients in the walls and in the propellant grains of the rocket. Perturbations in temperature caused by the presence of the thermocouple structures in rockets under test have been evaluated, and, as a result, new designs for such structures have been proposed.

The material bearing on these heat flow problems exists in the form of notes ^{17, 18} by the Applied Mathematics Group of New York University.

For certain powder-burning rockets of relatively long burning time, there was fear of failure of the steel casings because of excessive heating, unless suitable coatings and other countermeasures were employed. As a help in designing such countermeasures, mathematical investigations of related heat flow problems were undertaken.¹⁷ These included a study of temperature variation with time in a steel slab about 0.3 cm thick, heated on one side by a hot gas with mass flux depending on the time. A similar study

allowed for variations in conductivity and heat capacity with temperature. It was proposed also to determine the cause of and remedy for the observed phenomenon of removal of steel from the inner part of the nozzle and its subsequent deposition on the throat of the nozzle.

A later note¹⁸ contained estimates of stresses caused by thermal gradients, which indicated unexpectedly high tensions in the cooler sides of the steel walls. Under certain circumstances, there appeared to be danger of a total stress locally exceeding the yield stress and therefore initiating rupture starting from the cooler side.

Chapter 2

UNDERWATER EXPLOSIONS AND HYDRODYNAMIC INVESTIGATIONS

2.1 UNDERWATER EXPLOSIONS

2.1.1 Introduction

THE MATERIAL of this section relates to AMP investigations of the gas bubble resulting from an underwater explosion. These studies led to significant contributions to the relevant mathematical theory and to results of considerable practical value.

The detonation of an explosive under water results in a gas bubble which has an enormous initial pressure, expands rapidly to a very low pressure, contracts to a small minimum size (with a resulting new pressure wave), and then rapidly expands again. The second pressure pulse of the underwater explosion is potentially of great importance in causing damage to targets. Its importance is influenced by changes in position of the bubble caused by the facts that the buoyancy of the gas causes the bubble to rise, the bubble is attracted by rigid walls, and it is repelled by the free surface of the water. Many interesting experimental and theoretical problems are suggested by the interplay of these three influences on the motion of the bubble, the relation of the pressure, momentum, and energy of different pulses to the damage produced on targets of various mechanical properties and the general question of changes in the shape of the gas bubble during its motion.

Consulting service, based on these investigations, was rendered in connection with certain specific projects. Most important of these projects was a study of the possibility of damaging the dams of water reservoirs by underwater attacks. Similar considerations entered into a study of probable damage to warships by underwater explosions of great magnitude at some distance from the target. Various problems arose involving the best location for explosions in underwater attack.

2.1.2 Summary of Principal Results

A broad program of theoretical studies in England and this country preceded the work done under the

direction of AMP. The principal results of the Panel's work can be summarized as follows.

1. An improved theory of the motion of the gas bubble was developed. This involved much numerical work and close contact with experiments, most of which were carried out by the Woods Hole Oceanographic Institution [WHOI]. The most significant accomplishment was an improved treatment of the differential equations of motion of the bubble so that this motion could be followed up to close proximity to rigid walls.

2. A very important phenomenon was investigated in connection with the situation where the various forces governing bubble motion so interact that the pulsating bubble remains at approximately the same point. Under such circumstances, one can expect a maximum effect from the pressure radiation in the second pulse. This phenomenon received extensive theoretical analysis which was later confirmed by experiments.

3. The surface phenomena resulting from underwater explosions were investigated, especially the breaking of the surface by the bubble and the appearance of "spray dome" and "plumes." Estimates were made of the time intervals between different surface events in terms of the depth of explosion, depth of water, size of charge, and type of explosive.

4. A refined theory which takes into account changes in the shape of the bubble during its motion was evolved.

The studies were pursued in coordination with experimental work by WHOI, the Navy Ordnance Laboratory [NOL] and Division 6 of the National Defense Research Committee [NDRC].

2.1.3 The Problem of Best Location

If a mine containing a given weight of explosive is to be placed near the sea bed, what position should it have to cause maximum damage to a target at the surface?

A comparatively slow pulsation of the gas bubble,

consisting of the burned gases, follows after the initial shock wave. The second, sometimes even the third, pulse of this motion results in a pressure of considerable strength. Even though these later pulses may have only ten to fifteen per cent of the peak pressure of the initial shock wave, they may last about twenty times as long and have a destructive effectiveness comparable to that of the initial shock. Model experiments and damage analysis support this statement. Hence considerable practical importance attaches to the understanding and control of the factors influencing the effectiveness of the second pulse.

It was shown¹ in AMP work on the present problem that the peak pressure of the second pulse possesses a decided maximum if the gas bubble is stationary at the moment of contraction. For practicable depths of water and weights of explosive, this stationary condition can be achieved by balancing the gravitational force with the attractive force of the sea bed and the repulsive force of the water surface.

Roughly speaking, for mines containing 500 to 2,000 lb of explosive in water 70 to 150 ft deep, the optimum position is about one maximum bubble radius (approximately 20 ft) above the sea bed.

The peak pressure is quite sensitive to changes in depth, even near the optimum, so that a change of a few feet may reduce the peak pressure by one-half. If a mine is placed directly on the sea bed, then, according to experimental evidence, the secondary pulse is weak and erratic.

The optimum depth for the secondary pulse improves the effectiveness of the shock wave in comparison with a location on the sea bed. The influence of the sea bed on the shock wave depends on the nature of the sea bed. Accordingly, as it is more or less rigid, it adds to the effectiveness of a mine resting on it. However, this is more than compensated by the decrease in distance from the surface when the mine is raised to the best position for secondary pulse.

Underlying the determination of the best location is the following principle of stabilization: *For a given mass of explosive, the maximum peak pressure in the secondary pulse is obtained if the gas bubble produced by the explosion is kept motionless at the time of its minimum size.*

As a plausible physical argument for this principle, consideration should be given to the fact that the total energy of the bubble and water is divided into the kinetic energy of the water surrounding the

bubble and the internal energy of the gas inside the bubble. If the bubble is moving at the time of its minimum size, some of the total energy is diverted into kinetic energy of the water and is therefore not available for the internal energy of the gas. Consequently, the pressure inside the gas and the pressure in the water are reduced. The stabilization principle was demonstrated¹ mathematically. The analysis takes account of the interplay of the gas pressure in the bubble and the motion of the water in contributing to the pressure in the water. The above physical argument ignores the second type of contribution, which is later proved mathematically to be relatively unimportant.

In connection with maximizing the damage caused by the second pulse, it should be noted that all damage theories indicate that when a pressure pulse is of long duration relative to the time constant of the target the damage is approximately proportional to the peak pressure rather than to impulse or energy. Because the second pulse lasts about twenty times as long as the shock wave, it appears that maximizing the peak pressure of this pulse should increase the damage. Table 1 gives numerical values resulting from the analysis.

TABLE 1. Best depths for certain mines.

Wt of TNT (lb)	Depth of sea bed from sea level (ft)	Best height for mine above sea bed
1,500	150	21.0
1,000	150	20.2
1,000	100	17.0
500	100	15.5

The graph in Figure 1 is drawn for a mine with 1,500 lb of TNT in water 150 ft deep. The graph shows the relative magnitudes of the peak pressure in the secondary pulse when the mine is placed at varying distances from the bottom of the sea. The best location is 21 ft from the bottom. Computations give, as the resulting peak pressure at any point in the water, $2,015/R$ atmospheres, where R is the distance in feet from the point to the center of the contracted bubble. If the mine is initially placed at some other distance from the bottom, then Figure 1 gives a factor by which the above value for peak pressure should be multiplied.

The sharpness of the graph suggests that if a mine is placed either 17 or 29 ft from the bottom, the peak pressure is only one-half the maximum.

2.1.4 Mathematical Study of the Secondary Pressure Pulse

High-pressure pulses are produced only when the gas bubble is near its minimum size. At such time, the buoyant force due to gravity is small. Also, the proximity of rigid walls or free surfaces does not materially affect the motion of the bubble because their influences depend on the ratio of bubble radius to distance from the bubble. At this stage of minimum size, therefore, the bubble can be thought of as immersed in an infinite body of water and subject to no outside forces. Under these circumstances, the pressure pulse produced by the bubble was investigated.¹ During contraction to minimum size, the bubble and

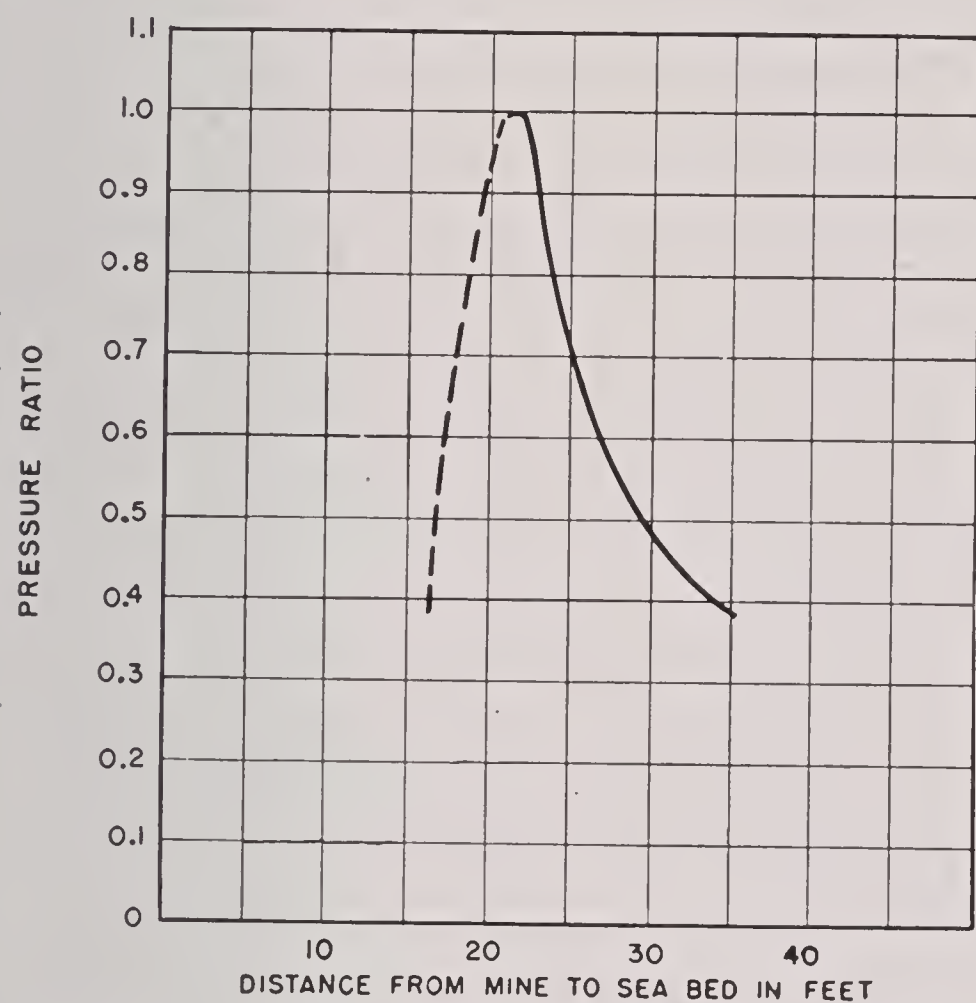


FIGURE 1. Pressure factor for mine of 1,500 lb of TNT in water 150 ft deep. (Ratio of peak pressure produced by mine placed at varying distances from the sea bed to the peak pressure produced when placed 21 ft above sea bed.)

surrounding water have a linear momentum which remains practically constant while the bubble passes through the minimum size stage when the outside influences can be neglected. The pressure pulse produced by the bubble depends on the linear momentum acquired by the bubble. In deriving the form of this dependence, the following assumptions are made:

1. The water is an ideal incompressible fluid.
 2. The bubble remains spherical in shape.
 3. The gas inside the bubble is in thermal equilibrium at each instant and follows the adiabatic law.
- The violations of the assumptions, in the very short

time interval when the bubble radius is small, involve corrections in the theory which do not significantly affect the principle of stabilization.

Classical theory furnished equations for the velocity potential describing the flow around a moving, pulsating sphere in an infinite body of water; the kinetic energy of the water; and the potential energy U of the system of gas bubble and water.

These equations were then simplified¹ by the use of nondimensional quantities with appropriate scaling factors; the scaling factor L for length being approximately the maximum radius of the bubble and that for time C being about two-thirds the period of pulsation of the bubble in the absence of such outside influences as rigid walls or free surfaces. On the basis of experimental evidence, it is found that

$$L = 13.2 \sqrt[3]{\frac{W}{D_0}} \text{ ft} \quad (1)$$

$$C = 2.85 \frac{W^{\frac{1}{3}}}{D_0^{\frac{5}{6}}}$$

in the case of W pounds of TNT, with center of explosion ($D_0 = 33$) ft below sea level. The depth D_0 is measured 33 ft above sea level to allow for the pressure of the atmosphere.

When the radius A of the bubble is small — in other words, during the interesting part of the motion — higher powers of $a = A/L$ become relatively insignificant in the energy equation. With the aid of this fact and the Lagrangian equations of motion, an explicit equation for \dot{a} is obtained, and the minimum radius \bar{a} is then readily obtained by setting $\dot{a} = 0$. The quantities required to characterize the bubble's motion near its minimum size can then be computed.

If A denotes the radius of the bubble, ρ the density of the water, and B the height above the sea bed, then the pressure at a distance R (not too small) from the center of explosion is found to be approximately

$$P = \frac{A}{R} \left(\frac{1}{2} \rho A'^2 + \frac{1}{4} \rho B'^2 + p(A) \right), \quad (2)$$

where the primes denote time derivatives and $p(A)$ is the internal pressure of the gas. *The principle of stabilization asserts that $p(A)$ is the most important term of equation (2) to such a degree that it should be maximized even at the expense of the dynamic terms*

$$\frac{1}{2} \rho A'^2 + \frac{1}{4} \rho B'^2.$$

The principle of stabilization, as just interpreted, was mathematically established,¹ along with the

statements that the peak pressure occurs at the time of the minimum size of the bubble and that the optimum peak pressure \bar{P}_{opt} in the secondary pulse for a given mass of explosive is obtained by keeping the bubble motionless at the time of its minimum size. The formula

$$\bar{P}_{\text{opt}} = 176 \frac{W^{\frac{1}{3}}}{R} \text{ atmospheres} \quad (3)$$

was obtained and compared with the experimentally established peak pressure

$$P_{\text{shock}} = 1160 \frac{W^{\frac{1}{3}}}{R} \text{ atmospheres} \quad (4)$$

of the primary shock wave.

The impulse I per unit area, carried by the secondary pulse, is the time integral

$$I = \int P dT \quad (5)$$

over the period during which $P > 0$. Approximately

$$I = \frac{0.83}{D_0^{\frac{1}{6}}} \frac{W^{\frac{2}{3}}}{R} \text{ atmosphere-seconds.} \quad (6)$$

In the case of a depth of 100 ft ($D_0 = 133$), this gives

$$I = 0.37 \frac{W^{\frac{2}{3}}}{R} \text{ atmosphere-seconds} \quad (7)$$

for the impulse carried by the secondary pulse, as compared with

$$I_{\text{shock}} = 0.12 \frac{W^{\frac{2}{3}}}{R} \quad (8)$$

for the impulse carried by the primary shock wave. The indication of three times the shock, while significant, should not be directly interpreted in terms of damage to a structure because the contribution to damage from a relatively long period of low pressure might be negligible.

From relations involving pressures and impulses of secondary pulse and shock, it appears that the secondary pulse lasts about eighteen times as long as the initial shock wave.

2.1.5 Stabilization by Gravity and the Sea Bed

In terms of the scaling factor L of equation (1), the nondimensional radius of the bubble and the nondimensional distance of its center above the sea bed are given, respectively, by

$$A = La \quad \text{and} \quad B = Lb, \quad (9)$$

and the nondimensional linear momentum, when the bubble is near minimum size, is

$$\bar{s} = \frac{1}{3} a^3 \dot{b}, \quad (10)$$

where the dot denotes differentiation with respect to the nondimensional time $t = T/C$. [See equation (1).] It is \bar{s} that determines the peak pressure produced by the bubble at the time of its minimum size, and the best location of the mine can be obtained by equating the momentum \bar{s} to zero. Hence it is important to calculate the effects of gravity and of a rigid wall on \bar{s} during a complete pulsation of the bubble.

In evaluating the period and momentum, it is assumed that the time \bar{t} and linear momentum \bar{s} at the minimum size of the bubble are twice the respective corresponding quantities at the maximum size ($\bar{t} = 2t_1$, $\bar{s} = 2s_1$), and that during the first half of the period of pulsation (until time t_1), b is small and can be taken as zero, so that b remains essentially equal to $b_0 = B_0/L$, where B_0 is the initial distance of the bubble from the sea bed. Both these assumptions agree satisfactorily with results of certain numerical integrations as well as with experimental evidence. An equation for $d = D/L$, under the conditions $\bar{s} = 0$ (which should produce maximum pressure, by the principle of stabilization), is

$$d = 6.2b_0^2 + 3.3b_0 + 0.4. \quad (11)$$

As for the migration of the bubble, an empirical formula is developed by combining a theoretical argument with results of numerical integration. The influence of the free surface (a repellent force) aids the downward force of the sea bed. A satisfactory approximate analysis replaces a complete discussion, which would require a knowledge of the velocity potential function and of several other relatively complicated functions. A situation is developed in which the influence of the free surface of the water on the period of the bubble cancels the influence of the rigid bottom. The validity of the approximations was tested by numerical integrations of the exact differential equations governing the motion of the bubble. The numerical integration was carried out by the Mathematics Tables Project operating under the Applied Mathematics Panel.

2.1.6 Effect of a Rigid Wall on the Bubble Motion

A study was made² of the motion of a gas bubble as influenced by the presence of a plane infinite rigid

wall. The method employed can be applied to the case of a spherical wall. This study was motivated partly by consideration of the fact that if a bubble, during its initial pulsation, moves closer to the target, then the secondary high pressure pulse produced when the bubble is near its minimum size, may cause more damage than the initial shock wave.

Earlier investigations³ dealt with the manner in which a bubble, relatively far from a rigid wall, is attracted by the wall, especially during the contracting state. A new method was introduced² which applies to all cases of this problem, even when the explosion takes place near the wall. General conclusions were based on the differential equations, a detailed solution of which required² numerical methods.

After the initial shock wave has passed, the water has an outward motion. The ensuing motion was studied under the assumptions that the water is incompressible and that the bubble remains spherical. If a denotes the radius of the bubble and b the distance from its center to the wall, the motion can then be described by giving a and b as functions of t . Differential equations for the determination of these functions are derived by concentrating attention on the liquid, whose hydrodynamic state is described by a velocity potential ϕ , where $\phi_{xx} + \phi_{yy} + \phi_{zz} = 0$ subject to the following boundary conditions (see Figure 2).

$$-\frac{\partial \phi}{\partial r} = \dot{a} + \dot{b} \cos \theta \quad \text{on the sphere} \quad (12)$$

$$-\frac{\partial \phi}{\partial r} = 0 \quad \text{on the plane}$$

and the condition $\phi = 0$, $-\text{grad } \phi = 0$ at infinity. After ϕ is determined, the total kinetic energy T of the liquid is calculated from

$$T = \frac{1}{2} \rho \iiint (-\text{grad } \phi)^2 d\tau, \quad (13)$$

which, in turn, leads to the Lagrange equations of motion.

It was shown,² on the basis of the resulting differential equations in a and b , that db/dt is negatively large during the contracting stage; in other words, that the bubble moves rapidly toward the wall. At the beginning, for a very brief interval of time, there appears, on the basis of the analysis, to be a very slow motion away from the wall, but it is so slow and brief that it would be hardly perceptible.

For a detailed analysis of the motion of the bubble, a numerical integration of the equations of motion was found necessary. An interesting case in the discussion is that of an explosion occurring at a distance from the rigid wall equal to the maximum radius of the spherical bubble.

The influence of gravity on bubble motion is neglected in general. However, for a rigid horizontal wall (above or below the bubble) it was found possible to include it with slight alteration in the basic equations. For a nonhorizontal wall (slanting or vertical), a third degree of freedom must be introduced in the form, for example, of the vertical depth c of the bubble center. There would then be three equations of motion.

2.1.7 Effect of Nonspherical Shape

Consider a pulsating gas bubble from an underwater explosion rising under the buoyant force caused by gravitation. The problem of its motion was investigated⁴ under various restrictive hypotheses. Earlier hypotheses were weakened by allowing small deviations from spherical symmetry and by avoiding the assumption that the bubble rises slowly. The need for such a modified discussion arose from the fact that significant deviations from earlier theoreti-

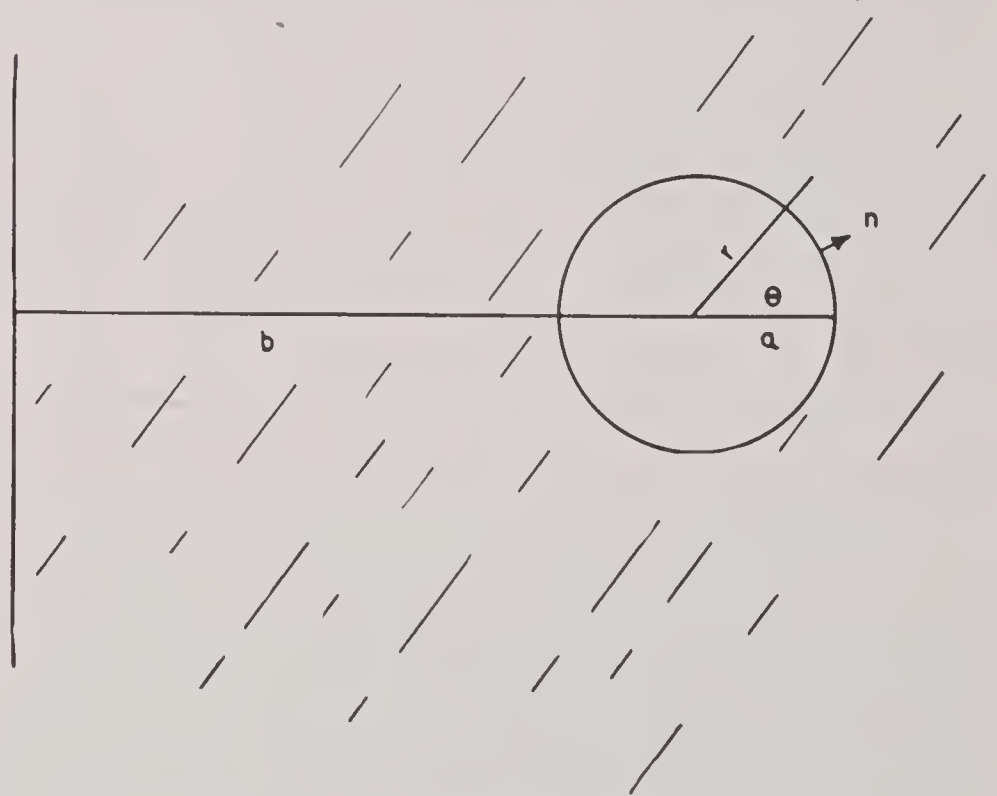


FIGURE 2. Spherical bubble near a rigid wall.

cal results had been found experimentally, for example, a larger high pressure pulse than predicted from a contracting bubble near its minimum size. Qualitative indications were presented⁴ that this phenomenon may be explained by deviations from spherical shape. However, numerical integration of

equations would be required for any reliable quantitative statements.

The surface of the bubble, in view of its rotational symmetry about a vertical axis, can be described by an equation $R = R(\theta)$ in polar coordinates with a suitably chosen pole inside the bubble. The pole is chosen in a manner to simplify an expansion of the function $R(\theta)$ in Legendre polynomials. In case of a surface with only moderate deviations from the spherical, the choice of pole is unique. It has the property that, in the Legendre polynomial expansion, a first order approximation leaves the volume of the bubble unchanged. The velocity potential, with boundary conditions, is determined by a method of successive approximations, whereupon the motion of the gas bubble can be found by equating the water pressure to the gas pressure at the surface of the water. This motion is thus obtained by substituting an approximate expression for the velocity potential in the Bernoulli equation for the pressure P of the water, evaluating at the surface of the bubble and retaining only first-order terms. A series of differential equations is obtained by expanding the Bernoulli equation into Legendre polynomials and equating the coefficients to zero. The first three such equations are amenable to mathematical analysis and form a basis for a discussion of the bubble motion. These equations require numerical solution.

Among the effects of deviation from spherical shape, as compared with earlier analyses which omitted such deviations, the following results may be noted: a less rapid rise of the bubble, a contraction of the gas bubble to a smaller size, and consequently a higher pressure than previously predicted at a specified point in the water.

It should, on the other hand, be remarked that the upward motion of the bubble, although it causes the contraction to take place nearer the target (assumed to be above the explosion), prevents the bubble from attaining so small a radius and hence produces a correspondingly weaker pressure pulse.

The work just summarized introduces corrections in earlier theory which are in the right direction from the point of view of experimental results. Numerical integration of the basic equations would be required to establish any quantitative agreement.

Many theoretical results serve chiefly to indicate directions in which valuable experiments might be performed. From the practical wartime viewpoint of application in combat, experiments suggested by the present theory become increasingly urgent. For

many purposes it is not possible to obtain sufficient information from model experiments, and full-scale tests are then needed.

2.1.8 Miscellaneous Considerations

Another problem in underwater explosives arose in connection with the question of blasting a path through obstacles, such as coral reefs, submerged in shallow water. A note in the form of an informal draft⁵ pointed out that the use of large charges released from planes or surface vessels would involve a waste of explosives and would at best be of strictly local effect. The burned gases from the explosion would break surface before their energy could be used for the desired purpose. As an alternative, the distribution of many small charges was suggested, so employed as to be detonated at the bottom and so small that the resulting gas globes would not break surface. Thus not only the first shock wave from the explosions but also the effects of the second and perhaps the third pulsations would be concentrated against obstacles. It is emphasized that the suggestions are based on idealized considerations and should be used, first of all, as a basis for planning experiments.

Some study was made of surface phenomena as an indication of underwater events. The investigations were based on experiments involving the dropping of charges from aircraft as well as the employment of statically detonated charges. Observations were made of such events as the formation of the spray dome and of various associated disturbances of the normal surface of the water, including the emergence of a vertical column of water and the appearance of plumes. Among the objects of such experimentation are the determination of the depth of explosion of a charge dropped from an airplane and the bubble periods of small charges fired near the surface. Certain experiments⁶ at WHOI made advisable a more complete treatment of the interaction of the gas bubble with the surface and the bottom, involving a comparison of theoretical with experimental results.

At the time when the OSRD contract terminated, many phases of the work on underwater explosions remained incomplete. The research is being continued under a Navy contract by essentially the same New York University group that worked on these problems under AMP. Among the unsolved problems are those associated with surface phenomena as related to underwater events and the problem of

CONFIDENTIAL

optimum position of an explosion for charges near the surface and for charges dropped from fast-flying aircraft.

2.2 AIR-WATER ENTRY OF SOLIDS

2.2.1 Introduction

A general survey of underwater ballistics forms Part 4 of this volume. In the present section, merely the initial phase of the entry problem (the so-called *impact phase*) is discussed and that only for vertical entry of a sphere or, more generally, a projectile with a nose of spherical shape. This impact phase is followed by the formation and collapse of the air bubble, provided the speed is high, after the projectile has completely or partially entered the water.

The present discussion is included here because of its close relation in mode of attack to the underwater bubble studies reported in Section 2.1. In fact, the work done by the AMG-NYU on the gas bubble studies enabled this same group to attack the entry problem with the aid of rigorous and powerful mathematical tools. They adapted to the purpose a method employed by Sommerfeld in the problem of diffraction of light and based on the use of potential functions in a Riemann space. It thus became possible to present a complete solution of this particular hydrodynamical problem of air-water entry. A numerical treatment based on the theory proved to be in satisfactory agreement with experiments. A better approximation was obtained in an extension of the work in which account was taken of the splash and disturbance of the plane water surface by the entering projectile. Furthermore, an attack was made on the entry problem for bodies of different shapes and also for oblique entry. As a result, mathematical methods were developed for theoretical treatment of the impact phase of the entry problem (probably incidentally for the impact of a shell on steel) which can account for the forces associated with the entry and which may be found applicable to other related problems, for example, the impact forces of airplanes landing on water.

During the impact stage of air-water entry, commencing with the initial contact and terminating with the formation of a cavity behind the projectile, the latter undergoes its greatest deceleration. Hence it is of great practical importance to obtain a quantitative estimate of the impact force in order to determine possible damage to the mechanism and nose

and to gain some information regarding associated impulsive force and torques, which influence the underwater trajectory of the projectile.

2.2.2 Summary of Methods and Results in the First Approximation

The upward force P on a sphere in the impact stage of air-water entry can be expressed in terms of a dimensionless *impact-drag coefficient* C_p . If A denotes the radius of the sphere, U_0 its velocity (assumed vertical) on impact, and ρ the density of the water, then

$$P = \frac{1}{2}\rho U_0^2 \cdot \pi A^2 \cdot C_p. \quad (14)$$

The coefficient C_p , regarded as a function of time, is equal to zero at the initial contact, increases rapidly to a maximum and then decreases. One of the important results⁷ is:

The maximum value of C_p is 0.95. It occurs when the lowest point of the sphere is about one-quarter of a radius past the original level of the water.

If B denotes the depth below the original water level of the lowest point of the sphere, then C_p as a function of the ratio B/A has the form revealed in Figure 3, the maximum occurring, as stated in the

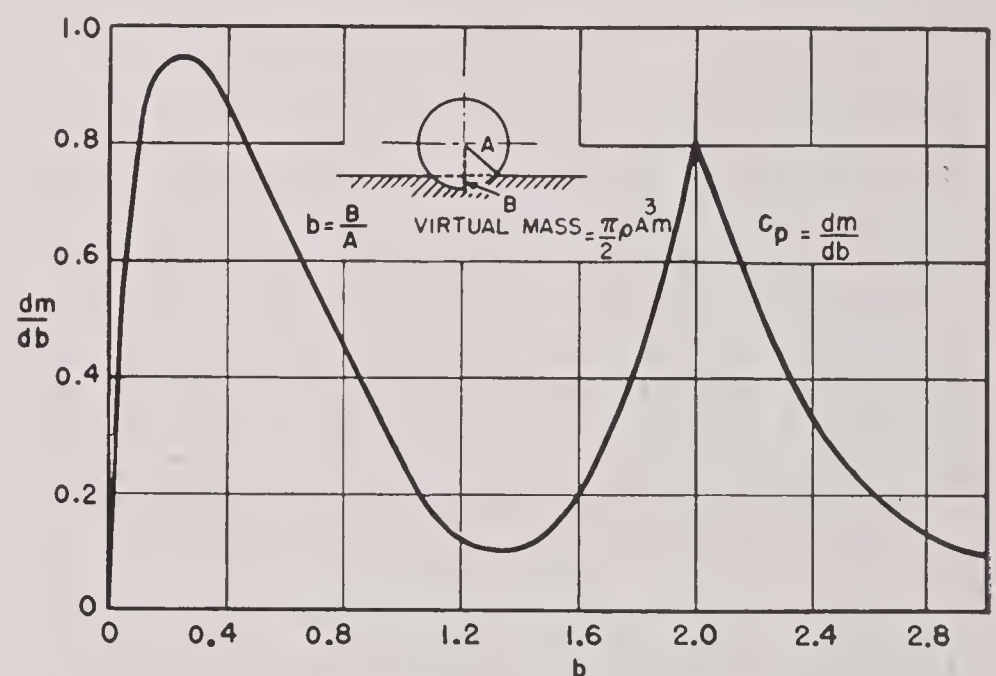


FIGURE 3. Impact drag coefficient as a function of depth of penetration.

preceding paragraph, approximately for the value 0.25. The graph should not be used beyond the point where a cavity is formed, generally somewhere between $B/A = 1/4$ and $B/A = 1$. In case the initial velocity U_0 is so small that no cavity occurs, the graph remains valid for the entire range of B/A .

The average pressure \bar{p} on the portion of sphere in contact with the water at any time is significant from the viewpoint of possible damage to the struc-

ture and mechanism of the projectile. In terms of the radius a of the circle of intersection of the sphere with the initial water level,

$$\bar{p} = \frac{P}{\pi a^2} = \frac{1}{2} \rho U_0^2 \cdot K_p, \quad (15)$$

where

$$K_p = \frac{A^2}{a^2} C_p. \quad (16)$$

The dependence of K_p on B/A , as exhibited in Figure 4, should be qualified by the remark that

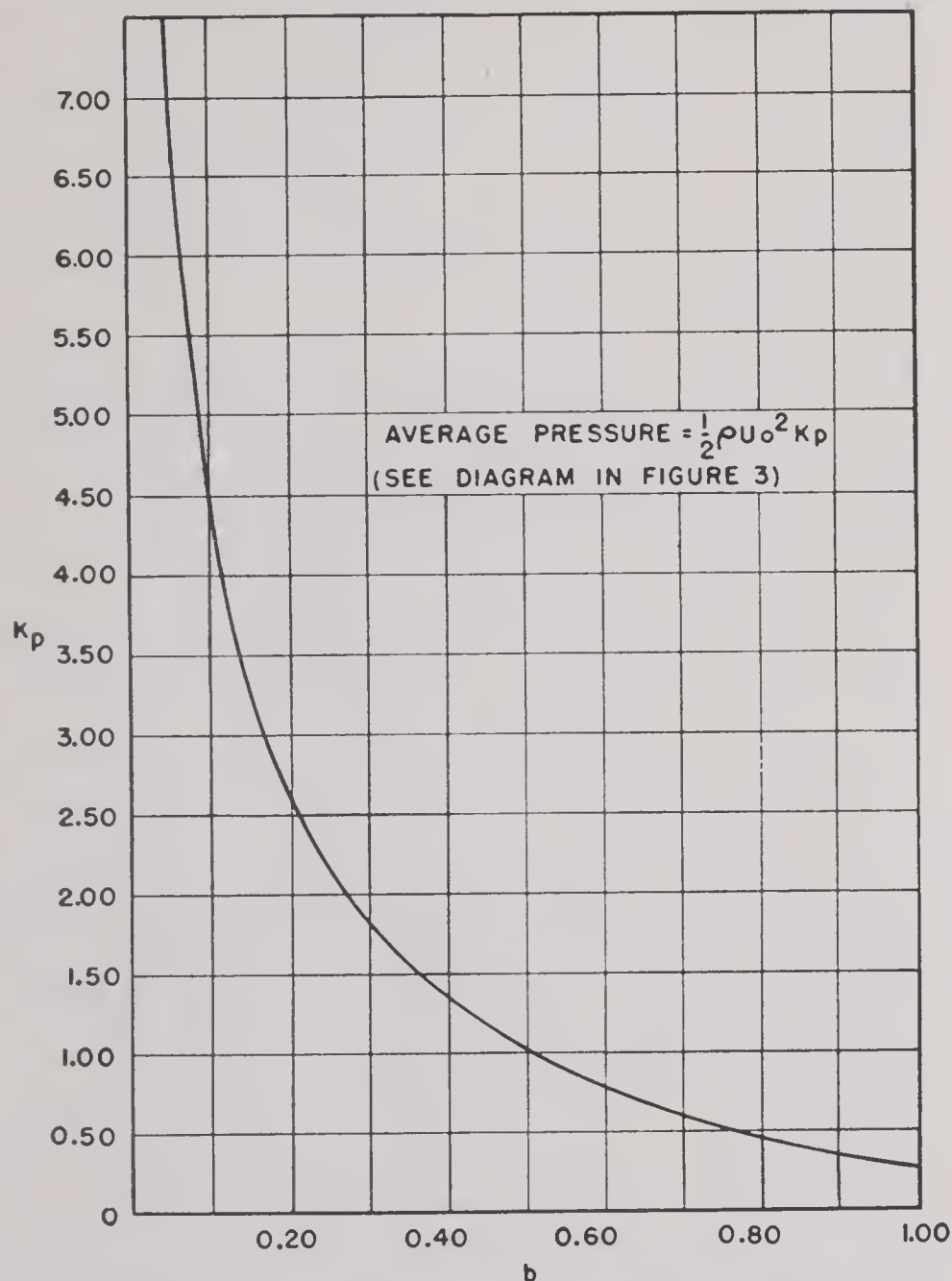


FIGURE 4. Average pressure coefficient as a function of depth of penetration.

because of the slight compressibility of water the initial pressure \bar{p} is only $\rho c U_0$ (where c is the speed of sound in water), instead of infinity, as suggested by the graph.

In the first approximation,⁷ motion of the surface was neglected, along with squares of velocities on the surface. On the free surface, the boundary condition then becomes $\Phi = 0$, where Φ is the velocity potential characterizing the flow. This assumption makes it possible to regard the results obtained as merely a first approximation. A second approxima-

tion⁸ took account of the disturbance of the water's surface by the entry of the body.

In the first approximation, the flow at each instant corresponds to that about a symmetrical lens, as indicated in Figure 5. It is the explicit determination

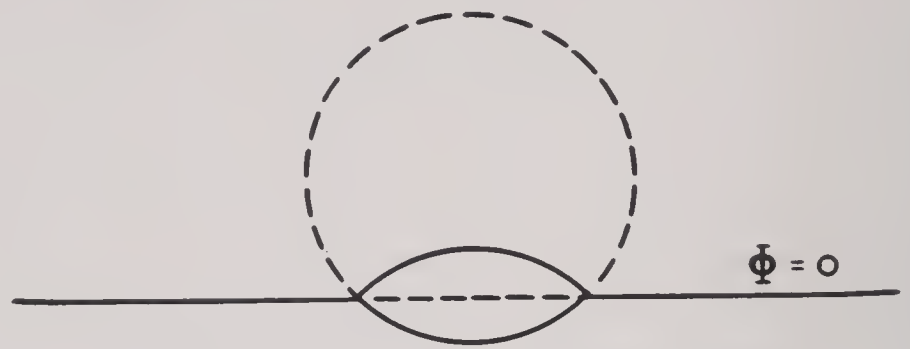


FIGURE 5. Lens as approximation to sphere.

of this flow about a lens which constitutes the principal mathematical contribution. The adaptation of Sommerfeld's method, which yielded the results, is of potential usefulness in analyzing other hydrodynamical and sound phenomena.

Near the edge of the lens in Figure 5, it is clear that a good approximation to the case of the sphere is not to be expected, since the water is free to stream along the back surface of the lens, whereas it can only rise along the sides of the sphere.

Let the depth below initial water level of the lowest point of the sphere be expressed as a function of the time: $B = B(t)$. It was then first established⁷ that

$$P = \frac{d}{dt}(M\dot{B}), \quad (17)$$

where $\dot{B} = dB/dt$ and

$$M = \rho \iint_{W+S} \Phi dx dy, \quad (18)$$

W being the wet portion of the sphere and S the free surface. The quantity M is considered the effective momentum mass of the water. The equation expressing conservation of momentum readily takes the form

$$(M + M_0)\dot{B} = M_0 U_0 \quad \text{or} \quad \dot{B} = \frac{U_0}{1 + \mu}, \quad (19)$$

where M_0 is the mass of the oncoming projectile and $\mu = M/M_0$.

Essentially, the problem is to find M or a useful approximation thereto.

As in many other problems, the use of dimensionless quantities is convenient. Hence the following dimensionless virtual mass and depth of penetration were employed,

$$m = \frac{M}{\frac{1}{2}\pi\rho A^3} \quad \text{and} \quad b = \frac{B}{A}. \quad (20)$$

In terms of these quantities, Figure 4 has its interpretation as representing dm/db as a function of b , with the maximum $dm/db = 0.95$ occurring for $b = 0.24$.

If an energy equation were used instead of a momentum equation, a more detailed analysis of the free surface would be required, since the spurts running up the side of the sphere carry considerable energy but little vertical momentum. Energy losses due to sound waves in the water and elastic vibrations of the projectile would also require some attention.

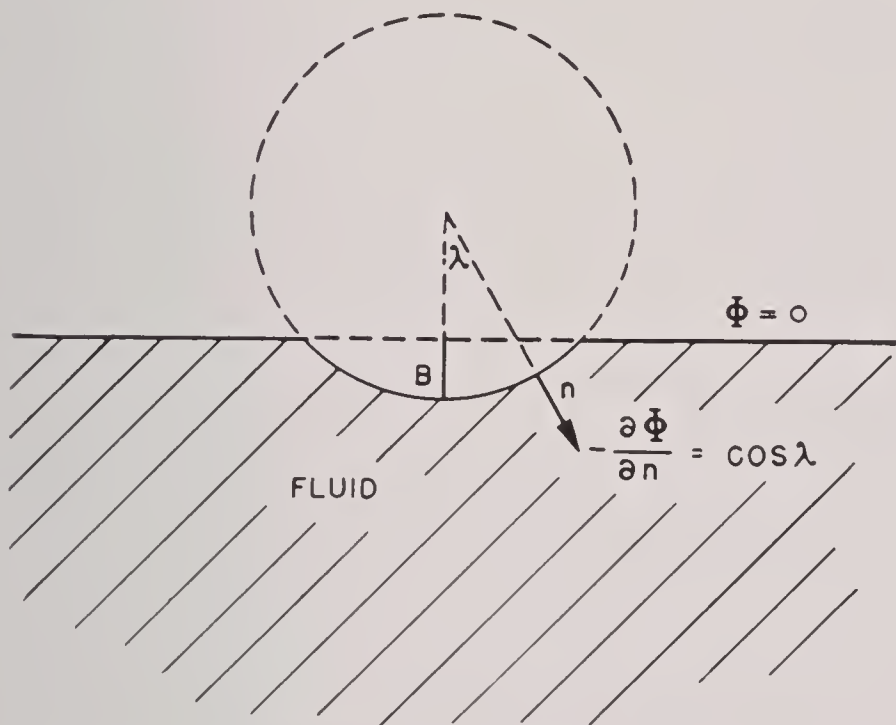


FIGURE 6. Boundary conditions for flow pattern.

The basic mathematical treatment is based on a description of the flow pattern of the fluid at time t by a velocity potential $\dot{B}\Phi(x,y,z,t)$, where

$$\Phi_{xx} + \Phi_{yy} + \Phi_{zz} = 0$$

with boundary conditions (see Figure 6)

$$-\dot{B} \frac{\partial \Phi}{\partial n} = \dot{B} \cos \lambda \text{ on the sphere} \quad (21)$$

$$\Phi = 0 \text{ on the plane, } z = 0 \text{ (water level).}$$

When it is attempted to construct Φ by the classical method of images, a difficulty is encountered because the sphere *intersects* the free surface; consequently, some of the successive images of the process lie in the fluid below the sphere, and dipoles (singularities) which violate the assumptions of the problem result inside the fluid. To obviate this difficulty, multivalued dipoles are employed, with images in the various sheets of a Riemann space. These images do not give rise to singularities in the portion of the space which is of interest in the problem. It is in the construction of the multivalued dipoles that an

adaptation of a method used by Sommerfeld was employed.⁷

For certain cases, tables of values for m and dm/db were computed by the Mathematical Tables Project, operating under the Applied Mathematics Panel. They were used, for example, in plotting the graph of Figure 4. For purposes of checking the theory, the virtual mass was calculated by other means in a few easy special cases.

2.2.3 Summary of Methods and Results in the Second Approximation

The second approximation² revealed that surface disturbance leads to two types of corrections in the earlier results. First, the upward rise of the surface of the water wets a larger portion of the entering body and thus increases the water resistance. Second, the rising surface causes a decrease in the impact force. These two partly counterbalancing forces were analyzed by a combination of theory and experiment. The results, which deviate somewhat from those of the first approximation, are in satisfactory agreement with experiment.

The next problem which it might be well to solve is that of oblique entry. Efforts are being continued in this direction, with the aid of the theory developed for vertical entry.

As in the first approximation, the projectile was first thought of as having a nose of spherical shape, and the entire mass of the projectile was then considered to be concentrated in a sphere of the same radius as the nose. The impact-drag coefficient C_p was defined as before and so was the virtual mass M of the fluid, namely, a quantity such that MU is the total vertical impulse communicated to the fluid during the time interval t :

$$P = \frac{d}{dt}(MU). \quad (22)$$

With the dimensionless virtual mass m defined by equation (20), it is shown that

$$C_p = \frac{\frac{dm}{db}}{\left(1 + \frac{3m}{8\sigma}\right)^3}, \quad (23)$$

where σ is the specific gravity defined by

$$\sigma = \frac{\text{mass of projectile}}{\frac{4}{3}\pi\rho A^3}. \quad (24)$$

For values of σ from 1 to ∞ , C_p rises very rapidly to a peak of about 1 (Figure 7), the peak occurring at a penetration of from one-tenth to one-fifth of a radius below the initial surface level. For smaller σ , the general behavior of the graph is retained, with a shift downward and to the left.

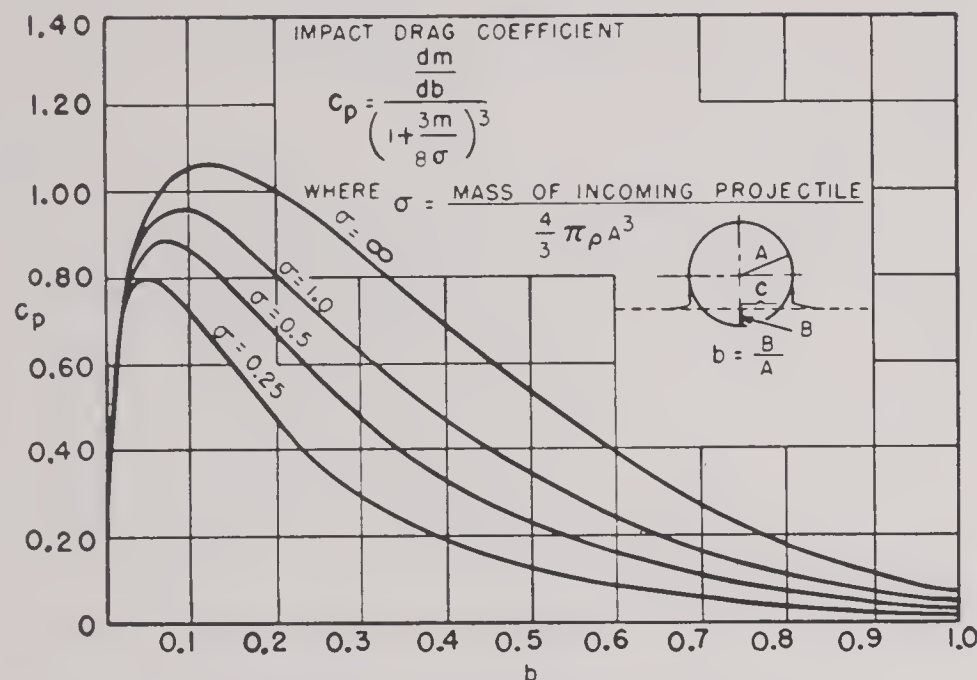


FIGURE 7. Impact drag coefficient.

In Figures 8 and 9, the first and second approximations to virtual mass m and impact-drag coefficient C_p are compared. In the corrected estimate of C_p , the maximum is somewhat larger and is displaced to the left.

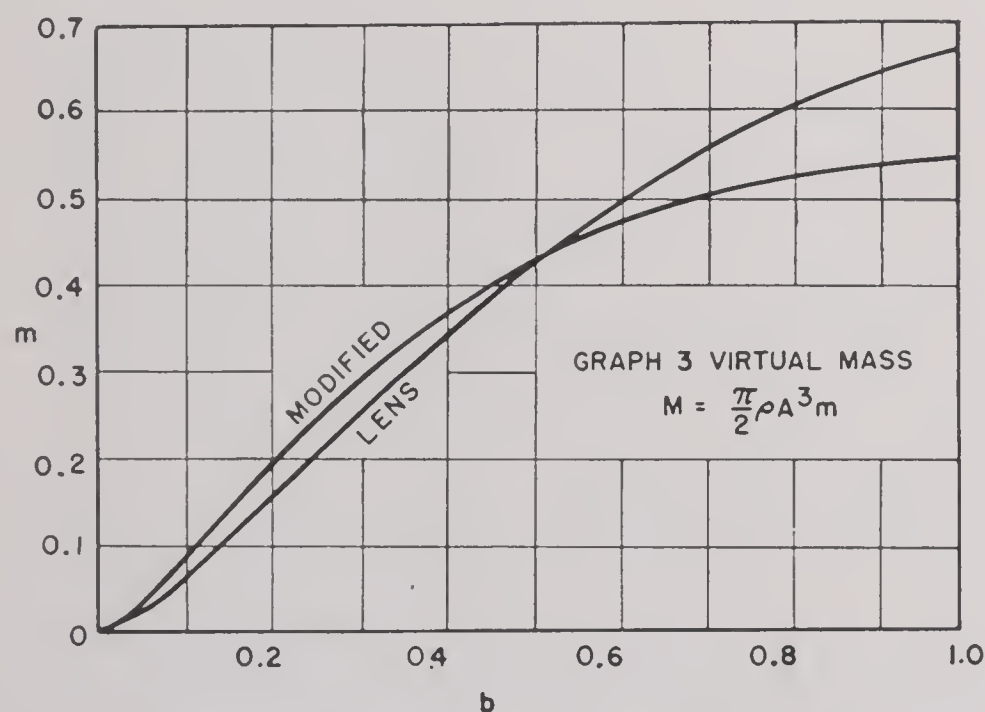


FIGURE 8. Virtual mass, $M = (\pi/2)\rho A^3 m$.

In the second approximation, the two types of correction suggested above can be thought of as a *wetting correction* and a *surface correction*. The value of C_p , with the two corrections included, was compared with experimental measurements of the impact force on a sphere, including the careful experiments of S. Watanabe.¹⁸ Other experiments serve chiefly to give an idea of the order of magnitude of the impact

forces and of their duration. The agreement between experiment and theory is satisfactory.

In view of equation (23), the determination of C_p requires merely the determination of the dimensionless virtual mass m . In formulating the problem, effects of compressibility and viscosity of the fluid are neglected. The flow of the fluid is irrotational and is described by a velocity potential $\Psi(x, y, z, t)$, where the velocity of the fluid at the instant t and position x, y, z is given by $-\text{grad } \Psi$; $\Psi_{xx} + \Psi_{yy} + \Psi_{zz} = 0$, with subscripts denoting differentiation; and the formula

$$\frac{p}{\rho} + \frac{1}{2}(\text{grad } \Psi)^2 - \frac{\partial \Psi}{\partial t} = 0 \quad (\text{Bernoulli's equation}) \quad (25)$$

connects pressure p in excess of hydrostatic pressure with the potential function. The form $\Psi = \dot{B}\Phi$ of the potential, used in the first approximation, exhibits separately the effect of the velocity \dot{B} of the sphere.

The impact force exerted on the sphere is obtained, as in Section 2.2.2, by use of the principle of conservation of momentum.

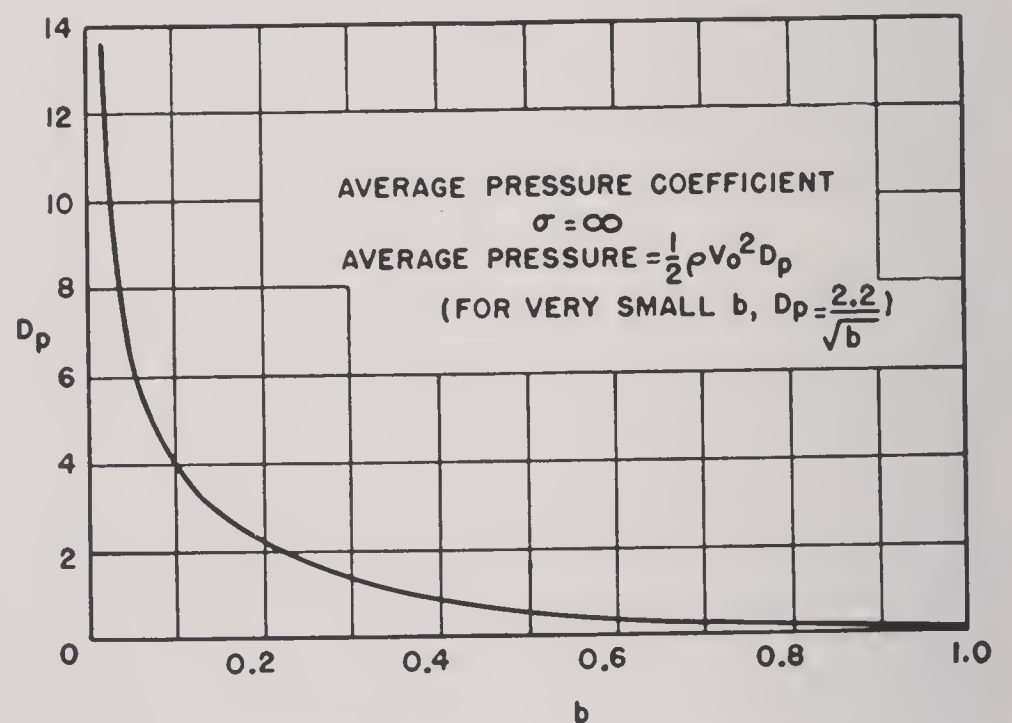


FIGURE 9. Average pressure coefficient.

The exact boundary condition on the free surface of the sphere is $P = 0$ or, by (25),

$$\frac{\partial \Psi}{\partial t} = \frac{1}{2}(\text{grad } \Psi)^2. \quad (26)$$

Avoiding the difficulties caused by the nonlinearity of this exact condition, the first approximation employed $\partial \Psi / \partial t = 0$, neglecting $(\text{grad } \Psi)^2$. In analyzing the corrections here introduced, the expression

$$M = \rho \iint_{W+S} \phi dx dy = \rho \iint_W \phi dx dy + \rho \iint_S \phi dx dy \quad (27)$$

for virtual mass is useful, since it breaks M into two integrals corresponding to the notions of the wetting and surface corrections.

Figure 10 is suggestive for the wetting correction. The separation (more or less arbitrary) of the part of the fluid which has risen by the horizontal line QQ corresponds to the notion of a thick base of water below QQ' , the influence of which is the same as if it extended to ∞ ; that is, as if the water level were raised to Q . In the report,⁸ the choice of Q is clarified and mathematically determined to a certain extent.

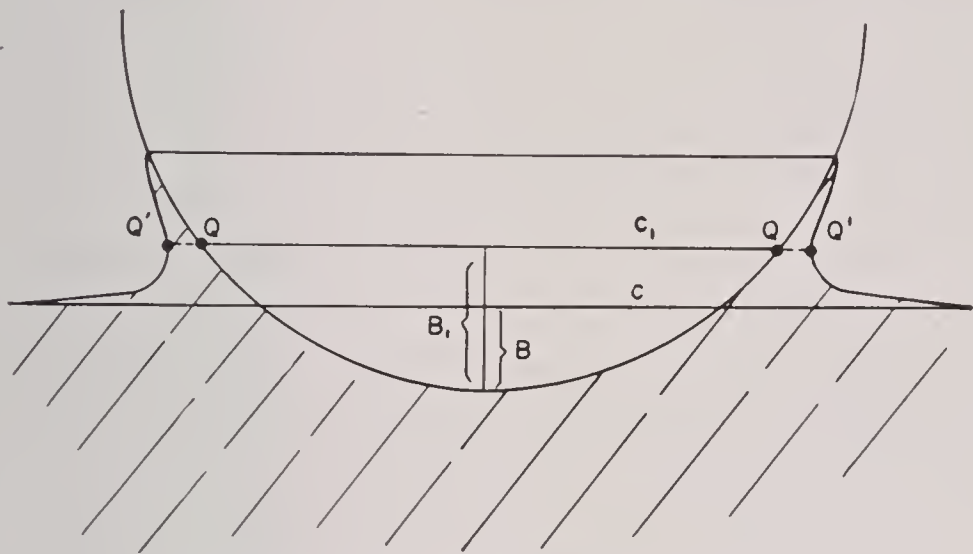


FIGURE 10. Rise of fluid near sphere.

In the wetting correction, it is the spherical segment below Q which becomes the so-called wetted portion W ; and the *effective* depth B_1 (Figure 10) replaces B , and so forth. The flow of the fluid is caused by the *effective* (or wetted) portion W and is approximately that caused by the lens of the first approximation, increased by using B_1 in place of B .

The exact dependence of $b_1 = B_1/A$ on b presents extreme theoretical difficulties, but it was found possible to determine it approximately with the aid of experimental results.

The free surface correction arises from the last term in equation (27) and the fact that the exact boundary condition (26) is to be used in place of $\Psi = 0$. It was established that the surface correction is negative, in accordance with the statement that the two corrections partly compensate one another.

2.3 JET PROPULSION IN WATER

2.3.1 Introduction

In addition to jet propulsion in air, an extensive study was undertaken⁹ concerning jet propulsion under water. Experimentation has not yet reached a stage permitting verification of the theoretical material developed in these latter studies. The work was

done in connection with Project NA-195 (Bureau of Aeronautics, Navy Department). It includes an analysis of various problems concerning the mechanics of the exhaust stroke in a hydropulse motor. Specific assumptions as to engineering aspects of the development were avoided in favor of a broad, fundamental approach to the subject.

In the devices under consideration, the propulsive element is a duct open at both ends (Figure 11). It is assumed to be traveling through the water with a certain velocity V ; for example, it might be propelling a ship or a torpedo. At a certain time, a chemical is injected into the duct and reacts with the water to produce a volume of gas, as indicated in the figure. The gas expands and imparts momentum to the water. If the duct in front of the gas is sealed off by

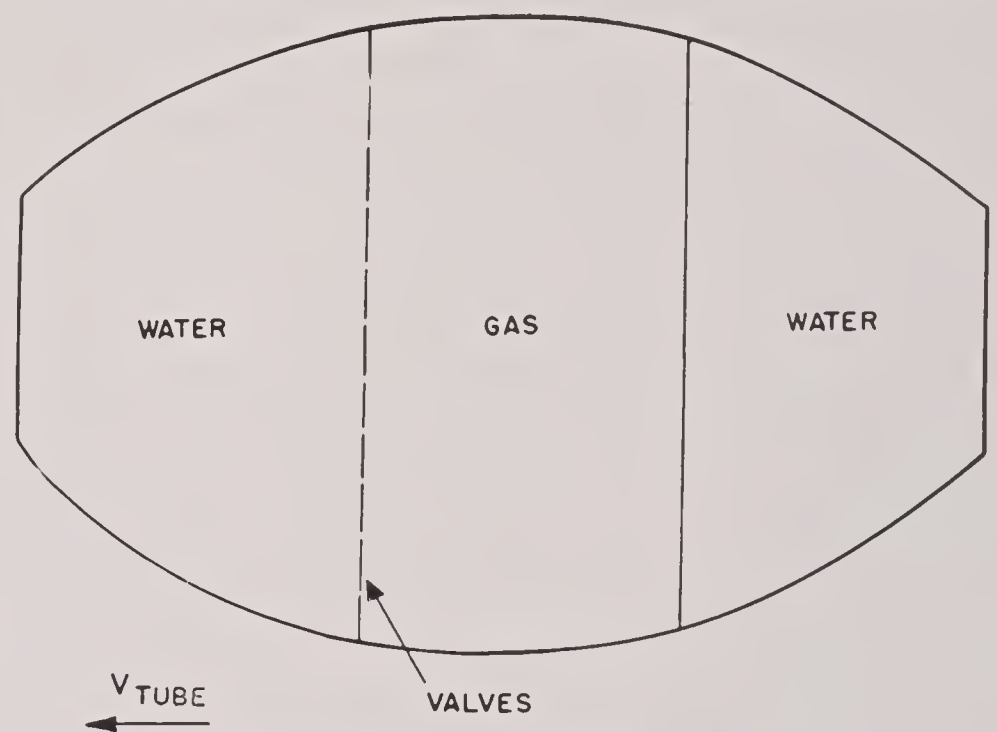


FIGURE 11. Duct of hydropulse.

closing valves, a thrust in the forward direction will result. For a sufficiently high forward velocity and a suitable design of the front intake part of the duct, it might be possible to dispense with valves and permit a continuous injection of fuel. At moderate velocities, however, it appears likely that valves would be necessary for efficient operation of the device. A complete cycle in the operation, commencing with the expulsion of the water, would consist of opening the valves, refilling the chamber, injection of the fuel, expansion of the gas, expulsion of the water, and so on.

The investigations⁹ were largely confined to phenomena which could be treated without detailed knowledge of the mechanical operation of the motor. Attention was thus directed primarily to that part of the cycle during which the gas was expanding and pushing water out of the tube. The motion was considered up to the time when the gas expanded down

to the exit pressure, and the time required for such expansion was called the *time of stroke* or, more simply, the *stroke*.

In the development of the theory, the water is treated as incompressible and nonviscous. Its motion is assumed to be irrotational, and its velocity distribution over any cross-section of the tube is replaced by the average over the section. The gas is assumed uniform in state throughout its volume at each instant of time and is assumed to expand adiabatically. The interface between gas and water is taken as a plane surface at right angles to the axis of the tube. The pressure at the exit of the tube is assumed constant during the entire stroke. These assumptions underlie a study of the motion of the water in the tube, the impulse delivered over the stroke, and the time of the stroke. These objects of study constitute the mechanics of the hydropulse operation as distinguished from the associated chemical and thermodynamic problems.

2.3.2 Method of Attack

The equation of motion of the water during a single stroke is derived, along with a formula for impulse, on the basis of classical principles (energy balance, conservation of momentum, and so on). This part of the work leads to an initial value problem for a nonlinear, ordinary differential equation of second order. An important simplification is achieved by expressing the essential variables and parameters in dimensionless form.

2.3.3 Duct of Variable Cross Section

Despite the apparent simplicity of the mathematical formulation just mentioned, an enormous amount of calculation would be needed for a complete discussion of the obvious physically important quantities involved in the problem. The complications are associated with the impossibility of explicitly integrating the equation of motion. Methods of numerical integration must be resorted to. However, even without a complete integration of the equations, useful approximate formulas were found for the quantities of the greatest practical importance. These quantities include: the impulse I_s per stroke; the ratio I_s/M_g of impulse to mass of fuel injected per stroke, referred to as *specific impulse* or effective velocity; the time of stroke t_s ; and the average thrust $\bar{F}_s = I_s/t_s$. The approximate formulas

yield rigorous upper bounds for I_s and \bar{F}_s and a rigorous lower bound for t_s . The formulas have been demonstrated to yield, in many cases, results accurate within 2 per cent for I_s and 5 to 15 per cent for t_s , as long as the initial pressure ratio exceeds 10 and the duct is a sufficiently close approximation to a straight tube of uniform cross section.

The problem of maximizing the impulse with respect to changes in the shape of the hydropulse tube has been discussed.⁹ For a small forward speed of the hydropulse, a straight cylindrical tube is as good as any other. This follows from the calculated fact that such a tube yields an impulse very close to a rigorously established upper bound of I_s for all shapes of tubes. For a rapidly moving hydropulse, for which the velocity of the water in the tube is high at the start of the stroke, the impulse I_s is more sensitive to changes in the shape of the tube. Indications are that some sort of flared-out forward part joined to a straight cylinder extending to the exit may be best from the viewpoint of maximizing I_s .

2.3.4 Approximate Solutions for the Tube of Constant Cross Section

The general approximate formulas mentioned in Section 2.3.3 were developed explicitly for the case of a straight tube in such a way as to permit a complete discussion for the full ranges of all essential parameters. These formulas express the dependence of the four quantities enumerated in Section 2.3.3 on the initial pressure ratio p_i/p_e , the ratio M_g/M_w of the mass of gas M_g injected per stroke to the initial mass M_w of water in the tube, the initial velocity U_i of the water in the tube, the adiabatic constant γ , and the initial temperature and molecular weight of the gas.

2.3.5 Performance of the Tube of Constant Cross Section

The effective velocity I_s/M_g , which measures the efficiency of the device, exhibits only a slow increase, especially for higher initial velocities, once the initial pressure ratio p_i/p_e exceeds 30.

Hence, from the viewpoint of fuel consumption, no great advantage would result from going to pressure ratios above 30. Efficiency is promoted by keeping the amount of fuel injected per stroke as low as is consistent with other requirements.

The time of stroke t_s is not very sensitive to

changes in p_i/p_e if this pressure ratio exceeds 30 or 40. If the fuel ratio M_o/M_w alone is varied (in particular, while keeping p_i/p_e fixed), then t_s tends to zero and to infinity with the fuel ratio. There are, of course, practical limits to the variation of M_o/M_w with p_i/p_e held fixed.

The average thrust, $\bar{F}_s = I_s/t_s$, increases steadily with p_i/p_e . With respect to M_o/M_w , \bar{F}_s decreases steadily from a finite value for $M_o/M_w \rightarrow \infty$ and approaches half that same value as $M_o/M_w \rightarrow 0$, a statement to be considered in conjunction with the limitations on M_o/M_w as p_i/p_e is held fixed.

Since the effective velocity tends to its maximum value for $M_o/M_w = 0$, it is strongly suggested that *the hydropulse should be operated at high frequency with injection of small amounts of fuel per stroke. These amounts of fuel should be kept as low as is compatible with maintenance of a minimum initial pressure ratio (perhaps 30 or 40), so that the average thrust will be maintained at the value necessary to overcome the drag on the hydropulse.*

As functions of the time, the gas pressure has a very rapid initial decrease and the velocity of the water a very rapid initial increase. Thereafter, for the rest of the stroke, both quantities remain nearly constant.

Some consideration was given⁹ to the effect of replacing the assumed instantaneous creation of the initial high pressure of the gas by a linear building up of that pressure, followed of course by an adiabatic expansion down to exit pressure. This more realistic approach reveals, for the few cases considered, that a gradual buildup in pressure may be favorable for the operation of the hydropulse, since the impulse delivered per stroke for a given quantity of fuel comes out substantially larger than in case of an instantaneous pressure rise. It is noted, however, that the method of comparison might be open to objections on physical grounds.

2.3.6 Straight Tube with Elastic Energy Storage

Calculations reveal a very rapid change in gas pressure and velocity of the water in the tube at the beginning of the exhaust stroke. It appears that a more even distribution of the thrust and the exit velocity might be in the interests of efficiency. Such a distribution might be accomplished by some sort of elastic storage of energy during the early part of the stroke and a delivery of that energy during the later

part. A mechanical model was investigated⁹ in the report, in an exploratory spirit, as a sort of preliminary appraisal of this possibility. The rigid wall (valves) closing the left end was thought of as replaced by a piston of a certain mass attached to a spring. It was found that considerable influence could be exercised on the time distribution of the thrust and on the velocity of the water by suitable selection of mass and spring; in particular, a successful smoothing out of the abrupt initial variations in thrust and velocity appeared practicable.

An alternative method of providing elastic storage might be a type of fuel injection which would create two gas volumes separated by a mass of water. The calculations bearing on this method⁹ cover only a very small number of possibilities, but they reveal the feasibility of thus modifying the time distribution of thrust and velocity.

2.3.7 The Valveless Hydropulse

In a tentative canvassing⁹ of the possibility of operating a hydropulse without valves, the tube was assumed to be open at both ends but to have a constricted front portion. A flow of water was assumed in the tube at the time when the gas, at relatively high pressure, was injected (behind the constriction). The flow was analyzed, under the usual assumptions, up to the time when gas pressure decreased to the value at the exit. For any particular set of parameter values, the solution required numerical integration of a pair of second-order nonlinear differential equations. On the basis of the four cases treated, the following conclusion was reached.

As far as the total impulse for a single stroke is concerned, a hydropulse without valves could be designed to compare favorably in performance with the hydropulse with valves. A fairly long narrow forward or nose section apparently would be needed. Such a constricted forward portion, however, is shown to be very unfavorable for the scavenging or refill portion of the whole cycle of operations.

2.3.8 Scavenging

At the end of the exhaust stroke, the gas pressure has just fallen to exit pressure. The inertia of the moving mass of the water leads to a further expansion of the gas, which could be employed to cause valves to open, by virtue of water pressure in front of the valves. A study of the subsequent motion of both

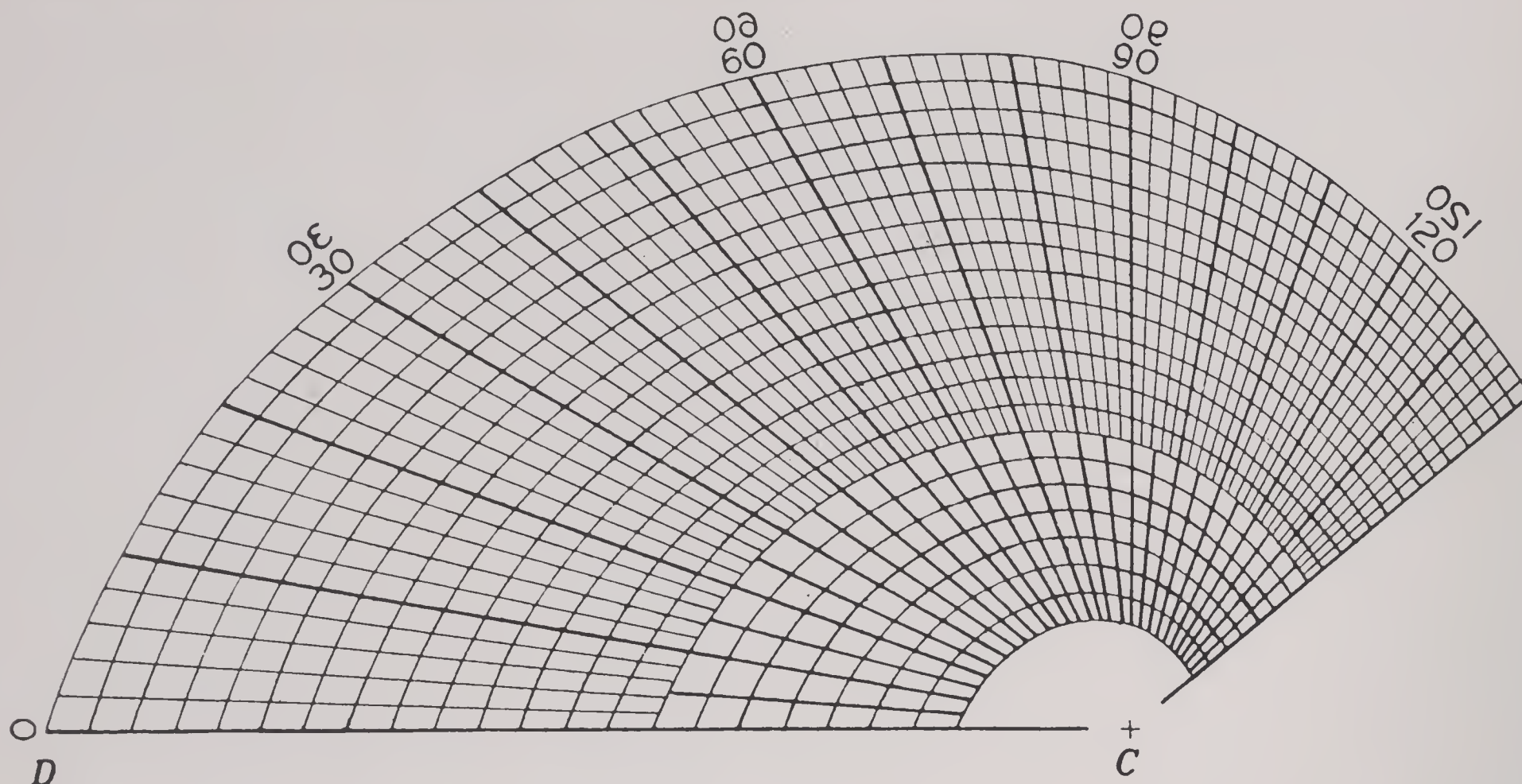


FIGURE 12. Cusp loci.

layers of water was made⁹ under the usual assumptions. This study involved numerical integration of a pair of second-order differential equations dependent on a considerable number of parameters, for which reasonable values were assumed. In general, the scavenging operation turned out to be very slow. In the numerical case treated, three times the time of the exhaust stroke is required for the gas pressure to reach its minimum after the valves open, and even then the refilled volume is less than the volume of the gas layer at the time the valves open. Because it is essential to efficiency that the scavenging phase does not occupy an excessive portion of the full cycle, it appears that this phase may present problems of crucial importance. Some possible remedies were suggested, along with an indication of the problems requiring further investigation.

2.3.9 Effect of Finely Distributed Gas Bubbles

In practice, the fuel may be so injected into the water as to create, not a single layer of gas, but a large number of minute bubbles distributed over a certain volume. The motion of the water in this case also was shown⁹ to yield to treatment. On the basis of a number of simplifying assumptions, it was concluded that the motion in the tube is the same as if there were a single layer of gas of smaller total volume. Only two-thirds of the volume of the water containing gas bubbles is effective.

2.4 WAVE PATTERNS FROM SURFACE VESSELS

2.4.1 Introduction

In 1887, Lord Kelvin showed that the bow waves from a ship always make an angle of $19^{\circ} 28'$ with the vertex at the bow, regardless of the ship's size and speed. The speed of the ship is indicated by the spacing of cusps along these bow waves. The existence of numerous photographs of Japanese ships, almost always in turns, made it highly desirable to extend Lord Kelvin's analysis to turning ships.

The theoretical analysis of ship speeds¹⁰ was checked experimentally on the basis of a series of photographs of ships maneuvering at known speeds and rudder angles. Particular attention was given to the case of a circular course at a constant velocity, and a method was then developed for determining the speed of maneuvering ships from aerial photographs. Rather deep water was assumed, 150 to 200 ft or more for speeds of 30–35 knots. The agreement of theory and observation was very good, within a few per cent for both speed and turning radius.

The method developed by AMP was adopted by the Photographic Interpretation Center, which incorporated much of the research in an official handbook.¹¹

The Kelvin theory and the extension carried out under AMP become purely geometric once a single formula from hydrodynamics is given, namely, the

formula for the amplitude of the annular surface waves created by a sudden impulse at a point of the surface. The hydrodynamic problem of the amplitudes of the waves created by a turning ship and of the effect of finite depth of water on the wave pattern are subjects for continuing study.

A related general investigation of wave patterns created by surface vessels was undertaken in response to a request from the Bureau of Ships in connection with countermeasures against pressure mines. Existing theories were to be extended by taking into account the effects on the pressure pulse of the length of a run and of the ship's acceleration during the run. Great difficulties arise in studying the properties of well-known exact solutions, in the form of integral representations, when the parameters are varied, and the only methods which have thus far proved successful are tedious numerical computations and asymptotic developments. The work is being continued at New York University under Navy contract NOa(s)-7370.

2.4.2 Rules for Determining the Speed

In general, the most prominent feature in the photographs of turning ships is a series of waves on the inside of the curve. Frequently the waves appear to end in cusps. The curve on which such cusps lie is called the cusp locus. The method for determining the ship's speed is based on the spacing of the waves along the inner cusp locus. This method is founded on the following theoretical results:

A. Any two cusp loci have the same form but they differ in scale according to the radius R of the circle in which the ship is turning.

B. Once the turning radius R has become fixed, the spacing of the waves along the cusp loci depends solely on the speed c of the ship.

The procedure for determining the speed falls into the following four steps:

1. A set of inner cusp loci drawn on a transparent sheet (Figure 12) is placed over an aerial photograph, so that the inner cusp locus fits one of the curves or lies between two of them, with the bow of the ship somewhere on CD . Then C is the center of the circle in which the ship turns. The radius is determined if the ship's length is known.

2. A sequence $(0), (1), \dots, (n)$ of $(n + 1)$ clearly distinguishable successive cusps is selected (in general, as long a sequence as the photograph permits),

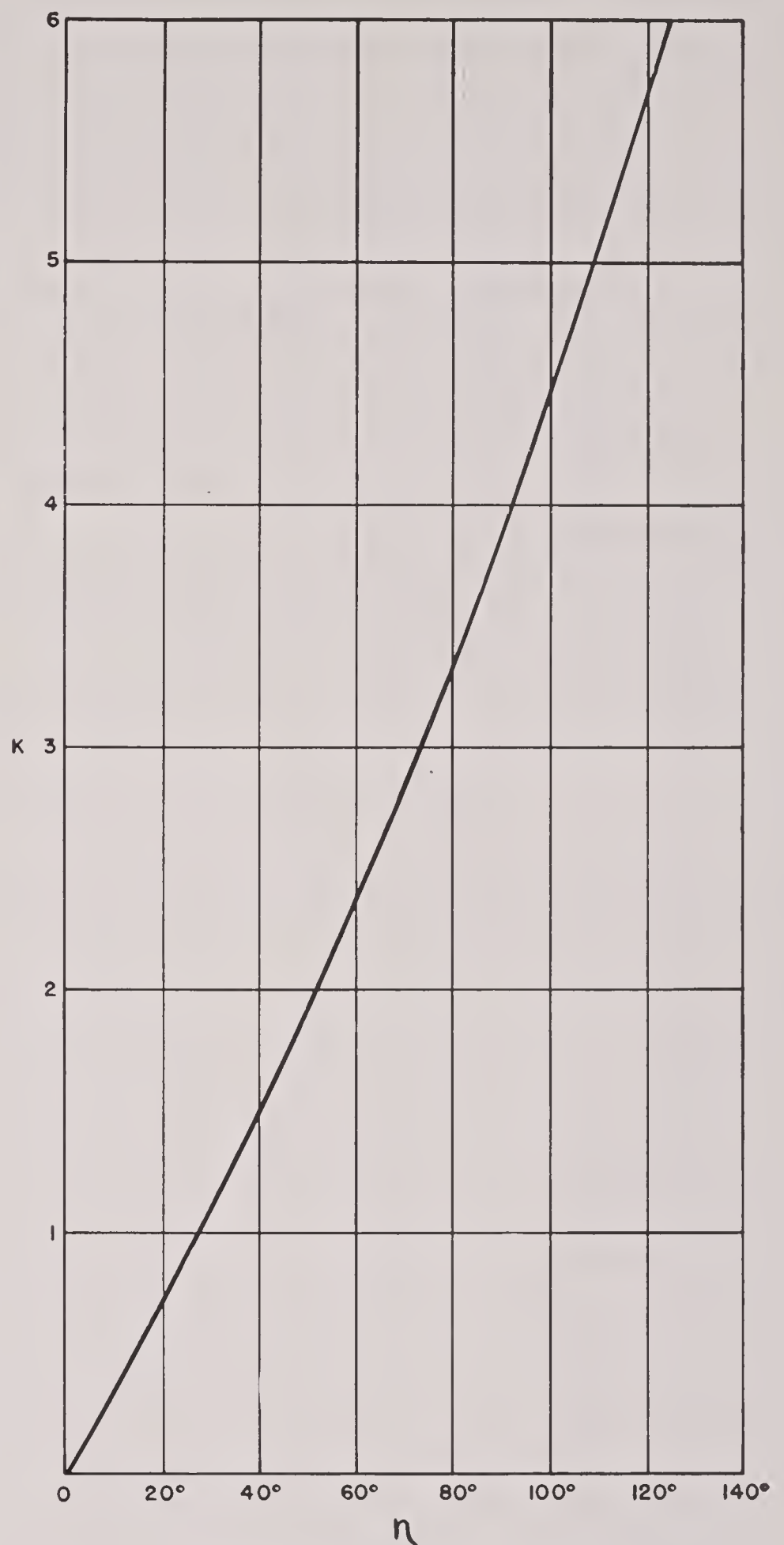


FIGURE 13. Graph of K versus η .

and the angles η_0 and η_n from CD to the first and last cusps are read off from the graph with the aid of the device of Figure 12. The notation is so assigned that $\eta_n - \eta_0$ is positive.

3. A second graph (Figure 13), whose construction involved the general theory quite completely, yields values K_0 and K_n , corresponding to η_0 and η_n , respectively.

4. The speed c of the ship, in knots, is given by

$$c = 0.949 \sqrt{\frac{R(K_n - K_0)}{n}}, \quad (28)$$

where R is in feet.

The above procedure was devised on the basis of available photographic material on enemy ships, which, as a rule, are shown making sharp turns. This procedure would need modification, with the aid of the fundamental theory, for turns with a comparatively large turning radius.

2.4.3 Basis for the Theory

The following simplifying assumptions were employed:

1. The ship is a moving point, sending out pulses in the form of annular waves.
2. The amplitudes and slopes of the resulting surface waves, and the velocity of the water, are small.
3. The depth of the water is infinite.

The theory is based on a classical approximate formula

$$z \cong k \frac{t^3}{r^4} \sin \left(\frac{gt^2}{4r} \right) \quad (29)$$

for the amplitude z of the annular waves, relative to

the undisturbed surface, resulting from a pressure impulse applied at the origin; where k depends on the magnitude of the pressure pulse and on the density of the water, t is time after the impulse was applied, r is distance from the origin, and g is gravitational acceleration. Any phase (as a crest or trough) is given by a constant value of

$$\phi = \frac{gt^2}{4r}. \quad (30)$$

Hence such phases are propagated each with a constant acceleration, though different phases are accelerated at different rates.

The total amplitude at a fixed point (x,y) resulting from a portion of a ship's path is obtained by integrating the expression for z relative to the time along the arc of the course in question, where r is now the length of the vector from (x,y) to the point of integration. The resulting integral was dealt with approximately first by Kelvin for straight-line courses at constant speed and second under AMP for circular courses at a constant speed.

PART II

WAVE PROPAGATION AND ELECTRONICS

CONFIDENTIAL

Chapter 3

WAVE TRANSMISSION THROUGH METAL SHELLS—UNDERWATER ACOUSTIC PROBLEMS

3.1 INTRODUCTION

IN DETECTION by echo ranging, using, for example, certain acoustic submarine detection devices, a sound beam from a projector is reflected by an obstacle and then received by the face of the projector, which functions also as a sound detecting device. In its dual role, it is referred to as a *transducer*. Such acoustic equipment requires protection when fastened to a ship traveling at even a moderate speed. Otherwise, noise from water and bubble motion about the transducer plates might effectively blanket the reception of the reflected sound beam. The required protection is afforded by streamlined convex shells, called *domes*, which enclose the transducers. The domes are fastened rigidly to the hulls of ships and are filled with water, oil, or some other liquid. Within a dome, the projector is free to sweep the azimuth and in some cases can be directed downward.

Theoretical solutions ^{1, 2, 3, 4} of the dome problem were given first for homogeneous shells, then for shells of nonhomogeneous structure, and finally for shells separating liquids of different acoustic properties. The theoretical solutions served to suggest desirable lines of further investigation, both experimental and theoretical, and to throw light on practical problems of design. It is clearly essential, in the matter of design, that a dome have the structural strength to withstand the thrusts it must encounter and that it does not seriously impair the directivity pattern of the beam.

Progress was made ^{5, 6, 7} in various related attempts to solve rigorously certain problems in wave motion involving disks or spheroids. Solutions of such problems would have wide applicability. The efforts are being continued, in connection with a gun-blast program, by a group at New York University, operating under Navy Department Contract NOas-7370.

3.2 THE MATHEMATICAL THEORY

3.2.1 Physical Assumptions and Formulation of the Problem

The problem of the influence of a dome on sound propagation can be formulated as an explicit boundary value problem of a partial differential equation of wave propagation with discontinuity conditions across the dome. The problem, so formulated, was explicitly solved ¹ in such a manner as to exhibit the dependence of the disturbance on thickness, density and shape of the shell, velocity of sound, and so on.

A. It is assumed that:

1. The original sound beam is stationary and periodic, with a certain frequency ω . All other relevant phenomena are subject to similar assumptions.

2. The shell of the dome behaves like a liquid whose density and bulk modulus (or sound velocity) may differ markedly from those of the liquids inside and outside of it.

3. The thickness of the shell of the dome is small in comparison with the wave length of the sound transmitted through it.

4. The undisturbed acoustic pressure, if the dome is not present, is given by the real part of a complex function, as follows: $\text{Re } p(x, y, z) e^{-i\omega t}$. It is assumed that the complex pressure amplitude p and its derivatives are known, either theoretically or experimentally.

Assumption 2 results in leaving flexural vibrations of the dome out of account. Experimental evidence suggests that this is reasonable.

The third assumption is reasonable for the domes and frequencies employed. It serves to make possible a useful approximate solution.

The original beam, subject to assumption 4, has a position in space which will be thought of as de-

pending on the position of the projector relative to the dome, the latter being considered fixed.

When it is stated that the pressure p represents a beam, the following is meant in analytic terms.

B. At distances $r = \sqrt{x^2 + y^2 + z^2}$ from the projector, which are large relative to the diameter of the projector, the pressure amplitude can be approximately represented as a product

$$p \approx B \cdot f(r), \quad (1)$$

where the factor B depends only on direction and where

1. $|B| = |B_0|$, a maximum, in the direction 0 , of the beam.

2. $|B_1/B_0|$ is small if B_1 is the value of B in a direction 1, not very close to 0 .

As for part 2, a beam is considered satisfactory if $|B_1/B_0|$ is less than 0.1 except for directions very close to that of the main beam. The side lobes in the directivity pattern then turn out to be at least 20 decibels below the main beam and hence readily distinguishable therefrom.

The influence of the dome causes a modification in the pressure, replacing $p(x, y, z)$ by a new function, which it is convenient to represent in the form

$$P = p + hq, \quad (2)$$

where h is the thickness of the dome shell. The relative directional disturbance caused by the presence of the dome is readily found to be

$$\left| \frac{p_1 + hq_1}{p_0 + hq_0} \right| - \left| \frac{p_1}{p_0} \right| = \left| \frac{p_1}{p_0} \right| \operatorname{Re} h \left(\frac{q_1}{p_1} - \frac{q_0}{p_0} \right) + \text{higher powers of } h. \quad (3)$$

The basic differential equation is, of course,

$$\nabla^2 P + k^2 P = 0, \quad (4)$$

where ∇^2 denotes the operator $\partial^2/\partial x^2 + \partial^2/\partial y^2 + \partial^2/\partial z^2$ and where

$$k = \begin{cases} k_0 = \frac{\omega}{c_0} & \text{in water} \\ k_1 = \frac{\omega}{c_1} & \text{in the shell of the dome,} \end{cases} \quad (5)$$

c_0 and c_1 being the velocities of sound in water and the shell of the dome respectively.

C. It is assumed that, for large values of r , P behaves like $C \cdot e^{ik_0 r}/r$, where C does not depend on r , i.e., an outgoing wave form.

D. It is also assumed that the pressure P and the acceleration of any particle are continuous across the

two interfaces of the dome shell. Analytically, if ρ is the density, this means that P and $(1/\rho)(\partial P/\partial n)$ are continuous, where $\partial P/\partial n$ is a normal derivative relative to the interface. Since ρ is discontinuous, P , and therefore q , will have known discontinuities in their normal derivatives at the interfaces. Elsewhere, except at the sources of the beam, P is assumed regular.

3.2.2 Approximate Solutions and Qualitative Conclusions

The exact unique solutions, known to exist, for the boundary value problem for P appear to be entirely unmanageable from the viewpoint of practical applications. A good working approximation, however, can be based on the assumption that h is small enough to make higher powers negligible when P is developed in powers of h . The shell is effectively regarded as a discontinuity surface S in the water, across which, in the limit, q satisfies the following "jump" conditions

$$[q] = \left(\frac{\rho_1}{\rho_0} - 1 \right) \frac{\partial p}{\partial n} \quad (6)$$

$$\left[\frac{\partial q}{\partial n} \right] = \frac{\rho_0}{\rho_1} (k_0^2 - k_1^2) p - \left(1 - \frac{\rho_0}{\rho_1} \right) \left(\frac{\partial^2 p}{\partial n^2} + 2H \frac{\partial p}{\partial n} \right),$$

where the square brackets signify the difference between values on either side of S and where H is the mean curvature of S . The function q also satisfies

$$\nabla^2 q + k_0^2 q = 0. \quad (7)$$

It is regular save on S , and it behaves like P at great distances from the projector. Under these conditions, q is given uniquely by

$$q = \frac{-1}{4\pi} \iint_S \left[\frac{\partial q}{\partial n} \right] \frac{e^{ik_0 r'}}{r'} dS + \frac{1}{4\pi} \iint_S [q] \frac{\partial}{\partial n} \left(\frac{e^{ik_0 r'}}{r'} \right) dS, \quad (8)$$

where r' is the distance from a fixed point (x, y, z) , at which q is to be determined, to a variable point on the surface of integration S .

Thus the disturbance appears as the effect of a layer of simple sources and a layer of dipoles on S . Their intensities are known, by equation (1), in terms of p . The relative directional disturbance (3) is obtainable, to a first approximation, from the relationship (8).

The following practical conclusions are suggested by the work.

I. The disturbance can be minimized by using for

the shell a material which agrees as nearly as practicable with water in density and in velocity of sound. Thus aluminum should be much better than steel.^a

II. Wherever the original pressure p or its gradient is high, the dome should be as thin as practicable; greater thickness (for the sake of structural strength) is permissible in places where p and its gradient are low.

III. Stiffening ribs which present a small area to the action of the original beam should not be a serious source of disturbance, if they are relatively sparsely distributed where p and its gradient are high in value.

IV. Strong curvatures and sharp edges should be avoided where $\partial p / \partial n$ is large. [Compare the term involving H in (11).] Such edges and curvatures should be kept clear of the beam.

V. A thin layer of oil or, even worse, air coating the inside of the dome could produce serious disturbances.

3.2.3 Outline of Mathematical Methods

From equations (4), (2) and the equation like (4) for the undisturbed pressure p , the following equation is obtained for q :

$$\nabla^2 q + k_0^2 q = \frac{1}{h}(k_0^2 - k^2)p, \quad (9)$$

where $k_0^2 = \omega^2 / c_0^2$, with c_0 the sound velocity in water, and where k is determined according to the medium in which q is being considered. Thus $k = k_0$ inside and outside the dome, but $k \neq k_0$, in general, in the material of the shell, where the equation is therefore nonhomogeneous. Here the assumption is employed that the material of the shell behaves like a liquid, in the sense that shear waves can be ignored.

The mathematical problem of determining q and hence P completely is formulated, for convenience, in terms of a special coordinate system. The coordinate curves are the lines of curvature on the inner surface of the shell and the normals to that surface. Even when these appropriate coordinates are employed, the problem remains complicated. It is accordingly replaced by a simpler limit problem obtained by letting the thickness h approach zero,

^a Unfortunately, rapid corrosion of aluminum shells leads to bad scattering.

under reasonable assumptions regarding the behavior of q , its normal derivatives and its Laplacian in the material of the shell. The process leads to a limit function q , which is found to be subject to the discontinuity conditions (6). It is then shown that q , as given by (8), satisfies the required differential equation (7), has the proper discontinuities, and behaves as required at infinity.

Practical applications involve values hq of the pressure disturbance (or values hq/p of the relative disturbance) at large distances from the dome. A purely imaginary value of hq/p would signify merely a phase shift. Disturbances in amplitude lead to consideration of the relative change

$$\frac{|p + hq| - |p|}{p}$$

in amplitude. Its development in powers of h commences with $\text{Re}(hq/p)$, the relative amplitude disturbance, for which $|hq/p|$, the relative disturbance, is a convenient upper bound. In practice, a comparison is generally desired between the acoustic pressure in an arbitrary direction and that in the direction of maximum pressure (the main beam). This leads to the *directional disturbance*

$$\left| \frac{p_1}{p_0} \right| h \text{Re} \left(\frac{q_1}{p_1} - \frac{q_0}{p_0} \right)$$

[see (3)]. The directional disturbance in intensity, however, is measured to within first-order terms in h by

$$2 \left| \frac{p_1}{p_0} \right|^2 h \text{Re} \left(\frac{q_1}{p_1} - \frac{q_0}{p_0} \right),$$

because the intensity is proportional to the square of the pressure amplitude.

A dome may be considered satisfactory if the common logarithm of this quantity is below 0.2 in value (20 decibels) for all directions.

The energy flow from the sound source was also analyzed,¹ as affected by the presence of the dome. The analysis involves the displacement vector $\mathbf{W}(x, y, z, t)$ and the acoustic pressure $\pi(x, y, z, t)$, as related through the wave equation

$$\rho \ddot{\mathbf{W}} = -\nabla \pi, \quad (10)$$

with

$$\pi = -\mu \nabla \cdot \mathbf{W}, \quad (11)$$

where ρ is the density of the medium, μ is the bulk modulus, dots refer to time differentiation, $\nabla \pi$ is the gradient of π , and $\nabla \cdot \mathbf{W}$ the divergence of \mathbf{W} . Both

π and \mathbf{W} were written in periodic form, and the principle was used that, if R is the region between a surface S_1 and an enclosing surface S_2 , then the energy flux across S_1 during an entire period is the same as that across S_2 . The analytic expression of this principle is referred to as the *energy balance relation*.

If a source of sound is maintained constant, there will be differences in the amount of energy transmitted from the source, according to whether or not a dome is present. This fact explains what is meant by loss in energy caused by the presence of a dome. It is usually assumed that the amplitude of the vibrator is unaltered by the presence of the dome. Alternatively, the energy output might be required to remain constant, depending on details of construction of the vibrator and its electric circuit.

3.2.4 Disturbance of Plane and Spherical Waves

Disturbance of a plane wave by a plane sheet and disturbance of a spherical wave by a spherical sheet admit explicit, exact theoretical solutions of such a nature as to permit an assessment of the accuracy of the approximate solutions discussed in Section 3.2.2. They are of interest, however, not merely for the sake of assessing the approximate solutions but also because the results for the two problems contrast in a manner which is suggestive in connection with desirable further investigations. It appears likely, in fact, that the plane and the spherical cases present extremes between which lie the results for actual domes; especially in so far as overall losses in intensity (rather than redistributions) are concerned.

The approximate limit solution for the case of the plane sheet is a straightforward application of the approximate methods in Section 3.2.2, with suitable modifications of the condition at infinity. In its analytic form, the expression for the disturbance q suggests a reflected part on one side of the sheet and a transmitted part on the other. To the first order in h , the amplitude disturbances comes out zero. The approximation involved in using this limit solution for the case of a thin sheet of given thickness decreases in accuracy when the original oncoming wave approaches the sheet at glancing angles.

The exact solution of the plane problem is known in the literature. It agrees to a first-order approximation in powers of h , with the solution of the limit problem. In general, only small percentage errors

result from using the approximate limit solutions, for thicknesses of the order of 0.02 in., angles of incidence within 80 degrees of normal incidence, and a frequency of 24 kc.

Consider next a spherical sound wave emanating from the center of a spherical shell. By contrast with the plane case, the solution to the limit problem now yields an amplitude disturbance significantly different from zero. Indeed, computations reveal that relative amplitude disturbances might be 40 per cent or higher in practical situations.

Again, it is found that the exact solution coincides with the limit solution up through first-order terms in h . Numerical computations reveal reasonably accurate results for the limit solution in the case of steel and aluminum shells of radius 20 cm and thickness $h = 0.1$ cm.

The contrast in loss of sound intensity between the plane and the spherical situations was suggested as an aid in understanding why much larger losses in intensity are observed for certain small domes constructed in a torpedo shape than for large ones with straight sides. This comment was mentioned primarily as a possible guide to experimental procedure.

Spherical shells of steel and aluminum were compared, and aluminum was shown to involve a much smaller loss in the intensity of the sound. The superiority of the aluminum was more marked for a directional beam from the center of a spherical shell than for the spherical wave just considered.^a

In practical situations, the vibrator has dimensions of the same order of magnitude as the cross section of the dome. Hence a significant loss of accuracy may be entailed in the assumption of a point source of sound.

3.2.5 Effects of Various Liquid Fillings

For a plane wave incident upon a plane metal sheet and a spherical wave internally and concentrically incident upon a spherical shell, let it be assumed that the metal separates water (on the far side) from oil, or another liquid, on the side where the sound originates.

If the radius is large enough in the spherical case and if the incidence is normal in the plane case, then no disturbance will occur because of the use of the oil, provided the oil has the same acoustic impedance ρc as water. For nonnormal incidence, in the plane case, the oil should match water not only in acoustic

impedance ρc but also in velocity of sound; in other words, it should agree with water in the values of ρ and c separately, not merely in the value of their product. Where such agreement cannot be secured, formulas indicate that it is desirable to choose an oil the sound velocity of which somewhat exceeds that of water, but the density of which is less, for example, liquid. E.C. and Lubric oil X200 at 25 C. As the temperature falls, the sound velocity relative to water increases. No great disturbance is expected even at 0 C for angles of incidence up to 80 degrees from the normal.

Various tables have been prepared,¹ giving (1) the relative amplitude of the transmitted wave for steel and aluminum and a number of oils in the plane case, (2) the magnitude of the amplitude disturbances in the case of a spherical shell of thickness 0.1 cm for steel and aluminum filled with Fluolube and water, and (3) the impedance ratios of various liquids with the corresponding extreme values of the percentage amplitude disturbance.

For a dome of arbitrary shape filled with a liquid referred to hereafter as oil, only slightly different from water in acoustic properties, a *perturbation procedure* is applicable. It consists of a power series development with respect to the difference

$$K = k_2 - k_0 = \frac{\omega}{c_2} - \frac{\omega}{c_0} \quad (12)$$

between values of the ratios ω/c for the water and oil. With respect to first-order approximations, the influences of the oil and the dome are additive; hence the influence of the dome, the constants of which would be identified by the subscript 1, is here omitted. Instead, it is assumed that all space is filled with water except a region R bounded by a surface S and filled with oil. The problem then is to determine the pressure P when sound sources of a definite character are prescribed inside R . This is a boundary value problem of the sort described in Section 3.2.1. The perturbation method involves setting

$$P = p + Kq_2, \quad (13)$$

where p is the original wave, and Kq_2 the disturbance caused by replacing water by oil in R . Then q_2 satisfies

$$\nabla^2 q_2 + k_2^2 q_2 = \frac{(k_0^2 - k_2^2)p}{K} \quad \text{inside } R \quad (14)$$

$$\nabla^2 q_2 + k_0^2 q_2 = 0 \quad \text{outside } R$$

with appropriate transition conditions across S . The

difficulties of this general problem are obviated when K is small by considering only first-order effects relative to K ; that is, rejecting higher powers. The explicit approximate solution thus obtained is

$$q_2 = \frac{k_0}{2\pi} \iiint_R \frac{e^{ik_0 r'}}{r'} p dv - \frac{\rho_0}{4\pi K} \left(\frac{1}{\rho_2} - \frac{1}{\rho_0} \right) \iint_S \frac{e^{ik_0 r'}}{r'} \frac{\partial p}{\partial n} dS. \quad (15)$$

This solution was compared with an exact solution for the case where R and the sound wave are both spherical, with a common center. In this case the approximate solution gives, for the disturbance outside the oil-filled region,

$$q_2 = \frac{e^{ik_0 r}}{r} \left[iR + ie^{ik_0 R} \left(\frac{\lambda \rho}{ik_0 R} - \frac{1}{k_0} - \lambda \rho_0 \right) \sin k_0 R \right], \quad (16)$$

where R is the radius of the sphere of oil. For the exact solution, the term of first-degree K agrees precisely with (16). Similar agreement is found inside the sphere. It should be emphasized that the approximate method just outlined yields good results only if the two media almost agree in density as well as in values of c .

The above method was also applied to estimate the disturbance caused by using oil inside a spherical dome in the case of a directional beam. An estimate for the maximum expected disturbance was obtained by calculating q_2 only on the axis of the original beam at a large distance r from the origin, where q_2 is given by (15). Assuming r large permits one to obtain a good approximation by neglecting higher powers of D/r , where D is the distance from the origin to the point of integration. This makes it possible to evaluate (15) explicitly. Hence one can obtain the relative amplitude disturbance

$$\frac{|p + Kq_2| - |p|}{|p|},$$

which is given by $\text{Re}(Kq_2/p)$ up to a first-order approximation in terms of K . Tabulated values¹ reveal, except in the case of Lubric oil, that a sharp directional beam is more strongly affected by the use of oil inside a dome than is a spherical wave.

3.3 ACOUSTIC SCATTERING, WITH APPLICATIONS

In accordance with the theory just outlined, it appears desirable to keep the shells thin and to

strengthen them, in so far as necessary, with ribs and rods. Hence it became important to assess the disturbing influence of such strengthening elements on a sound beam.²

It was found that when stiffening ribs are arranged in grids with suitable spacing, the disturbing influence on the sound beam is less than if the same total mass of the same material were used in thickening a homogeneous shell. The disturbing effect for the grids, in certain important cases, is only about 10 per cent that of the corresponding homogeneous shells. Consequently, it is advisable to achieve the required structural strength by using thin stiffening ribs and rods rather than by thickening the dome.

Although a complete mathematical analysis of the scattering of sound by rods, ribs, and grids has never been made, such an analysis was carried far enough to permit quantitative estimates of the relevant effects.

3.3.1 Summary of Methods

Pressure gradients inside the solid portions of thin rods and grids differ from those of thin shells in a way to account largely for the differences in their sound-scattering properties. For a pattern, as in a rectangular network, of rods with thickness small in comparison to wavelength and with links small in comparison to space variations in pressure, the contribution to scattered amplitude can be resolved into that caused by a shell of equal mass and extent with suitable physical constants.

The investigation led to flexible forms of equations for treating various scattering problems. As a basic hypothesis, it was assumed that the solids, as well as the liquids, behaved in hydrodynamic fashion, an assumption which can be shown in many cases to involve only negligible inaccuracies.

The basic assumptions lead to an association of sound with a small pressure increment Π , variable in time, satisfying the wave equation, and fulfilling (along with the normal acceleration component) continuity conditions at the interface between two media. Analytically, in terms of a *complex amplitude* P for which $\Pi = \text{Re } P e^{-2\pi i \omega t}$, this means

$$\nabla^2 P + k_0^2 P = 0 \quad \text{in medium [0] (water)}$$

$$\nabla^2 P + k_0^2 P = -(k_1^2 - k_0^2)P \quad \text{in medium [1]}$$

(the scatterer) and, at the interface between [0] and [1],

$$P_0 = P_1 \quad \text{and} \quad \frac{1}{\rho_0} \frac{\partial P_0}{\partial n} = \frac{1}{\rho_1} \frac{\partial P_1}{\partial n}. \quad (17)$$

Application of Green's theorem to the two differential equations in the system (17) and use of the boundary conditions lead to various integral equations whereby P is expressed in terms of primary and secondary sources. The latter are introduced on and in the scattering bodies as a device for satisfying the boundary conditions. When the boundaries have certain simple shapes, orthogonal series or suitable integral forms lead to explicit solutions.

The employment of integral equations as a device for finding improved approximate solutions to (17) leads, in the case of thin scattering bodies in the form of shells, rods, and spheres, to explicit asymptotic expressions for P and its gradient. These were numerically checked for nonzero thicknesses encountered in actual rods and grids.

For the case of a thin infinite cylinder, an incident plane wave p was expressed in terms of cylindrical Bessel functions, and similar expressions were obtained for the total complex amplitude P inside and outside the cylinder. The terms of the expansions were asymptotically expressed, with the following result. In and on the cylinder,

$$P_1 \sim p_1$$

$$\nabla_1 P_1 \sim \frac{2}{1 + \frac{\rho_0}{\rho_1}} \nabla_1 p_1 - \left(\frac{\rho_1 - \rho_0}{\rho_1 + \rho_0} \right) \mathbf{k} \frac{\partial p_1}{\partial z_1}, \quad (18)$$

where \mathbf{k} is the unit vector along the axis (z) of the cylinder. A similar treatment for spheres gives the asymptotic form

$$P_1 \sim p_1$$

$$\nabla_1 P_1 \sim \frac{3}{2 + \frac{\rho_0}{\rho_1}} \nabla_1 p_1. \quad (19)$$

These expressions are numerically accurate within 2 per cent for steel cylinders and spheres of radii not more than one-thirtieth of a wavelength.

3.3.2 Application to Grids

With the aid of special integral theorems, the information obtained from asymptotic developments and from methods of integral equations was applied² to express the scattering by grids in terms of scattering by corresponding shells which can be treated from the viewpoint of discontinuity conditions. In the cases of grids and shells, complex amplitudes were expressed by asymptotic developments which agree in general form and differ only in the values of certain

coefficients. A modification of the discontinuity conditions (6), involving constants dependent on the grid and a corresponding shell, is useful in describing the scattering at large distances from the grid.

3.3.3 Thin Rings and Rods

In the case of thin rings and rods, the integral equations can be altered so that line integrals replace volume integrals.² This permits relatively simple evaluations with the aid of tabulated functions, in the case of scattering from a thin circular ring, provided the source is on the axis of the ring. When several rings are involved, the use of a superposition gives quite accurate results. In the case of straight rods lined up with the origin of the source function, fairly simple expressions exist for the scattering functions. Other positions of such rods introduce complications.

3.3.4 Spherical Sources and Shells

A study was made² of the dependence of scattering on the radii of concentric spherical sources and domes for directional beams. In this connection, the self-shielding of a finite source and a point source were compared, and resonance effects were studied with the aid of asymptotic relations. The asymptotic forms employed involve only about 2 per cent error in the case of highly directional beams. Highly directional beams are represented by taking the first few terms of an expansion of p in terms of spherical Bessel and Legendre functions. In this case, the effect of the scattering is to multiply the unperturbed complex amplitude by a factor which is quite sensitive to changes in the radius of the spherical source, the radius of the dome and the frequency of the sound wave.

3.3.5 Beam Distortion When Projector Is Close to Nose of Dome

For a particular proposed type of dome and projector, it was required that the distance from projector to shell be much smaller than in usual domes and that the shell fulfill more severe requirements as to mechanical strength. The theoretical considerations just outlined were applied³ to the problem of designing the device so as to reduce beam distortion due to a semifocused back pressure from the nose. Various recommendations were made to sharpen the beam by such methods as making the nose as flat as

practicable, having the projector follow the curvature of the nose, adjusting amplitudes and relative phases of the individual crystals of the projector, and suitably locating any necessary reinforcing members.

3.4

SHIELDING

It is customary to employ fairly large rigid shields in domes in order to reduce sound interference, such as from a ship's propellers. Calculations were carried out⁶ bearing on the efficiency of such shields when they are about five wavelengths in diameter. Graphical curves, based on the calculations, revealed an optimum size for the shielded area. General analytic representations were given for integrals involved in the problem and were later adapted for use in a comprehensive report on shielding by Division 6 of the NDRC.

The analytical study formulated a fairly general method for dealing with questions of acoustic shadowing or shielding. By contrast with optical shadowing mathematical problems of considerable difficulty result from the fact that all the dimensions are of the order of a very few wavelengths at most.

The principal idealization among those employed to make the problem amenable to mathematical analysis involved the treatment of the transducer. In actuality, this mechanism would lead to unwieldy mathematical boundary conditions. However, it is thought of as removed, and its place occupied merely by a part of the water body or by a transparent disk. Figures 1 and 2 are suggestive of both the practical

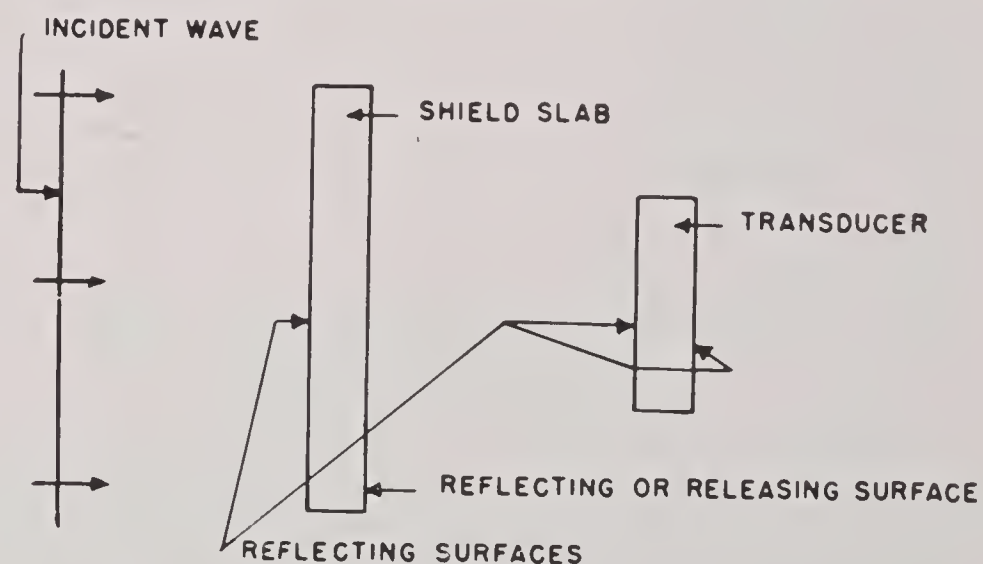


FIGURE 1. Block plan of actual apparatus.

device and the idealization. An alternative idealization consisting of replacing the transducer by a perfectly reflecting disk, while more realistic, leads to excessive mathematical complications. The shadow effect of the shield is measured by the quotient R

of the amplitude of the total acoustic pressure on the transparent disk in the presence of the shield divided by the amplitude thereof in the absence of the shield. This ratio R is briefly referred to as the ratio of the *shaded* to the *unshaded* pressures.

An exact expression for R was given in the case of a shield disk with acoustic pressure release on the

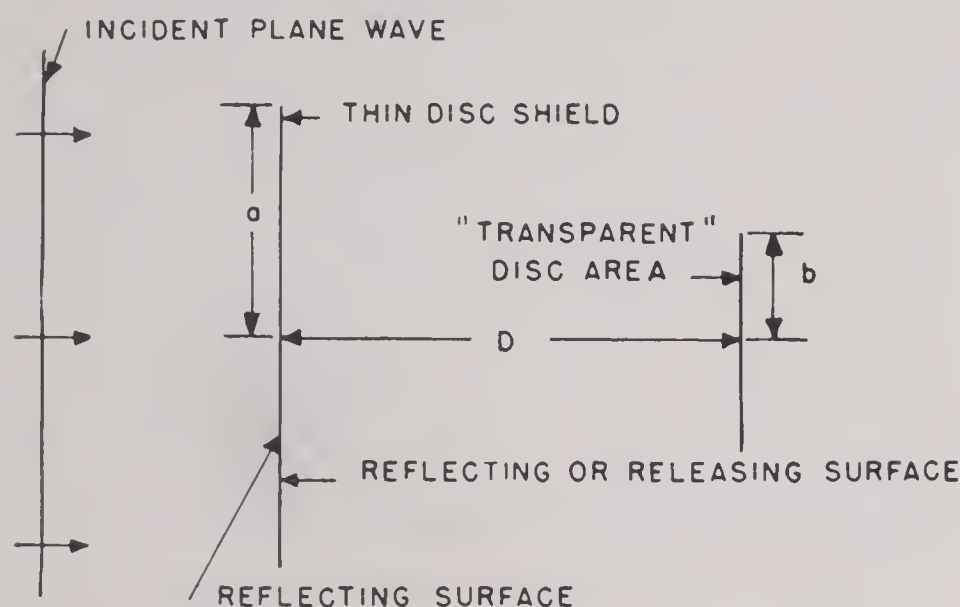


FIGURE 2. Plan of idealized apparatus.

shaded side and with pressure doubling on the exposed side (a condition here associated with almost perfect reflection from all but a narrow circumferential region of the exposed sides). The expression involves an integral which was evaluated by series in order to obtain useful graphs of R . One of these graphs (Figure 3), which can be understood in terms of the notation shown in Figure 2, indicates how greatest efficiency in shielding can be achieved by choosing a suitable radius for the transducer, so that R is nearly at its minimum. The calculations were restricted to ranges of a , b , and D that are of greatest interest for certain transducers widely used in submarine detection. (For a 20,000-cycle transducer 5 in. in radius, b equals 10 units, the unit being $\lambda/2\pi$.)

3.5 ACOUSTIC REFLECTIONS AND IMAGES IN DOMES

With the aid of the theoretical studies reviewed in Section 3.2 above, the occurrence of annoying reflections from large domes when the projector points in certain directions was explained.⁴ Corrugation of the side walls was proposed as a possible remedy, with the outer walls of the dome restored to smoothness, if practicable, by a plastic agreeing in acoustic properties with water. Alternative proposals involved doubled or stepped walls.

The reflections, which tend to occur when the axis

of the beam of sound deviates considerably from the axis of the dome, are quite troublesome in connection with direction finding. The mode of investigation employed was a treatment of the reflections with the aid of acoustic images, in the form of elliptical disks with suitable source distributions and with orientations depending on average angles of incidence and reflection. Exact calculations were carried through

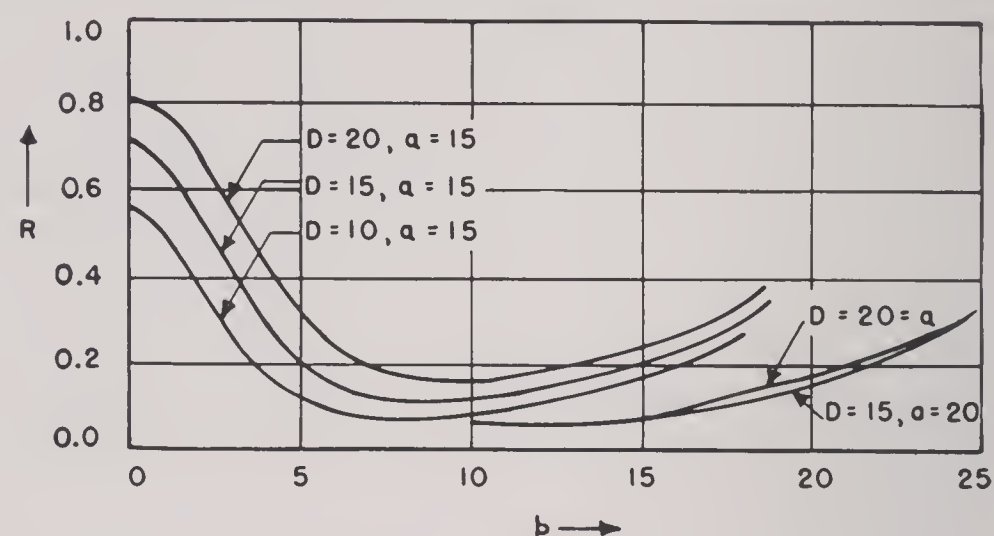


FIGURE 3. Ratio of shaded to unshaded pressures.

for an idealized but representative case, and the principal features of the main case were discussed. The elliptical form of the images arises from the shape of that part of the flat section of a dome intercepted by the strong part of a sound beam with a circular cross section. The image disk is obtained by a certain backward projection of the reflected rays through this intercepted area. In the idealized case, the curvatures of the shell and wave front are neglected, along with the variation in amplitude of the incident waves.

3.6 RADIATION PATTERN FROM A VIBRATING PLATE

Methods were investigated⁵ for controlling the directivity of sound radiated from a plate vibrating in an infinite baffle. A complete mathematical solution was given for the problem of obtaining a prescribed radiation pattern by a suitable distribution of amplitudes and phases over a vibrating plate. While this mathematically idealized solution can only be approximated in actuality, it can serve as a guide to the engineering problem of how to distribute amplitudes and phases over the various members of a mosaic of vibrating elements constituting a projector.

The work here reviewed is supplementary to other treatments by the Harvard Underwater Sound Laboratory and by Division C, Section 4, of NDRC in which the vibrators were composed of line sources

and point sources. In the present treatment, a two-dimensional array of sound sources is assumed to be so densely packed as to justify the hypothesis of a continuous surface distribution over a vibrating plate. The dimensions of the plate and the frequency of vibration are assumed to have been specified.

The plate is assumed to be in the x,y plane and vibrating in z direction. Attention is confined to a circular plate, with center at the origin and with such a vibration that the equation of the surface of the plate at time t has the form

$$z = \text{Re} [f(R)e^{-i\omega t}] \quad (20)$$

where

$$R = \sqrt{x^2 + y^2}.$$

The complex amplitude function of the acoustic pressure at a point (x_0, y_0, z_0) , namely

$$P = \frac{\rho\omega^2}{2\pi} \iint_{\text{plate}} \frac{e^{ikr}}{r} f(R) dx dy, \quad (21)$$

where $r = \sqrt{(x - x_0)^2 + (y - y_0)^2 + z_0^2}$ was studied⁵ at large distances from the plate. In terms of an arbitrary preassigned radiation pattern, a function $f(R)$ was derived which produced the given pattern to a close approximation. For large plates, the difference between the approximation and the desired pattern becomes negligible.

In practical cases, a vibrating plate cannot be so constructed as to achieve an arbitrary continuous variation of the complex amplitude of vibration over its surface. However, it has been found possible to break up a disk into a central circular portion and concentric annuli, over each of which the complex amplitude of vibration is constant though it varies from section to section. By this method, a desirable "mode of vibration" function $f(R)$ can be approximated, for example, one which reduces the angle of the principal conical portion of a beam and which also eliminates, or reduces, the sidelobes. Some par-

ticular cases were briefly considered,⁵ as illustrations of the method. A similar method can be applied to vibrating plates which are not circular, for example, rectangular plates. It consists of dividing the plate into a mosaic of small sections vibrating with their own complex amplitudes, which are adjusted to approximate to a desirable continuous vibration function, $f(x,y)$, and hence to produce a radiational beam of the desired sort.

3.7 SCATTERING OF PLANE WAVES FROM CYLINDERS

In connection with a certain underwater sound ranging apparatus, computations were required for the scattering of plane waves from elliptic cylinders and from various arrangements of parallel circular cylinders for different impedances of these cylinders. The behavior of the field close to the cylinders was of special importance.

The purpose of the mathematical investigations was to assist Division 6 of the NDRC in improving the design of the JP baffle, a part of a listening device used on submarines to determine the source of a sound, as from an enemy ship. Fairly complete results were obtained⁷ which proved useful as a guide to subsequent experimental work at the New London Underwater Sound Laboratory. The situation was idealized by regarding the cylinders as infinitely long and the baffle as an elliptical cylinder, or a set of circular cylinders, with various boundary conditions. The following indicated results of the mathematical work may be mentioned:

1. Directivity is appreciably improved by relatively small increases in the back-to-front thickness of a baffle covered with sponge rubber.
2. It is possible to avoid reversals in directivity at low frequencies and to improve general performance by constructing the covering layer on the baffle so as to have a small specific impedance.

Chapter 4

THE SCATTERING CROSS SECTION OF SPHERES FOR ELECTROMAGNETIC WAVES

4.1

INTRODUCTION

THE INVESTIGATION is concerned with the analysis of inconsistencies and common misinterpretations found in several standard books and research papers dealing with the problem of diffraction of light by spherical obstacles. It is the object of this investigation to clarify these inconsistencies and to provide a physical interpretation of theoretical results that is in accord with experiments.

The problem of the scattering of light by small spherical obstacles is an old one in theoretical physics, and goes back to Rayleigh, Debye, and Mie, whose papers on the subject became classics. The theory is known to give very good results as far as angular distribution of secondary radiation is concerned. It checks well with experiments, provided scattering particles are true spheres of well-defined radius. However, there appears to be a serious difficulty about the absolute value of the total amount of energy loss per second (energy lost by the beam and partly absorbed in the sphere, partly reradiated in all directions).

V. K. LaMer⁹ pointed out that the theoretical value for the energy scattered per second by the sphere as computed, for example, by using the formulas given by Stratton² is about twice as great as the experimental one. LaMer and Sinclair suggested that the customary calculation, according to a pattern proposed by Mie, ought to be in error at the point where the superposition of two independent beams of polarized light is used to obtain the formulas for natural light. It is true that many authors, including Rayleigh made errors at this stage of the computation.¹³

It is demonstrated that another reason for this discrepancy is far more fundamental, and it is shown that if one uses the usual method of computing the energy scattered per second by the sphere for *polarized incident light*, the scattering cross-section area Q_s for a reflecting sphere of large radius a is $Q_s = 2\pi a^2$, which is twice the value given by geometric optics.

Moreover, this difficulty is not connected with the shape of the body, as can be seen from certain British computations^{11,12} which treat the problem of light scattering by a solid cylinder of radius a and obtain an apparent scattering cross section, which for a wavelength that is small compared with the radius of the cylinders tends to a value $4a$ instead of $2a$ (per unit length of the cylinder).

The true explanation of such discrepancies is found to lie in the proper interpretation of the use of Poynting's flux theorems and in the special role played by the shadow of the body. In order to obtain the correct value for the scattering cross section, it is necessary to take into account the electromagnetic fields in the shadow region and in the scattered radiation.

The difficulties connected with the role of the shadow do not arise in the problem of radiation pressure, since all the energy radiated at small angles of deflection does not contribute to the radiation pressure. This explains why Debye obtains the correct result for the radiation pressure on a metallic sphere of large radius. The problem is a fundamental one in wave theory, and similar considerations apply to acoustics.

The following section is devoted to a brief summary of the optical properties of spheres and the amounts of light they scatter when the problem is analyzed from the point of view of geometrical optics and elementary physical optics.

4.2 ELEMENTARY APPROACH TO THE PROBLEM

Geometrical optics is known to give a correct answer whenever the dimensions of all instruments involved are much larger than the wavelength λ . In our problem this means that the radius a of the sphere and the distance R of observation should be considerably larger than λ

$$a \gg \lambda, \quad R \gg \lambda. \quad (1)$$

For the case of a metallic sphere, acting as an ideal mirror, the result is:

- Scattering cross section = actual cross section = πa^2 .
 - Light scattered with uniform distribution all around the sphere.
 - A perfectly dark shadow inside a cylinder of radius a behind the sphere.
- (2)

In this shadow, the electric field is exactly zero.

Elementary physical optics is usually based on Huyghens' principle. It is known to yield only a very rough first approximation of a more correct theory of wave propagation. This method does not take into account the transverse character of electromagnetic waves and treats longitudinal or transverse waves in exactly the same way, which is bound to be wrong. Furthermore, this theory makes no provision for the exact shape of the boundary nor for specific boundary conditions. In our problem, Huyghens' principle yields similar results for a dark circular disk, an absorbing sphere, or a reflecting sphere, and such a complete similarity between widely different problems cannot be taken seriously.

This theory, however, is known to give information of real practical value and the corresponding results are summarized briefly here. The theory is found in all textbooks on optics.¹

As is well known, the fringe patterns are similar when observed either behind an aperture of a given shape or behind a screen of the same shape. This is the "principle of Babinet."^{1a} The fringes behind a circular aperture have been known for a long time; their intensity distribution is governed by a J_1 Bessel function, and the first black rings correspond to

$$p = 0.61 \frac{\lambda}{a}; \quad 1.115 \frac{\lambda}{a}; \quad 1.619 \frac{\lambda}{a} \dots \quad \lambda \ll a, \quad (3)$$

where a is the radius of the circular aperture, λ the wavelength and p the ratio

$$p = \frac{r}{R} = \sin \theta,$$

r the radius of a dark ring on a screen located at a distance R from the aperture; θ the angular deflection.^{1b} Similar rings should be observed in the light scattered by a sphere. They occur for small angles θ and constitute conical fringes around the geometrical shadow.^{2c} In addition, the theory also predicts a white *bright fringe* of interference all along

the z axis, just in the middle of the geometrical shadow.

Let us define a cone with a small angle θ_s that would include the first rings (3) and the shadow, and choose

$$\theta_s \approx \sin \theta_s = K \frac{\lambda}{a} \quad (4)$$

$$K \approx 1 \text{ to } 3.$$

We can give a rather crude description of the shadow structure in physical optics in the following way (see Figures 1 and 2).

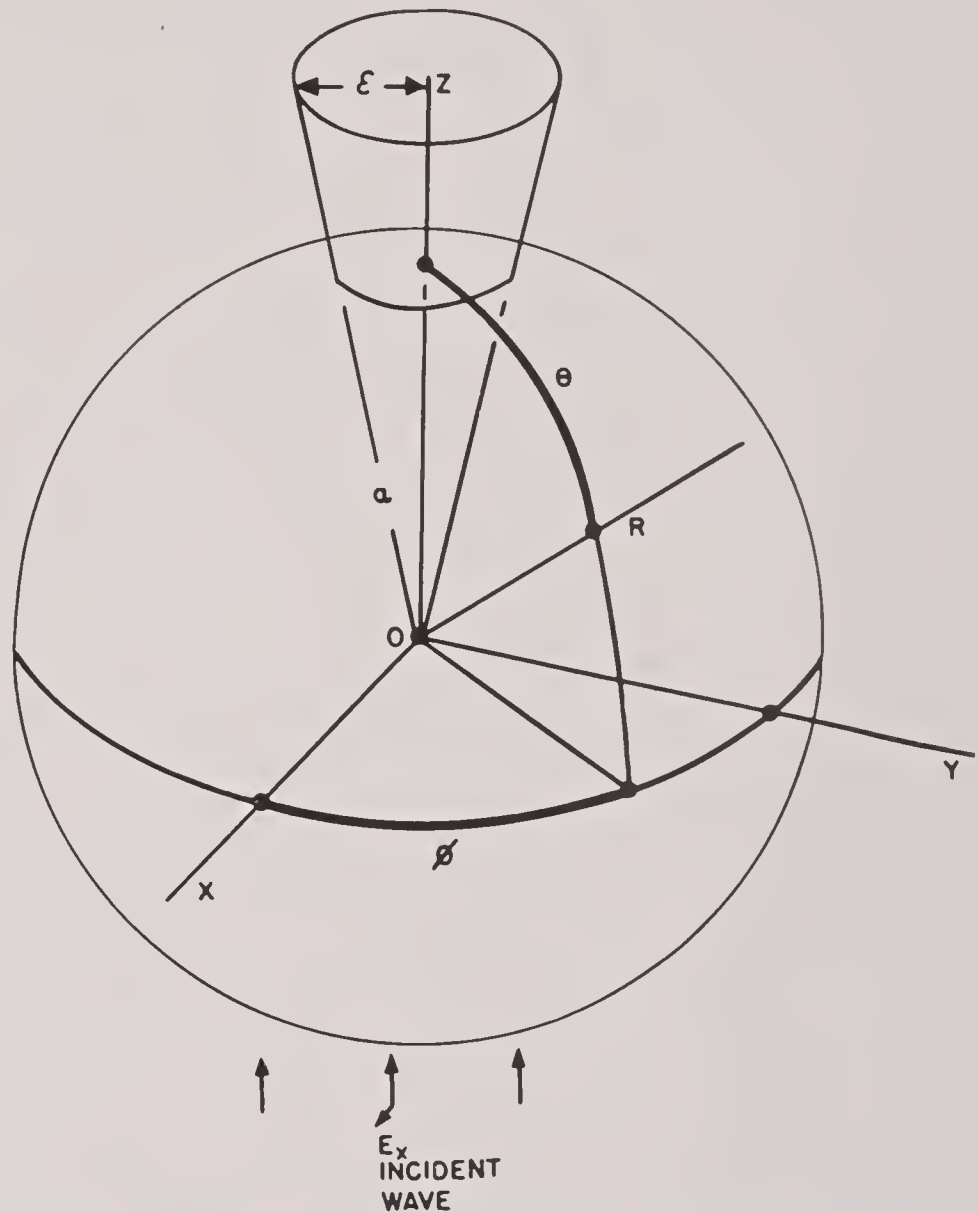


FIGURE 1. Coordinate system for shadow structure.

A plane wave falling upon the sphere should give a sort of conical shadow region S where the intensity of light ought to be extremely small except for a bright fringe along the axis OSR . This shadow would extend up to a distance R ,

$$\frac{a}{R} = \theta_1 = K \frac{\lambda}{a}, \quad (5)$$

$$R = \frac{1}{K} \frac{a^2}{\lambda}.$$

Around the shadow, one should find a sort of penumbra P , exhibiting a succession of interference rings caused by the superposition of the incident field E_i

and of the secondary field E_r . Outside the penumbra, the fields corresponding to direct wave and scattered wave could be distinguished from each other on account of their different polarization and direction of propagation.

When the wavelength λ is decreased indefinitely, the angle θ_s decreases and the penumbra region shrinks together, while the regular shadow extends farther and farther. More detailed explanations will be found at the end of the present paper and in Appendix III.

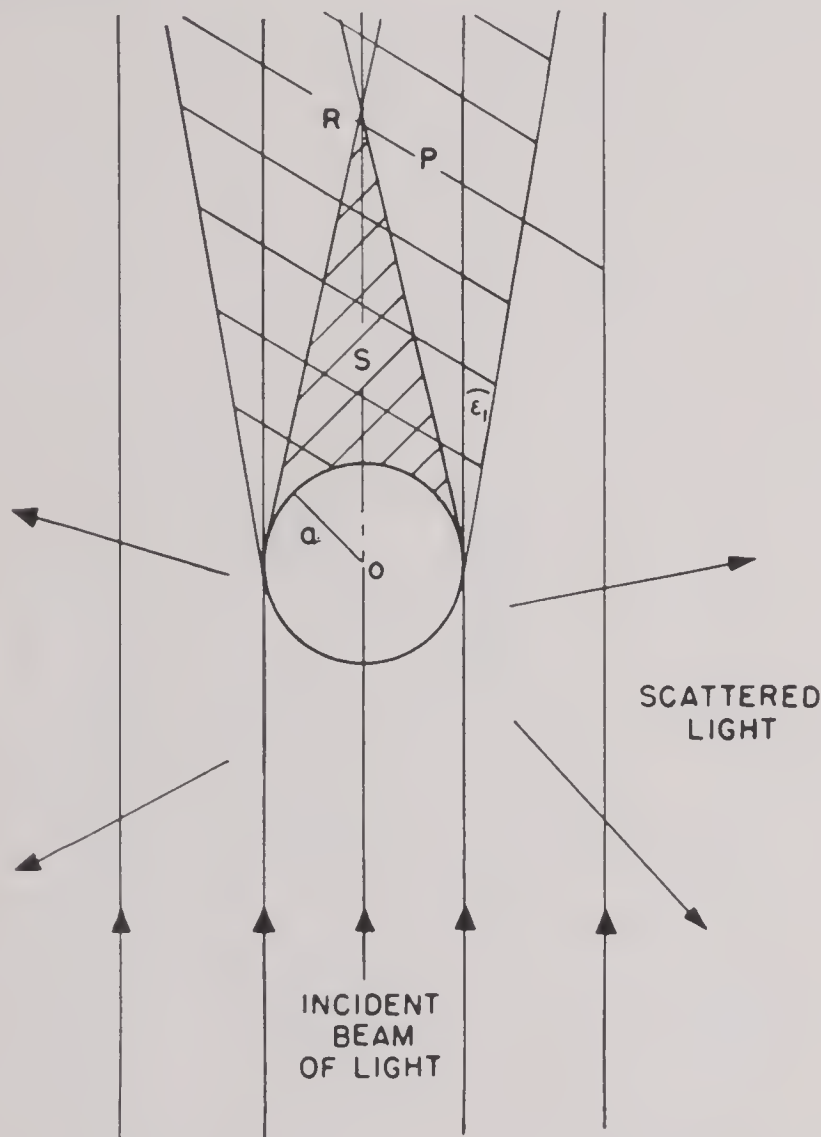


FIGURE 2. Shadow structure for plane wave on a sphere.

4.3 A RIGOROUS ELECTROMAGNETIC THEORY; THE PROBLEM OF THE FACTOR 2

The theory of light diffraction is usually built along the following lines. An incident wave (field E_i) falls upon an obstacle (a sphere) and the resulting field distribution is analyzed as the sum of two terms:

$$\mathbf{E} = \mathbf{E}_i + \mathbf{E}_r, \quad (6)$$

where \mathbf{E}_i is the incident wave, as it would be obtained without perturbation if the sphere was not scattering any radiation, and \mathbf{E}_r is the secondary wave, including the scattered radiation and the corrective field in the shadow region.

The energy flow for the scattered radiation is com-

puted by taking the Poynting vector corresponding to $\bar{\mathbf{E}}_r$ and integrating over all directions. The resulting energy flow is expressed by the scattering cross section Q_s , the area which receives equal energy flow from the incident waves. The theory is in the literature.^{2a} The computation of the electromagnetic field around the scattering sphere is given with all details by Stratton² (this part being essentially a summary of the original papers by Debye and Mie) and is absolutely correct. When the general formulas are used in connection with the assumption $\lambda \ll a$ (λ is the wavelength, a the radius of the sphere), the scattering cross section is found to be twice the cross section of the sphere

$$Q_s \longrightarrow 2\pi a^2, \quad \lambda \ll a, \quad (7)$$

as will be shown in more detail in the following sections. This result was first explicitly stated in a paper by Stratton and Houghton.⁸ Their Figure 1 is a graph of the variation of a coefficient

$$K = \frac{|A|}{2\pi a^2},$$

where $|A|$ is the total energy scattered, which tends to the limit *one* for large values of a/λ . That is the result stated in (7).

Comparing formulas (2) and (7) we note a *discrepancy by a factor 2* in a problem where the sphere is very much larger than the wavelength.

This discrepancy is due to a real difficulty in the definitions. Let us *first* assume the validity of *geometrical optics*, with its results (2) and investigate their translation in the more elaborate method sketched in equation (6). The resultant field at any point outside the sphere is the sum of the primary and secondary field

$$\begin{aligned} \mathbf{E} &= \mathbf{E}_i + \mathbf{E}_r, \\ \mathbf{H} &= \mathbf{H}_i + \mathbf{H}_r \end{aligned}$$

where \mathbf{E}_i , \mathbf{H}_i are the electric and magnetic field as they would be found in the incident beam of light if it could propagate without perturbation. \mathbf{E}_r , \mathbf{H}_r are the additional field components resulting from the perturbation due to the sphere. Stratton also calls this the "reflected field," hence the subscript r .

This is where a dubious physical picture is introduced. The secondary field \mathbf{E}_r , \mathbf{H}_r contains two different things: the *reflected or scattered wave*, spreading all around the sphere in all directions (let us call it \mathbf{E}_{r1} , \mathbf{H}_{r1}) and the *shadow* (\mathbf{E}_{r2} , \mathbf{H}_{r2}). This second part is a field distribution which must compensate almost completely (but for some inter-

ference fringes) the unperturbed incident field $\mathbf{E}_i, \mathbf{H}_i$ in a region behind the sphere. Because $\mathbf{E}_i, \mathbf{H}_i$ is taken as the unperturbed incident wave, the secondary field $\mathbf{E}_{r2}, \mathbf{H}_{r2}$ must contain the correction to the incident wave in the region known as the shadow of the sphere.

$$\begin{aligned}\mathbf{E}_r &= \mathbf{E}_{r1} + \mathbf{E}_{r2}, \\ \mathbf{H}_r &= \mathbf{H}_{r1} + \mathbf{H}_{r2},\end{aligned}\quad (8)$$

where the secondary field = scattered radiation + compensating field in the shadow.

The first point being clear, let us come back to the Stratton-Mie discussion. The radial component of the complex Poynting vector is ^{2b}

$$S_R^* = \frac{1}{2}(E_\theta \bar{H}_\phi - E_\phi \bar{H}_\theta) \quad (9)$$

where the bar over the letter means complex conjugate. If we compute the field radiated at very large distance from the sphere, we may use the well-known result

$$H_\phi \approx \eta E_\theta, \quad H_\theta \approx -\eta E_\phi, \quad \eta = \sqrt{\frac{\mu}{\epsilon}}, \quad (10)$$

where η is the characteristic impedance of free space. Introducing the transverse component E_t of the electric field, we write:

$$S_R^* = \frac{\eta}{2} [|E_\theta|^2 + |E_\phi|^2] = \frac{\eta}{2} |E_t|^2, \quad (11)$$

a relation which checks with Stratton.^{2c} This expression can be resolved by virtue of (6) into three groups

$$S_R^* = \frac{\eta}{2} [|E_{ti}|^2 + |E_{tr}|^2 + 2(E_{ti} \bar{E}_{tr})]. \quad (12)$$

The first term contains the field of the unperturbed incident wave, the second term represents the contribution of the secondary wave, and the last one the interaction between both fields. Let us now integrate over a sphere at large distance (radius $R \gg a$). We notice immediately that the first term does not contribute anything, while the integral of S_R^* yields the total energy absorbed by the sphere, hence the following relation ^{2d}

$$W_a = -\text{Re} \iint S_R^* R^2 \sin \theta d\theta d\phi = -W_r + W_{ir},$$

where

$$W_r = \text{Re} \frac{\eta}{2} \iint |E_{tr}|^2 R^2 \sin \theta d\theta d\phi,$$

(the W_s of Stratton),

(13)

$$W_{ir} = -2\text{Re} \frac{\eta}{2} \iint (E_{ti} \bar{E}_{tr}) R^2 \sin \theta d\theta d\phi,$$

(the W_t of Stratton).

Here the subscripts have been changed to r and ir , instead of s and t (Stratton), to show the disagreement with Stratton about the physical interpretation of the different terms.

The point of view of Stratton is the following: "The second term [in E_{tr}] obviously measures the outward flow of the secondary or scattered energy from the diffracting sphere, and the total scattered energy is W_s . W_t measures, therefore, the total energy derived from the primary wave and dissipated as heat and scattered radiation." As a matter of fact, for a metallic sphere $W_a = 0$ and $W_s = W_t$.

The explanations given in equation (8) clearly show that the Mie-Stratton interpretation of the different terms is not quite correct in the case of geometrical optics and that it rests on an incorrect physical picture. This will be investigated on a specific example to explain how it makes for the factor 2. Let us consider a metallic sphere of radius a much larger than the wavelength. The approximations of geometrical optics yield the following results.

A. *Scattered radiation.* The tangential component is

$$E_{tr1} = \frac{C}{R} E_{i0}, \quad |C|^2 = \frac{a^2}{4},$$

where E_{i0} is the amplitude of the electric field in the incident wave. This results from the well-known fact that a reflecting sphere scatters light uniformly in all directions and that the total amount of energy scattered per second amounts to the total incident energy falling per second on the cross section πa^2

$$\begin{aligned}W_{\text{scattered}} &= R^2 \frac{\eta}{2} \iint |E_{tr1}|^2 \sin \theta d\theta d\phi = \frac{\eta}{2} 4\pi |C|^2 E_{i0}^2 \\ &= \pi a^2 \frac{\eta}{2} E_{i0}^2 = \pi a^2 S_2,\end{aligned}\quad (14)$$

$$S_2 = \frac{\eta}{2} E_{i0}^2,$$

where S_2 is the mean energy flux in the incident wave.

B. *Shadow.* The field of the incident wave is completely compensated over an area πa^2 behind the sphere, hence a compensating field

$$E_{tr2} = -E_{i0} \quad \text{in the shadow } \pi a^2. \quad (15)$$

According to (8), the secondary field E_r is the sum of these two terms, and

$$\begin{aligned}|E_{tr}|^2 &= |E_{tr1} + E_{tr2}|^2 = |E_{tr1}|^2 + |E_{tr2}|^2 \\ &\quad + 2(E_{tr1} \cdot \bar{E}_{tr2}).\end{aligned}\quad (16)$$

Integrating over a sphere at large distance we notice that the last term of (16) gives practically zero, since

at large distance E_{tr_1} decreases as $1/R$ while the area of integration $R^2 \sin \theta \Delta \theta \Delta \phi$ keeps a constant value πa^2 (area of the shadow). Hence:

$$W_r = \frac{\eta}{2} \iint |E_{tr_1}|^2 R^2 \sin \theta d\theta d\phi + \frac{\eta}{2} \iint |E_{tr_2}|^2 R^2 \sin \theta d\theta d\phi \quad (17)$$

$$W_r = W_{\text{scattered}} + \pi a^2 \frac{\eta}{2} |E_{tr_2}|^2 = 2\pi a^2 \frac{\eta}{2} E_{i_0}^2$$

using (14) and (15). The flux of the negative field (15) over the area πa^2 of the shadow obviously gives an additional contribution just equal to that of the scattered radiation.

Let us now turn to the mixed term W_{ir} [equation (13)]. In this integral the scalar product $(E_{ti} \cdot \bar{E}_{tr})$ splits into

$$(E_{ti} \cdot \bar{E}_{tr}) = (E_{ti} \cdot E_{tr_1}) + (E_{ti} \cdot E_{tr_2}).$$

The first one is zero in average, and the second one is to be integrated over the area of the shadow

$$W_{ir} = -\eta \int (E_{ti} \cdot \bar{E}_{tr_2}) dS = +\pi a^2 \eta E_{i_0}^2 = W_r. \quad (18)$$

So we reach the following conclusion: In the case of a well-defined geometrical black shadow, the assumptions of Mie and Stratton yield a scattered energy twice as large as the actual scattering.

4.4 QUALITATIVE DISCUSSION BASED ON PHYSICAL OPTICS

The case of geometrical optics, which we have just discussed, obviously represents a dangerous oversimplification of the real problem, and we immediately feel that there is no such thing as the sharply defined shadow of the geometrical theory.

Referring to equations (3), (4), (5), and Figure 2, we note that the actual shadow limit must extend from $\theta = 0$ up to an angle θ_s , which may become small when $a \gg \lambda$ but can never be exactly zero.

Geometrical optics leads to the conclusion that (1) energy scattered all around the sphere corresponds to a cross section πa^2 equal to the geometrical cross section; (2) an equal amount of secondary energy flow is found exactly on the angle $\theta = 0$, thus yielding an additional πa^2 contribution to the cross section. The total makes $2\pi a^2$ and checks with Stratton's result in equation (7) above.

According to physical optics, we understand that the first contribution should remain unchanged and

that the second one should spread over a small but finite angle θ_s .

The theoretical problem can now be stated in the following way. A plane electromagnetic wave with its electric vector in the x direction is propagating upwards along the z axis. It strikes a sphere centered on the origin O of coordinates and is scattered around the sphere. If the sphere is large enough to produce a shadow, the shadow will extend about the positive z axis. Using spherical coordinates (Figure 1) R, θ, ϕ ($R = a$, radius of the sphere), the shadow corresponds to angles $0 < \theta < \epsilon_1$ where ϵ_1 is a small quantity which is to be conveniently chosen.

According to the preceding discussion, it is necessary to compute first the amount of energy scattered in all directions, except for the shadow region;

$$\begin{aligned} R &\gg a \text{ far away from the sphere,} \\ \epsilon_1 &< \theta \leq \pi \text{ outside the shadow,} \\ 0 &< \phi \leq 2\pi \text{ all around the sphere.} \end{aligned} \quad (19)$$

The problem is to take the expressions for the Poynting vector, as obtained by Stratton² and to carry the integration of energy flow according to conditions (19), instead of doing it for all angles $0 < \theta \leq \pi$ as Stratton did. This last procedure is objectionable since it includes the shadow region, and incorporates into the scattered field radiation the whole field distribution inside the shadow, which is physically to be distinguished from the scattered radiation.

4.5 EXPERIMENTAL CHECKS OF THE THEORY

As stated in the first section, the present investigation was prompted by some discrepancies between experiment and theory. Those who discovered such discrepancies also found another source of error, caused by inconsistent definitions for the intensity of a beam of light. The errors caused by inconsistent use of different systems of units are pointed out in AMP Report 87.2R.¹⁰

When the preceding errors have been corrected, the Mie-Stratton theory is found to work very well for all cases

$$\begin{aligned} \lambda &\geq \frac{1}{2}a, \\ \rho_1 &= 2\pi \frac{a}{\lambda} < 15, \end{aligned} \quad (20)$$

and experimental results check very well with theoretical formulas. The values of the total scattering,

observed in LaMer's laboratory for sulfur or oleic acid droplets, agree very well with the theory.

For very small spheres and long wavelength ($\lambda \gg a$) the theory still gives the correct result for Rayleigh scattering, as pointed out by Stratton.^{2e}

The problem discussed in Sections 4.2 and 4.3 is related to the case of large ρ_1 values

$$\rho_1 > 15, \quad \lambda < \frac{1}{2}a. \quad (21)$$

In the following experiments by Sinclair, for instance,

$$\begin{aligned} a &\approx 15\mu, \\ \lambda &\approx 0.5\mu, \\ \rho_1 &\approx 190. \end{aligned} \quad (22)$$

There, according to experimental conditions, the observed scattering cross section is πa^2 when the limit angle ϵ_1 (see Section 4.3) is larger than 10 degrees and goes up to $2\pi a^2$ for smaller ϵ_1 values as obtained for large distances R of observation.

The following account, written by Dr. Sinclair, summarizes the experimental checks:

"We have recently made a few observations of the size of lycopodium spores of fairly uniform size. The radius of these spores, as measured in a light microscope, was found to be 15.0 ± 0.9 micron.

"The spores were allowed to settle on a glass plate which was then placed in a beam of light of parallel rays and in a slightly divergent beam from a point source. Measurements were made of the angular diameter of two orders of both the light and dark diffraction rings in both red and green light. From these measurements we calculated the spore radius to be 15.5 ± 0.2 micron, in good agreement with the microscope measurements.

"We also placed the plate of lycopodium spores in a parallel beam in front of a photocell. The reading of the photocell increased by the factor 2 to 1 when the distance from the plate to the photocell was decreased from 18 feet to 6 inches. This result was predicted by Professor Brillouin. Calculation checked this result and showed that at 18 feet the observed scattering cross section was $2\pi a^2$ and at 6 inches $a^2\pi$. In other words, the true scattering cross section is $2\pi a^2$."

4.6 STRATTON'S PRESENTATION OF THE MIE THEORY

The general method^{2f} is to expand the incident plane wave into an infinite series of terms, each of which corresponds to a specific spherical harmonic, then to assume a similar expansion with arbitrary coefficients for the scattered or secondary wave and to obtain the coefficients by matching both fields

on the surface of the sphere to satisfy boundary conditions.

The solution is thus obtained as an expansion in spherical harmonics and would be perfectly suitable if we were in a position to observe separately each term in the series. Unfortunately this is not the case, and we are only able to measure the total field scattered in any given direction. Hence we are faced with the very difficult task of rebuilding a function that is given as a rather clumsy expansion.

The point of departure is the set of formulas given by Stratton.^{2g} The incident wave is taken as

$$\begin{aligned} E_{ix} &= E_0 e^{-i\omega t + ikz}, \\ H_{iy} &= -\eta_0 E_0 e^{-i\omega t + ikz}, \end{aligned} \quad (23)$$

$$k = \frac{2\pi}{\lambda} = \frac{\omega}{c} = \omega \sqrt{\epsilon_0/\mu_0}, \quad \eta_0 = \sqrt{\epsilon_0/\mu_0}, \quad (24)$$

where $\epsilon_0 = \mu_0$ is the permittivity and permeability in the surrounding medium (free space), in mks units. The sphere has its center at O and a radius a . Its electric and magnetic properties are specified by the values ϵ_1, μ_1 , which may be complex if necessary to include absorption, and

$$k_1 = \omega \sqrt{\epsilon_1/\mu_1}. \quad (25)$$

The solution of the problem is obtained by writing the continuity conditions on the surface of the sphere. When this is done, the field outside the sphere comes out as the sum of two terms,

$$\mathbf{E} = \mathbf{E}_i + \mathbf{E}_r, \quad \mathbf{H} = \mathbf{H}_i + \mathbf{H}_r, \quad (26)$$

where $\mathbf{E}_i, \mathbf{H}_i$ are the fields corresponding to the unperturbed incident wave (23) while $\mathbf{E}_r, \mathbf{H}_r$ represent the corrective terms, which contain the reflected or scattered waves spreading out from the sphere and the corrective field which compensates the incident wave in the shadow region.

Stratton gives^{2h} the complete formulas for the secondary fields $\mathbf{E}_r, \mathbf{H}_r$, which appear as a sum of terms corresponding to the radiation of electric n poles (amplitude b_n) or magnetic n poles (amplitude a_n). The field components of the secondary field are

$$\begin{aligned} E_{rR} &= E_0 e^{-i\omega t} \sum_{n=1}^{\infty} i^{n-1} \frac{(2n+1)}{\rho} b_n h_n(\rho) P_n^1 \cos \phi, \\ E_{r\theta} &= E_0 e^{-i\omega t} \sum_{n=1}^{\infty} i^n \frac{2n+1}{n(n+1)} \left[a_n \frac{h_n}{\sin \theta} P_n^1 \right. \\ &\quad \left. - i b_n \frac{1}{\rho} (\rho h_n)' \frac{\partial P_n^1}{\partial \theta} \right] \cos \phi, \end{aligned}$$

$$E_{r\phi} = E_0 e^{-i\omega t} \sum_n i^n \frac{2n+1}{n(n+1)} \left[-a_n h_n \frac{\partial P_n^1}{\partial \theta} + i b_n \frac{1}{\rho} (\rho h_n)' \frac{P_n^1}{\sin \theta} \right] \sin \phi, \quad (27)$$

$$H_{rR} = -\eta_0 E_0 e^{-i\omega t} \sum_n i^{n+1} \frac{2n+1}{\rho} a_n h_n P_n^1 \sin \phi,$$

$$H_{r\theta} = -\eta_0 E_0 e^{-i\omega t} \sum_n i^n \frac{2n+1}{n(n+1)} \left[-b_n \frac{h_n}{\sin \theta} P_n^1 + i a_n \frac{1}{\rho} (\rho h_n)' \frac{\partial P_n^1}{\partial \theta} \right] \sin \phi,$$

$$H_{r\phi} = -\eta_0 E_0 e^{-i\omega t} \sum_n i^n \frac{2n+1}{n(n+1)} \left[-b_n h_n \frac{\partial P_n^1}{\partial \theta} + i a_n \frac{1}{\rho} (\rho h_n)' \frac{P_n^1}{\sin \theta} \right] \cos \phi,$$

where the prime indicates a ρ derivative and $\rho = kR = (2\pi R)/\lambda$.

It may be noted here that the same formulas can be used for the representation of the incident plane wave as a superposition of waves from electric and magnetic multipoles:

$$\begin{aligned} &\text{Plane wave polarized along } x \text{ and} \\ &\text{propagating along } z: \text{ take } a_n = b_n = 1 \\ &\text{and replace } h_n(\rho) \text{ by } j_n(\rho). \end{aligned} \quad (27a)$$

The only trouble about these series is their very poor convergence. If the equations in series (27) are used according to (27a) to represent a plane wave, the terms of importance run up to $n > \rho = kR$, which is a very large figure.

Coming back to the scattered radiation (27), we shall find a simplification, since the coefficients a_n and b_n become very small when $n > \rho_1 = ka$ and may often be neglected. In order to compute the scattered energy, all we need is the field at a great distance R ,

$$R \gg a, \quad \rho \gg \rho_1, \quad \rho = kR, \quad \rho_1 = ka, \quad k = 2/\lambda, \quad (28)$$

hence

$$kR \gg n.$$

This condition enables us to use Debye's approximate formulas²ⁱ and to take the asymptotic expressions of the spherical Bessel functions

$$\begin{aligned} h_n^1(\rho) &= \sqrt{\frac{\pi}{2\rho}} H_n^1 + \frac{1}{2}(\rho) \approx \frac{1}{\rho} e^{i(\rho - [(n+1)/2]\pi)}, \\ j_n(\rho) &= \sqrt{\frac{\pi}{2\rho}} J_n + \frac{1}{2}(\rho) \approx \frac{1}{\rho} \cos\left(\rho - \frac{n+1}{2}\pi\right) \quad (28a) \\ \frac{1}{\rho} \frac{\partial}{\partial \rho} [\rho h_n^1] &\approx \frac{i}{\rho} e^{i(\rho - [(n+1)/2]\pi)} = i h_n^1. \end{aligned}$$

If these simplified expressions are used in Stratton's fundamental equations (27), the secondary field at a great distance is obtained. The factor i^n in equation (27) partly compensates $e^{-i[(n+1)/2]\pi}$ from (28a),

$$i^n e^{-i[(n+1)/2]\pi} = -i,$$

and we find

$$E_{rR} = H_{rR} = 0,$$

$$E_{r\theta} = \frac{1}{\eta_0} H_{r\phi} = \frac{-i}{\rho} E_0 e^{-i\omega t + i\rho} \sum_n \frac{2n+1}{n(n+1)} \left(a_n \frac{P_n^1}{\sin \theta} + b_n \frac{dP_n^1}{d\theta} \right) \cos \phi, \quad (29)$$

$$E_{r\phi} = \frac{-1}{\eta_0} H_{r\theta} = \frac{i}{\rho} E_0 e^{-i\omega t + i\rho} \sum_n \frac{2n+1}{n(n+1)} \left(a_n \frac{dP_n^1}{d\theta} + b_n \frac{P_n^1}{\sin \theta} \right) \sin \phi.$$

The field at a great distance is transverse and satisfies the usual relation

$$\mathbf{H} = \eta_0 (\mathbf{I}_1 \times \mathbf{E}), \quad (30)$$

where \mathbf{I}_1 is a unit vector in the R direction of propagation. The complex Poynting's vector is directed along R

$$S_R^* = \frac{1}{2} (E_{r\theta} \bar{H}_{r\phi} - E_{r\phi} \bar{H}_{r\theta}) = \frac{1}{2} \eta_0 (|E_{r\theta}|^2 + |E_{r\phi}|^2), \quad (31)$$

where the bar over the letter means "conjugate imaginary." As stated before, the secondary field [equation (29)] represents the scattered radiation plus the compensating field in the shadow. What we want to compute is the energy radiated in all directions, shadow excluded. This can be done by integrating the Poynting's vector for angles θ ranging from a small but finite value ϵ_1 up to π .

$$W_s = \text{Re} \int_0^{2\pi} d\phi \int_{\epsilon_1}^{\pi} d\theta S_R^* R^2 \sin \theta, \quad (32)$$

where Re means "Real part of . . ." The amount of energy scattered is better expressed by giving the scattering cross section Q_s ,

$$Q_s \frac{1}{2} \eta_0 E_0^2 = W_s, \quad (33)$$

which means that the amount W_s scattered is equal to the energy of the incident wave falling on an area Q_s . Finally

$$Q_s = \frac{\text{Re}}{k^2} \int_0^{2\pi} d\phi \int_{\epsilon_1}^{\pi} d\theta \sum_n \sum_m \frac{2n+1}{n(n+1)} \frac{2m+1}{m(m+1)}.$$

$$\left[\left(a_n \frac{P_n^1}{\sin \theta} + b_n \frac{dP_n^1}{d\theta} \right) \left(\bar{a}_m \frac{P_m^1}{\sin \theta} + \bar{b}_m \frac{dP_m^1}{d\theta} \right) \cos^2 \phi \right. \\ \left. + \left(a_n \frac{dP_n^1}{d\theta} + b_n \frac{P_n^1}{\sin \theta} \right) \left(\bar{a}_m \frac{dP_m^1}{d\theta} + \bar{b}_m \frac{P_m^1}{\sin \theta} \right) \sin^2 \phi \right] \sin \theta. \quad (34)$$

The ϕ integration is obvious,

$$\int_0^{2\pi} \cos^2 \phi d\phi = \int_0^{2\pi} \sin^2 \phi d\phi = \pi.$$

Hence

$$Q_s = \frac{\pi}{k^2} \operatorname{Re} \int_{\epsilon_1}^{\pi} d\theta \sum_n \sum_m \frac{2n+1}{n(n+1)} \frac{2m+1}{m(m+1)} \cdot \\ \left\{ (a_n \bar{b}_m + a_m \bar{b}_n) \left[P_n^1 \frac{dP_m^1}{d\theta} + P_m^1 \frac{dP_n^1}{d\theta} \right] + (a_n \bar{a}_m + b_n \bar{b}_m) \cdot \right. \\ \left. \left[\frac{P_n^1 P_m^1}{\sin \theta} + \sin \theta \frac{dP_n^1}{d\theta} \frac{dP_m^1}{d\theta} \right] \right\}. \quad (34a)$$

This is easily compared with Stratton's formula.²⁷ Stratton takes $\epsilon_1 = 0$ in which case the first θ integral is zero and the second is different from zero only when $m = n$, where it yields

$$\int_0^{\pi} \left(\frac{P_n^1 P_m^1}{\sin \theta} + \sin \theta \frac{dP_n^1}{d\theta} \frac{dP_m^1}{d\theta} \right) d\theta = 2 \frac{n^2(n+1)^2}{2n+1}. \quad (35)$$

Hence

$$Q_{\text{Stratton}} = \frac{2\pi}{k^2} \sum_n (2n+1) (|a_n|^2 + |b_n|^2). \quad (36)$$

Thus, taking an angle $\epsilon_1 = 0$ simplifies the formulas very much. But we need to keep a small angle $\epsilon_1 \neq 0$ and the general expression (34a):

$$Q_s = \frac{\pi}{k^2} \sum_{n,m} \frac{2n+1}{n(n+1)} \frac{2m+1}{m(m+1)} \operatorname{Re} [I_1 (a_n \bar{b}_m + a_m \bar{b}_n) \\ + I_2 (a_n \bar{a}_m + b_n \bar{b}_m)], \quad (37)$$

with

$$I_1 = \int_{\epsilon_1}^{\pi} \left(P_n^1 \frac{dP_m^1}{d\theta} + P_m^1 \frac{dP_n^1}{d\theta} \right) d\theta = P_n^1 P_m^1 \Big|_{\epsilon_1}^{\pi}, \quad (38) \\ I_2 = \int_{\epsilon_1}^{\pi} \left(\frac{P_n^1 P_m^1}{\sin \theta} + \sin \theta \frac{dP_n^1}{d\theta} \frac{dP_m^1}{d\theta} \right) d\theta = \sin \theta P_m^1 \frac{dP_n^1}{d\theta} \Big|_{\epsilon_1}^{\pi} \\ + n(n+1) \int_{\epsilon_1}^{\pi} P_n^1 P_m^1 \sin \theta d\theta.$$

[See Section 4.10, equation (87).] These are our fundamental formulas for the following discussion.

4.7 USE OF APPROXIMATE EXPRESSIONS FOR THE LEGENDRE FUNCTION

The problem is to obtain approximate values for the integrals I_1 and I_2 of (38). Using formula (93) of Section 4.10 for the lower limit ϵ_1 and remembering P_n^1 to be zero for π , we obtain

$$I_1 = P_n^1 P_m^1 \Big|_{\epsilon_1}^{\pi} \approx \sqrt{nm} \frac{2}{\pi \sin \epsilon_1} \sin \left[\left(n + \frac{1}{2} \right) \epsilon_1 \right. \\ \left. + \frac{3\pi}{4} \right] \sin \left[\left(m + \frac{1}{2} \right) \epsilon_1 + \frac{3\pi}{4} \right], \quad (39)$$

$$I_1 = \frac{\sqrt{nm}}{\pi \sin \epsilon_1} [\sin (n+m+1)\epsilon_1 - \cos (n-m)\epsilon_1]$$

when

$$n, m \gg 1,$$

where ϵ_1 is small and $\sin \epsilon_1$ can be replaced by ϵ_1 , while $(n+m+1)\epsilon_1$ and $(n-m)\epsilon_1$ may become rather large.

As for the integral I_2 , we can apply the same treatment to the first term, but if we use approximate expressions for $P_n^1 P_m^1$ in the second integral, we cannot extend it up to π but only to $\pi - \epsilon_2$, hence

$$I_2 \approx \sin \theta P_m^1 \frac{dP_n^1}{d\theta} \Big|_{\epsilon_1}^{\pi} + n(n+1) \int_{\epsilon_1}^{\pi-\epsilon_2} P_n^1 P_m^1 \sin \theta d\theta, \\ \approx -\frac{2n}{\pi} \sqrt{nm} \sin \left[\left(n + \frac{1}{2} \right) \epsilon_1 + \frac{3\pi}{4} \right] \cos \left[\left(n + \frac{1}{2} \right) \epsilon_1 \right. \\ \left. + \frac{3\pi}{4} \right] - \frac{\sqrt{nm}}{\pi} n(n+1) \int_{\epsilon_1}^{\pi-\epsilon_2} [\sin (n+m+1)\theta \\ - \cos (n-m)\theta] d\theta, \quad (40)$$

$$I_2 \approx \frac{+n \sqrt{nm}}{\pi} \left[+ \cos (n+m+1)\epsilon_1 \right. \\ \left. + \sin (n-m)\epsilon_1 + (n+1) \frac{\cos (n+m+1)\theta}{n+m+1} \right. \\ \left. + (n+1) \times \frac{\sin (n-m)\theta}{n-m} \Big|_{\epsilon_1}^{\pi-\epsilon_2} \right].$$

The last term is the most important one, especially when n and m do not differ too much, and $n+1/n-m$ is very large. For $n = m$ we have

$$\left| \frac{\sin (n-m)\theta}{n-m} \right|_{\epsilon_1}^{\pi-\epsilon_2} = \left| \theta \right|_{\epsilon_1}^{\pi-\epsilon_2} = \pi - \epsilon_1 - \epsilon_2, \\ n = m \gg 1 \quad (41)$$

$$I_2 = \frac{n^2}{\pi} [\cos (2n+1)\epsilon_1 \\ + \frac{1}{2} \cos (2n+1)\theta \Big|_{\epsilon_1}^{\pi-\epsilon_2} + n\pi - n\epsilon_1 - n\epsilon_2] \approx n^3.$$

According to our assumptions, n is supposed to be large compared to 1 and ϵ_1, ϵ_2 are small, but $n\epsilon_1, n\epsilon_2$ may be of the order of some units. Anyhow, in formula (41), the term $n\pi$ is by far the largest one in the brackets, and our approximate result compares favorably with the correct one (Stratton, $\epsilon_1 = \epsilon_2 = 0$)

$$I_2 = \frac{2n^2(n+1)^2}{2n+1} \approx n^3 \quad n \gg 1. \quad (42)$$

In our general formula (37), we note that the large values of n, m give the largest contribution, since integral I_2 is of the order of n^3 and even after multi-

plication by $\frac{2n+1}{n(n+1)} \frac{2m+1}{m(m+1)}$ it still increases

with n . This remark enables us to write separately the term $n = m$, which practically coincides with the one kept by Stratton, and to state

$$Q_{\text{Stratton}} Q_s = + Q_{\text{corr}} \\ Q_{\text{corr}} = \frac{\pi}{k^2} \sum_n \sum_{m \neq n} \frac{2n+1}{n(n+1)} \frac{2m+1}{m(m+1)} \text{Re}[2I_1 a_n \bar{b}_m \\ + I_2 (a_n \bar{a}_m + b_n \bar{b}_m)]. \quad (43)$$

In the double sum on n and m we have replaced $a_n \bar{b}_m + a_m \bar{b}_n$ by its equivalent $2a_n \bar{b}_m$. The quantity Q_{corr} yields the correction to Stratton's original formula for the scattering cross section.

4.8 LARGE METALLIC SPHERES; COMPUTATION OF THE COEFFICIENTS a_n, b_n

The preceding formulas should be used as point of departure for the discussion of the scattering cross section for large spheres.

$$\rho_1 = \frac{2\pi a}{\lambda} \gg 1 \quad a \geq \lambda. \quad (44)$$

The approximations involved will mean neglecting terms in $1/\rho_1$ compared with unity.

For a perfect metallic sphere, the a_n and b_n coefficients have the following values ^{2k}

$$a_n = -\frac{j_n(\rho_1)}{h_n^1(\rho_1)}; \quad b_n = -\frac{[\rho_1 j_n]'}{[\rho_1 h_n^1]'}; \quad \rho_1 = ka = 2\pi \frac{a}{\lambda}, \quad (45)$$

where j_n, h_n^1 are the spherical Bessel functions, as in equation (28a) and the prime denotes the derivative with respect to ρ_1 .

These formulas (45) may be written in a slightly different way, if we start from an expression

$$\rho_1 h_n^1 = A_n e^{i\phi_n}; \quad A_n \text{ real, positive}, \quad (46)$$

where amplitude A_n and phase angle ϕ_n of the h_n^1 functions are explicitly used. Then

$$\rho_1 j_n = \text{Re} \rho_1 h_n^1 = A_n \cos \phi_n \quad (46a)$$

and

$$a_n = -\cos \phi_n e^{-i\phi_n}. \quad (47)$$

Taking the derivatives, we find

$$[\rho_1 h_n^1]' = [A_n' + iA_n \phi_n'] e^{i\phi_n},$$

$$[\rho_1 j_n]' = \text{Re}[\rho_1 h_n^1]' = A_n' \cos \phi_n - A_n \phi_n' \sin \phi_n.$$

Here, two cases should be considered separately

$$(A) \quad \phi_n' \gg \frac{A_n'}{A_n} \quad b_n \approx -i \sin \phi_n e^{-i\phi_n}, \quad (48)$$

$$(B) \quad \phi_n' < \frac{A_n'}{A_n} \quad b_n \approx -\cos \phi_n e^{-i\phi_n} = a_n.$$

These results are identical with those of Stratton,^{2b} except for the fact that Stratton uses an angle

$$\gamma_n = \frac{\pi}{2} - \phi_n.$$

The important point is that the a_n, b_n coefficients are large (order of magnitude 1) when $n \leq \rho_1$ and decrease very rapidly when $n > \rho_1$. In order to prove this and to find approximate expressions to be used in each case, we must distinguish three different cases:

- I $n < \rho_1 \quad \rho_1 \gg 1$
- II $n \approx \rho_1$
- III $n > \rho_1$

and discuss the corresponding approximate expressions given by Debye.⁷

Case I. For ($n < \rho_1 \gg 1$), the approximate formulas to be used are

$$n < \rho_1, \quad \tau_n \approx \frac{\pi}{2} - \frac{n + \frac{1}{2}}{\rho_1}; \quad (49)$$

$$\sin \tau_n \approx 1, \quad \phi_n \approx \rho_1 - \frac{\pi}{2}(n + 1); \quad (50)$$

$$\rho_1 j_n \approx \cos \phi_n \rho_1 h_n^1 \approx e^{i\phi_n}. \quad (51)$$

In formulas (50), we notice that τ_n varies very slowly with n , while ϕ_n exhibits a rapid variation. Hence in equation (46) the amplitude $A_n = (\sin \tau_n)^{-\frac{1}{2}}$ varies very slowly and we may use formulas (46) and (47),

$$a_n = -\cos \phi_n e^{-i\phi_n} \\ b_n = -i \sin \phi_n e^{-i\phi_n}, \quad (52)$$

from which we compute

$$\begin{aligned} a_n \bar{b}_m &= -i \cos \phi_n \sin \phi_m e^{i(\phi_m - \phi_n)}, \\ a_n \bar{a}_m + b_n \bar{b}_m &= \cos(\phi_m - \phi_n) e^{i(\phi_m - \phi_n)}. \end{aligned} \quad (53)$$

Case II. For $n \approx \rho_1 \gg 1$, the approximate expressions for the Bessel spherical functions are more complicated and have been computed.^{4,7} They yield

$$\rho_1 = n + \frac{1}{2}, \quad \phi_n = -\frac{\pi}{3}. \quad (54)$$

Case III. For $n > \rho_1 \gg 1$, the approximate expressions given by Debye must be corrected to include the real part ψ_n in ζ_n , which Debye drops out. It is actually true that ψ_n is much smaller than the imaginary part of ζ_n , but it is safer to keep it, and to write

$$\zeta_n = \rho_1 h_n^1 = \psi_n - i \frac{e^{\rho_1 f_n^1} n}{\sqrt{sh\tau_n^1}}, \quad (55)$$

$$\psi_n = \rho_1 j_n = \frac{1}{2} \frac{e^{-\rho_1 f_n^1} n}{\sqrt{sh\tau_n^1}} \ll \zeta_n, \quad (56)$$

where

$$f_n^1 = -sh\tau_n^1 + \tau_n^1 ch\tau_n^1 > 0, \quad \tau_n^1 > 0 \text{ real}, \quad (57)$$

$$ch\tau_n^1 = \frac{n + \frac{1}{2}}{\rho_1}. \quad (58)$$

The factor $\frac{1}{2}$ in ψ_n (or j_n) was first omitted by Debye and discovered later by F. Emde.⁹ The phase angle ϕ_n in ζ_n is given by

$$\tan \phi_n = -2e^{2\rho_1 f_n^1}, \quad (59)$$

which, for the lower limit of the interval ($n = \rho_1 - \frac{1}{2}$), yields $\tan \phi_n = -2$, or ϕ_n slightly below $-\pi/3$, while for increasing n the angle ϕ_n reaches $-\pi/2$ as

$$\phi_n = -\frac{\pi}{2} + \frac{1}{2} e^{-2\rho_1 f_n^1}. \quad (60)$$

Under such conditions, we may use formulas (47) and (48) to compute the coefficients a_n and b_n ,

$$a_n \approx b_n \approx -\cos \phi_n e^{-\phi_n} \approx \frac{1}{2} e^{-2\rho_1 f_n^1}. \quad (61)$$

When n increases, both a_n and b_n decrease very rapidly and tend exponentially to zero,

$$n \gg \rho_1, \quad (62)$$

$$ch\tau_n^1 \approx sh\tau_n^1 \approx \frac{1}{2} e^{+\tau_n^1} = \frac{n + \frac{1}{2}}{\rho_1},$$

$$\rho_1 f_n^1 = (n + \frac{1}{2})(\tau_n^1 - 1) = (n + \frac{1}{2}).$$

$$\left(\log \frac{2n+1}{\rho_1} - 1 \right) = (n + \frac{1}{2}) \log \frac{2n+1}{e\rho_1}, \quad (63)$$

$$\zeta_n = -i \sqrt{\frac{2}{e}} \left(\frac{2n+1}{e\rho_1} \right)^n \rightarrow \infty,$$

$$\psi_n = \frac{1}{\sqrt{2e}} \left(\frac{e\rho_1}{2n+1} \right)^{n+1} \rightarrow 0, \quad (64)$$

$$a_n = b_n = \frac{i}{2} \left(\frac{e\rho_1}{2n+1} \right)^{2n+1}. \quad (65)$$

Following the same line as in Case I, we compute the values of the combinations we need in our formulas, namely

$$a_n \bar{b}_m = \frac{1}{4} e^{-2\rho_1(f_n^1 + f_m^1)} \rightarrow \frac{1}{4} \left(\frac{e\rho_1}{2n+1} \right)^{2n+1} \left(\frac{e\rho_1}{2m+1} \right)^{2m+1}, \quad (66)$$

$$a_n \bar{a}_m + b_n \bar{b}_m = \frac{1}{2} e^{-2\rho_1(f_n^1 + f_m^1)} \rightarrow \frac{1}{2} \left(\frac{e\rho_1}{2n+1} \right)^{2n+1} \left(\frac{e\rho_1}{2m+1} \right)^{2m+1}.$$

It is interesting to draw a few curves in order to visualize the results just obtained. As noticed in (47) and (48), we are especially interested in the phase angle ϕ_n , from which our a_n, b_n coefficients can be readily computed.

In Case I ($n < \rho_1 - \frac{1}{2}$) the phase angle ϕ_n decreases regularly from $\rho_1 - (\pi/2)(n=0)$ down to $-\pi/4(n = \rho_1 - \frac{1}{2})$, this last point being reached with a horizontal tangent, but we have to stop using the formulas of Case I before we reach this limit, which corresponds to Case II. There the angle ϕ_n exhibits a slow decrease with $-\pi/3$ as its actual value when $n = \rho_1 - \frac{1}{2}$. For larger values of n , we turn to the formulas of Case III, which show a decrease from $-\pi/3$ to $-\pi/2$. These results are summarized on the curve of Figure 3, which should be considered only as qualitative.

From the ϕ_n curve, one may readily deduce the variation of a_n, b_n . The curves on top of Figure 3 show the behavior of $|a_n|$ and $|b_n|$, which oscillate like $|\cos \phi_n|$ and $|\sin \phi_n|$ in Region I, then decrease in Region II and tend exponentially to zero in Region III.

The sum $|a_n|^2 + |b_n|^2$ is equal to 1 in Region I, decreases rapidly in II and is practically zero in III (second curve on top of Figure 3). This typical behavior had been noticed by Debye, who consequently replaced the curve by a rectangular one:

$$|a_n|^2 + |b_n|^2 = \begin{cases} 1 & n < \rho_1 - \frac{1}{2} \\ 0 & n > \rho_1 - \frac{1}{2} \end{cases}$$

When this approximation is used in equation (36), it yields

$$Q_{\text{Stratton}} \approx \frac{2\pi}{k^2} \sum_{n=1}^{n=\rho_1} (2n+1) = \frac{2\pi}{k^2} ka(ka+2) \approx 2\pi a^2,$$

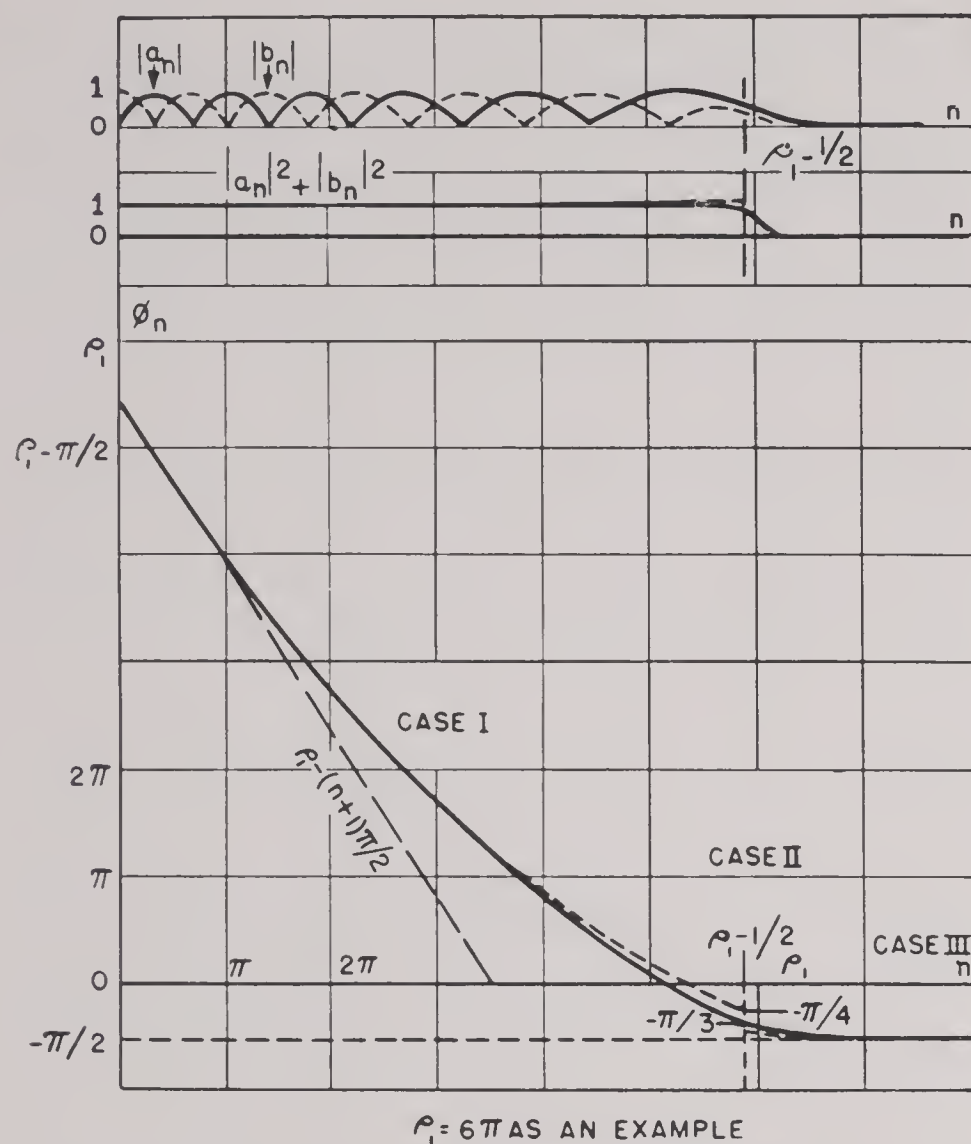


FIGURE 3. Behavior of the phase angle and the coefficients.

since $\rho_1 = ka$. This shows directly how Stratton's scattering cross section comes out twice the actual cross section [equation (7)].

Some quantitative data are summarized by the curves of Figure 4, which have been plotted from the Lowan tables "scattering angles for spherical coordinates."

The circles, just near the curve $\rho_1 = 10$, correspond to points computed from Debye's formulas. They lie very near the curve, a result which suggests that for $\rho_1 > 10$ these asymptotic expressions can already be used for practical computation.

4.9 COMPUTATION OF THE SCATTERING CROSS SECTION

The formulas obtained in the preceding sections must now be used for a discussion of the scattering cross section of a metallic sphere. We start from formula (43),

$$Q_s = Q_{\text{Stratton}} + Q_{\text{corr}}, \quad (67)$$

where Q_{Stratton} is the value obtained by Stratton, which tends to the limit $2\pi a^2$ for large spheres, and Q_{corr} is the correction, which should amount to $-\pi a^2$ for large spheres, in order to bring Q_s back to the expected value πa^2 . Formula (43) gives Q_{corr} and we

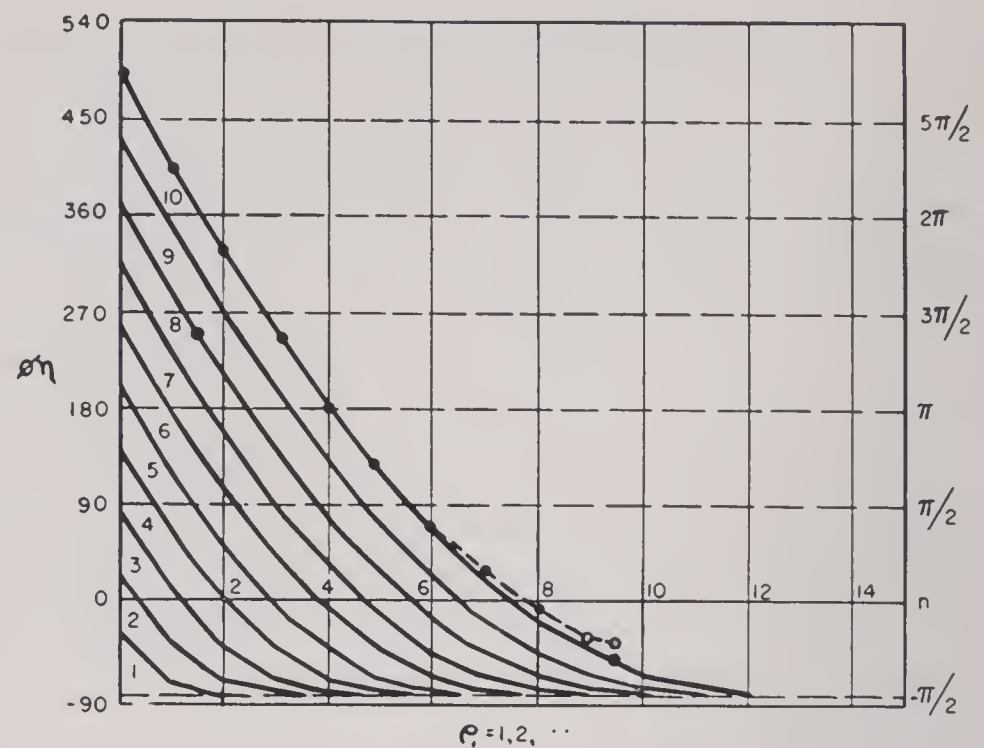


FIGURE 4. The phase angle for various values of ρ_1 .

take I_1 and I_2 from equations (39) and (40). Remembering that n and m may practically take all values up to ρ_1 , while ϵ_1 is small but finite, we note that I_1 is certainly much smaller than I_2 and that the most important terms in I_2 are those with the denominator $n - m$. Hence we may use the approximation

$$I_1 \approx 0, \quad (68)$$

$$I_2 \approx \frac{n\sqrt{nm}}{\pi} \left[-\frac{m+1}{m-n} \sin(m-n)\epsilon_1 - (-1)^{m-n} \frac{n+1}{m-n} \sin(m-n)\epsilon_2 \right], \quad (69)$$

$$\rho_1 = ka \gg 1.$$

The difference in the behavior of the terms in ϵ_1 and ϵ_2 is striking. Terms in ϵ_1 may pile up to a finite value, since they all keep the same sign, while alternative signs on the ϵ_2 terms will prevent them from yielding any large contribution (see Section 4.11). We shall be satisfied with keeping the ϵ_1 terms only, and we may introduce a new integer

$$\nu = m - n \neq 0 \quad \nu = +1, +2, +3 \dots \quad (70)$$

$$Q_{\text{corr}} \approx -\frac{1}{k^2} \sum_n \frac{(2n+1)^2}{n+1} \sum_{\nu \neq 0} \left(1 + \frac{2}{2n+1} \right) \left(1 + \frac{\nu}{n} \right)^{-\frac{1}{2}} \frac{\sin \nu \epsilon_1}{\nu} \text{Re}(a_n a_{n+\nu} + b_n b_{n+\nu}). \quad (71)$$

As a further approximation, we assume that the most important contribution will be given by small ν values, and we put

$$|\nu| \ll n, \quad 1 + \frac{2\nu}{2n+1} \approx 1 + \frac{\nu}{n} \approx 1.$$

Then we use formula (53), which refers to the most important case, $n < \rho_1$, as discussed in Section 4.8,

and we simply drop all terms for which n or $n + \nu$ is larger than ρ_1

$$\operatorname{Re}(a_n \bar{a}_{n+\nu} + b_n \bar{b}_{n+\nu}) = \cos^2(\phi_{n+\nu} - \phi_n) \quad (72)$$

$$Q_{\text{corr}} \approx -\frac{1}{k^2} \sum_{n=1}^{\rho_1} \frac{(2n+1)^2}{n+1} \sum_{\nu \neq 0} \frac{\sin \nu \epsilon_1}{\nu} \cos^2(\phi_{n+\nu} - \phi_n). \quad (73)$$

The $\cos^2(\phi_{n+\nu} - \phi_n)$ is $1/2$ on the average^a and

$$\sum_{\nu > 0} \frac{\sin \nu \epsilon_1}{\nu} = \frac{\pi - \epsilon_1}{2} \quad \epsilon_1 > 0. \quad (74)$$

[See Section 4.11, equation (95).] The sum for negative ν values yields the same result, hence

$$\sum_{\nu \neq 0} \frac{\sin \nu \epsilon_1}{\nu} = \sum_{\nu > 0} + \sum_{\nu < 0} = \pi - \epsilon_1, \quad (75)$$

and

$$Q_{\text{corr}} = -\frac{\pi - \epsilon_1}{2k^2} \sum_{n=1}^{\rho_1} \frac{(2n+1)^2}{n+1} \approx -2 \frac{\pi - \epsilon_1}{k^2} \sum_{n=1}^{\rho_1} n \approx -2 \frac{\pi - \epsilon_1}{k^2} \frac{\rho_1^2}{2}. \quad (76)$$

We may assume ϵ_1 small compared to π and obtain finally

$$Q_{\text{corr}} \approx -\pi \frac{\rho_1^2}{k^2} = -\pi a^2, \quad (77)$$

which is the expected result.

A discussion of the approximations involved in this last step would now appear desirable.

The computation rests on the approximate formula for the Legendre function [Section 4.10, equation (93)], as used in Section 4.7, and this approximation is good only when the small angle ϵ_1 is larger than $4/n$ [Section 4.10, equation (94)].

$$\epsilon_1 \geq \frac{4}{n} \quad n \gg 1. \quad (78)$$

On the other hand, we took the sum from $n = 1$ to $n = \rho_1$ in equation (76). This may not seem quite consistent with the assumption $n \gg 1$. Let us discuss the point more carefully and assume that in equation (76) we take the sum from

$$n = \frac{2}{10} \rho_1 \quad \text{to} \quad n = \rho_1, \quad (79)$$

both values are much larger than unity, as needed. Then our sum becomes

^a For a more precise discussion, see end of Section 4.11. $\phi_{n+\nu} - \phi_n$ for small ν values is practically $\nu(\partial\phi/\partial n)$, and $\partial\phi/\partial n$ is comprised between $-\pi/2$ and $-\pi/6$, as shown on Figures 3 and 4.

$$\sum_{0.2\rho_1}^{\rho_1} n = \int_{0.2\rho_1}^{\rho_1} n dn = \frac{\rho_1^2}{2} \left(1 - \frac{4}{100}\right), \quad (80)$$

which makes a very small correction. Combining conditions (78) and (79), we obtain

$$\epsilon_1 \geq \frac{4}{n} \geq \frac{20}{\rho_1}, \quad \rho_1 = ka = \frac{2\pi a}{\lambda}, \quad (81)$$

or

$$\epsilon_1 = K \frac{\lambda}{a}, \quad K \approx 3,$$

and ϵ_1 must still be much smaller than π . Here again let us be satisfied with an error $4/100$,

$$\frac{20\lambda}{2\pi a} \leq \frac{4\pi}{100},$$

or approximately $\lambda/a \leq 0.04 = 1/25$, hence

$$\rho_1 = \frac{2\pi a}{\lambda} \geq 160 \quad \frac{a}{\lambda} > 25. \quad (82)$$

When conditions (81) and (82) are satisfied, the energy flow of the radiation scattered over angles comprised between ϵ_1 and π correspond within a few per cent per energy flow in the incident wave over a cross section πa^2 . The secondary radiation inside an angle ϵ_1 , if it were alone, would correspond to an energy flow measured by another equal cross section πa^2 .

An attempt is made in Appendix III to rebuild the total field by the superposition of the direct and secondary waves, for these small angles. When

$$\theta < \theta_s, \quad \theta_s = \frac{2}{\rho_1} = \frac{\lambda}{\pi a}, \quad (83)$$

the total field is very small, but there is a bright fringe of interference along the z axis, when

$$\theta < \theta_F, \quad \theta_F = \frac{2}{\rho} = \frac{\lambda}{\pi R}, \quad (84)$$

where a is the radius of the sphere and R the distance of observation. This bright fringe along the axis is a well-known experimental fact, usually explained on the basis of Huyghens' principle; it is obtained here on the basis of rigorous theory of electromagnetism.

The curve drawn on Figure 5 represents an attempt at summarizing our results, but the calculations developed in the present report do not give enough information to enable us to draw a complete and precise graph.

No experimental device can measure the scattered radiation down to a deviation zero, hence there will

always be a lower limit ϵ_1 to the deviation angle. The assumption made in (81) and (82) corresponds to

$$\epsilon_1 = \frac{4}{100}\pi \quad \text{or} \quad \epsilon_1 = 7^\circ.$$

The measurements are performed for all ratios λ/a and plotted in Figure 5, with $\rho_1 = 2\pi(a/\lambda)$ as parameter and the scattering cross section Q_s as ordinate. For small values of ρ_1 (up to $\rho_1 \approx 20$) the small finite

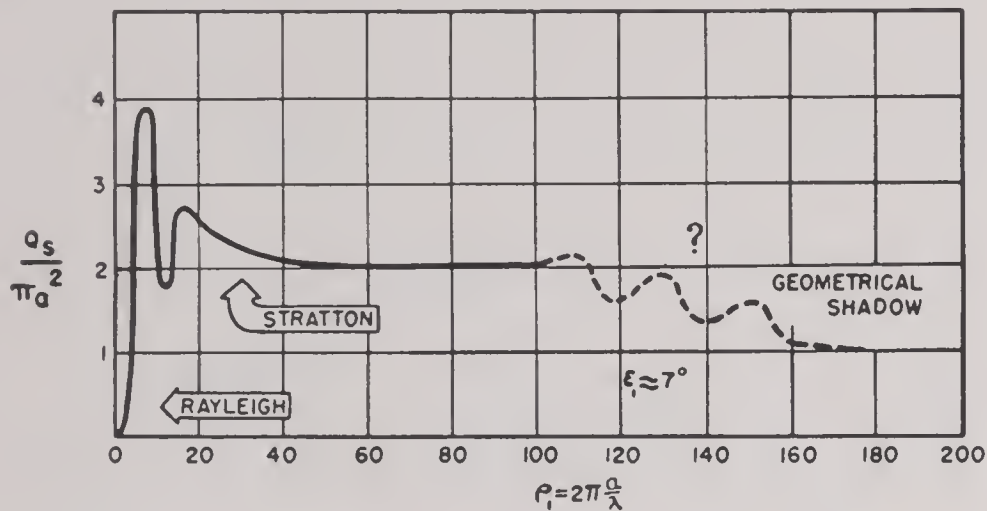


FIGURE 5. Qualitative representation of scattering cross section.

value of ϵ_1 does not play any appreciable role, and the scattering cross section Q_s is practically equal to the value computed by Stratton (taking $\epsilon_1 = 0$). It oscillates up and down, and finally reaches a value near $2\pi a^2$. For shorter wavelengths (larger ρ_1 values), a transition will be observed, and the curve will go down to the limit πa^2 which corresponds to geometrical optics. The final value πa^2 is practically reached for $\rho_1 \approx 160$ in our typical example.

We did not obtain any information about the shape of the curve in the intermediate region, but the curve should exhibit a few sharp maxima and minima, since our limit $\epsilon_1 > K(\lambda/a)$ where $K = 3$ includes all the first classical diffraction rings [equation (4)].

4.10

APPENDIX I

SOME FORMULAS CONNECTED WITH LEGENDRE FUNCTIONS

Legendre functions $P_n(x)$ satisfy the following equation¹³

$$\frac{1}{\sin \theta} \frac{d}{d\theta} \left(\sin \theta \frac{dP_n^1}{d\theta} \right) + \left(n(n+1) - \frac{1}{\sin^2 \theta} \right) P_n^1 = 0. \quad (85)$$

This formula can be used in connection with the integral

$$I_2 = \int_{\epsilon}^{\pi-\epsilon_2} \left(\frac{P_n^1 P_m^1}{\sin \theta} + \sin \theta \frac{dP_n^1}{d\theta} \frac{dP_m^1}{d\theta} \right) d\theta. \quad (86)$$

Integration by parts on the second term yields

$$I_2 = \sin \theta P_m^1 \frac{dP_n^1}{d\theta} \Big|_{\epsilon_1}^{\pi-\epsilon_2} + \int_{\epsilon_1}^{\pi-\epsilon_2} P_m^1 \left[\frac{P_n^1}{\sin \theta} - \frac{d}{d\theta} \left(\sin \theta \frac{dP_n^1}{d\theta} \right) \right] d\theta \quad (87)$$

$$I_2 = \sin \theta P_m^1 \frac{dP_n^1}{d\theta} \Big|_{\epsilon_1}^{\pi-\epsilon_2} + n(n+1) \int_{\epsilon_1}^{\pi-\epsilon_2} P_n^1 P_m^1 \sin \theta d\theta.$$

If ϵ_1 and ϵ_2 are zero, the conditions for orthonormalization of the P_n^1 give

$$I_2 = \begin{cases} 0 & \text{if } n \neq m \\ n(n+1) \frac{2}{2n+1} \frac{(n+1)!}{(n-1)!} = \frac{2n^2(n+1)^2}{2n+1} & \text{if } n = m. \end{cases} \quad (88)$$

The Legendre function P_n^1 can be represented by the expansion^{3a}

$$P_n^1 = \frac{n(n+1)}{2} \sin \theta \cdot \left[1 - \frac{(n-1)(n+2)}{4} (1 - \cos \theta) \dots \right]. \quad (89)$$

This shows that P_n^1 is zero for $\theta = 0$ (and $\theta = \pi$).

When $\theta \rightarrow 0$

$$P_n^1 = \frac{n(n+1)}{2} \theta \left[1 - \frac{\theta^2}{6} - \frac{(n-1)(n+2)}{8} \theta^2 \dots \right]$$

$$\frac{dP_n^1}{d\theta} = \frac{n(n+1)}{2} \left[1 - \frac{\theta^2}{2} - \frac{3}{8} (n-1)(n+2) \theta^2 \dots \right]. \quad (90)$$

$$R_n^1 = -\frac{P_n^1}{\sin \theta} + \frac{dP_n^1}{d\theta} \quad (91)$$

is zero for $\theta = 0$ and becomes appreciable (for large n) when $n^2\theta^2/4$ can no longer be neglected in comparison to 1 or when

$$\theta \sim \frac{2}{n}. \quad (92)$$

The Legendre function P_n^1 starts from zero at $\theta = 0$ and exhibits a series of oscillations between $\theta = 0$ and $\theta = \pi$. These oscillations can be represented by the approximate formula^{3b} (see Figure 1).

$$P_n^1 \approx -\sqrt{\frac{2n}{\pi \sin \theta}} \sin \left[\left(n + \frac{1}{2} \right) \theta + \frac{3\pi}{4} \right], \quad (93)$$

when $n \gg 1$, $\epsilon < \theta < \pi - \epsilon$.

The limit ϵ corresponds to the neighborhood of the first zero of P_n^1 . This first zero practically coincides with the second zero of the approximate expression (94), namely

$$(n + \frac{1}{2})\theta_1 = \frac{5\pi}{4} \quad \theta_1 \approx \frac{5\pi}{4n}, \quad (94)$$

a limit larger than (92) but of the same order of magnitude.

4.11

APPENDIX II

SOME ELEMENTARY RESULTS CONCERNING THE FOURIER SERIES AND CONDITIONS FOR STATIONARY PHASE

The following Fourier series is known to yield a saw-toothed curve, with discontinuities at $x = 0, \pm 2\pi, \dots$

$$f(x) = \sum_{p=1}^{\infty} \frac{\sin px}{p} = \begin{cases} \frac{-\pi - x}{2} & -2\pi < x < 0 \\ \frac{\pi - x}{2} & 0 < x < 2\pi. \end{cases} \quad (95)$$

The sudden jump from $-\pi/2$ to $+\pi/2$ when x crosses the zero point is of special importance for our discussion.

In the problem discussed in the report, the series to be computed is not exactly (95), but a similar series whose summation can be reduced to the case (95).

The series involved in equation (73) is

$$F(x) = \sum_{p=1}^{\infty} \cos^2 p\psi \frac{\sin px}{p} = \frac{1}{2} \sum_{p=1}^{\infty} \frac{\sin px}{p} + \frac{1}{2} \sum_{p=1}^{\infty} \cos 2p\psi \frac{\sin px}{p} \psi = \frac{\partial \phi}{\partial n}, \quad (96)$$

where x is small and positive, while ψ is an angle between $-\pi/2$ and $-\pi/6$. The first series is given by (95) and the second series is split in two similar ones:

$$F(x) = \frac{1}{4}(\pi - x) + \frac{1}{4} \sum_{p=1}^{\infty} \left[\frac{\sin p(x + 2\psi)}{p} + \frac{\sin p(x - 2\psi)}{p} \right]. \quad (97)$$

Here, we must note that

$$\begin{aligned} x + 2\psi &< 0 \\ x - 2\psi &> 0 \end{aligned}$$

which leads to the two different cases of (95):

$$\begin{aligned} F(x) &= \frac{1}{4}(\pi - x) + \frac{1}{8}[\pi - x - 2\psi - \pi - x + 2\psi] \\ &= \frac{\pi}{4} - \frac{x}{2}, \end{aligned} \quad (98)$$

a result that could have been guessed, since it practically amounts to taking $\cos^2 p\psi$ with its average value $1/2$ in the original formula (96).

4.12

APPENDIX III

It was noted in the general discussion in Section 4.9 that a sharp distinction between incident wave and secondary wave is impossible to draw for small angles of deflection θ , and that the right way to attack the problem is to discuss the total field distribution as given by the superposition of incident and secondary waves.

Both waves are represented by the expansions given in Section 4.6, namely:

$$\begin{aligned} &\text{secondary wave (S), equations (27);} \\ &\text{plane incident wave (I), equation (27a).} \end{aligned} \quad (99)$$

Both $h_n^1(\rho)$ and $j_n(\rho)$ functions were computed in Section 4.8 and their approximate expressions were used to obtain the a_n and b_n coefficient for a rather large metallic sphere ($a > \lambda$).

$$\rho_1 = ka \gg 1, \quad \rho = kR, \quad k = 2\pi/\lambda, \quad (100)$$

where a is the radius of the sphere and R the distance of observation. The discussion in Section 4.8 proved that the a_n, b_n coefficients become negligible when n is larger than ρ_1 [Case III, equation (65)], hence the expansion of the secondary wave will practically contain ρ_1 terms only.

We build up the resultant or total field by superimposing both expansions (99) of primary I and secondary S waves. The preceding remarks show that the ρ_1 first terms only will be affected by this superposition, while the remaining terms $n > \rho_1$ in the expansion of the plane primary wave remain unchanged.

$$\text{Total field} = \sum_{n=1}^{n=\rho_1} (I + S) + \sum_{n=\rho_1}^{\infty} I. \quad (101)$$

The last group of terms results directly from equation (27a) without any change. Let us now discuss the first group. We are especially interested in the behavior in the *shadow region*, which corresponds to small angles θ , and we assume condition (92) to be fulfilled,

$$\theta < \theta_s = 2/\rho_1 \quad n \leq \rho_1. \quad (102)$$

Under such conditions we may use equation (90) and the following approximations are justified:

$$\frac{\partial P_n^1}{\partial \theta} \approx \frac{P_n^1}{\sin \theta} \approx \frac{1}{\theta} P_n^1 \frac{n(n+1)}{2}. \quad (103)$$

This simplifies the general expansions (27). If we study the field at a great distance, the radial component E_R is negligible and we are left with the θ and ϕ components only:

$$E_\theta = E_0 e^{-i\omega t} \sum_{n=1}^{\rho_1} i^n \frac{2n+1}{n(n+1)} \frac{P_n^1}{\rho \theta} \left[\begin{aligned} &+a_n \rho h_n - i b_n [\rho h_n]' \\ &+ \rho j_n - i [\rho j_n]' \end{aligned} \right] \cos \phi, \quad (104)$$

$$E_\phi = -E_0 e^{-i\omega t} \sum_{n=1}^{\rho_1} i^n \frac{2n+1}{n(n+1)} \frac{P_n^1}{\rho \theta} \left[\begin{aligned} &+a_n \rho h_n - i b_n [\rho h_n]' \\ &+ \rho j_n - i [\rho j_n]' \end{aligned} \right] \sin \phi.$$

This refers only to the first group of terms in (101). Terms in $a_n, b_n h_n$ represent the contribution of the secondary wave, while the j_n terms come from the direct wave. The brackets are identical in both formulas. Let us discuss their values for the problem stated in Section 4.8, Case I,

$$\begin{aligned} n &< \rho_1 \\ \psi_n &= \rho j_n = \cos \phi_n \\ a_n &= -\cos \phi_{ln} e^{-i\phi_{ln}} \\ \phi_{ln} &= \rho_1 - \frac{\pi}{2}(n+1) \end{aligned} \quad (105)$$

$$\rho_1 = 2\pi \frac{a}{\lambda} \gg 1$$

$$\zeta_n = \rho h_n = e^{i\phi_n} = -i[\rho h_n]'$$

$$b_n = -i \sin \phi_{ln} e^{-i\phi_{ln}}$$

$$\phi_n = \rho - \frac{\pi}{2}(n+1).$$

The primes indicate $\partial/\partial\rho$ derivatives, which amount to $\partial/\partial\phi_n$, and ϕ_n, ϕ_{ln} should not be confused with the angular coordinate ϕ .

$$\begin{aligned} a_n \zeta_n - i b_n \zeta_n' &= -\cos \phi_{ln} e^{i(\phi_n - \phi_{ln})} \\ &\quad - i \sin \phi_{ln} e^{i(\phi_n - \phi_{ln})} = -e^{i\phi_n}, \end{aligned} \quad (106)$$

hence the bracket of formula (104) reduces to

$$-e^{i\phi_n} + \cos \phi_n + i \sin \phi_n = 0.$$

This means that the first group of terms in (101) drops out entirely and that we obtain the following *very important results*,

$$\theta < \theta_s = \frac{2}{\rho_1} = \frac{\lambda}{\pi a} \quad \rho_1 = \frac{2\pi a}{\lambda} \quad (107)$$

$$\text{Total field} \approx \sum_{n=\rho_1}^{\infty} (\text{incident field terms}).$$

In the *shadow region*, the resulting field is obtained by erasing the first ρ_1 terms in the expansion of the incident wave.

$$E_\theta \approx \frac{E_0 e^{-i\omega t}}{\rho} \sum_{n=\rho_1}^{\infty} i^n \frac{2n+1}{n(n+1)} \left[\psi_n \frac{P_n^1}{\sin \theta} - i \psi_n' \frac{\partial P_n^1}{\partial \theta} \right] \cos \phi \quad (108)$$

$$E_\phi \approx -\frac{E_0 e^{-i\omega t}}{\rho} \sum_{n=\rho_1}^{\infty} i^n \frac{2n+1}{n(n+1)} \left[\psi_n \frac{\partial P_n^1}{\partial \theta} - i \psi_n' \frac{P_n^1}{\sin \theta} \right] \cos \phi,$$

where $\psi_n = \rho j_n$.

Here we may attempt to use again the Debye approximations (see Section 4.8), and state

$$n \ll \rho \quad \psi_n \approx \cos \phi_n = \cos \left[\rho - \frac{\pi}{2}(n+1) \right] \quad (109)$$

$$n \gg \rho \quad \psi_n \approx 0,$$

hence sums in (108) extend practically from

$$n = \rho_1 \text{ to } n = \rho. \quad (110)$$

Equations (108) through (110) represent an approximate solution for the field in the shadow region, as defined by (107). The P_n 's are oscillating functions, with an order of magnitude $\sqrt{n/\sin \theta}$, according to (108), whenever θ does not become too small. Hence for such moderately small angles the sums (108) should remain very small and yield a very low light intensity.

A different situation arises when θ becomes *extremely small*

$$\theta < \theta^F = \frac{2}{\rho} = \frac{\lambda}{\pi R}$$

$$\theta^F = \frac{a}{R} \theta_s \quad (111)$$

where R is the distance of observation and a the radius of the sphere. We may now use (103) again in sum (108) and obtain

$$E_\theta \approx \frac{E_0 e^{-i\omega t}}{\rho} \sum_{n=\rho_1}^{\infty} i^n (n + \frac{1}{2}) (\psi_n - i \psi_n'), \quad (112)$$

and a similar formula for E_ϕ . The upper limit in the sum is still of the order ρ , but because of the $(n + \frac{1}{2})$ factor, terms increase up to the limit, and it is impossible to use Debye's approximation, since the most important contribution to the sum is now given by terms $n \approx \rho$, for which no practical approximation was obtained (Section 4.8, Case II). Let us try a more accurate method, starting from the rigorous formula,²ⁿ

$$e^{i\rho} = \sum_{n=0}^{\infty} i^n (2n+1) j_n(\rho) \quad \gamma = 0. \quad (113)$$

Next we use the recurrence formula,^{2o}

$$j_n' = \frac{n}{2n+1} j_{n-1} - \frac{n+1}{2n+1} j_{n+1} \approx \frac{1}{2} (j_{n-1} - j_{n+1}) \quad n \gg 1. \quad (114)$$

Turning back to (112),

$$\frac{1}{\rho}(\psi_n - i\psi'_n) = j_n - \frac{i}{\rho}[\rho j_n]' \approx j_n - \frac{i}{2}(j_{n-1} - j_{n+1})$$

$$\rho \gg 1. \quad (115)$$

For large n and ρ values, the sum in (112) reduces to

$$\sum_{n=\rho_1}^{\infty} i^n n (\psi_n - i\psi'_n)$$

$$\approx \sum_{n=\rho_1}^{\infty} \left\{ i^n n j_n + \frac{1}{2} [i^{n-1}(n-1)j_{n-1} + i^{n+1}(n+1)j_{n+1}] \right\}$$

116

since

$$n + \frac{1}{2} \approx n \approx n - 1 \approx n + 1.$$

With the same approximation, (113) yields

$$\frac{1}{2}e^{i\rho} = \sum_0^{\infty} i^n n j_n. \quad (117)$$

In the three sums (116), small n values contribute very little. If and when we can add to the sums the small missing terms corresponding to $0 < n < \rho_1$, all three sums are identical with (117) and finally we obtain

$$\theta < \theta^F = \frac{\lambda}{\pi R}, \quad (118)$$

$$E_\theta \approx E_0 e^{-i\omega t + i\rho},$$

which yields a bright fringe all along the z axis.

Chapter 5

COILS YIELDING A SINGLE DIPOLE MOMENT

5.1 INTRODUCTION AND SUMMARY

IN A NUMBER of problems of electrotechnics, a system of coils is needed with a mutual inductance varying as the cosine of the angle between the axes of symmetry of the coils. Such problems are found in many instrumental devices such as ammeters, galvanometers, and the like. A similar problem arose in connection with the design of a direction finder and the present discussion was aimed at finding a solution of very high accuracy.

This report starts with a theoretical discussion of the multipole problem (Sections 5.2, 5.3, and 5.4), which was necessary, since no adequate discussion was found in most textbooks. All the applications were based on formula (6), a direct proof of which was needed. Section 5.4 discusses more specifically the structures of spherical shape and Section 5.5 deals with the problem of the magnetic field produced by a spherical coil.

In Section 5.6, the magnetic flux collected by a second coil is computed, and the law of variation of the flux with the angle χ between the axes of the coils is given in equation (44). A general formula for the mutual inductance of two spherical coils with axial symmetry is obtained in Section 5.7, equation (48), and compared with a similar formula computed by Schelkunoff.⁶ These formulas represent the basis for practical applications that can be divided in two groups, as shown in Section 5.8.

A. How to build a coil yielding a single dipole moment.

B. How to build a pair of coils with a sine law for their mutual induction.

Practical solutions of problem A are discussed in Sections 5.9 through 5.12 and the results summarized at the end of Section 5.13.

Solutions of problem B are given in Section 5.13 and found to yield the accuracy of 10^{-4} in the most favorable case.

5.2 GENERAL THEORY OF ELECTRIC MULTIPOLES

Let us investigate the electric properties of a "complex of charges," as Mason and Weaver¹ call it, namely a system of charges contained within a finite volume. Let e_i be one of the charges, at a distance l_i from the origin in a direction making an angle γ_i with the direction r . The potential is to be

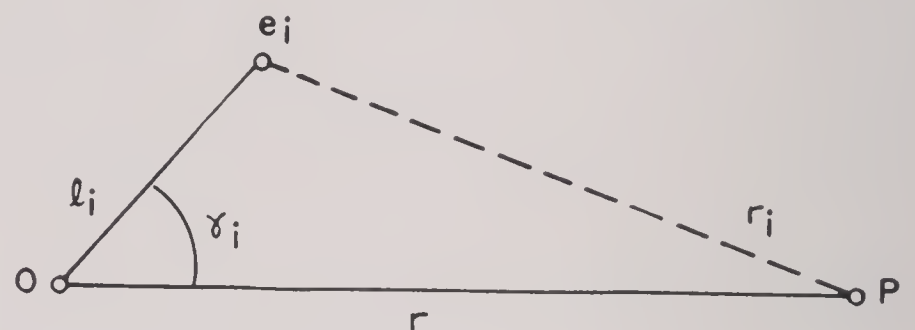


FIGURE 1. Notation for computation of potential along a line.

computed at point P outside the complex of charges (Figure 1), r being larger than all the l_i , and we may use the well-known expansion

$$\frac{1}{r_i} = \frac{1}{r} \sum_{n=0}^{\infty} \left(\frac{l_i}{r} \right)^n P_n(\cos \gamma_i), \quad P_n \text{ Legendre polynomial}, \quad (1)$$

hence the potential Φ at point P (mks units) is

$$4\pi\epsilon_0\Phi = \frac{1}{r} \sum_i e_i + \frac{1}{r^2} \sum_i e_i l_i \cos \gamma_i \cdots + \frac{p_n}{r^{n+1}} \cdots, \quad (2)$$

where we define the p_n component of the multipole n in the direction r by the formula

$$p_n = \sum_i e_i l_i^n P_n(\cos \gamma_i). \quad (3)$$

The preceding method gives the potential along the line OP on Figure 1. In order to find the potential in all directions, we must use another well-known transformation formula on Legendre polynomials^{3a}

$$\begin{aligned}
 P_n(\cos \gamma) &= P_n(\cos \alpha)P_n(\cos \theta) \\
 &+ \sum_{m=1}^n 2 \frac{(n-m)!}{(n+m)!} P_n^m(\cos \alpha)P_n^m(\cos \theta) \cos m(\phi - \beta) \\
 \cos m(\phi - \beta) &= \cos m\phi \cos m\beta + \sin m\phi \sin m\beta. \quad (4)
 \end{aligned}$$

γ is the angle between the directions (α, β) where the charge e is located and (θ, ϕ) which gives the observa-

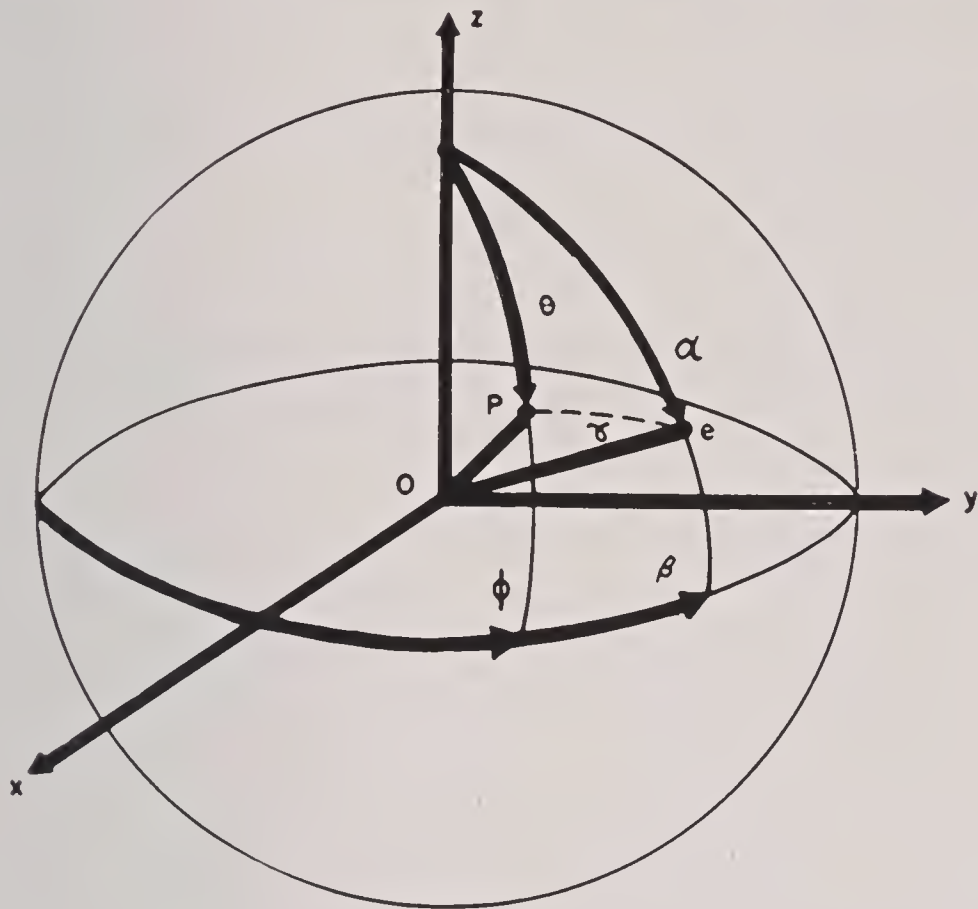


FIGURE 2. Notation for computation of potential in all directions.

tion point P (Figure 2). Using (4) in equations (2) and (3), we obtain

$$\begin{aligned}
 4\pi\epsilon_0\Phi(r, \theta, \phi) &= \sum_{n=0}^{\infty} \frac{1}{r^{n+1}} \sum_i e_i l_i^n \left[P_n(\cos \alpha)P_n(\cos \theta) \right. \\
 &+ \left. \sum_{m=1}^n 2 \frac{(n-m)!}{(n+m)!} P_n^m(\cos \alpha)P_n^m(\cos \theta) \cos m(\phi - \beta) \right]. \quad (5)
 \end{aligned}$$

Let us now define the $2n + 1$ components of the multipole number n in the form

$$p_n = p_{n0c} = \sum_i e_i l_i^n P_n(\cos \alpha_i), \quad p_{n0s} = 0 \quad (6a)$$

$$\begin{aligned}
 p_{nmc} &= \sum_i 2 \frac{(n-m)!}{(n+m)!} e_i l_i^n P_n^m(\cos \alpha_i) \frac{\cos m\beta_i}{\sin m\beta_i}; \\
 m &= 1, 2, \dots, n. \quad (6b)
 \end{aligned}$$

This enables us to write our potential as

$$\begin{aligned}
 4\pi\epsilon_0\Phi(r, \theta, \phi) &= \sum_{n=0}^{\infty} \frac{1}{r^{n+1}} \sum_{m=0}^n P_n^m(\cos \theta) \cdot \\
 &[p_{nmc} \cos m\phi + p_{nms} \sin m\phi]. \quad (7)
 \end{aligned}$$

This checks with Stratton's expansion^{3c} if one states

$$\begin{aligned}
 \text{(Stratton)} \quad p^n a_{nm} &= p_{nmc} \\
 p^n b_{nm} &= p_{nms}, \quad (8)
 \end{aligned}$$

but our discussion yields directly the important formulas (6), which define the multipole components in terms of the distribution of charges in the complex.

5.3 PROBLEMS WITH CYLINDRICAL SYMMETRY

We shall be interested in a structure exhibiting *cylindrical symmetry* about the z axis, which means that the distribution of the e_i charges does not depend upon the angle β_i . This results in

$$p_{nmc} = 0, \quad p_{nms} = 0, \quad m = 1, 2, \dots, n, \quad (9)$$

and the potential function no longer depends on ϕ . The only term left is

$$p_n = p_{n0c} = \sum_i e_i l_i^n P_n(\cos \alpha_i). \quad (10)$$

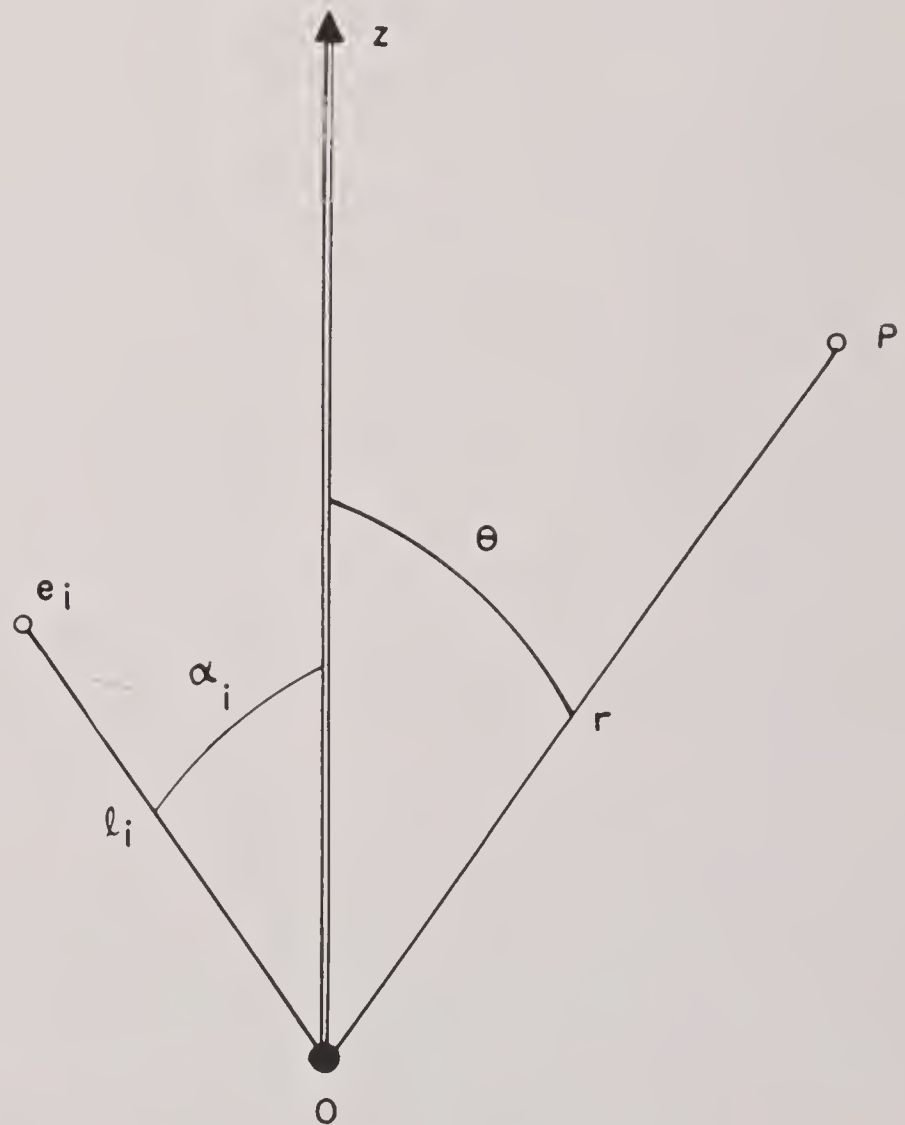


FIGURE 3. The case of cylindrical symmetry.

The n th multipole has just one axial component (Figure 3) and the potential is

$$4\epsilon_0\Phi(r, \theta) = \sum_{n=0}^{\infty} \frac{p_n}{r^{n+1}} P_n(\cos \theta). \quad (11)$$

Taking $\theta = 0$, we obtain the potential along the z axis. Since $P_n(1) = 1$, our formula (11) reduces to (2). Furthermore, if the charges are distributed exclusively along the z axis (axial problem), equation (6a) yields

$$p_n = \sum_i e_i l_i^n = \sum_i e_i \zeta_i^n, \quad \alpha_i = 0, \quad P_n(\cos \alpha_i) = 1, \quad (12)$$

which is Stratton's definition of an axial multipole of n th order.^{3b} Here electronic moments and multipole components are similar.

The following formulas are important:

$$P_n = \frac{1, 3, 5, \dots, (2n-1)}{n!} \left[\zeta^n - \frac{n(n-1)}{2(2n-1)} \zeta^{n-2} + \frac{n(n-1)(n-2)(n-3)}{2 \cdot 4(2n-1)(2n-3)} \zeta^{n-4} \dots \right] \quad n = 0, 1, 2, \dots, \quad (13)$$

$$P_{-n} = P_{n-1}, \quad (14)$$

hence $P_{-1} = P_0$

$$(2n+1)P_n = P'_{n+1} - P'_{n-1}, \quad (15)$$

where

$$P'_n(\zeta) = \frac{dP_n}{d\zeta}.$$

Asymptotic expressions:

$$n \gg 1, \quad \epsilon < \theta < -\epsilon, \quad 0 < \epsilon \ll \pi/6,$$

$$P_n(\cos \theta) = \sqrt{\frac{2}{\pi n \sin \theta}} \left[\left(1 - \frac{1}{4n}\right) \sin \psi - \frac{1}{8n} \cot g \theta \cos \psi \right] \approx \sqrt{\frac{2}{\pi n \sin \theta}} \sin \psi \quad (16)$$

$$\psi = \left(n + \frac{1}{2}\right)\theta + \frac{\pi}{4}.$$

Other useful relations may be found in the Jahnke and Emde "Tables of Functions."⁵

5.4 SPHERICAL SHAPES

To take another specific example, let us assume a distribution of electric charges on a sphere of radius R with symmetry about the z axis:

$$l_i = R, \quad e_i \text{ function of } \alpha_i \text{ only.} \quad (17)$$

The multipole components p_n , equation (10), are now given by

$$p_n = R^n \sum_i e_i P_n(\cos \alpha_i). \quad (18)$$

If the sphere is covered with a uniform layer ρ we shall take

$$e_i = 2\pi\rho R^2 \sin \alpha_i d\alpha_i \quad (19)$$

$$p_n = \rho R^{n+2} 2\pi \int_0^\pi P_n(\cos \alpha) \sin \alpha d\alpha \\ = 2\pi\rho R^{n+2} \int_{-1}^1 P_n(\zeta) d\zeta, \quad \zeta = \cos \alpha \quad (20)$$

$$p_n = \frac{2\pi\rho}{2n+1} R^{n+2} \left[P_{n+1} - P_{n-1} \right]_{-1}^1 = 0 \\ n = 1, 2, \dots, \quad (21)$$

since the P 's are all equal to 1 for $x = 1$ and to ± 1 according to their parity, for $x = -1$. The only nonzero term is

$$p_0 = \text{total charge} = 4\pi\rho R^2, \quad (22)$$

a result which can be obtained from the general formulas (21). Let us now consider a piece of a

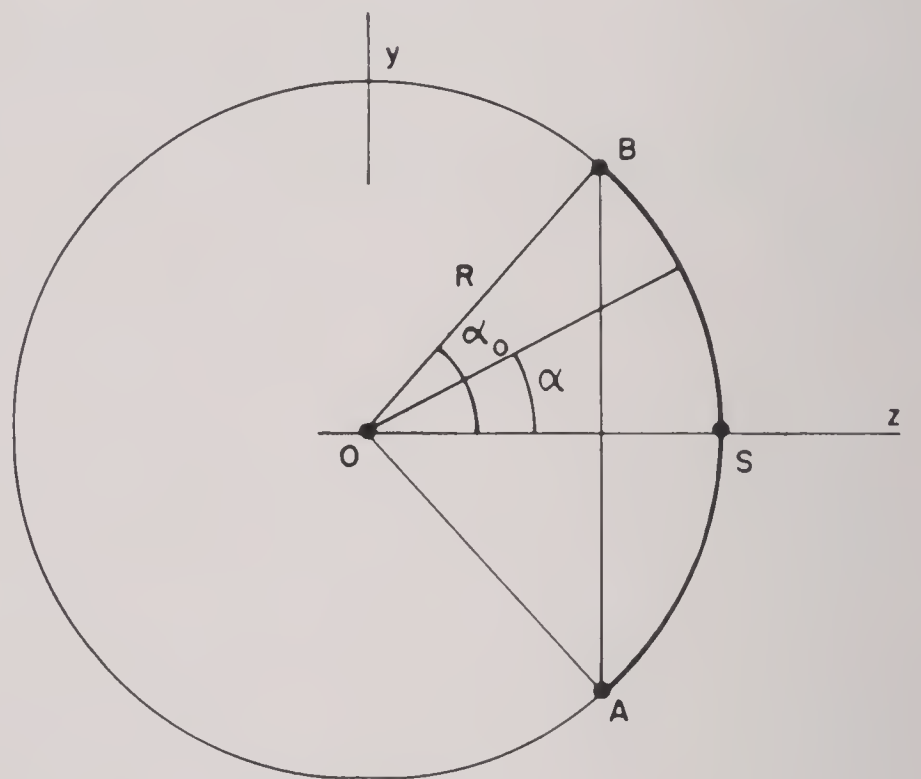


FIGURE 4. Spherical shell.

spherical shell (Figure 4) extending from $\alpha = 0$ to $\alpha = \alpha_0$ on a sphere of radius R , with uniform density. The multipole p_n is given by the same formula (21) as before, but with different limits:

$$p_n = \frac{2\pi\rho}{2n+1} R^{n+2} \left[P_{n+1} - P_{n-1} \right]_{\cos \alpha_0}^1 \\ = \frac{2\pi\rho}{2n+1} R^{n+2} [P_{n-1}(\zeta_0) - P_{n+1}(\zeta_0)] \quad (23)$$

calling $\zeta_0 = \cos \alpha_0$.

The total charge of this shell is

$$Q = 2\pi\rho R^2(1 - \zeta_0). \quad (24)$$

If the spherical shell is covered with dipoles, we may compute the corresponding multipole components. Let us, for instance, assume two concentric

spherical shells bearing the same charge $\pm Q$, and having different radii

$$R_1(\text{for } +Q), \quad R_2(\text{for } -Q), \quad (25)$$

$$R_1 - R_2 = \Delta R, \quad \text{same angle } \alpha_0. \quad (26)$$

We first rewrite (23)

$$p_n = \frac{Q}{2n+1} R^n \frac{P_{n-1}(\zeta_0) - P_{n+1}(\zeta_0)}{1 - \zeta_0}. \quad (27)$$

Hence for our spherical *double layer*, we obtain, in case of a small but finite thickness ΔR ,

$$p_n = \frac{Q}{2n+1} \frac{P_{n-1}(\zeta_0) - P_{n+1}(\zeta_0)}{1 - \zeta_0} \left[nR^{n-1}\Delta R + \frac{n(n-1)}{2}(\Delta R)^2, \dots \right], \quad (28)$$

where we may substitute the dipole surface density and make ΔR tend to zero

$$\bar{\omega} = \rho \Delta R \quad \Delta R \rightarrow 0 \quad (29)$$

$$p_n = \frac{2n\pi\bar{\omega}}{2n+1} R^{n+1} [P_{n-1}(\zeta_0) - P_{n+1}(\zeta_0)]. \quad (30)$$

This case is schematically represented in Figure 5. It corresponds to a spherical shell with uniform

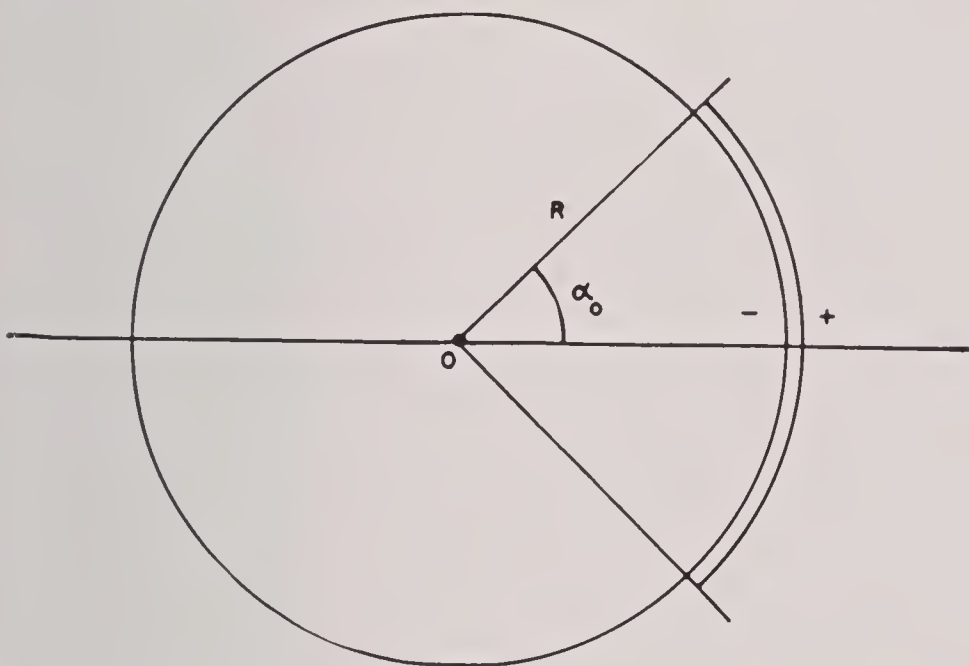


FIGURE 5. Spherical shell with dipoles pointing along radii.

dipole density, when the *dipoles always point along the radii*, and the double layer extends from $\alpha = 0$ to α_0 ($\zeta_0 = \cos \alpha_0 \leq \zeta \leq 1$).

5.5 MAGNETIC PROBLEM — GENERAL DISCUSSION

If instead of an electrical double layer we consider a similar *magnetic double layer*, also with uniform dipole surface density, we know that it is equivalent to a current on the circular loop at α_0 . In such a magnetic problem, ϵ_0 should be replaced by μ_0 in equation (7).

If we assume a current distribution on the sphere, with a current density $I_1 F_1(\zeta)$ (per unit of length z), we have ^{4a}

$$d\bar{\omega} = \mu_0 I_1 F_1(\zeta) R d\zeta \quad (31)$$

and the total multipole is

$$p_{1n} = \int_{\zeta=-1}^{\zeta=1} dp_n = \mu_0 I_1 \frac{2n\pi}{2n+1} R^{n+2} \int_{-1}^1 (P_{n-1} - P_{n+1}) F_1(\zeta) d\zeta. \quad (32)$$

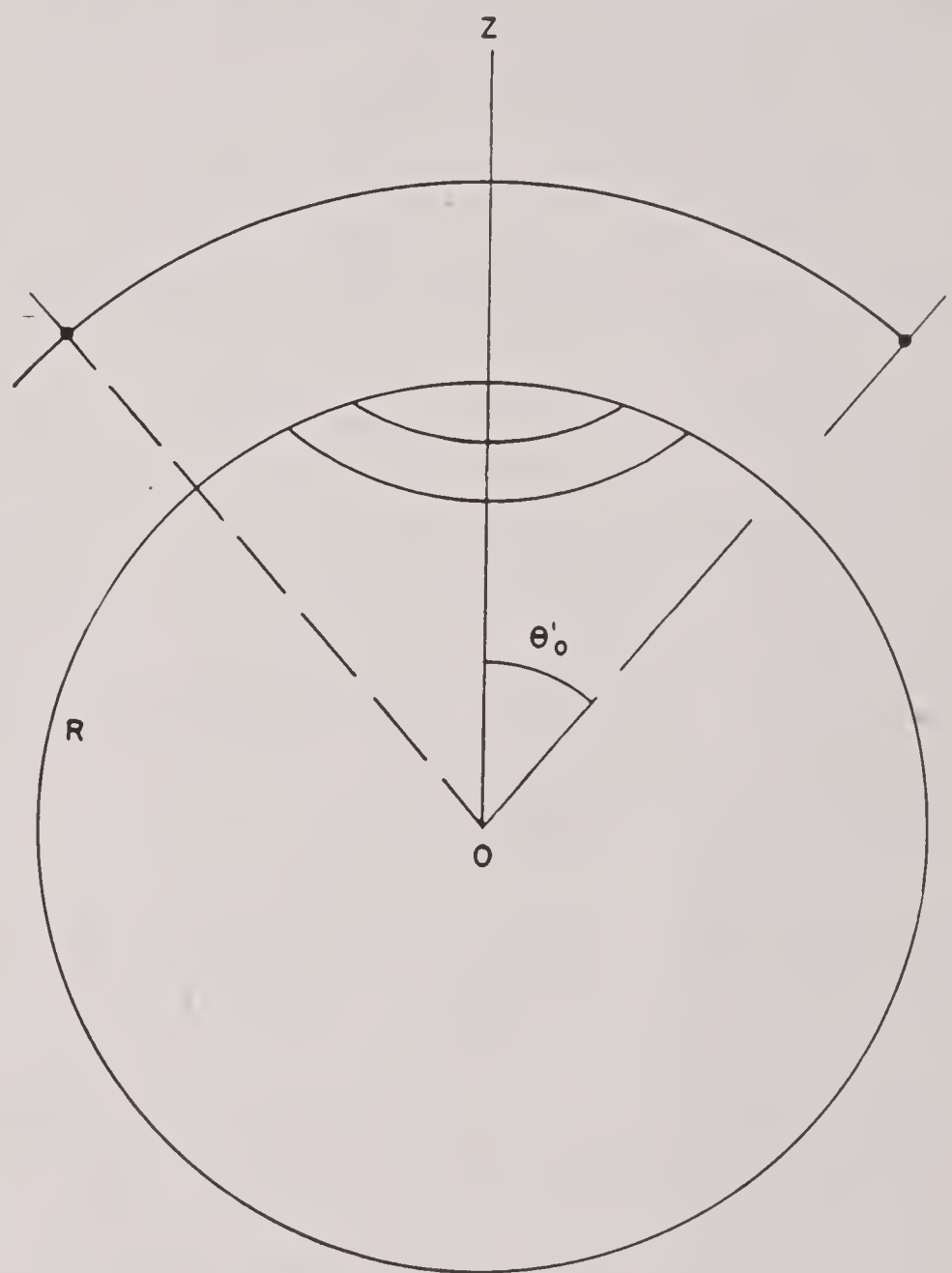


FIGURE 6. Spherical coil and collecting loop with center on z axis.

As an example, let us consider a uniform winding, with $F_1(\zeta) = 1$. Equation (15) is used for computing the integral:

$$p_{1n} = \mu_0 \frac{2n\pi}{2n+1} I_1 R^{n+2} \left[\frac{P_n - P_{n-2}}{2n-1} - \frac{P_{n+2} - P_n}{2n+3} \right]_{\zeta=-1}^{\zeta=1}. \quad (33)$$

Remembering the relation (14) and the fact that P 's of the same parity have all the same value $+1$ at $\zeta = 1$ and ± 1 at $\zeta = -1$, one easily finds:

$$p_{10} = 0 \text{ total charge zero (since } 2n\pi = 0 \text{ when } n = 0) \quad (34)$$

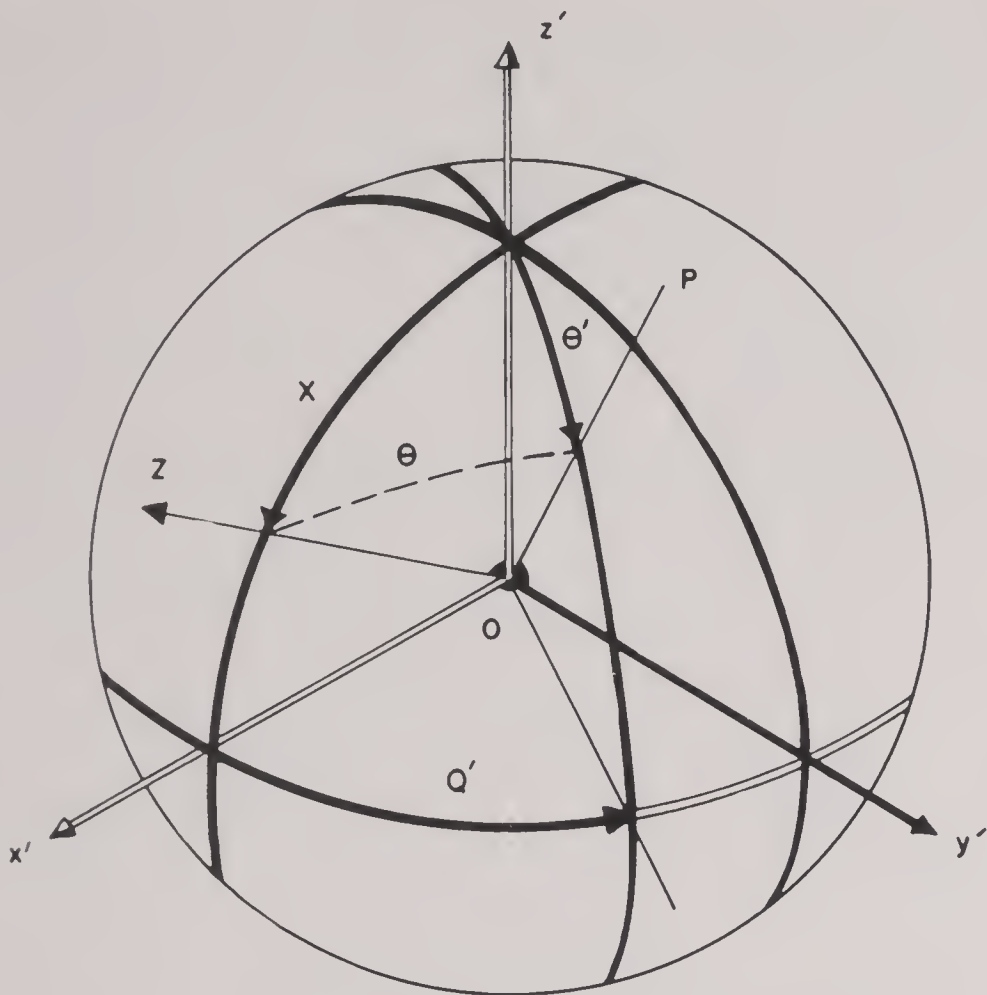


FIGURE 7. Notation when axis of coil is at an angle with the z axis.

$$p_{11} = \mu_0 \frac{4}{3} \pi R^3 I_1 \quad p_2 = p_3 = \dots = 0. \quad (35)$$

Such uniform winding yields only a dipole component, but it is not very practical, and we shall discuss later some other structures.

5.6 THE INDUCTION FLUX THROUGH A COLLECTING COIL

The magnetic potential of the field created by a first coil results from equations (7) and (11) for a first coil exhibiting cylindrical symmetry,

$$\Phi = \sum_n \Phi_n, \quad \Phi_n = \frac{1}{4\pi\mu_0} \frac{p_n}{r^{n+1}} P_n(\cos \theta), \quad (36)$$

where Φ_n is the potential due to the n th multipole of the first coil [equation (32)]. The magnetic induction field, in the direction r , is given by μ_0 times the magnetic field:

$$B_r = -\mu_0 \frac{\partial \Phi}{\partial r} = \sum_n B_{rn}, \quad (37)$$

$$B_{rn} = -\mu_0 \frac{\partial \Phi_n}{\partial r} = \frac{1}{4\pi} \frac{n+1}{r^{n+2}} p_n P_n(\cos \theta); \quad (38)$$

it obtains its maximum value on the z axis when $\cos \theta = 1$ and $P_n = 1$. The field is observed by the amount of flux flowing through a collecting coil. Let us first assume the coil to be a single loop, with its center on the z axis, and collect the field, at a dis-

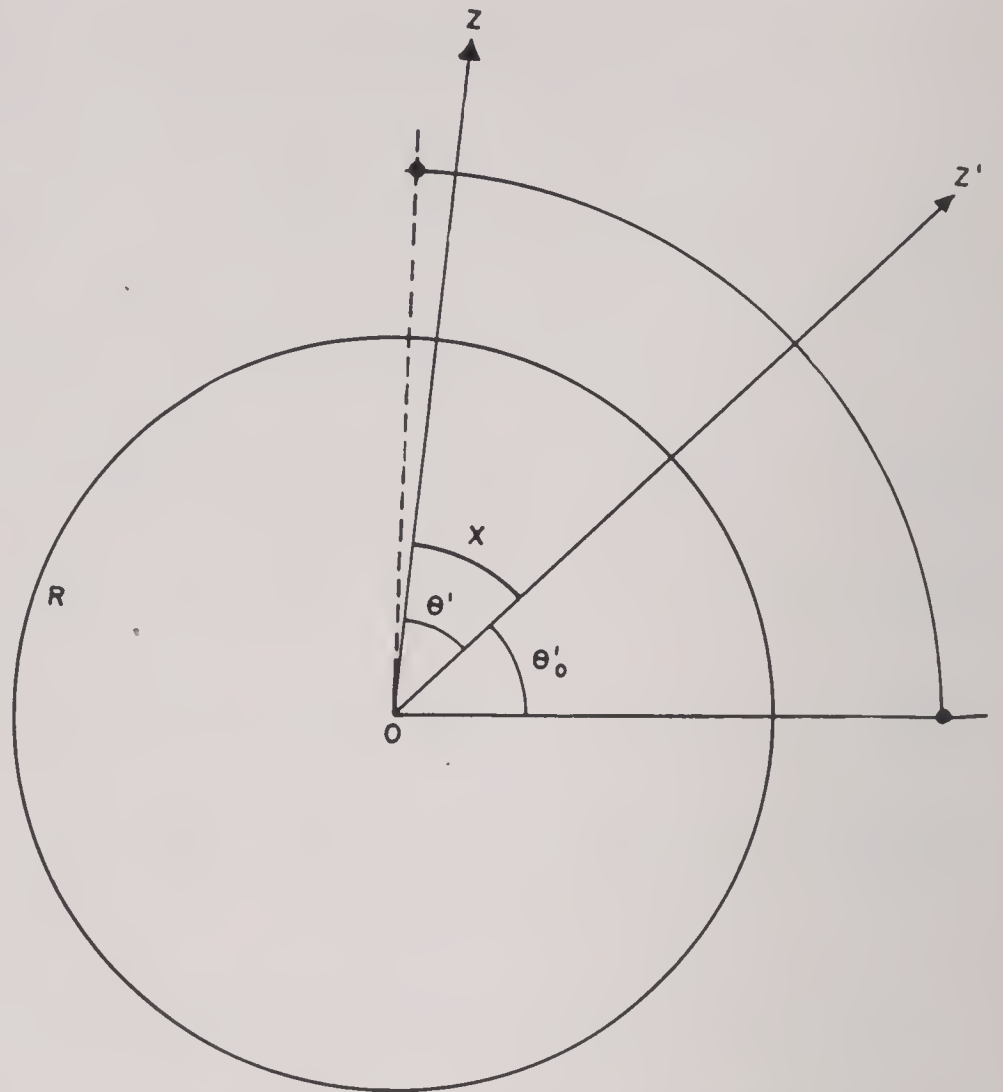


FIGURE 8. Spherical coil and collecting loop with different axes of symmetry.

tance r , for angles $0 < \theta' \leq \theta_0$. For the n th multipole, the flux ψ_n amounts to

$$\psi_n = \int_0^{\theta_0} B_{rn} 2\pi r^2 \sin \theta' d\theta' = \frac{n+1}{2r^n} p_{1n} \int_{\zeta_0}^1 P_n(\zeta') d\zeta', \quad (39)$$

$$\zeta'_0 = \cos \theta_0.$$

Here we make use of (15) and integrate

$$\begin{aligned} \psi_n &= \frac{n+1}{2n+1} \frac{p_{1n}}{2r^n} \left[P_{n+1} - P_{n-1} \right]_{\zeta_0}^1 \\ &= \frac{n+1}{2n+1} \frac{p_{1n}}{2r^n} [P_{n-1}(\zeta_0) - P_{n+1}(\zeta_0)]. \end{aligned} \quad (40)$$

The total induction flux through coil 2, due to coil 1, is

$$\psi = \sum_n \psi_n, \quad (41)$$

where the p_n 's are the multipoles of the first coil, as given by equation (33). This solves the problem for a second coil on the z axis. Next we must discuss the flux through a coil whose axis Oz' makes an angle χ with the z axis (Figures 7 and 8). Calling θ' , ϕ' the spherical coordinates with respect to x' , y' , z' , we obtain a formula similar to (4),

$$\begin{aligned} P_n(\cos \theta) &= P_n(\cos \theta') P_n(\cos \chi) \\ &+ \sum_{m=1}^n 2 \frac{(n-m)!}{(n+m)!} P_n^m(\cos \theta') P_n^m(\cos \chi) \cos m\phi'. \end{aligned} \quad (42)$$

This formula, together with (38), gives the radial induction field B_r as a function of the new angles θ' , ϕ' .

The collecting coil is again supposed to be a single loop collecting the field through an area

$$\begin{aligned} 0 < \phi' < 2\pi \\ 0 < \theta' < \theta_0. \end{aligned} \quad (43)$$

In the ϕ' integration, all terms in $\cos m\phi'$ cancel out, and the only contribution is given by the first term of (42). Hence the flux $\psi_n(\chi)$ for the coil whose axis makes an angle χ with the z axis is simply given by

$$\psi_n(\chi) = \psi_n(0)P_n(\cos \chi), \quad (44)$$

where $\psi_n(0)$ is the flux computed in (39). Since $P_n(\cos \chi)$ is always smaller than 1 in absolute value, this proves that the flux of the n th multipole through the collecting coil is maximum for the coil centered on the z axis ($\chi = 0$, $P_n = 1$).

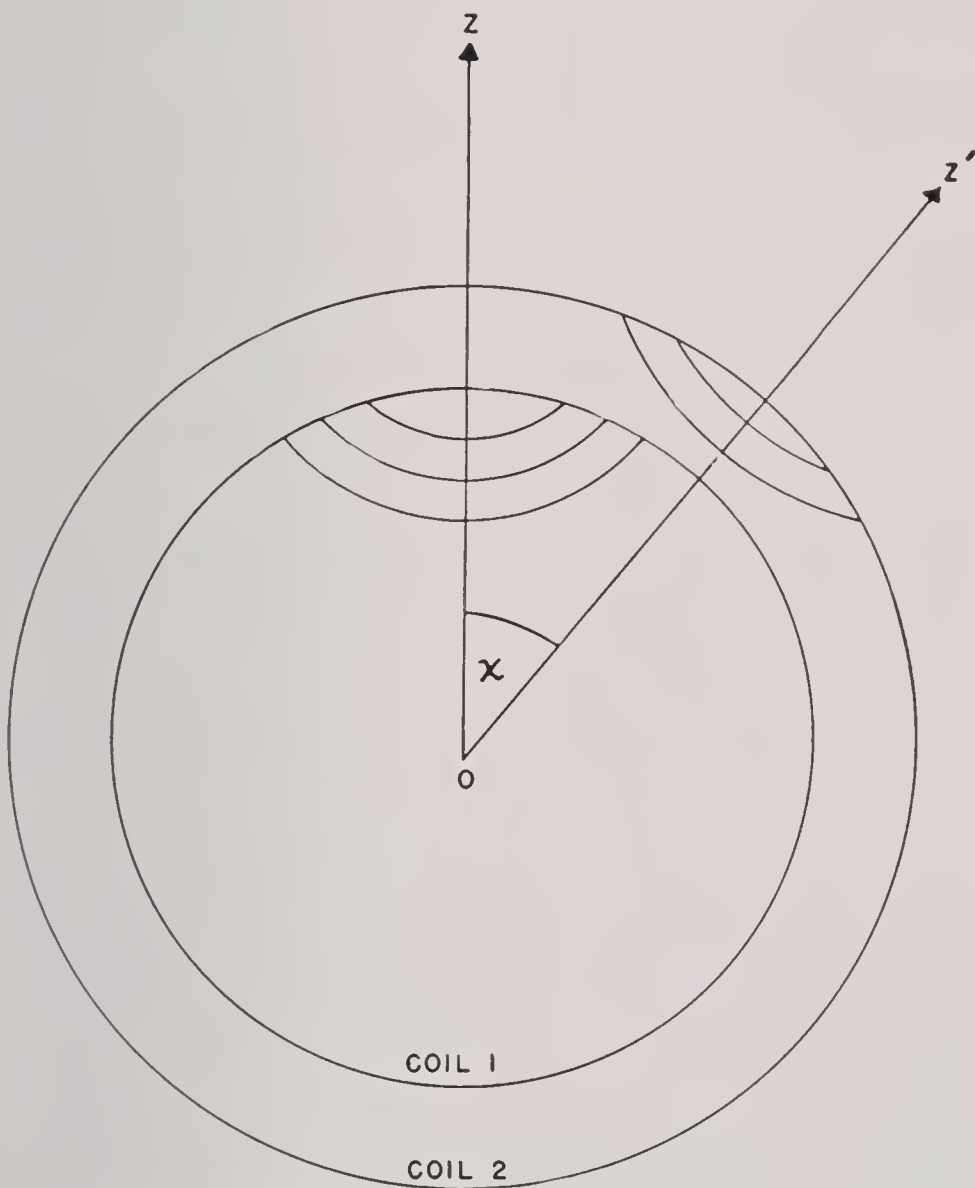


FIGURE 9. The case where the second coil consists of several loops.

5.7 MUTUAL INDUCTANCE OF TWO AXIALLY SYMMETRIC SPHERICAL COILS

Instead of a single loop, we can assume the second coil to consist of a number of loops on a sphere of radius r (Figure 9), with a distribution function

$F_2(\zeta')$ playing a similar role to the $F_1(\zeta)$ function of the first coil in equation (31). The magnetic induction flux ψ_n due to the n th multipole of the first coil takes the new value

$$\psi_n = \frac{n+1}{2n+1} \frac{p_{1n}}{2r^n} P_n(\cos \chi) \int [P_{n-1}(\zeta') - P_{n+1}(\zeta')] F_2(\zeta') r d\zeta' \quad (45)$$

obtained by integrating equation (40) over all the loops of the second coil. In this formula we recognize an expression similar to that of the n th multipole p_{2n} of the second coil, according to equation (32):

$$p_{2n} = \mu_0 \frac{2n\pi}{2n+1} r^{n+2} I_2 \int_{-1}^1 (P_{n-1} - P_{n+1}) F_2(\zeta') d\zeta', \quad (46)$$

where I_2 is the current in the second coil. Hence finally

$$\psi = \sum_n \psi_n, \quad (47)$$

$$\psi_n = \frac{n+1}{\mu_0 4n\pi} \frac{I_1}{r^{2n+1}} \frac{p_{1n}}{I_1} \frac{p_{2n}}{I_2} P_n(\cos \chi).$$

This yields for the mutual inductance of two axially symmetric spherical coils

$$L_{12} = \frac{\psi}{I_1} = \sum_n \frac{n+1}{\mu_0 4n\pi} \left(\frac{R}{r}\right)^n R \left(\frac{p_{1n}}{R^{n+1}I_1}\right) \left(\frac{p_{2n}}{r^{n+1}I_2}\right) P_n(\cos \chi), \quad (48)$$

where R is the radius of the small sphere (coil 1) and r is the radius of the large sphere (coil 2).

$$\frac{p_{1n}}{R^{n+1}I_1} = \mu_0 \frac{2n\pi}{2n+1} R \int (P_{n-1} - P_{n+1}) F_1 d\zeta, \quad \zeta = \cos \theta. \quad (49)$$

Instead of the distribution functions $F_1 F_2$, one may use density functions $f_1 f_2$, giving the number of loops per angle as θ ,

$$\begin{aligned} R F_1 d\zeta &= -f_1 d\theta \\ r F_2 d\zeta' &= -f_2 d\theta'. \end{aligned} \quad (50)$$

The following transformation formula can also be proved

$$P_{n-1} - P_{n+1} = \frac{2n+1}{n(n+1)} P_n^1 \sin \theta. \quad (51)$$

Let us now call

$$u_{1n} = \int_0^\pi f_1(\theta) P_n^1 \sin \theta d\theta. \quad (52)$$

We obtain the relation

$$\frac{p_{1n}}{R^{n+1}I_1} = \mu_0 \frac{2\pi}{n+1} u_{1n} \quad (53)$$

and a similar one for the second coil. Hence

$$L_{12} = \pi\mu_0 R \sum_n \left(\frac{R}{r}\right)^4 P_n(\cos \chi) \frac{u_{1n}u_{2n}}{n(n+1)}, \quad (54)$$

which is a formula obtained by Schelkunoff.

5.8 PRACTICAL PROBLEMS INVOLVED

There are many electrotechnical problems where the preceding theory is used as a basis for discussion of practical applications.

A. Given a *magnetic field* distribution with *cylindrical symmetry*, the problem is to build a coil such that the *flux collected* by this coil varies as $\cos \chi$, χ being the angle between the axis of symmetry of the field and the axis of the coil, as in Figure 9.

Assuming, for instance, the magnetic field to be created by another coil 2, coil 1 should be built in such a way as to keep only the term $P_1(\cos \chi)$, which is equal to $\cos \chi$, and to cancel all other P_n 's in expansions (48) or (54). This means that the exact solution of the problem is

$$p_{11} \neq 0 \quad p_{1n} = 0 \quad n \neq 1. \quad (55)$$

The coil must give just one single dipole and no other multipoles. This can be obtained with a uniform winding on a spherical coil [equation (35)], but this solution is not practical, and structures made out of individual coils are preferred, each of them being lodged in a separate groove. The larger the number of multipoles made to zero, the better the approximation. A practical solution may yield

$$\begin{aligned} p_{11} \neq 0, \quad p_{12} = p_{13} \cdots = p_{1N} = 0 \\ p_{1,N+1} \neq 0, \quad p_{1,N+2} \neq 0 \cdots \end{aligned} \quad (56)$$

B. Assuming a system of two coils, both of which can be built at will, we may want to obtain a *sine law in the mutual inductance* L_{12} of equations (48) or (54). This means again keeping only the term in $P_1(\cos \chi)$ in the formulas. If the first coil is built according to conditions (56), we may now increase the accuracy by using a second coil for which $p_{2,N+1}$ would be made zero, thus killing one more perturbation term in the expansion.

5.9 A SPHERICAL COIL SYSTEM YIELDING A SINGLE DIPOLE

Let us discuss a structure comprising h coils, all of the same thickness b , distributed on one hemisphere $0 < \zeta < 1$, with symmetrical coils on the

other hemisphere $-1 < \zeta < 0$. This symmetry automatically cancels out all even numbered multipoles. As represented in Figure 10, we call $\zeta_1, \zeta_2, \dots, \zeta_n$

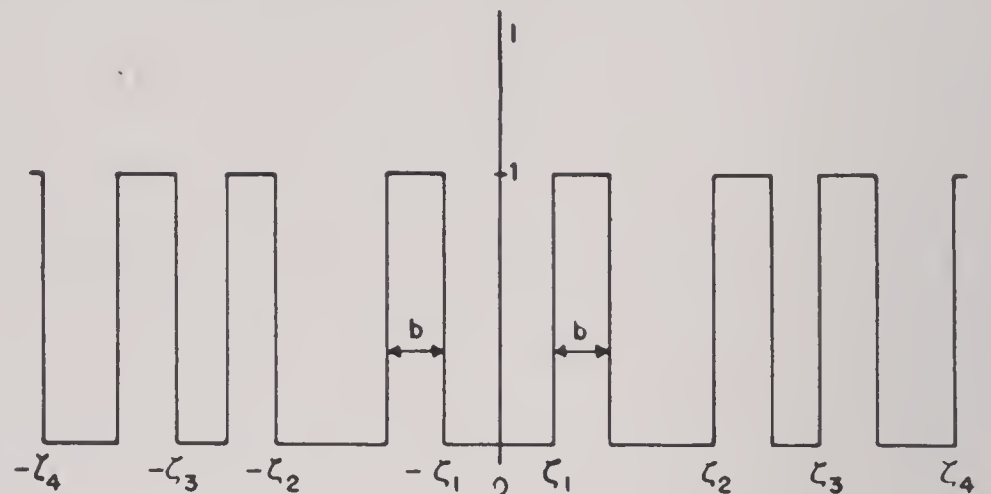


FIGURE 10. Portions of first windings of coils.

the positions of the first winding of the coils. This means that equation (32) becomes

$$\begin{aligned} p_{1n} &= \mu_0 \frac{4n\pi}{2n+1} R^{n+2} I_1 \int_0^1 F_1(\zeta) (P_{n-1} - P_{n+1}) d\zeta, \\ F_1(\zeta) &= \begin{cases} 1 & \zeta_k \leq \zeta \leq \zeta_k + b \text{ on a coil,} \\ 0 & \zeta_k + b < \zeta < \zeta_{k+1} \text{ between coils,} \end{cases} \end{aligned} \quad (57)$$

where $n = 2g + 1$, $g = 0, 1, 2, \dots$, odd multipoles. The integration is carried out as in (20) or (33) and yields

$$p_{1n} = \mu_0 \frac{4n\pi}{2n+1} R^{n+2} I_1 (G_{n-1} - G_{n+1}) \quad (58a)$$

with

$$\begin{aligned} G_m &= \int_0^1 F_1(\zeta) P_m d\zeta \\ &= \frac{1}{2m+1} \sum_{k=1}^{k=h} \left[P_{m+1}(\zeta_k + b) - P_{m+1}(\zeta_k) \right. \\ &\quad \left. - P_{m-1}(\zeta_k + b) + P_{m-1}(\zeta_k) \right], \end{aligned} \quad (58b)$$

$m = 0, 2, \dots, 2g, \dots$

As previously said, all even p_n 's are zero by symmetry and we are left with the odd n values only, which mean even m 's. For $n = 1$ ($g = 0$), we obtain the dipole moment

$$p_{11} = \mu_0 \frac{4\pi}{3} R^3 I_1 (G_0 - G_2), \quad (59)$$

where equation (58) can still be used for G_0 provided one replaces P_{-1} by P_0 , which gives a nonzero result, as in (35). Higher multipoles can be made zero, according to formula (58), if we state

$$G_{2g} = G_{2g+2} \cdots = C, \quad m = 2g, 2g+2, \dots, \quad (60)$$

all integrals (58) being equal to a constant C .

For very *narrow coils* and *small g values*, we may use a power series expansion to compute integral (58),

$$G_{2g} = \sum_k \int_{\zeta_k}^{\zeta_k+b} P_{2g} d\zeta = \sum_k \int_{-b/2}^{b/2} \left[P_{2g} \left(\zeta_k + \frac{b}{2} \right) + \xi P'_{2g} + \frac{\xi^2}{2} P''_{2g} \cdots \right] d\xi, \quad (61)$$

where the bracket is an expansion of

$$P_{2g} \left(\zeta_k + \frac{b}{2} + \xi \right).$$

When higher terms in ξ can be neglected, this yields

$$G_{2g} \approx \sum_k \left[b P_{2g} \left(\zeta_k + \frac{b}{2} \right) + \frac{1}{3} \left(\frac{b}{2} \right)^3 P''_{2g} \left(\zeta_k + \frac{b}{2} \right), \cdots \right] = C. \quad (62)$$

This is, according to (60), the expression that must equal a constant C . Since P''_{2g} is roughly of the order of $rg^2 P_{2g}$, this expansion can be used only when gb is a very small quantity, which means narrow coils and lower multipoles. For higher multipoles, it is impossible to ignore the thickness of the coils.

Using *one very thin coil*, we can make the third pole zero by taking

$$\begin{aligned} p_3 &= 0, \quad P_4(\zeta) = P_2(\zeta) = C \\ P_4 - P_2 &= \frac{1}{8}(35\zeta^4 - 30\zeta^2 + 3) - \frac{1}{2}(3\zeta^2 - 1) \\ &= \frac{7}{8}(5\zeta^4 - 6\zeta^2 + 1) = 0, \end{aligned} \quad (63)$$

the roots of which are

$$\zeta^2 = \frac{1}{5}, \quad \zeta^2 = 1.$$

The last one cannot be used, since it yields a coil of radius zero, hence we must take

$$\zeta = \frac{1}{\sqrt{5}} = \cos \alpha \quad \alpha = 63^\circ 27'. \quad (64)$$

5.10 A SMALL NUMBER OF VERY THIN COILS ON THE SPHERE

In case of a small number N_c of very thin coils, we assume b to be negligible; in practical cases, our ζ would determine the average position of the coil, which was called $\zeta + b/2$ in (62). Next we rewrite our equations (62), neglecting the b^3 terms, and replacing C by $\sum_k P_2$;

$$\sum_{k=1}^{N_c} (P_{2g}(\zeta_k) - P_2(\zeta_k)) = 0, \quad g = 2, 3, \cdots, N+1. \quad (65)$$

These conditions insure the zero value of the multipoles number 3, 5, \cdots , $2N+1$. Let us write the first few polynomials, which we call

$$R_g(\xi) = P_{2g}(\zeta) - P_2(\zeta) \quad \xi = \zeta^2. \quad (66)$$

This R_g is a polynomial of degree g in ξ , with one of its roots equal to 1. For instance,

$$\begin{aligned} R_2 &= \frac{7}{8}(5\xi^2 - 6\xi + 1), \\ R_3 &= \frac{1}{16}(231\xi^3 - 315\xi^2 + 81\xi + 3). \end{aligned} \quad (67)$$

These polynomials being known, equations (65) now read

$$\sum_{k=1}^{N_c} R_g(\xi_k) = 0, \quad g = 2, 3, \cdots, N+1. \quad (68)$$

Let us introduce the averages of the successive powers of the ξ_k 's:

$$N_c a_m = \sum_{k=1}^{N_c} \xi_k^m \cdots \quad (69)$$

What we obtain from conditions (68) is the value of all these averages. The conditions (68) yield

$$\sum_k R_2 = 0, \quad 5a_2 - 6a_1 + 1 = 0, \quad (70)$$

$$\sum_k R_3 = 0, \quad \text{or } 231a_3 - 315a_2 + 81a_1 + 3 = 0. \quad (71)$$

As an example, let us discuss the case $N = 2$, where we must satisfy both equations (70). We may attempt to use *two equal coils* located at

$$\xi_1 = a_1 + b, \quad \xi_2 = a_1 - b, \quad \text{and their symmetricals.} \quad (72)$$

This yields

$$a_2 = \frac{1}{2}(\xi_1^2 + \xi_2^2) = a_1^2 + b^2, \quad (73)$$

$$a_3 = \frac{1}{2}(\xi_1^3 + \xi_2^3) = a_1^3 + 3a_1 b^2. \quad (74)$$

Our equations (70) and (71) now give,

$$\begin{aligned} 5(a_1^2 + b^2) - 6a_1 + 1 &= 0, \quad a_1^2 + b^2 = \frac{6}{5}a_1 - \frac{1}{5}, \\ 231a_1(a_1^2 + 3b^2) - 315(a_1^2 + b^2) + 81a_1 + 3 &= 0, \\ \text{or} \end{aligned} \quad (75)$$

$$-462a_1^3 + \frac{4158}{5}a_1^2 - \frac{2178}{5}a_1 + 66 = 0.$$

This equation in a_1 can be freed of its trivial solution $a_1 = 1$ and reduced to the second degree

$$(a_1 - 1)(-462a_1^2 + 369.6a_1 - 66) = 0, \quad (76)$$

which yields two possible a_1 solutions, hence two different groups of two coils which have no multipole moments p_3 or P_5 .

A *first solution* is

$$\begin{aligned} a_1 &= 0.53093, \quad b = 0.39399, \\ \xi_1^2 &= \xi_1 = a_1 + b = 0.92492, \\ \xi_2^2 &= \xi_2 = a_1 - b = 0.13694, \end{aligned} \quad (77)$$

hence the positions of the coils

$$\zeta_1 = 0.962, \quad \zeta_2 = 0.370. \quad (78)$$

The *second solution* reads

$$\begin{aligned} a_1 &= 0.26907, \quad b = 0.22468, \\ \zeta_1^2 &= \xi_1 = a_1 + b = 0.49375, \\ \zeta_2^2 &= \xi_2 = a_1 - b = 0.04439, \end{aligned} \quad (79)$$

hence the coils at

$$\zeta_1 = 0.703, \quad \zeta_2 = 0.211. \quad (80)$$

5.11 A LARGE NUMBER OF THIN COILS ON THE SPHERE. METHODS FOR SYSTEMATIC CORRECTION

If we decide to use a rather large number of coils on a sphere, we may start from a distribution approximating the uniform winding of equations (33) and (35), compute the error due to the use of discrete coils, and attempt to correct this error by small displacements in the positions of the coils. Let us take a practical example, using 10 coils, with the values $\zeta_1, \zeta_2, \dots, \zeta_{10}$. These ζ 's are the values of $\cos \theta$ for the middle of the coil, as noticed in equation (65). Each coil is furthermore given a thickness $b = 1/20$. First of all, we compute the successive even powers of the ζ_k 's and their averages (69),

$$\xi_k = \zeta_k^2, \quad a_m = \frac{1}{10} \sum_{k=1}^{10} \xi_k^m = \frac{1}{10} \sum_{k=1}^{10} \zeta_k^{2m} \quad (81)$$

and we obtain the averaged polynomials

$$\bar{P}_2 = P_2(a), \quad \bar{P}_4 = P_4(a), \dots \quad (82)$$

The next step is to account for the thickness of the coils, as indicated in (62). Hence we compute

$$\bar{P}_2'' = P_2''(a), \quad \bar{P}_4'' = P_4''(a), \dots, \quad (83)$$

and obtain the $G_{n-1} - G_{n+1}$ expressions which, according to (58) give the value of the multipole n . For instance, using (62) and (82), $n = 2g + 1$

$$\begin{aligned} G_{2g} - G_{2g+2} &= 10b \left[\bar{P}_{2g} - \bar{P}_{2g+2} \right. \\ &\quad \left. + \frac{b^2}{24} (\bar{P}_{2g}'' - \bar{P}_{2g+2}'') \right]. \end{aligned} \quad (84)$$

Let us call this bracket ϵ_{2g+1}

$$\epsilon_{2g+1} = \bar{P}_{2g} - \bar{P}_{2g+2} + \frac{b^2}{24} (\bar{P}_{2g}'' - \bar{P}_{2g+2}''). \quad (85)$$

We use ten coils, of thickness $b = 1/20$, hence

$$\frac{b^2}{24} = \frac{1}{9,600} \quad (86)$$

and the b^2 correction is always very small. The term

ϵ_{2g+1} measures the error to be corrected since the moment of the multipole $2g + 1$ is given by (58),

$$\begin{aligned} p_n &= \mu_0 \frac{4n\pi}{2n+1} R^{n+2} I_1 10b \epsilon_n = \mu_0 \frac{2n\pi}{2n+1} R^{n+2} I_1 \epsilon_n, \\ (n &= 2g + 1). \end{aligned} \quad (87)$$

Let us now make some slight changes in the position of the coils and take

$$\zeta_1 = \zeta_1 + y_1, \dots, \quad \zeta_{10} = \zeta_{10} + y_{10}. \quad (88)$$

We achieve a first correction if we assume

$$\begin{aligned} \Delta \bar{P}_{2g} - \Delta \bar{P}_{2g+2} &= \frac{1}{10} \sum_{k=1}^{10} y_k [P'_{2g}(\zeta_k) - P'_{2g+2}(\zeta_k)] \\ &= -\epsilon_{2g+1}, \end{aligned} \quad (89)$$

which means that the change in the averaged P makes up for the error (85), for which we want to compensate. Here we use equation (15):

$$P'_{2g} - P'_{2g+2} = -(4g + 3)P_{2g+1}, \quad (90)$$

hence the condition

$$\frac{(4g + 3)}{10} \sum_{k=1}^{10} y_k P_{2g+1}(\zeta_k) = \epsilon_{2g+1}. \quad (91)$$

The ζ_k values from which we start are equidistant in order to approximate uniform winding:

$$\zeta_k = 0.05, 0.15, 0.25, 0.35, 0.45, 0.55, 0.65, 0.75, 0.85, 0.95, \quad (92)$$

and each ζ value corresponds to an interval $\Delta\zeta = 1/10$. Hence for small g values, when P_{2g+1} is a slowly varying function, we may replace the sum (91) by an integral

$$\frac{1}{10} \sum_k y_k P_{2g+1}(\zeta_k) = \sum y P_{2g+1} \Delta\zeta \approx \int_0^1 y(\zeta) P_{2g+1} d\zeta, \quad (93)$$

where $g = 1, 2, 3$.

When (93) can be used, we obtain independent correction of the first multipoles, by taking advantage of the orthogonality of Legendre polynomials. Stating

$$y_k = \sum_h \epsilon_{2h+1} P_{2h+1}(\zeta_k), \quad (94)$$

we obtain

$$\int_0^1 y_k P_{2g+1} d\zeta = \sum_h \epsilon_{2h+1} \int_0^1 P_{2g+1} P_{2h+1} d\zeta = \frac{\epsilon_{2g+1}}{4g + 3}, \quad (95)$$

since

$$\int_0^1 P_{2g+1} P_{2h+1} d\zeta = \begin{cases} 0 & h \neq g \\ \frac{1}{4g + 3} & h = g. \end{cases} \quad (96)$$

Hence (94) is the solution to our conditions (91) and (93). This method was used repeatedly until a convenient approximation was obtained, with values of the first ϵ 's well below the tolerable error.

5.12 NUMERICAL RESULTS

Let us first give the errors resulting from the "set 0" corresponding to the values (92).

TABLE 1. Set 0.

	$\epsilon_n = -P_{n+1} + P_{n-1}$
\bar{P}_2 - 0.001250	
\bar{P}_4 - 0.004154	$\epsilon_3 = 0.002904$
\bar{P}_6 - 0.008598	$\epsilon_5 = 0.004444$
\bar{P}_8 - 0.014163	$\epsilon_7 = 0.005565$
\bar{P}_{10} - 0.019880	$\epsilon_9 = 0.005717$
\bar{P}_{12} - 0.023993	$\epsilon_{11} = 0.004113$

Starting from these values and applying a method very similar to the one described in Section 5.11 results in the following set of values:

TABLE 2.*

$\zeta = 0.0493, 0.1483, 0.2483, 0.3493, 0.4505, 0.5509, 0.6495, 0.7466, 0.8456, 0.9555$

	$\epsilon_n = -\bar{P}_{n+1} + \bar{P}_{n-1}$
\bar{P}_2 - 0.001729	
\bar{P}_4 - 0.001824	$\epsilon_3 = + 0.00095$
\bar{P}_6 - 0.002065	$\epsilon_5 = + 0.000241$
\bar{P}_8 - 0.002628	$\epsilon_7 = + 0.000563$
\bar{P}_{10} - 0.014375	$\epsilon_9 = + 0.011747$
\bar{P}_{12} - 0.025429	$\epsilon_{11} = + 0.011054$
\bar{P}_{14} - 0.031490	$\epsilon_{13} = + 0.006061$
\bar{P}_{16} - 0.028601	$\epsilon_{15} = - 0.002889$

* H. Harrison, Eastman Kodak Company.

Harrison's set of values provides a pretty good solution for a system of very thin coils, but it should be used with coils of thickness 1/20, for which the correction of equation (85) results. These errors can be corrected according to equation (94).

TABLE 4. ζ Values.

0.0495	0.1486	0.2486	0.3495	0.4504
0.5508	0.6496	0.7473	0.8465	0.9543

It results in a very accurate compensation of the first three multipoles.

The set of values of Table 5 represents the best solution found for the practical problem which we are considering.

This concludes the discussion about problem A of Section 5.7; practical solutions have been obtained for (64) with *two* symmetrical thin coils, next (77) or (80) for *four* symmetrical thin coils, and finally the solution of Table 4 for *20 coils* on a sphere.

5.13 TWO COILS WITH A SINE LAW IN THE MUTUAL INDUCTANCE

This last problem was stated as *B* in Section 5.7 and can be solved by taking any one of the solutions proposed in the preceding Section 5.11 and associating it with a collecting coil on a sphere of radius *r* larger than the radius *R* of the inner coil. Assuming the outer collecting coil to be a very thin coil, we may choose its dimensions in such a way as to kill

TABLE 3. Coil thickness correction.

	$-P_{n+1} + P_{n-1}$	Correction to ϵ_n	Former ϵ_n	Final ϵ_n	
$\bar{P}_2'' = 3$					
$\bar{P}_4'' = 9.9395$	-6.9395	-0.000724	0.000095	-0.000629	ϵ_3
$\bar{P}_6'' = 20.6638$	-10.7243	-0.001120	0.000241	-0.000879	ϵ_5
$\bar{P}_8'' = 34.8852$	-14.221	-0.001483	0.000563	-0.000920	ϵ_7
$\bar{P}_{10}'' = 52.09$	-17.20	-0.001788	0.011747	+0.009959	ϵ_9

TABLE 5*

	$\epsilon_n = -\bar{P}_{n+1} + \bar{P}_{n-1}$	Coil thickness correction	Final ϵ_n
\bar{P}_2 -0.001638			
\bar{P}_4 -0.002387	$\epsilon_3 = 0.000749$	-0.000724	0.000025
\bar{P}_6 -0.003566	$\epsilon_5 = 0.001179$	-0.001120	0.000059
\bar{P}_8 -0.005139	$\epsilon_7 = 0.001573$	-0.001483	0.000090
\bar{P}_{10} -0.015751	$\epsilon_9 = 0.010612$	-0.001788	0.008824
\bar{P}_{12} -0.025127	$\epsilon_{11} = 0.009376$	-0.002200	0.007176

* Computed from the tables of Hj. Tallqvist, Sechstellige Tafeln der 16 Ersten Kugelfunctionen $P_n(x)$, Helsingfors, 1937.

one more term in the expansion (48) for the mutual inductance.

Assuming that the first coil has $P_{1,N+1}$ as its first nonzero multipole [equation (56)], we must make the corresponding term zero for the second coil

$$p_{2,N+1} = 0. \quad (97)$$

When this is done, we compute the next term in $p_{1,N+2}$, $p_{2,N+2}$ in the same expansion, and we choose the ratio R/r of the radii small enough to make this first troublesome term negligible. Higher terms will generally be negligible, too, on account of the higher power of R/r involved. According to equations (32) and (51), the $N+1$ th multipole is zero when

$$P_{N+1}^1(\zeta) = 0, \quad \zeta = \cos \theta. \quad (98)$$

This will be illustrated in the following examples.

I. *First coil with two symmetrical loops* [equation (64)]. The first nonzero multipole is number

$$N+1 = 5,$$

and (98) is satisfied when we choose for the *second coil*

$$\theta = 40^\circ 5' \quad \text{or} \quad 73^\circ 26', \quad (99)$$

as suggested by Schelkunoff.⁶

II. *First coil, consisting of four symmetrical loops* according to equations (78) or (80). This structure of the first coil kills the third, the fifth, and all even multipoles. The next one to be compensated is

$$N+1 = 7$$

and this is obtained for any one of the following angles

$$\theta = 29^\circ 20', \quad \text{or} \quad 53^\circ 44', \quad \text{or} \quad 77^\circ 55'. \quad (100)$$

The *second coil* should be built on one of these angles.

III. *First coil, with 20 symmetrical grooves*, as discussed in Section 5.11. This first coil (Table 5) kills

the multipoles 3, 5, 7 and all even multipoles. The next nonzero multipole is

$$N+1 = 9,$$

which can be compensated by choosing for the *second coil* an angle θ making

$$P_9^1(\cos \theta) = 0, \quad (101)$$

such as

$$\theta = 42^\circ 40', \quad \text{for instance.}$$

In the preceding examples, the uncompensated perturbation is for

$$\begin{array}{ll} \text{Case I} & N+2 = 7 \\ \text{Case II} & N+2 = 9 \\ \text{Case III} & N+2 = 11. \end{array} \quad (102)$$

The corresponding Legendre polynomial P_{N+2} equals ± 1 for $\chi = 0$ or $\chi = \pi$ and takes much smaller values in between. In Case III, for instance, the polynomial P_{11} is less than $1/2$ for all angles,

$$6^\circ < \chi < 174^\circ, \quad (103)$$

hence the perturbation is limited to small χ angles (see Figure 9) and becomes negligible for all other angles. In Case III we obtained in Table 5 an error $\epsilon_{11} = 0.007$. Let us now take a ratio

$$\frac{R}{r} = \frac{1}{\sqrt{2}}$$

for the radii of both coils, the eleventh term in the expansion comes out with a relative order of magnitude

$$\left(\frac{R}{r}\right)^{11} \epsilon_{11} = 0.00015,$$

as seen from equation (48). This error could be still decreased by choosing a smaller value for the ratio R/r .

PART III

MECHANICS

CONFIDENTIAL

Chapter 6

MECHANICS OF PARTICLES AND RIGID BODIES

6.1 INTRODUCTION

AMONG THE VARIOUS studies undertaken by AMP at the request of branches of the Armed Forces, several involve portions of the theory of the mechanics of a particle and of a rigid body, such as the Lagrange equations of motion of a rigid body and the theory of the damped motion of a particle on a straight line under various forces. Such studies are considered in this chapter. They are arranged in more or less natural order based upon similarities in the procedures employed.

6.2 COLLIDING LINEAR OSCILLATORS

The study of the motion of colliding linear oscillators was initiated in order to analyze and predict the behavior of a device known as the *spring hammer box* [SHB] used by the United States Navy in acoustic mine sweeping.^{1,2} The device consists essentially of a closed box, one side of which is a clamped diaphragm. The box is immersed in the sea, and the diaphragm, which is in contact with the water, is made to vibrate by repeated blows from a mechanically driven heavy hammer inside the box. The hammer is attached to one end of a spring, the other end of which is made to perform an oscillatory motion by means of a connecting rod and crank or simply by a driving eccentric. This provokes a vibratory response in the hammer. By means of a guide, such as a leaf spring, the hammer is constrained to move on a line perpendicular to the diaphragm. The separation of the hammer and diaphragm when the hammer is in its equilibrium position is small enough to insure collisions when the amplitude and frequency of the driving motion are given.³ The fundamental problem concerns the manner in which the operation of the SHB depends on the various physical parameters of the system, such as the mass of the hammer. Of paramount interest is a discussion of the periodic modes of operation.

The interaction of the diaphragm and water is complex. Hence, a theoretical investigation is carried out of the simplified model of the SHB described below. Indeed, it was this model that was first proposed for investigation by the David Taylor Model Basin [DTMB].

6.2.1 The Simplified Model

The mechanism of the SHB is idealized to a system of two linear oscillator units. The first unit, which is called the hammer unit, is a mass on one end of a spring, the other end of which is made to perform a simple harmonic motion in the direction of the axis of the spring. The second unit, which is called the diaphragm unit, is simply an undriven mass and spring, which, however, experience viscous damping. Thus the vibrating diaphragm and water of the SHB are

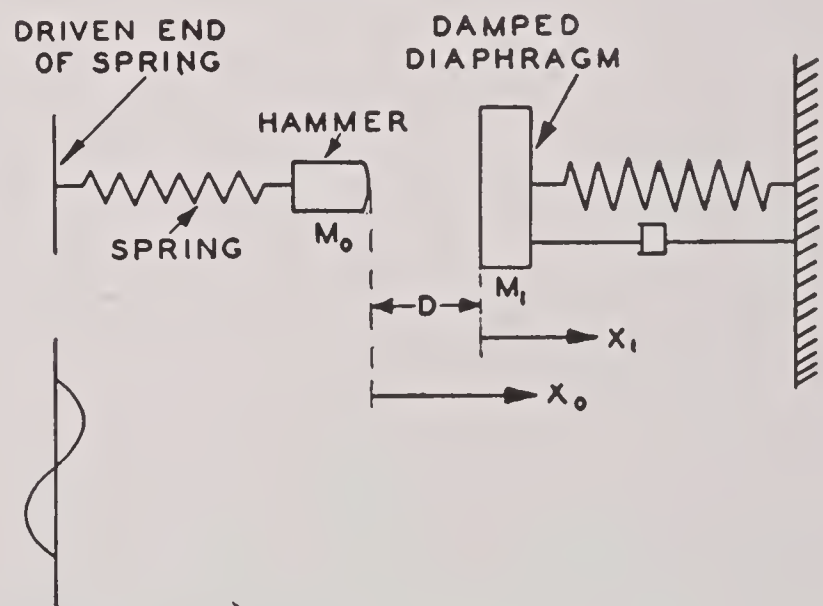


FIGURE 1. Simplified mechanical model of the SHB.

idealized to an equivalent mass and spring. Since the vibrating diaphragm has infinitely many degrees of freedom, and the mass and spring constitute a linear oscillator with one degree of freedom, the above idealization is equivalent to assuming that the SHB diaphragm vibrates only in its fundamental mode.

Figure 1 is a schematic diagram of the linear oscillator units. The oscillators are coupled by the

impacts between the hammer and the diaphragm. The dashpot represents the viscous damping of the diaphragm. The damping is introduced to simulate the energy lost from the diaphragm into the adjacent water.

In the following, the letters SHB refer to the simplified model of Figure 1.

6.2.2 Formulation of the Problem

PARAMETERS OF THE SYSTEM

The following notations are employed: M_0 and M_1 are the masses of the hammer and diaphragm; X_0 and X_1 are the displacements of the hammer and diaphragm from their equilibrium positions; t is the time; Ω_0 , Ω_1 , and ω are the circular frequencies (in radians per unit time) of the free vibration of the hammer, the free vibration of the diaphragm, and the simple harmonic motion of the driven end of the hammer spring; A is the amplitude of the simple harmonic motion of the driven end of the hammer spring; D is the clearance between the masses at equilibrium; ϵ is the coefficient of restitution at impact of the hammer and diaphragm, and in general $0 < \epsilon < 1$; σ is the coefficient of viscous damping of the diaphragm.

In the actual analysis, it is convenient to introduce the following dimensionless parameters formed from those above:

$$\begin{aligned} \omega_0 &= \frac{\Omega_0}{\omega}, \quad \omega_1 = \frac{\Omega_1}{\omega}, \quad m_0 = \frac{M_0}{M_0 + M_1}, \\ m_1 &= \frac{M_1}{M_0 + M_1}, \quad x_0 = \frac{X_0}{D}, \quad x_1 = \frac{X_1}{D}, \quad a = \frac{A}{D}. \end{aligned} \quad (1)$$

Now $m_0 + m_1 = 1$, whence m_0 and m_1 are not independent. The SHB is thus characterized completely by the six parameters

$$m_0, \omega_0, \omega_1, a, \epsilon, \sigma. \quad (2)$$

The values of m_0 and m_1 depend only on the quotient M_0/M_1 of the masses.

THE REQUIRED SOLUTIONS

Between impacts, the motion of the SHB is governed by two linear second-order differential equations in $x_0(t)$ and $x_1(t)$. However, because of the impacts, the system is nonlinear. In order to solve the problem in general, it is necessary to make a separate determination of $x_0(t)$ and $x_1(t)$ for each interval between impacts. This general problem is not considered. Instead, consideration is restricted to solu-

tions that are periodic and are such that there is exactly one collision of the hammer and diaphragm per period. Also, only stable solutions are considered, i.e., the motion of the system must satisfy the *condition of stability* which states that periodic motions of the system must be insensitive to small disturbances. This implies that nonperiodic solutions which are sufficiently close to a periodic solution must eventually settle down to the periodic solution.

It is obvious that in addition the so-called *noninterpenetration condition*

$$x_1(t) \geq x_0(t) - 1 \text{ for all } t$$

must be satisfied, as otherwise the solution corresponds to the hammer penetrating the diaphragm. It is assumed that the impacts are inelastic.

6.2.3 Determination of Required Solutions

The period of the periodic motion is denoted by T' . The ratio n of T' to the period $2\pi/\omega$ of the driving motion must be an integer. In practice n is usually unity.

THE UNDAMPED SYSTEM

In this section the effect of the viscous damping is neglected, so that $\sigma = 0$. The theory of periodic stable motions has been worked out in greatest detail for this case in AMP 36.5R.¹⁸ As regards stability, the assumption $\sigma = 0$ is probably not as serious as it might seem, for there is dissipation of energy at the inelastic impacts.

The Displacement Functions. A special time unit is introduced which is such that $\omega = 1$. Thus the period of the driving motion is 2π , and T' is equal to $2n\pi$. The differential equations governing the motion of the system between impacts is then

$$\begin{aligned} \ddot{x}_0 + \omega_0^2 x_0 &= a\omega_0^2 \cos(t + \delta), \\ \ddot{x}_1 + \omega_1^2 x_1 &= 0, \end{aligned} \quad (3)$$

where the superimposed dots denote differentiations with respect to time, and δ is a phase angle. It is assumed that an impact occurs at $t = 0$. Successive impacts then occur at $t = 2n\pi, 4n\pi, 6n\pi, \dots$. In the time interval $0 \leq t \leq 2n\pi$, the solution of (3) has the form

$$\begin{aligned} x_0 &= a_0 \sin \omega_0 t + b_0 \cos \omega_0 t + U \sin t + V \cos t, \\ x_1 &= a_1 \sin \omega_1 t + b_1 \cos \omega_1 t, \end{aligned} \quad (4)$$

where a_0, b_0, a_1 and b_1 are arbitrary constants, and U and V are constants depending on a, ω_0 and δ .

Since x_0 and x_1 must be periodic, it follows that

$$x_0(0) = x_0(2n\pi), \quad x_1(0) = x_1(2n\pi).$$

Also, the masses are in contact at $t = 0$, whence

$$x_0(0) - x_1(0) = 1.$$

Finally, at the impact, momentum must be conserved, and the ratio of the relative velocities of the masses before and after the impact must equal the negative of ϵ . In all, there are thus five boundary conditions. These lead to the relations

$$\begin{aligned} a_0 &= -p \frac{m_1}{\omega_0}, \quad b_0 = -p \frac{m_1}{\omega_0} \cot \frac{\alpha}{2}, \\ a_1 &= p \frac{m_0}{\omega_1}, \quad b_1 = p \frac{m_0}{\omega_1} \cot \frac{\beta}{2}, \end{aligned} \quad (5)$$

$$U = p \frac{1 - \epsilon}{1 + \epsilon}, \quad V = 1 + p \left(\frac{m_0}{\omega_1} \cot \frac{\beta}{2} + \frac{m_1}{\omega_0} \cot \frac{\alpha}{2} \right),$$

$$\frac{a^2}{(1 - \omega_0^{-2})^2} = U^2 + V^2, \quad (6)$$

where p is defined by the equation

$$2p = [\dot{x}_0(2n\pi) - \dot{x}_1(2n\pi)] + [\dot{x}_1(0) - \dot{x}_0(0)], \quad (7)$$

and

$$\alpha = 2n\pi\omega_0, \quad \beta = 2n\pi\omega_1.$$

It is to be noted that p is the average of the absolute values of the relative velocities of the masses before and after impact.

Equation (6) is a quadratic equation in p . Only positive real roots have significance. Thus, corresponding to a given set of values of the parameters (2), there are two, one, or no possible periodic solutions (4), depending on whether (6) has two, one, or no positive roots. Once p is known, the values of the constants in (4) follow from the above.

The Noninterpenetration Condition. When damping is absent, the noninterpenetration condition takes the following simple form. *A necessary and sufficient condition for noninterpenetration is*

$$\frac{1}{p} > \max [G(t)] \quad (0 < t < 2n\pi), \quad (8)$$

where

$$G(t) = \frac{1}{2} \csc^2 \frac{t}{2} \left[\frac{1 - \epsilon}{1 + \epsilon} \sin t + \left(\frac{m_0}{\omega_1} \cot \frac{\beta}{2} + \frac{m_1}{\omega_0} \cot \frac{\alpha}{2} \right) \cos t - \frac{m_0 \cos (\omega_1 t - \frac{1}{2}\beta)}{\omega_1 \sin \frac{1}{2}\beta} - \frac{m_1 \cos (\omega_0 t - \frac{1}{2}\alpha)}{\omega_0 \sin \frac{1}{2}\alpha} \right].$$

In any given case, $G(t)$ is plotted and each positive root p of (6) is tested to see if (8) is satisfied.

There are various other ways of checking for noninterpenetration. Most attention was directed to the development of graphical methods. These use the noninterpenetration condition in the form

$$x_0(t) - x_1(t) < 1, \quad (0 < t < 2n\pi).$$

The left side in this inequality is the sum of several harmonic terms, and the condition is checked by the use of rotating vector diagrams. In special cases much time can be saved by these methods. In general, however, the task of checking the noninterpenetration condition is tedious and takes much time.

THE DAMPED SYSTEM

The problem considered here is the same as the one just considered, except that damping is now included. There is one impact per period of the system, and the ratio of the period of the system to the period of the driving motion is an integer n .

The theory of the damped system, which appears in AMP 36.3R, was developed before that of the undamped system and in a somewhat different notation which is not so convenient. However, the results of this theory will be presented here in the original notation, which is as follows. M_1 and M_2 are the masses of the hammer and the diaphragm, x_1 and x_2 are the displacements of the hammer and the diaphragm measured from a common origin; t is the time; ν_0 , ν_1 , and ν_2 are the circular frequencies of the simple harmonic motion of the driven end of the hammer spring, the free vibration of the hammer and the free vibration of the diaphragm; A_0 , A_1 , and A_2 are the amplitudes of the driving motion, the free vibration of the hammer, and the damped motion of the diaphragm; L is the clearance between the masses at equilibrium; δ_0 , δ_1 , and δ_2 are phase angles; ϵ is the coefficient of restitution at impact of the hammer and diaphragm; σ is the coefficient of viscous damping of the diaphragm.

The Displacement Functions. A special time unit is introduced such that the period of the driving motion is unity. Thus it follows that $\nu_0 = 2\pi$. The unit of length is chosen equal to the amplitude of the forced motion, which is $A_0[1 - (\nu_0/\nu_1)^2]^{-1}$.

The interval between successive impacts is $0 < t < n$, and it is found that in such an interval

$$\begin{aligned} x_1 &= \cos(2\pi t + \delta_0) + A_1 \cos(\nu_1 t + \delta_1), \\ x_2 &= L + A_2 e^{-\sigma t} \cos(\nu_2 t + \delta_2). \end{aligned} \quad (9)$$

Only the case $n = 1$ is considered. Thus the periods of the driving motion and the system as a whole are

equal. The periodic motion of the system in this case is referred to as a *simple periodic motion*.

The constants δ_0 , δ_1 , δ_2 , A_1 , and A_2 are to be determined in terms of the given parameters ν_1 , ν_2 , ϵ , $M = m_2/m_1$, and σ . By means of the conditions of periodicity and impact, the following sequence of procedures and formulas which lead to the required constants is established:

1. The value of δ_1 is found from

$$\delta_1 = \begin{cases} -\frac{1}{2}\nu_1 & \text{for } \sin \frac{1}{2}\nu_1 < 0, \\ \pi - \frac{1}{2}\nu_1 & \text{for } \sin \frac{1}{2}\nu_1 > 0. \end{cases} \quad (10)$$

2. The value of δ_2 is found from

$$\delta_2 = \begin{cases} -\frac{1}{2}\nu_2 + \beta & \text{for } \sin \frac{1}{2}\nu_2 > 0, \\ \pi - \frac{1}{2}\nu_2 + \beta & \text{for } \sin \frac{1}{2}\nu_2 < 0, \end{cases} \quad (11)$$

where β is such that

$$\tan \beta = -\frac{\tanh \frac{1}{2}\sigma}{\tan \frac{1}{2}\nu_2} \quad (-\frac{1}{2}\pi < \beta < \frac{1}{2}\pi).$$

3. The quotient A_2/A_1 is found from

$$\frac{A_2}{A_1} = \frac{2\nu_1}{M\nu_2} \frac{|\cos(\frac{1}{2}\nu_2 + \beta) \sin \frac{1}{2}\nu_1|}{|\sin \nu_2|}. \quad (12)$$

4. The quantity \bar{A}_1 , which equals $A_1 \sin \delta_0$, is found from

$$\bar{A}_1^{-1} = \frac{|\sin \frac{1}{2}\nu_1| \nu_1}{2\pi M \nu_2 \sin \nu_2} \left[\sigma(\cos 2\beta + \cos \nu_2) + \nu_2 \sin 2\beta - \nu_2 \frac{1-\epsilon}{1+\epsilon} (1+M) \sin \nu_2 \right]. \quad (13)$$

This equation also determines $\text{sign} [\sin \delta_0]$.

5. The quantity \bar{A}_2 , which equals $A_2/\sin \delta_0$, is found from the relation

$$\bar{A}_2 = \bar{A}_1 \frac{A_2}{A_1} \quad (14)$$

by use of the results of steps 3 and 4.

6. The phase angle δ_0 is found from

$$\sin(\delta_0 + \tau) = \frac{L}{K}, \quad (15)$$

where $K = [(\bar{A}_1 \cos \delta_1 - \bar{A}_2 \cos \delta_2)^2 + 1]^{\frac{1}{2}}$, and τ is a constant such that $0 \leq \tau \leq \pi$ and

$$\sin \tau = \frac{1}{K}, \quad \cos \tau = \frac{\bar{A}_1 \cos \delta_1 - \bar{A}_2 \cos \delta_2}{K}. \quad (16)$$

In general, equation (15) yields two values for δ_0 . Thus there are in general two possible periodic motions of the type under consideration for each given set of values of the fundamental parameters ν_1 , ν_2 , τ , M , and σ . One or both of the values of δ_0 must be

discarded if $\text{sign} [\sin \delta_0]$ disagrees with the results of step 4.

With regard to the uniqueness of a simple periodic solution, the following result is established. If the clearance L between the masses at equilibrium is less than the amplitude $A_0[1 - (\nu_0/\nu_1)^2]^{-1}$ of the forced response of the hammer, there can be at most one simple periodic motion of the SHB corresponding to a given set of values of the fundamental parameters ν_1 , ν_2 , ϵ , M , and σ .

The Noninterpenetration Condition. In the present notation, the noninterpenetration condition is $x_0 < x_1$. This condition can be checked by straightforward computation of $x_0(t)$ and $x_1(t)$ for $0 < t < 1$. Since x_0 and x_1 involve various harmonic terms, the condition can also be checked by the use of rotating vector diagrams, as for undamping, though in the present case the damping complicates matters a little. However, once facility in the use of this method has been attained, a considerable saving of time can be made.

6.2.4 Stability Conditions

It was not until nearly a year after the first report on the SHB appeared that a mathematical formulation of the condition of stability for periodic solutions was obtained. It was derived in a very general fashion which yielded necessary and sufficient conditions for the stability of periodic motions of a dynamical system of n degrees of freedom subject to discontinuous impulses. The simplified model of the SHB is a special case of this, and the stability conditions for the undamped system appear in a surprisingly simple form. The system of n degrees of freedom will now be considered.

SYSTEM WITH n DEGREES OF FREEDOM

Systems are considered which are governed by the equations

$$\frac{dX_i}{dt} = f_i(X_1, X_2, \dots, X_m, t), \quad (i = 1, 2, \dots, m) \quad (17)$$

for the unknown functions X_i of t , where f_i are periodic in t of period T' . It is assumed that the f_i are defined for all values of the variables and possess continuous first-order derivatives. In addition, at any time t_0 when the variables satisfy the relation

$$L(X_1, X_2, \dots, X_m) = 0, \quad (18)$$

where L is a given function, the functions X_i are to have the discontinuities

$$\Delta X_i \equiv X_i(t_0 + 0) - X_i(t_0 - 0) \\ = \phi_i(X_1, X_2, \dots, X_m), \quad (i = 1, 2, \dots, m). \quad (19)$$

In (18) and (19) the symbols X_i are understood to mean $X_i(t_0 - 0)$, i.e., the value of X_i immediately preceding the jump. It is assumed that the above system has a periodic solution \bar{X}_i , and investigation of the stability of \bar{X}_i is required.

This general problem includes that of the stability of periodic motions of a Lagrangian dynamical system with n degrees of freedom acted upon by continuous forces and discontinuous impulses. In this case the unknown functions X_i are the n generalized coordinates and the n generalized velocities, so that $m = 2n$. For the SHB, it then follows that $m = 4$. The four functions X_i are the displacements and velocities of the two masses, equation (18) is the condition that the two masses be in contact, and the functions ϕ_i are deduced directly from the conditions of impact, which are that the momentum is conserved and the ratio of the relative velocities before and after impact is equal to the negative of ϵ .

The classical theory of stability according to Liapunoff and Poincaré deals only with continuous motions. The general problem set forth above is solved in AMP 36.5R¹⁸ by extending this classical theory to include impulsive motions. An indication will now be given of the lines which this extension follows.

First, a rigorous definition of stability is made. The periodic solution $\bar{X}_i(t)$ is compared with a disturbed solution $X_i(t)$ which satisfied the condition

$$X_i(0) = \bar{X}_i(0) + a_i, \quad (i = 1, 2, \dots, m), \quad (20)$$

where a_i are small in comparison with the ranges of \bar{X}_i . The disturbed solution need not be periodic. The periodic solution $\bar{X}_i(t)$ is said to be stable if, by choosing a_i sufficiently small, the deviations $X_i(t) - \bar{X}_i(t)$ can be made arbitrarily small for all t greater than zero, except in the vicinity of discontinuities of \bar{X}_i .

At the end of a period of \bar{X}_i , i.e., when $t = T'$, the deviations have the values

$$b_i = X_i(T') - \bar{X}_i(T'), \quad (i = 1, 2, \dots, m),$$

which are determined completely once the a_i are specified. This defines a *continuous transformation* θ over a neighborhood of the origin in the m -dimensional space. This transformation is termed stable if, when it is iterated on a given point sufficiently close to the origin, the point becomes arbitrarily close to the origin.

A matrix of the first derivatives of θ is introduced. It is called the *companion matrix* to θ , and represents θ to a linear approximation. A criterion for stability of θ is established in terms of this companion matrix evaluated at the point where the stability is in question (the point $a_i = 0$ in the present case). The basic theorem proved in this regard is that the stability of the nonlinear transformation θ (aside from the exceptional cases) depends only on the stability of the linear transformation described by the companion matrix. It is well known that such a linear transformation is stable if and only if the characteristic roots are all less than unity in absolute value.

The problem is thus reduced to finding the companion matrix A of the transformation θ . This is done by splitting θ into two transformations to be applied successively. The first is obtained by disregarding the jump conditions (18) and (19) and defining a *continuous* solution of equations (17) which is determined by initial conditions disturbed from those of $\bar{X}_i(t)$ by small quantities a_i . This continuous solution carries the initial disturbance a_i into a new set of values b_i at the end of the period T' of $\bar{X}_i(t)$, and hence defines a transformation in the m -dimensional space. The companion matrix of this transformation is denoted by M . The required matrix A is obtained as the product of M and a second matrix τ , which is the companion matrix of the transformation corresponding to the jump. In order to find τ , a further decomposition of the transformation corresponding to the jump is necessary.

For the sake of simplicity, the matrix A is obtained only in the case where the trajectory $\bar{X}_i(t)$ crosses the discontinuity manifold $L = 0$ only once per period, at $t = 0$. This corresponds to the case when there is only one impact per period. Explicit expressions for τ and M are found in terms of the given functions f_i , ϕ_i , and L of equations (17), (18), and (19). The results of this general stability investigation are summarized as follows: *The periodic solution $\bar{X}_i(t)$ is stable or unstable according as the absolute values of the characteristic roots of the matrix*

$$A = \left[E + N - \frac{1}{\gamma}NR - \frac{1}{\gamma}(R - R') \right] M \quad (21)$$

are all less than 1 or are not all less than unity.

The symbols appearing in (21) will now be defined in turn. The phrase "characteristic roots" has the usual meaning, i.e., if a_{ij} are the elements of A , then the characteristic roots of A are the roots of the polynomial $|a_{ij} - \lambda\delta_{ij}| = 0$ in λ , where δ_{ij} is the

Kronecker delta (which is equal to 1 or zero, according as i is equal or not equal to j).

The matrix M is given by

$$M = [\xi_i^{(r)}(T')] \quad (r, i = 1, 2, \dots, m), \quad (22)$$

where i is constant in any one row, and $\xi_i^{(r)}(t)$ are the solutions of the linear differential equations

$$\frac{d\xi_i}{dt} = \sum_{k=1}^m \frac{\partial f_i}{\partial X_k} \xi_k \quad (i = 1, 2, \dots, m),$$

satisfying the initial conditions

$$\xi_k^{(r)}(t) \big|_{t=0} = \delta_{kr}. \quad (24)$$

The superimposed bar in (23) indicates that after differentiation, X_k is to be replaced by \bar{X}_k . It is remarked that explicit solutions of (23) can be obtained only in very special cases, such as when the f_i are of the form

$$f_i = \sum_{\nu=1}^m \alpha_{\nu} X_{\nu} + F(t),$$

where the α_{ν} are constants. Fortunately, in the case of the SHB, f_i has this particular form.

The matrix E is the unit matrix of order m ,

$$E = (\delta_{ij}) \quad (i, j = 1, 2, \dots, m). \quad (25)$$

The matrix N is given by

$$N = \left(\frac{\partial \phi_i}{\partial X_j} \right) \quad (i, j = 1, 2, \dots, m), \quad (26)$$

where i is constant in any one row, and, after differentiation, X_i is to be replaced by $X_i(-0)$. The matrix R is given by

$$R = \left(\frac{\partial L}{\partial X_j} \frac{\partial \bar{X}_i}{\partial t} \right) \quad (i, j = 1, 2, \dots, m), \quad (27)$$

where i is constant in any one row; in the derivatives of L it is necessary to replace X_i by $\bar{X}_i(-0)$, and the time derivatives are to be evaluated at $t = -0$. The matrix R' is also given by (27), but in the derivatives of L it is now necessary to replace X_i by $\bar{X}_i(+0)$, and the time derivatives are to be evaluated at $t = +0$. Finally

$$\gamma = \sum_{k=1}^m \frac{\partial L}{\partial X_k} \frac{\partial \bar{X}_k}{\partial t}, \quad (28)$$

where, in the derivatives of L , it is necessary to replace X_i by $X_i(-0)$, and the time derivatives are to be evaluated at $t = -0$.

It is remarked that the stability matrix A applies only to the case when the periodic solution $\bar{X}_i(t)$ crosses the manifold $L = 0$ once per period, i.e., there is one impact per period. It is shown that the

stability of a periodic solution $\bar{X}_i(t)$ which crosses the manifold p times (where p is any integer) during a period can be handled in an analogous fashion, and the stability matrix in this case is set up in terms of the matrices already defined.

APPLICATION TO THE SHB

The stability theory developed above is applied to the simplified model of the SHB without damping. This model has been considered above, and the displacements $x_0(t)$ and $x_1(t)$ of the hammer and diaphragm determined. The effect of damping could be included only at the expense of increasing the complexity of the numerical computations.

For the undamped system, the matrix A appears in AMP 36.5R,¹⁸ equation (51). It is too complex to be reproduced here. It is a square matrix with sixteen elements which involve m_0 , m_1 , ω_0 , ω_1 , ϵ , the angles α and β defined just below equation (7), and a quantity k which has the value

$$k = -\frac{1}{2}(1 + \epsilon) \left[\frac{1}{p} + \frac{m_0}{\omega_1} (1 - \omega_1^2) \cot \frac{\beta}{2} + \frac{m_1}{\omega_0} (1 - \omega_0^2) \cot \alpha \right], \quad (29)$$

where p is determined from equation (6). Necessary and sufficient conditions are found that the roots of the characteristic equation (which is a quartic) be less than 1 in absolute value. These conditions appear as three relations of the form

$$g_i(m_0, m_1, \omega_0, \omega_1, \epsilon, k) < 0 \quad (i = 1, 2, 3). \quad (30)$$

The functions g_i are too lengthy to reproduce here. Their explicit forms can be seen in AMP 36.5R,¹⁸ relations (54) to (56). The final results are thus:

To a given choice of the parameters M_0 , M_1 , Ω_0 , Ω_1 , ω , D , A , and ϵ there corresponds a stable periodic motion with one collision per period of the undamped SHB system, a period being equal to n periods of the driving motion, if and only if equation (6) has a positive root p such that the three stability conditions (30) and the noninterpenetration condition (8) are satisfied, the quantity k being given in equation (29).

APPLICATION TO ONE LINEAR OSCILLATOR

Because of the complexity of stability considerations, some study was devoted to a simplified SHB in which the diaphragm was considered as a rigid wall. This system has one degree of freedom. The stability of this system was investigated with satisfactory results by workers outside NDRC. However,

the method employed was inadequate to treat the system of two colliding oscillators.

An application of the general stability theory developed above for a system of n degrees of freedom yields the following single condition that is necessary and sufficient for stability:

$$(1 + \epsilon^2)^{-1} \left| k'(1 + \epsilon) \frac{\sin \alpha}{\omega_0} - 2\epsilon \cos \alpha \right| < 1, \quad (31)$$

where k' is analogous to the quantity k defined for the system of two colliding oscillators.

STABILITY OF A GENERAL MOTION

It is to be emphasized that, although necessary and sufficient conditions for stability have been obtained, these apply only to the case of periodic motions and to rather special periodic motions at that. Even more important, to use these conditions one must first specify the type of periodic motion being considered and assign values to the physical parameters in order to decide on stability. Thus, although stability can be decided in each particular case, little general information is obtained. Consequently, if one visualizes a parameter space made up of the physical parameters of the system and considers each particular set of numerical values of these parameters as a point in this space, it would require the investigation of countless individual numerical cases to discover in what regions of this parameter space the motion of the SHB is stable and in what regions it is unstable. Moreover, no information at all is obtained on the stability of nonperiodic motions which would enable one to predict the nature of the motion to which an SHB would eventually settle down (if at all) when it is started up under arbitrary initial conditions.

Some progress in these directions has been made for the case of the one-mass system of a hammer striking a rigid wall. In place of a sinusoidal driving force, a so-called square-wave driving motion is considered. A graphical procedure is developed,⁴ based on the so-called Meissner method.⁵ It leads to the following.

1. It is possible to chart the course of a motion corresponding to an arbitrary set of initial conditions and parameter values. Thus, it can be decided, for example, whether a given set of initial conditions and parameter values leads to a periodic motion eventually.

2. The possible periodic motions having only one collision per period which can occur for given parameter values can be determined.

3. The stability of any specified periodic motion of the system can be investigated.

Several interesting examples are studied. In one case two simple periodic motions are found to arise from a given set of parameter values. One is stable and the other unstable. However, it is found that one state of motion near the unstable periodic state will converge, after some 17 cycles, to the stable periodic motion. This leads to the conjecture that regardless of the initial conditions, if the parameter values are compatible, the system always eventually settles down to some stable periodic motion.

6.2.5 Application to Numerical Cases

A considerable application of the theory discussed above is made to numerical cases.⁶ The simplified model of the SHB, consisting of two linear oscillators without damping, is considered. The parameters m_0 , m_1 , ϵ and a are given fixed numerical values, and ω_0 and ω_1 are each given eight different values, making a total of 64 cases. These cover a typical working range in practice.

In each case it is asked whether there exists a stable, simple, periodic motion. Consequently, in each case it is necessary to verify the stability and noninterpenetration conditions. Computational work arising in the use of the stability conditions (30) is considerably shortened by the use of a reformulated version of these conditions which is suited to variation of the parameters ω_0 and ω_1 alone. A graphical method of verifying the noninterpenetration condition is evolved; this also takes advantage of the fact that ω_0 and ω_1 alone vary from case to case.

A numerical determination is made of the maximum displacement of the diaphragm in each of the 64 cases considered above.⁷ The maximum displacement is also determined, since a numerical study is made of the periodic solutions arising when all the parameters are fixed except the ratio of the masses, which is given six different values. In this way the response of the diaphragm to changes in M_0/M_1 is investigated at different frequencies. In each such case it is necessary to verify whether the given choice of parameters leads to a simple periodic motion which satisfies the conditions of stability and noninterpenetration.

6.2.6 Electric Analogue of SHB

At DTMB, experiments were carried out on a mechanical model of the idealized SHB system. Un-

fortunately, these experiments were not too successful because, first, it was difficult to vary the essential parameters of the machine over sufficiently wide ranges and second, accurate measurement and description of motions were not possible.

Consequently, an electric analogue of the SHB was developed at Brown University⁸ simultaneously with the theoretical investigations, since it appeared that such a device would minimize the difficulties experienced with the mechanical model. The purpose of this analogue was to check theoretical results and obtain information beyond the scope of the theory.

DESCRIPTION OF ANALOGUE

The electrical analogue is an electric circuit which is governed by equations similar to those governing the simplified model of the SHB shown in Figure 1, except that damping is absent. In a strict sense, the analogy between the electrical system and mechanical system is not exact; to render it so, it would be necessary to replace the impact by a mechanism consisting of a light but very stiff spring, together with a dashpot which is suddenly attached to the two masses when they come together. After yielding momentarily, this coupling forces the two masses apart with a relative velocity of the proper magnitude. The coupling is then broken. All this is required to take place during a time which is very small in comparison with the interval between successive impacts.

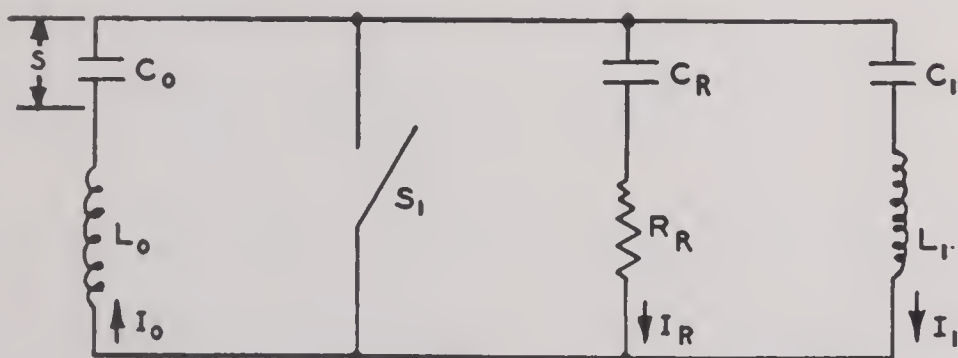


FIGURE 2. A first circuit for the electric analogue to the SHB.

Figure 2 shows an electric circuit. The symbol s , which equals $(Q_0/C_0) + (Q'_0/C_0) \cos \omega t_R$, denotes the sum of the voltages due to the oscillating free charge of the system and the impressed voltage due to a charge generated with a frequency ω . This latter voltage corresponds to the forced motion of the hammer in the mechanical problem. Kirchhoff's laws are written down, integrated, and rearranged. This yields

$$L_0 \frac{d^2 Q_0}{dt_R^2} = -\frac{1}{C_0} (Q_0 - Q'_0 \cos \omega t_R) - \alpha f, \quad (32)$$

$$L_1 \frac{d^2 Q_1}{dt_R^2} = -\frac{Q_1}{C_1} + \alpha f, \quad (33)$$

where

$$f = \frac{Q_0 - Q_1 + Q_k}{C_p} + R_R \frac{d}{dt_R} (Q_0 - Q_1).$$

The multiplier α has the value zero when the switch S_1 is closed and the value unity when S_1 is open. The symbol Q_k denotes the minimum charge difference of condensers C_0 and C_1 . The other notations appear in Figure 2 or are obvious. When $Q_0 < Q_1 + Q_k$, the switch is closed and the circuits $L_0 - C_0$ and $L_1 - C_1$ are isolated. When $Q_0 = Q_1 + Q_k$, the switch is opened electrically and the restitution circuit $R_R - C_R$ comes into play. This corresponds to the introduction of the spring and dashpot between the masses.

A comparison of equations (32) and (33) with the equations governing the motion of the undamped mechanical system indicates the following correspondences:

$$L_0, L_1 \sim M_0, M_1; \frac{1}{C_0}, \frac{1}{C_1} \sim k_0, k_1;$$

$$Q_0, Q_1, Q_k \sim X_0, X_1, X_k.$$

Here, k_0 and k_1 are the spring constants. The symbol X_k denotes the separation of the masses when the spring and the dashpot come into play.

In order to determine when the switch S_1 is to be operated, a condenser C_M , common to all three circuits, is introduced, as shown in Figure 3. The

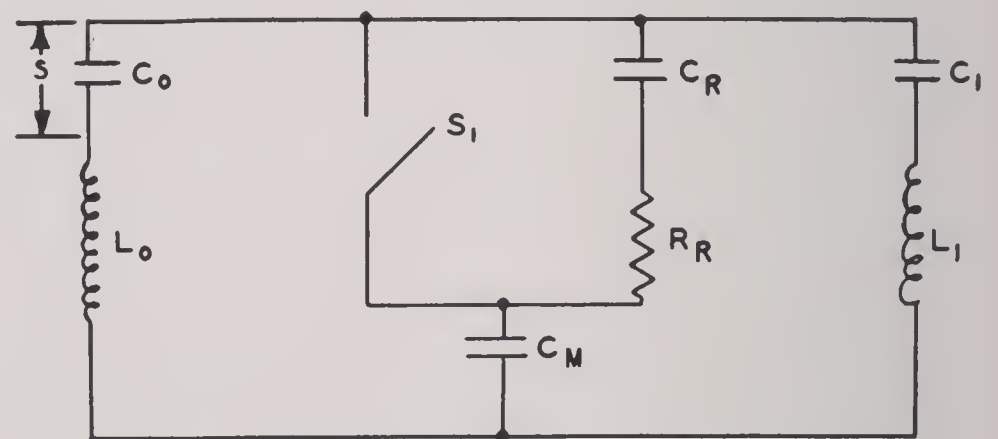


FIGURE 3. A second circuit for the electric analogue to the SHB.

voltage across this condenser is amplified and used to detect "impacts." The capacity C_M is much larger than C_0 and C_1 , so that the circuits have a small interaction, except when impact takes place. A theoretical investigation of this interaction is given in Appendix I of AMP 36.6R.¹⁹

In the electrical and mechanical systems there exists a certain amount of damping. This introduces the terms $-I_0 R_0$ and $-I_1 R_1$ into the right sides of equations (8) and (9) respectively. Since, in the

Figure 4 shows the circuit of the electric analogue actually used in studying the SHB.

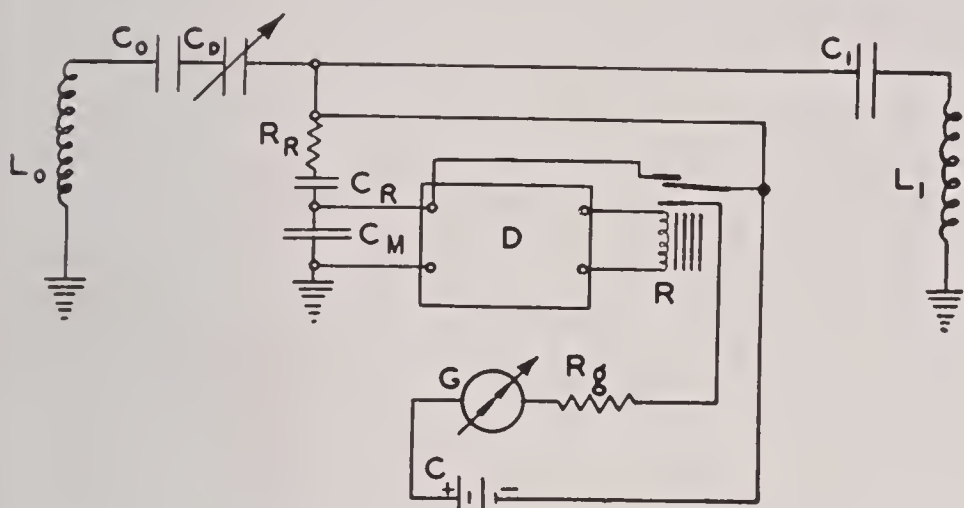


FIGURE 4. The final circuit for the electric analogue to the SHB.

The electrical analogue was operated under conditions which simulate a wide variety of values of the fundamental constants of the mechanical system. Tests were run to check the 64 cases investigated theoretically in AMP 36.1M²⁰ and AMP 36.2M.²¹ A table is given in AMP 36.6R¹⁹ by means of which a direct comparison of the results of the two approaches can be made.

In general, the results obtained by the use of the electrical analogue are complex, but their character is summarized below. A stable periodic solution is termed an $n - m$ solution if there are n impacts in one period of the system and if the period of the system is equal to m periods of the driving motion. It is recalled that $a = A/D$, $\omega_0 = \Omega_0/\omega$, where A is the amplitude of the driving motion, D is the clearance between the masses at equilibrium, and Ω_0 and ω are the circular frequencies of the free hammer system and the driving motion.

When the ratio of the mass and the frequency ω are given certain specific values, it is found that those values of a and ω_0 for which stable periodic solutions can be obtained are as shown in Figure 5. In the general region of resonance ($\omega_0 = 1$), values of a larger than about 0.6 invariably give $n - 1$ solutions. When a is less than 0.6, the results can be subdivided according to the values of ω_0 . When ω_0 is greater than unity (subresonant driving), $n - m$ solutions with $n/m \simeq 1$ are found only for a small range of values of a . As resonance is approached, the range widens, and at resonance $1 - 1$ solutions seem to be the rule. When ω_0 is less than unity (superresonant driving),

FIGURE 5. Regions where stable periodic motions of the SHB are obtained.

A significant quantity governing the applicability of the electric analogue to a study of the SHB is the ratio of the "time of impact" to the period of the system. In practice, this ratio had the range 0.02 to 0.2 and in most cases favored the lower value. Also, the various fundamental parameters of the SHB, such as the coefficient of restitution ϵ and the ratio of the masses, were simulated in the electric analogue to within a probable error which ranged up to about 6 per cent.

The servomechanism was considered,⁹ which consists of an input shaft and an output shaft, the rotations of these shafts being denoted by θ_i and θ_0 , respectively. The rotation θ_i is assigned, and it is desired to make the output shaft follow the input shaft by applying to the output shaft a torque proportional to the error $\epsilon = \theta_i - \theta_0$. There is the added restriction that this torque cannot exceed a given constant M , no matter how large the error.

The equations governing the motion of the system are

$$\begin{aligned} J\ddot{\theta}_0 + \dot{f}\dot{\theta}_0 &= C(\theta_i - \theta_0) && \text{for } C \mid \theta_i - \theta_0 \mid \leq M, \\ J\ddot{\theta}_0 + \dot{f}\dot{\theta}_0 &= \pm M && \text{for } C \mid \theta_i - \theta_0 \mid > M, \end{aligned}$$

where the superimposed dots denote differentiation with respect to time, J is the moment of inertia of the motor driving the output shaft, f is the coefficient of viscous damping in the motor, and C is a constant proportionality factor. The *critical error*

ϵ_c is defined as the error at which torque saturation is reached, i.e., $C\epsilon_c = M$. The above equations are written in the form

$$T\ddot{\theta}_0 + \dot{\theta}_0 = K_v(\theta_i - \theta_0) \quad \text{for } |\theta_i - \theta_0| \leq \epsilon_c, \quad (34)$$

$$T\ddot{\theta}_0 + \dot{\theta}_0 = \pm K_v\epsilon_c \quad \text{for } |\theta_i - \theta_0| > \epsilon_c, \quad (35)$$

where T and K_v are constants called the *motor time constant* and the *velocity error constant*, respectively.

The case is considered where the system is initially at rest and θ_i is suddenly increased from zero to a constant value ϵ_0 , i.e., θ_i is a step function. The quantity ϵ_0 is thus the initial error.

6.3.2 Results

If ϵ_0 is less than ϵ_c , equation (34) applies, saturation is never attained, and the servo behaves exactly as a servo without saturation.

When ϵ_0 is greater than ϵ_c , the *relative excess error* $Q = (\epsilon_0 - \epsilon_c)/\epsilon_c$ is introduced. There is a time interval t_0 during which ϵ decreases from ϵ_0 to ϵ_c and equation (35) applies. It is found that t_0 satisfies a transcendental equation which can be solved graphically. When Q is much larger than K_vT , an approximate root of this equation is $t_0 = 1 + (Q/K_vT)$. In the time interval $t_0 < t < \infty$, the motion of the system is as described in one of the two following circumstances.

1. At a certain time t_1 , the error passes the negative critical value $-\epsilon_c$, and overshoots into the saturated domain.

2. The absolute value of ϵ remains below ϵ_c for $t_0 < t < \infty$, and aside from the initial period $0 < t < t_0$ the servo behaves exactly as a servo without saturation.

It is found that if K_vT is greater than 3.03, case 1 arises and the system overshoots one or more times. However, the number of overshoots is finite, and the oscillations gradually die out. If K_vT is less than 3.03, case 2 arises.

6.4 GUN EQUILIBRATORS

The vertical and horizontal axes about which a gun can be rotated are called the axes of train and elevation, respectively. In a *navy gun*, these two axes intersect, or very nearly intersect, and the center of gravity of the mass on the trunnions is close to this point of intersection. Thus, a navy gun is practically in equilibrium at all angles of elevation and train. In an *army gun*, however, the axis of elevation is at some distance from the axis of train, since the trunnions are located much closer to the

breech than in a navy gun. Also, the center of gravity of the mass on the trunnions in an army gun is well forward of the axis of elevation, and the gun is kept in equilibrium at all angles of elevation by a system of springs constituting a *gun equilibrator*.

The purpose of the present study is to throw some light on the feasibility of mounting army guns on board ship. An obvious advantage to such an arrangement is that the axis of elevation can be much closer to the deck than in the case of a navy gun, and a considerable saving in weight can thus be effected. However, when the ship pitches and rolls, couples must be applied to the army gun by means of the gear trains controlling elevation and train in order to keep the gun trained on the target, and these couples might become so large that smooth operation of the gun would be impossible. The present study is concerned, then, with a determination of these couples.

A preliminary attack was made on the problem,¹⁰ and the couples were determined for a gun of medium size on a very large ship. Because of mathematical complexity, it was necessary to use extensive approximations, and the results do not apply to small ships. It was learned subsequently that numerical results were desired for a specific 3-in. gun mounted on four specific small ships. Accordingly, a second attack on the problem was made.¹¹ No further mention of the original work will be made here, since the results obtained were never used and since the method used in both cases is the same and is contained in full in the second report. The attack used in the second report will be considered in the next section.

In order to ascertain the smoothness of operation of a gun on a pitching and rolling ship, it is customary to subject it to a certain test in the factory. In this test the gun is mounted on a level floor and is made to execute a simple harmonic oscillation in train simultaneously with a simple harmonic oscillation in elevation. Obviously, the similarity between this test and actual conditions on board ship is not too good. A study was made of this test, and the couples delivered to the gun by the gear trains were ascertained in order to evaluate the reliability of the factory test.¹² This study will be considered in the section after the next.

6.4.1 Gun Equilibrators I

The gun under consideration is the 3-in. 50-mount Mark 24, Model 1, modified to the extent that the

center of gravity of the mass on the trunnions is ahead of the axis of the trunnions, the distance between the axis of the trunnions and the train axis is greatly increased, and the gun has an equilibrator. The four small ships which are to be considered are referred to as Types (a), (b), (c), and (d). Significant numerical data about these ships are contained in Table 1.

TABLE 1. Data on the four types of ships considered.

Type of ship	Length at water line (ft)	Beam at water line (ft)	Metacentric height (ft)	Period of roll (sec)
(a)	310	21	1.5	11.1
(b)	173	23	2.0	7.2
(c)	180	33	3.9	7.4
(d)	135	24.5	2.7	6.5

MOTION OF THE SHIP

The ship is assumed to follow a straight course on rough water at constant speed v . At a general time, the position of the ship differs by a rigid body displacement D from the position it would occupy if the water were smooth. The displacement D involves a rigid body rotation; it is assumed that this rotation is always much smaller than one radian, hence this rotation can be decomposed uniquely into pitch, roll, and yaw. Such a decomposition permits a simple mathematical treatment of the motion of the ship, but it has the disadvantage of introducing into the results relative errors comparable with the amplitudes of the angles of pitch and roll. The following assumptions are also made:

1. Yaw is negligible, as compared with pitch and roll.

2. The axes of pitch and roll are mutually perpendicular, do not intersect in general, and are *horizontal at all times*. It may appear to some that these axes should instead be made to follow the ship, either wholly or in part, as it pitches and rolls. Such a question is of no consequence, for the results obtained in all such cases would differ only by quantities comparable with the probable errors of these results.

3. The angles α and β of pitch and roll are given by the expressions

$$\alpha = \bar{\alpha} \sin \omega_p t, \quad \beta = \bar{\beta} \sin \omega_r (t - \bar{t}). \quad (36)$$

Here, α and β are positive when counterclockwise, as observed from the starboard side and the bow respectively; $\alpha = \beta = 0$ when the ship rests on an even keel; $\bar{\alpha}$ and $\bar{\beta}$ are the amplitudes of pitch and

roll, are constants, and are much smaller than unity; t is the time; \bar{t} is a constant specifying the phase difference between pitch and roll when $t = 0$; ω_p and ω_r are the angular frequencies of pitch and roll.

4. The amplitudes $\bar{\alpha}$ and $\bar{\beta}$ have the values $\bar{\alpha} = 1/10$ radian, $\bar{\beta} = 1/5$ radian.

5. The frequency of pitching is twice the frequency of rolling, i.e., $\omega_p = 2\omega_r$.

THE COORDINATE SYSTEMS

Figure 6 shows a diagram of the gun; Δ_1 is the axis of train; the axis of elevation is through P perpendicular to the page; C is the center of gravity of the mass on the trunnions; G is the couple exerted on the gun by the equilibrator; θ is the angle of elevation of the gun.

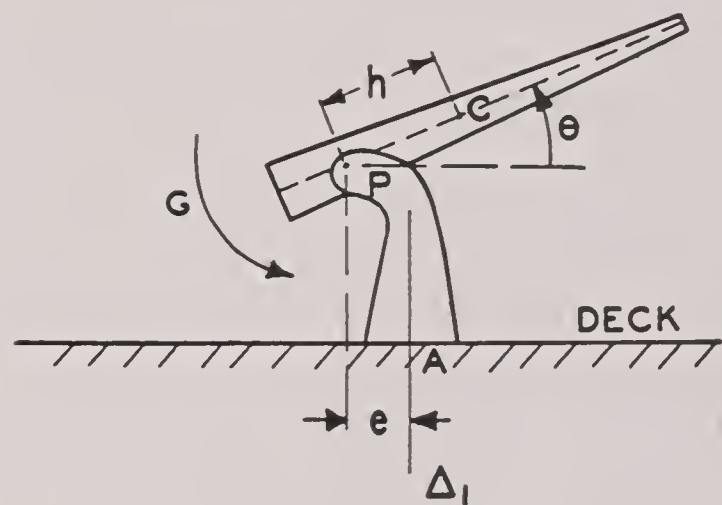


FIGURE 6. The gun.

Figure 7 shows the axis of pitching Δ_2 and the axis of rolling Δ_3 . A Cartesian coordinate system S is introduced. The origin O is on Δ_3 at that point which is closest to Δ_2 . The y axis coincides with Δ_3 and the z axis is vertical as shown. The axes of S thus point in the same directions at all times, but the system as a whole moves forward at a constant speed v .

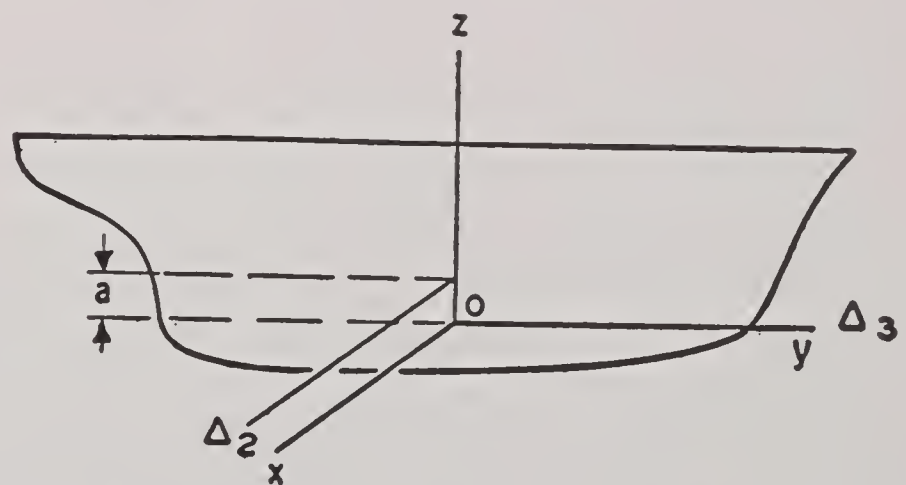


FIGURE 7. The ship; Δ_2 and Δ_3 are the axes of pitch and roll.

A second Cartesian coordinate system S' is introduced. The axes of S' are rigidly attached to the ship and coincide with the axis of S when the ship rests on an even keel. Figure 8 shows the system S' , and also

the quantities specifying the position of the gun on the ship; the line PC again represents the axis of the gun barrel, and ϕ is the angle of train. A third Cartesian coordinate system S'' is also introduced, as shown in Figure 8. The y'' axis coincides with the axis of the gun barrel, and the x'' axis is parallel to the deck at all times.

LAGRANGE'S EQUATIONS

Lagrange's equations of motion are used to obtain the couples delivered to the gun by the gear trains controlling elevation and train. If Q_θ and Q_ϕ denote these couples, it is readily seen from these equations that

$$\begin{aligned} Q_\theta &= \frac{d}{dt} \left(\frac{\partial T}{\partial \dot{\theta}} \right) - \frac{\partial T}{\partial \theta} + \frac{\partial V}{\partial \theta} - G, \\ Q_\phi &= \frac{d}{dt} \left(\frac{\partial T}{\partial \dot{\phi}} \right) - \frac{\partial T}{\partial \phi} + \frac{\partial V}{\partial \phi}, \end{aligned} \quad (37)$$

where T and V are respectively the kinetic and potential energies of the system and the superimposed dot denotes differentiation with respect to time.

THE METHOD OF APPROXIMATION

In order to obtain Q_θ and Q_ϕ , it is only necessary to compute T and V by use of the three coordinate systems S , S' , and S'' , and then substitute in equations (37). This yields very involved expressions for Q_θ and Q_ϕ . Many of the terms in these expressions are small, and since the results already contain a certain probable error, there is no point in retaining those terms that are smaller than the probable error. Accordingly, a systematic method of approximation is introduced whereby a uniform yardstick based on the probable error is introduced and the order of magnitude of each term is estimated. On this basis, it is found that practically all the terms in the expressions for Q_θ and Q_ϕ can be dropped safely.

This method of approximation is called the ϵ method. It has been noted above that the probable error is comparable with the amplitudes of the angles of pitch and roll. The numerical data indicate that the average of these amplitudes is about one-seventh. Accordingly, a dimensionless quantity ϵ is introduced, where $\epsilon = 1/7$. This is the so-called yardstick. In order to indicate the magnitude of a dimensionless quantity n , the expression $n = n_\epsilon \epsilon^\sigma$ is considered, where σ is an integer to be chosen so that n_ϵ is comparable with unity. The quantity σ is thus a measure of the magnitude of n . In order to treat dimensional quantities in a similar fashion, a standard length l equal to

100 ft and a standard time ω_r^{-1} are introduced. Thus, to indicate the magnitude of the velocity v of the ship, the expression $v = l\omega_r^{-1}v_\epsilon \epsilon^\sigma$ is considered, where σ is an integer to be chosen so that v_ϵ , which is dimensionless, is comparable with unity. The quantity σ is thus a measure of the magnitude of v . For a variable which runs through a wide range of values, it is often necessary to consider separately the cases where the variable has different orders of magnitude.

RESULTS

A gun is said to be *amidships* when it is less than forty feet from the center of the deck. It happens that when a gun is amidships the expressions for Q_θ and Q_ϕ differ from those when the gun is not amidships. This is so because the order of magnitude of the quantity c in Figure 8 varies for different positions of the gun on the ship. The results are:

1. When the gun is not placed amidships:

$$\begin{aligned} Q_\theta &= -mc_p h \alpha \cos \theta, \\ Q_\phi &= m(h \cos \theta - e) [\alpha^2(d_p - \alpha c_p)^2 + \beta^2(d_r - \alpha c_p)^2]^{\frac{1}{2}} \cos(\phi + \eta'). \end{aligned}$$

2. When the gun is placed amidships:

$$\begin{aligned} Q_\theta &= mh [-(\alpha^2 d_p^2 + \beta^2 d_r^2)^{\frac{1}{2}} \sin(\phi + \eta) \sin \theta \\ &\quad + (-\alpha c_p + \beta b_r) \cos \theta], \\ Q_\phi &= m(h \cos \theta - e)(\alpha^2 d_p^2 + \beta^2 d_r^2)^{\frac{1}{2}} \cos(\phi + \eta). \end{aligned}$$

In these, the notation is as follows:

$$\begin{aligned} m &\text{ is the mass on the trunnions,} \\ b_r &= \omega_r^2 b, \quad c_p = \omega_p^2 c, \\ d_p &= \omega_p^2 d + g, \quad d_r = \omega_r^2 d + g, \\ \tan \eta &= \frac{\alpha d_p}{\beta d_r} \quad (0 \leq \eta < 2\pi), \\ \tan \eta' &= \frac{\alpha(d_p - \alpha c_p)}{\beta(d_r - \alpha c_p)} \quad (0 \leq \eta' < 2\pi). \end{aligned}$$

To obtain Q_θ and Q_ϕ at any time, it is only necessary to substitute for α and β in the above expressions from equations (36).

Further, a determination is made of two quantities M_θ and M_ϕ , which are defined respectively as the maximum values which $|Q_\theta|$ and $|Q_\phi|$ can attain for given θ and ϕ at any given position on the ship as it pitches and rolls. In other words, M_θ and M_ϕ are obtained by maximizing $|Q_\theta|$ and $|Q_\phi|$ with respect to α and β . Hence M_θ and M_ϕ are functions of the position of the gun on the ship and of θ , ϕ , h and e . The expressions obtained for M_θ and M_ϕ are too complicated to reproduce here. It is assumed that

$m = 3,750$ lb, and numerical values of M_θ and M_ϕ are computed for the previously mentioned 3-in. gun mounted at seven different positions on each of the four ships referred to in Table 1. Of these seven positions, five are equally spaced along that center line of the deck which is parallel to the keel and two are located at the ends of that center line of the deck which is perpendicular to the keel. These results are presented in the form of a number of graphs from which the values of M_θ and M_ϕ can be determined when the gun is mounted at any one of the seven positions on any one of the four ships and the quantities θ , ϕ , h and e have any given values. For example, when the gun is at the bow of ship (a) and $\theta = 30$ degrees, $\phi = 120$ degrees, $h = 2.5$ ft, and $e = 0.75$ ft, it is found that $M_\phi = 2,120$ lb-ft.

6.4.2 Gun Equilibrators II

As mentioned above, a determination was made of the couples delivered to a gun by the gear trains controlling elevation and train when the gun is mounted on a horizontal floor and is made to execute simultaneously simple harmonic oscillations in elevation and in train. The gun was the same one considered in Section 6.4.1, namely, the 3-in. 50-mount Mark 24, Model 1, modified to include an equilibrator.

THE METHOD

The approach to the problem is precisely that used in Section 6.4.1, but with the motion of the ship set equal to zero. The gun is as shown in Figure 6. The coordinate systems S and S' coincide at all times, and the origins of these systems are taken at the point where the axis of train cuts the deck (or factory floor). Thus, in the notation of Figure 8, $b = c = 0$ and $d = f$. Equations (37) are again used for the determination of the required couples Q_θ and Q_ϕ . The method of approximation is not required, since the motion of the ship and the attendant probable error in the results do not enter here.

THE RESULTS

It is found that:

1. The required couples Q_θ and Q_ϕ are given by the expressions

$$\begin{aligned} Q_\theta &= \ddot{\theta}(K+B) + \dot{\phi}^2 K \sin \theta (\cos \theta - L), \\ Q_\phi &= K \{ \ddot{\phi} [(\cos \theta - L)^2 + N] - 2\dot{\phi}\dot{\theta} \sin \theta (\cos \theta - L) \}, \end{aligned}$$

where the superimposed dots denote differentiations with respect to time, m is the mass on the trunnions, A is the moment of inertia of the mass m about an axis

through its center of gravity and perpendicular to its axis, B is the axial moment of inertia of the mass m , I is the moment of inertia about the train axis of the rotating parts of the gun exclusive of the mass m , and

$$K = mh^2 + A - B, \quad L = \frac{mhe}{K},$$

$$N = \frac{I + B + m^2}{K} - L^2.$$

These results are derived with no assumptions as to the type of motion the gun is to perform.

The particular factory test is considered in which

$$\theta = \frac{\pi}{4} + \frac{\pi}{6} \sin\left(\omega t - \frac{\pi}{2}\right), \quad \phi = \frac{\pi}{6} \sin\left(\omega t - \frac{\pi}{2}\right),$$

where t is the time and ω is the so-called circular frequency of oscillation. It is to be noted that the elevation θ oscillates about $\theta = \pi/4$ with amplitude $\pi/6$, the train ϕ oscillates about $\phi = 0$ with ampli-

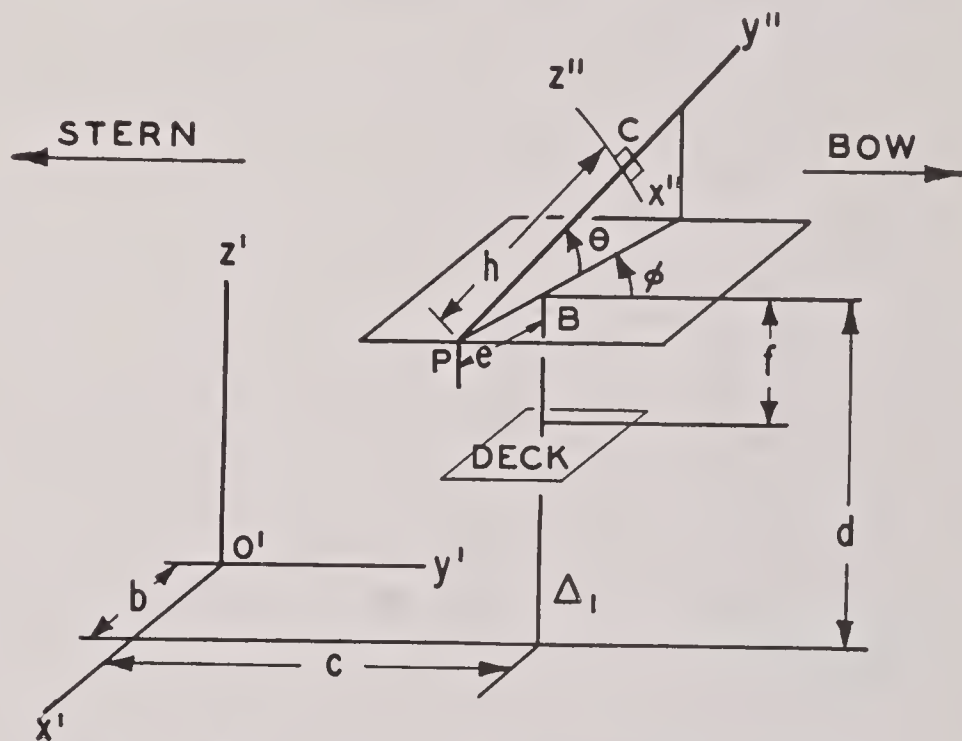


FIGURE 8. The position of the gun on the ship; PC is the axis of the gun barrel.

tude $\pi/6$, and $t = 0$ when the gun is at the low point of its swing. In this case, the maximum values of $|Q_\theta|$ and $|Q_\phi|$ are denoted by $M'(e, h)$ and $M(e, h)$, where e and h are as shown in Figure 6. It is found that:

2. For the factory test under consideration

$$M'(e, h) = \frac{\pi}{6} \omega^2 (mh^2 + A),$$

if and only if

$$e \leq \frac{(mh^2 + A)(12 + \pi) - \pi B}{4\pi mh \cos \pi/12}, \quad (38)$$

and this value of M' is assumed at the top and bottom of the oscillation. Condition (38) is satisfied when $0 \leq e \leq h$.

In all practical cases, the mounting of the gun is such that $e \leq h$, and the formula for $M'(e, h)$ given here holds. It is to be noted that $M'(e, h)$ is independent of e . An analogous theorem for $M(e, h)$ cannot be obtained easily.

The problem is also considered of choosing e and h so that M' and M are minima. In the case of M' , the answer follows easily from theorem 2 above. In the case of M , the problem is much more difficult. However, the following numerical data are introduced:

$$m = \frac{3,750}{32.2} \text{ slugs, } I = 1,500 \text{ slug-ft}^2,$$

$$A = 1,200 \text{ slug-ft}^2, \quad B = 2.93 \text{ slug-ft}^2,$$

and Q_ϕ is tabulated for $0 \leq h \leq 4$ ft and $e \leq h$. From these tabulations, Q_ϕ is graphed for various values of e and h in the ranges indicated. An examination of these graphs leads to the following result, which is valid, of course, only in the indicated ranges:

3. For the factory test under consideration, if h is such that $0 \leq h^2 \leq \sqrt{3}(A - B)/m$, then M is a minimum when $e = h \cos \pi/12$; this minimum is

$$R = \frac{\pi}{6} \omega^2 \left[(A - B) \cos^2 \frac{\pi}{6} + I + B \right],$$

and occurs at the bottom of the oscillation. As e is increased from zero to $h \cos \pi/12$, M decreases monotonically to its minimum value R . On the other hand, if h is such that $h^2 > \sqrt{3}(A - B)/m$, then M is a minimum when $e = \sqrt{6}(mh^2 + A - B)/4mh$; this minimum is

$$\frac{\pi}{6} \omega^2 \left[(mh^2 + A - B) \frac{mh^2 + 3(A - B)}{8mh^2} + I + B \right],$$

and occurs at the bottom of the oscillation.

In all practical cases, $h^2 < \sqrt{3}(A - B)/m$ and hence the minimum value obtainable for M is R .

6.5 CLEARANCE OF LAND MINES

A mathematical analysis was performed of two mechanical devices for exploding land mines.¹³ Both types consist essentially of a drum mounted with its axis horizontal and made to rotate about its axis. Attached to the surface of the drum are a number of short chains (or ropes with weights at their ends) which flail the ground. For purposes of identification, the two types will be referred to as Types A and B.

6.5.1

Type A

In Type A, the radius of the drum is relatively small, and the length of the chains is a little more than the clearance between the drum and the ground. The drum is rotated at high speed, and the ends of the chain do a certain amount of digging into the surface of the ground.

It is required to find the power expenditure of the machine. In order to obtain this, the ground is treated as a rigid body with a plane horizontal surface, and the power expenditure is attributed to the following: (1) the kinetic energy lost on impact of the chain and ground, (2) the work done on dragging the chain over the ground.

In order to obtain a rough approximation to the energy lost on impact, a system is considered which consists of two homogeneous rigid bars OA and AB , hinged together at A and mounted to rotate about a horizontal axis through O . The distance from this axis to the ground is equal to the length of the bar OA ; the bar AB thus represents that portion of the chain which eventually comes in contact with the ground. It is assumed that at the moment of impact the bars OA and AB form a straight line and possess the same angular velocity ω . By means of the standard theory of impacts, the energy lost on impact is readily found to be

$$E_i = \frac{1}{24} m a^3 \omega^2 n (1 + n) (4 + 3n),$$

where m is the mass per unit length of the bars and a and na are the lengths of the bars OA and AB , respectively. This energy is lost once during each revolution. The power expenditure is thus

$$P_1 = \frac{\omega}{2\pi} E$$

for each chain.

To obtain a rough approximation to the work done in dragging the chain along the ground, the system considered above is again introduced, but with the bar AB replaced by a chain of the same length. It is assumed that, on the average, one half of this length of chain is in contact with the ground during the entire dragging operation, and hence the work done during this operation is readily found to be

$$W = \mu m g b \sqrt{2ab}.$$

The power expenditure is then

$$P_2 = \frac{\omega}{2\pi} W$$

for each chain.

The total power expenditure for each chain is $P_1 + P_2$. This value is far below that encountered in actual practice, which indicates that considerable power is expended in breaking up the ground. Because of this and the fact that the breaking up of the ground produces a heavy cloud of dust which obscures the vision of the operator, it was deemed advisable to devise a mechanical mine exploder that flailed the ground without actually breaking it up. This exploder is the one referred to above as Type B.

6.5.2

Type B

In the mechanical mine exploder of Type B the radius of the drum is much larger than for Type A, and the clearance between the drum and ground is just sufficient to permit the passage of the drum over the normal small irregularities of the surface of the ground. Flexible flails are attached to points on the surface of the drum.

If R is the radius of the drum and ω is its angular velocity, the drum is pushed forward with a velocity V which is just a little smaller than $R\omega$. In this way the flails are alternately wound onto the drum and slapped against the ground. Also, the flails strike the ground with almost normal velocity and in being wound onto the drum they are dragged along the ground only enough to keep them taut. This minimizes the expenditure of power and the creation of dust.

Of course the mass of a flail can be distributed along its length in an arbitrary manner. However, for mathematical convenience the flail is assumed to consist of a length of light rope with a concentrated mass attached to the end. By use of the Lagrange form of the equations of motion, it is found that the determination of the trajectory of the mass hinges on the differential equation

$$\frac{d^2p}{d\tau^2} = 1 + \eta(\cos \sqrt{2p} + \tau),$$

where η is a constant ($\eta = g/R^2$, g being the acceleration due to gravity). In most practical cases, η is much smaller than 1 and a solution of this differential equation can be obtained easily in the form of a power series in η . The trajectory of the mass follows from this solution, and the impact speed of the mass and the resultant energy loss can then be computed. Since there are $\omega/2\pi$ impacts per flail per unit of time, the total power expenditure of the machine can be determined easily.

It is suggested that the flails consist of about 6 ft of light rope, with 2 ft of heavy chain attached to it. It is also suggested that a model of Type B be constructed and tested to obtain the effect on the operation of the machine of various parameters, such as the clearance of the drum above the ground and the distribution of mass along the flail. This model could conveniently be such that the axis of the drum is fixed and the flails strike a moving belt which serves as the ground.

6.5.3

Conclusions

The mechanical mine exploder of Type A wastes considerable power in digging up the surface of the ground and at the same time generates a cloud of dust which obscures the vision of the operator. In Type B, this power loss is not present, and the design is such as to reduce the dust to a minimum.

Type A has been in operation for some time. Recent reports indicate that Type B has been tested and has proved superior to Type A.

6.6

THE WILLIAMS GAGE

Evaluation of the readings obtained with a Williams gage requires the discussion of the following problem. A piston moves into one end of a cylinder which is closed at the other end. The motion of the cylinder is engendered by the action of an outside pressure which is a known function of time. It is required to find the displacement of the piston when it first reverses its direction of motion. A preliminary study was carried out.¹⁴ This study, which does not tackle this problem but is rather concerned with the physical assumptions to be introduced in its ultimate study, will now be surveyed.

Two modes of attack are suggested. According to the first, it is assumed that at any given instant all the air inside the cylinder is under the same pressure, which then can be computed from the volume of this mass of air by means of the adiabatic law. This approach is justified only if the velocity of the piston is considerably below the velocity of sound. The second manner of attack, much more complicated but exact, takes account of the pressure waves set up by the moving piston and of their successive reflections at the closed end of the cylinder and at the moving piston.

In order to get an approximate idea of the difference between results furnished by these two ap-

proaches, the following simplified problem is studied. A piston, starting from rest, is pushed with a constant velocity into a cylinder which is closed at the other end. It is required to find the pressure exerted on the piston by the enclosed air as a function of time (or displacement of the piston).

For the first manner of approach, the answer can be given immediately. If p denotes the pressure and ρ the density, the adiabatic law is $p = p_0(\rho/\rho_0)^k$, where $k = 1.4$, and p_0 and ρ_0 are the initial values of p and ρ . By hypothesis, at any instant the density throughout the air enclosed in the cylinder is constant. If at the time t the piston has moved a distance x into the cylinder and if l denotes the original length of the enclosed column of air, then

$$p = p_0 \left(\frac{l}{l-x} \right)^{1.4}. \quad (39)$$

For the second manner of approach, the solution is more complex and will now be discussed briefly.

6.6.1 Compression Shock Waves

At the time $t = 0$ the piston is at the open end $x = 0$ of the cylinder, and its velocity is increased instantaneously from zero to W . This velocity is imparted to the air particles in contact with the piston, and at a later time t' this velocity will have been transmitted to all the air particles situated originally between the plane $x = 0$ and some plane $x = \xi$. Of course t' must be small enough so that ξ is less than the length l of the cylinder. Thus, for $x < \xi$, the air has a velocity W and constant pressure p_1 , density ρ_1 , and absolute temperature T_1 . For $\xi < x < l$, the air is at rest and has a constant pressure p_0 , density ρ_0 , and absolute temperature T_0 . The discontinuity surface $x = \xi$ is termed a *shock wave*. This shock wave moves with a constant velocity D , so that $\xi = t'D$.

The condition of continuity and the theorems of momentum and energy furnish conditions which must be satisfied by p , ρ , and T at the two sides of the shock wave. This yields the relations

$$\begin{aligned} \sigma &= 1 + 3\tau + (7\tau + 9\tau^2)^{\frac{1}{2}}, \\ \rho_1 &= \frac{6\sigma + 1}{6 + \sigma} \rho_0, \quad D = \frac{W}{5} \left(\frac{6\sigma + 1}{\tau} \right)^{\frac{1}{2}}, \end{aligned} \quad (40)$$

where $\sigma = p_1/p_0$ and $\tau = W^2 \rho_0 / 5p_0$.

When the shock wave reaches the end of the cylinder, it is reflected toward the piston in such a way that the air between the reflected wave and the

closed end of the cylinder is again at rest. This air has a constant pressure p_2 , density ρ_2 , and absolute temperature T_2 . By proceeding as in the case of equations (40), it is found that

$$\begin{aligned} \sigma' &= 1 + 3\tau' + (7\tau' + 9\tau'^2)^{\frac{1}{2}}, \\ \rho_2 &= \frac{6\sigma' + 1}{6 + \sigma'} \rho_1, \\ D' &= \frac{W}{5} (6 + \sigma') [\tau' (6\sigma' + 1)]^{-\frac{1}{2}}, \end{aligned} \quad (41)$$

where $\sigma' = p_2/p_1$ and $\tau' = W^2 \rho_1 / 5p_1$.

When this shock wave reaches the piston it is reflected toward the closed end of the cylinder. After this reflection it moves into a region at rest from a region possessing the constant velocity W , so that in order to obtain the values p_3 and ρ_3 valid in the region between the piston and the second outgoing shock wave, it is only necessary to apply equations (40) with p_0 , ρ_0 and p_1 , ρ_1 replaced by p_2 , ρ_2 and p_3 , ρ_3 .

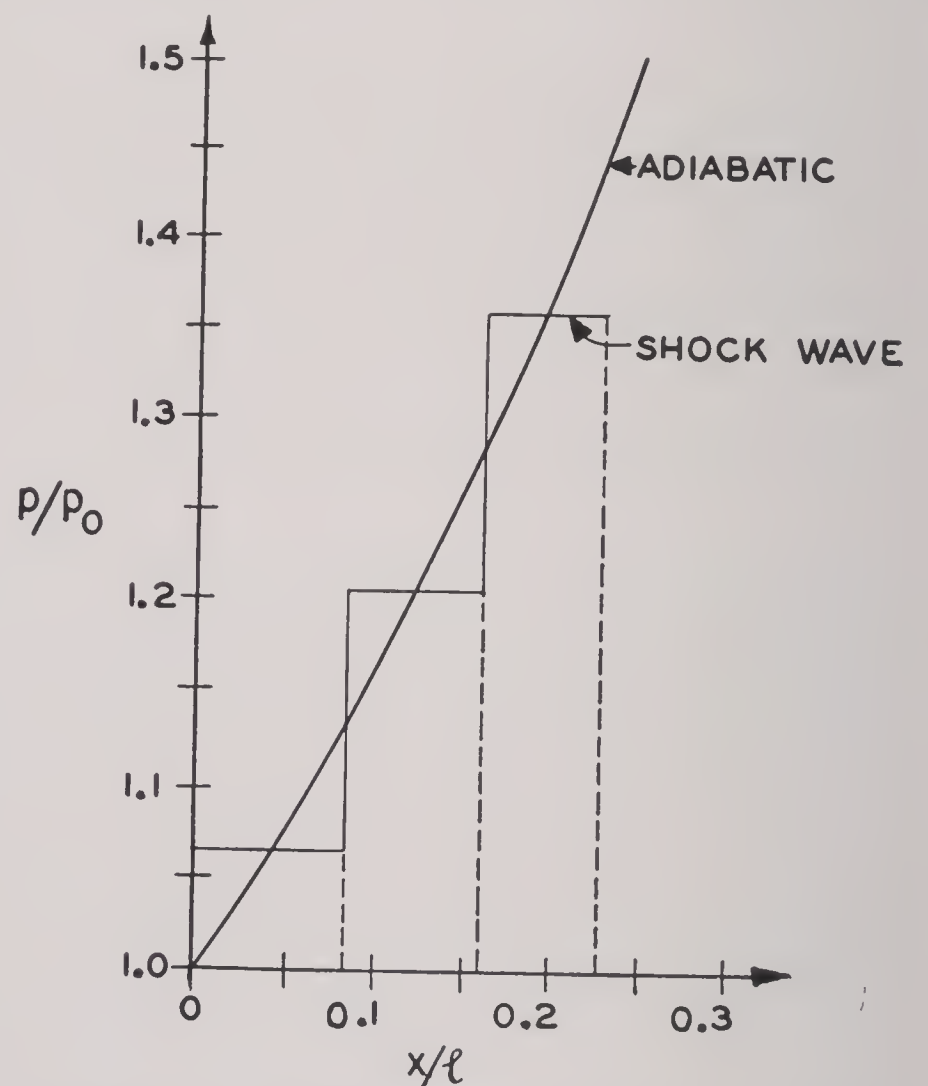


FIGURE 9. Pressure distribution when $W = 50$ fps.

In similar fashion, by the alternate use of equations (40) and (41) it is possible to determine at any given time the values of p and ρ as well as the position and velocity of the shock wave. If then, the length l , the piston velocity W and the initial conditions in the cylinder are specified, the pressure on the piston can be determined as a function of the displacement x of the piston.

The shock wave approach to the problem predicts constant pressure on the piston for short intervals during its motion; the pressure-displacement curves are consequently just step functions. The magnitude of the pressure over each constant interval and the lengths of successive intervals depends on the piston velocity W .

Two specific examples throw considerable light on the relative predictions of the adiabatic and shock wave approaches. In the first a large piston velocity $W = 300$ fps is considered; in the second the comparatively slow speed of $W = 50$ fps is considered. The initial conditions assumed for the air in the cylinder are standard conditions of temperature, pressure, and density. Figures 9 and 10 show the pressure-displacement curves obtained for the two piston velocities; in these figures, p_0 is the standard atmospheric pressure and p/p_0 is plotted against x/l where l is the length of the cylinder. Both the adiabatic and shock wave predictions are drawn for comparison.

It is apparent that the agreement between the adiabatic and the shock wave predictions is much better in the case of the lower piston velocity; the pressure jumps are much smaller in this case and occur at positions of the piston which are much nearer to each other.

6.6.2 Maximum Displacement of Piston

The preceding results are based on the assumption that the piston is pushed into the cylinder with constant velocity. Actually the piston is exposed to an outside pressure which rises very quickly to a high value and then drops off to practically zero in a very short time. For purposes of a first estimate, such an exterior pressure might be idealized into an impulse which instantaneously communicates a certain initial velocity to the piston. From then on, the piston moves under the influence of atmospheric pressure on the outside and the pressure of the enclosed air on the inside. The maximum displacement of the piston can then be found from the energy principle if the law according to which the inside pressure varies with the displacement of the piston is known. If this pressure law is denoted by $p = F(x)$, the maximum displacement X is found from the following formula

$$\frac{1}{2}mv_0^2 = \int_0^X p_0 A \left(\frac{F(x)}{p_0} - 1 \right) dx. \quad (42)$$

The left side of this equation is the change in kinetic energy experienced by the piston of mass m in coming to rest from its initial velocity v_0 , while the right side is the work done, A denoting the area of the cross section of the cylinder.

If the integral on the right side of (42) is evaluated for both the graphs of $F(x)/p_0$ appearing in Figure 9, it is found that the results differ by little. Hence it is permissible to use the simple expression given in (39) for $F(x)$ in order to evaluate X by means of (42). For a certain brass piston it is found that $X = 0.54l$. A similar procedure in the case of Figure 10 indicates that if the simple expression (39) is used for $F(x)$, the resulting value of X cannot be relied upon. Thus for the lower piston velocity the adiabatic approach seems adequate, while for the higher piston velocity this is not the case.

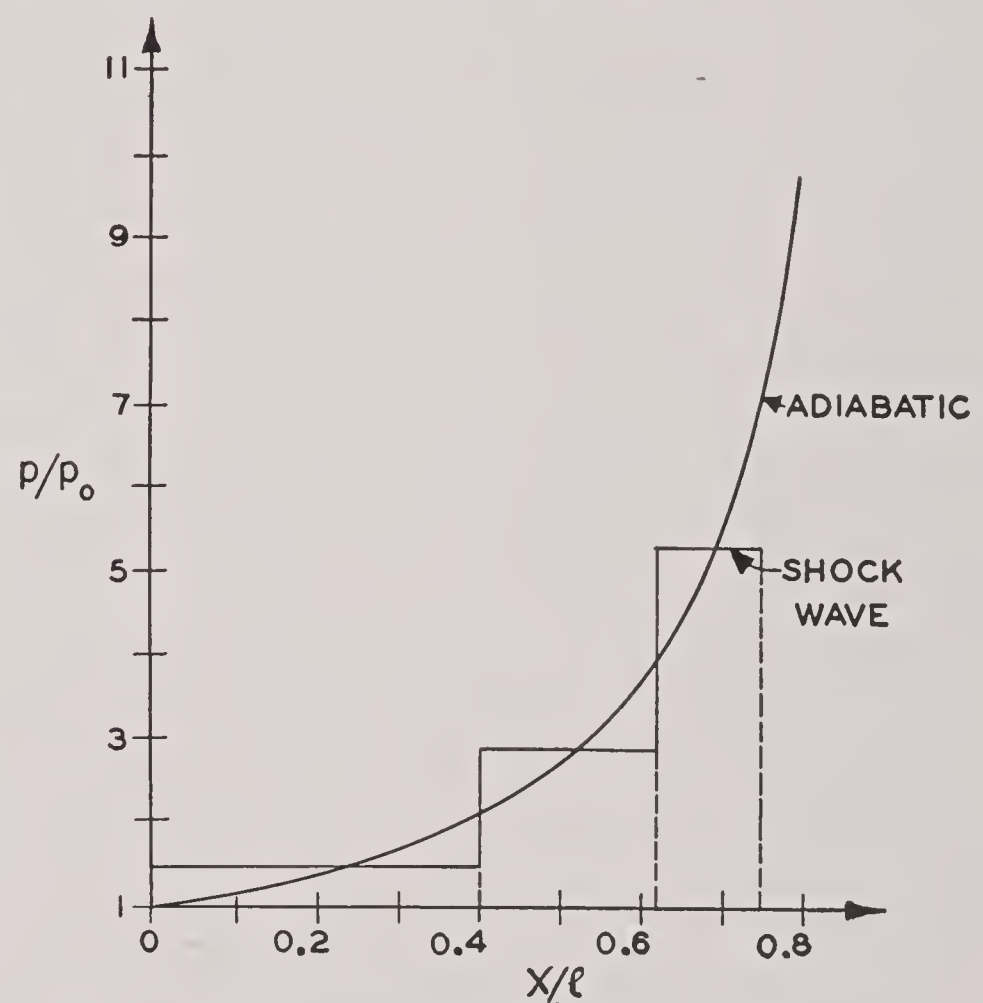


FIGURE 10. Pressure distribution when $W = 300$ fps.

6.7 CENTRIFUGAL CASTING

In connection with consulting work for the War Metallurgy Division of NDRC, a study was carried out by dimensional analysis concerning the influence of various variables on the De Lavaud process of centrifugal casting of pipes.^{15, 17}

For the convenience of the discussion, the De Lavaud process is divided into two stages, *pouring* and *solidification*. The pouring is primarily controlled by mechanical variables, while the solidification is controlled by the heat transfer across the walls of the mold.

In the case of a *mold with horizontal axis*, the mechanical variables which appear to be of importance are: d , the diameter of the pipe; t , the thickness of the wall of the pipe; n , the number of revolutions per minute of the mold; V , the speed of the mold in the direction of its axis; Q , the pouring rate (expressed as volume per unit time); ρ , the density of the molten metal; μ , the viscosity of the molten metal at the pouring temperature. The dimensionless parameters characterizing the pouring stage are then

$$\frac{Q}{nd^3}, \frac{d}{t}, \frac{V}{nd}, \frac{nd^2\rho}{\mu}.$$

If the *axis of the mold is inclined under the angle β against the horizontal*, the additional parameter

$$\frac{g \sin \beta}{n^2 d}$$

should be introduced (g = acceleration of free fall). From this consideration of these parameters the following rule is derived: *for a set of pipes of various diameters but constant ratio d/t , the pouring rate should be proportional to the diameter, the axial speed of the mold inversely proportional to the diameter, the rotational speed of the mold inversely proportional to the square of the diameter, and the inclination of the axis of the mold measured by $\sin \beta$ should be inversely proportional to the cube of the diameter*. In establishing these rules, the pouring temperature has been assumed constant and all effects of the heat transfer across the walls of the mold have been disregarded.

As regards the solidification stage, at least the following additional variables must be taken into account: h is the coefficient of heat transfer, i.e., the heat energy flow across the wall of the mold per unit area and unit time and per degree of temperature difference inside and outside the mold; c is the specific heat of the molten metal (per unit of mass); θ is the difference between the pouring temperature and the temperature of the outer surface of the mold; and k is the increase of viscosity per degree of temperature drop. The introduction of these variables necessitates the introduction of the following additional parameters:

$$\frac{k\theta}{\mu}, \frac{h}{ncd\rho}.$$

If the pouring temperature is kept constant, the following additions must therefore be made to the rules given above: *the temperature drop across the walls should be kept constant, while the coefficient of heat*

transfer should be inversely proportional to the diameter. The limitations of the method of dimensional analysis have been discussed.

6.8 OPTICAL BARS OF RANGE FINDERS

This study¹⁶ is concerned with the problem whether the thermal deflections of the optical bar of a range finder can be reduced by suitable cutouts in the webs of this bar. The optical system of a range finder is usually mounted in a hollow bar which is supported in a statically determinate manner. For obvious reasons this bar, like all other parts of the range finder, should be as light as possible. On the other hand, the customary type of optical system is extremely sensitive to any bending of the bar, such as may be produced by its weight or by accidental temperature differences existing across its width. Thus there arises the problem of designing a bar which, for a given weight per unit length has maximum bending stiffness under transverse loads (weight of bar and optical system) as well as under temperature differences existing across its width. As is well known, the deflections produced by the bar's own weight can be reduced by suitable cutouts in the webs of the bar. The question arises whether such cutouts would also prove useful in reducing the thermal deflection of the bar.

The report on this study begins with a review of the basic equations of thermoelasticity, with particular mention of the equivalent loads, i.e., the fictitious body and surface forces which would produce the same deformations as the given temperature changes. It is shown that the thermal stresses produced by a given temperature change $\theta - \theta_0$ are obtained by superimposing the hydrostatic pressures $\alpha K(\theta - \theta_0)$ on the stresses produced by the equivalent loads (α = coefficient of thermal expansion, K = bulk modulus, θ_0 = uniform initial temperature). In particular, it is shown that the thermal stresses vanish whenever the gradient of the temperature θ is constant, provided the surface of the body is free from stresses. In this case a cutout will not influence the thermal deformations. Indeed, the vanishing of the thermal stresses shows that there is no interference between the thermal deformations of adjacent portions of the body. The cutting away of a portion of the body has therefore no influence on the thermal deformations of the remainder.

Before these results can be applied to the problem on hand, an assumption must be made regarding the

temperature field by which the thermal deformations and stresses in the optical bar are produced. Actually, the optical bar is mounted in a thermoinsulated tube. Since the temperature distribution on the outer surface of this tube may vary considerably, there is little sense in trying to apply the theory of heat conduction to the determination of the temperature distribution in the interior of the tube. Instead, it seems reasonable to assume certain temperature fields inside the tube and to determine the corresponding deformations. It is true that the actual temperature field will be influenced to a certain extent by the design of the bar. For instance, when a constant temperature difference is maintained across the width of the surrounding tube, the temperature difference across the width of an optical bar inside the tube may be smaller for a solid bar than for a bar with numerous cutouts. This is certainly so if heat convection through motion of the air inside the tube is excluded. The opposite may be true, however, when such convection is taken into account. In view of this un-

certainty, discussion of too complicated temperature fields does not seem justified.

A uniform temperature increase produces a uniform expansion of the bar which has no detrimental influence on the optical system.

A temperature increase of constant gradient produces pure flexure of the bar. Since the optical system is extremely sensitive to this flexure, the question arises whether the amount of bending produced by a given temperature gradient can be reduced by giving an appropriate shape to the bar. Unfortunately, the result discussed above shows that this is not possible.

Since the amount of thermal flexure of a bar made of a given isotropic elastic material cannot be reduced by giving an appropriate shape to the bar, other means of circumventing the difficulty are suggested. One possibility is to reduce the temperature gradient inside the insulating tube by forced convection caused by a small fan. Redesign of the optical system so as to make it less sensitive to flexure of the optical bar is also suggested.

Chapter 7

MECHANICS OF A CONTINUUM

7.1 INTRODUCTION

THE MATHEMATICAL theory of elasticity deals with a theoretical treatment of bodies which are deformed when acted upon by forces but which resume their original states when the forces are removed. On the other hand, the mathematical theory of plasticity deals with a theoretical treatment of bodies which are deformed when acted upon by forces but which do not resume their original states when the forces are removed. In other words, plastic bodies undergo permanent distortion while elastic bodies do not. A number of studies undertaken by AMP involve the mathematical theories of elasticity and plasticity. These studies are considered in this chapter.

7.2 ENERGY IN A PLASTIC DIAPHRAGM

In this study a plane diaphragm is considered¹ which is clamped along its circular contour and then permanently deformed by the action of an explosion occurring at some distance from the diaphragm. The center of the explosion is situated on the normal to the plane of the circular diaphragm drawn through its center, consequently the deformation of the diaphragm can be expected to have rotational symmetry. Now if the energy absorbed in the plastic deformation of the diaphragm could be evaluated it would furnish an indication of the intensity of the explosion. The question to be answered is whether this energy of deformation can be evaluated if only the final (permanent) deformation of the diaphragm is known and not the intermediate states of deformation through which it has passed. More precisely, this report aims at a complete statement of the problem as well as a clear discussion of the assumptions which must be made concerning the plastic behavior of the diaphragm material in order to make such an evaluation of the energy of deformation possible.

7.2.1 True Stress and True Strain

The study of this question is complicated by the fact that, for the diaphragms under consideration, the

deformation can by no means be described as infinitesimal. Consequently the notion of stress and strain as defined in the theory of elasticity is no longer adequate.

The simple case of a tension test is first considered. In the classical theory of small deformations, the stress σ and strain ϵ are defined by the relations

$$\sigma = \frac{P}{A_0}, \quad \epsilon = \frac{L - L_0}{L_0},$$

where P is the load, A_0 is the area of the original cross section, L_0 is the original length, and L is the final length. These definitions are hardly justified in the testing of materials where the average strains at rupture may run from 30 to 60 per cent. To overcome this difficulty, P. Ludwigh² proposed to define "true tensile strain" in the following manner. The process of stretching is decomposed into infinitesimal steps. The unit extension at a given step is found by dividing the increase of elongation dL at that step by the instantaneous length L . The total unit extension is defined by integrating these results, that is,

$$\epsilon = \int_{L_0}^{L_1} \frac{dL}{L} = \log \frac{L_1}{L_0} \quad (1)$$

where L_0 is the initial length and L_1 is the final length. The strain ϵ , as defined in equation (1), is known as the *logarithmic strain* or *true strain*. The average true tensile stress σ at any phase of the test is defined by

$$\sigma = \frac{P}{A},$$

where P is the axial force and A the actual cross-sectional area at the given instant. Analogously, the *true reduction in area* q can be defined by the relation

$$q = \log \frac{A_0}{A}.$$

These concepts can be generalized to a state of three-axial stress³ without much difficulty, as follows. A rectangular parallelepiped is considered, the sides of which have the original lengths $L_{1,0}$, $L_{2,0}$,

and L_3 , and the faces of which carry the normal loads P_1 , P_2 , and P_3 , as shown in Figure 1. At a given

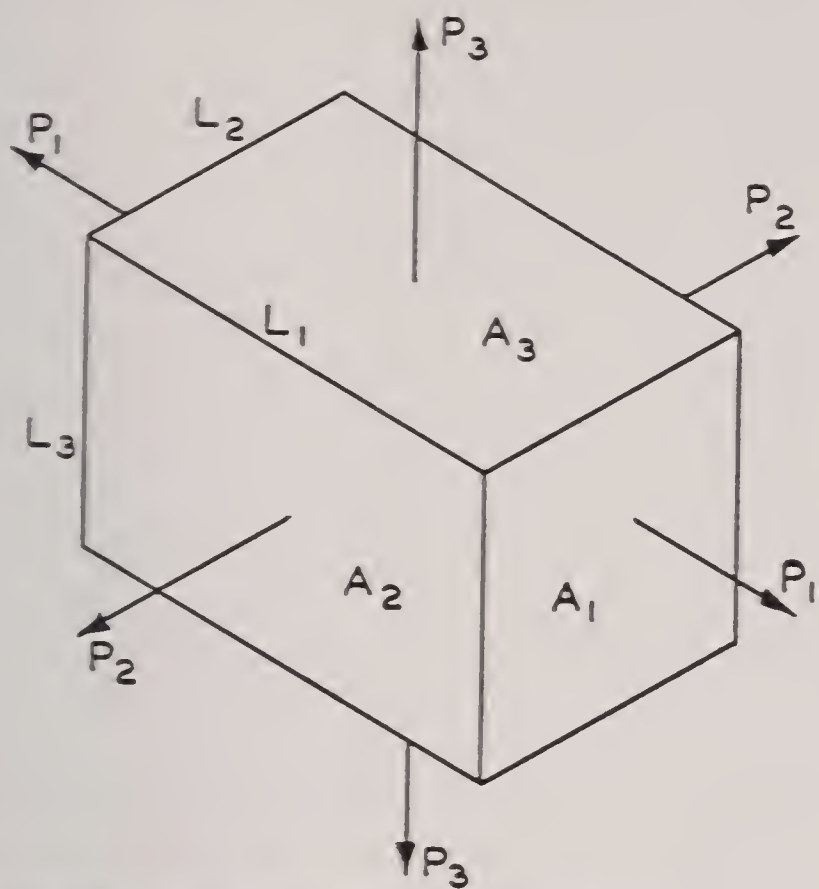


FIGURE 1. The state of three-axial stress.

instant, when the lengths of the sides of the parallelepiped are L_1 , L_2 , and L_3 , the true strains are

$$\epsilon_1 = \log \frac{L_1}{L_{1,0}}, \quad \epsilon_2 = \log \frac{L_2}{L_{2,0}}, \quad \epsilon_3 = \log \frac{L_3}{L_{3,0}}.$$

The true stresses are defined by the relations

$$\sigma_1 = \frac{P_1}{A_1}, \quad \sigma_2 = \frac{P_2}{A_2}, \quad \sigma_3 = \frac{P_3}{A_3},$$

where A_1 , A_2 , and A_3 are the instantaneous areas of the faces carrying the loads P_1 , P_2 , and P_3 , respectively. The "true cubic dilatation" is defined to be $\log (V/V_0)$, where V is the instantaneous volume and V_0 is the original volume. Thus

$$\log \frac{V}{V_0} = \log \frac{L_1 L_2 L_3}{L_{1,0} L_{2,0} L_{3,0}} = \epsilon_1 + \epsilon_2 + \epsilon_3 = 3\epsilon,$$

if ϵ is by definition equal to $(\epsilon_1 + \epsilon_2 + \epsilon_3)/3$. For an incompressible material $\epsilon = 0$. The "true reduction in area" for the face A can be shown to be

$$q_1 = -(\epsilon_2 + \epsilon_3),$$

or $q_1 = \epsilon_1$ for an incompressible material.

7.2.2 Work of Deformation

It is assumed that throughout the deformation the loads remain normal to the faces on which they act and these faces remain perpendicular to each other, that is, the principal axes of stress and strain are supposed to coincide and remain fixed with respect

to the material. While the sides of the parallelepiped increase in length by amounts dL_1 , dL_2 , and dL_3 , the forces P_1 , P_2 , and P_3 perform the work

$$\begin{aligned} dW &= P_1 dL_1 + P_2 dL_2 + P_3 dL_3 \\ &= V_0 e^{3\epsilon} (\sigma_1 d\epsilon_1 + \sigma_2 d\epsilon_2 + \sigma_3 d\epsilon_3). \end{aligned}$$

The work per unit volume of the undeformed body is given by the relation

$$W = \int e^{3\epsilon} (\sigma_1 d\epsilon_1 + \sigma_2 d\epsilon_2 + \sigma_3 d\epsilon_3),$$

where the integration covers the entire deformation from the undeformed initial state to the present deformed one. If the material is incompressible,

$$W = \int \sigma_1 d\epsilon_1 + \sigma_2 d\epsilon_2 + \sigma_3 d\epsilon_3. \quad (2)$$

It is to be noted that these results hold only for the assumptions made about the principal axes of stress and strain. Fortunately these assumptions are permissible in the problem in question.

7.2.3 Stress-Strain Relations for Incompressible Material

The following expressions are formed by use of the true components of stress and strain:

$$S = \sqrt{\frac{1}{2}[(\sigma_1 - \sigma_2)^2 + (\sigma_2 - \sigma_3)^2 + (\sigma_3 - \sigma_1)^2]}^{\frac{1}{2}},$$

$$E = \sqrt{\frac{2}{9}[(\epsilon_1 - \epsilon_2)^2 + (\epsilon_2 - \epsilon_3)^2 + (\epsilon_3 - \epsilon_1)^2]}^{\frac{1}{2}}.$$

If the material is incompressible, then $\epsilon_1 + \epsilon_2 + \epsilon_3 = 0$, and the last expression takes the form

$$E = \sqrt{\frac{2}{3}[\epsilon_1^2 + \epsilon_2^2 + \epsilon_3^2]}^{\frac{1}{2}}.$$

The following conditions are expected to hold for the problem in question:

1. Throughout the deformation, the principal axes of stress and strain coincide and remain fixed with respect to the material.

2. The material is incompressible, that is, $3\epsilon = \epsilon_1 + \epsilon_2 + \epsilon_3 = 0$ throughout the deformation.

3. The strains determined the stresses only to within a hydrostatic state of stress. In other words, a state of stress in which no shearing stresses occur and in which the magnitude of the normal stress is independent of the orientation of the surface element may be added without affecting the strains.

Thus it is natural to introduce the stress deviation, a tensor which has the same principal axes as the stress tensor and the principal values

$$s_i = \sigma_i - \sigma, \quad (i = 1, 2, 3),$$

where $\sigma = (\sigma_1 + \sigma_2 + \sigma_3)/3$ is the mean normal stress. Similarly, the strain deviation is a tensor

which has the same principal directions as the strain tensor and the principal values

$$e_i = \epsilon_i - \epsilon, \quad (i = 1, 2, 3).$$

If the material is incompressible, $e_i = \epsilon_i$.

4. The strain deviations are such that the ratio of e_1 to e_2 to e_3 is constant at any given point in the material throughout the deformation. This assumption means that the final state of stress E is reached in just one way. If the strain at any point in the material is represented by a point E in a space with coordinate axes e_1 , e_2 , and e_3 as shown in Figure 2, this assumption

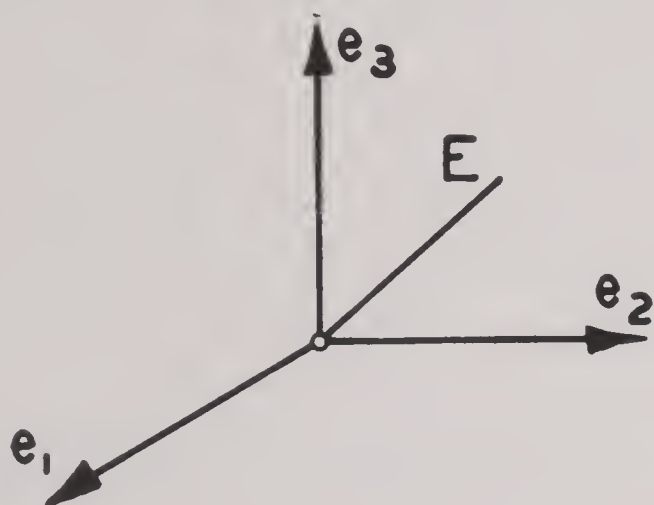


FIGURE 2. The principal strain space.

tion requires that the state of strain be reached by traveling on a straight line from the origin to E . In general, the state of stress in a plastic material is not independent of the way in which the final strain is reached; consequently, such an assumption is needed to compute the work of deformation on the basis of the final strain alone.

5. No reversal of the sense of deformation occurs. In other words, the rate of flow $\dot{E} = dE/dt$ is positive throughout the deformation.

6. The rate of flow $\dot{E} = dE/dt$ varies so little that its influence on the stress-strain relations may be neglected.

Under these assumptions the stress-strain laws may be expected to reduce to equations between the tensors of stress and strain only. To each strain tensor, there corresponds a unique stress tensor independent of how the state of strain has been reached; the converse need not be true, however. It has been observed from certain experiments^{4, 5} that the following relations hold:

$$\frac{s_1}{e_1} = \frac{s_2}{e_2} = \frac{s_3}{e_3}. \quad (3)$$

Equation (3) states that the point S corresponding to the strain E will lie on the same straight line through

the origin as E , as shown in Figure 3. This equation may be rewritten in the form

$$\frac{\sigma_1 - \sigma_2}{\epsilon_1 - \epsilon_2} = \frac{\sigma_2 - \sigma_3}{\epsilon_2 - \epsilon_3} = \frac{\sigma_3 - \sigma_1}{\epsilon_3 - \epsilon_1} = \lambda, \quad (4)$$

a relation previously noted by Nadai.⁶

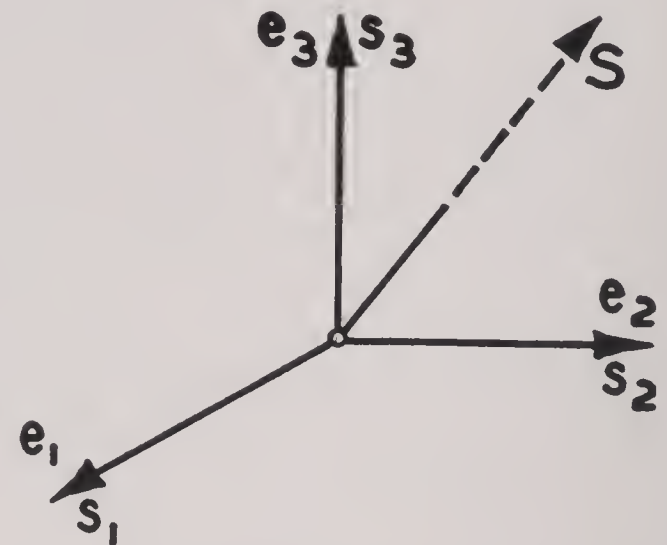


FIGURE 3. The stress-strain relations in the stress-strain space.

If in the tensile test it is found that $\sigma_1 = f(\epsilon_1)$, it is to be expected that for more general types of stress $S = f(E)$. For instance, C. W. MacGregor has found⁷ that true-stress vs true-strain curves for the tension test become straight lines after the point of maximum load is reached.

Elementary manipulations with the definitions of E and S as well as equations (4) yield the relations

$$\sigma_1 = \sigma + \frac{2S}{3E}\epsilon_1, \quad \sigma_2 = \sigma + \frac{2S}{3E}\epsilon_2, \quad \sigma_3 = \sigma + \frac{2S}{3E}\epsilon_3,$$

from which it can be shown that

$$W = \int_0^E f(E) dE = F(E). \quad (5)$$

Thus, as long as no unloading occurs, the work done depends only on the final value of E . If the material is purely plastic, no deformations occur upon unloading and $W = F(E)$ without restriction as to the avoidance of unloading. For most technical materials, the amount of energy regained by unloading is small if large deformations have been produced. Consequently equation (5) can be considered as valid to a rather high degree of accuracy for the problem in question.

7.2.4 Application to a Deformed Circular Diaphragm

Equation (5) shows that if the function $f(E)$ is known from experiment, or more directly the function $F(E)$, then the energy absorbed in deformation can be computed once E is known. This section will

be devoted to showing how E can be computed for a circular diaphragm.

The diaphragm is assumed to have no bending stiffness. In other words, if x_1 and x_2 are coordinates in the plane of the diaphragm and x_3 the coordinate normal to the diaphragm, then

$$\sigma_1 = \sigma_1(x_1, x_2), \quad \sigma_2 = \sigma_2(x_1, x_2), \quad \sigma_3 = 0.$$

It is not assumed, however, as in the case of a membrane, that $\sigma_1 = \sigma_2 = \text{constant}$. For the type of loading under consideration, it can be shown that assumption 1 of Section 7.2.3 is fulfilled and that the principal axes are the radius vector from the center to an arbitrary point in the diaphragm, the normal to the plane of the diaphragm, and the perpendicular to these two directions. Any point on the circle of radius r in this diaphragm will have displacement components u in the direction of the radius and w perpendicular to the plane of the diaphragm. If h_0 is the original thickness of the diaphragm and h the thickness after deformation, then the circumferential strain ϵ_t , the normal strain ϵ_z , and the radial strain ϵ_r are given by the relations

$$\begin{aligned} \epsilon_t &= \log \left(1 + \frac{u}{r} \right), \quad \epsilon_z = \log \frac{h}{h_0}, \\ \epsilon_r &= \frac{1}{2} \log \left[\left(1 + \frac{du}{dr} \right)^2 + \left(\frac{dw}{dr} \right)^2 \right] \\ &= \log \left[1 + \frac{du}{dr} + \frac{1}{2} \left(\frac{dw}{dr} \right)^2 \right] \end{aligned} \quad (6)$$

for deformations which are not too large.

These strains can be measured experimentally in the following way. The diaphragm is covered with concentric circles and radii. Then ϵ_t may be found directly by measuring the extension of an arc of a circle between two radii making a small angle with each other, for it is simply \log (new length/old length). By measuring the thickness before and after the deformation, one can compute ϵ_z from equations (6). If the material is assumed to be incompressible, the radial strain ϵ_r is given by the relation

$$\epsilon_r = -(\epsilon_t + \epsilon_z).$$

Thus the energy of deformation can be computed from these measured strain values according to equation (5), provided the relationship between W and E is known for the material under consideration.

7.3 ROCKET PROPELLANTS

In connection with a much wider program of research on rocket projectiles being carried on by the

Allegany Ballistics Laboratory, the Applied Mathematics Group at Brown University was asked to study possible explanations of the breakup in cylindrical powder grains used in the H-4.5 rocket.⁸ Two such mechanisms have been considered, buckling of the grain as a thin column and yielding of the grain with particular reference to the influence of differences in pressure between the inside and outside burning surfaces. A sketch of the grain is shown in Figure 4. In particular, the grain studied has as

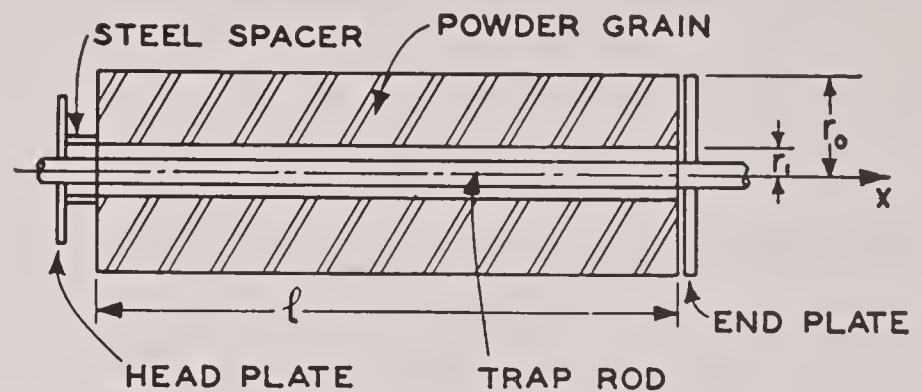


FIGURE 4. The H-4.5 powder grain.

dimensions in the unburned state the inside radius $r_1 = 7/32$ in., outside radius $r_0 = 39/64$ in., and length $l = 20$ in. Since burning takes place both inside and outside, the inside radius increases and the outside radius decreases during flight. Any changes in length caused by burning are ignored. The steel spacer prevents horizontal motion of the grain during ordinary handling, but it does not prevent elongation of the grain caused by elastic forces during burning.

The grain is subject to the following system of forces during flight: a uniformly distributed inertia or setback force caused by the acceleration of the rocket, a normal pressure distribution on the outside of the grain, and a normal pressure distribution on the inside of the grain.

7.3.1 Buckling of Powder Grains

The possibility of buckling of the powder grain is split into two parts, buckling under uniformly distributed inertia forces and buckling under variation of gas pressure along the length of the grain. In a strict sense, both loadings should be considered simultaneously; such a division, however, simplifies the mathematical considerations and shows the relative importance of each of these factors. The end conditions are assumed to be those of pin end supports. This seems to be within the limits of accuracy set for the whole problem.

A thin elastic beam on pin supports is considered, subject to a uniformly distributed load of intensity q

lb in.⁻¹ as well as an end thrust of P pounds. The total length of the bar is l , the Young's modulus of the material is E , I is the polar moment of inertia of the cross section about an axis through the centroid perpendicular to the plane of bending, and the x and y axes are directed as shown in Figure 5. The differ-

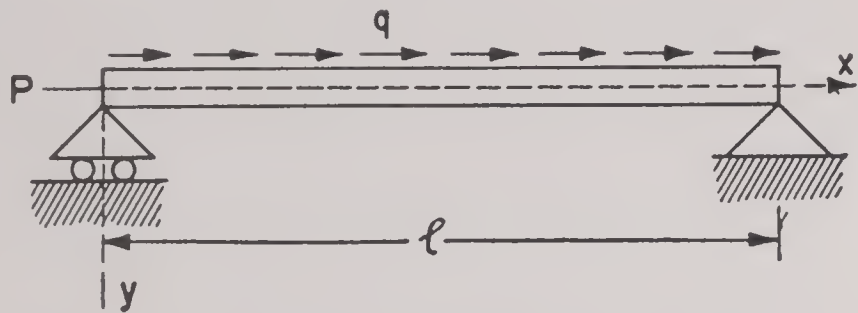


FIGURE 5. Forces in acceleration buckling.

ential equation governing the deflection, the boundary conditions, and the buckling loads are given by S. P. Timoshenko.⁹ The deflection $y(x)$ must satisfy the differential equation

$$\frac{d^4 y}{dx^4} + \frac{qx + P}{EI} \frac{d^2 y}{dx^2} + \frac{q}{EI} \frac{dy}{dx} = 0, \quad (7)$$

and the boundary conditions

$$y(x) = \frac{d^2 y(x)}{dx^2} = 0 \quad \text{at} \quad x = 0 \quad \text{and} \quad x = l. \quad (8)$$

Now equation (7) is homogeneous. Consequently, there are no nontrivial solutions $[y(x) \neq 0]$ which satisfy the boundary conditions for all values of q and P . There are such solutions only for certain critical values which define the critical or buckling loads. For the problem under consideration, $P = 0$ and the critical load is found to be

$$ql = 1.86 \frac{\pi^2 EI}{l^2}.$$

The total inertia force is given by $ql = NW$, where N is the acceleration of the grain expressed in G 's and W is the weight of the grain. If γ denotes the specific weight of the grain, r_0 the outside radius, and r_1 the inside radius during any stage of burning, the critical acceleration in G 's is given by

$$N_{cr} = \frac{1.86 \pi^2 E}{r l^3 \gamma} (r_0^2 + r_1^2). \quad (9)$$

Experimental evidence indicates that the area S of the burning surface remains constant. Therefore r_0 and r_1 are related by the formula

$$S = 2\pi(r_0 + r_1)l. \quad (10)$$

Since S can be calculated from the dimensions of the unburned grain, equations (9) and (10) can be used

to find N_{cr} as a function of r for various values of E . The results of this computation are shown in Figure 6. Since flight records indicate maximum accelerations of over 200 G 's, Figure 6 shows that the critical

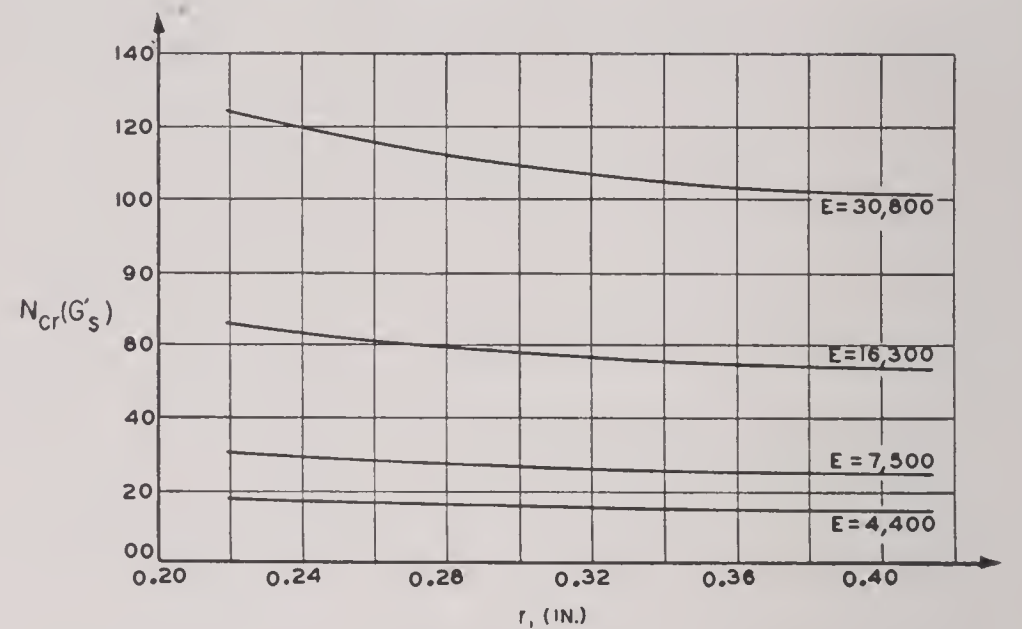


FIGURE 6. Critical acceleration (N_{cr}) versus inside radius (r_1) for various values of Young's modulus (E).

accelerations are far exceeded and buckling takes place.

A second type of buckling is that caused by variation in the gas pressure along the length of the grain. In particular, it is assumed that the gas pressure varies linearly, i.e., the pressure $p(x)$ is given by the relation

$$p(x) = \bar{p}_0 \left(1 - k \frac{x}{l} \right),$$

where \bar{p}_0 is the pressure at the head end ($x = 0$). The grain, pressure distribution, coordinate axes, and end conditions are shown in Figure 7. The basic

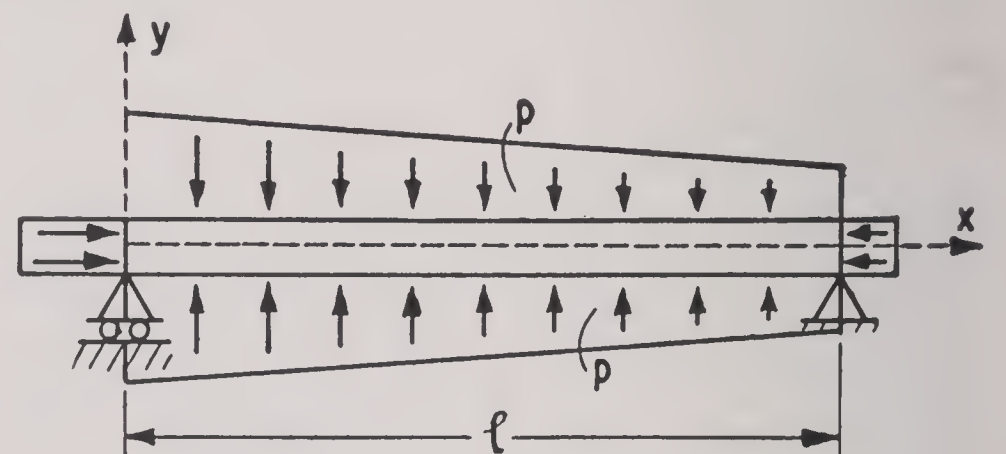


FIGURE 7. Forces in pressure buckling.

differential equations can be derived by first determining the resultant of the gas pressure on a curved element. A simple consideration of the geometry of the deformed element will show that this resultant is $-pAy''dx$ acting in the negative y direction (A is the area of the cross section). The forces acting on the element (gas pressure, pulls P , shears S , and bending moments M) are shown in Figure 8. Equilibrium

conditions and the Euler-Bernoulli law for the bending of this beam lead to the differential equation

$$\frac{d^2M}{dx^2} + \frac{kP}{EI}M = 0, \quad (11)$$

where P is the total head force ($P = \bar{p}_0 A$). The boundary conditions are

$$M(0) = M(l) = 0. \quad (12)$$

Equation (11) can be solved in terms of Bessel functions of order $1/3$. Again, solutions cannot be

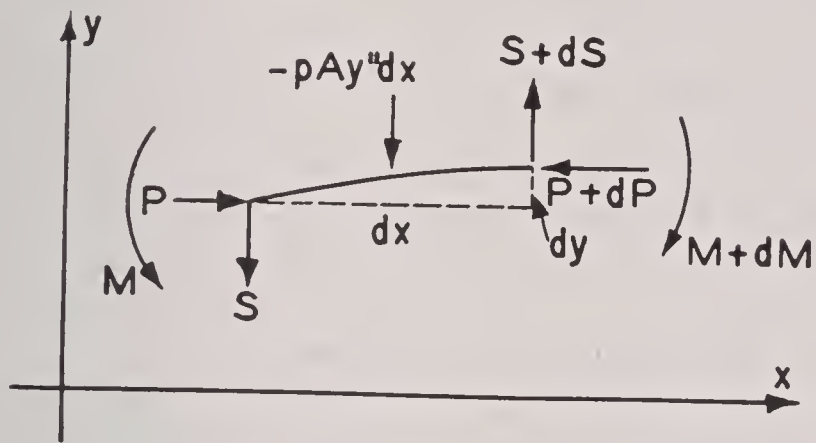


FIGURE 8. An element of the grain in the buckled state.

found which satisfy the boundary conditions (12) for all values of P but only certain critical loads. It can be shown that the critical head pressure is given by the relation

$$(\bar{p}_0)_{cr} = 18.956 \frac{E}{4kl^2} (r_0^2 + r_1^2). \quad (13)$$

Experimental evidence indicates that $k = 0.07$ for the H-4.5 rocket. Equation (13) has been evaluated under the assumption in equation (10) which indicates a constant burning surface; the results are shown in Figure 9. These graphs indicate that for

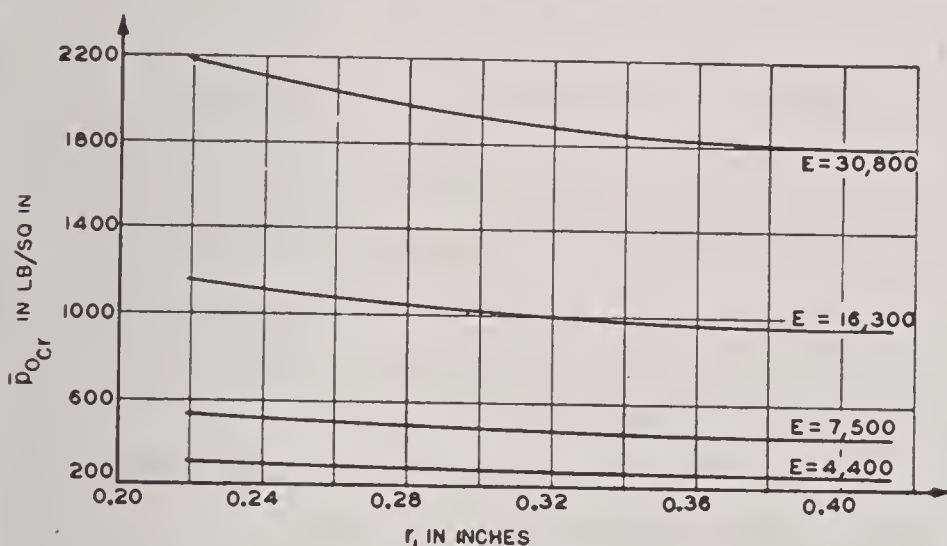


FIGURE 9. Critical head pressure $[(p_0)_{cr}]$ versus inside radius (r_1) for various values of Young's modulus (E).

small values of Young's modulus, 16,300 lb in.⁻², 7,500 lb in.⁻², and 4,400 lb in.⁻², the critical pressures are far below those encountered either in flight tests or static tests. On the other hand, the critical

values corresponding to $E = 30,800$ lb in.⁻² are within the range of some of the pressures found in tests.¹⁰ It is possible that under these conditions buckling is not caused by gas pressure. This is somewhat more plausible if account is taken of the supporting action of the trap wire and increased support from the end conditions. Under these circumstances, the grain may not fail in static tests where only gas pressure exists but it may very well fail in flight when high acceleration loads are added.

In the case of acceleration loads as well as in the case of pressure loads, the performance is improved if E is increased or the length l of the individual grain is decreased. Both critical loads vary directly with Young's modulus; the critical acceleration varies as $1/l^3$ and the critical pressure as $1/l^2$. A decrease in the length of the grain to perhaps two-thirds its present size would be a considerable improvement.

7.3.2 Yielding of Powder Grains with Overpressure

It is possible that the internal stresses in the powder grain may be so high that the yield condition for the material is exceeded and failure results. In particular, differences in gas pressure between the inside wall and the outside wall may have a noticeable affect on plastic deformation. This section is an attempted study of such effects.

The grain is assumed to undergo the following loading conditions: a pressure p_1 distributed over the outer surface of the grain, a pressure p_0 distributed over the inner surface of the grain, a constant pressure \bar{p}_0 applied at the head end of the grain, and an acceleration stress in the axial direction $-N\gamma z$ where N is the acceleration in G 's and γ is the specific weight. Such a distribution of loads gives rise to three internal stresses, an axial stress σ_z , a radial stress σ_r , and a hoop stress σ_θ . These stresses depend only on r and z and not on θ .

The yield condition is assumed to be of the Hendy-von Mises type,¹¹ which reduces to

$$(\sigma_r - \sigma_z)^2 + (\sigma_r - \sigma_\theta)^2 + (\sigma_\theta - \sigma_z)^2 = \text{constant}. \quad (14)$$

The left side of equation (14) represents the equivalent tensile stress t . The maximum value of this equivalent tensile stress, which is denoted by t_{\max} can be found by evaluating equation (8) by use of the analysis of stresses in a thick tube under constant pressure.¹² The final equation becomes

$$t_{\max} = \left[3 \left(\frac{p_1 - p_0}{r_0^2 - r_1^2} \right)^2 r_0^4 + \left(\frac{p_1 r_1^2 - p_0 r_0^2}{r_0^2 - r_1^2} + N\gamma z + \bar{p}_0 \right)^2 \right]^{\frac{1}{2}}. \quad (15)$$

Equation (15) has been evaluated for various combinations of the parameters involved including several different overpressures $p_1 - p_0$. The yield stress is exceeded in all cases as the wall thickness diminishes in burning, and the higher the overpressure the earlier this will occur. Consequently, circular vents in the grain should decrease overpressure and this tendency toward failure. A more complete discussion of this possibility depends on an accurate experimental study of the mechanical properties of the material used in forming the grain. At present, this information is unfortunately lacking.

7.4 SHELL STRESSES

At the request of Division 1 of NDRC, a summary was prepared of the work done in this country and in England on the problem of the design of projectiles from the point of view of strength.¹³ This problem is significant, since the shell must not fail structurally on passing through the gun barrel and since the shell must be as light as possible in order to maximize the charge carried, insure proper fragmentation, and minimize wear on the gun.

7.4.1 The Shell

Figure 10 shows a sketch of a fairly typical shell. The side walls of the shell are thin and the base rela-

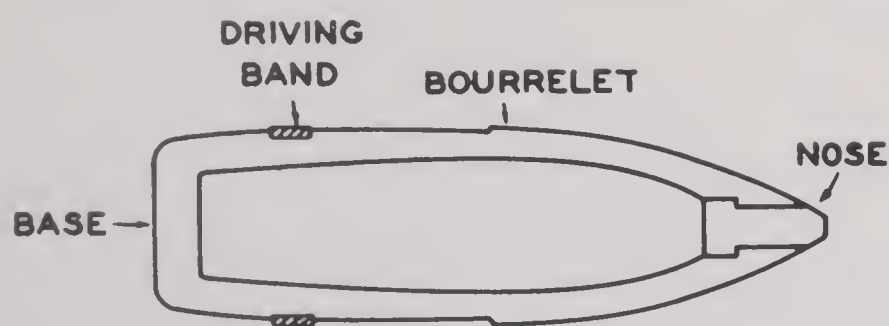


FIGURE 10. A typical shell.

tively thick. A driving band of soft metal such as copper is shrunk into a groove in the side walls, as shown. The outside diameter of this driving band is greater than the bore of the gun, and when the shell is forced into the gun the driving band is "engraved" by the rifling. As a consequence, a good seal is effected and the shell is set in rapid rotation about its axis as it passes down the gun barrel. The bourrelet is made to fit the gun barrel snugly, so that the shell will be centered in the gun barrel.

The forces acting on the shell can be classified as three types:

1. The gas pressure p_G , which acts on the base and the portion of the side walls back of the driving band. In practice, p_G is of the order of 30,000 to 40,000 psi.
2. The pressure p_B exerted by the driving band. Static tests indicate that p_B ranges from 30,000 to 90,000 psi.
3. Inertia forces due to the forward and angular acceleration imparted to the shell and filling.

7.4.2 Summary of Work in the U.S.A.

Work on the problem apparently has been done or is planned by four different groups in this country. Each group will be considered in turn.

WORK AT ORDNANCE DEPARTMENT

Methods are used which permit an approximate determination of the stresses in the shell by analytical means. The forward acceleration of the shell is computed by neglecting the retarding force due to friction between the driving band and the inner surface of the gun barrel. Once this acceleration is known, it is possible to calculate the pressure p_F exerted on the base of the shell by the filling. The radial stresses in the base are then computed from the theory of a thin circular plate subjected to a pressure $p_G - p_F$, even though the base does not qualify too well as a thin plate.

In the side walls of the shell, the stress due to the pressure exerted by the driving band is neglected. The following stresses are taken into account: (1) the stress exerted across a cross section perpendicular to the axis of the shell and due to the inertia forces of the part of the shell ahead of the cross section; (2) the stress due to the inertia forces rising from the rotation of the shell and its filling. The results obtained here suffer from the fact that formulas are used which apply strictly to a cylinder of uniform thickness, of infinite length, and subjected to loads which do not vary along the cylinder.

In general, the above procedures lead to values of stresses in base and side walls which are too low.

WORK AT CATHOLIC UNIVERSITY

This work consists of a mathematical part and an experimental part. In the former, an analytical determination is made of the stresses and deformations in an infinite uniform hollow cylinder acted upon by a pressure distributed uniformly over a narrow ring

around the outside of the cylinder. The solution is in the form of an infinite series.

In the experimental work, a 37-mm shell is forced into a 6 in. long section of a 37-mm gun tube which has been turned down on the outside so that the outside diameter has been reduced considerably. The band pressure is inferred from the increase in the outside diameter of the tube. Pressures of the order of 40,000 psi are found.

WORK AT WATERTOWN ARSENAL

Work has been done at the Watertown Arsenal which is similar to the experimental work done at Catholic University, except that the 75-mm gun is used. Band pressures ranging from 30,000 to 90,000 psi have been found, and no good explanation of this wide variation has been given.

At the Watertown Arsenal an experimental determination of the strains in a gun during actual firing is being carried out. This is being done by means of strain gauges placed on the gun barrel in such a way as to measure both longitudinal and circumferential strains. It is hoped that it will be possible to separate the effects of powder pressure and band pressure.

WORK AT ABERDEEN PROVING GROUND

A revision and clarification of shell design formulas is being carried out. Also, an attempt is being made to introduce the effect of band pressure into design formulas.

7.4.3 Summary of Work by the British

Much more work has been done on shell design by the British than by this country. A set of formulas has been devised for the approximate analysis of the stress in shells. It is proposed to check these formulas in the case of a wide range of designs by comparison with stresses computed accurately by means of the so-called relaxation process. This method is essentially one in which the equations of elasticity are replaced by equivalent difference equations which are solved by iteration. This method is laborious and in addition it must be carried out for each shell design. It has been found, among other things, that the band pressure tends to reduce the stresses in the base by almost 50 per cent in some cases.

The British have also experimented with shells having a very low safety factor. Results indicate that the factor of safety could be reduced much below customary values without risk of failure.

The magnitude of the band pressure has been studied in actual firings in which the strains on the outside of the gun are measured. It is found that the band pressure is of the order of 30,000 to 40,000 psi, which is the same as the order of the powder pressure.

The proper design of the driving band has been considered also. A shell with two driving bands was tested. The front band was turned down so that there was no excess copper, and the rear band was designed to effect the seal. Strain gauges attached to the gun barrel indicate that the band pressure is negligible in this case.

This summary of work by the British is incomplete, since many relevant documents were not available to the author of AMP 75.1R.¹³ A partial bibliography is given in this report.

7.5 THERMAL INSULATION

It has been observed that certain materials used for thermal insulation fail to give the proper insulation when they are compressed. For example, if a person sits on a down quilt placed on a cold object, the cold comes through quickly. On the other hand, if a piece of reindeer fur is used, good insulation is obtained. The reason for this is that the down quilt is compressed and loses its air spaces, which should supply the insulation, while the reindeer hairs, which are hollow tubes and are arranged almost parallel to the reindeer skin, do not collapse and hence continue to provide insulation.

Since reindeer fur is rather bulky, a study was undertaken¹⁴ to throw some light on the possibility of manufacturing a thermal insulator which would stand up under compression, this insulator to consist of hollow circular tubes arranged much as the cigarettes in a pack, the direction of the compression being perpendicular to the axes of the tubes.

7.5.1 The Mathematical Problem

A pad is considered consisting of a large number of hollow circular tubes packed closely together with their axes parallel. The cross section of the pad perpendicular to the axes is a rectangle. The four sides of the pad are subjected to a uniform pressure p , and the ends of the pad, which are perpendicular to the axes of the tubes, are free. It is desired to determine mathematically the maximum stress in the tubes.

Each tube inside the pad touches each of the six

adjacent tubes along a narrow surface. It is assumed that the resultant reaction P at each contact is

$$P = \frac{2\pi R_1}{6} p,$$

where R_1 is the outer radius of each tube. In order to obtain a rough approximation to the required maximum stress, the following are found: (1) the maximum stress at the contact surface; (2) the maximum stress in a hollow tube subjected to an external pressure p .

7.5.2

Results

In the case of (1), it is found from the known theory of elastic bodies in contact that the width b of the contact strip and the maximum stress q_0 (which occurs at the center of this strip) have the values

$$b = 1.1R_1 \sqrt{\frac{p}{E}}, \quad q_0 = 0.6 \sqrt{pE},$$

where E is Young's modulus, and Poisson's ratio is

taken to be 0.3. It is to be noted that q_0 is independent of the wall thickness.

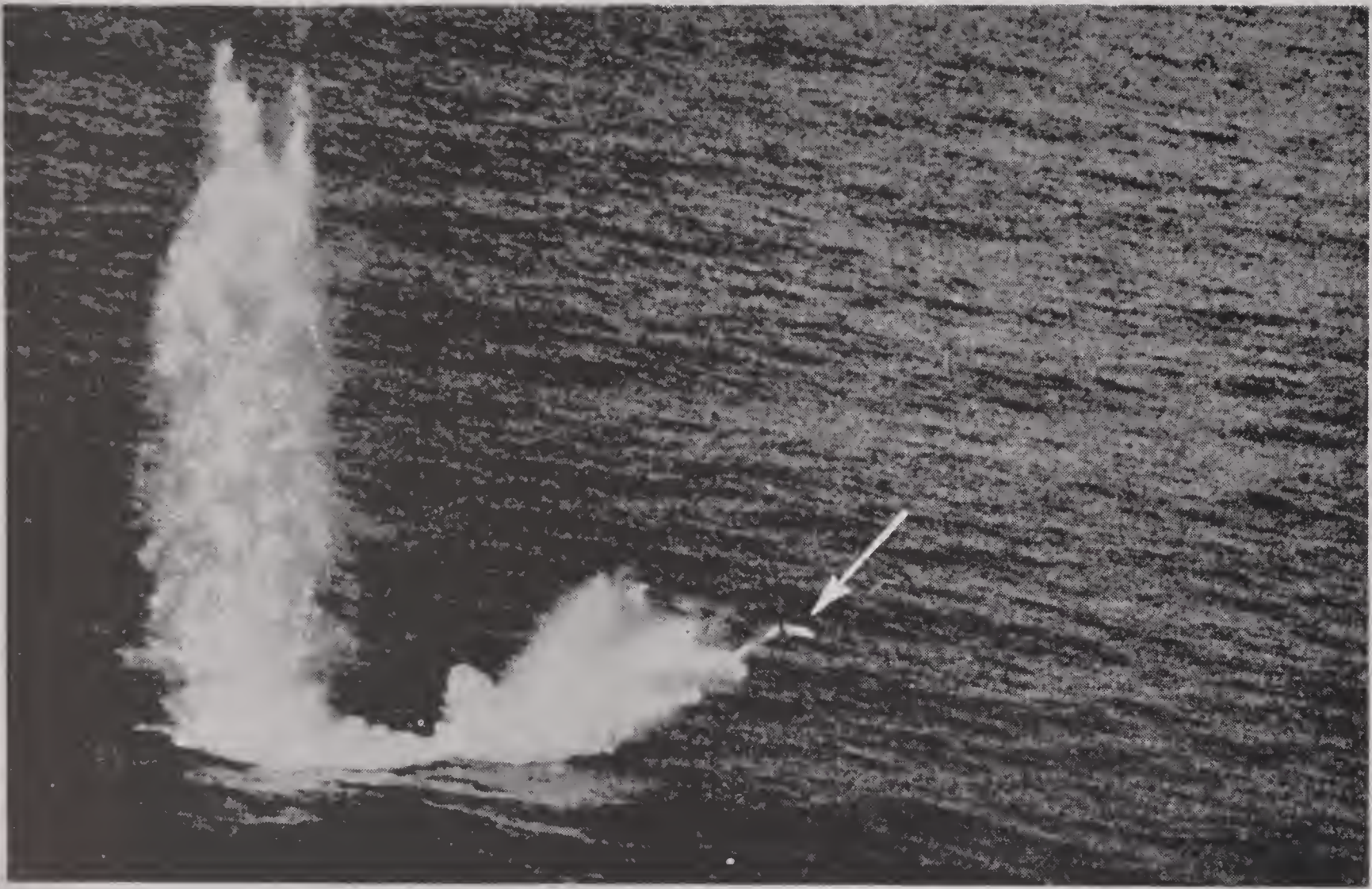
In the case of (2), the theory is well known. The maximum stress q_1 occurs on the inner boundary and has the value

$$q_1 = \frac{2pR_2^2}{R_2^2 - R_1^2}, \quad (16)$$

where R_2 is the inner radius. If the tube has thin walls, equation (16) can take the form $q_1 = p/\epsilon$, where $R_2 = (1 - \epsilon)R_1$.

A glass fibre is considered of outside diameter 0.1 mm and thickness such that $\epsilon = 1/10$. The pressure p is taken to be 4 psi. (This is about the body pressure that occurs in practice.) It is found that $q_0 = 2,400$ psi and $q_1 = 400$ psi. Since the breaking stress of glass is of the order of 25,000 psi, it thus appears that glass could be used safely. Rayon could also be used.

The case was also considered where the tubes are arranged in layers with the axes of the tubes at right angles in alternate layers. Stresses of the same order of magnitude as those above are obtained.



Ricochet of aircraft depth bomb (NOL).

PART IV

UNDERWATER BALLISTICS

CONFIDENTIAL

Chapter 8

DESCRIPTIVE SUMMARY

8.1 STATEMENT OF PROBLEM

WE SHALL be concerned here with the mechanics of entry and underwater motion of projectiles entering the water at high speeds. Although it is not the purpose of this report to enter in detail into

They apply to all aircraft-launched torpedoes and mines and all depth charges (attacks from the air or surface against submarines). They apply to bombs, rockets, and HE shell intended to explode underwater (where damage to the target is usually greatest), as well as to cases where ricocheting bombs, artillery shell, or small-caliber bullets might endanger the releasing aircraft or bystanders (see Figures 1 and 2). They also apply to the mechanism of wounding by bullets and high velocity fragments of bombs, grenades, and shell, to ricochet of artillery shell from dirt surfaces, etc.^{12a,15,36}

For this reason, the physical variables involved cover a wide range of numerical values. Entry speeds range from 25 fps ("ash cans" rolled from destroyers) to 2,500 fps (high-velocity shell) or even more (bomb fragments at 8,000 fps). The entry angles range from 3° with the horizontal ("Shark" antisubmarine projectile fired from ship's deck) to nearly 90° (high-altitude mines, etc.). The head shape is often flat, hemispherical, or ogival, but many other shapes occur. The length may vary from one or two calibers (heavy bombs and mines) to sixteen (3.5-in. rocket).

Very few aspects of underwater ballistics can be covered by exact mathematical formulas, although it does seem that we can assume that resistance is proportional to the velocity squared and that incompressible fluid theory and differential equation theory can be successfully applied to the problem if judgment is used.

On the other hand, most of the fundamental physical principles involved are now (1945) understood, in the sense that almost all of the phenomena actually observed can be explained rationally on the basis of the laws of mechanics.

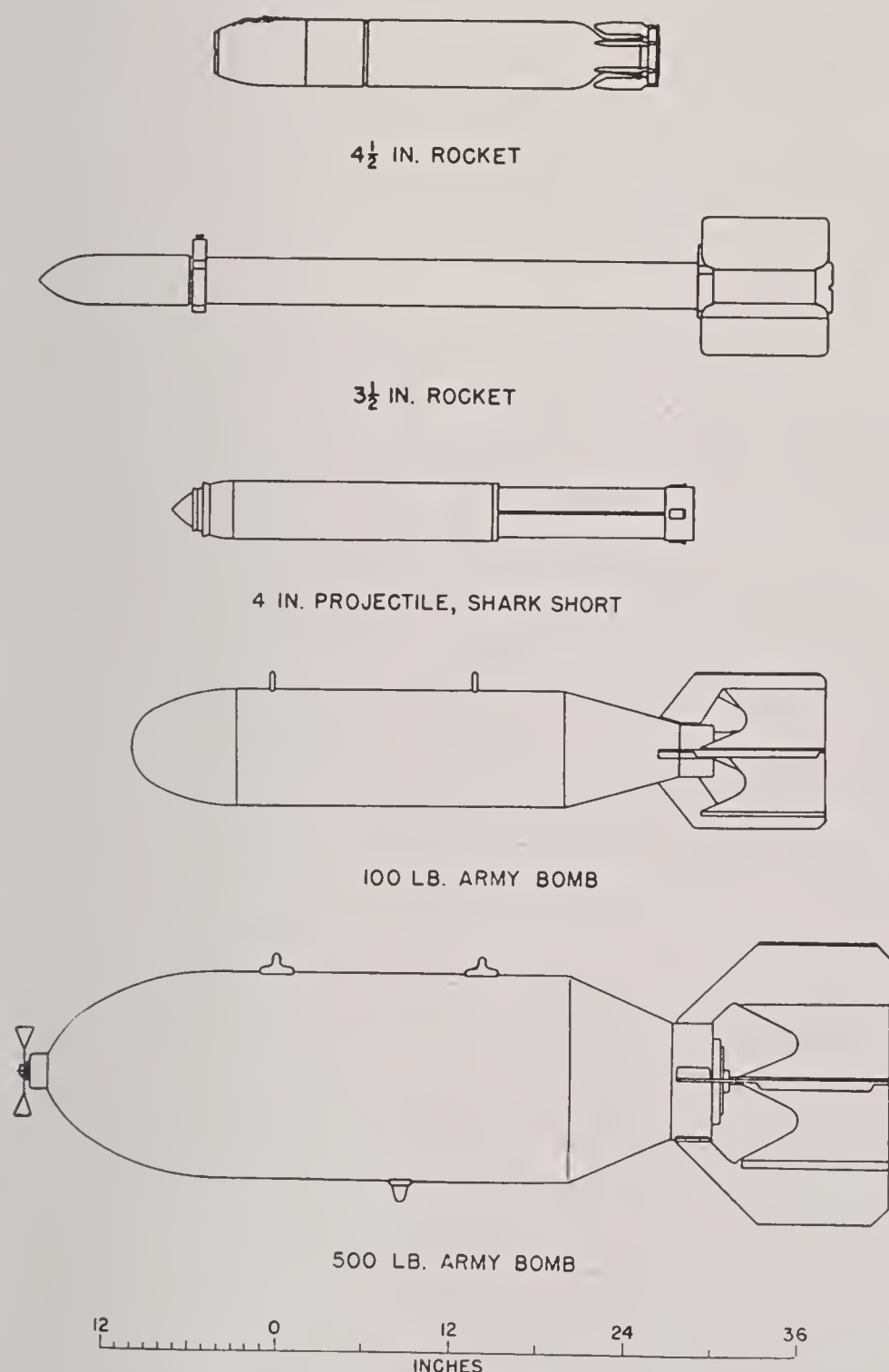


FIGURE 1. Projectile models.

the naval or military aspects of the subject,^a it may be of interest to mention some of the situations to which the considerations involved apply.

^a For a brief discussion of some related practical questions, see notes by Capt. R. C. Hovenden and Capt. G. I. Schuyler.^{1a}

8.2 PHASES OF MOTION

The flight of projectiles through the air has been thoroughly treated in many places, and not much attention will be given to it here. Suffice it to say that many heavy projectiles launched at low altitudes

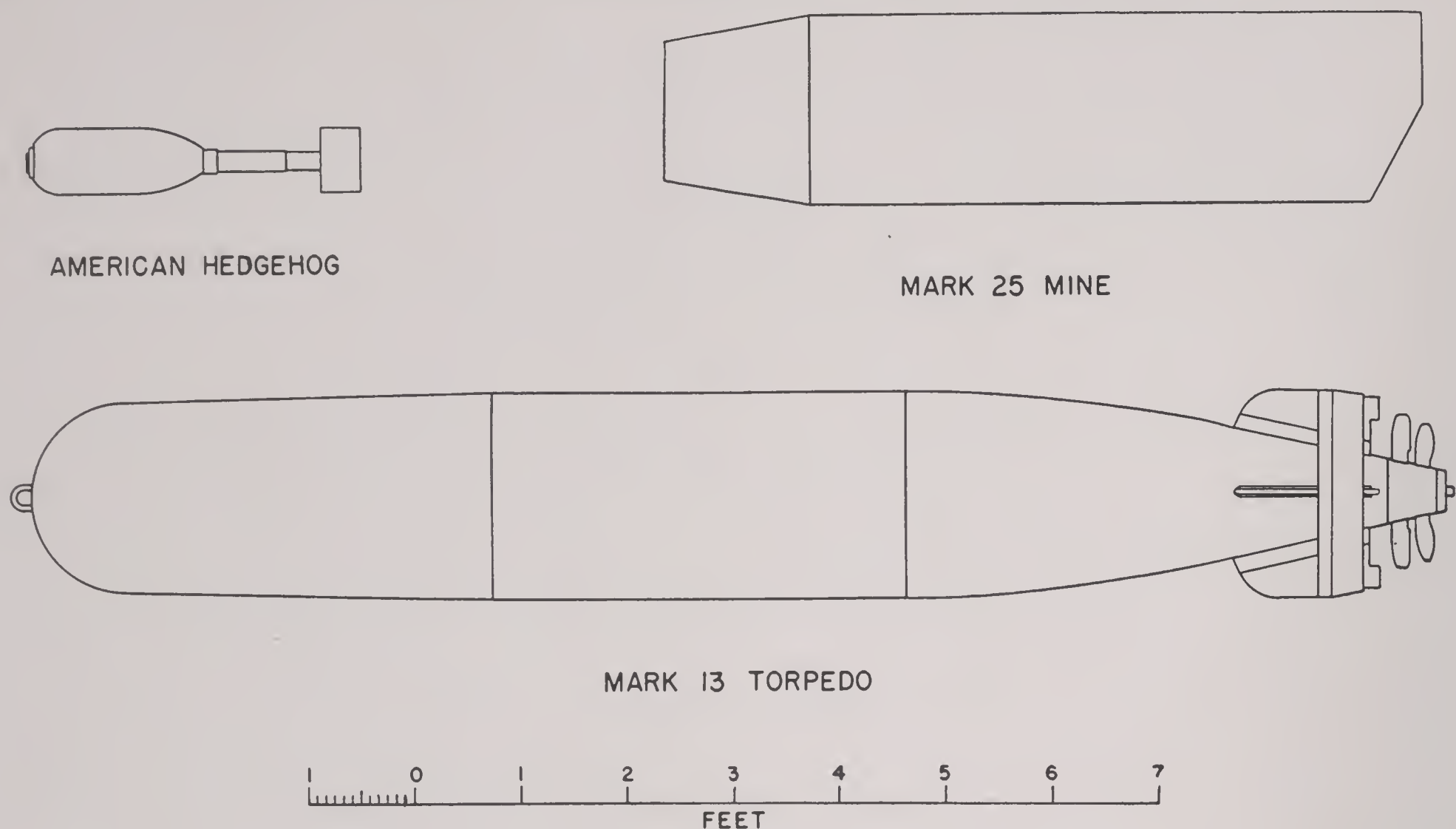


FIGURE 2. Projectile models.

follow an approximately parabolic path in air and that most projectiles enter the water with axis inclined less than 5° to the trajectory,^b although some torpedoes have been very unstable, i.e., entered the water at a large angle of pitch.

We shall assume that the direction and speed of travel and the orientation and angular velocity, $\omega = dv/dt$, of the projectile (see Figure 5) are given at the time of entry into the water. The phases of motion after the entry into water will be considered. Especially in Chapter 11 it will often be assumed for simplicity that the projectile, when it strikes the water, is moving only in the vertical plane. For symmetric projectiles, the motion should then continue in a vertical plane, which greatly simplifies the problem analytically,³⁷ although it is still difficult enough.

The first phase which will be considered in detail will thus be the *impact phase*, which may be loosely defined as constituting the phase during which the head of the projectile is being submerged. This phase is discussed in Chapter 9; it is the phase in which the projectile is subjected to the largest forces and is most likely to suffer damage.

^b It should be mentioned that wind will impart to a projectile a pitch and yaw (called "slew" by the British) relative to the water, even though the projectile is perfectly stable (moves with its axis tangent to the trajectory in coordinates moving with the air). Also, surface waves may alter the effective entry angle.

During the impact phase a sheet of splash is thrown off by the projectile (see Figure 3), and even afterwards the water is deflected away from the projectile path with such violence that a large air-filled or vapor-filled cavity (void) is left in its wake. Indeed, a projectile entering the water nearly tangent to its trajectory usually travels one to five lengths with only its nose pressing against the water; during this period the direction of travel is nearly a straight-line continuation of the air path, though the projectile is decelerating rapidly. The moment of the pressure on the nose imparts a large angular velocity to the projectile, so that after this preliminary travel it swings over and hits one side of the cavity with a resounding "tail slap." This may bend the tail or cause other damage.

During the same interval of time, the shape of the cavity is also constantly changing. At first it grows rapidly in both length and diameter, but it ultimately pinches off or "seals" some distance behind the projectile, often at the surface. The cavity is discussed in detail in Chapter 10, but it may be noted here that after being sealed the entrapped air follows behind the projectile in a long bubble, which is gradually stripped away.^c Figure 4 shows a typical cavity history.

^c If the speed is, say, above 100–200 fps, a large cavity filled with water vapor is formed even when the projectile is launched underwater.

Meanwhile the projectile is decelerating rapidly. Its velocity v , underwater travel distance s , and travel time t are related by the approximate equations

$$v = v_1 e^{-\alpha s}, \quad \alpha t = \frac{1}{v} - \frac{1}{v_1} = \frac{(e^{\alpha s} - 1)}{v_1}, \quad (1)$$

where v_1 is the entry speed and $\alpha = C_D/2\sigma l_a$ is a suitable deceleration coefficient.^d The net result is that a projectile in water will lose half its velocity every

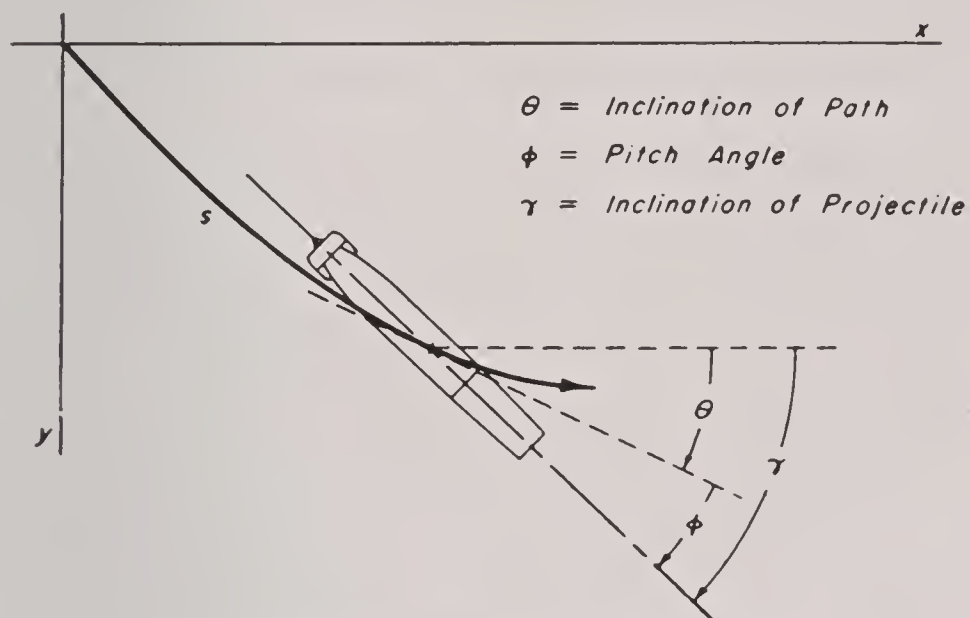


FIGURE 5. Diagram of projectile.

two to thirty lengths of travel until gravity or internal propulsion devices determine its motion. Unless propelled, it will then sink approximately vertically with a nearly constant terminal velocity $v_t = \sqrt{2gl_a(\sigma - 1)/C_D}$. (It will, of course, rise if $\sigma < 1$, i.e., for buoyant projectiles.)

If the entry angle is small enough, i.e., below a critical angle, depending on the projectile shape, entry speed, and other variables, it may be deflected back out of the water into the air. This will usually occur only after the projectile has been totally submerged during part of its underwater travel, in which case we have what is technically called a "broach."^e But at grazing angles, it may ricochet back into the air without ever having been totally submerged, although even in this case it will usually skim along the surface for a considerable distance (called the *plough*).

^d Here C_D is a drag coefficient usually between 0.1 and 1, σ is the specific gravity, and l_a is an average length. C_D may vary by as much as 100 per cent over a single trajectory. See also Section 11.3.

^e The word ricochet has traditionally been used to include all cases where a projectile had a renewed air flight with, say, 10 per cent or more of its impact speed. But specialists in underwater ballistics prefer to follow the distinction made here. It is not always realized how rare ricochet, as defined here, is.

The underwater trajectory is discussed in more detail in Chapter 11. Figure 5 defines the principal trajectory variables.

8.3 TYPES OF UNDERWATER MOTION

Type I. Ricochet of Spheres. Anyone who has seen high-speed motion pictures of projectiles entering water will classify the trajectories into several fairly distinct types, even though this classification does not seem to have been made prior to World War II.

The simplest type of motion occurs with the ricochet of spheres (see Figure 6); this type was also the first to be studied.^f

For a sphere of specific gravity σ , the critical angle θ_c , below which ricochet occurs off smooth water, is approximately

$$\theta_c = \frac{18^\circ}{\sqrt{\sigma}} \quad (2)$$

for impact speeds through the range 200 to 2,000 fps; the increase in θ_c through this range of speeds is apparently less than 20 per cent. Moreover, the exit angle θ_2 is always less than the impact angle θ_1 ; this makes multiple ricochet possible (if $\theta_1 \leq \theta_c$, then $\theta_2 \leq \theta_c$). More precisely,

$$0.8 \leq \frac{\theta_2}{\theta_1} \leq 1.0, \quad (3)$$

the ratio θ_2/θ_1 apparently being nearest unity when θ_1/θ_c is small and the impact speed v_1 is high.

Ricochet does not consist in bouncing off the surface; the sphere will usually skim along the surface partly submerged for 10 to 50 diameters before leaving the water. It is easily seen that in this condition the water will exert more pressure on the lower than on the upper side of the sphere and hence tend to lift the sphere out of the water; the magnitude of the force as a function of immersion^g is shown in Figure 7.

It will be noted that there is some lift even on a totally submerged sphere traveling horizontally, and there are instances of broaching, where a sphere has left the water even after being totally submerged.

^f Experimentally (using steel spheres) by Jonquières¹¹¹ and in reference 30. Theoretically, in an attempt to explain the refraction of supposedly spherical light corpuscles, by d'Alembert.^{5a} Formula (2) was derived theoretically and experimentally in reference 8. (See Section 9.5.)

^g As determined by Ramsauer¹¹²; we have converted to C_L . At speeds below 50 fps spheres may, however, refract down; this was discovered by the Morris Dam Group at California Institute of Technology.

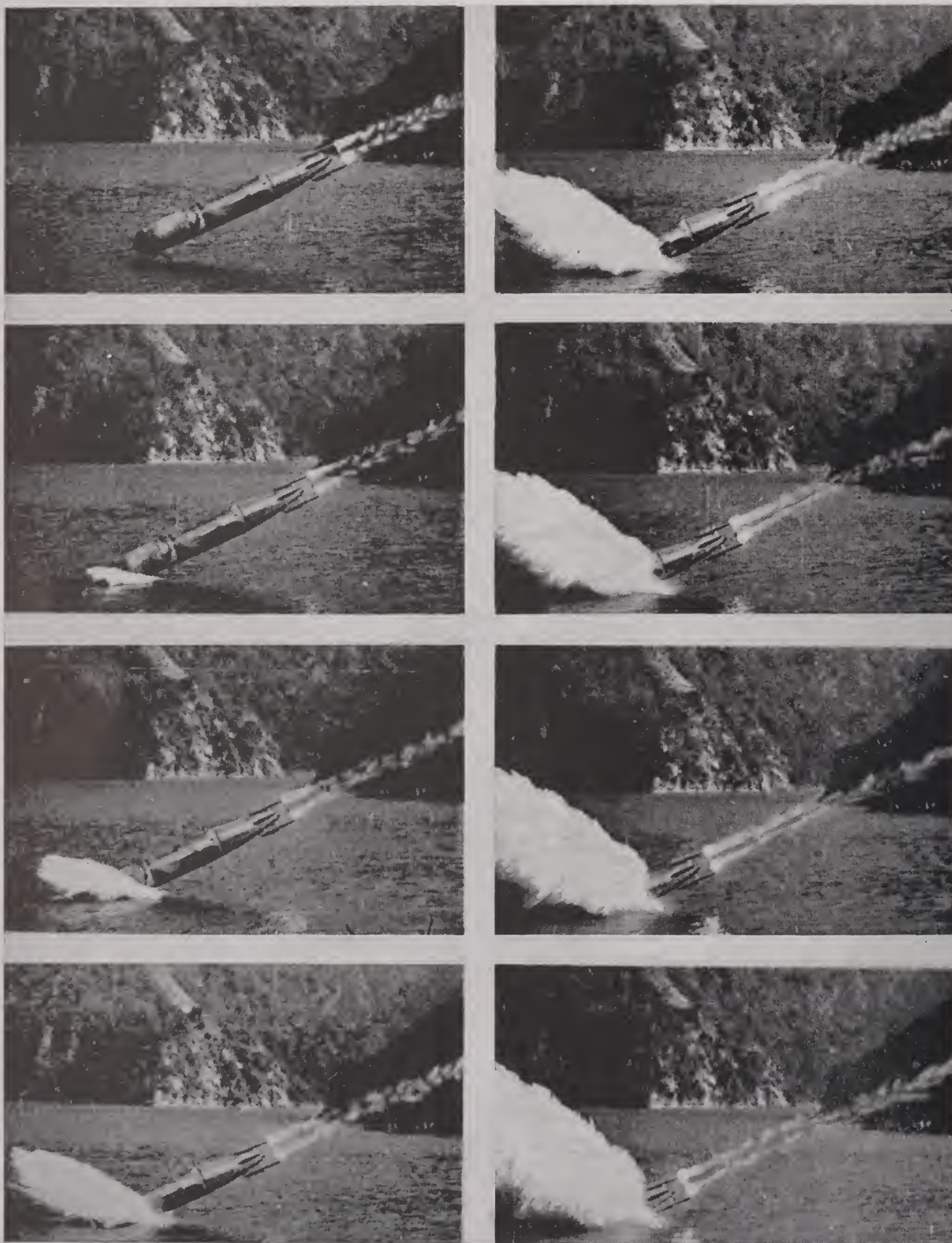


FIGURE 3A. Splash (CIT).

CONFIDENTIAL

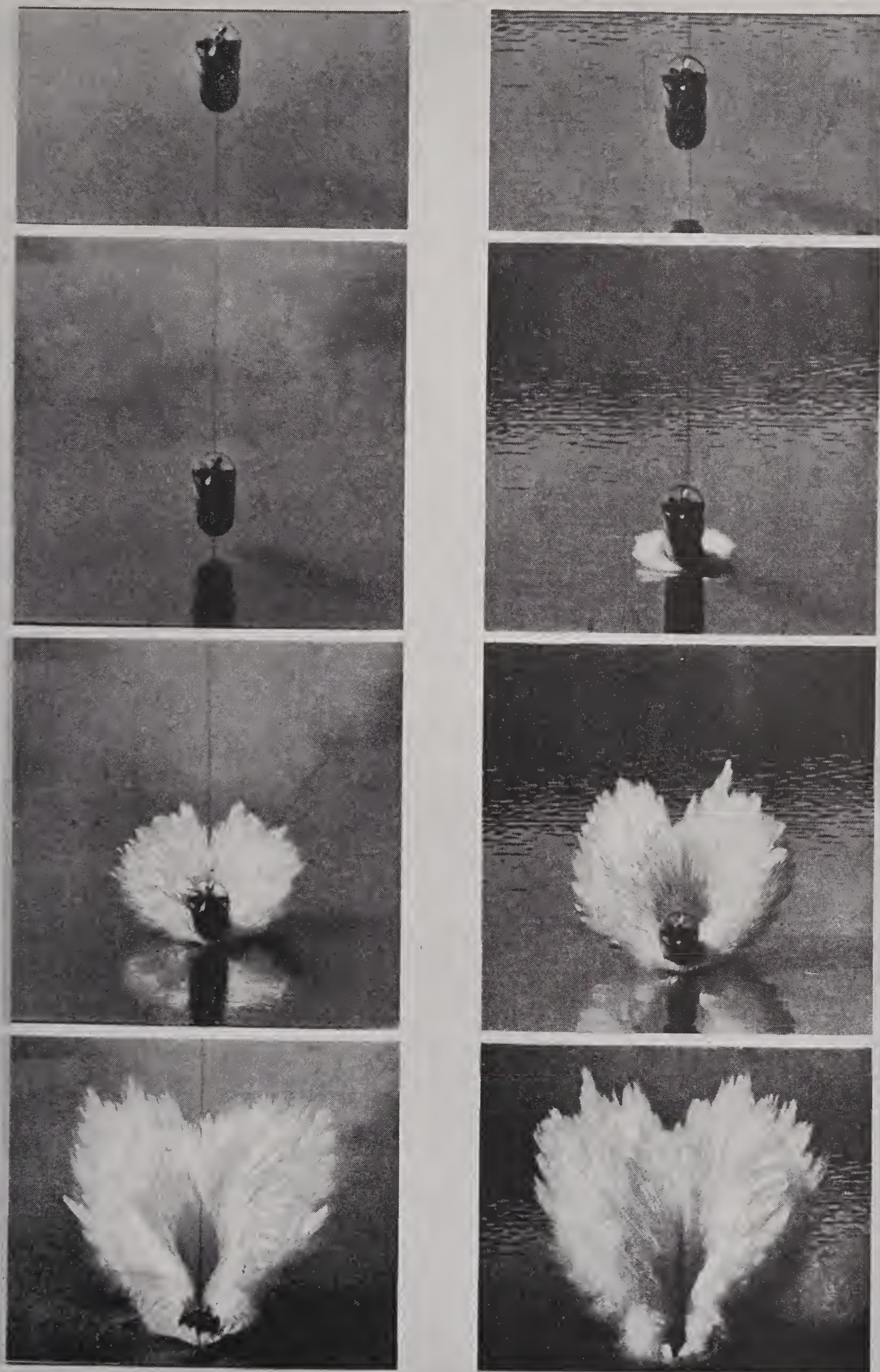


FIGURE 3B. Splash (CIT).

CONFIDENTIAL



FIGURE 4A. Typical cavity history (AHL).

CONFIDENTIAL

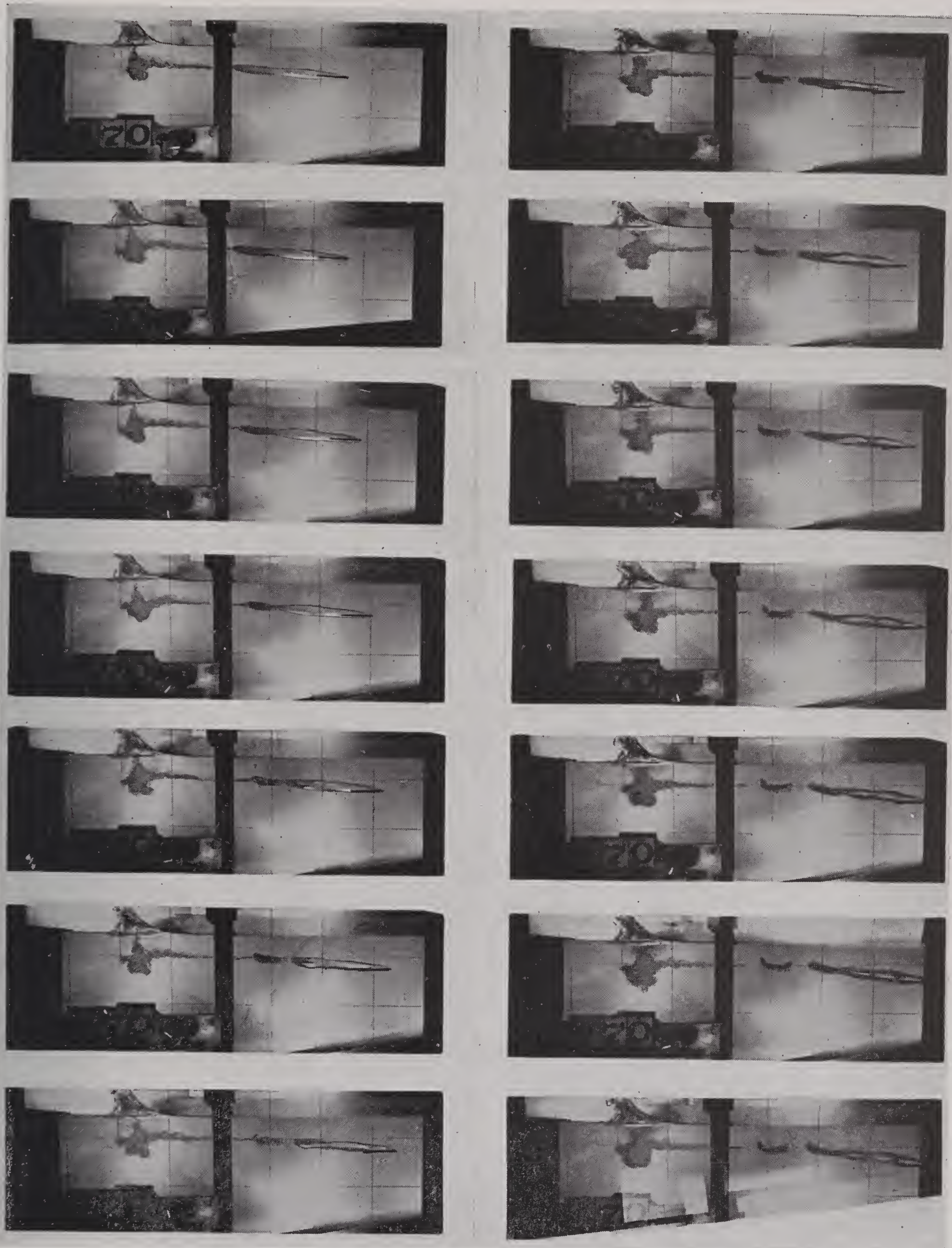


FIGURE 4B. Typical cavity history (AHL).

CONFIDENTIAL



FIGURE 6. Ricochet of aluminum sphere (AHL).

CONFIDENTAIL

This lift, due to the nearby "free surface," is correlated with an asymmetrical cavity (see Section 10.3); both effects disappear three to four diameters below the surface.

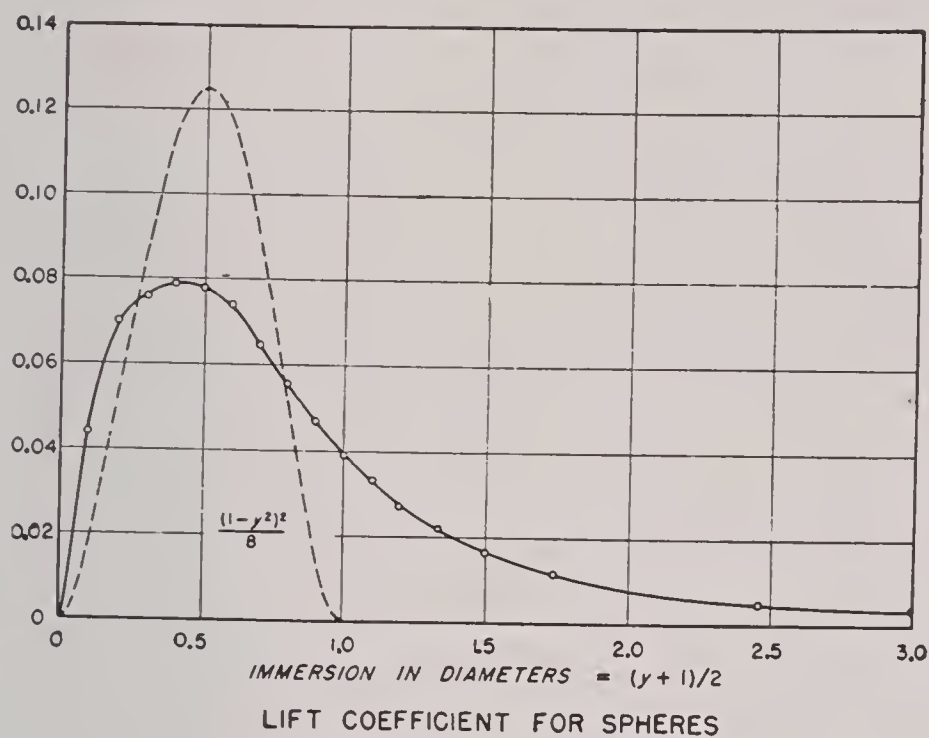


FIGURE 7. $C_L(y)$.

However, with projectiles other than spheres, the lift due to pitch is much greater than that due to free surface effects, and therefore broaching is mainly due to pitch forces. The free surface effect^h is usually important only because of the "whip" it imparts during the brief phase of partial submergence. We now consider such broaching.

Type II. Circular Arc Motion. In the next simplest type of underwater motion, the projectile leans against one wall of the cavity at a more or less constant angle (see Figures 8 and 9). This type of motion is observed with most British and American rockets, with the American Mark 13 torpedo (full scale), and with various experimental models (M30 GP bomb with rigid box tail and fuze cap, torpedo with CG back, etc.).^{11, 39, 40, 41, 42}

By elementary hydrodynamics, the lift coefficient C_L should then be constant, and the motion should be in a circular arc, until the projectile loses its cavity (see Chapter 11). It follows that *broach should be possible at any entry angle*, if the entry speed is high enough so that the projectile does not shed its cavity first. Actually, the trajectory has a straight portion preceding the tail slap, so that $\theta_2 \geq \theta_1$ (see Figure 8),

$$\theta_1 \leq \theta_2 \leq 1.5\theta_1. \quad (4)$$

The radius R/l_a of curvature in projectile lengths may be from ten to sixty, depending largely on the

head shape; the curvature l_a/R is greatest (motion most unstable) with conical and ogival heads. It is also greater, even relatively, with short projectiles than with long ones. It is clear that the horizontal "plough" should be approximately $2R \sin \theta_1$, the maximum depth of submergence should be $\frac{1}{2}R \sin^2 \theta_1$, and the exit speed v_2 should satisfy $v_2/v_1 = e^{-2\alpha R\theta}$, if θ is measured in radians.

In the case of projectiles having sufficiently steep (i.e., nose-down) pitch at entry, the tail will swing to the top of the cavity and the circular arc will curve down instead of up. Hence broach will never occur, no matter how small the entry angle, unless the momentum is enough for the projectile to execute a complete circle and leave the water *behind* the entry point. Such a motion is called a "dive."

This possibility is especially important for torpedoes entering shallow water. If there is enough steep pitch to swing the tail up, the torpedo may dive 100 to 2,000 ft.^{34, 43} Small models entering at low speeds may dive even though they do not have steep pitch at entry. In any case, circular arc motion ceases when the cavity is shed.

Type III. Broadside Motion. Many projectiles entering water at high speeds have their stable mode of motion traveling broadside (see Figure 10). Fins or other stabilizing devices are required to prevent ordinary bombs and other aircraft-launched missiles from broadsiding in air, and these stabilizing devices are often bent or torn off (sometimes intentionally) during motion through water.ⁱ This is, for example, the case with American GP bombs, with some depth charges having hydrostatic fuzes set for shallow action, with high-altitude mines (which often have asymmetrical heads to produce rapid broadsiding), and with other tailless mines. An example is shown in Figure 10.

In typical cases, broadsiding occurs after three to five lengths of travel. A symmetric projectile with a convex head^j noses up on impact unless entry pitch is steep or the entry speed slow. While the projectile is broadsiding, a lift force on the side curves the trajectory up.

The critical angle θ_c for broaching is usually between

ⁱ Water, which is 750 times as dense as air, gives rise to dynamic forces 750 times as great at the same velocity.

^j If water behaves like an ideal fluid, so that all forces are normal to the surface, then no turning moment is developed by a spherical cap centered at the center of gravity. In general, heads which are more convex than this develop up-pitch at impact; those which are flatter develop down-pitch (see Section 9.5).

^h Thus C. J. Cranz^{12b} mentions the pitch force as primary. The first complete treatment based on this hypothesis was given by H. P. Hitchcock.³⁹

8° and 25°, but depends very much on the impact speed v_1 . Thus it may double when v_1 is doubled^{4a,21} in the range 100 to 200 fps; but above a certain speed there seems to be little further increase in θ_c , i.e., it approaches a fixed maximum value asymptotically.

At shallow entry angles, we have approximately

$$2\theta_1 \leq \theta_2 \leq 3\theta_1 \quad (5)$$

in many cases. Nearer the critical angle we tend to have $\theta_1 \leq \theta_2 \leq 2\theta_1$; hence, on the average,^k $\theta_2 \sim 2\theta_1$.

Since a broadsiding model decelerates rapidly, we cannot expect long underwater travel to precede broaching; the length of plough never seems to exceed $15l_a$ (15 projectile lengths). On the other hand, even at the shallowest entry angles (say 4° when $\theta_c = 15^\circ$), the plough seems to be as much as $3l_a$. Moreover, the model always turns through nearly 45° and loses at least 25 per cent of its speed before broaching. Actually, in most cases the projectile emerges with its nose vertical or even tilted slightly backward, and a large nose-forward angular velocity is imparted during exit from the water.

Type IV. Oscillatory and Spiral Motion. All the flat-headed projectile models which we have photographed oscillate about a position of zero pitch, the amplitude of the oscillation being greatest with short models (see Figure 11). So does the British hemispherically nosed aircraft torpedo^{1c} with propellers,¹ and so do some of the GP bomb models with convex heads and rigid box tails which we have studied.

On the other hand, very similar models performed circular arc motion.^{11,25,39,42} The physical causes differentiating between oscillatory and circular arc motion are not clearly understood in all cases, though moving the CG forward tends to encourage oscillatory motion (see Section 11.12). A distinction is made between the motion of projectiles which oscillate symmetrically between the two sides of a cavity (oscillatory motion) and the motion of projectiles

which execute damped oscillations about a position leaning against one side of the cavity, or about a broadside position.^m

Projectiles performing oscillatory motion usually have low critical angles θ_c for broaching, in the range 5° to 15°. If a broach occurs, it almost always occurs on the first oscillation, and the broach angle θ_2 usually lies between θ_1 and $1.5\theta_1$. The length of plough thus tends to be short (five to ten projectile lengths), even more so than in the case of broadside motion, though it may take a longer distance to cause the same deceleration.

Projectiles which are spin-stabilized in air will be unstable in water, since the "stability coefficient"^{16a} is only $1/750$ as big.ⁿ However, the spin is sufficient to convert the broadsiding tendency of the projectiles into a spiral or corkscrew motion, which somewhat resembles the oscillatory motion just discussed. Such projectiles also have a low critical angle, 5° to 15°, for broaching.

Type V. Tail-up Ricochet. Projectiles with flat, stepped, or inverted cone heads striking the water at a low angle θ_1 as well as other projectiles with a large steep entry pitch (say 70°), will be given a nose-down rotation at impact; moreover, as they swing tail over head they will be subject to a large lift force. This may carry them out of the water before the direction of rotation has been reversed, causing "tail-up" ricochet (see Figure 12). Cases have even been observed where the projectile turned end over end two or three times before finally ricocheting.

This tail-up ricochet and sphere ricochet represent the only cases where ricochet is more common than broaching.

A more detailed description of the types of underwater motion observed with projectiles, including physical explanations of why these types are observed in specific cases, is given in Sections 11.8 to 11.11.

^k This relationship was first announced²⁵ by Marston Morse and Capt. Russell Baldwin. It contrasts markedly with Sections 8.3 and 8.4.

¹ Without propellers, the 1-in. model used performed circular arc motion, like the American Mark 13 torpedo.

^m We still call the latter circular arc and broadside motion, though the projectiles oscillate about the positions in question.

ⁿ The usual criterion for spin stability is that the stability coefficient exceed unity (for safety, 1.5).



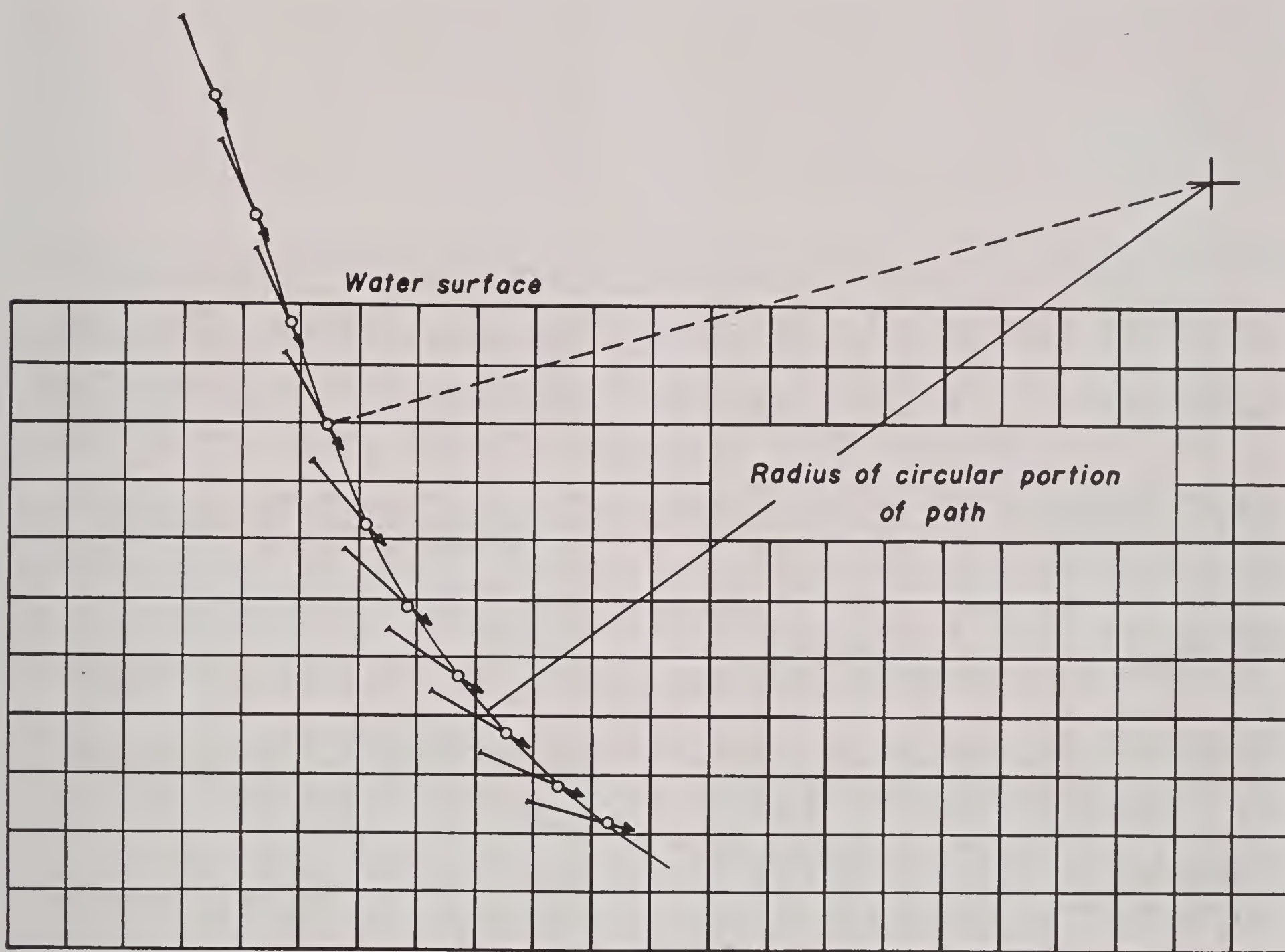
FIGURE 8. Circular arc motion (AHL).

CONFIDENTIAL



FIGURE 9A. Circular arc motion ("tallboy").

CONFIDENTIAL



Aspects of projectile at equal time intervals.

FIGURE 9B. Circular arc motion.

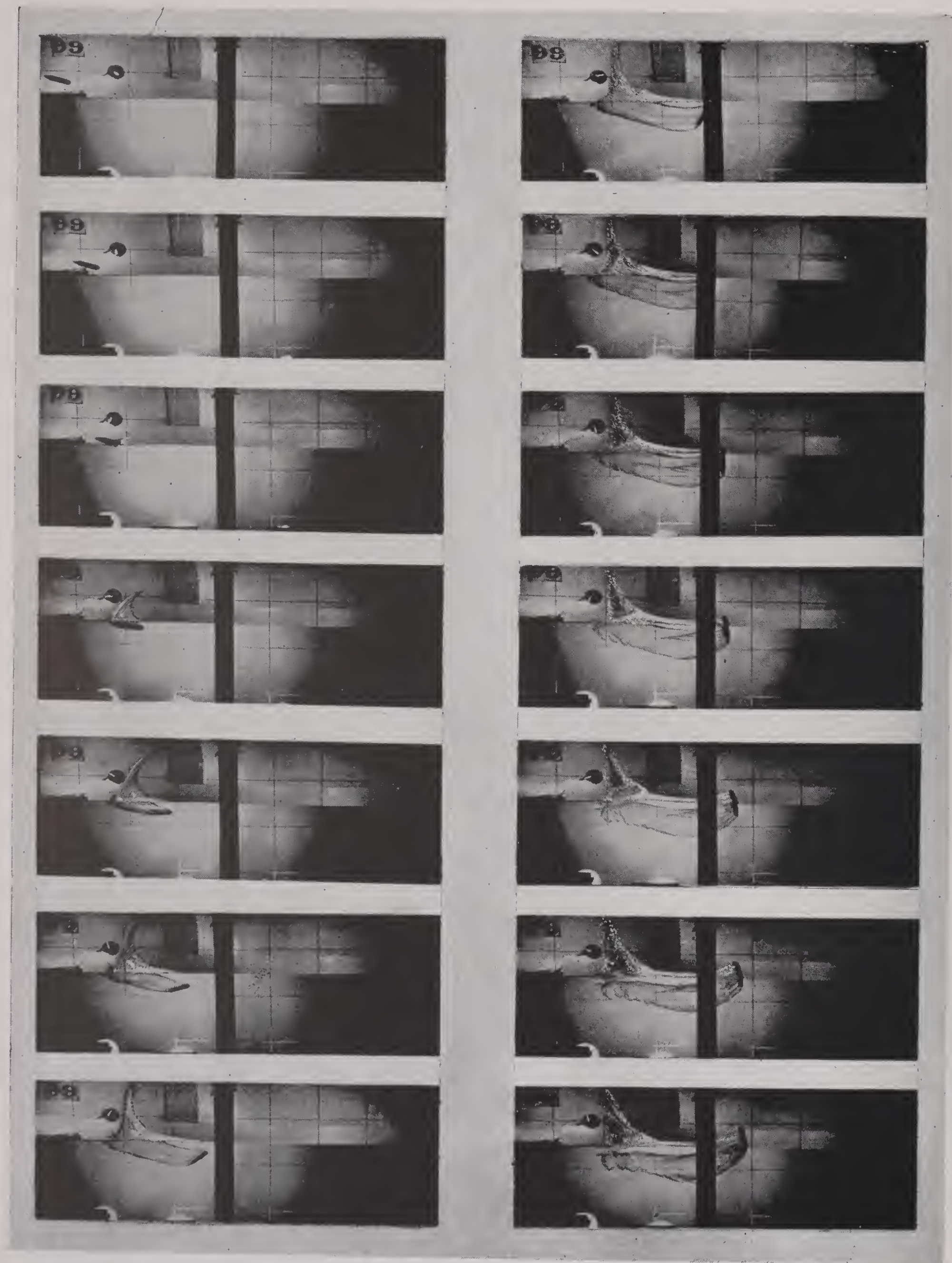
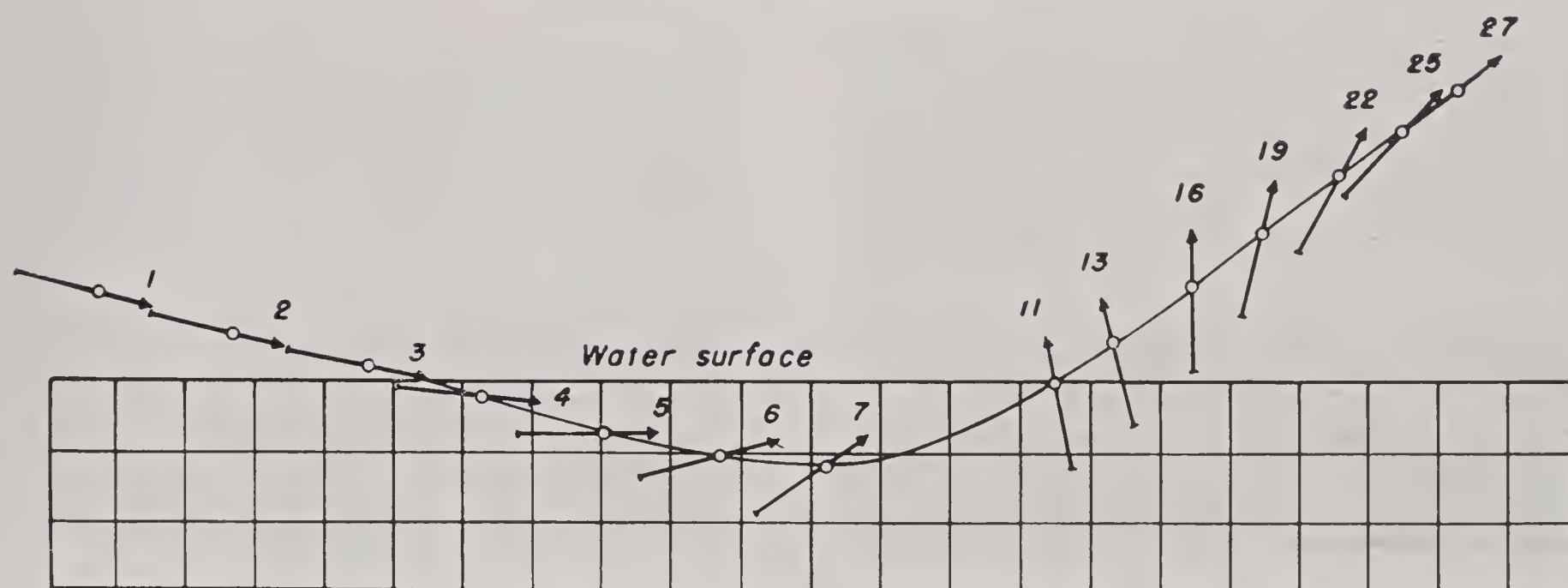


FIGURE 10A. Broadside motion (AHL).

CONFIDENTIAL



FIGURE 10B. Broadside motion (AHL).



Frame numbers indicate time intervals.

FIGURE 10C. Broadside motion.

CONFIDENTIAL



FIGURE 11A. Oscillatory motion (AHL).

CONFIDENTIAL

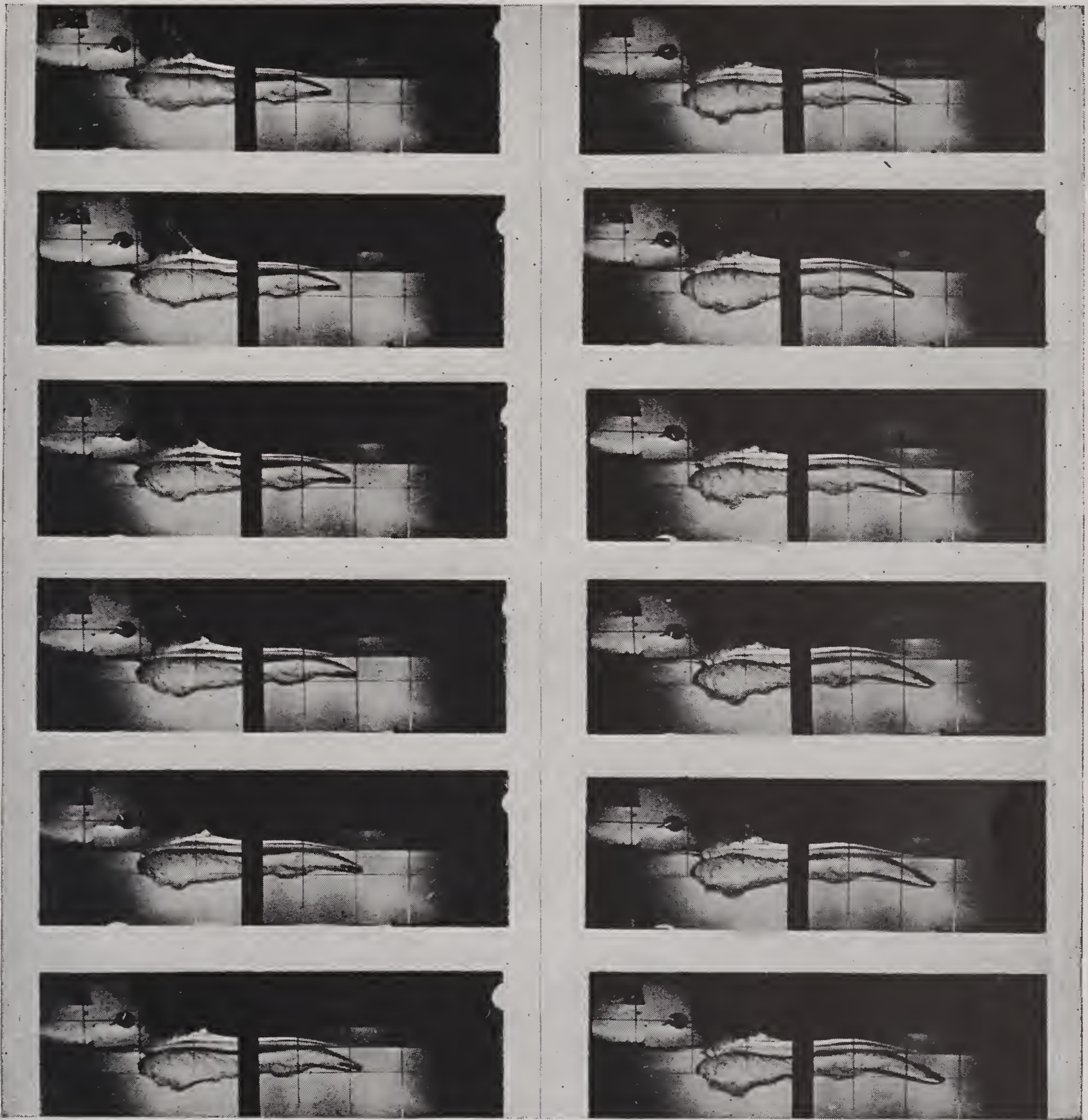
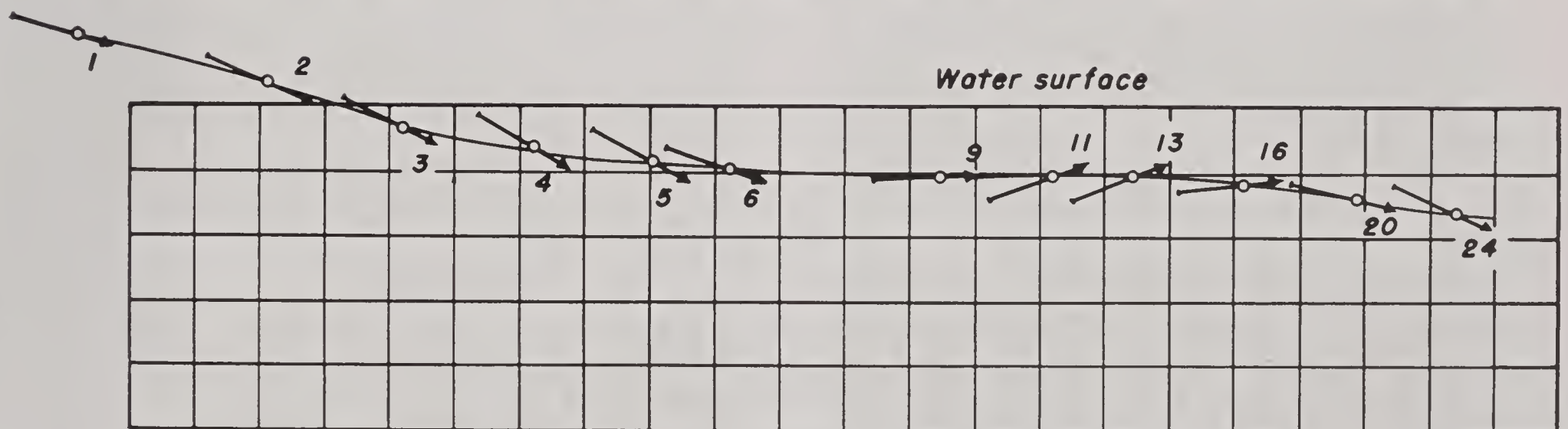


FIGURE 11B. Oscillatory motion (AHL).



Frame numbers indicate time intervals.

FIGURE 11C. Oscillatory motion.

CONFIDENTIAL

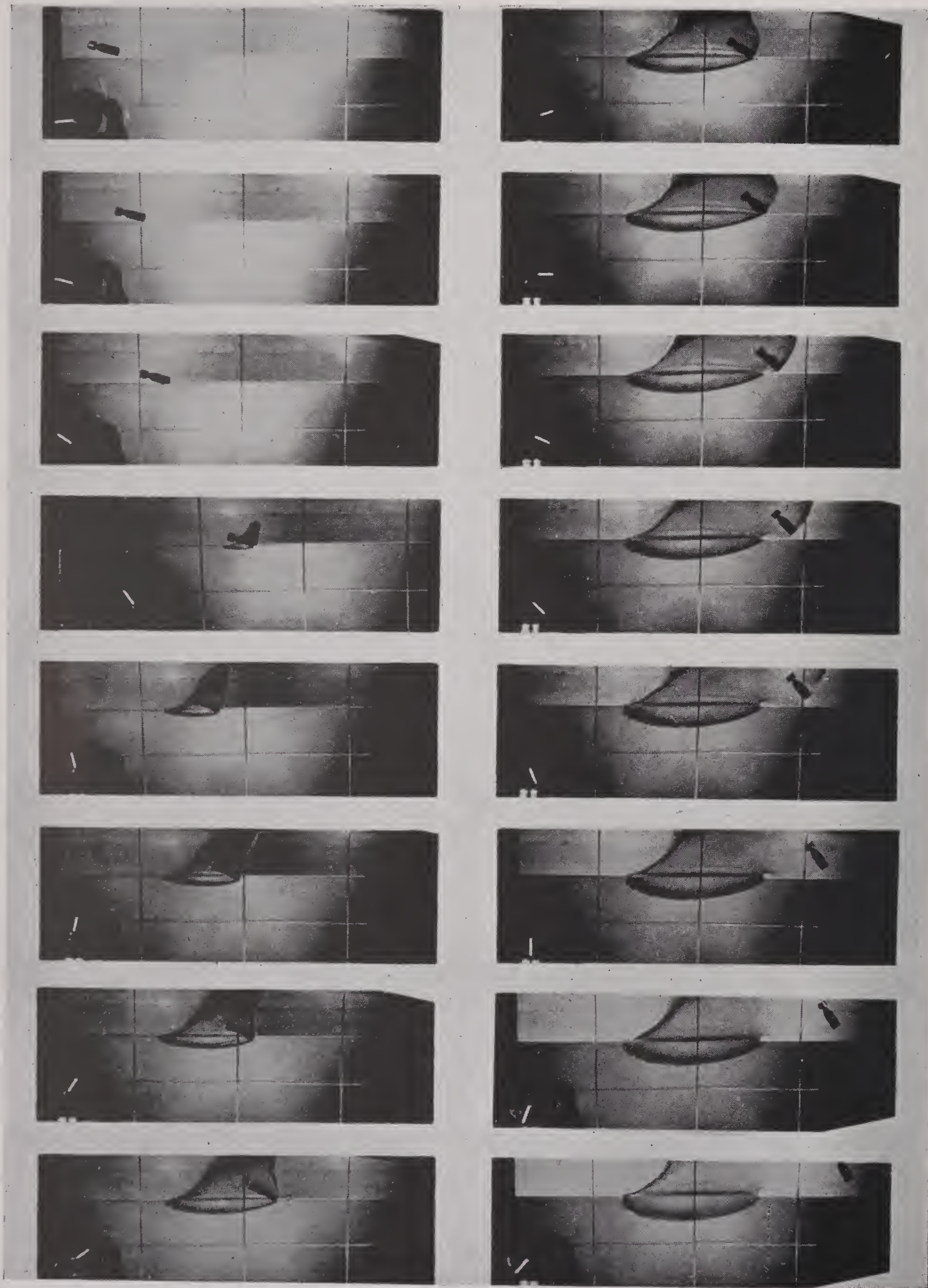


FIGURE 12. Tail-up ricochet (AHL).

CONFIDENTIAL

Chapter 9

IMPACT FORCES

9.1 IMPORTANCE

THE IMPACT forces which occur when the nose of a projectile is entering water are important for many reasons.

Thus the moment of these forces imparts a large angular velocity, or "whip," to the projectile, which often decides whether the projectile (which is generally unstable at zero pitch) will swing to the upper or lower side of the cavity, e.g., broach or dive. This whip is discussed in Section 9.5.

Again, these impact forces may damage the case of an HE missile. Or they may cause a fuze, intended to operate when the missile strikes a ship or submarine hull, to go off prematurely on striking the water. In other words, they may cause "prematures" with what are intended to be water-discriminating contact fuzes. Or, finally, they may damage machinery components in a torpedo or fuze components (vacuum tubes, etc.) in mines.

Analogous effects may occur during the tail slap (see Section 8.2); in particular, there is a possibility of damage to the rudders of a torpedo or of premature operation of hydrostatic fuzes set on the lower side of convex-headed depth charges. Various general discussions of impact forces may be found.^{6, 34, 44}

From the theory of vibration¹⁷ we know that the maximum stress S on an elastic projectile component at impact is determined largely by the maximum *impulse*

$$I^* = \text{Max} \left[\int_t^{t+T} F(t) dt \right]$$

communicated during a quarter-period T of oscillation of the component. In fact,

$$\frac{1}{\sqrt{2}} I^* \leq S \leq \sqrt{2} I^*$$

in general. In order to estimate the cause of damage, it is therefore important to know the *peak force* and *duration* of the forces encountered by the projectile at entry, as well as the period of the component.

These will now be discussed. Though the projectile is treated as a rigid body, most HE projectiles actually vibrate considerably on impact. This is shown in the tail flare records¹⁷ taken by the Morris Dam Group at California Institute of Technology [CIT]. Although there is no reason to believe that the vibration affects significantly the hydrodynamic forces, it does mean that the period of most machinery, etc., components is larger than might otherwise be supposed.

Even if there were no special forces acting during entry, the hydrodynamic forces would be larger then than at any later time. Thus the drag D_0 at constant velocity v is roughly proportional to the velocity squared, $D_0 = \frac{1}{2} \rho A v^2 C_D$, where C_D is nearly independent of v and A . For a Mark 13 torpedo entering water at 400 fps, v might decrease 30 per cent and hence D_0 would be halved in 0.04 sec.

Actually, due to *induced mass* (the inertia of the water during the establishment of a flow pattern in it), the drag may be $1.5D_0$ to $3D_0$ during the first half-diameter of entry; in the case considered, during the first 0.003 sec.

And finally, due to *elastic shock* at impact, the force and especially the *peak pressure* at the point of impact (which would be infinite if water were incompressible) may be ten or more times the constant-velocity drag. Thus certain readings^{1b} averaged over the first 0.002 to 0.005 sec after entry gave $C_D = 0.703, 0.87; 2.12, 3.85, 7.83; 1.00, 1.57, 1.49$ and 1.93 in cases when the steady-state C_D for axial travel might be 0.2 to 0.8. This peak pressure is, however, of extremely short duration. Which of the forces is measured by a particular accelerometer depends on the natural period (or reaction time) of the accelerometer. This, together with the difficulty of statically calibrating instruments measuring dynamic forces, explains why accelerometer data have been so unreliable in the past. In fact, some accel-

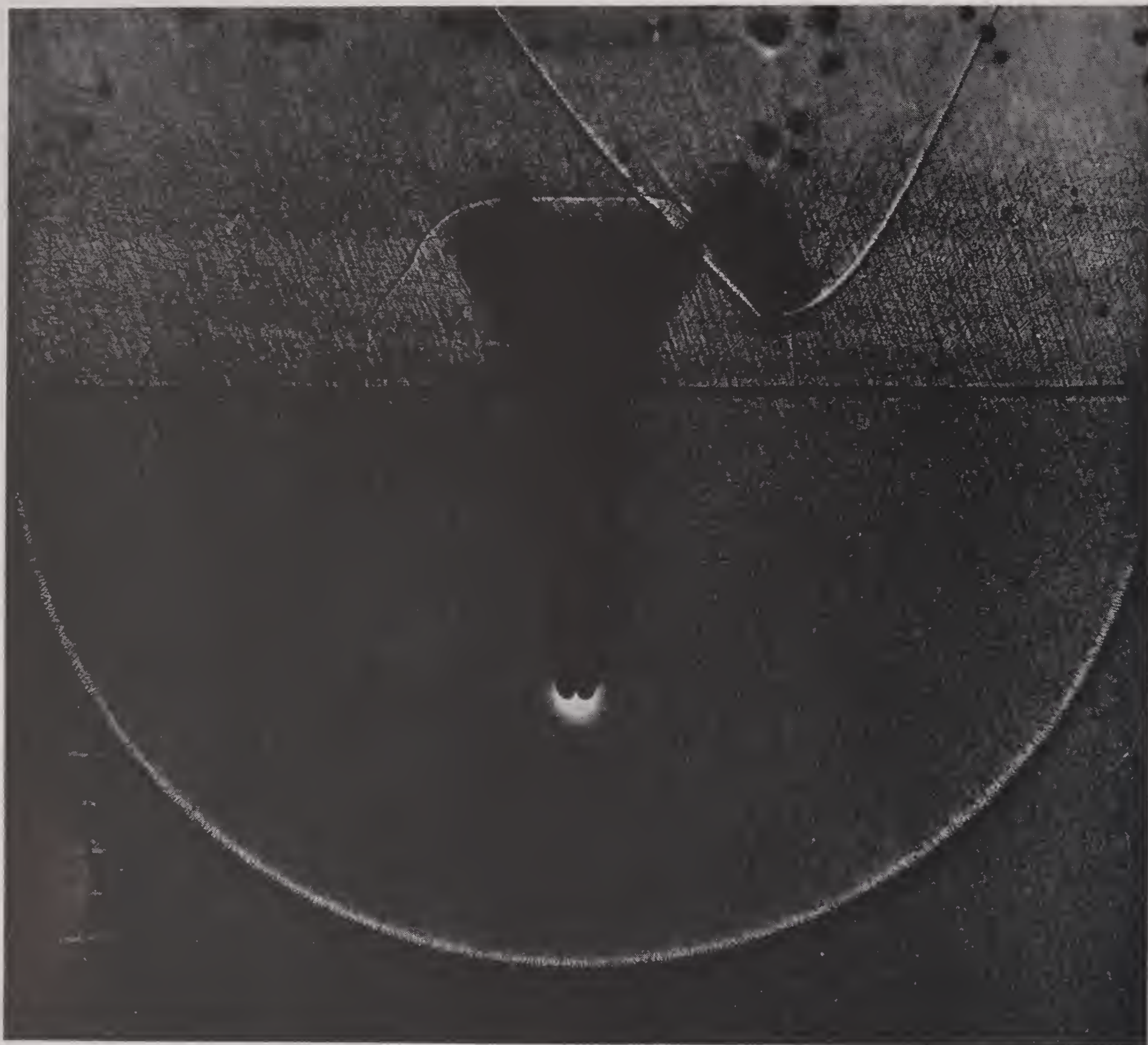


FIGURE 1. Shock wave (E. N. Harvey and J. H. McMillen).

erometers have been found ^a to give the same reading mounted forward as backward!

The forces just referred to will now be discussed in more detail.

9.2 ELASTIC SHOCK FORCE

If the entire surface of a rigid flat plate strikes the surface of an incompressible fluid simultaneously, it will impart a finite velocity to a finite volume of fluid instantaneously. Hence it will impart a finite amount of energy to the fluid instantaneously; this can happen only if the peak pressure is infinite. Moreover, an elementary consideration of infinitesimals, given in Appendix II, shows that infinite pressure must still

develop if a smooth surface (i.e., one without a point or edge) impinges on the incompressible fluid.

Since water is not actually incompressible, we conclude that *the peak impact pressure can only be computed by considering the compressibility of water.*

A line of reasoning ^b shows that for *normal* impact of a plane or smooth surface on a compressible fluid, a peak pressure of $\rho c v_1$ will be developed, where ρ is the fluid density, c is the speed of travel of the "shock wave" (roughly that of sound) in the fluid, and v_1 is the impact speed. It should be remarked that such a shock wave is visible when, as in Figure 1,^c a sphere strikes the water, even at speeds much less than the speed of sound in water.

^a By B. G. Neal of the British Admiralty.

^b Suggested by David Gilbarg and presented in Appendix II.

^c E. N. Harvey's photograph.

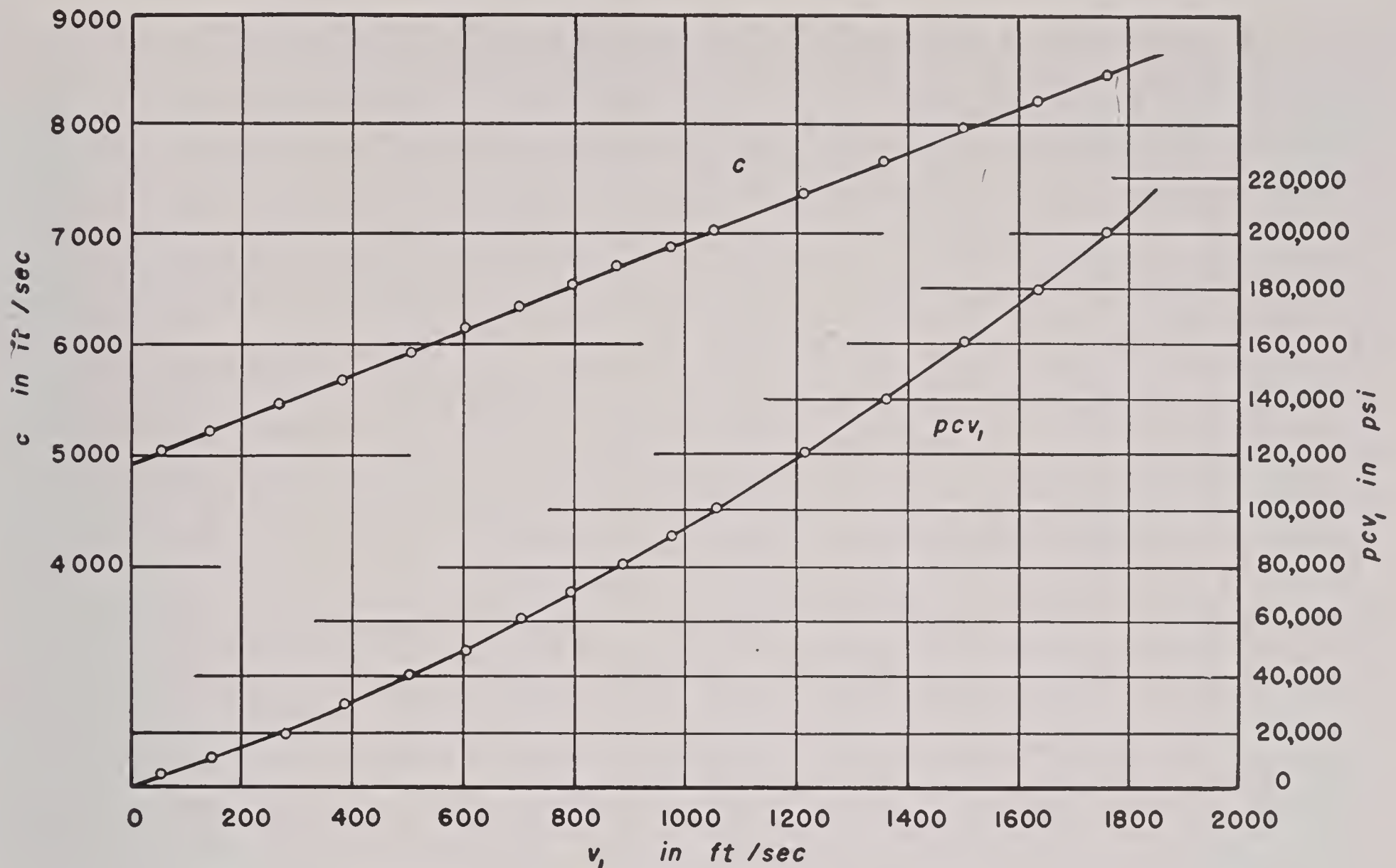


FIGURE 2. Graph of shock wave pressure.

The peak pressure, occurring with *oblique* impact at an angle θ_1 with the horizontal, will presumably be less than that occurring with normal impact, but at least as great as the pressure $\rho c v_1 \sin \theta_1$ which would occur if the tangential velocity component were suppressed. For a horizontal plane striking a compressible nonviscous surface, the peak pressure would be exactly $\rho c v_1 \sin \theta_1$. But with convex projectile heads, the "piling up" of water causes larger pressures to be observed in front than at the exact point of impact. Hence the following inequality holds.

$$\rho c v_1 \sin \theta_1 \leq \text{peak pressure} \leq \rho c v_1. \quad (1)$$

Numerically, $\rho c v_1$ is about 7,000 psi in fresh water if v_1 is 100 fps. Actually c is greater in sea water than in fresh water, and it increases, due to the shock intensity, as the impact speed increases, although the increase is small until v_1 exceeds 1,000 fps, or about $0.2c$. A graph of c and $\rho c v_1$ as a function of v_1 for fresh and salt water is given in Figure 2; it is based on tables prepared by A. B. Arons and R. R. Halserson.⁴⁵

The best available measurements (by diaphragm deformations^d) are in reasonable agreement with (1),

^d Handy pressure plugs, which mount a thin copper diaphragm, have been developed by the Morris Dam Group at CIT to measure peak pressures. However, one is always faced with the difficulty of calibrating statically an instrument to measure dynamic forces, which will, moreover, be affected by the presence of the plug.⁴⁶

allowing for the scatter in the observed data. This is shown in Table 1.

TABLE 1*

v_1 (fps)	225	300	400	500	600	390	1,650
Peak pressures in 1,000 psi							
$\rho c v_1 \sin \theta_1$	5.1	6.8	9.1	11.4	13.7	8.9	100
At point of impact	4.0	7.0	8.0	9.5	13.0		
Highest peak	4.5	8.0	13.0	18.0	23.0	9.0	37-48
$\rho c v_1$	15	20	26.8	33.5	40	32.7	120

* The first six columns are averages of pressure-plug data taken with $\theta_1 = 19^\circ$ at Morris Dam; the first five on the Mark 13 (hemispherical) torpedo head; the sixth with the "Ager bulge." The seventh column represents measurements with indenter and diaphragm gauges mounted in the nose pin of a 5-in. HVA rocket fired into salt water.^{4d, 47} This mounting probably accounts for the low observed value.

The shock-wave peak pressure (1) is generally believed (from frequency and duration computations) to be responsible for damage to the case and to vacuum tubes mounted in mines. However, the total impulse is small, and it is believed that other components have too long a period to be affected by it.

On the basis of tests at Newport, it has been inferred that a cylindrical plywood "pickle barrel" (see Figure 3), introduced to stabilize the air flight, reduces the peak impact pressure on a Mark 13 torpedo by as much as 40 per cent (with corresponding damage to the case). A possible explanation, using formula (1), is that the leading edge causes aeration

of the water by creating a cavity. This would greatly increase the compressibility $dp/\rho dp$ of water and hence decrease $c = \sqrt{dp/d\rho}$. Actually, there are pressure-plug readings which give a peak force one-half as great as without the pickle barrel.^e



FIGURE 3. Pickle barrel.

Finally, it should be noted that no such large peak pressure as predicted by (1) and no shock wave are to be expected from a pointed head entering water. Some confirmation of this was found in the low peak pressures recorded by pressure plugs with the more or less pointed Ager head tried at Morris Dam.^f

9.3 TIME-DECELERATION CURVE FOR VERTICAL ENTRY

The best method of estimating the time-deceleration curve during entry after the elastic shock is due to von Kármán and is a potential-theoretic one.¹⁸ He assumes in effect that the water is an incompressible nonviscous fluid moving everywhere vertically on the water level and that water which rises above this level can be disregarded. Figure 4 shows the actual flow pattern for a conical projectile shortly after entry. Each chain of dots represents the successive positions of a tiny bubble of air as revealed by four successive exposures on a single plate. The validity of this assumption (which, as explained in Section 9.2, predicts infinite peak pressure) is discussed in Appendix II; for the present, only its theoretical consequences are considered.

The instantaneous potential flow will then be that around a lens-shaped solid $S + S'$ consisting of the portion S of the projectile which is below water level and its mirror image S' under reflection in the water surface (see Figure 2 of Appendix V). If the induced mass

$$m' = \frac{K}{v^2} \quad (2)$$

of the water (where K is the kinetic energy of the potential flow around $S + S'$) can be computed, then for vertical entry one can use the momentum

^e Oral communication from Harold Wayland.

^f Direct confirmation is found in an unpublished picture by Newton Harvey of a sharp needle entering water.

equation (3) to determine the time-deceleration curve.

$$(m + m')v = mv_1. \quad (3)$$

It should be emphasized that in (3) $v(y)$ and $m'(y)$ are the velocity of the projectile and the induced mass of the flow for a given depth y of submergence; v_1 is the initial velocity of the projectile and m its mass. Differentiating (3) with respect to y , we get

$$(m + m')\frac{dv}{dy} + \frac{dm'}{dy}v = 0, \quad (3')$$

which can easily be solved for deceleration $a = dv/dy$.

The computation of K was accomplished by von Kármán¹⁸ for wedges. Recently Shiffman and Spencer^{48, 94} have succeeded in finding the explicit solution of the potential flow problem for spheres. The computed time-deceleration curve is shown in Figure 5.

The virtual mass forces just discussed are intermediate between the peak forces of Section 9.2 and the steady-state forces for the entry speed of Chapter 11, both as regards duration and magnitude. For this reason they are hard to isolate experimentally,^g and

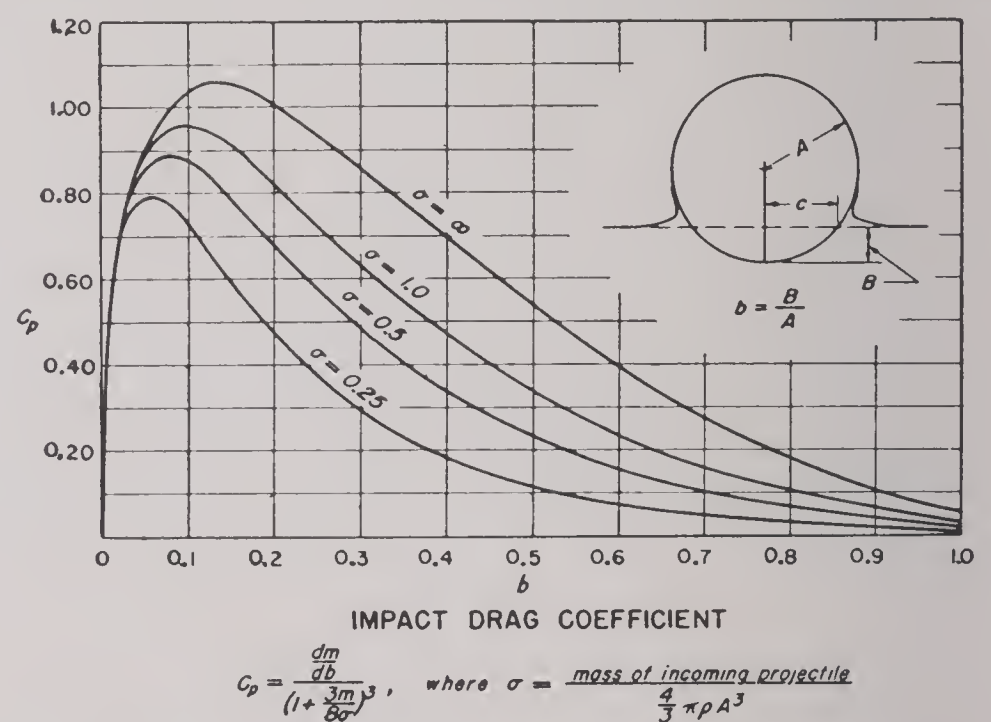


FIGURE 5. Time-deceleration curve (AMP-NYU).

no experimental values can be compared with the curves of Figure 5. However, it might be mentioned that the earlier peak decelerations, obtained at Morris Dam with copper-ball and other accelerometers, gave readings for oblique entry at 19° that had the predicted order of magnitude.

Other experimental results which reveal induced mass deceleration are described in Section 9.4.

^g With the present Rule optical whip recorder, it does not seem feasible to measure the drag component accurately enough to get the time-deceleration curve. It is, however, hoped that time-distance measurements on a special slit-illumination drum camera at the Naval Research Laboratory will give more information.

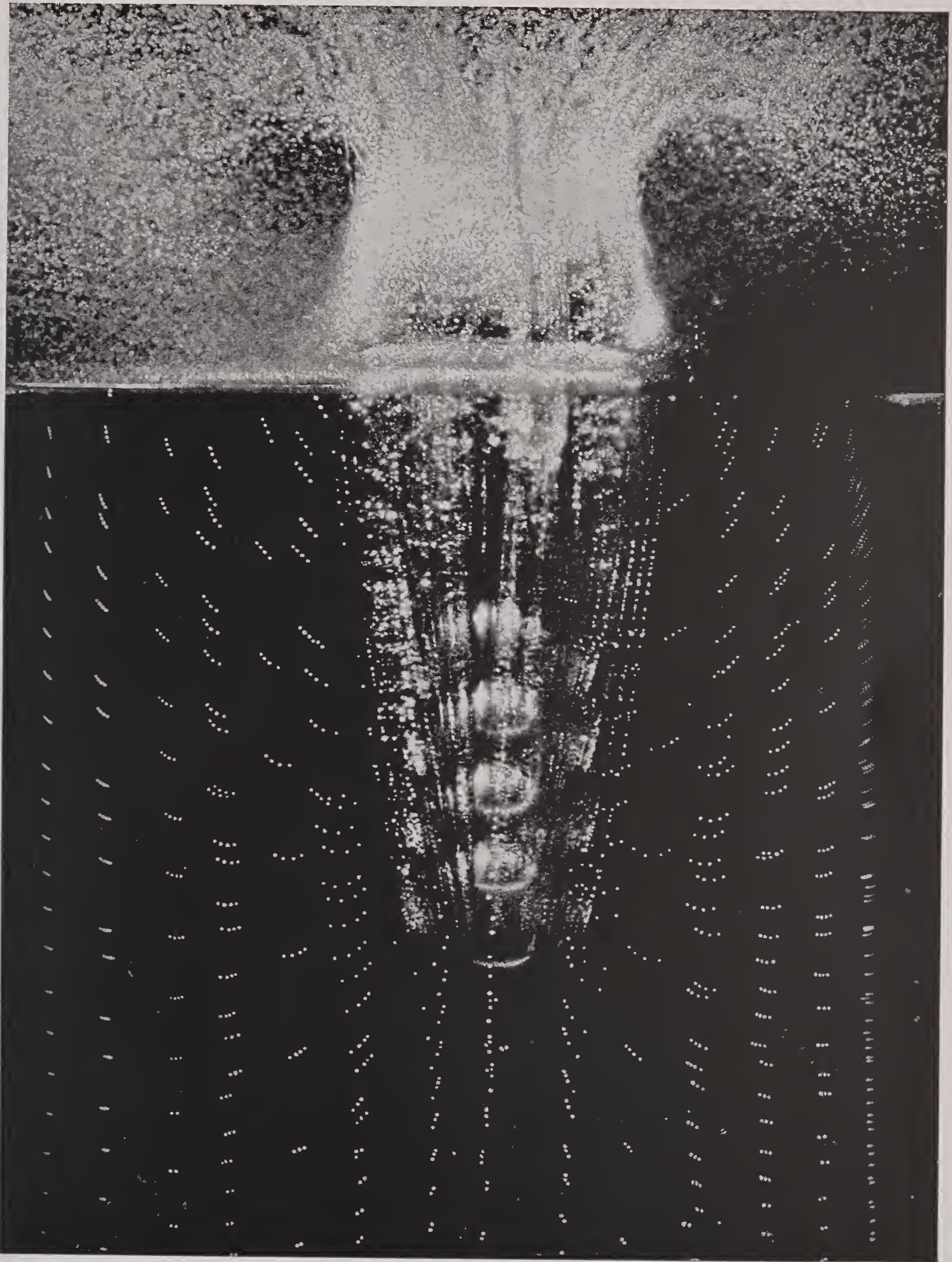


FIGURE 4. Pin-point bubbles (CIT).

CONFIDENTIAL

9.4 INDUCED MASS VELOCITY LOSS

By curve-fitting, one can find the α and v which give the closest fit of formula (1) of Chapter 8, $\alpha t = (e^{\alpha s} - 1)/v$ to the observed time-distance curve after total submergence. One finds that the pseudo-initial velocity v obtained by extrapolating backwards in this way is less than the actual impact velocity. If we assume that the difference is due to the induced mass effect, called the skin effect, we get an estimate, as in (3), of $m' = m(v_1 - v)/v$. The most significant experiments have been made with light bodies entering perpendicularly, because the effect is most easily measured in this case.

We have reproduced in Table 2 empirical measurements of m' for various bodies; for convenience, we have tabulated the ratio m'/M of the measured m' to the mass M of water in a sphere of the same diameter for bodies of revolution traveling axially. For two-dimensional bodies (plates and wedges), M is the mass of water in a cylinder having the same diameter as the body. We have also tabulated the ratio m'_i/M , where m'_i is the theoretical induced mass of the head plus its mirror image (as used in von Kármán's theory).

TABLE 2*

	Sphere	Disk	45° cone	60° cone	90° cone	Cyl- inder	174° wedge	157° wedge	150° wedge
$\frac{m'_i}{M}$	0.5	1.0				1	1.95	1.8	1.7
$\frac{m'}{M}$	0.4-0.44	0.9-10.3	0.3	0.4	0.7		2.6	1.9	1.5

* Data for this table are available in reference 49 of the bibliography for sphere, disk, and cones, and in reference 50 for disk and wedges.

In R. L. Kreps' tests,⁵⁰ an increase in m' of as much as 80 per cent through the range 4 to 15 fps is observed. This may be due to the transition from entry without to entry with a cavity, which occurs in this range. At least Kreps and F. P. Mayo and E. A. Richardson⁴⁹ find little variation in m' above 15 fps.

These experimental results indicate that von Kármán's theory will give results of the correct order of magnitude for the first half-diameter of entry; this point is discussed in detail in Appendix II.

9.5 WHIP WITH OBLIQUE ENTRY; HEMISPHERICAL HEAD

When a symmetrical projectile strikes the water, the lower side of the head is subject to the fluid pres-

sure, which is normal to the projectile surface,^h sooner than the upper side (see Figure 6). In the case of a convex (e.g., hemispherical, conical, ogival, or elliptical) head, this pressure has a *counterclockwise* moment (see Figure 6A); in the case of a flat head, the

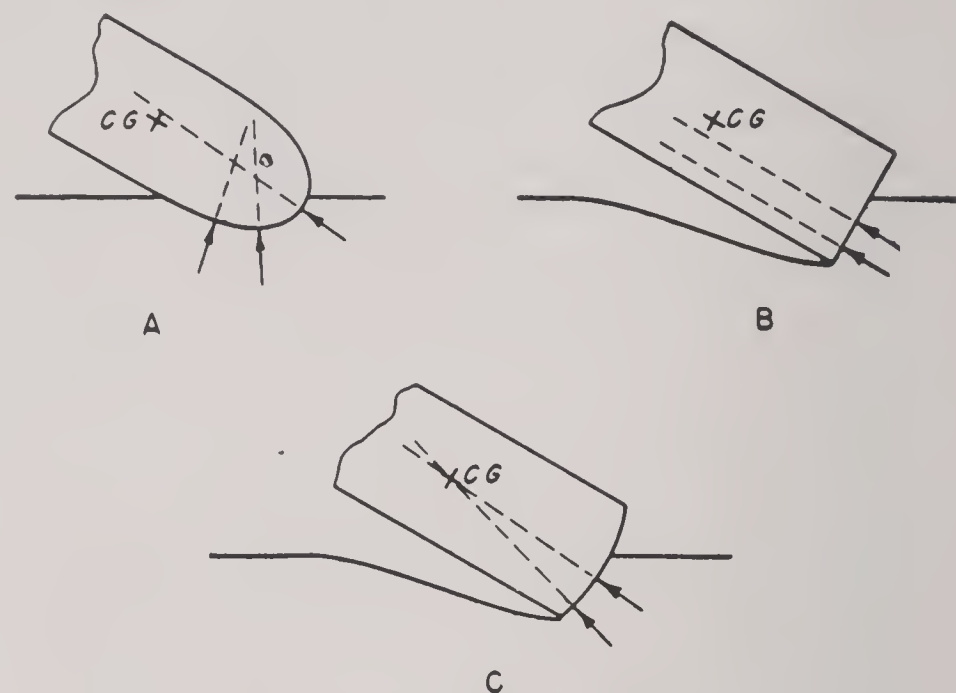


FIGURE 6. Whip impulse.

moment is *clockwise* (see Figure 6B). The dividing line (for the case of zero moment) is furnished by a projectile the head of which is a spherical cap centered at the center of gravity (see Figure 6C and Chapter 8, footnote i). This special design, which has been suggested independently by various individuals, was actually adopted in the German torpedo-bomb.⁵²

After the head is submerged, there is no moment if the pitch is zero. With large down-pitch the moment is ordinarily clockwise, except in the case of a projectile with a flat or nearly flat head, as noted above; with up-pitch, it is counterclockwise. Hence the decision as to whether a projectile noses down or up depends on its *pitch* at entry, as well as on its head shape. But for the present we shall discuss only the relation to head shape.

The qualitative discussion above agrees generally with observation, except that actually small projectile models with streamlined head shapes, entering at 125 fps or less, may nose down at entry instead of nosing up. This phenomenon is discussed in detail in Sections 12.3 and 12.4.

A way to estimate roughly the quantity of the

^h This is a postulate of theoretical fluid dynamics. In fact, measurements with the Rule optical whip recorder showed that the tangential force was less than 2 per cent of the normal force.⁵¹ The entry whip is usually so much larger than the entry angular velocity ω_1 due to air that one can neglect the latter. Thus only θ_1, ϕ (and entry yaw and roll) need be considered.

torque impulse I_M at entry, based on the following three crude assumptions, will now be given.

Assumption 1. The pressure p on an infinitesimal surface element dS whose outward normal makes an angle $\psi \leq \pi/2$ with the line of forward motion is normal to dS and is

$$p = \frac{1}{2}\rho v^2 \cos^2 \psi. \quad (4)$$

Assumption 2. This pressure p is applied to the surface elements below water level and to no others.

Assumption 3. The velocity and pitch are nearly constant during the impact phase.

The basis for making these assumptions is discussed in Appendix III; for the present, we shall only list some of the theoretical formulas to which they lead and compare these with experiment.

For a sphere moving horizontally with its horizontal diametral plane y radii below the water, we get $C_L(y) = (1 - y^2)^2/8$; this is compared with Ramsauer's empirical measurements in Figure 7 of Chapter 8. The discrepancy for shallow ploughs is possibly due to the piling up of water ahead of the sphere. This is also seen in a British report.⁵³ For nearly horizontal travel, as with ricochet, by integrating the approximate differential equation $y'' = 3(1 - y^2)^2/64\sigma$ corresponding to $C_L(y) = (1 - y^2)^2/8$, we get a predicted critical angle $\theta_c = 18^\circ/\sqrt{\sigma}$ for ricochet, which agrees closely with observation. The calculations are outlined in Appendix III; they were first performed by d'Alembert.^{5b} D'Alembert, however, used the coefficient 2 (Newton's formula) instead of $1/2$ in equation (4).

We are also led to the prediction that $\theta_2 = \theta_1$; that impact and ricochet angles are equal; actually, $\theta_2 = 0.9\theta_1$ on the average; the discrepancy is presumably due to virtual mass effects, making $C_L(y)$ 20 per cent greater on the descending than on the ascending part of the plough.

The predicted plough does not, however, conform closely to experiment. The observed plough seems to conform to the prediction that increasing density in the ratio $1/\sigma$ increases length of plough in the ratio $1/\sigma$ without increasing its depth. It also conformsⁱ to the prediction that the plough will become indefinitely

long as $\theta \rightarrow \theta_c$, if deceleration does not reduce the speed to the point where gravity becomes dominant. The prediction that the plough will increase (indefinitely) as θ approaches zero is, however, not fulfilled. Actually, conforming to Ramsauer's experimental determination of $C_L(y)$ for shallow submergence, the plough seems to decrease until $\theta = 0.06\theta_c$ at least.

For any projectile whose head is a section of a sphere (hemisphere or spherical cap), entering with zero pitch, the counterclockwise moment impulse I_M is bI_L , where I_L is the lift impulse, and b is the distance from the center of gravity forward to the center of the spherical cap. With a hemispherical head, by Appendix III,

$$I_L = \frac{\rho V_h}{15} v \cot \theta_1 \quad (V_h = \text{volume of head}). \quad (5)$$

This case is interesting, because we can compare the theory with experimental results for the Mark 13 torpedo entering at 19° . In this case,^j the impulsive change $\Delta\omega$ in angular velocity ω is $\Delta\omega = 0.0039 v_1$ radians per sec; observation³⁴ gives $0.0044 v_1$ radians per sec, with some experimental scatter.

The approximate proportionality (5) between entry whip and $\cot \theta$, which was first predicted in reference 8, has recently been confirmed by 1 in. diameter model experiments. The optical whip recorder developed by B. H. Rule of the Morris Dam Group now permits extraordinarily accurate measurements on entry whip.

We can also get a simple nondimensional theoretical formula valid for Mark 13 model experiments at arbitrary entry speeds and angles. We have an angular velocity of about $0.019 \cot \theta_1$ radians per length (14 ft) of travel; moreover (see Chapter 12), this should be independent of size and entry speed.

However, it is not independent of the entry pitch ϕ_1 . The drag component exerts an average moment during entry of $D b \phi = \frac{1}{8} \rho V^2 \pi r^2 b \phi_1$ (since^{17a} $C_D = 0.25$, apparently^k), through a distance $r(\cot \theta_1 + \csc \theta_1)$, or an impulse of $(45\phi/16)bI_L(1 + \sec \theta_1)$. Hence the predicted whip is³⁴

$$0.019 \cot \theta_1 [1 - 2.8\theta_1(1 + \sec \theta_1)] \frac{\text{radians}}{\text{length}}. \quad (6)$$

ⁱ Thus Ramsauer³⁰ gets ploughs corresponding to different values of θ_1/θ_c as follows, $\sigma = 7.8$:

θ_1/θ_c	0.15	0.30	0.45	0.60	0.74	0.91	0.96	1
Plough	10d	12d	13d	18d	25d	50d	85d	∞

We experimented with Lucite spheres ($\sigma = 1.3$) and at very low angles ($\theta_1/\theta_c = 0.06$ to 0.12) obtained ploughs of about $5d$, or $\sqrt{1.3/7.8} \times (10d - 12d)$.

^j Since $b = 5$ ft, $V = 2\pi r/3$, $r = 11.2$ in., so that $\rho V_h = 100$ lb, and $bI_L = 33V \cot \theta_1$. Moreover, the moment of inertia is $25,000$ lb-ft² = 800 slug-ft².

^k At steeper θ_1 , it is probable that C_D is bigger, possibly 0.5 , which would correspond to (9) under full submergence. Recent data, suggested that $C_D = 0.29$, which would predict $\phi_c = 8^\circ$.

When $\theta_1 = 19^\circ$, this reduces to

$$0.054(1 - 5.8\phi_1) \frac{\text{radians}}{\text{length}} = 3^\circ \frac{(1 - \phi_1/10^\circ)}{\text{length}}. \quad (6')$$

Formula (6) explains the observed tendency for the critical pitch ϕ_c yielding zero whip to decrease as θ_1 increases, and the observed linear dependence of entry whip on entry speed (see Figure 7).

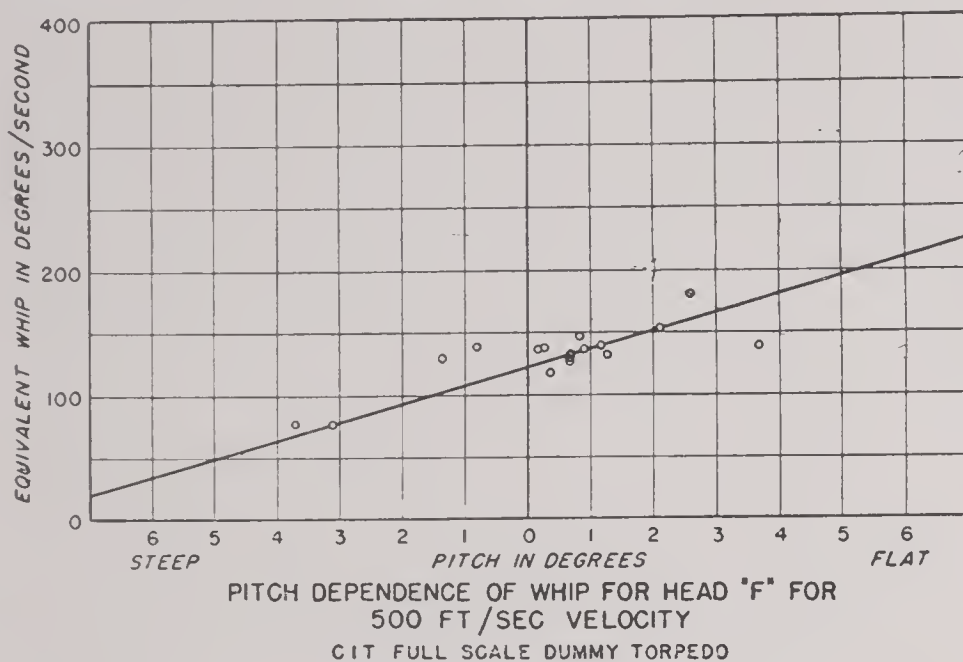


FIGURE 7. Whip graph.

With 8-in. diameter models of the Mark 13 torpedo, the observed⁵⁴ whip is only about 1.5° per length at zero pitch, instead of 3° , and the "pitch whip" [coefficient of ϕ_1 in (6')] is apparently nearer 0.6 than 0.3. (We see that we have a scale effect if the experimental results are taken at their face value.) On the full-scale torpedo, the steep pitch giving zero whip is³⁴ probably 8° , instead of the 10° predicted by (6'). With a 1-in. model entering at 100 fps, an entry whip of 500° per sec = 5° per ft = 3° per length was observed⁵⁵ at zero pitch, as predicted by (6'). This increased to 2000° per sec at the time of tail slap.

A rough explanation of this increase (which has not been observed on the full scale torpedo) is in terms of the moment of the drag force. Assuming $C_D = 0.25$, we have a moment $\frac{1}{8}\rho v^2 \pi r^2 b \phi = I(d\omega/dt)$ as before. We can introduce the integrating factor $d\phi/dt = \omega$ to get $\frac{1}{8}\rho v^2 \pi r^2 b \phi - I\omega^2 = \text{constant}$. Setting $\phi = 9.5^\circ = \frac{1}{6}$, $v = 105$ fps, $r = \frac{1}{24}$, $b = 5/22.4$, and $I = 25,000/22.4$,⁵ we get $\omega = 100\phi = 1000^\circ$ per sec. This is of the right order of magnitude.

9.6 WHIP WITH GENERAL SYMMETRICAL HEAD; ROLL

In general, the counterclockwise torque impulse I_M of an axially symmetric body entering with zero pitch is the sum of lift and drag components

$$I_M = bI_L - I_{MD}. \quad (7)$$

Here b is the distance from the line of action of the lift forces to the center of gravity, I_L is the lift impulse, and may be expressed as

$$I_L = \frac{1}{2}\rho v \cot \theta_1 \int \cos^2 \psi dV, \quad (8)$$

integrated with respect to distance w along the projectile axis, so that $dV = r^2 dw$ (see Figure 8), and

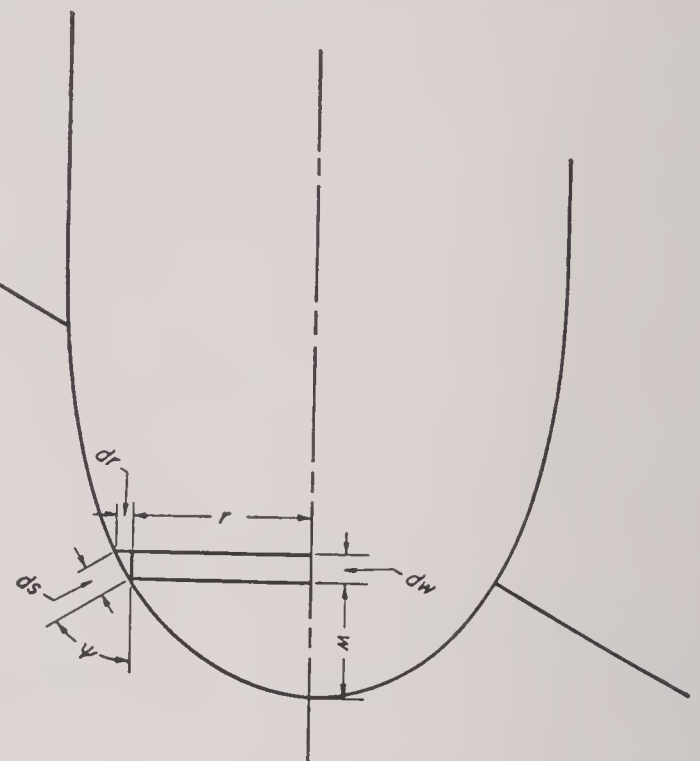


FIGURE 8. Integral formula.

$\cos^2 \psi = dr^2/(dr^2 + dw^2) = dr^2/ds^2$. And I_{MD} is the torque of the drag impulse; the theoretical formula for it, based on assumptions 1 to 3 is

$$I_{MD} = \frac{1}{2}\pi\rho v \cot \theta_1 \int r^3 \cos^2 \psi dr. \quad (9)$$

In the case of a flat head of radius a , evidently $I_L = 0$ and $I_M = -I_D = -\frac{1}{8}\pi\rho a^4 v \cot \theta_1$. For a scatter-bomb model tested at the Alden Hydraulic Laboratory with $d = 1.25$ in. and $I = 279$ gm-in.², the predicted whip in radians per foot is thus about $\cot \theta_1/30$. This gives 0.24, 0.19, and 0.15 for $\theta_1 = 8^\circ$, 10° , 15° ; the average observed values were 0.33, 0.22, and 0.13.

More generally, with a conical head of radius a and vertex angle 2β , $I_D = \frac{1}{8}\pi\rho a^4 v \cot \theta_1$, $I_L = \frac{1}{2}\pi\rho v V_h \sin^2 \beta \cot \theta_1$, and the line of action of the lift forces passes through the center of gravity of the cone.

It will be seen from (7) that long projectiles will have a tendency to receive on entry a counterclockwise angular impulse and short flat ones a clockwise impulse.

Another interesting case occurs with a tilted flat or wedge-shaped head, such as has been used with certain mines. These will be subjected to a continuous torque on entry which can be computed for an arbitrary pitch angle and so freed from Assumption 3.

Blackwell⁹⁰ gives the rate of turning in radians

per feet as $\pi \rho a^3 b v \gamma_L \cot \theta_1 / I$, where γ_L is 0.06 for a 1 caliber radius head (crh) and is 0.055 for a 3 crh of ogival shape.

The effect of yaw at entry on the roll of a torpedo should perhaps be mentioned in an account of impact forces. If the tail yaws to the *right*, as viewed from the rear, there is a counterclockwise roll of about $(100^\circ/\text{sec})$ yaw¹ with the Mark 13 torpedo and about half as much with small "minimum" fins, the

center of gravity being on the axis. If the center of gravity is below the axis, the effect is increased. The explanation of this is not entirely clear, though it has been observed that a vertical whip would cause the fins to roll in the observed direction during tail slap.

¹ Oral communication from Wayland. Qualitatively, the effect mentioned has been confirmed independently at Gosport, England.

Chapter 10

THE CAVITY

10.1 IMPORTANCE

AS ALREADY described in Section 8.2, air almost always follows in the wake of a solid entering water faster than 40 fps, and frequently with entry speeds as slow as 10 fps. Below 10 fps, the water usually closes in behind without entrapping any air.³⁵ Under exceptional circumstances (hydrophilic surface, etc.) no cavity is formed at 50 fps (see Appendix VIII). The air usually trails behind the solid for 5 to 60 diameters. Ultimately water closes in behind the air, and the cavity becomes a bubble from which the air is gradually stripped away by the water flowing past the solid.

This cavity may have important practical effects. Thus in the case of an HE projectile, it may provide a vent through which fragments and blast effects may pass to the open air, possibly endangering aircraft, etc. More frequently, the bubble will cushion the explosive blast, reducing its effectiveness by perhaps^a 15 per cent to 25 per cent. Again, the cavity (as well as dynamic pressure) will greatly affect the action of a hydrostatic fuze, especially if improperly located.¹²

The presence of a cavity, especially before tail slap occurs, will also inhibit the functioning of steering controls and propellers on a torpedo, as well as (see Section 9.6) cause a large underwater roll. For this reason, attempts have been made to secure head shapes producing a small cavity^b by means of prods [i.e., nose extensions (see Figure 1)] or other devices.⁵⁷

^a Informal oral communications from E. B. Wilson, based on underwater explosions of charges placed inside air-filled boxes.

^b The idea seems to have been suggested by Townend; discussion may be found in minutes of the British Aircraft Torpedo Entry Subcommittee. Mason of CIT has attempted to eliminate the bubble by sheathing the projectile in a container which, by flaring out, would prevent the air from entering the water. See Appendix I, Section 8.

And above all, the presence of the cavity alters the trajectory of any projectile. Thus projectiles which would travel in a fairly straight line without a cavity actually often travel in a "circular arc."

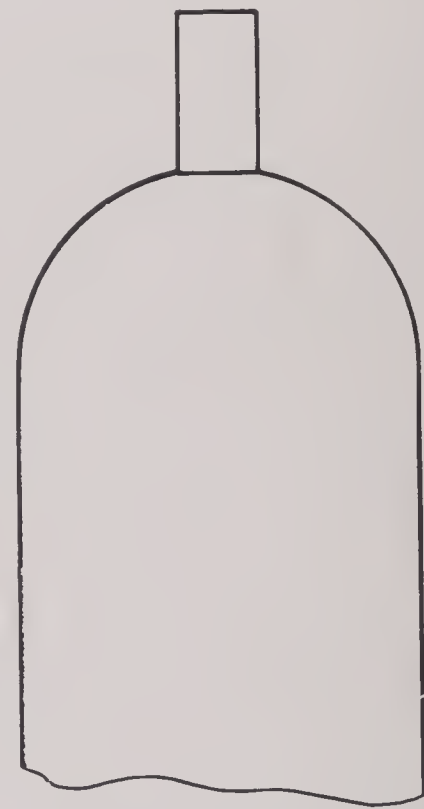


FIGURE 1. Nose prod.

The air-filled cavity formed when a projectile enters water should be clearly distinguished from the boiling or true cavitation which occurs locally around any solid body (propeller or turbine) when the pressure falls below vapor pressure.¹⁹ Rapid acceleration can cause true cavitation. By Bernoulli's theorem, true cavitation ordinarily happens when the dimensionless "cavitation parameter"

$$K = \frac{2(p - p_v)}{\rho v^2} = \frac{(p - p_v)}{q} \quad (1)$$

falls below a "critical" value^c K_c between 0.2 (for

^c Here $p = (2,120 + 62.4y)$ lb per square foot is the hydrostatic pressure, the vapor pressure p_v is usually small, and $\rho = 62.4$ lb. per cubic foot is the density of water; $q = \rho v^2/2$ is the dynamic pressure at the stagnation point.

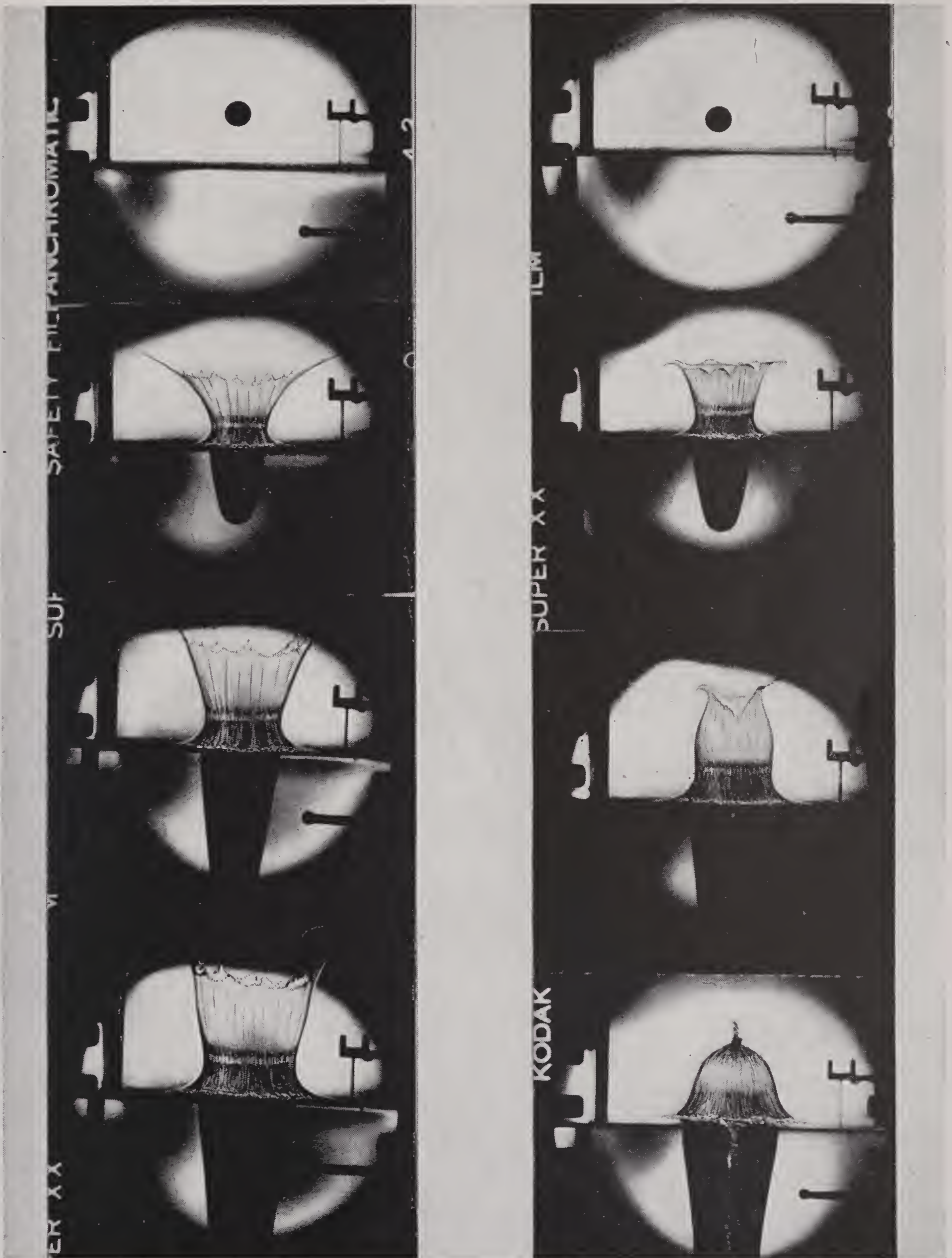


FIGURE 2. Details of cavity behavior (Experimental Lab, Cambridge University, England).

CONFIDENTIAL

streamlined bodies) and 2; hence cavitation usually occurs when

$$v \geq \sqrt{\frac{2(p - p_v)}{\rho K_c}} = \frac{50}{\sqrt{K_c}} \text{ fps} \quad (1a)$$

10 ft below the surface, under standard atmospheric conditions. The cavitation bubble becomes large when $K = K_c/2$, hence ordinarily at 50 to 165 fps. Further details may be found in Section 10.10.

10.2 SPLASH AND SURFACE SEAL

When a projectile strikes the water at high speed, it throws out a sheet of splash tangential to its surface in all directions (see Figure 3). This sheet may move forward with four to five times the projectile speed, and its edge dissipates into spray. The volume of the splash has never been accurately measured. It is presumably less than the projectile volume, but at low altitudes of release it has been known to damage the tail controls of an airplane.^d In addition, it will always be enough to wet the nose (cause a supersensitive fuze in the nose to function), even at the shallowest entry angles.

But the main importance of splash arises from its transition to a "surface seal," choking off the access of air to the cavity. Small-scale pictures (see Figures 2, 3, and 6) of entry into water^{1,10,13} show that the splash forms into a sheath about the air rushing into the cavity. (The practical importance of surface seal was first pointed out by Blackwell.¹⁰) The underpressure of the intruding air causes the upper part of the splash to come together and form a dome which blocks the entrance to the cavity. With spheres entering vertically at speeds below 300 fps, this happens when the sphere is 5 to 8 diameters below the surface. (The instant of surface seal is hard to locate exactly.) With oblique entry, and also at higher entry speeds, surface seal takes much longer. Figure 3 shows the development of the splash and surface seal in the case of a 1½-in. steel sphere entering at 15° and 300 fps. The shape of the head will also affect the time of surface seal. Thus surface seal is more rapid (surprisingly) with a disk entering vertically than with a sphere.

Instead of being blown into the cavity, the dome appears to stay in a more or less fixed position and

^d Aberdeen Proving Ground, Firing Record B-7296, Aug. 1-3, 1944, made by Lieutenant Yanik; the release altitude was 25 ft. The possibility that a fuze might remain unwetted was raised by Captain Schuyler.

to thicken from the sides, so that no more air can enter the cavity. At entry speeds greater than 100 fps, the cavity is still expanding under its own momentum when this happens. This adiabatic^e expansion causes a large underpressure to develop in the cavity, and prevents it from growing as large as it would otherwise. At very high entry speeds, a pulsation of the bubble, similar to that observed with underwater explosions, becomes more and more marked.^{15a} The period of oscillation is about $10^{-5} \sqrt[3]{E}$ sec where E is the impact energy in ergs.

The preceding explanation of surface seal and its effects has been checked by Taylor and Davies,¹³ who showed that if the air density is reduced to nearly zero the splash is not blown inwards and a much larger cavity is created.^{1f} Recent experiments^f at NOL give further confirmation (see Figure 4). It was also shown experimentally¹³ that surface tension has hardly any effect on surface seal. Worthington observed^{35a} that the formation of the splash into droplets is, however, caused by surface tension. (See also Appendix VIII, Section 2.)

One would expect the blast from an air gun to act in just the opposite way from reduced density, accelerating surface seal and diminishing cavity size; this has, in fact, been observed at NOL.^f Pictures at the Alden Hydraulic Laboratory show that the blast may follow a 1.5-in. diameter projectile for a distance of 10 ft. in air. (See Figure 4.)

As the sequence of events just described seems to occur also in the few available full-scale photographs,^g presumably the detailed observations made on photographs of models apply also to full-scale projectiles.

10.3 CAVITY SHAPE

The cavity formed by a projectile entering the water vertically is, of course, axially symmetric. At slow speeds the cavity is curved and has at first a roughly paraboloidal shape. For fast shots and before surface seal the instantaneous cavity is roughly con-

^e That is, with air, pressure is proportional to $V^{-1.4}$, where V is the cavity volume. This is because the time is too short for conduction of heat to be appreciable.

^f By David Gilbarg.

^g See Bomb-Firing Tank Note No. 7, "New Design of the 250-lb A/S Bomb. Main Tank Trials on Design C with 10° Skew Nose," especially Figures 5 and 6, where the "shoulder" of surface seal is clearly visible. Various persons have expressed skepticism regarding surface seal for full-scale projectiles, and, indeed, it might be wondered whether the splash would form an airtight sheet or a permeable spray.

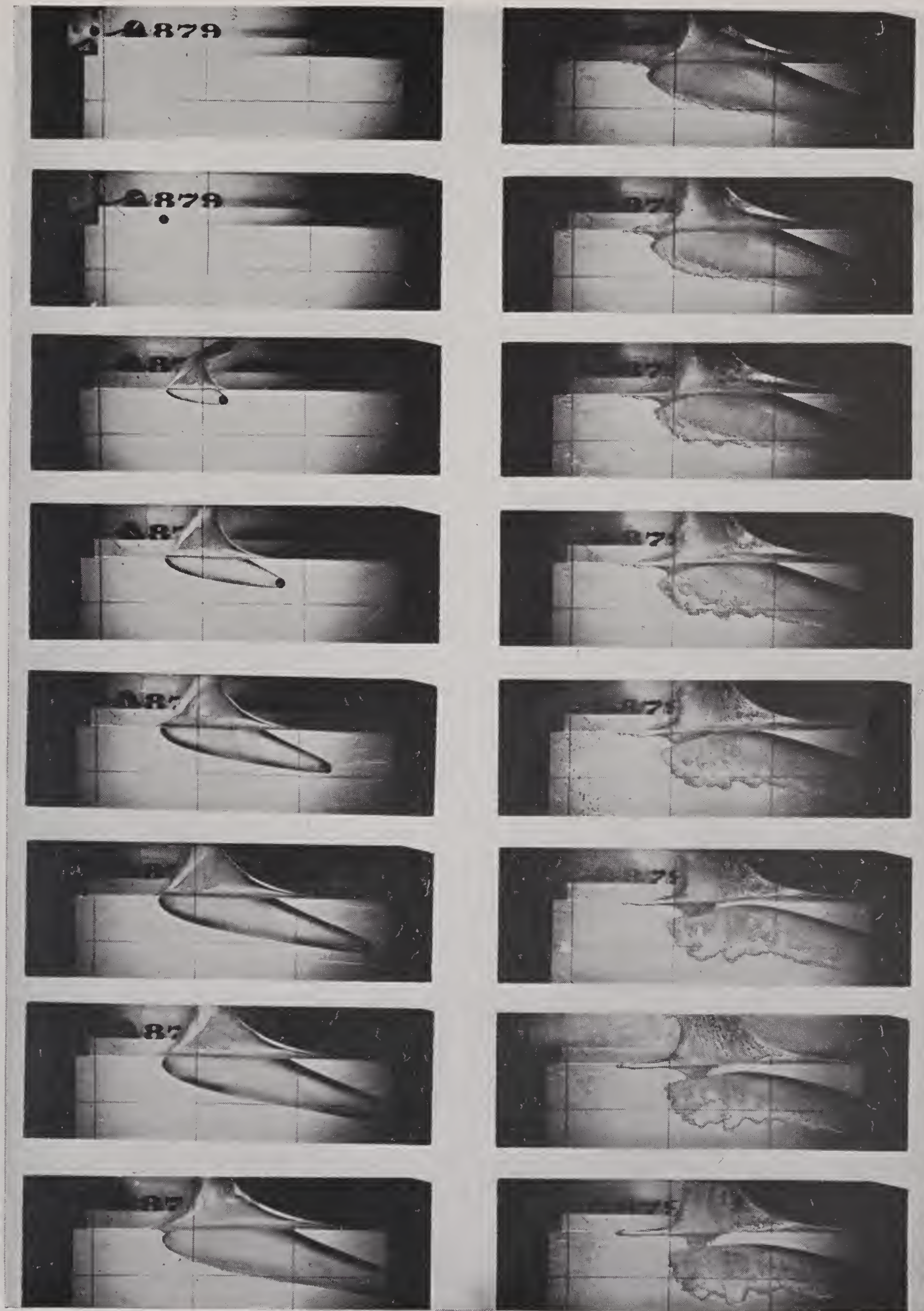


FIGURE 3. Surface seal (AHL).

CONFIDENTIAL



FIGURE 4. Blast effect on cavity (NOL).

CONFIDENTIAL

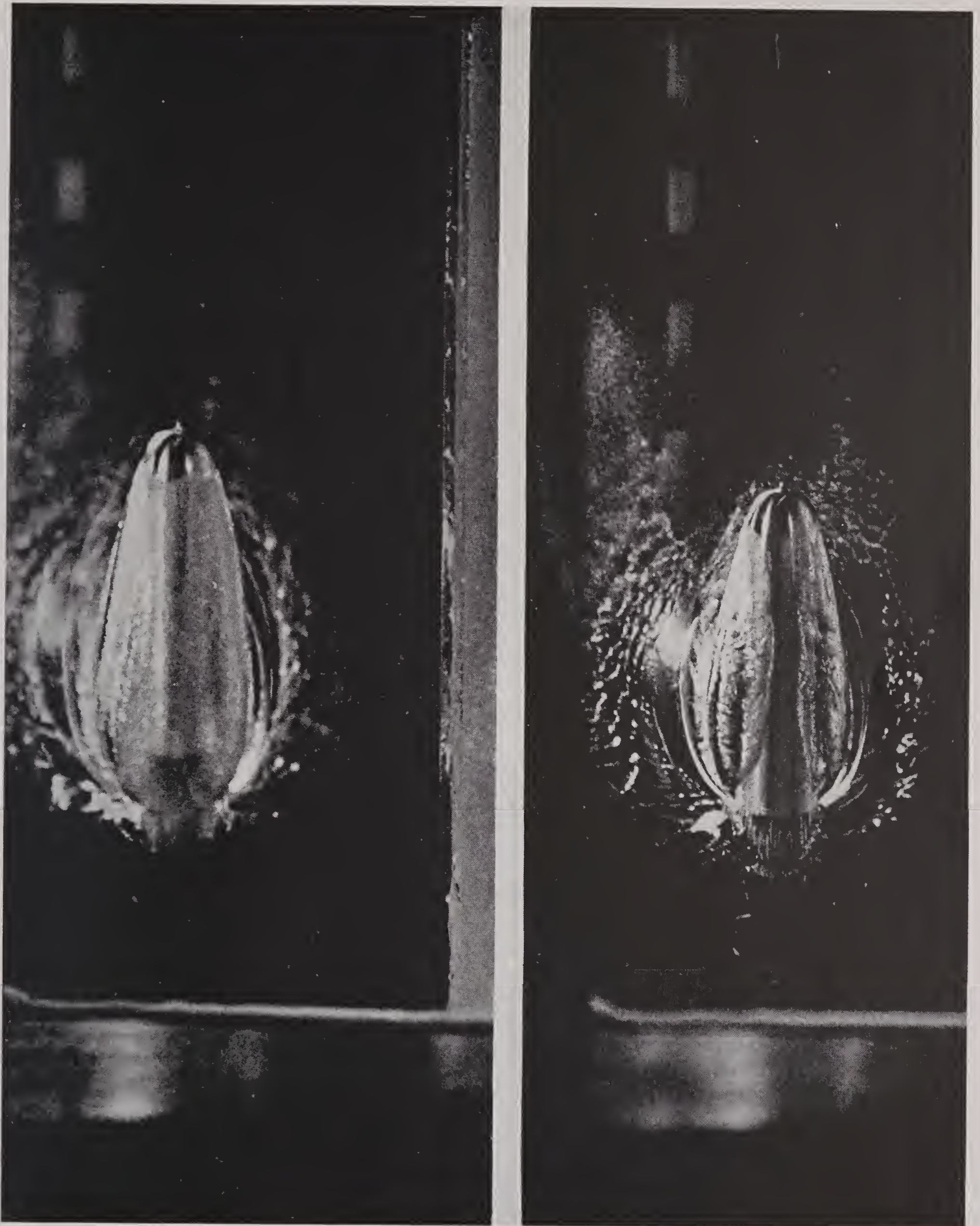


FIGURE 5. Bubble from below (CIT).

CONFIDENTIAL

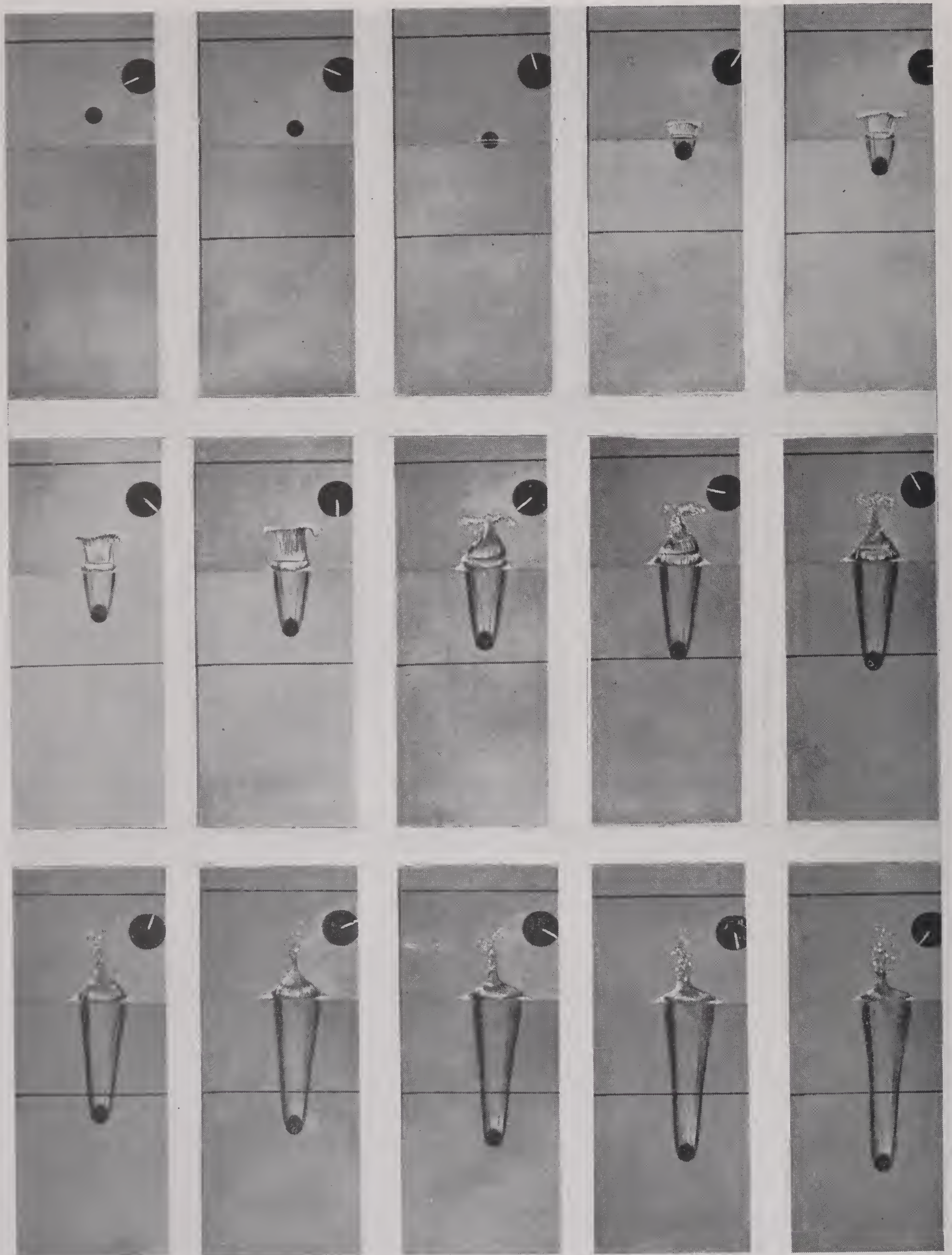


FIGURE 6A. Vertical entry of steel spheres (AHL).

CONFIDENTIAL

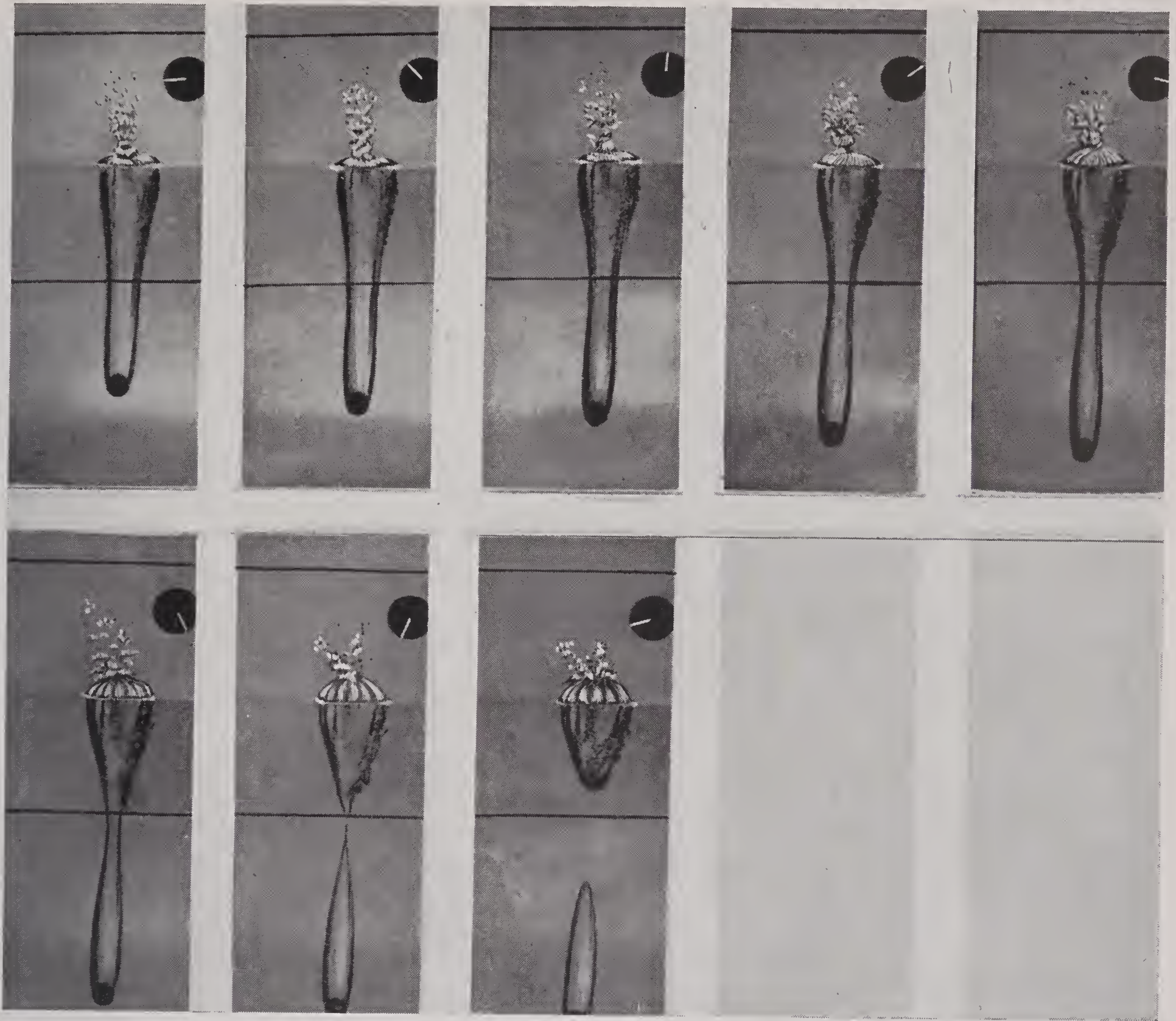


FIGURE 6B. Vertical entry of steel spheres (AHL).

cal over the middle portion, the cone semiangle (cavity angle) being, for spheres, about 6° to 7° .^h After surface seal, with the increase of underpressure in the cavity, the cone angle may decrease toward zero. However, the shape of the stretch of the cavity profile extending for 1 or 2 diameters behind the circle of separation on the projectile nose is largely independent of the projectile velocity and of the shape of the remainder of the cavity. Unlike the cone semiangle, it is thus determined almost entirely by the head shape. Moreover, its width at a fixed point gives a good measure of the drag, wider cavities going with higher drag coefficients (see equation (8ff)).

^h For an extreme case, see Plates BII-BV of reference 15 showing spark shadowgraphs of 3/32-in. steel spheres entering at about 3,000 fps.

After oblique entry, the water at the top side of the cavity is nearer the surface and yields more to the side thrust of the moving projectile, so that the early cavity is oval in cross section, the path of the projectile nose lying near the bottom side of the oval (see Figure 3b). The rear lip of the cavity may in fact be in contact with the model as it passes. Photographs taken from underneath the cavity by B. H. Rule of the Morris Dam Group at CIT (see Figure 5) show that at low speeds (30 to 100 fps) and with long slender noses this contact between projectile and cavity is maintained along the whole length of the projectile, while at higher speeds the cavity breaks away at the usual circle of separation on the nose.

This phenomenon helps to explain a previously unexplained trajectory anomaly. High-speed photo-

CONFIDENTIAL

graphs of GP bombs and a model of a navy practice bomb, filmed at the Alden Hydraulic Laboratory, show a consistent tendency to nose up at high entry speeds and to nose down at lower speeds. The same tendency has been shown even more noticeably in slender-headed torpedo models shot at CIT. This effect is discussed further in Section 12.4.

The head of the moving projectile gives to the cavity wall an outward velocity away from the trajectory of the nose. Under the influence of gravity and the underpressure in the cavity following surface seal (and possibly the dynamic underpressure of the air rushing into the cavity) this motion is slowed down and reversed. At moderate Froude numbers (say $F < 10,000$) the intruding walls of the cavity first collide on the axis at a point between the model and the surface, dividing the cavity into two parts, the upper one remaining relatively motionless and the lower one following the model down and further subdividing. This is the deep seal.^{10,35,58} (See Figure 6.) If the entry speed is very small ($F = v^2/rg =$ about 40, where v , r , and g are the entry velocity, radius of the projectile, and acceleration of gravity respectively) the surface seal does not occur at all, only the deep seal. The cavity volume stops growing before enough air has been pulled into the cavity to cause a surface seal. With slightly faster speeds ($F = 350$) the surface seal may form and then be blown open by the overpressure in the contracting cavity. At Froude numbers $F > 5,000$, the surface seal is permanent. At high Froude numbers ($F = 70,000$), the deep seal may never occur, the collapse of the cavity wall onto the axis occurring continuously at the rear end of the cavity so that the cavity follows the projectile. This occurs especially at low entry angles, where the gravity gradient along the trajectory and the underpressure are small (the latter due to the late surface seal), so that the factors contributing to a deep seal are minimized.

An interesting phenomenon associated with closures in the case of vertical entry is the appearance of jets moving rapidly along the axis in both directions away from the seal, caused by the radial flow of water symmetrically onto the axis at the time of seal.^{13,35b} (See Appendix V.) The down jet from surface seal may pass down the full length of the cavity and strike the projectile. This was conjectured by Worthington, who saw the jet pass through the narrowing neck of the deep seal, but was first seen recently in small-scale motion pictures taken in silhouette at NOL. The force of the impact of the jet

on the model was in one case sufficient to knock the model out of the cavity. This jet impact may explain the observed and previously unexplained "chatter" in hydrostatic fuzes in the tails of mines and depth charges.

Figure 7 shows the development of the down jet from the surface seal. It collides with the newly formed upward jet from the deep seal and will later be obliterated by this growing upward jet, but meanwhile, as evident in the last four frames of the picture, it breaks through the bottom of the upper half of the cavity, carrying air with it.

10.4 A QUANTITATIVE THEORY OF CAVITY COLLAPSE

The contents of this section are treated in detail in Appendix V, and the statement made here should be considered only as a summary.

In 1865 Hélie observed that the total volume of the crater formed by a projectile fired into dirt is proportional to the initial energy of the projectile. This is not surprising in view of the fact that if a projectile enters water vertically the maximum cross-section area at different levels is roughly proportional to the space rate at which the projectile loses energy as it crosses the level, which has been explicitly formulated as a law.^{15b} Associated with this approximate law is the physical concept that the energy lost by a projectile passing a given level goes into the work of pushing out the cavity wall at that level against a pressure difference. This hypothesis yields a simple mathematical relation

$$E_0 = \pi(\rho g y + \bar{p}_u)(R^2 - r_0^2) \quad (2)$$

[see equation (1), Appendix V] between the maximum cavity width R , the energy E_0 lost by the projectile, and the average underpressure \bar{p}_u in the cavity. The maximum cavity widths computed from this formula are about 20 per cent greater than the measured widths.

The actual motion of the cavity wall has received some study. Blackwell¹⁰ fitted the graphs of cavity width against time by parabolas and derived a descriptive theory of the kinematics of the cavity which successfully predicted the approximate time and depth of deep closure. Actually, careful graphs of cavity width against time are often better fitted by ellipses than by parabolas. In Appendix V, a new theory of the transient cavity is sketched which predicts this elliptic shape in the case of constant cavity

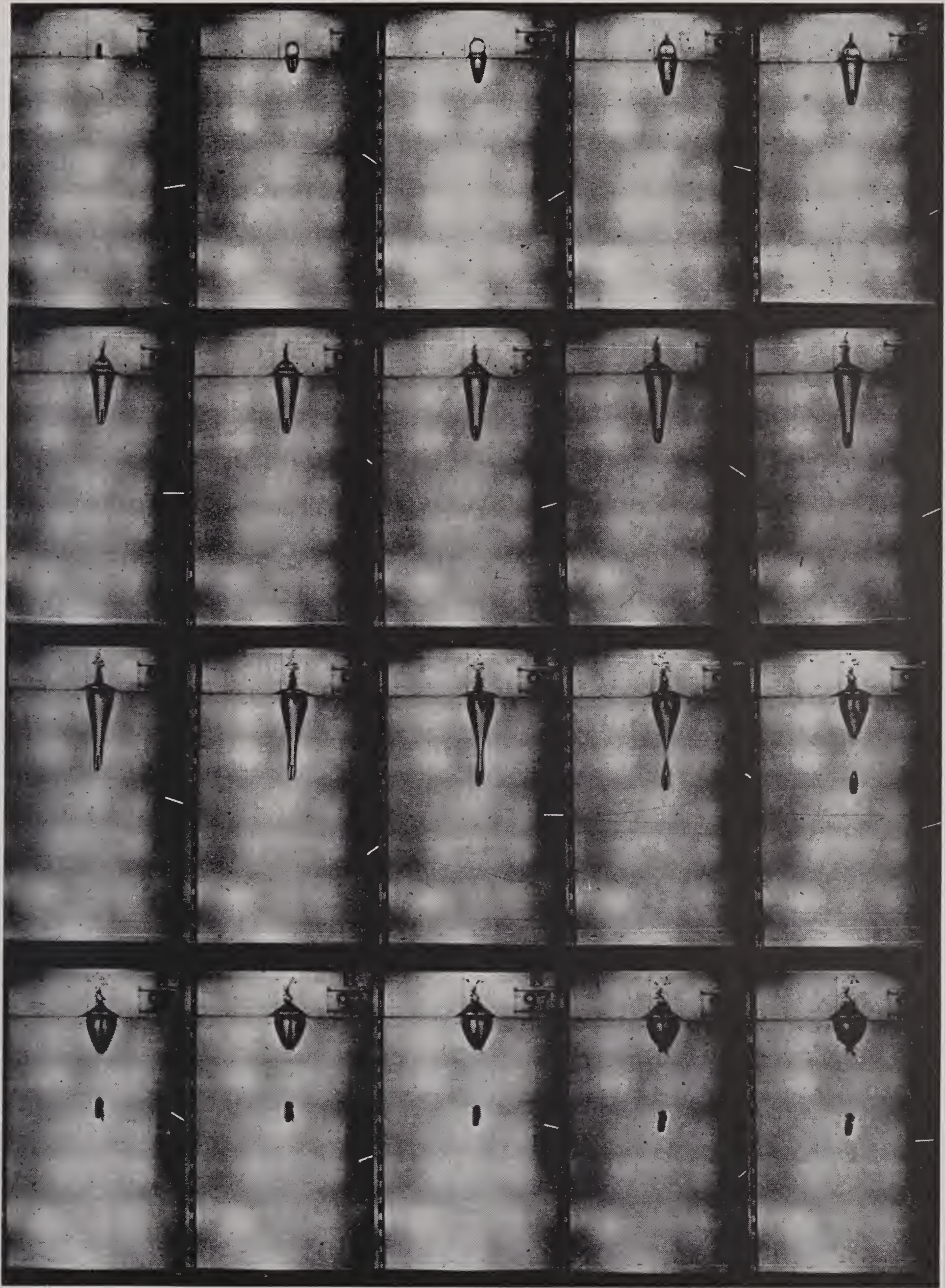


FIGURE 7. Jet and surface seal (NOL).

CONFIDENTIAL

pressure and which has the added advantage that it predicts the motion of the cavity wall from a simple assumption about the velocity pattern of the surrounding water, without introducing arbitrary empirical constants. Departures from elliptical shape for the graph of cavity width vs time are ascribed to varying cavity underpressure, and the underpressure can even be estimated roughly from the graph, though this application is more doubtful. The times and depths for deep seal predicted by this theory agree well with experiment.

10.5 CAVITY DRAG COEFFICIENTS; GENERAL REMARKS

The resistance or drag D experienced by a body moving through a fluid with speed v is most conveniently expressed in terms of the dimensionless "drag coefficient,"

$$C_D = \frac{2D}{\rho v^2 A}$$

where

$$-\frac{mdv}{dt} = D = \frac{\rho v^2 A C_D}{2}, \quad (3)$$

where ρ is the fluid density and $A = \pi r^2$ is the maximum cross section. If the body is in a cavity, we call C_D the cavity drag coefficient. We shall discuss below such cavity C_D ; it will be instructive to compare these with the corresponding noncavity C_D .

Clearly the cavity C_D will be independent of the shape of the unwetted part of the body; hence, in general, it will be determined by the shape of the head. This contrasts sharply with the situation as regards the noncavity C_D , which depends very much on the tail assembly and afterbody streamlining.ⁱ In fact the noncavity C_D can be reduced nearly to zero by proper streamlining^{29a} in the rear, whereas the only way to obtain a low cavity C_D is to use a tapered head. The fact that the cavity C_D may exceed the noncavity C_D leads to a peculiar anomaly. The velocity of a depth charge will decrease steadily until gravity balances the hydrodynamic resistance, when

$$mg = \frac{\rho v^2 A C_D}{2} \quad \text{or} \quad v = \sqrt{\frac{2\sigma l_a g}{C_D}}, \quad (4)$$

the "terminal velocity." If the depth charge has not yet shed its cavity, however, v will then increase

ⁱ This point was made some years ago by H. L. Dryden.

again as the cavity is shed, because in (4) the C_D decreases from its cavity to its noncavity value.^j

Again, the theoretical noncavity C_D of any body is zero by the d'Alembert paradox.^{29b} Whereas, if we assume a cavity (air wake with free boundary) extending to infinity, we get a theoretical C_D between zero and one which can be compared with experiment.^k

Thus, for a flat plate inclined at an angle ϕ to the direction of motion, $C_D = 2\pi \sin \phi / (4 + \pi \sin \phi)$ theoretically, which reduces to $C_D = 0.88$ for broad-

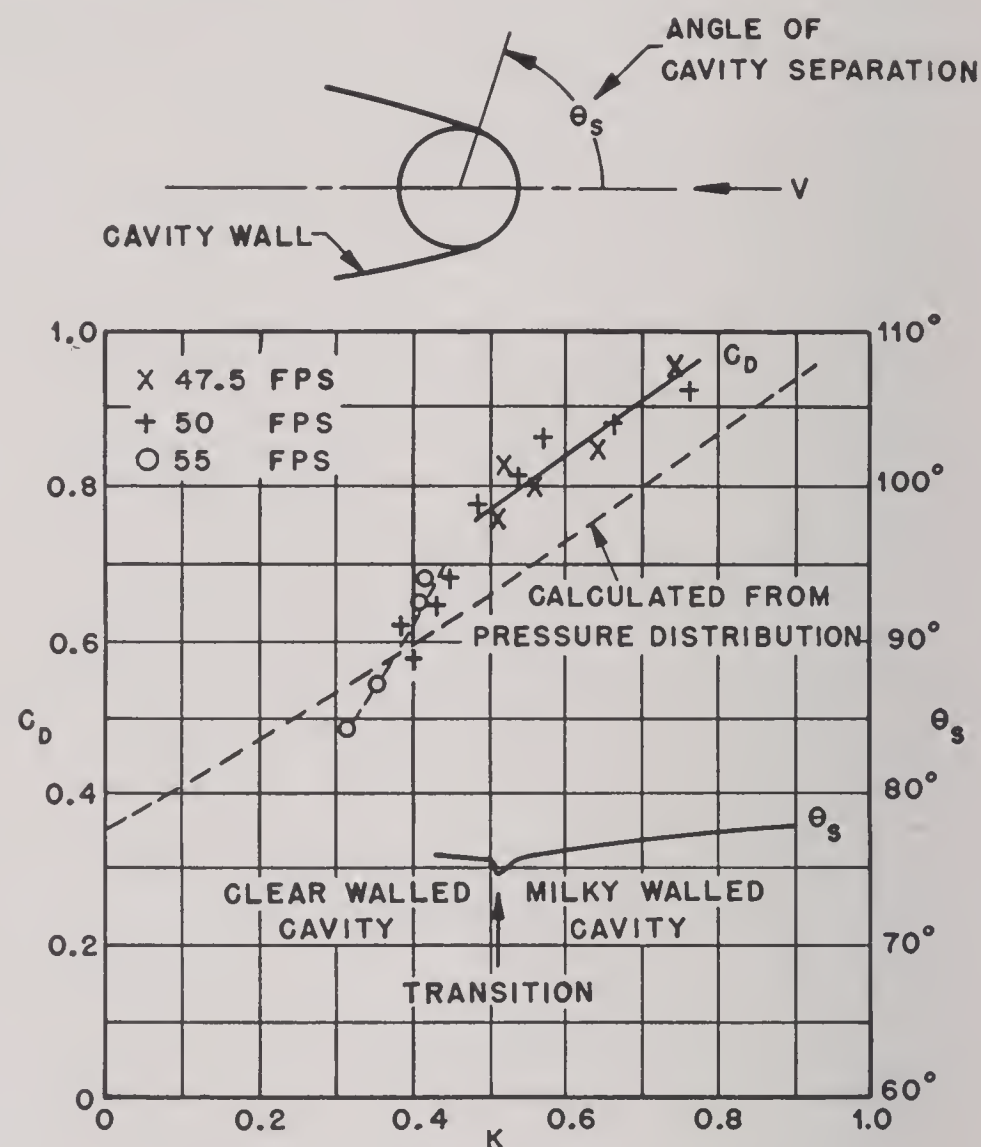


FIGURE 8. Cavitation C_D of cylinder.

side motion ($\phi = 90^\circ$); this was shown by Helmholtz and Rayleigh. More recently, S. Brodetsky has shown^{59,66} that the cavity C_D of a nearly circular cylinder moving broadside was 0.56.

We have shown that the presence of walls in a channel 40 diameters wide will increase the *theoretical* cavity C_D by 60 per cent (see Section 5, Appendix IV). However, if only because of finite

^j See Fairlie Sound Range Internal Report 197, "The terminal velocity of the squid." This is 40 fps at 150-ft, and 53 fps at 300-ft depth. With oblique entry, before vertical descent begins, the velocity may also fall below terminal velocity.

^k It is precisely the wake drag coefficient considered in Chapter 12 of reference 27, where the cases of inclined plates and wedges are treated. A general formula for cavity C_D is given in Section 2, Appendix IV.

cavity length due to gravity, it is doubtful if the actual wall effect is as great as that predicted theoretically.

There is little to check these theoretical results against. The cavity C_D of a cylinder moving broadside has been estimated photographically^{8a} as 0.58 and 0.38 in two determinations at the David Taylor Model Basin. The variation of C_D with K in a water tunnel is drawn in Figure 8; the experimental points (but not the extrapolated dashed line) agree reasonably well with Brodetsky's computation. A fuller description of $C_D(K)$ for this and other shapes has recently been published by R. T. Knapp.⁷¹

10.6 CASE OF AXIAL SYMMETRY

The majority of experimental results concern the cavity C_D of bodies of revolution moving axially under deceleration; to interpret them accurately, it is necessary to correct them for “virtual mass.” Recent water-tunnel experimental results exist,⁷¹ but the variation in C_D with K in these experiments is so large that it is hard to apply them to predictions of underwater deceleration.

It is well known¹ that a body in noncavity motion along a straight line without rotation through an ideal fluid is resisted by a force

$$D' = m'a = \frac{m'}{m\sigma} \left(\frac{4\pi\rho r^3}{3} \right) a, \quad (5)$$

where

$$a = \frac{dv}{dt} = \text{acceleration},$$

proportional to the acceleration times the mass m' of a certain volume of the fluid. This m' is called the theoretical “induced” or “carried” mass; it is the m'_i of Table 2, Section 9.4. The corresponding theoretical induced mass in the case of motion with an infinite cavity is infinite. [In a perfect fluid, $m'v^2/2$ is the kinetic energy of the water, but in cavity motion, we have shown that this is always infinite (Section 4, Appendix IV).] Nevertheless, it is reasonable to assume that in the case of actual motions, with finite cavities, the experimentally determined drag is the sum of an “induced mass” drag D' proportional to the acceleration ($D' = m'a$ for a

suitable constant m') and a residual, steady-state drag D^* independent of the acceleration. Then

$$D^* = D - D' = -(m + m')a = \left(1 + \frac{m'}{m}\right)D. \quad (6)$$

For objects of different specific gravity σ but with the same shape, m/σ is constant and m' should be constant. If we let k be the constant $m/m'\sigma$ and if $C_D^* = 2D^*/\rho v^2 A$ is the steady-state drag coefficient, we obtain from (6) the relations

$$C_D^* = \left(1 + \frac{k}{\sigma}\right)C_D, \quad C_D = \frac{C_D^*}{\left(1 + \frac{k}{\sigma}\right)}. \quad (7)$$

In particular, the measured C_D of light spheres should be less than that of heavy spheres.

These predictions are fulfilled in the case of spheres, and the best fit to observed decelerations is obtained if we use (7) and set $C_D^* = 0.3$ to 0.34 and $k = 0.4$ to 0.45 (just as in Table 2, Section 9.4). Direct water-tunnel measurements for hemispherical heads give $C_D^* = 0.30$ (Ackeret, large correction) and 0.31.²⁴ Full-scale measurements at CIT give $C_D = 0.29$, based on hemisphere diameter.

The data on other C_D are not numerous enough to permit an empirical estimate of k . Deceleration measurements at $v = 80$ fps give for spherical caps of radius R on a cylinder of radius r ⁶⁰

r/R	0.00	0.25	0.50	0.67	0.83	1.0
C_D	0.77	0.71	0.61	0.61	0.40	0.28

The extreme cases clearly correspond to a disk resp.-hemisphere. For conical heads of vertex angle 2α , deceleration measurements at Farnborough,⁶¹ Helensburgh, and the David Taylor Model Basin^{8a} give

2α	180°	150°	120°	90°	60°	45°	30°	Source
C_D	0.77	0.71	0.63	0.52	0.38	...	0.20	Farnborough
C_D	0.47	0.36	0.25	...	Helensburgh
C_D	0.8–0.85	0.6*	0.36	0.28	...	Model Basin†

* Measurement by Morris Dam Group; pitch increased C_D .

† The photographs were measured and the C_D computed by T. L. Smith

Water-tunnel measurements at Haslar²⁴ give the values $C_D^* = 0.31$ for a hemisphere, $C_D^* = 0.22$ for a one-caliber ogive, and $C_D^* = 0.13$ for a 3-caliber ogive at $K = 0.13$. Knapp⁷¹ gets $C_D^* = 0.77$ for a disk.

10.7 “THEORETICAL” ESTIMATES

There are no reliable theoretical values that can be compared with the preceding empirical values. It is conjectured that there is exactly one axially

¹ For the theoretical treatment of the cases of a cylinder and a sphere see reference 27a. The idea of virtual mass was considered by Kirchhoff in 1869 and also by Thompson and Tait.¹⁰² Virtual mass effects of the predicted magnitude are observed experimentally.

symmetric potential flow with wake ^m which is physically plausible around a given axially symmetric head. It is further hoped that the theoretical drag for this flow will be equal to the measured cavity drag coefficient.

However, all theoretical estimates ^{8b, 31, 33, 62, 63} have been based on approximations that affect the drag coefficient by 30 per cent to 50 per cent. All that we know is that the theoretical cavity profile is asymptotic to $r = c\sqrt{x}$ in two dimensions and apparently to

$$r = \left(\frac{c\sqrt{x}}{\sqrt[4]{\log x}} \right) \left[1 - \frac{1}{8} \frac{(\log \log x)}{\log x} + O\left(\frac{1}{\log x} \right) \right] \quad (8)$$

for axially symmetric flows in three dimensions.^{22, 33} The theoretical drag is proportional to c^2 in two dimensions and to c^4 (the *fourth* power of the cavity diameter) in three.¹¹ The c^2 and c^4 relations follow from the fact that $(\ln r / \ln x) \rightarrow 1/2$ as $x \rightarrow \infty$ (see Sections 2 and 3, Appendix IV). It is interesting that, under the most plausible theory of an axially symmetric *transient* cavity (see Appendix V), the drag

than formulas with $\cos^3 \psi$ ($p \propto \cos^2 \psi$) in the case of *noncavity* motion. However, the fact that the cavity may clear the tapering portion of the head makes the use of $\cos^3 \psi$ ($p \propto \cos^2 \psi$) more plausible for tapered heads (ogives, spherogives, etc.). Both formulas will give bad estimates for heads with prods.

R. A. Shaw ³¹ suggests estimating the cavity forces on a projectile by measuring the *noncavity* pressure distribution empirically and integrating over the forward zone of positive pressure. This method avoids introducing an empirical numerical factor (0.67 or 0.77). Finally, at CIT, rough estimates of the cavity C_D have been made by integrating the "pressure coefficient" $2p/\rho v^2$ over the region forward of the observed line of separation (beginning of the cavity), interpolating smoothly between the overpressure coefficient of 1 at the stagnation point and the theoretical zero pressure where separation occurs.

These methods are only useful as indicators of orders of magnitude and of trends; comparisons of (9) and (10) with the experimental data of (6) are given below.⁶⁵

Spherical Caps $r/R = \tau$							Cones $2\alpha = \tau$					
τ	0.00	0.25	0.50	0.67	0.83	1.0	150°	120°	90°	60°	45°	30°
Exp.	0.8	0.71	0.61	0.61	0.40	0.31	0.71	0.63	0.55	0.37	0.28	0.20
(9)	0.67					0.33	0.63	0.50	0.33	0.17	0.10	0.04
(10)	0.77					0.51	0.74	0.67	0.55	0.38	0.29	0.20

should be approximately proportional to the *square* of the maximum diameter.

In the absence of genuine theoretical predictions, various formulas involving definite integrals have been proposed as giving rough estimates of cavity C_D .

In an earlier report it was suggested that the pseudo-Newtonian ⁿ integral ^{8c}

$$C_D = 0.67 \int \cos^3 \psi dS \quad (9)$$

would give estimates which were not too bad. A better fit to the observed C_D of cones is given by the pseudo-Eulerian integral

$$C_D = 0.77 \int \cos^2 \psi d\psi. \quad (10)$$

A comprehensive empirical formula has recently been given which gives promising results.⁶⁴ Formulas with $\cos^2 \psi$ ($p \propto \cos \psi$) are known to give better fits

^m That is, an axially symmetric flow having a velocity potential $U(x, r)$ which satisfies in space Laplace's equation $\Delta^2 U = 0$, is regular at infinity and has a wake $r = f(x)$ for which the slope $f'(x)$ tends to zero as x becomes infinite.

ⁿ Newton's formula would replace 0.67 by 2. Formula (9) assumes two-thirds of the pressure of (4) of Chapter 9, an estimate of the decrease due to the absence of impact virtual mass forces.

10.8 CAVITY LIFT COEFFICIENTS

Very little is known about cavity lift coefficients, although a few reliable statements can be made. For example, although *noncavity* $C_L(\phi)/\phi$ and $C_M(\phi)/\phi$ are usually gradually decreasing functions of ϕ , the corresponding *cavity* coefficients experience an abrupt change near the pitch angle where the tail makes contact with the cavity wall. By symmetry, $C_L(-\phi) = -C_L(\phi)$ and $C_M(-\phi) = -C_M(\phi)$ in both cavity and *noncavity* motion.

Since the pressure acts normally to the projectile surface, with *flat* heads we should have $C_L = -C_D \tan \phi = -(0.6 \text{ to } 0.8) \tan \phi$ below the cavity angle, i.e., until the tail strikes the cavity wall. We also expect, by symmetry, $C_L = 0$ with *hemispherical* heads below the cavity angle. (Speaking anthropomorphically, the water has no way to discover that it is not flowing past a sphere. Below the cavity angle, the C_D of a flat head is presumably still in the range 0.6 to 0.8.) In the case of ogives, the pressure on the upstream side of the head increases rapidly with pitch, hence $C_L(\phi)$ has the same sign at ϕ .

Preliminary measurements made at the David

Taylor Model Basin by T. L. Smith, using a very simple apparatus, support these conjectures. A model was suspended in a water tunnel by a rod inside a faired sheath, down which air was conveyed to maintain a cavity. This seems the most practical setup for measuring cavity force coefficients. Short, flat-headed models experienced negative lift for pitch angles up to 30° or more, with a maximum C_L when ϕ is not too far from 20° . With $\phi < 10^\circ$, $C_L(\phi)$ was around 0.4ϕ for a short hemispherically headed model and about 1.2ϕ for an ogival-headed model; the cavity did not clear these models, even at low pitch angles. Preliminary water-tunnel data may also be found in reference 71.

All other measurements of cavity C_L are based on trajectory differentiation. We have by algebraic transformation from $mv^2 d\theta/ds = L$ [(1) of Chapter 11]

$$C_L = \frac{2\sigma}{R} = \frac{8m}{\pi d^2 R} \frac{l_a}{l_a} \quad (11)$$

$$\text{Avg } C_L = \frac{4\sigma l_a \sin \theta_1}{X},$$

where R is the radius of curvature, $l_a = V/A$ (volume/area) is the "average projectile length," X is the plough, and θ_1 is the entry angle.^o This R is most easily observed, and hence C_L has been most frequently computed for *circular arc* motion. But, in interpreting data, one should keep the following situation in mind.

The "stable pitch angle" for circular arc motion depends on the location of the CG and on the L/D ratio (discussed in detail in Section 11.8). Moreover, C_L increases rapidly with ϕ , since tail lift is first exerted above the cavity angle. Hence the observed C_L varies with the L/D ratio and CG position (distance head to CG/total length), as shown in the following table for cone-headed projectiles.⁶¹ (The

TABLE 1

C_L	0.24	0.16	0.13	0.10	0.07	0.16
$2a$	45°	60°	45°	60°	45°	60°
L/D	11	11	18	18	18	18
CG	0.40	0.40	0.45	0.45	0.40	0.40

stable pitch angles were not tabulated.) Values of C_L in the same range have been observed for other models. Thus,^{11a} $C_L = 0.02$ for the 3.5-in. aircraft

^o Since actually $\theta_1 \neq \theta_2$, we should average and use $(\theta_1 + \theta_2)/2$ instead.

rocket with $L/D = 16$ and a special ogive head (1j); it was about 0.06 to 0.08 for 1.4-caliber ogive heads. It is only 0.08 for the 11.75-in. rocket with $L/D = 10$. It averaged about 0.17 to 0.20 for an "egg" projectile model^p having a flat head with three fins inscribed in a 90° cone in front and slender fins along an unusual tapering conical afterbody. An M30 bomb model with prod gave $C_L = 0.17$.

We have also estimated C_L for flat-headed scatter-bomb models in *oscillatory* motion; $C_L = 0.14$ to 0.21 , depending on the model. The agreement with $C_D \tan \phi$ ($C_D = 0.59$), averaged over an oscillation from $\phi = 0^\circ$ to $\phi = 26^\circ$ and back, is quite good.

Finally, in *broadside* motion, when ϕ passes through 45° , C_L is much larger (the curvature is pronounced near this point). Thus, with a tailless model having a one-caliber ogive head and $L/D = 3.5$, we get^q an average as large as $C_L = 0.5$.

10.9 CAVITY MOMENT COEFFICIENTS

Even less is known about the cavity moment coefficient. A flat-nosed projectile encounters a *restoring* moment at small pitch angle; this is predicted in classical hydrodynamics for a disk in noncavity motion and has been observed in Knapp's water tunnel. For the hemispherical nose below the cavity angle, the drag produces a small destabilizing moment; an ogival-headed projectile encounters a large destabilizing moment due to lift.

In the hypothetical case of oscillatory motion with a restoring force proportional to the pitch, the distance Δs required for a half-oscillation will satisfy approximately, by elementary oscillation theory,

$$\Delta s = \pi \sqrt{\frac{2\sigma l_a}{C_M' r^2}} \quad (C_M = C_M' \phi). \quad (12)$$

This formula can be used to estimate C_M' for flat-headed projectiles from trajectory tracings. Other estimates of C_M , for broadside motion, are intertwined with estimates of the damping force.⁷ For circular arc motion, $C_M = C_D r^2/R$, but this determines only the stable pitch angle ϕ and not C_M as a function of variable ϕ .

Various attempts have been made to change $C_M(\phi)$ by altering the head shape ("spades," etc.) to improve stability at entry and later. These are discussed in Appendix I.

^p See reference 110; $\phi = 10^\circ$ to 30° , depending on minor variations.

^q From measurements of tracings obtained from photographs made at Alden Hydraulic Laboratory for AMG-H.

10.10 STEADY-STATE CAVITATION

Steady-state cavitation conditions occur in high-speed water tunnels (see Figure 9), especially under reduced external pressure and with missiles (torpedoes, etc.) propelled through the water at very high constant speed.



FIGURE 9. Fully developed cavitation (Admiralty Experimental Works).

Cavitation ordinarily sets in when the pressure falls below vapor pressure p_v locally.^r

The pressure at any point is approximately

$$p = p_0 + \frac{1}{2}\rho v_0^2 \left(\frac{1 - v^2}{v_0^2} \right) \quad (13)$$

by Bernoulli's theorem, since p_v is usually small

^r Extensive experimentation has been carried out by Knapp at CIT. A program is also under way at the University of Iowa under H. Rouse.¹²¹ Deaeration of water and other special laboratory treatments may permit large negative pressures to occur without cavitation. This interesting scientific phenomenon is discussed in Appendix VIII.

enough to be neglected. Here p_0 denotes the pressure in the free stream and v_0 the velocity of the projectile relative to the stream. The dimension-

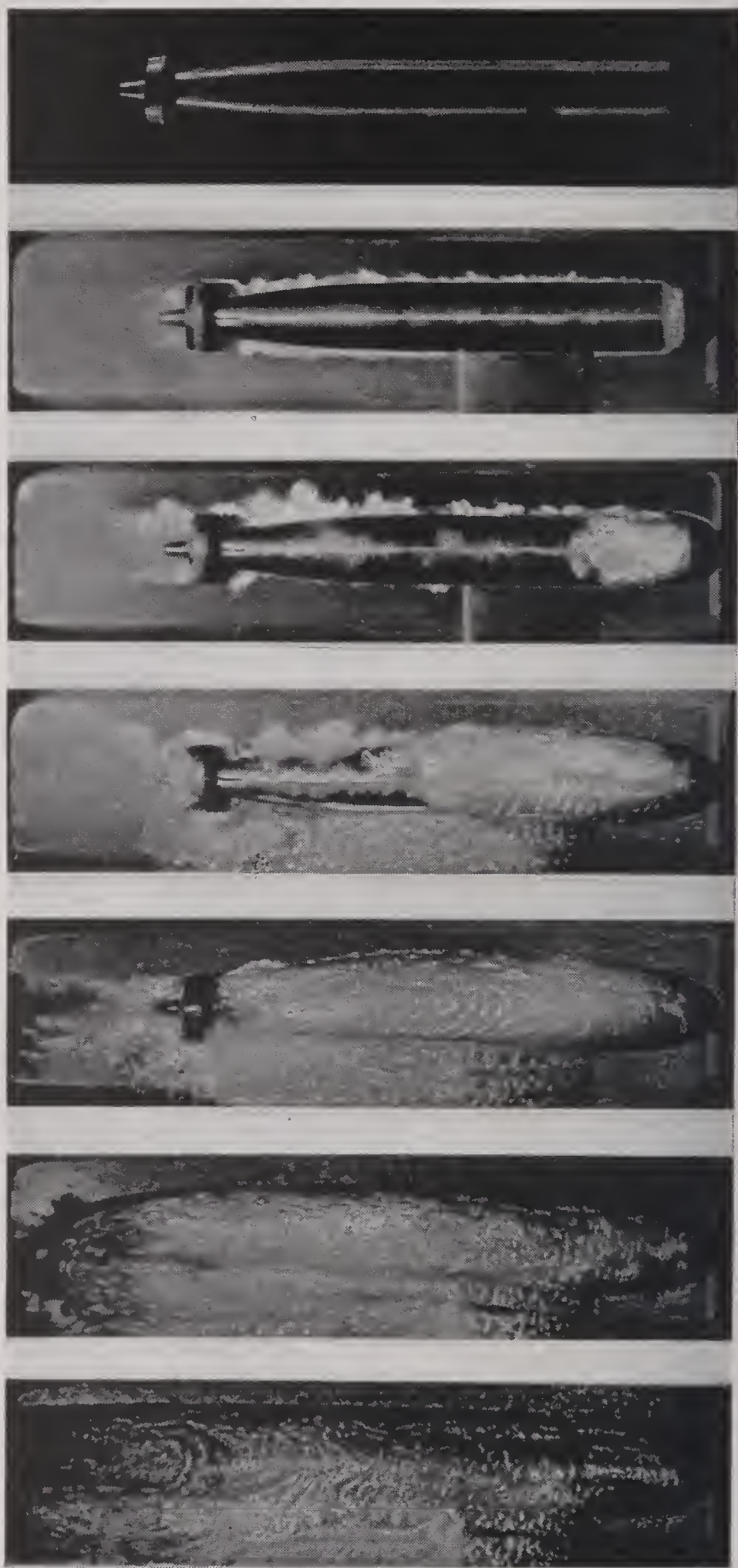


FIGURE 10. Degrees of cavitation (CIT).

less quantities v/v_0 , $k = v_{\max}/v_0$, and $(p - p_0)/q$ depend theoretically exclusively, and actually almost exclusively, on the shape of the projectile. Hence cavitation should begin or be "incipient" at the point where $v = v_{\max}$ when $p_0 = \frac{1}{2}\rho v_0^2(k^2 - 1)$, or $v_0 = \sqrt{2p_0/\rho(k^2 - 1)}$, since this expresses the condition that $p = 0$ in (13). At this

speed, the "cavitation parameter" K assumes its critical value K_c .

$$K_c = \frac{2(p_0 - p_v)}{\rho v_0^2} = k^2 - 1 \quad \text{approximately.} \quad (14)$$

We can also estimate K_c by plotting $(p - p_0)/q$ along the boundary, where $q = \frac{1}{2}\rho v^2$ and p is measured by manometers; cavitation will occur where p is a *minimum* and

$$K_c = \frac{p_0 - p_{\min} - p_v}{q}.$$

Incipient cavitation is marked by the appearance of a thin circle of fine or microscopic foam at the cavitation point (see Figure 10). Since most projectiles have streamlined afterbodies, the zone of minimum pressure is usually near the head, though cavitation can also begin near the tail assembly. This incipient cavitation does not affect the force coefficients, but the bubbles collapsing under the force of surface tension produce a noise which may disturb sound-ranging equipment.

As cavitation becomes more pronounced (i.e., at higher speeds or lower pressures), the region of cavitation extends farther and farther back. The cavity surface has a foamy appearance, and the drag coefficient of most streamlined bodies mounts steadily. Thus Knapp has supplied the following preliminary data for the Mark 13 torpedo.

K	0.7	0.6	0.55	0.50	0.4
C_D^* (sphere)	0.13	0.13	0.135	0.15	0.22
Bubble length	Incipient	0.06 d	0.17 d	0.5 d	2 d

Similar data are given elsewhere.^{9a, 71} For a cylinder moving broadside, $0.5 < C_D^* < 0.6$ was found as $0.8 > K > 0.5$ (see below). At $K = 0.5$, the cavity wall was transparent. (See Section 10.5, Figure 8.)

Ultimately the cavity wall becomes perfectly transparent, the cavity extends well behind the projectile, and the C_D^* may decrease again. The reason for this can be seen if we suppose $p = p_0 + \frac{1}{2}\rho v^2$ is stagnation pressure at the front end, while $p = p_v$ at the rear end of a model. Then

$$C_D^* = \frac{2(p_0 + \frac{1}{2}\rho v^2 - p_v)A}{\rho v^2 A} = 1 + K, \quad (15)$$

which is the maximum C_D^* possible for any K . It is 1 when $K = 0$.

As observed in Section 10.6, we should expect the steady-state C_D^* to be greater than the C_D under deceleration,

$$C_D^* = \left(1 + \frac{k}{\sigma}\right)C_D, \quad (16)$$

where k is the ratio of the virtual mass of the water to the volume of water displaced and σ is the specific gravity. Usually k should be in the interval $0.1 < k < 1$.

Finally we note that a projectile followed by a cavity of finite length has a theoretical drag equal to zero (d'Alembert's paradox). This means that some of the "theoretical" work which has been done computing cavity drag coefficients using ideal flow theory is essentially self-contradictory.

Chapter 11

UNDERWATER TRAJECTORIES

11.1 COMPLEXITY OF THE PROBLEM

VARIOUS FACTORS complicate the analysis and prediction of underwater trajectories.

In the air flight of bombs,^{14a, 26} we get a good idea of the trajectory by considering only gravity and the drag D ; the lift L , moment M , and damping force H of stable bombs are important largely in so far as they cause motion to occur at nearly zero pitch angle ϕ . Moreover, since ϕ is nearly zero, the theory of stability involves *linear* differential equations, and simple criteria can be given for stability.

However, in underwater motion, motion at large pitch angles is common, and (see Section 10.8) D , L , M , and H are *nonlinear* functions of ϕ . Moreover, because of the high density of water, one must consider virtual mass forces,^a as well as buoyancy forces and (during entry) free surface forces. For these reasons, the situation is much more complicated.

This complication is closely related to the large dispersion often found in experimental results, under almost identical conditions (nearly identical projectiles entering the water at small yaw and pitch and nearly the same entry angle). The reason for this dispersion is that *we often operate near the dividing line between different stable modes of motion*. Thus the addition of an apparently insignificant fuze cap may cause a projectile to be stable leaning against one wall of the cavity instead of oscillating between two walls, and hence to ricochet at 20° instead of only at 10° . This was first observed with the M30 projectile⁸; observations on models of the Mark 17 depth charge at the David Taylor Model Basin have confirmed it. It is analogous to what happens when a just-stable spin-stabilized projectile undergoes a reduction of spin and becomes just unstable. Again, a steep pitch of 5° at entry will cause a Mark 13 torpedo to swing

toward the top instead of the bottom of the cavity and produce a dive of 200 ft instead of 35 ft.

However, once we have determined the stable mode of motion of a projectile, we can get a good quantitative estimate of its trajectory by integrating the differential equations of motion. We can also get from these differential equations a qualitative idea of the trends that may be expected when parameters are varied, including the transition from one stable mode of motion to another. More than that cannot be obtained in our present state of knowledge.

11.2 NATURE OF FORCES INVOLVED

The trajectory of a rigid body moving through a fluid in a vertical plane is completely specified by the three functions $x(t)$, $y(t)$, $\gamma(t)$, where t is the time, and x , y , and γ are as in Figure 5 of Chapter 8. If the body is subject only to the gravity force mg and the reactions of the fluid (hydrodynamic forces), we have^b by elementary mechanics^{37a}

$$\begin{aligned} \frac{dx}{dt} &= v \cos \theta, & \frac{dy}{dt} &= v \sin \theta, & \frac{d\gamma}{dt} &= \omega \\ m \frac{dv}{dt} &= -\bar{D} + mg \sin \theta, & m v \frac{d\theta}{dt} &= \bar{L} + mg \cos \theta, & (1) \\ I \frac{d\omega}{dt} &= \bar{M}. \end{aligned}$$

Hence, from sufficiently accurate high-speed motion pictures of the trajectory, we can, theoretically, determine the hydrodynamic forces by measurement and double differentiation (double differencing). Actually, the process is more complex and involves resolving the overall hydrodynamic forces \bar{D} , \bar{L} , \bar{M} into various constituents.

First, we have the hydrostatic *buoyancy* force

^a See references 27 and 102. However, the references mentioned neglect the much more important lift and drag forces.

^b We assume only that electromagnetic forces, etc., are negligible. The distinction between \bar{D} , \bar{L} , \bar{M} and D , L , M is largely academic in air flight.^{16c}

mg/σ , though it should be noted that Archimedes' law (buoyancy equal to the mass mg/σ of displaced fluid) need not apply in cavity motion. The displaced fluid may be largely air or water vapor, so that the force of buoyancy may be considerably less than mg/σ .

Then we have the steady-state hydrodynamic forces $D(v, \phi)$, $L(v, \phi)$, $M(v, \phi)$ for pure translation. These are measured by letting water flow with constant speed v in a water tunnel or towing tank past a projectile suspended at a constant pitch angle ϕ and subtracting the forces due to gravity and buoyancy.

A projectile undergoing translation and (slow) rotation, as under rotation on a whirling arm or oscillation in a wind or water tunnel,^c will be subject to an additional *damping force* H , the most important constituent of which is its moment (damping moment). In fact, in Fowler's theory of the aerodynamics of a spinning shell, the other components are neglected (noted by Synge).

Again, even if v and ω are zero (i.e., there is no velocity of translation or rotation) and σ is 1 (i.e., buoyancy cancels gravity), the projectile is subject to a well-known *virtual mass*^a force vector if it is accelerated either in translation or rotation (see Appendix VII).

Finally, if the projectile moves rapidly partly submerged or just submerged, there is an upward steady-state hydrodynamic "free surface" force even if $\phi = 0$. This force, first measured by Ramsauer,³⁰ is due to the fact that the water above the projectile opposes less inertia to its motion than that below. It was mathematically predicted for partly submerged bodies (but not for totally submerged ones) by d'Alembert.^{5a} We ignore the Magnus effect, although this frequently occurs with imperfect spheres (e.g., two hemispheres loosely screwed together); this is a term in L proportional to $v\omega$.

11.3 DIFFERENTIAL EQUATIONS OF MOTION

We note that if the hydrodynamic forces \bar{D} , \bar{L} , \bar{M} depend^d only on $x, y, \gamma, t, \dot{x}, \dot{y}, \dot{\gamma}, \ddot{x}, \ddot{y}, \ddot{\gamma}$, then equa-

tion (1) is a *sixth-order* system of ordinary differential equations. Hence by very general theorems on differential equations,⁹⁷ the trajectory is determined from the initial position $x = y = 0$, and the initial velocity v_0 , trajectory angle θ_0 , pitch angle ϕ_0 , and angular velocity ω_0 .

If the speed is so high that gravity is negligible, and if by dynamic similarity the dynamic drag coefficient C_D is constant,^e then from (1) we get,

$$mv \frac{dv}{ds} = -\frac{1}{2} \rho A v^2 C_D \quad \text{or} \quad d(\ln v) = -\alpha ds, \quad (2)$$

where $\alpha = \rho A C_D / m$ is constant. Experimentally, the deceleration coefficient α is measured and $C_D = (m/\rho A)\alpha = \sigma l_a \alpha$ then computed.

Various methods of estimating α from observations are feasible. Integrating (2) by elementary methods, we get

$$v = v_0 e^{-\alpha s}, \quad \alpha s = \ln(1 + \alpha v_0 t), \quad \frac{1}{v} - \frac{1}{v_0} = \alpha t. \quad (3)$$

If we know v at two points, we can solve for α by the first and third equations; however, this involves two measurements of $\Delta s / \Delta t$ (hence four of s, t), in practice over intervals so large that v is far from constant. If we know v_0 at entry, and a single other position-time state, we can solve for α from the second equation by constructing nomograms for various α and interpolating. [This method ignores the skin effect, or loss of speed at impact due to virtual mass (see Chapter 9).] These methods have all been used.

When high-speed motion pictures are used, it is most direct to fit three time-position readings (say at $t = t_0$, $t = t_0 + \Delta t$, $t = t_0 + n\Delta t$) to the second equation; rules for the numerical computations have been published,³⁸ together with numerical tables to shorten the computations. A still more accurate procedure is to obtain a best-curve fit to a whole series of readings,^{104, 12c} still using the second equation of (3). The problem in air is somewhat different, because v changes so much more slowly.

From the third equation of (3) we see incidentally that the *time* required for the velocity to fall to v_1 never exceeds $(1/v_1)\alpha$, no matter how large the entry speed. By the second equation, we see that doubling the entry speed will only add $7/10 \alpha$ to the underwater range; thus to increase underwater range, it is more important to decrease C_D and to increase l_a than it is to increase impact velocity.

^e In practice, this means that ϕ is nearly constant and the cavity angle is nearly constant; theoretically, it means that drag is inertial and pitch constant. (See Chapter 12.)

^c A "whirling arm" swings the model in a circle whose radius is 15 or more projectile lengths. Models whose pitch oscillates in a fluid current are also subjected to a damping force; the two will be the same if the hydrodynamic force is a function only of v, ϕ , and ω .^{14b}

^d Differentiation with respect to time t is denoted by a dot; double differentiation by two dots; thus $\ddot{x} = d^2x/dt^2$.

Another simple type of motion consists of free fall vertically; the *terminal velocity* v_t , where gravity and buoyancy balance hydrodynamic drag, occurs by (1) when $mg(1 - 1/\sigma) = \frac{1}{2}\rho A v_t^2 C_D$, so that

$$v_t = \sqrt{\frac{2gl_a(\sigma - 1)}{C_D}} \quad \text{and} \quad C_D = \frac{2l_ag(\sigma - 1)}{v_t^2}. \quad (4)$$

The rate of sinking of stable depth charges can easily be estimated from (4).

11.4 REDUCTION OF ORDER BY SYMMETRY

It is a general mathematical principle that if a system of ordinary differential equations of order n possesses a degree of symmetry, then we can reduce its integration to the integration of a system of order $n - 1$, followed by a quadrature. The principle has been discussed theoretically by L. E. Dickson.¹⁰⁵ The application to Lagrangian dynamical systems is usually covered by the phrase "ignorable coordinates";¹⁰⁶ we are here applying the principle to non-Lagrangian systems. This principle will be applied to the differential equations (1).

We can eliminate t from (1) by writing $d/dt = vd/ds$; this assumes (see Section 11.3) that \bar{D} , \bar{L} , \bar{M} are independent of t (*temporal homogeneity*). This is reasonable if we neglect the dissipation of the cavity. A formal solution assuming exponential decay of the cavity has been proposed by N. A. Haskell.⁶⁹

All forces except free surface forces are presumably also *spatially homogeneous*, dependent only on γ , x , y , γ , \dot{x} , \dot{y} , $\ddot{\gamma}$. Because of the invariance under the two-parameter translation group,^f we should be able to reduce the order by two; this we accomplish formally as follows: We first write $D^* = \bar{D} - mg \sin \theta$, $L^* = \bar{L} + mg \cos \theta$. We then observe

$$\frac{d^2}{dt^2} = v \frac{d}{ds} \frac{vd}{ds} = \frac{-D^*}{m} \frac{d}{ds} + \frac{v^2 d^2}{ds^2}.$$

Now write $\gamma = \phi + \theta$, whence $d\omega/dt = d^2\phi/dt^2 + d^2\theta/dt^2$, where

$$\begin{aligned} \frac{d^2\theta}{dt^2} &= \frac{-D^*}{m} \frac{L^*}{mv^2} + \frac{v^2 d L^*}{ds mv^2} \\ \frac{d^2\phi}{dt^2} &= \frac{-D^*}{m} \frac{d\phi}{ds} + \frac{v^2 d^2\phi}{ds^2}. \end{aligned}$$

^f It should be observed that in air ballistics, the atmospheric density decreases with altitude; hence \bar{D} , \bar{L} , \bar{M} depend also on y , and only half the reduction is possible.

Substituting in (1), we get $t = \int ds/v$, and

$$\frac{dx}{ds} = \cos \theta, \quad \frac{dy}{ds} = \sin \theta \quad (5)$$

$$\frac{d(\ln v)}{ds} = \frac{-D^*}{mv^2}, \quad \frac{d\theta}{ds} = \frac{L^*}{mv^2} \quad (5')$$

$$\frac{Id^2\phi}{ds^2} - \frac{D^*}{mv^2} \frac{d\phi}{ds} = \frac{D^*L^*}{m^2v^4} + \frac{d}{ds} \frac{L^*}{mv^2} + \frac{\bar{M}}{v^2}. \quad (5'')$$

In appearance, (5') and (5'') constitute a fourth-order system of differential equations expressing v , θ , ϕ , and $d\phi/ds$ as functions of s . Since s appears only in the form d/ds (because of invariance under the group $s \rightarrow s + c$), we can reduce to a *third-order* system by writing $d/ds = (d\phi/ds)d/d\phi$.

Hydrodynamic forces (excepting again free surface forces) are also *isotropic*, i.e., invariant under the rotation group $\theta \rightarrow \theta + \alpha$. Hence, at speeds high enough so that gravity is negligible^g (and so that the cavity is fully developed), we get a further reduction. In fact, (5'') and the first equation of (5') constitute a *third-order* system of differential equations in v, ϕ and $d\phi/ds$, from which $\theta = \int L^*(v, \phi, d\phi/ds) ds$ can be obtained by a quadrature. As before, we can eliminate s and reduce to a *second-order* system, by writing $d/ds = (d\phi/ds)d/d\phi$.

Finally, hydrodynamic forces are approximately *inertial*^h or of dimension t^{-2} (proportional to v^2). It is clear that if $D^* = v^2 f_D(\phi, d\phi/ds, d^2\phi/ds^2)$, and similarly for L^* and \bar{M} , then (5'') is a *second-order* differential equation in ϕ , $d\phi/ds$ alone. This follows more generally, as discussed earlier (see Section 11.4), if we have dynamic similarity under $v \rightarrow kv$; hence it applies to virtual mass forces. But in this case the eliminations required to make this apparent are more complicated (see Appendix VII).

To summarize, for high-speed projectiles several diameters below the surface, the *differential equations of motion can be reduced by symmetry to a second-order equation in ϕ , $d\phi/ds$ like (5''), plus the quadratures*

$$\begin{aligned} v &= v_0 e^{\int \frac{-\bar{D}}{mv^2} ds}, \quad \theta = \int \frac{\bar{L}}{mv^2} ds \\ x &= \int \cos \theta ds, \quad y = \int \sin \theta ds, \quad t = \int \frac{ds}{v}. \end{aligned}$$

Moreover, by writing $d/ds = (d\phi/ds)d/d\phi$ (invariance under $s \rightarrow s + c$), we can eliminate s and get a *first-order differential equation in ϕ , $d\phi/ds$* .

^g A rough estimate, based on $C_L = 0.1$, is that gravity curves the trajectory as much as the hydrodynamic forces when $F^* = v^2/g\sigma l_a$ is about 20, or $F = v^2/gd = 200$.

^h This is discussed in detail in Chapter 12, together with the experimental evidence. It is an assumption always made in effect when yaw is discussed in air ballistics.

11.5 SIMPLIFIED DIFFERENTIAL EQUATIONS OF MOTION

In Section 11.2 an account has been given of the forces involved in underwater motion. Here we shall study the differential equations (1), taking the forces \bar{D} , \bar{L} , and \bar{M} as the steady-state hydrodynamic forces. We neglect gravity, buoyancy, damping effects, virtual mass, and free-surface effects. Thus we have

$$\begin{aligned} m \frac{dv}{dt} &= -\frac{1}{2} \rho A v^2 C_D(\phi), \\ m v \frac{d\theta}{dt} &= \frac{1}{2} \rho A v^2 C_L(\phi), \\ I \frac{d\omega}{dt} &= -\frac{1}{2} \rho A v^2 l_a C_M(\phi). \end{aligned}$$

These equations are very useful in spite of the formidable list of neglected forces. By using $v(d/ds) = d/dt$, we can rewrite the first two equations as

$$v \frac{dv}{ds} = -\frac{C_D v^2}{2\sigma l_a}, \quad \frac{d\theta}{ds} = \frac{C_L}{2\sigma l_a}. \quad (6)$$

The last equation, using $\gamma = \theta + \phi$, becomes

$$k^2 v \frac{d}{ds} \left(v \frac{d\theta}{ds} + v \frac{d\phi}{ds} \right) = -\frac{C_M v^2}{2\sigma}.$$

Using (6), this becomes

$$\frac{d^2\phi}{ds^2} + \left(\frac{C_L' - C_D}{2\sigma l_a} \right) \frac{d\phi}{ds} + \frac{C_M}{2\sigma k^2} - \frac{C_D C_L}{4\sigma^2 l_a^2} = 0, \quad (7)$$

which involves ϕ and s only. We observe that the coefficient of $d\phi/ds$ is an even function of ϕ and the last two terms in the equation are odd functions of ϕ . In case ϕ is small and C_D is treated as a constant and C_L and C_M as linear functions of ϕ , (7) becomes a linear equation with constant coefficients and can be solved explicitly.

Usually C_D , C_L , and C_M will be more complicated, and the analysis of (7) leads to a problem in "non-linear mechanics." Moreover consider the coefficient $(C_L' - C_D)/2\sigma l_a$ of the "damping term" in $d\phi/ds$ from (7). Its average over $(0, 2\pi)$ is exactly equal to the average of $-C_D/2\sigma l_a$, the average of $-C_L' = dC_L/d\phi$ being zero. This is decidedly negative, and so a purely mathematical analysis of (7) would lead one to expect "tumbling" solutions in which the projectile rotates over and over about an axis perpendicular to the plane of its motion, and $|d\phi/ds|$ increases in every complete rotation.

Such motions are prevented in practice by the large damping moment which slows up rotations with large $d\phi/ds$. It is strong enough in water also to rule out in practice mathematical solutions of (7) of the form $\phi(s) = Cs + P(s)$, where $C > 0$ is a constant and $P(s)$ is periodic (except in rare instances of tail-up ricochet described in Section 11.11). The damping moment is discussed further in Section 11.6.

For motion involving small $|\phi|$, however, the damping moment is of no importance. In this case we have, from (7), even if C_D , C_L' and C_M are far from constant,

$$\frac{d^2\phi}{ds^2} - \alpha(\phi) \frac{d\phi}{ds} - \beta(\phi) = 0, \quad (8)$$

where

$$\alpha(\phi) = \frac{C_D - C_L'}{2\sigma l_a}, \quad \beta(\phi) = \frac{C_D C_L}{4\sigma^2 l_a^2} - \frac{C_M}{2\sigma k^2}. \quad (9)$$

In the case of cavity motion, if the head of the projectile is more convex than a spherical cap with center at the center of gravity of the projectile, $C_M(\phi)$ is an overturning moment and thus has the opposite sign of ϕ . For small $|\phi|$, the C_M term is the dominant one in $\beta(\phi)$ and thus, $\beta'(0) > 0$. Using this in (8) we find for small $|\phi|$ the approximate result

$$\phi'' - \alpha(0)\phi' - \beta'(0)\phi = 0. \quad (10)$$

Since $\beta'(0) > 0$ we see that the solution $\phi = 0$ is unstable. Thus head-on motion is nearly impossible for convex-headed projectiles in a cavity.

If the head is flat or almost flat, the above argument is no longer true, because $\beta'(0) < 0$. However, when the head is almost flat, $C_L(\phi)$ has the sign of $-\phi$, due mainly to head forces. Thus $C_L'(0) < 0$ and

$$\alpha(0) = \frac{C_D(0) - C_L'}{2\sigma l_a} > 0.$$

Again using (10) we see now that the solution $\phi = 0$ is unstable because of the negative damping due to $\alpha(0) > 0$. Thus head-on motion is also impossible for a flat-headed body. (This last result is true even if there is no cavity, provided there is deceleration.)

11.6 DAMPING MOMENT

The damping moment H has been introduced in the study of air flight of bombs on empirical grounds.²⁶ If it is assumed⁶ that the projectile is a streamlined body with tails and fins, then the damping forces can be treated as arising from these latter. If \bar{p} denotes average pressure on the vanes and the moment arm of the point of application of the pressure with

respect to the center of gravity is denoted by $c_1 l_a$, then $\bar{p} = c \rho v c_1 l_a \omega$, where c is an empirical dimensionless constant. Again H , the damping moment, is given by $\bar{p} c_1 l_a A_v$, where A_v is the area of the vanes. Thus

$$H = c c_1^2 \rho l_a^2 A_v \omega v.$$

Or, introducing the dimensionless quantity,

$$\frac{2c c_1^2 A_v}{A} = C_H \quad (11)$$

we have

$$H = \frac{1}{2} \rho A l_a^2 \omega v C_H(\phi).$$

This damping term appears on the right side of the $I(d\omega/dt)$ equation with a negative sign and prevents tumbling.

By introducing this term and proceeding as in Section 11.5, we get the modified equation²⁰

$$\frac{d^2\phi}{ds^2} + \frac{C_L' - C_D}{2\sigma l_a} + \frac{l_a C_H}{2\sigma k^2} \frac{d\phi}{ds} + \frac{C_M}{2\sigma k^2} + \frac{C_L C_H}{4\sigma^2 k^2} - \frac{C_D C_L}{4\sigma^2 l_a^2} = 0 \quad (12)$$

in place of (7). However (6) is still valid.

Here again, if C_D and C_H are treated as constants and C_L and C_M as linear in ϕ , equation (12) becomes linear with constant coefficients and can be solved at once. For future reference, we define

$$\chi = \frac{d\phi}{ds}, \quad \alpha(\phi) = \frac{C_D C_L'}{2\sigma l_a} - \frac{l_a C_H}{2\sigma k^2}, \quad (13)$$

$$\beta(\phi) = \frac{C_D C_L}{4\sigma^2 l_a^2} - \frac{C_M}{2\sigma k^2} - \frac{C_L C_H}{4\sigma^2 k^2},$$

and put equation (12) in the form

$$\frac{d\chi}{ds} = \chi, \quad \frac{d\chi}{ds} = \alpha(\phi)\chi + \beta(\phi). \quad (14)$$

11.7 POINCARÉ CYLINDER (PHASE-PLANE); TYPES OF MOTION

If we write $\chi = d\phi/ds$, the approximate differential equations of motion (5'') and (8) assume the form

$$\frac{d\phi}{ds} = \chi, \quad \frac{d\chi}{ds} = F(\phi, \chi). \quad (15)$$

By a study of the curves in (ϕ, χ) space (or "phase space") defined by (15) and of related physical considerations, we are led to a mathematical classification of cases which parallels the physical classification into oscillatory, circular arc, and broadside motions made in Chapter 8. The details of this classification are given in Appendix VI.

Briefly the idea is that any solution of (15) must²⁸ either tend to a periodic solution, as $t \rightarrow +\infty$, or else $\chi \rightarrow 0$ and $\phi \rightarrow \phi_0$, where ϕ_0 is a constant. In the latter, depending on whether ϕ_0 is zero, small, or large, we have head-on circular arc or broadside motion. In the former, ϕ tends to a periodic function in t and, depending on whether the mean $\bar{\phi}$ of the periodic function is zero, small, or nearly 90° , we have oscillatory, circular arc, or broadside motion respectively.

It was shown in Section 11.5 that stable head-on motion is impossible for a projectile decelerating in a cavity. Hence the only stable types of *cavity* motion which occur are oscillatory, circular arc, and broadside.

11.8 CIRCULAR ARC TRAJECTORIES

The types of underwater motion discussed in Sections 8.3 to 8.7 will now be correlated with the laws of dynamics and hydrodynamics, referring where convenient to the differential equations of motion. We shall begin with circular arc motion.

We recall that because the projectile travels in a more or less straight line until tail slap occurs (see Section 8.4), we have $\theta_1 \leq \theta_2 \leq 1.5\theta_1$ ordinarily, and not $\theta_1 = \theta_2$, as would occur with pure circular arc motion. Again, the oscillations about the stable pitch angle ϕ_s , which occur initially, often cause a sequence of bends, near the points where the up-pitch $-\phi$ is a maximum, to describe the curved portion of the trajectory more accurately than a smooth circular arc. However, films of a tailless "tallboy" rocket model taken at the Alden Hydraulic Laboratory¹²² fitted exactly a circular arc after tail slap (see Figure 9 of Chapter 8). This suggests the possibility of exact prediction of underwater trajectories.

Furthermore, if the down-pitch is large enough or v_1 small enough, especially with slender heads, the tail may swing to the top and not to the bottom of the cavity, causing the projectile to "dive." And finally, as the cavity narrows and $-\phi$ tends to zero, there is an induced mass effect (see Section 11.15) which causes the trajectory to curve down. This effect is accentuated by gravity for nonbuoyant models.

We can correlate the curvature of the trajectory with $C_L(\phi_s)$ by the elementary formula

$$C_L = \frac{8m}{\pi \rho d^2} \frac{d\theta}{ds} = 1.2 \frac{m}{d^2} \frac{d\theta}{ds} \quad (16)$$

if m is measured in pounds, d and s in inches, and θ

in degrees. Some values for C_L , computed from equation (11) of Chapter 10,

$$C_L = \frac{4l_a\sigma \sin \theta}{X}, \quad \theta = \frac{1}{2}(\theta_1 + \theta_2),$$

where X is the length of plough, are as follows: 3.5-in. and 11.75-in. U. S. rockets (Bowen), $C_L = 0.10$ and 0.08 respectively; for egg,¹¹⁰ $C_L = 0.19$; for the navy practice bomb and M30P, $C_L = 0.10$ and 0.17 , respectively.

It has been suggested by Blackwell⁹ that $C_L(\phi_s)$ can be roughly predicted for rockets and other high-velocity, ultralong projectiles on the assumption that, because of the cavity, the hydrodynamic force results entirely from a cross force on the afterbody and tail (centered, say, $0.8l_a$ back from the nose) and a thrust on the head.³ This may be described as the assumption of "two-point contact."

If $\phi = \phi_s$ is constant, then $d\phi/ds = d^2\phi/ds^2 = 0$. If also $C_L = C_L(\phi)$ is independent of velocity, then (5'') reduces to

$$\frac{D^*L^*}{m^2v^2} + \bar{M} = 0. \quad (17)$$

Following Blackwell, we note that \bar{M} is much the more variable of these terms, hence we can simplify (17) to the rough equation $\bar{M} = 0$. Further, if the tail lift L_2 is centered $0.8l_a$ behind the nose (for this Blackwell quotes experimental evidence), it will cause a restoring moment of $(0.8 - k)l_aL_2$, where the CG is kl_a from the nose. If the head has a drag D_1 and a lift L_1 , the destabilizing moment is approximately $(L_1 + D_1\phi)kl_a$. Equating, we get after simplification,

$$L_1 + D_1\phi_s = L_2\left(\frac{0.8}{k} - 1\right). \quad (18)$$

An interesting special case is that of a hemispherical noseⁱ; this is especially simple since $L_1 = 0$. Hence $\bar{L} = L_2 = k\phi_s D_1/(0.8 - k)$. Since ϕ_s increases as L_2 increases, we see that the curvature of the trajectory of the Mark 13 torpedo should increase at least as fast as $k/(0.8 - k)$ when the CG is moved back.

In general, assuming $C_L = C'_L\phi$ approximately, where $C'_L = \partial C_L(\phi, v)/\partial \phi$, we get by similar calculations

$$\bar{L} = L_1 + L_2 = \phi_s \frac{kC_D - 0.8 C'_L}{0.8 - k}.$$

ⁱ Here we can even include the D^*L^*/m^2v^2 term in (17). We get $[(0.8 - k)L_2 - k\phi_s D_1] = D_1 L_2 / l_a m^2 v^2$.

Hence the curvature of the trajectory of *any* projectile should increase at least as fast as $1/(0.8 - k)$.

Note that all these formulas underestimate \bar{L} , because we have neglected the term D^*L^*/m^2v^2 in (18).

It should be noted that pointed heads (ogival or conical) give rise to a large C'_L . This is also true for a *spigot-ended* hemispherical or conical head. For in this case the cavity created by the spigot causes a highly asymmetrical pressure on the rest of the nose.^{1g} This is why such projectiles are observed to whip around violently in experiments. Rapid curving of the trajectory was also observed with a short model with a truncated cone head having a 22.5° vertex semiangle and a 0.6 diameter flat.

This "unstable" behavior is even more violent with "short" models having low L/D ratio.

11.9 BROADSIDE MOTION

Models of medium L/D ratio with weak tails, with the center of gravity at 0.35 to 0.4 lengths from the nose and with hemispherical or ogival head-shape, usually perform broadside motion. Thus this is true of the series of GP bombs, M30, M43, M44, M65, etc., used by the Army Air Forces in World War II.

The most noticeable property of projectiles broaching after broadside motion is the large ratio θ_2/θ_1 of impact angle to exit angle, which averages around two. This was first observed by Morse and Baldwin,²⁵ who gave the approximate rule $\theta_2 = 2\theta_1$. Measurements by the Applied Mathematics Group at Harvard of more accurate films of the M43 taken at Aberdeen Proving Ground showed that actually θ_2/θ_1 is largest when θ_1 is small.^{8d} Thus θ_2 was nearly 24° throughout the range $8^\circ < \theta < 14^\circ$; an explanation is given below. The next most prominent property is the short plough, due to rapid deceleration after broadsiding.

The large ratio of θ_2 to θ_1 , which is inconvenient in skip bombing (low ricochets being desired), may be explained as follows. During entry, a finite whip $(d\phi/ds)_0$ is received. Moreover there is further overturn torque thereafter, so that $\phi = as + bs^2 + \dots$, where $a, b > 0$. At low pitch angles also, $C_L(\phi)$ is roughly linear in ϕ (though convex upwards) so that

$$\begin{aligned} \frac{d\theta}{ds} &= a_1s + b_1s^2 + \dots, \\ \theta &= a_2s^2 + b_2s^3 + \dots, \end{aligned} \quad (19)$$

where again $a_2, b_2 > 0$, and in fact b_2 may be bigger than a_2 . This implies that for θ_1 small, θ_2 lies between

$2\theta_1$ and $3\theta_1$; we omit the mathematical discussion of infinitesimals.

As θ_1 increases, we tend to the case where ϕ swings over to 90° during the plough. Moreover, if we neglect the impulse whip during entry, the change $\Delta\theta$ in θ as ϕ increases from 0° to 90° (i.e., $\theta_1 + \theta_2$) should be independent of θ_1 . Hence $\theta_2 = \Delta\theta - \theta_1$ should cease to increase and should even decrease as θ_1 approaches the critical angle for ricochet. These predictions are fulfilled by broadside motion.

Experiments with models performing broadside motion revealed a number of scale effects which were not anticipated in reference 8. Thus they revealed a considerable variation of critical angle for broaching with entry speed and with model shape. At very low entry speeds models have a tendency to nose down and dive. At higher entry speeds they nose up but are influenced by gravity as they lose speed. As the entry speed increases, the relative effect of gravity is decreased and the critical angle for broaching increases up to a certain point. Beyond this point, however, increasing the entry speed does not cause broaching. This phenomenon has been observed with the tailless models of GP bombs²¹ and for the A Mark VIII mine.⁴

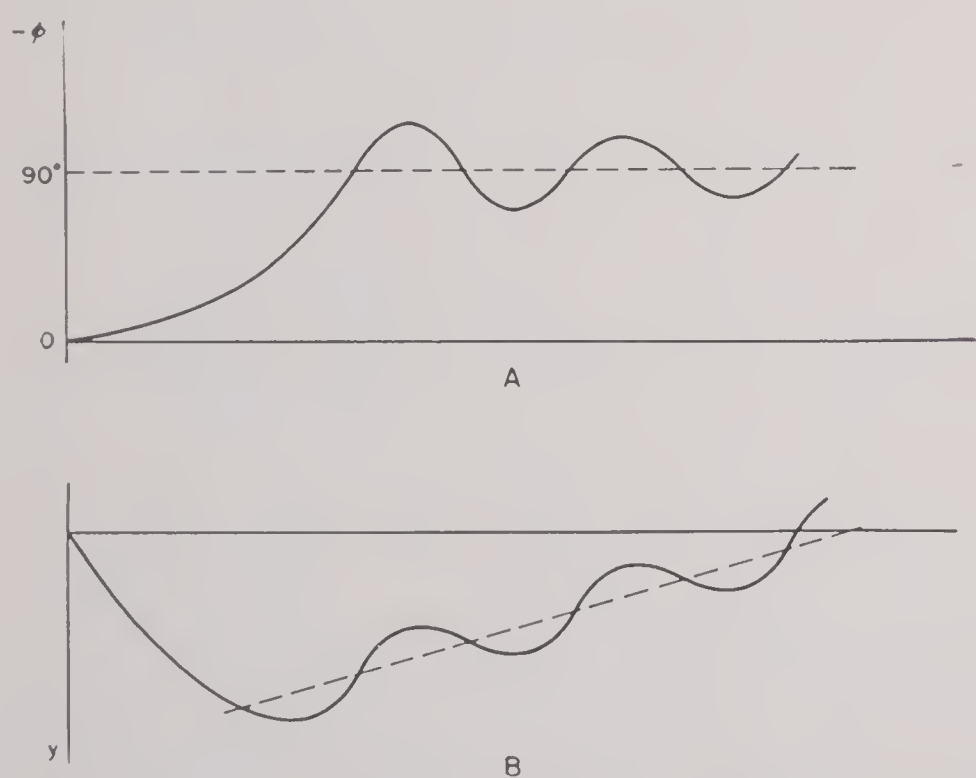


FIGURE 1. Pitch with broadside motion. Effect of damping.

An explanation for this tendency of critical angle to increase with entry speed up to a certain point and then remain fixed is revealed by high-speed films. The up-pitch, $-\phi$ in our notation, is plotted against s for a typical case in Figure 1A. We observe that $-\phi$ oscillates about a mean position M with a period of four or five model lengths. M , for models that broach, is only slightly less than 90° . Associated

with M there is a mean lift nearly zero on the model which would cause the model to follow the dotted straight line of Figure 1B. The oscillations in ϕ , however, cause the trajectory to have the form indicated by the solid curve in Figure 1B. If the model had high enough entry velocity, it could follow the trajectory shown and emerge from the water at the fifth arch of the sinusoid. However, in fact this velocity is outside the practical range because the high drag the model encounters once it broadsides slows it down so that the trajectory curves down under the influence of gravity before the fifth arch can be reached. In going from the top of the third arch to the point of emergence shown in the sketch the velocity would decrease by about 80 per cent or 90 per cent. The velocity required to make the model reach the top of even the third arch is usually much greater than that indicated by Froude scaling from the full scale. Increasing the impact angle θ_i beyond the point where emergence occurs at the top of the third arch will necessitate emergence at the fifth arch; in other words, it will require a fourfold increase in impact speed. Thus we see why the critical angle can be increased up to a certain point by increasing entry speed, although no realizable increase in impact speed will cause broaching above this point.

Another important scale effect is that full-scale bombs generally have less tendency than small models to broach at the same entry speed, and have more tendency to broach at the same Froude number. This effect is discussed further in Sections 12.4 to 12.6.

In cases where the full-scale model has a weak tail structure and broadsides, tailless models simulate full-scale performance far better than models with stiff tails.²³ In fact, models with bendable tails shot at the Alden Hydraulic Laboratory broached with $\theta_1 = 20^\circ$, and hence gave even better simulation of full-scale trajectories. However, in simulating full-scale behavior, great care has to be taken to prevent down-pitch at entry and to simulate the extent of bending of the tail.

11.10

OSCILLATORY MOTION

This name describes motion in which the pitch angle oscillates about the mean position zero. As we have seen in Section 11.5, there are steady-state motions involving oscillation about a pitch angle ϕ_0 different from zero. These latter, however, are de-

scribed as circular arc and broadside, depending on whether ϕ_0 is under 30° or nearly 90° .

Since the mean pitch angle is zero for oscillatory motion, the mean trajectory, aside from gravity and free-surface effects, is a straight line. Thus broaching does not occur unless θ_1 is small. For the $1\frac{1}{4}$ -in. model of the flat-headed scatter bomb and for several variations of this model, the limiting value of θ_1 for broaching was about 11° . High-speed films also show that if a broach occurs, it is during the first phase of oscillation of the model, when its trajectory is on the first upward arch of its sinusoidal path.

Oscillatory motion occurs with many convex-headed models having rigid tails, especially if the center of gravity is well forward. It is often hard to determine from the shape of such models and from their physical constants whether they will perform oscillatory motion or circular arc motion. Thus the $1\frac{1}{4}$ -in. diameter models of the GP bombs with rigid tails and the M38 performed oscillatory motion, while the M30 and M43 performed circular arc. Again, the British torpedo oscillates, while the U. S. Mark 13 does circular arc motion, although the two are very similar indeed.

Flat-headed models also perform oscillatory motion. This is true not only of models having comparatively small L/D ratio, but even for an L/D ratio of 16. This latter result was established at AHL.

Flat-headed models differ from most other models in that they have uplift with down-pitch and conversely. This is because the large force acting on the flat head is normal to the flat and therefore has an upward component with respect to the trajectory when the pitch is down.^j For small pitch angles the nose force is the only force acting, since the lateral area and tail of the model are in the liquid free cavity. Even for long models, where the latter is not entirely true, the great magnitude of the force on the flat nose causes it to predominate in influence. We see therefore that $C_L(\phi)$, the lift coefficient, is of the opposite sign of ϕ itself, at least so long as $|\phi|$ is not too large.

It is also the case that, when the pitch is up, the lower part of the flat head will be further upstream than the upper part and therefore will receive the greater part of the force. This means that the moment due to the nose force will be a restoring moment. Since the moment due to body and tail forces is

certainly restoring, the term $C_M(\phi)$, the moment coefficient, is a restoring term and thus of the same sign as ϕ .

These two facts, $C_L(\phi)$ and $C_M(\phi)$ being of the opposite and same sign respectively as ϕ , are enough to assure that the singular point (0,0) on the phase cylinder is an unstable focal or nodal point surrounded by a limit cycle. This can be seen by referring to the differential equations of motion (3) ff. of Appendix VI. Another way of describing the behavior of the model for small $|\phi|$ is that the model is statically stable but dynamically unstable near (0,0).

In the case of the scatter bomb, a $4\frac{1}{4}$ -in. long flat-headed $1\frac{1}{4}$ -in. diameter model, the oscillation of ϕ has an amplitude of 26° and a period of 3.2 ft of trajectory length. Over half of a period, 1.6 ft, the pitch is down and therefore the lift is up. Over the other half, the lift is down. Thus the trajectory itself contains a sinusoidal component of the same period as the pitch angle. The striking effect of this on the cavity shape is shown clearly in Figure 10 of Chapter 8. Putting a cylindrical plug in front of the flat head of the model shortened the length of the period of oscillation as measured along the trajectory curve.

11.11

TAIL-UP RICOCHET

A rarely occurring example of pure ricochet is "tail-up" ricochet.² This happens when the model receives an initial positive (nose-downward) average moment and *also receives* enough lift on the nose to keep the model at the surface. These conditions are met in the case of a flat-headed model entering at very low angle. Tail-up ricochet might also be expected to occur in the case of a round-headed projectile entering at very low angle with large positive (nose-down) pitch, though this has not been observed so far as we know.

Flat-headed models may ricochet tail first (rotating tail over head in the air) after the first impact, or, if the lift force is insufficient and the head is submerged to a couple of diameters, the tail may also catch the surface after it rotates over the head. In this case the model "cartwheels" along the surface for several revolutions before it clears the surface. This has been observed in a film taken at the David Taylor Model Basin.

An example of tail-up ricochet is shown in Figure 12 of Chapter 8.

^j The first explanation of the performance of flat-headed models appeared in reference 2.

11.12 VARIATION OF CENTER OF GRAVITY POSITION

In Sections 11.12 to 11.16, we shall study the variation in entry characteristics with CG location, length/diameter ratio, density, radius of gyration, entry pitch, and entry speed.

Moving back the CG is a well-known way of increasing the static instability. The criterion for static stability is that the center of pressure [CP] lie behind the CG. Moving the CG back will lengthen the moment arm of the overturn forces near the head of the projectile and shorten the moment arm of the tail forces. Thus the pitch angle will increase until the tail digs deep enough into the cavity wall to balance the moment of the head forces.

In the case of circular arc motion, moving back the CG increases the pitch angle and therefore the lift on the model. For this reason, broaching occurs more easily, as shown experimentally by CIT data on the Mark 13.⁷⁰ It is also confirmed by an experimental torpedo model²⁰ which, when its CG was shifted back, broached at an entry angle as high as 35°.

Of course, if the CG is moved too far back, the model will broadside rather than perform circular arc motion. If it is moved even farther back the model will swing around to a tail-first position. In the case of a model which does broadside motion, moving the CG farther back does not necessarily increase the broaching tendency.²⁰ The reason for this is that although the initial dive is less because the model broadsides faster, it also turns to 90° faster and thus the lift has less time to act.

In the case of oscillatory motion, one series of experiments with a torpedo model indicated that moving back the CG tends to cause the model to do circular arc or broadside motion.

11.13 LENGTH TO DIAMETER RATIO AND STABILITY

The improved stability of projectiles brought about by increasing the length to diameter ratio L/D has been utilized in practice in the case of the Shark and other designs. In a series of experiments performed by AMG-H at AHL, models of similar shape but with L/D ratio varying from 16 to 6 were tested. Whether the nose shape was flat, hemispherical, or ogival, an increase in L/D caused an increase in stability. The trajectories of long models

had much larger radii of curvature, even when measured in model lengths, than did the short models.

In the case of cavity motion, the improved stability is partly explained by the paraboloidal cavity shape. This makes the tail lie against the cavity wall at a smaller stable pitch angle ϕ when L/D is large than when it is small. But there is also a deeper reason, which applies both to cavity and noncavity motion.

Namely, at least for small pitch angles, C_M is only slightly affected by changes in L/D , while C_H , by (11), is proportional to A_v/A , which in turn is proportional to $DL/D^2 = L/D$. Thus, in the differential equation of motion, for small ϕ we can regard C_L , C_D , and C_M as invariant, while C_H varies as L/D . The effect of increasing L/D is to increase C_H . Thus $\alpha(\phi)$ in (13) becomes more negative, which means that the damping of the pitch angle oscillations is increased. In the case of a model doing oscillatory motion, the increase in damping would shrink the limit cycle on the Poincaré cylinder enclosing the origin. In other words, the motion would be more nearly along a straight line.

In the case of broadside or circular arc motion, it is necessary to study $\beta(\phi)$. For pointed noses or even the slightly convex ones usually associated with this type of motion, $C_M(\phi)$ is of the opposite sign of ϕ for small $|\phi|$ and $C_L(\phi)$ of the same sign. Thus setting $\beta(\phi) = 0$, we have

$$-C_M = \frac{C_L}{2\sigma} \left(C_H - \frac{k^2}{l_a^2} C_D \right).$$

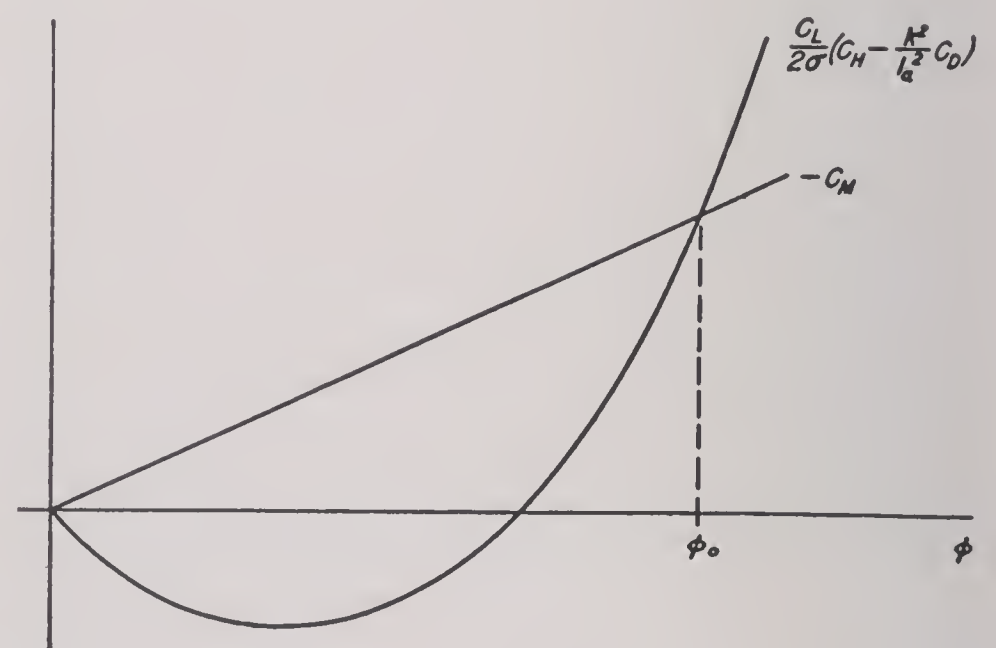


FIGURE 2. Graph of stability.

From the graph (Figure 2) we see that increasing C_H would move the point ϕ_0 to the left. That is, the angle of attack of the projectile decreases and therefore the motion becomes more nearly rectilinear.

11.14 DENSITY AND RADIUS OF GYRATION

If the shape and location of the CG of a projectile are unaltered but its specific gravity σ is increased, how is the motion affected? If H is neglected and if the radius of gyration is altered in the same proportion as $\sqrt{\sigma}$, the trajectory is unaffected except in so far as all distances are increased proportionally to σ . This can be seen from (7). If we set $S = s/\sigma$, then (7) becomes

$$\frac{d^2\phi}{dS^2} + \frac{C_L' - C_D}{2l_a} \frac{d\phi}{dS} + \frac{C_M}{2k^2/\sigma} - \frac{C_D C_L}{4l_a^2} = 0. \quad (20)$$

From (20) we see that if k^2/σ is held fixed, the equation remains invariant. Clearly, holding k^2/σ fixed is equivalent to keeping k proportional to $\sqrt{\sigma}$.

Turning to (12) and again setting $S = s/\sigma$, we find

$$\frac{d^2\phi}{dS^2} + \left(\frac{C_L' - C_D}{2l_a} + \frac{l_a C_H}{2k^2} \right) \frac{d\phi}{dS} + \frac{C_M}{2k^2/\sigma} + \frac{C_L C_H}{4k^2} - \frac{C_D C_L}{4l_a^2} = 0.$$

Here we note that if only σ is increased the effect can be analyzed by setting $\beta(\phi) = 0$, much as in (13). Using a similar graph, we see that for circular arc motion increasing σ will increase ϕ_0 , the angle of attack. However, by the increase of s with σ , this effect is offset so far as change in the curvature of the trajectory is concerned.

11.15 INDUCED MASS EFFECTS

For small $|\phi|$, we have [(15), Appendix VII], taking account of induced mass effects,

$$\frac{d\theta}{ds} = \frac{C_L(\phi)}{2\sigma l_a} + \frac{j\lambda' - \lambda''}{\sigma} \frac{d\phi}{ds}, \quad (21)$$

where λ' and λ'' are dimensionless constants associated with transverse and axially induced mass respectively. For a projectile with length at least several times greater than its diameter, λ'' is very much less than λ' . The term j depends on the degree of immersion of the lateral area of the projectile. It is 1 for a projectile completely in contact with the water and is zero for a projectile in a cavity or a bubble. It takes on an intermediate value for a projectile that is partially imbedded in the cavity wall or is only partially enclosed by a bubble.

Let us now consider the following situation: A

projectile moves with up-pitch $\phi < 0$ and with $d\phi/ds > 0$. Under these conditions, the second term in the right-hand member of (21) has the opposite sign from the $C_L(\phi)$ term. Hence the trajectory of a convex-headed projectile with up-pitch may actually curve down (or, in the same way, a projectile with down-pitch curve up). And even when the last term does not exceed the C_L term, the trajectory may be considerably flatter than is indicated by the magnitude of the pitch angle. This has been observed in several cases.

Thus induced mass effects may be relevant in connection with the systematic occurrence of extremely flat portions in the trajectory of the 1½-in. model of the navy practice bomb. This model performs circular arc motion. On impact with the water at moderately high velocities, it pitches up, $\phi < 0$. The tail and rear body dig well into the cavity wall before the direction of rotation is reversed and the model turns, with $d\phi/ds > 0$, toward (but in general not through) zero pitch angle. During this phase the induced mass term is brought into play, speeding up the flattening of the trajectory as indicated by (21).

In the phase of motion that follows the flattening of the trajectory, the model again gets more up-pitch, the trajectory turns up and in some cases broaches.

Another case where the induced mass effect under consideration appears to be relevant is that of the Mark 13.2. This model has been studied exhaustively at CIT.^k On striking the water at an angle of 19°, and with small pitch angle, this model curves down during a late phase of its motion even though its pitch is up, $\phi < 0$. During this phase of curving down, $d\phi/ds > 0$ and the order of magnitude of the induced mass term is larger than the C_L term. Moreover, the air and vapor cavity appears to extend along only the upper surface of the model and therefore j is not small. Incidentally, the model is buoyant in water and appears to be sufficiently in contact with the water to compensate for the downward force due to its weight.

The trajectory curvature in the case of the tailless models of the army bombs is strongly conditioned by effects other than that due to $C_L(\phi)$ itself in the broadside phase of its motion. However, the observed phenomena in the trajectory curvature as ϕ passes through 90° are exactly the opposite from those predicted by equation (9) of Appendix VII. Whether

^k Remarks here are based on CIT data and on photographs in reference 55.

this means that the treatment of induced mass as given in Appendix VII is oversimplified to the point of being false for certain ranges of ϕ or whether there are other more relevant effects which we have neglected entirely is not clear.

11.16 CRITICAL ANGLE

The critical angle, or entry impact angle $\theta = \theta_c$, of a model for which broaching occurs depends on entry pitch and on entry speed.

The effect of entry pitch angle on broaching is hardly surprising. Flat pitch causes round-nosed models to nose up and hence to broach. In the case of flat-nosed models, steep pitch causes broaching, since for these models the lift forces on the nose predominate and therefore steep pitch is associated with upward lift.

The dependence of entry angle for broaching with entry speed may be explained in large part by the effect of gravity on models with $\sigma > 1$. Gravity plays a trivial role as long as the model is moving at high speed, but as the drag slows it down the effect of gravity becomes important. Thus a model that broaches when entering the water at high speed may fail to broach when the speed is reduced somewhat, because in the latter case the influence of gravity becomes enough to pull the model before it can reach the surface.

Various slender-nosed 1-in. to 1.5-in. diameter projectile models have shown a tendency to nose down when entering at speeds below 100 fps, though they nose up when entering at speeds above 150 fps. In the case of the navy practice bomb a relevant effect may be the impact of the tail on the water, which is shown by the films to occur at low-angle entry. The point where the tail first hits the water depends on the cavity shape, which in turn appears to be dependent on the impact velocity. The dependence of pitch on striking velocity is discussed in Section 12.4 below.

11.17 EFFECTS OF SPIN

There are fewer experimental and theoretical data on the ricochet of bullets and other spinning projectiles off water.

Some data on the ricochet characteristics of the Navy 3.0-in. Mark III with 4R ogive and 6.0-in. Mark XX may be found in reference 38. Striking at 1,115 fps, these projectiles ricocheted from impact at 12.5° but not from 16.5° or more. A rough estimate of the velocity loss is 65 per cent or more, with impact angle 12.5°.

Reference 113 indicated 8° as the critical angle¹ for a small-caliber shell striking at 1,500 fps.

R. H. Kent⁷² observes that 0.30-in. rifle bullets fired into shallow water with a muddy bottom ricocheted up to 28°, but not at 31°. This greater tendency to ricochet may be attributed to the slender ogive.

For the Navy 3.0-in. and 6.0-in., underwater trajectories were determined by screens. The observed trajectories fitted qualitatively Hitchcock's hypothesis³⁸ that deviation from a straight line was due to the lift caused by yaw. It would be interesting to repeat Hitchcock's work, using cavity ballistic coefficients instead of the noncavity coefficients observed by Hitchcock. It would also be interesting to use an observed entry whip (using the Rule optical whip recorder) instead of an entry whip introduced to obtain the best fit to the later trajectory.

There has been much data on torpedo roll (i.e., spin) collected during this war⁷³; however, because of the small axial moment of inertia (large L/D ratio), it does not seem to affect the trajectory as much as in the case of ordinary shells, which usually make a complete revolution in 15 to 30 diameters of travel.

Spinning may have other interesting effects. Thus there has been some concern over the possibility that the "Magnus effect" of combined spin and broadside motion may cause depth charges rolled off a destroyer deck to curve back under the destroyer. Again,⁷⁴ the Germans considered spinning bombs so that the Magnus effect would make them dive at entry, instead of ricochet. Another practical application of spinning is discussed in Section 7, Appendix I.

¹ Highly qualitative visual data were reported in reference 114.

Chapter 12

MODELING AND SCALE EFFECTS

12.1 GENERAL REMARKS

THE USE OF SMALL models to simulate full-scale projectiles is a common practice in underwater ballistics, as it has long been in ship design, airfoil tests, and other domains of practical fluid dynamics.

Nevertheless, it must be admitted that the laws of modeling in underwater ballistics are not yet fully understood, in spite of the great progress achieved in World War II. For this reason, no model experiments can be accepted as absolutely conclusive until they have been checked against at least some full-scale tests.

In a general way, experiments using geometrically and dynamically similar models with diameters λ times full-scale size give reasonable simulation of underwater trajectories if a suitable entry speed, somewhere between $\sqrt{\lambda}$ times the full-scale velocity (Froude scaling) and the actual full-scale velocity, is used. Froude-scaled velocity works better with blunt-nosed projectiles, in general, and full-scale velocity with slender-nosed models. However, the appropriate entry speed is hard to determine a priori, and there seem to be two complicating factors.

The first of these is the tendency of slender-nosed models to dive at entry speeds below 100 fps. This is discussed in Section 12.4. It appears to be due to the viscosity of air, and a mathematical treatment of it would seem to be extremely complicated. L. B. Slichter has found an ingenious method for avoiding it experimentally by "ventilation." He encourages early separation of water from the nose of the model by peppering its surface with minute air vents leading into the (hollow) interior of the model. Small circular grooves around the nose can also be used. However, so far the correct amount of ventilation can be determined only by trial and error. Details of Slichter's results and theoretical interpretation will be found in reference 115.

A second complication is the fact that cavity-sealing phenomena are hard to model. This difficulty is given a mathematical treatment below. It is shown

that if viscosity effects can be avoided by "ventilation" or other means, the best prospects for success in the use of small models may be hoped for if sealed tanks of "heavy gases" at suitably reduced pressures are used. More precisely (Section 12.9), *the only way approximately to model surface seal and the equation of state for air is by reduced-pressure Froude scaling with a heavy gas.*

12.2 MATHEMATICAL THEORY OF DYNAMIC SIMILARITY

Two physically or mathematically defined motions will be called *dynamically similar* when one can be obtained from the other by a transformation of space-time of the form

$$x' = \lambda x, y' = \lambda y, z' = \lambda z, t' = \mu t, \quad (1)$$

where λ and μ are constants.

This will multiply vector velocities by the scalar λ/μ , accelerations by λ/μ^2 , etc.

In hydrodynamics, the laminar flow of a fluid around a rigid body is determined mathematically from its initial conditions by the equations of *continuity, state, and motion*, which involve, in addition to the variables x, y, z, t , the pressure variable $p(x, y, z, t)$ and the density variable $\rho(x, y, z, t)$. Therefore, if we are given a full-scale physical flow, which we will call Σ , it should be possible to obtain a dynamically similar "model" motion as follows.

Find a transformation (1) and transformations of p and ρ

$$\begin{aligned} \rho'(x', y', z'; t') &= F(\rho, x, y, z), \\ p'(x', y', z'; t') &= G(p, x, y, z; t), \end{aligned} \quad (1')$$

which preserve to a high degree of approximation the equations of continuity, state, and motion, both in the full-scale and in the model. Then launch the model system Σ' under conditions obtained from those of Σ by the transformation (1). The state of the system Σ' should then be obtainable from Σ at all later times by (1). And conversely, where direct observation of

Σ is difficult, it should be possible to know the behavior of Σ by observing that of Σ' and applying the inverse of transformation (1), namely

$$x = \frac{x'}{\lambda}, y = \frac{y'}{\lambda}, z = \frac{z'}{\lambda}, t = \frac{t'}{\mu}. \quad (1'')$$

This general consideration reduces the problem of hydrodynamic modeling to that of *finding which transformations (1), (1') preserve the equations of continuity, state, and motion.*

The equations of continuity and state are taken care of by the two following results, whose proof is given in Appendix VIII, Section 5.

Theorem 1. The equation of continuity is preserved by any transformation (1) for which

$$\rho'(x', y', z'; t') = \alpha \rho(x, y, z; t), \quad (2)$$

α being a constant depending only on the material (e.g., it need not be the same for air as water).

Theorem 2. The equation of state of an incompressible fluid is preserved under any transformation (1). The equation of state

$$\begin{aligned} \rho &= \rho_v & \text{if } p < p_v \\ \rho &= \rho_1 & \text{if } p > p_v, \end{aligned}$$

[where p_v = vapor pressure and ρ_v = vapor density (see Figure 1)] is preserved under any transforma-

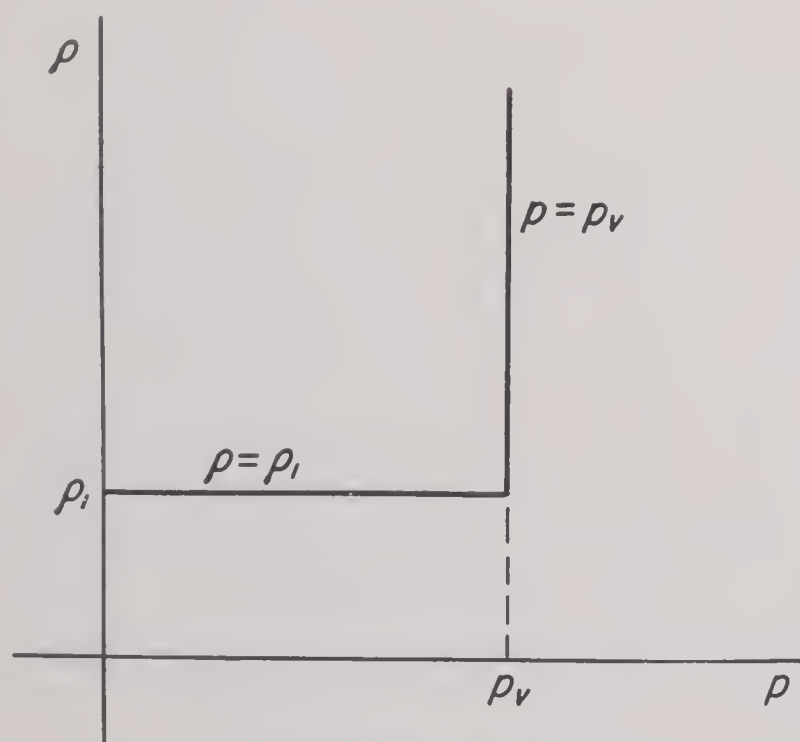


FIGURE 1. Pressure-density ratio.

tion (1) in which $\rho' = \rho$; p' is a monotone increasing function of p ; and $p'_v = p_v$. The equation of state $\rho = Cp^\gamma$ of a perfect gas is preserved under (1) when the equation of continuity is preserved, if and only if $p' = \beta p$ for some β , depending on the material.

The equation $\rho = \rho_1$ if $p > p_v$ clearly approximates

the condition of water without cavitation, the condition $\rho = \rho_v$ the condition in the cavity.

The discussion of the equations of motion is more ambiguous, because everything depends mathematically on what forces are neglected. Throughout the mathematical discussion below, we shall neglect the forces of viscosity, surface tension, and adhesion; their effect is discussed in Appendix VIII. We shall also neglect turbulence.

This leaves us with the forces of *inertia, gravity, and compression* to treat mathematically. By the Helmholtz-Kelvin theorem, we can assume irrotational flow except at surfaces of discontinuity.^a Hence there exists a velocity potential U , and the equations of fluid motion are the space derivatives of

$$\frac{\partial U}{\partial t} + \int \frac{dp}{\rho} + \frac{1}{2}(u^2 + v^2 + w^2) = gy, \quad (3)$$

where u, v, w are the velocity-components of the fluid. Rewriting (3) in the form

$$dp = \rho \left[g dy - (u du + v dv + w dw) + d \left(\frac{\partial U}{\partial t} \right) \right],$$

we see that, if ρ is sufficiently small, $\Delta p = \int dp$ must also be extremely small in any connected portion of fluid. We conclude:

Theorem 3. The pressure within connected portions of air is nearly constant, in so far as the density of air is negligible.

Actually, though the density of air under standard conditions is only 1/750 that of water, we shall see later that it plays a fundamental role in surface seal and is sometimes important also in determining the rate of deep seal.

However, to the extent to which it is valid, it greatly simplifies the scaling problem. Before sealing, since there is an infinite reservoir of air at the original air pressure, it implies that water has a "free boundary" at constant pressure. After sealing, it implies that the upper surface remains at this pressure, while the pressure at any instant on the cavity surface is constant. This cavity pressure can be determined from the free air pressure by the equation of state, knowing the ratio of cavity volume to the volume at the instant of sealing. (To the extent that it is not quite constant, the average cavity

^a As at the water surface or where the cavity seals. The mathematics may be found in reference 29, Chapter 9. We have neglected to mention before the boundary conditions of (1) pressure continuity and (2) continuous normal velocity component; these are clearly preserved under any transformation [(1), (1'), and (1'')].

pressure will satisfy the same condition.) In either case, the motions of the water and the projectile are mathematically determined by this boundary condition and their own differential equations.

The scaling rules for particular mathematical theories of the entry and underwater motion of projectiles will be considered now, remembering that the problem has been reduced to the question of the scaling of the equations of motion.

12.3 THEORY OF INERTIAL MODELING

The simplest type of scaling is inertial scaling. Let Σ be any system consisting of a rigid body moving in a vertical plane through air and water. (This hypothesis simplifies the mathematics, but the results hold equally well for a rotating projectile.) The motion of the body is specified, as in Figure 5 of Chapter 8, by $x(t)$, $y(t)$, $\gamma(t)$; the flow of air and water by the functions, u, v, w, ρ, p of position and time.

Definition: By an *inertial* model of Σ , we mean a system Σ' obtained from Σ by (1'') and

$$\rho' = \rho \quad \text{and} \quad p' = \frac{\lambda^2 p}{\mu^2} + p_0. \quad (4)$$

Physically, this means that the density of air, water, and the projectile must be preserved, with the exception that since the projectile is assumed to be rigid one need merely preserve the average density and scale geometrically the location of the center of gravity and radius of gyration. For large values of λ/μ , it follows from theorem 2 that the equation of state for air is not preserved even approximately, though that for water will be, as long as velocities do not exceed 1,000 fps.^b However, if we assume that, in view of its low density, air gives relatively constant pressure on the water surface, then (4) preserves our hypotheses.

Theorem 4. The equations of continuity and (if compressibility is neglected and cavitation avoided) of state of the water are preserved by (4). The equations of motion are preserved if gravity, viscosity, and surface tension are neglected. The condition of constant pressure on the air-water interface is also preserved, and so is the equation of motion (3) for air, if the compressibility term can be neglected.

Proof. The first statement follows from (1) and (2). For water, the second statement is obvious from

^b At this speed, $\rho v^2/2g < 10^6$ lb per sq ft = 465 atm, and less than 2 per cent increase in density is caused by steady-state motion. Transient pressures might be somewhat greater.

(3), since g is neglected; $\partial/\partial t$ is multiplied by $1/\mu$, velocities by λ/μ , and $\partial p/\rho \partial x$, etc., by λ/μ^2 . By choosing p_0 properly, we can make $p'_a = p_a =$ atmospheric pressure. The statement regarding (3) is equally obvious.

These remarks apply to the fluid and boundary; we now consider the projectile.

Hydrodynamic pressure differences are multiplied by λ^2/μ^2 ; the area over which they act by λ^2 ; hence the hydrodynamic forces D, L, M of drag, lift, and moment are multiplied by λ^4/μ^2 . But the inertia is multiplied by λ^3 ; hence the equations of motion are preserved if all accelerations are multiplied by λ/μ^2 . However, this is clear, since d^2s/dt^2 , d^2y/dt^2 are multiplied by λ/μ^2 . Likewise, torque is multiplied by λ^5/μ^2 and moment of inertia by λ^5 , and correspondingly, $d^2\gamma/dt^2$ by $1/\mu^2$.

12.4 SCALE EFFECTS WITH INERTIAL MODELING

Inertial scaling must be employed with great caution in underwater ballistics experiments, as there is a strong increase in the tendency to ricochet with increasing entry speed.

Inertial scaling seems quite successful in sphere ricochets. Thus^{8e} increasing the impact speed v_1 of 1.5-in. diameter spheres from 100–150 to 400–500 fps increased the critical angle θ_c for ricochet by only 10 per cent; the increase of v_1 to 2,000 fps increased θ_c only about 15 per cent more.

It also seems successful in measuring C_D . Thus the cavity C_D of steel spheres seems to be about 0.3, regardless of size or entry speed (see Table 1). But there is not much experimental evidence for non-spherical heads. Moreover, care should be taken to insure that v_1 is large enough so that the missile is traveling in a cavity throughout the range over which the C_D is being measured.

However, spheres seem to show a significant trend toward higher C_D with increasing speed; moreover, experiments by other groups, communicated informally to us but not reported, suggest the possibility that much larger spheres might have a cavity C_D nearer to 0.2–0.25 at entry speeds 100 to 300 fps. Also precise measurements by the Applied Mathematics Group at Harvard [AMG-H] show that the cavity C_D decreases after "deep seal."

Inertial scaling also predicts the entry whip of the full-scale Mark 13 torpedo at varying entry speeds,

although not that of models of various diameters (see Section 9.5).

Again, 1-in. diameter models of the Mark 12 and Mark 15 torpedoes were found to have the same cavity C_D as the 18-in. diameter full-scale.⁷⁵ In more elaborate experiments,⁷⁶ the cavity C_D of various 1-in. diameter cone-headed models was found to be independent of velocity.

150 fps and to nose down at speeds below 75 fps; the same tendency has been shown even more noticeably in slender-headed torpedo models shot at CIT.

Photographs by the Morris Dam Group correlate down-nosing with an absence of separation of the water from the lower side of the projectile, which is avoided if vents allow air to enter the cavity boundary or if the projectile is grooved to encourage separation.

TABLE 1*

d (in.)	0.25	0.25	0.25	1.5	1.5	1.5	0.1–0.25
v (fps)	30	60	100	95	180	275	3000
$10^{-5}R$	0.6	1.2	2	10.8	22	30	25–60
C_D	0.27–0.31	285	0.28–0.35	0.30–0.33	0.32	0.29–0.335	0.315

* Source, E. N. Harvey, AMG-H.

Tailless 1.5-in. diameter models of various GP bombs were shot into water at 80° from the horizontal by AMG-H; at entry speeds of 80 to 250 fps, they all turned broadside nose up after about four lengths of travel. The time t of "surface seal" with ordinary air also scales approximately inertially (i.e., roughly proportional to $1/v$, as shown by Blackwell¹⁰).

v (fps)	20	43	54	75
t (sec)	"deep"	0.028	0.017	0.012

But there is a significant trend to slower surface seal at higher entry speeds. In conformity with this, we have found that for spheres entering water vertically with ordinary density, surface seal occurs when the sphere is 5 to 8 diameters below the surface throughout the range from 50 to 200 fps. At higher speeds, surface seal is delayed further, presumably because the air in the cavity is considerably expanded at reduced density.

On the other hand, the critical angle θ_c for ricochet with broadside motion increases drastically with entry speed v_1 , and may be doubled when v_1 doubles, up to a certain asymptotic value, which is reached when $v_1 = 200$ fps or so with 1- to 1.5-in. diameter models.

Similarly, with circular arc motion, slower models throw a narrower cavity, and the cavity C_L under stable motion (trajectory curvature) is correspondingly less^c; hence there is less tendency to ricochet.

High-speed photographs of models of GP bombs and a navy practice bomb in particular show a consistent tendency to nose up at high speeds above

ration^d (see Figure 5, Chapter 10). This has since been checked by AMG-H with rocket models, but the down-nosing of the Navy practice bomb seems to be due to another cause; possibly the tail clips the water as it enters.

The concept of inertial modeling and scale effects throws light on the validity of some of the mathematical theories discussed earlier. Thus if cavity C_D and C_L can be determined by potential theory,⁶⁶ they must be independent of size and speed. Again, if von Kármán's method of estimating impact forces (see Sections 9.3 and 9.4) is valid,^e impact decelerations must scale inertially and virtual mass m' be independent of entry speed (see Table 1, Chapter 9). Similarly, our integral estimate for entry whip (Section 9.5) can only be reliable over ranges of sizes and entry speeds for which inertial modeling works. The same remark applies to the determination of trajectories by integrating differential equations of motion involving C_D , C_L , C_M , C_H , or virtual mass, as quantities independent of size and speed.

Hence, in view of the preceding data, all these theories must be employed with caution.

12.5 FROUDE MODELING; EFFECT OF GRAVITY

It is well known from model studies of the wave resistance of ships,^{29c} that the effect of gravity and inertial forces can be modeled by Froude scaling.

^d Preliminary computations by L. Slichter indicate that the reduced pressure under the nose may be maintained by viscous resistance to flow of air into the thin film of air near the separation point. This film is obtained with streamlined noses which closely hug the bubble. This explanation involves the Reynolds number of air.

^e The elastic shock pressure ρcv at impact does not scale inertially, but its effect on the trajectory is generally assumed to be negligible (see Section 9.2).

^c Oral communication of A. Graham, British Ministry of Aircraft Production, confirmed by observations at AMG-H. This contradicts the statement in reference 61 that speed effects on C_L were "only of the order that can be assigned to uncorrected gravity effects."

At the beginning of World War II, it was assumed, on the basis of oversimplified theoretical considerations, that Froude scaling would give faithful simulation of full-scale behavior.

Definition. A *Froude model* is an inertial model at the same Froude number $v^2/gr = F$.

Since g is fixed, this means that v^2/r is multiplied by 1, so that $(\lambda^2/\mu^2)/\lambda = 1$ or $\mu = \sqrt{\lambda}$ and velocities are multiplied by $\sqrt{\lambda}$. This is the usual Froude rule for scaling velocities when distances are scaled as $1:\lambda$.

Theorem 5. Froude models preserve the equations of motion of the projectile, water, and air, if viscosity and surface tension can be neglected. They preserve the equation of continuity; they also preserve the equation of state of water neglecting compressibility and that of constant pressure on the boundary. They do not preserve the equation of state of air nor the cavitation pressure of water.

*Sketch of proof.*³² Hydrostatic pressure differences ρgy [see (2)] in water are multiplied by λ ; if $\mu = \sqrt{\lambda}$, this scales with hydrodynamic pressures; hydrostatic forces are thus multiplied by λ^3 ; so are gravity forces on the body. A similar discussion applies to the equations of motion of air and to interface (boundary) conditions. The other equations were discussed above.

Clearly, Froude scaling is necessary and sufficient faithfully to model the down-curving of the trajectory by gravity and up-curving by buoyancy. This will alter the trajectory by 0.05 radians (about 3°) after a travel of $v^2/20g = F/40$ diameters. Hence it is important for slow-moving depth bombs and in long trajectories, as in air ballistics. But if a speed of 200 fps is maintained, the deflection by gravity will be less than 3° in 70 ft of travel. This hardly seems sufficient to explain even the small increase with v_1 in the critical angle for sphere ricochet (see Section 12.4).

But, in general, scale effects are more closely correlated with the size of the cavity. This is especially true of "circular arc" motion, which cannot occur without a fair-sized cavity. Broadside and oscillatory motion are less affected by the cavity, though it is conceivable that a model which would broadside in a cavity would travel nose-on otherwise.

Early theories of cavity sealing^{10, 32} stressed the role of gravity, which would certainly ultimately seal the cavity (see Section 10.4 for details of the present theory); if this were the main factor, we could expect cavity seal to scale under Froude modeling. But actually, at speeds of 300 fps and higher, the underpressure in the cavity due to volume expansion after

surface seal^f is more important. This depends on the equation of state for air, and hence should be identical in model and full-scale. Since dynamic pressures are multiplied by λ , this is more than enough underpressure to accelerate inward the cavity walls of the model to scale; hence Froude models should have cavities smaller than those of the full-scale.

This view has been confirmed by observation at Pasadena. Bubbles from a full-scale Mark 13.2 torpedo surfaced 80 ft from the entry point; bubbles from a 1-in. model with Froude scaled velocity appeared to surface at a point corresponding to 60 ft along the trajectory.

On the other hand, Froude scaling has worked successfully in many instances; full-scale mine designs^g based on Froude models, with *precision* models, have exhibited the same behavior as the models in all cases over a period of years.

These mines tend to be blunt, and it has been found at CIT^{1h} that blunt-nosed projectiles give better results under Froude scaling than slender-nosed cones. Thus⁷⁶ accurately compared trajectories of the 22.4-in. diameter Mark 13.2 torpedo and 1-in. models of it are very similar for the first 50 diameters (five lengths) of travel; the same is true of cone-headed models. However,⁷⁶ ellipsoidal-headed 1-in. diameter Froude models dive, whereas the full-scale does not; moreover, in general the tendency to nose down at low entry speeds does not obey Froude modeling.

One can also see directly that the tendency to nose down at low entry speeds, which is observed at around 70 to 100 fps, can hardly be explained as a gravity effect. In the first millisecond after entry, gravity displacements are less than 0.0002 in.; in the first 0.01 second, they are less than 0.02 in. The cavity angle of a projectile n calibers long should be changed by gravity only $nF/2$ radians at the tail; this turns out to be 1° for a 6-in. long model if $v_1 = 21$ fps. This makes an explanation in terms of air viscosity^d especially attractive.

12.6 MODELING BY EQUAL VELOCITIES

No discussion of modeling would be complete without a mention of *modeling by equal velocities*, i.e., inertial modeling with $\lambda = \mu$. (This is sometimes called "stress" or "Mach" modeling; it is always used in air ballistics.)

^f The importance of this was first stressed by Blackwell¹⁰; the Bernoulli underpressure before surface seal should be scaled by inertial, hence by Froude, modeling.

^g Oral information from L. C. Fisher of NOL.

Theorem 6. Models at equal velocity preserve the equations of motion of the projectile, water, and air, if gravity, viscosity, and surface tension can be neglected. They also preserve the equations of state of water and air and the equation of continuity.

Proof. Referring to the proof of theorem 4, we see that pressures and densities are preserved; hence, if initial temperature is preserved, the thermodynamic equation of state is preserved. In particular, if conductivity is negligible (this adiabatic approximation is excellent), since equal work per unit volume is done, the adiabatic equation of state is preserved.

Thus one can model *impact* forces perfectly, in cases where it may be feared that the compressibility of water plays an important role, such as with very high-speed rockets. In particular, no reason is apparent why scaled-down pressure plugs would not give the same readings if mounted on models, or why, if observations were multiplied by the model scale λ , decelerometers with proportionately quicker reaction times could not be mounted on models fired at equal velocities.

To estimate the effect of compressibility, we give some specific figures. Just at impact, the peak pressure (which was seen in Section 9.2 to be in the range $\rho cv \sin \phi$ to ρcv , where c is the speed of sound in water) may be 20,000 psi with impact speeds of 500 fps, but even this would make a compression of only about 4 per cent. Under steady-state conditions, moreover, the stagnation pressure is only $\rho v^2/2g = 2.5 \times 10^5$ psf = 115 atm., and the compression $\Delta\rho/\rho$ is about 0.005. (In general, $\Delta\rho/\rho = 4.54 \times 10^{-5}p$ in atmospheres.¹²³ However, peak pressures at impact of 50,000 psi have been measured on high-speed rockets; moreover, at the impact speeds of 3000 fps occurring in Dr. Newton Harvey's experiments, similar steady-state stagnation pressures should occur; this would correspond to a compression of 15 per cent.

Again, in a water tunnel, water vapor pressure is modeled, i.e., the pressure at which cavitation occurs. Hence *water-tunnel cavitation is modeled*, in so far as adhesion, surface tension, and gravity are negligible. (Gravity is actually less important than interference from the supporting strut in most water tunnels; moreover, the method of Section 12.7 is more practical than reproducing high speeds, hence this point is rather academic.)

If the time of sealing were modeled, as it may be with surface seal, the underpressure in the cavity due to expansion, as well as aerodynamic underpressure, will also be modeled. But the influence of gravity is

underestimated on a small model; hence with equal-velocity models, the duration of the cavity is relatively longer and the size relatively larger in the model than in the full-scale. However, at the extreme speeds ($v_1 = 3,000$ fps) used in Harvey's experiments, gravity is unimportant and so equal-velocity modeling should be satisfactory.

Since Froude scaling gives a cavity with too little air, we infer that *the full-scale trajectory should lie somewhere between that of a Froude model and that of an equal-velocity model*. With a blunt nose, the cavity is thrown wider, the surface seal is delayed, and deceleration is more rapid, hence gravity should be more important and Froude scaling should be more successful. With a slender nose, equal velocity scaling should be more successful; this has been found experimentally by Slichter.^{1h} This supposition is confirmed by experiments on torpedo models at CIT^{1h,21} and on GP bomb models at AHL.

12.7 REDUCED PRESSURE FROUDE MODELS

If both the static air pressure p_a and the velocity v can be varied, then one can preserve both the Froude number F and the cavitation parameter K . Clearly F is preserved if, in the notation of Section 12.2,

$$\mu = \frac{v'}{v} = \sqrt{\frac{r'}{r}} = \sqrt{\lambda}. \quad (5)$$

To preserve K , we need therefore only have

$$\frac{p'_a - p'_v}{p_a - p_v} = \frac{r'}{r} = \lambda. \quad (6)$$

If we assume p_v and p'_v are practically zero (see Appendix VIII) we thus get the approximate scaling rules

$$\frac{v'}{v} = \sqrt{\frac{r'}{r}}, \quad \frac{p'}{p} = \frac{r'}{r}. \quad (7)$$

The following simple alternative motivation for the second equation of (7) can be given. Atmospheric pressure is due to the weight of atmosphere. If we preserve atmospheric density and reduce the height of the atmosphere above the earth's surface in the ratio r'/r , then (gravity being the same), we would have $p'_a/p_a = r'/r$. By the same argument, at corresponding depths underwater,

$$p' = p'_a + \rho g y' = \frac{r'}{r} p_a + \rho g \frac{r'}{r} y = \frac{r'}{r} p.$$

Hence the second proportion of (7) also holds underwater.

Definition. By a *reduced-pressure Froude model*,

we mean a Froude model for the projectile and water, with air pressure scaled by (7).

Caution. A reduced-pressure Froude model is *not* a Froude model, or even an inertial model, because the density of air is not preserved.

Theorem 7. Reduced-pressure Froude models preserve the equations of nonviscous motion of the projectile and water. They also preserve all equations of continuity, the equation $p = C\rho^{1.408}$ of state of air, and (approximately) the equation of state of water, including the tendency to cavitation.

Hence to the extent that pressure is constant over connected regions of air, they also scale air pressure on the water *and* cavity surfaces. Thus the only physical properties not exactly scaled by reduced-pressure Froude models are: the equation of state of water, the dynamic pressure (i.e., density) of air, and viscosity, surface tension, and adhesion.

Proof. Each individual statement, except that about the equation of state of water, is contained as a special case of earlier theorems. The properties of water and the projectile are covered by theorem 6; those of air by theorems 1 to 3.

The equation of state of water involves both compressibility and (below vapor pressure) expansibility. The compressibility is not modeled, but is ordinarily negligible. The expansibility is determined by the cavitation parameter K of equation (1), Chapter 10. This is nearly modeled. It is the important thing in water-tunnel cavitation, and hence reduced-pressure Froude modeling should work in water-tunnel cavitation; this is at least approximately confirmed by experiment.

Reduced-pressure Froude scaling has also been successfully used in model underwater explosion tests, largely at the instigation of Sir Geoffrey Taylor.⁷⁷ Finally, J. H. McMillen's formula for cavity volume (given in Appendix V) is preserved under reduced-pressure Froude scaling.

There is as yet no direct experimental comparison of model and full-scale projectiles shot into water with reduced-pressure Froude scaling; hence the rest of the discussion will be based on indirect evidence. It is hoped that comparisons from NOL and from Knapp's reduced-pressure interface tank will soon be available.

12.8 EFFECT OF REDUCED DENSITY

It is plausible to assume that the approximation of theorem 3 is good. This plausible hypothesis leads one to the conclusions already stated: (1) that any

Froude model will scale correctly time of cavity (deep) seal and motion before sealing, and (2) that a reduced-pressure Froude model will scale correctly the entire trajectory.

However, it ignores the role of surface seal, which is caused by aerodynamic pressure, and is proportional to the *air density*. In fact, it would appear from Table 1 that *the time required for surface seal is approximately proportional* to the air density at entry speeds of 25 to 300 fps.

The qualitative part of this conclusion was reached experimentally by R. M. Davies¹³ and has been strikingly confirmed in recent experiments.^h

Hence reduced density allows a bigger volume of air to enter the cavity than would otherwise be possible, and we infer that *reduced density Froude scaling exaggerates cavity size*. This was not clearly realized when the present reduced-pressure launching tanks were planned; it implies that reduced-pressure Froude scaling should exaggerate the tendency to swerve and ricochet, especially for blunt-nosed projectiles.

Reduced-pressure Froude scaling presumably exaggerates cavity size for another reason. At high entry speeds, especially at shallow entry angles, aerodynamic underpressure $\rho v^2/2g$ may be important in helping to seal the cavity. Consider a Mark 13 torpedo entering water at 500 fps and 19°. Here $\rho v^2/2g = 2.1$ psi, the hydrostatic head due to 5 ft of water. Since the seal occurs at a depth of less than 10 ft, this is not negligible. In fact, if the density of air were 1 per cent of that of water, it would be the principal force tending to cause cavity closure.ⁱ

Reduced-pressure Froude modeling should, however, have the advantage of avoiding the tendency of models to nose down at low speeds. Assuming that negative *absolute* pressures are prevented by cavitation, the possibility of a large negative *relative* pressure is prevented by reduced-pressure scaling.

12.9 REDUCED-PRESSURE FROUDE MODELS WITH HEAVY GASES

In order to preserve density yet reduce pressure within the temperature range of the liquid state of

^h By David Gilbarg, NOL. (See Figures 3, 5, and 7 of Chapter 10.)

ⁱ In general, if air density/water density is σ , the ratio of aerodynamic pressure/hydrostatic head after a travel of 30 projectile diameters is

$$\frac{\rho^2 v/2}{30\rho^*gd \sin \theta} = \frac{v^2}{60gd \sigma \sin \theta} = \frac{F}{120\sigma \sin \theta}.$$

water, we must evidently use a "heavy gas", i.e., a gas of high atomic weight. The use of light models and liquids is also conceivable, but the author knows of no commercially available liquids that are much lighter than water.

More specifically, we must have $\rho' = \rho$ and $dp' = \lambda dp$ for the gas (see Sections 12.3, 12.4, and 12.7). But since $d\rho'/\rho' = d\rho/\rho$ for any scaling, this means that

$$\frac{\rho' dp'}{d\rho'} = \frac{\lambda \rho dp}{d\rho} \quad \text{or} \quad E' = \lambda E, \quad (8)$$

the *moduli of elasticity* (for adiabatic compression) must be in the ratio $1/\lambda$.

Definition. By a *density-pressure differential Froude model*, a Froude model is meant, in which the model gas may differ from air but such that model and prototype gas densities are equal, while pressure differentials are scaled in the ratio $1/\lambda$, as in Section 12.8.

Explanation. At ordinary pressures, the adiabatic equation of state of a gas is given by $\gamma \ln \rho = \ln p + \text{constant}$. But under any geometrical scale model,

$$\frac{d\rho'}{\rho'} = -\frac{dV'}{V'} = -\frac{dV}{V} = \frac{d\rho}{\rho}.$$

Hence, under any scale model,

$$\frac{dp'}{p'} = \frac{\gamma' d\rho'}{\rho'} = \frac{\gamma' d\rho}{\rho} = \frac{\gamma' dp}{\gamma p}.$$

If pressure differentials are to follow Froude scaling, $dp' = \lambda dp$; hence (solving algebraically),

$$\frac{p'_a}{p_a} = \frac{\lambda \gamma}{\gamma'}. \quad (9)$$

In the case of air ($\gamma' = \gamma$), this gives us the rule of Section 12.7 for pressure ratios. If another gas of relative atomic weight $R = N/29$ is used (with N the actual atomic weight), we have $\rho'_a = R(p'_a/p_a)\rho_a = (R\lambda\gamma/\gamma')\rho_a$ at prototype temperatures, by the Boyle-Avogadro law. Hence if $\lambda = \gamma'/\gamma R$, we can scale density and pressure differentials (or pressure differences and density differentials). This has the inconvenience that it permits only one scaling ratio for each gas.^j It gives, in general,

$$p' = \lambda \left[p + \frac{(\gamma - \gamma') p_a}{\gamma'} \right]. \quad (10)$$

We can summarize the results just obtained as follows.

^j It has the further inconvenience that, unless $\gamma' = \gamma$ (which is not to be expected),¹⁰⁷ we do not have $\Delta p' = \lambda \Delta p$. That is, higher-order pressure differences do not scale. In general, $1 < \gamma < 2$.

Theorem 8. If we use a gas with a density under standard conditions of R times that of air, and with an adiabatic equation of state $p' = c\rho'^{\gamma'}$, then a Froude model with $r'/r = \gamma'/\gamma R$ and pressure scaled by (8), will preserve (i) the equations of motion of the projectile, gas, and water, ignoring viscosity and surface tension, and (ii) the first differential effects of the expansibility of air (though not the equation of state, unless $\gamma' = \gamma$).

By scaling at least to a straight-line approximation, the cavity pressure after sealing is probably better than reduced-pressure Froude modeling with air. If we could find a heavy gas with the same γ as air, it would give perfect scaling in so far as viscosity, surface tension, adhesion forces, and water compressibility are negligible. Aerodynamic pressure is modeled; this is the improvement over reduced-pressure Froude scaling.

Physically, when a projectile enters water, there is no pure cavitation. (This is related to the fact that, under steady-state ideal flow, minimum pressures occur on the boundary; hence, where there is access to a gas well above the vapor pressure of water, there will be no pure cavitation.) Hence it is not important that density-pressure differential Froude modeling, like other Froude modeling, does not preserve the vapor pressure of water (unless $\gamma' = \gamma$).

As in all preceding cases, except equal velocity modeling, we fail to model effects due to the compressibility of water. The author could not find any other liquid to replace water in which $\rho' dp/d\rho' = \lambda \rho dp/d\rho$ for a λ differing notably from unity.

Chemically, the most practical commercially available, nontoxic and noncorrosive (in the dry state) heavy gases appear to be the Freon compounds used in refrigeration.^k These cover a wide range of atomic weights, as the brief table below shows.

Chemical formula	$R = N/29$	(Est)	$\gamma R/\gamma'$	Commercial name
$C_2Cl_3F_3$	187	6.3	1.1	8.0 F114
$C_2Cl_2F_4$	171	5.9	1.1	7.4 F113 (80¢-90¢ lb)
SF_6	146	5.0	1.1	6.4 (Fluorinated sulfur)
Xe	130	4.5	1.67	3.6
CCl_2F_2	121	4.2	1.2	4.9 F12 (40¢ lb)
$CHCl_2F$	103	3.6	1.2	4.2 F21
$CHClF_2$	86	3.0	1.2	3.5 F22 (\$1.00 lb)
CO_2	44	1.5	1.3	1.6

^k We are indebted to Fred Binns, of the Virginia Chemical Company, for the information presented here. The Freon compounds are apparently gaseous at atmospheric density and temperature (thus, at a fraction of atmospheric pressure).

The commercial cost appears to run from 40 cents to \$1.50 per pound. At atmospheric density and temperature, this would amount to \$80 to \$300 to fill a space $14 \times 30 \times 6$ ft.

APPENDIX 1

ANTIBROACH DEVICES

1. *Tactical Considerations.* In most low-altitude attacks by aircraft on naval targets, precautions must be taken to avoid broaching. Missiles (bombs, rockets, or depth charges) released horizontally at high speeds from low altitudes strike the water at angles so shallow that broaching will occur with most traditional projectile shapes. This is shown in Table 1, which tabulates the approximate altitudes in feet from which a missile released horizontally at speed v knots will enter the water at angles $\theta_1 = 5^\circ$, 10° , and 20° . It will be recalled that the critical angle for broaching exceeds 20° in many cases, 10° in most cases, and 5° almost always.

TABLE 1

	$v = 100$	200	300	400	600	1,000	2,000
$\theta_1 = 5^\circ$	3.4	14	31	55	124	343	1,374
$\theta_1 = 10^\circ$	14	55	120	221	496	1,366	5,514
$\theta_1 = 20^\circ$	59	235	523	940	2,115	5,876	23,504

Such low-altitude attacks include short-range attacks at speeds 150 to 300 knots with horizontally released missiles ("skip-bombing"), and attacks by rockets with velocities of 600 to 1,000 knots. Finally, they include all attacks on submarines or underwater hulls by deck guns.^a This is made clear in Table 2, which gives the approximate ranges from which a missile released horizontally at v knots will enter the water at angles $\theta_1 = 5^\circ$, 10° , and 20° .

TABLE 2

	$v = 100$	200	300	400	600	1,000	2,000
$\theta_1 = 5^\circ$	78	312	703	1,459	2,810	7,806	31,225
$\theta_1 = 10^\circ$	151	624	1,382	2,502	5,630	15,638	62,550
$\theta_1 = 20^\circ$	323	2,130	2,906	5,166	11,629	32,286	129,145

Finally, where the probable error in the direction of the target is large in comparison with the probable

^a The impact angle for a missile released in an upward direction is about half that for one released horizontally at the same range. Hence, if shallower entry angles are desired for attacks from a fixed range, this can be accomplished by releasing from a rising plane.

error in the release direction (say night attack with radar or attack on a squadron), shallow entry angles are desirable per se, because in this case the probability of hitting is roughly proportional to the length of that part of the missile trajectory which lies in the range of depths and altitudes occupied by the target. Shallow entry angles may also be needed to get a shallow explosion with a time-delay fuze.

For various reasons it is important to avoid broaching. The popular notion that broaching is a desirable feature of skip-bombing is highly erroneous. One reason is that it is almost impossible to obtain as long and low a broach as desired.^{78, 79} With a time-delay fuze, broaching may lead to an air burst which is less effective against the target and dangerous to the attacking pilot or plane. Safety is often achieved by using attacks at higher altitudes (longer ranges).^{80, 81} With a time-delay fuze, a high-drag antibroach device (e.g., broadsiding) is as effective as a low-drag one. Rough water discourages ricochet. With water-discriminating fuzes and with AP projectiles, broaching shortens the effective portion of the missile trajectory unless the plough is very long; the same is true at very shallow entry angles unless the drag is low. Hence *low-drag antibroach devices are needed*. If the underwater path is long (low drag) and the entry angle is fixed, the effectiveness of a missile is roughly doubled or quadrupled if a circular arc trajectory is used instead of a straight path. This applies to surface vessels but not to submerged targets.

In the case of missiles propelled in water (torpedoes, hydrobombs), antibroach devices are less important. But even then some precautions must be taken to avoid broaching at the tactically most convenient entry angles.^b

2. *Flat Head.* Independent experiments at the Aberdeen Proving Ground [APG] and at Dahlgren^c

^b High-velocity, low-drag rockets have underwater paths comparable in length with those of the jet-propelled hydrobomb. The Germans invented a low-drag antibroach "torpedo-bomb" not too much less effective and much cheaper to manufacture than torpedoes.^{82, 87}

^c The APG tests were on GP bombs, those at Dahlgren on depth bombs.^{83, 84}

led to the adoption of flat heads as substitutes for hemispherical and elliptical heads for antibroach properties. In principle, flat-headed bombs are also preferable because they have higher HE capacity. They have high drag but no higher drag than a broadsiding round-headed bomb.

However, they do not have very effective antibroach properties; a flat-headed projectile will broach at 10° to 15° if $L/D = 4$ to 6 is moderate. Tail-up ricochet with $\theta = 22^\circ$ and $v_1 = 240$ fps has been reported.⁸⁵

The broach angle can be reduced as much as 25 per cent by minor modifications such as beveling or rounding the edge.^d This will also have the advantage of reducing drag.

3. *Kopfring*. A flat head causes a projectile to nose down. A more subtle application of the same principle^e consists of projecting a flat part around the head of a convex-headed projectile in a ring.¹²⁴ Surprisingly small *Kopfrings* will stabilize projectiles and prevent them from broadsiding. Thus a 0.5-in. *Kopfring* entirely changed the entry characteristics of the

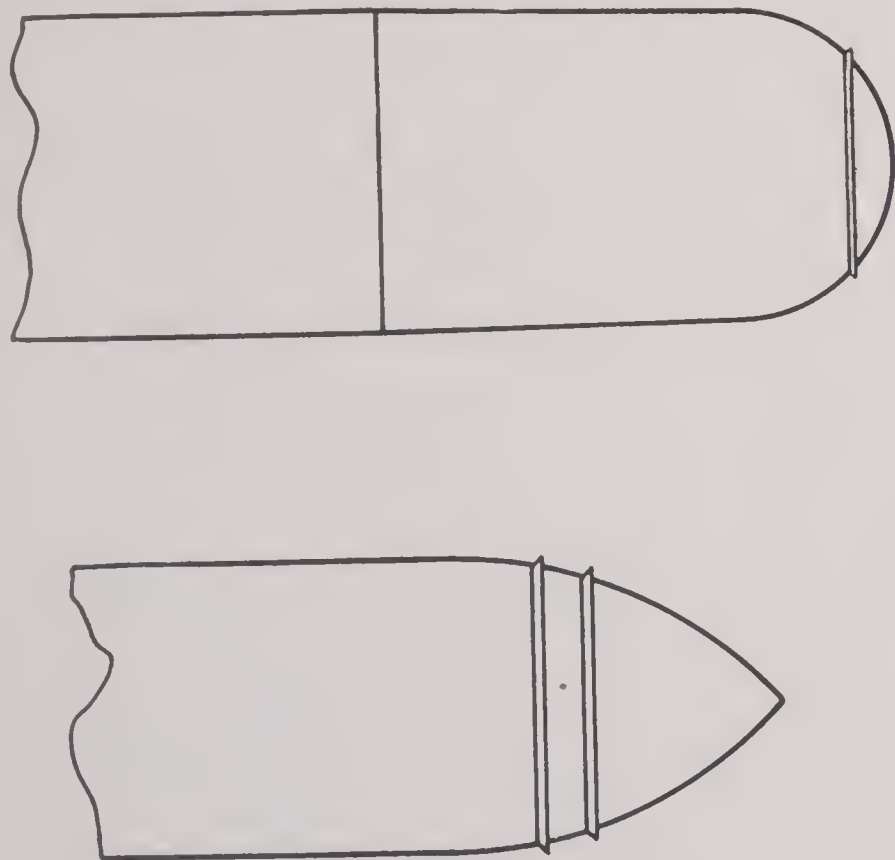


FIGURE 1. *Kopfring*.

22.4-in. diameter Mark 13 torpedo (see Figure 1), and one 0.75 in. thick prevented the violent broaching previously observed in the 28-in. diameter hydrobomb.

^d AMG-H data. The theoretical explanation for the improvement is that the axial component of lift, which causes broaching, is reduced (see Section 11.10). The 1945 navy cup attachment has a slightly rounded edge, but further rounding should improve its performance.

^e A communication from Lt. Comdr. H. E. Pavian states that this was first used in the Franco-Prussian War in an artillery attack on the underwater support of bridges.

However, *Kopfrings* greatly increase drag. (In the case of the hydrobomb, the *Kopfring* was intended to be blown off shortly after entry.) Moreover, in order to be effective in preventing broaching at really small angles, large *Kopfrings* must be used. In fact, the most successful use of *Kopfrings*^{1e} (see Figure 1) is nearly equivalent to a double flat (see Section 4); with this, entry without broaching was obtained at $\theta_1 = 3.5^\circ$, if $L/D = 10$, in the Shark, developed by Commander A. G. M. Small.

4. *Nose Extensions*. The fact that a small flat will throw a cavity of much larger diameter has led to considerable experimentation with flat noses 0.5 to 0.8 calibers or less in diameter.

It has been found that a flat head followed by a cone (see Figure 2) will be very unstable, unless the

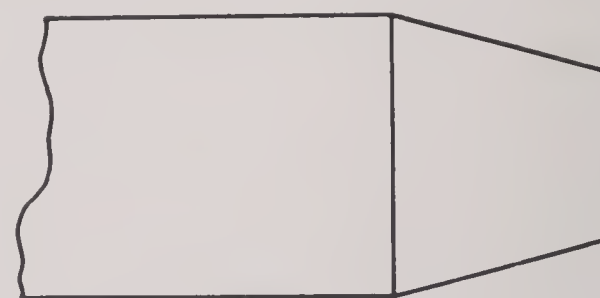


FIGURE 2. Frustum of cone.

cone semiangle α is small. Thus,^{11,86} with a 40-mm rotating projectile having $L/D = 4.5$, a $\frac{2}{3}$ caliber flat was found to be unstable unless $\alpha < 12^\circ$. The reason is presumably that with a moderate pitch there is a large overturn moment on the conical portion.

A more subtle procedure was suggested by Townsend in England. He suggested that a small prod extending axially ahead of a torpedo would give a smaller cavity,⁵⁷ hence speed up cavity collapse and let the torpedo controls act sooner, thus reducing the depth of dive. His conjecture was confirmed experimentally.⁸⁸ However, such a prod was found to increase instability with convex heads.^{1g, 1j} On a model of an M30 GP bomb with a rigid tail, a small fuze cap increased the critical angle from 8° to 25° .

Tests at the David Taylor Model Basin showed that a flat prod in front of a flat head was very effective in preventing broaching at entry angles as low as 5° , if suitably proportioned (see Figure 3). It greatly decreased the amplitude of the oscillations occurring with a flat head. Similar proportions were found most effective at the Admiralty Research Laboratory in England and at the California Institute of Technology [CIT].

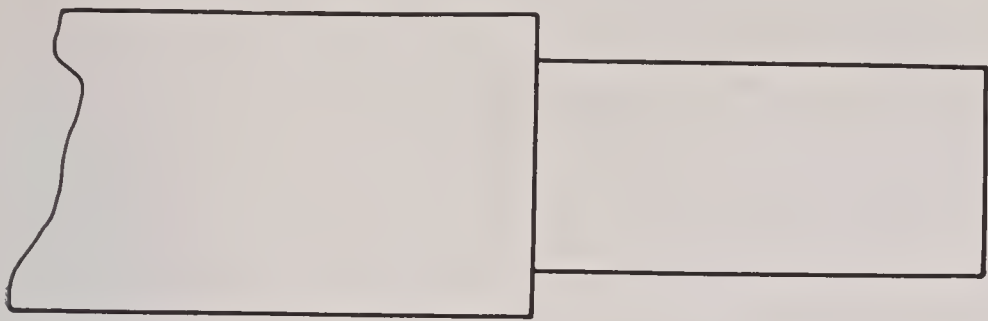


FIGURE 3. Prod, stepped head.

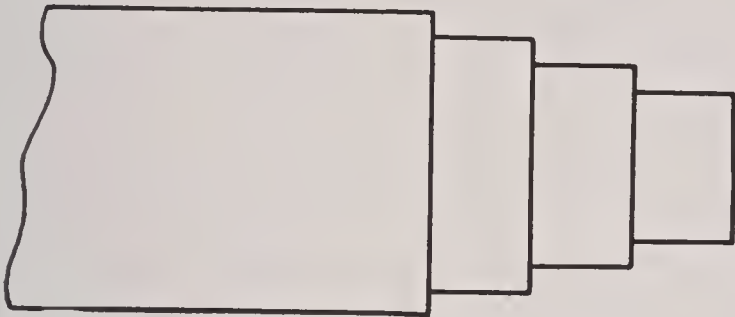


FIGURE 4. Cone attachments to GP.

A more complicated head with multiple steps has been tested by Commander Small for use in the Shark and at CIT with moderate success.^f

5. *Recessed Heads.* It seems logical to suppose that whatever antibroach virtues are possessed by a flat head (as contrasted with a convex head) will be possessed in even greater degree by an indented head. This idea has led to much experimentation with indented antibroach head shapes.

But actually, as we have seen (Section 2), a full-

^f Lt. Commander W. E. Bleick states that such a pagoda head (see Figure 3) was proposed by Thomas Edison for use in World War I. The principle is the same.

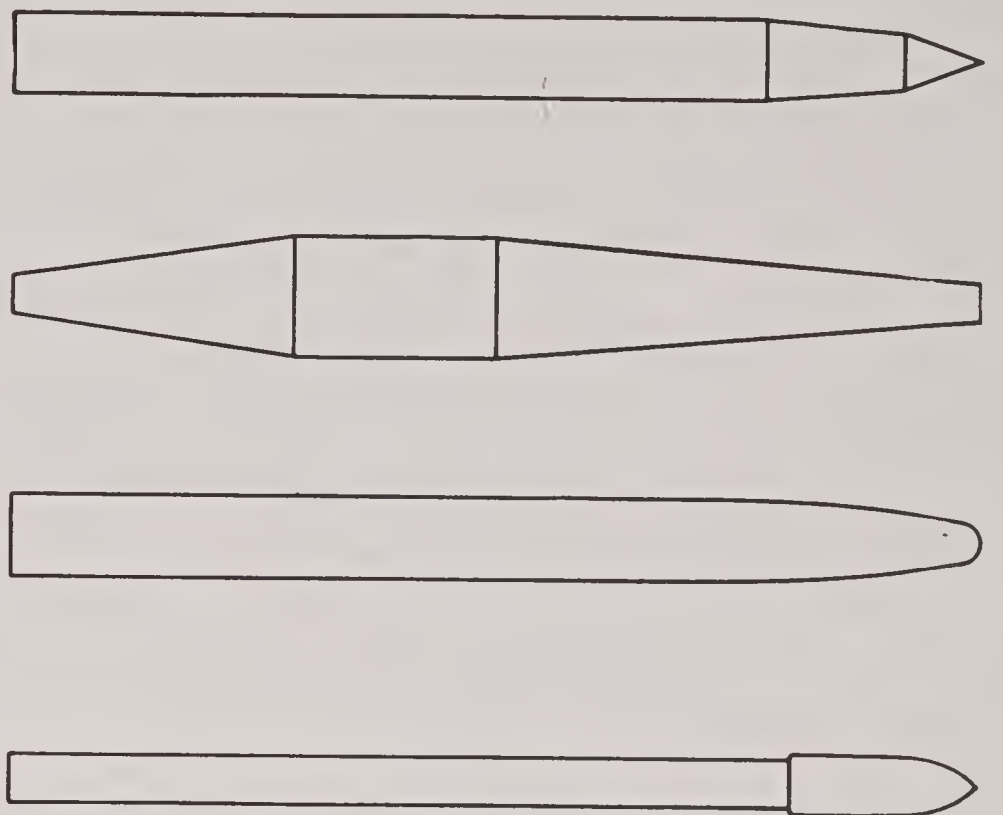


FIGURE 5. Long projectiles.

diameter flat head has *too much* flat area for an ideal antibroach device. This suggests that indenting (recessing) a flat nose will improve its antibroach characteristics only if it is not of full diameter.

This is found experimentally to be the case. Thus of two inverted cone attachments^g tried on GP bombs⁷⁹ and indicated in cross section in Figure 4, the smaller was the more effective. On the type C antisubmarine bomb, a skew recess^{89,90} raised the critical angle from 10° to 12° . On the 40-mm "stabilized rotated" projectile,¹¹ a shallow nose recess^h improved antibroach characteristics in the case of narrow flats.^{1k}

6. *Large Length/Diameter Ratio.* Probably the most effective antibroach shape consists of a very long, thin projectile with a small blunt nose and a gradually tapering head. (See Figure 5, where silhouettes of a German torpedo-bomb and three British and American rockets are drawn.) For the last, $\theta_c \leq 3^\circ$ was reported.

The effect of length is easy to explain. Since the cavity tapers, i.e., has a roughly paraboloidal cross section if $v = \text{constant}$, a long body leaning against one side of the cavity will assume a smaller pitch angle than a short one. Hence the trajectory curvature and the tendency to broach will be less. Thus the CIT double-ogive head, which gave sufficiently small trajectory curvature with $L/D = 16$, did not

^g Model experiments at AHL showed that the large cone attachment often caused the bomb to rotate through 180° .

^h Capt. G. N. Schuyler states that a similar device was used in the "Isham" projectile of World War I.

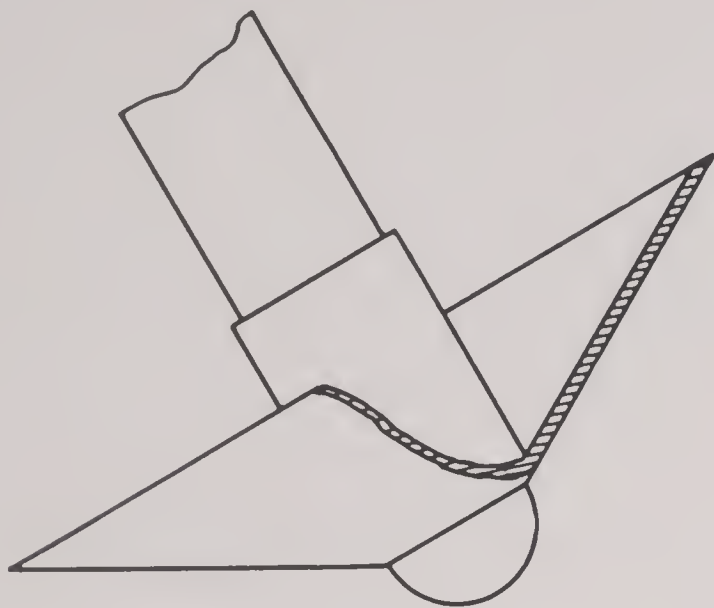


FIGURE 6. Bubble-shedding device.

with $L/D = 12$; it had to be replaced by a spherogive head^{91,92} to prevent broaching above 8° (see Section 11.8).

When a tapering head with a small blunt nose is used, the results are not only a small overturn moment at the stable pitch angle, but (because the cavity is thrown by a region of small diameter d') an extremely low drag coefficient $C_D = 8D/\pi\rho v^2 d^2$ based on the body diameter; $C_D = (d'/d)^2 C'_D$, where C'_D is the drag coefficient based on the wetted portion of the nose. These results, combined with the large sectional density due to length, lead to a very long underwater trajectory. (This means that tanks for testing models with large L/D ratio have to be correspondingly long.)

Though systematic tests have not been made, it would appear that the best results are obtained by having most surface elements of the head make angles $> 70^\circ$ or $< 15^\circ$ with the axis, and avoiding slants of 15° to 70° .

The principal limitation on using a large L/D ratio for stability is the strength of the projectile (its tendency to break in two).

7. *Tail Stabilization.* The fact that most nonrotating projectiles are effectively "fin-stabilized" in air (by a suitable tail) raises the question of why similar devices are not effective in water.

The answer is that the tail structure on most bombs is too weak to withstand the large hydrodynamic forces on entry and no longer behaves like a rigid structure. Moreover, thickening the tail may make it very heavy before it is strong enough, especially at the high entry speeds prevalent with modern aircraft. Because it moves the CG to the rear, a heavy tail is not only wasteful but is actually a destabilizing influence.

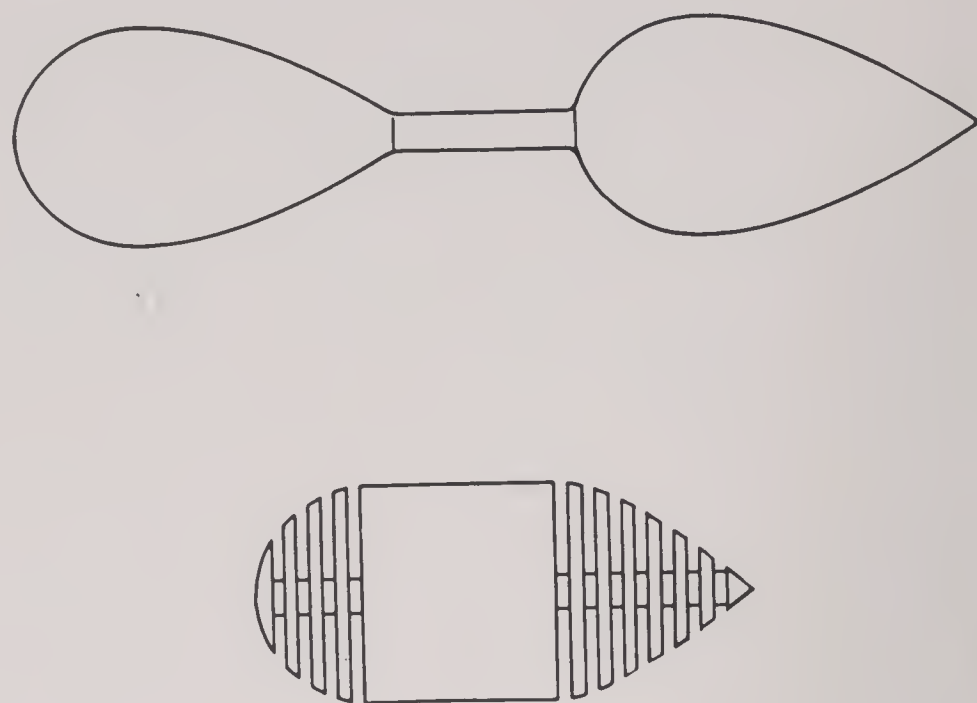


FIGURE 7. Slotted projectile.

However,^{1k} ring tails of welded $1/8$ -in. steel have been used successfully on 100-lb British antisubmarine bombs at 270 mph. The bombs failed to ricochet at release altitudes as low as 25 ft. Our tests at AHL also indicate that rigid tails will prevent broaching at entry angles above 8° , provided the head-shape is such as to cause oscillatory motion.

Col. Leslie Simon⁷⁴ reports that a conical "drag ring" on the tail had useful antiricochet properties.

In the case of depth bombs dropped on deeply submerged submarines, *spiral* tails are found to greatly decrease the dispersion.⁹³ [The dispersion is reduced by half or more by having the fins (vanes) tilted at 10° . The British have recognized the great value of this device.] This is presumably due to the fact that the normal lateral oscillations occurring in the free fall are converted by the rotation into helical oscillations. This will increase the effectiveness if the target is actually located or if a precise pattern of depth charges is desired.

8. *Other Devices.* If projectiles dropped vertically actually traveled in a vertical plane, a *vertical wedge* would be extremely effective in preventing ricochet. It has great stability in a vertical plane,⁵⁴ having the advantages of a flat head but with much smaller oscillations in a vertical plane. The wedge shape was found to have its entry whip less sensitive to changes in the entry pitch than any other shape. But unfortunately, it is as violently unstable in the horizontal plane as a cone-shaped head, quite apart from the difficulty of maintaining the vertical orientation of the wedge in free flight through air.

Much work has been done by the Morris Dam Group at CIT on bubble-shedding devices. (The idea appears to be due to Max Mason.⁹⁵) In princi-

ple, these devices consist of a light, strong sheath of large maximum diameter (see Figure 6) which enters the water with the projectile but is rapidly retarded due to its small momentum, while the projectile slides on through. This should prevent a large air cavity from following in the wake of the projectile. Hence, for torpedoes, it should let the torpedo controls act sooner and reduce the depth of dive, as the nose prod does. However, it will not diminish pure cavitation occurring with very high speed entry.

In any case, it seemed difficult to overcome practical difficulties, and the device was not perfected.

Moreover, it is hard to see in principle how a large overturn moment and binding could be avoided with oblique entry, as well as how a water vapor cavity of considerable cross section can be avoided until the projectile speed reduces, i.e., after considerable underwater travel.

Perhaps the most novel suggestion of all is a "slotted" projectile consisting of two or more pieces in tandem (see Figure 7).⁶ Since the transverse induced mass is much less than the axial induced mass, it should be highly stable. But it is hard to avoid a high drag, and no practical model based on this principle has been designed and tested.

APPENDIX II

IMPACT FORCES

1. *Elastic Shock Force.* Suppose that an infinite plane strikes a flat fluid surface perpendicularly with speed v_1 . There is a simple discontinuous solution of the hydrodynamical equations of motion according to which the water surface moves downward with speed v_1 below which (see Figure 1) there is a uniform

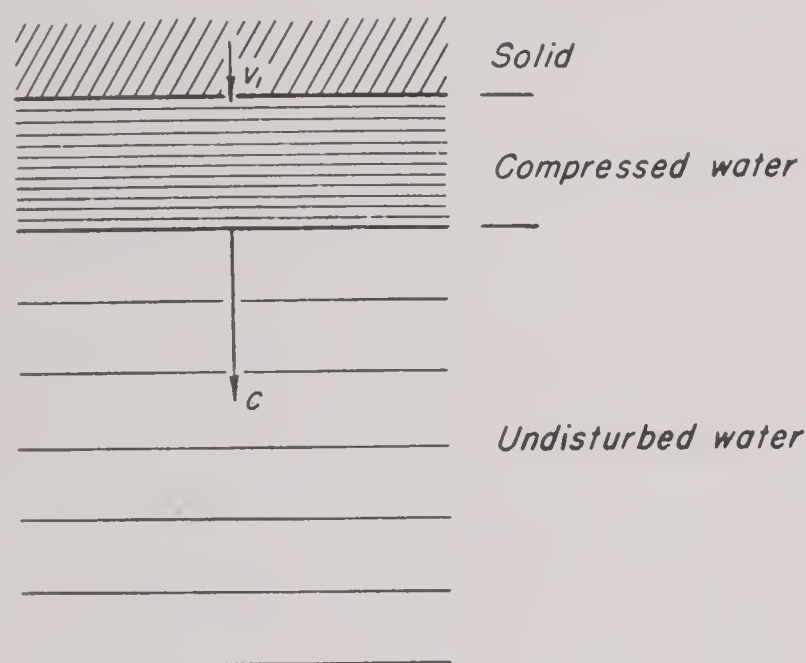


FIGURE 1. Elastic shock force.

compressed region of water also moving with speed v_1 , the lower boundary of which advances with the "shock wave" velocity c , which is ordinarily slightly above the speed of sound in water and can be computed more exactly using the so-called Rankine-Hugoniot equations; a table of $c(v_1)$ is given in Figure 2 of Chapter 9.

Momentum ρcv_1 is thereby imparted to the water per unit area and time; hence the pressure required to maintain the motion is $p = \rho cv_1$ and the drag coefficient is $C_D = 2c/v_1$. This is about 40 at an entry speed of 240 fps. Kinetic energy is not conserved, partly because of the energy used up in compressing the water (mechanical potential energy) and partly because compression heats the water (thermal energy). In fact, the work done per unit area and time is $pv_1 = \rho cv_1^2$, and the kinetic energy of the water is only $\frac{1}{2}\rho cv_1^2$; hence *the other half of the impact energy goes into the compression wave*. This gives an estimate of the energy of the shock wave formed when a flat slug hits water.

In actuality, if a finite curved surface strikes the water with normal velocity component v_1 , it is plausible to suppose that the initial pressure is still ρcv_1 (see Section 9.2). For the water has finite signal velocity, the radius of the wetted area increases initially at an infinite rate, and the shape is approximately flat, when greatly magnified.

2. *Asymptotic Inequalities with Incompressible Fluid and Finite Projectile Curvature.* If a cross section of area A is entering an incompressible fluid with normal velocity v_1 , then the outward flux through any membrane bounded by the edge of A is Av_1 . Hence, if we take equally spaced membranes (e.g., concentric hemispheres), the average velocity across the membrane is at least Av_1/A' , where A' is the membrane area. If we get a volume V composed of such membranes, we have a kinetic energy $K \geq \frac{1}{2}\rho V(Av_1/A')^2$.

For a circular area A of radius a , by using hemispheres we can make $A' = 2A$ and $V = 4A^{3/2}/3\sqrt{\pi}$; hence $K = (\rho/6\pi)A^{3/2}v_1^2$. For an elliptical area A with semiaxes $a > b$, rough calculations indicate that we can make $A' < 2A$ with $V = 4\pi ab^2/3$, and hence $V = 4A^{3/2}/3\sqrt{\pi a/b}$, and K is relatively less. Generally K is asymptotically $\tau\rho A^{3/2}v_1^2$, where the order of magnitude of τ is one-tenth.

It follows that *the total thrust* $dK/v_1 dt$ is $\tau'\rho v_1 \sqrt{A} dA/dt$, where the order of magnitude of τ' is one-seventh. For a projectile surface for which the principal radii of curvature (in the sense of differential geometry) are a, b we have asymptotically $A = 2h\sqrt{ab}$, where $h = v_1 t$ is the depth of submergence. It follows that *the total thrust* is $O(\sqrt{t})$ and *the average pressure* $O(1/\sqrt{t})$ initially. It is a corollary that the pressure would be infinite if water were strictly incompressible.

Incidentally, the preceding calculations give $(C_D)_{\max} \geq \frac{1}{2}$ for a sphere entering water; the von Kármán theory predicts $(C_D)_{\max}$ is approximately unity.

3. *Where von Kármán Theory Is Exact.* Suppose

that a rigid body P , symmetric in a vertical axis, is floating on a horizontal free surface. Suppose further that P is given a sudden impulse vertically downwards and that the fluid is incompressible.

Since the pressure is, by definition, constant on the free surface, the pressure gradient is everywhere perpendicular to the fluid boundary, and so the accelerations and hence the fluid velocity will be everywhere vertical at the instant of impact. Pictures taken by the Morris Dam Group at CIT^a physically confirm this mathematical reasoning. It follows that the potential flow around the part of P below water level and its mirror image (the shaded region of Figure 2)

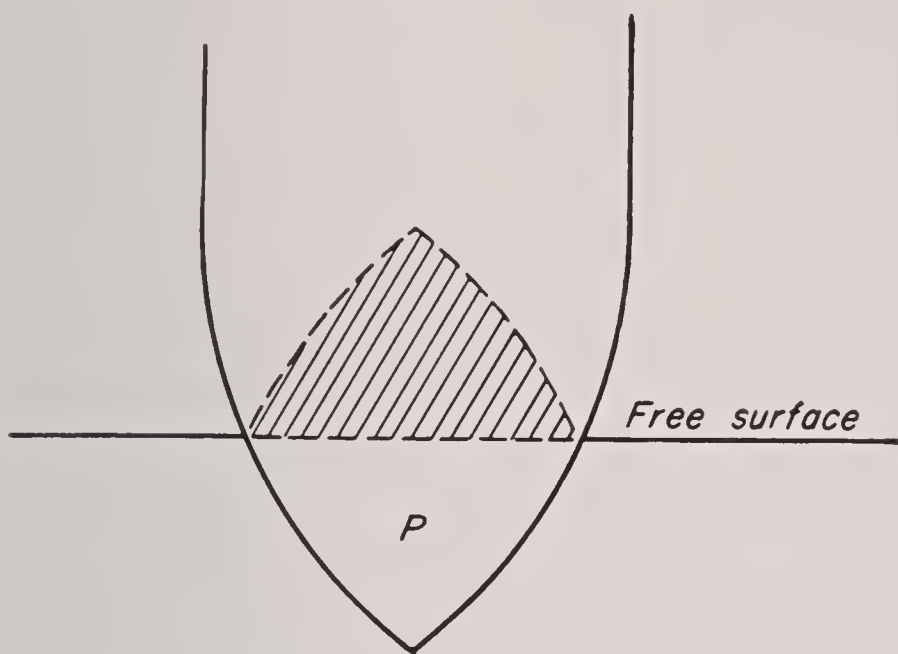


FIGURE 2. Lens.

will satisfy our boundary conditions; this is precisely the potential flow envisaged by von Kármán (see Section 9.3).

Moreover, although it is impossible to treat with mathematical rigor the case of impulsive motion of an incompressible fluid, our discussion of the elastic shock force makes it pretty certain that momentum is conserved, while half the kinetic energy will go into the shock wave,^b hence the energy equation cannot be used. But the vertical momentum of a finite region R bounded by a surface S is

$$\int M_y = \iiint_R \rho \left(\frac{\partial u}{\partial y} \right) dx dy dz = \rho \iint_S U dx dz.$$

Moreover, Theodorson⁹⁷ has shown that if S is a very long cylinder parallel to the y axis, then $\iint_S U dx dz$ tends to zero as S expands without limit.

^a Album of pictures to be issued.

^b Not into splash, as suggested by Th. von Kármán, L. G. Dunn, and J. Charyk.⁹⁶ On the other hand, our argument in the appendix of reference 116 is invalid; especially is this true of the criticisms of von Kármán's theory.

Hence the momentum of the fluid inside S is $\iint_P U dx dz$ extended over the projectile surface.

Therefore, if P is moving vertically with velocity v and we write $M_y = mv$, where $m = M_y/v$ is the "virtual mass" of P , we get

$$\begin{aligned} \frac{1}{2}mv^2 &= \frac{1}{2}v \iint_P \rho U dx dz = \frac{1}{2}\rho \iint_P U (v \cos \lambda) dS \\ &= \frac{1}{2}\rho \iint_P U \frac{\partial u}{\partial n} dS = \frac{1}{2}\rho \iiint (\Delta U \cdot \Delta U) dV, \end{aligned}$$

integrated over the exterior of P . Here λ is the angle made by an outward surface element dS with the (x,z) -plane. But the last expression is simply the total kinetic energy of the fluid, which is finite. This shows that *momentum virtual mass* (as defined by Theodorson) *equals the kinetic energy virtual mass*. It is the latter that is usually computed.

Finally, just half the momentum of the potential flow around P and its mirror image occurs below the water surface by symmetry. We conclude that, in the case just described, the impulsive loss of momentum will be exactly that predicted by von Kármán.

4. *Energy Equation; Remarks.* However, except in the case of a flat slug striking perpendicularly, the preceding description gives only a rough description of the observed facts.

In particular, we have a continuous acceleration of the water after the initial instant of contact. It follows that no energy is lost, either through compression, friction, or otherwise, hence *kinetic energy is conserved*, provided water behaves approximately as an incompressible, nonviscous fluid. Physically, this is true for those elements of the projectile surface making an angle of more than v/c radians with the water surface; as suggested by Harold Wayland, the compression wave can escape for such elements.

Since conservation of kinetic energy would imply about half the loss of momentum which occurs in the exact case of the von Kármán theory, we conclude that *an error of a factor of the order of two may occur with this theory*, except during the first quarter-diameter entry and for very flat head shapes.

We have tried to obtain inequalities which would give actual limits above and below to the loss of momentum, but without success. The preceding consideration suggests that the von Kármán theory *overestimates* the momentum loss. However, the fact that the projectile must push out of the way not only the fluid involved in the "exact case" of the von Kármán theory but also the fluid in the space occu-

pied by it suggests that it *underestimates* the momentum loss.^c

The conjecture that the symmetric flow of von Kármán minimizes the kinetic energy of the water is also false.^d Hence it seems impossible to make any

^c This line of reasoning has been pursued by P. Y. Chou.

^d It is suggested by the well-known fact that the potential flow through all space around a body minimizes the kinetic energy.¹¹⁷ Gilbarg suggested using "cavity virtual mass," de-

more definite statement about the von Kármán theory, beyond the statement that it is probably correct to within a factor of less than two for convex heads entering vertically, and that it is especially accurate during the first quarter-diameter of entry.

finer as above from the kinetic energy of cavity motion. But, as shown in Appendix IV, Section 4, this is always infinite and hence would predict a complete loss of momentum at entry.

APPENDIX III

THEORY OF ENTRY WHIP

1. *Discussion of Assumptions.* As in all known theories of hydrodynamic forces, the predictions based on assumptions 1 to 3 of Section 9.5 are only correct in so far as they reveal trends and the approximate amount of forces.

Newton's rough theory of hydrodynamic forces would give formula (4) of assumption 1 but with a coefficient 2 (for elastic collision) or 1 (for inelastic collision) instead of $\frac{1}{2}$. The factor $\frac{1}{2}$ was chosen to give the correct stagnation pressure in case $\psi = 0^\circ$, as computed by Bernoulli's formula; also because it gave a better fit with experiment. Euler's empirical formula $k \int \rho v^2 \cos \psi$ for pressure was discarded in favor of one of the Newtonian type, because the cavity causes zero pressure when ψ is nearly 90° ; this fits Newton's formula better than Euler's.

Assumption 2 is inexact because water "piles up" ahead of the projectile, but it was difficult to find any other assumption which would give a simple basis for computing the unbalanced forces during entry.

Assumption 3 is approximately valid except in the case of entry at very shallow angles. Thus the theoretically infinite whip as θ_1 tends to zero in formula (5) of Section 9.5 is not actually realized, because the head ricochets after a limited plough. However, with ordinary designs, less than 10 per cent of the velocity is lost during entry, and the change in aspect angle is less than 2° (less than 1° for the Mark 13 torpedo). This is usually less than the entry pitch.

The computation of the entry whip of a projectile entering with zero pitch, on the basis of assumptions 1 to 3, reduces to evaluating certain definite integrals.

2. *Cross-wind Impact Coefficient.* Suppose that a bomb is symmetric in a vertical plane P through its axis, and also in the plane through its axis perpendicular to P . Then there is associated with each infinitesimal surface element dS three other symmetric elements. Moreover after the upper two elements are submerged, in the case of zero yaw, the cross-wind forces on the four elements should exactly cancel by assumptions 1 and 2.

By assumption 3, there is a distance $2r \cos \theta \cot \alpha$,

where r is the radial distance from the axis (see Figure 8 of Chapter 9), when pressure acts on the lower two surface elements but not the upper two. This contributes $\int dL dt = \int 2r \cot \alpha \cos \theta dL/v$ to the cross-wind impulse.

In the case of *axial* symmetry, by assumption 1,

$$dL = 2pdS \cos \psi = \rho v^2 \cos^2 \phi dS \sin \phi \cos \theta. \quad (1)$$

Here ϕ is the angle between the outward normal to dS and the bomb axis, ψ is the angle between this normal and the upward component of cross-wind force, and θ is the longitudinal angle from the normal to the vertical plane through the bomb axis. We get by direct substitution that the total contribution from the four surface elements to the cross-wind impulse is

$$2\rho v \cot \alpha \cos^2 \phi \sin \phi \cos^2 \theta r d\theta ds.$$

Integrating with respect to θ from 0 to $\pi/2$, we see that the total cross-wind impulse should be

$$\begin{aligned} I_L &= 0.5\pi v \cot \alpha \int r^2 \cos^2 \phi \sin \phi ds, \\ &= 0.5\rho v \cot \alpha \int \cos^2 \phi dV, \end{aligned} \quad (2)$$

where $dV = \pi r^2 \tan \phi dr = \pi r^2 \sin \phi ds$ is the infinitesimal volume element between two nearby planes perpendicular to the axis. This implies that the dimensionless ratio

$$i_L = 2 \frac{\text{empirical cross-wind impulse}}{\rho v V_h \cot \alpha}, \quad (3)$$

where V_h is the volume of the head, depends only on the shape of the head ^a and not on its size, or the speed or angle of entry. We suggest that this should be tabulated for actual impacts at zero yaw and the results compared with the theoretical value $i_L = \int \cos^2 \phi dV/V_h$, which is always less than one.

We have computed the theoretical I_L for various head shapes. With a flat head, $I_L = 0$ since $V_h = 0$; it is meaningless to compute i_L . With a vertical wedge, since $dL = 0$ identically, $I_L = 0$ also. For a conical

^a This conclusion follows if any integral formula for the pressure thrust is used.^{12a}

head with a vertex angle 2ϕ , clearly (2) is easily integrated. For a hemispherical head, $i_L = \cos^2 \phi \sin^3 \phi d\phi = 2/15$, and so $I_L = \rho v V_h \cot \alpha / 15$. We can similarly compute the cross-wind impulse by elementary integrals whenever the head is a zone of a sphere or of an ogive.

3. *Overturn Impulse Moment.* Assumptions 1 to 3 also lead to an easy method of predicting roughly the overturn impulse moment of an axially symmetric bomb striking the water with zero yaw.

If the head is hemispherical, or any other section of a sphere, no further computation is necessary. Since all impulses are normal to the surface, their resultant acts through the center of the sphere, which necessarily lies on the bomb axis. Hence the overturn impulse moment is $I_M = bI_L$ where I_L is the cross-wind impulse and b is the distance from the center of gravity forward to the center of the spherical cap forming the nose of the bomb.

In general, we write $I_{MD} + I_L = I_M$, where I_{MD} is the overturn impulse moment resulting from drag components and I_L is that resulting from lift components or cross-wind components. In general, I_{MD} is downward while I_L is upward.

We note that the moment due to pressures cancels out, under our assumptions, except during the interval of length $2r \cos \theta \cot \alpha$ already mentioned, when the lower two of four symmetric elements are below the surface but not the upper. During this interval

the drag component of force is $v^2 \cos^3 \phi dS/2$, and the moment of this is $-\rho v^2 \cos^3 \phi dS r \cos \theta/2$. Hence the drag component of $\int M dt = sM/v$ is

$$I_{MD} = - \iint (\rho v \cos^3 \phi r d\phi ds) (r \cos \theta) (2r \cos \theta \cot \alpha) \quad (4)$$

or

$$I_{MD} = -0.5\pi\rho v \cot \alpha \int r^3 \cos^2 \phi dr. \quad (4')$$

In the case of a flat head of radius a , evidently $I_{MD} = -0.125\pi\rho a^4 v \cot \alpha$. More generally, with a conical head of radius a and vertex angle 2β (reducing to a flat head if $\beta = \pi/2$), $I_{MD} = -0.125\pi\rho a^4 v \sin^2 \beta \cot \alpha$.

The computation of I_L is even easier. The lift impulses from any circular zone all have the same moment arm $(z - z_0)$ about the center of gravity, and so

$$I_L = 0.5\rho v \cot \alpha \int \cos^2 \phi (z - z_0) dV. \quad (5)$$

In the case of a flat head, $dV = 0$ and so $I_L = 0$. With a conical head of radius a and vertex angle 2β , writing $dV = \pi r^2 dz$ and $\phi = \pi/2 - \beta$, we get

$$I_L = 0.5\pi\rho v V_h (\bar{z} - z_0) \sin^2 \beta \cot \alpha, \quad (6)$$

where \bar{z} is the center of gravity of the cone one-fourth of the way from the base to the vertex.

APPENDIX IV

STEADY-STATE CAVITY THEORY

1. *Introduction.* This appendix contains mathematical derivations of various useful results about steady-state cavities. They are all predicated on the assumptions of classical wake theory (Chapter 11 of reference 16), which amount to postulating that there is potential flow around the body, except for a semi-infinite air-filled cavity in back. This is assumed to be at constant pressure, hence, by Bernoulli's equation, its boundary must be a *free streamline* at constant pressure.

The first problem attacked is that of the asymptotic cavity shape. This is solved in Section 2 for a two-dimensional flow by the method of conformal mapping. The difficult axially symmetric case is treated^a in Section 3. These results, though of the greatest significance mathematically, have not yet been closely compared with experiment.

In Section 4, it is shown that the kinetic energy of cavity motion is always necessarily infinite; this indicates that it is useless to try to use cavity virtual mass in applying von Kármán's method of estimating impact forces.

In Section 5 a surprisingly large wall effect is shown to be theoretically predicted for two-dimensional flow. The implications for three-dimensional axially symmetric flows have not been worked out, nor is it certain that the theoretical results will be confirmed experimentally.

The results of Sections 4 and 5, like the formulation in Section 2 of Taylor's results, are the work of L. Loomis.

2. *Asymptotic Cavity Shape in a Plane in Two Dimensions.* We shall first show that the free stream-

lines of a two-dimensional potential flow around a symmetric barrier are asymptotic to a parabola, of which the focal length is proportional to the square root of the drag coefficient.

Let the flow lie in the z plane, parallel to the x axis at $-\infty$ and directed toward the positive x axis.

Since for a given flow pattern the drag is proportional to the square of the velocity at infinity, we can, without loss of generality, take the velocity at infinity to be one. The point of separation on the obstacle is taken at the origin. The potential function ϕ decreases in the direction of flow, and it and the stream function ψ are taken to be zero at the origin. If $w(z)$ is the analytic function $w = \phi + i\psi$ and if the variable ξ and the function $\omega(\xi)$ are defined by

$$w = -\frac{a^2}{4}\left(\xi + \frac{1}{\xi}\right)^2, \quad (1)$$

$$e^{-i\omega(\xi)} = -\frac{dw}{dz}, \quad (2)$$

then the drag on the barrier has, according to the classical Levi-Civita theory, the value^{27b}

$$D = \frac{1}{4}\pi a^2[\omega'(0)]^2. \quad (3)$$

The values corresponding to $\xi = 0$ are $w = \infty$, $z = \infty$, $dw/dz = -1$, $\omega = 0$. The function $\omega(\xi)$ is analytic at $\xi = 0$ and so has a power series development^b

$$\omega = A\xi + \dots$$

If we solve for ξ in (1), we get

$$\begin{aligned} \xi &= \frac{(-w)^{\frac{1}{2}}}{a} \left[1 - \sqrt{1 - \frac{a^2}{(-w)}} \right] \\ &= \frac{a}{2(-w)^{\frac{1}{2}}} + \frac{a^3}{4(-w)^{\frac{3}{2}}} + \dots \end{aligned}$$

^a Taylor³³ solved the problem in the two-dimensional case and wrote to AMG-H suggesting that they try the axially symmetric case. He wrote that he had proved that "a paraboloidal cavity would necessarily involve infinite resistance" and conjectured that "the true solution is a recondite solution involving logarithms." This was first shown and the actual formula for the asymptotic cavity shape derived by N. Levinson.²² His method principally involved new Tauberian techniques, though it also utilized certain suggestions by the rest of the committee.

^b This can be seen as follows: As $z \rightarrow +\infty$ along the free streamline, $w \rightarrow -\infty$ along the real axis, by (1) $\xi \rightarrow 0$ along the real axis. But $|dw/dz| = 1$ on the free streamline so that by (2) $\omega(\xi)$ is real. Thus $\omega(\xi)$ takes the real axis about $\xi = 0$ into the real axis about $\omega = 0$, and thus by the Schwarz reflection principle is analytic at $z = 0$.

Then

$$\begin{aligned}\frac{dz}{dw} &= -e^{i\omega(\xi)} = -\left[1 + i\omega(\xi) - \frac{\omega^2(\xi)}{2} - \cdots\phi\right], \\ &= -[1 + iA\xi + \text{higher-order terms}], \\ &= -\left[1 + \frac{iAa}{2(-w)^{\frac{1}{2}}} + \text{higher-order terms}\right].\end{aligned}$$

Hence

$$z = -(w - iAa(-w)^{\frac{1}{2}} + \text{a logarithmic term and negative powers of } (-w)^{\frac{1}{2}}).$$

On the negative real axis $w = -u$ we have,

$$z = (u + iAau^{\frac{1}{2}} + \cdots),$$

and

$$\begin{aligned}x &\sim u \\ y &\sim Aau^{\frac{1}{2}}\end{aligned}$$

so that

$$y \sim Aax^{\frac{1}{2}}$$

where $A = \omega'(0)$. By (3), we have $y \sim C^{\frac{1}{2}}x^{\frac{1}{2}}$ where $C = 4D/\pi$, the desired relationships.

3. Summary of Axially Symmetric Case in Space.

When a solid body moves at high speed through a liquid, only its fore part is wetted. The rear of the body is in a liquid-free cavity which contains either air or vapor.

We consider a homogeneous ideal incompressible fluid streaming through space with its velocity equal to v at ∞ and parallel to the x axis.

The fluid flows past a nose N , which is a surface of revolution with the x axis as its axis. Behind the nose there is a cavity extending back to ∞ which is free of fluid. The cavity wall W is also a surface of revolution with the x axis as its axis. In cylindrical coordinates the equation of the nose is $r = F(x)$, where $F(x)$ is a given function for $0 \leq x \leq a$. The equation of the cavity wall is $r = f(x)$, $a \leq x$, where $f(x)$ is a function we want to determine. We assume that there exists a flow with velocity potential given by $\phi(x, r) + vx$, subject to the conditions that (1) the velocity is v at ∞ , which is equivalent to

$$\frac{\partial \phi}{\partial x} \rightarrow 0, \quad \frac{\partial \phi}{\partial r} \rightarrow 0,$$

as $(r, x) \rightarrow \infty$; (2) on N and W there is no normal flow, which is equivalent to

$$\frac{d}{dn}[\phi(x, r) + vx] = 0,$$

where n is the normal direction; and on W , the velocity is v , which can be stated as

$$\frac{d}{ds}[\phi(x, r) + vx] = V,$$

where s is arc length along the meridian curve of $r = f(x)$.

Using Green's theorem over a finite portion of space and carefully moving the boundaries out to infinity, a representation of $\phi(x, r)$ in terms of the usual single and double layers on N and W is obtained. By letting (x, r) approach the surface W , a pair of singular nonlinear integrodifferential equations are obtained involving $f(x)$ and $\phi[x, F(x)]$ as unknowns.

Only one of these equations is used here. If we assume that $f(x) = x^k g(x)$, where $g(x)$ satisfies

$$\lim_{x \rightarrow \infty} \frac{xg'(x)}{g(x)} = 0, \quad (4)$$

then the integrodifferential equation can be simplified so that we obtain an equation involving two dominant terms and a third term of smaller size than either of these. If $k \neq \frac{1}{2}$, these dominant terms are of different orders of magnitudes, as $x \rightarrow \infty$ and therefore the equation is impossible.

If $k = \frac{1}{2}$, the equation becomes for large x

$$\int_a^x \frac{g^2(\xi)}{\xi} d\xi \sim 2g^2(x) \log x.$$

By a Tauberian approach, this last result yields for large x

$$\frac{1}{(\log x)^{4+\epsilon}} < g(x) < \frac{1}{(\log x)^{4-\epsilon}}$$

for any $\epsilon > 0$.

If (4) is replaced by the more restrictive assumption

$$\lim_{x \rightarrow \infty} \left| \frac{x \log x g'(x)}{g(x)} \right| < \infty,$$

then we find

$$f(x) \sim \frac{cx^{\frac{1}{2}}}{(\log x)^{\frac{1}{2}}} \left[1 - \frac{1}{8} \frac{\log \log x}{\log x} + o\left(\frac{1}{\log x}\right) \right].$$

When the asymptotic cavity shape is ascertained, one can, by using an axial distribution of sources to reproduce the cavity shape, find an asymptotic formula for the velocity valid at remote points.

If v_r and v_x denote the radial and axial components of fluid velocity, one can show that for large r and $x > r$

$$\begin{aligned}v_r &= \frac{vc^2}{2r\sqrt{\log x}} [1 + o(1)], \\ v_x &= \frac{vc^2 \log r}{4x(\log x)^{\frac{3}{2}}} + \frac{vc^2}{4x(\log x)^{\frac{1}{2}}} \left[1 - \frac{x}{\sqrt{x^2 + r^2}} \right] \\ &\quad + o\left(\frac{1}{x\sqrt{\log x}}\right). \\ &= v - \frac{vc^2 \log r}{4x(\log x)^{\frac{3}{2}}} + o\left(\frac{r^3}{x^3(\log x)^{\frac{1}{2}}}\right) + o\left(\frac{1}{x\sqrt{\log x}}\right).\end{aligned}$$

For large r and $-r < x < r$, we find

$$v_r = 0\left(\frac{1}{r\sqrt{\log r}}\right),$$

$$v_x = v + 0\left(\frac{1}{r\sqrt{\log r}}\right).$$

And for $|x|$ large and $x < -r$, we have

$$v_r = 0\left(\frac{r}{x^2(\log |x|)^{\frac{1}{2}}}\right),$$

$$v_x = v + 0\left(\frac{1}{|x|(\log |x|)^{\frac{1}{2}}}\right).$$

Next the momentum theorem¹¹⁸ is used over a closed surface consisting laterally of a circular cylinder of large radius on one end of a circular base of the cylinder and on the other end of the nose and cavity wall surfaces. Using the asymptotic values of the velocity in the momentum theorem, we find that the drag on the nose form is given by

$$D = \frac{1}{8}\pi\rho c^4 v^2,$$

where c is the constant in the formula for the asymptotic cavity shape.²²

4. *Kinetic Energy and Cavity Motion.* We shall show that if a body B moves steadily, though not necessarily irrotationally, with nonzero drag through an infinite ideal fluid, the kinetic energy of the fluid inside a sphere of radius R about a fixed point of B is at least aR , for some $a > 0$. In particular the kinetic energy of the fluid, and so the virtual mass of B , must be infinite.

B may consist of a finite body (including a finite solid plus a finite cavity), a finite solid plus a semi-infinite cavity, or a semi-infinite solid. For a finite body we obtain a rigorous proof of the d'Alembert paradox, and the general theorem may be considered as an extension of the paradox.

One implication of this result is that if a nonzero drag is to be calculated from a flow given by a distribution of sources and sinks, then the total mass or strength of the distribution must be infinite. This applies to any of the body types listed above, to singlet and doublet distributions, and holds in two dimensions as well as in three. A second implication is that an ideal flow which is used to compute a nonzero drag coefficient cannot also be used to compute impact decelerations by von Kármán's method.

Let B be a body bounded by a smooth surface and lying entirely on one side of some plane (and so, at worst, semi-infinite). Let the rest of space be filled with an incompressible, nonviscous fluid, and sup-

pose that B is moving "steadily" with constant velocity v_0 in the sense that a superimposed velocity $-v_0$ (bringing B to rest) reduces the fluid to steady-state motion.

We shall also make the physically obvious assumptions that as the distance from a fixed point of B approaches infinity the pressure tends to a limit p_∞ and the velocity to the limit zero. In the case of a semi-infinite solid (as distinguished from a finite solid with semi-infinite cavity) we shall have to assume that $p_\infty = 0$.

Let the time t_0 and the point Q be fixed. Let $S(r)$ be that part of the spherical surface about Q of radius r which lies exterior to B , and let $\beta(r)$ be that part of the surface of B lying interior to the spherical surface. Let $D(r)$ be the integral over $\beta(r)$ of the component in the direction of v_0 of the (outward) normal fluid pressure. Then, by definition, the drag D is the limit of $D(r)$ as $r \rightarrow \infty$.

If T is the kinetic energy of the fluid which was bounded by $S(r) + \beta(r)$ at the time t_0 , the classical energy equation^{27c} states that

$$\left.\frac{dT}{dt}\right|_{t_0} = - \iint_{S(r)+\beta(r)} (q \cdot n) dS, \quad (5)$$

where p is the fluid pressure, q the fluid (vector) velocity, and n the unit outward normal to the bounding surface. In connection with (5) we note that

$$|v_0| D(r) = - \iint_{\beta(r)} (q \cdot n) dS. \quad (6)$$

If we let $S(r)$ move with velocity v_0 (and so move with B), we can compute $dT/dt|_{t_0}$ by comparing T with the constant kinetic energy inside $S(r) + \beta(r)$. We obtain

$$\left.\frac{dT}{dt}\right|_{t_0} = \iint_{S(r)} \frac{|q|^2}{2} \rho (q - v_0 \cdot n) dS, \quad (7)$$

the integral being limited to $S(r)$, since $(q - v_0 \cdot n) = 0$ on $\beta(r)$. Thus, by equations (5) to (7),

$$|v_0| D(r) = \iint_{S(r)} \left[p(q \cdot n) + \frac{|q|^2}{2} \rho (q - v_0 \cdot n) \cdot S \right]. \quad (8)$$

By Bernoulli's theorem for steady-state motion

$$\frac{p}{\rho} + \frac{(q - v_0)^2}{2} = C,$$

where C in general varies with the streamline. Since the pressure is determined dynamically only to within a constant, we can add the constant pressure $-p_\infty$ and obtain $p = 0$ at infinity. This will in general

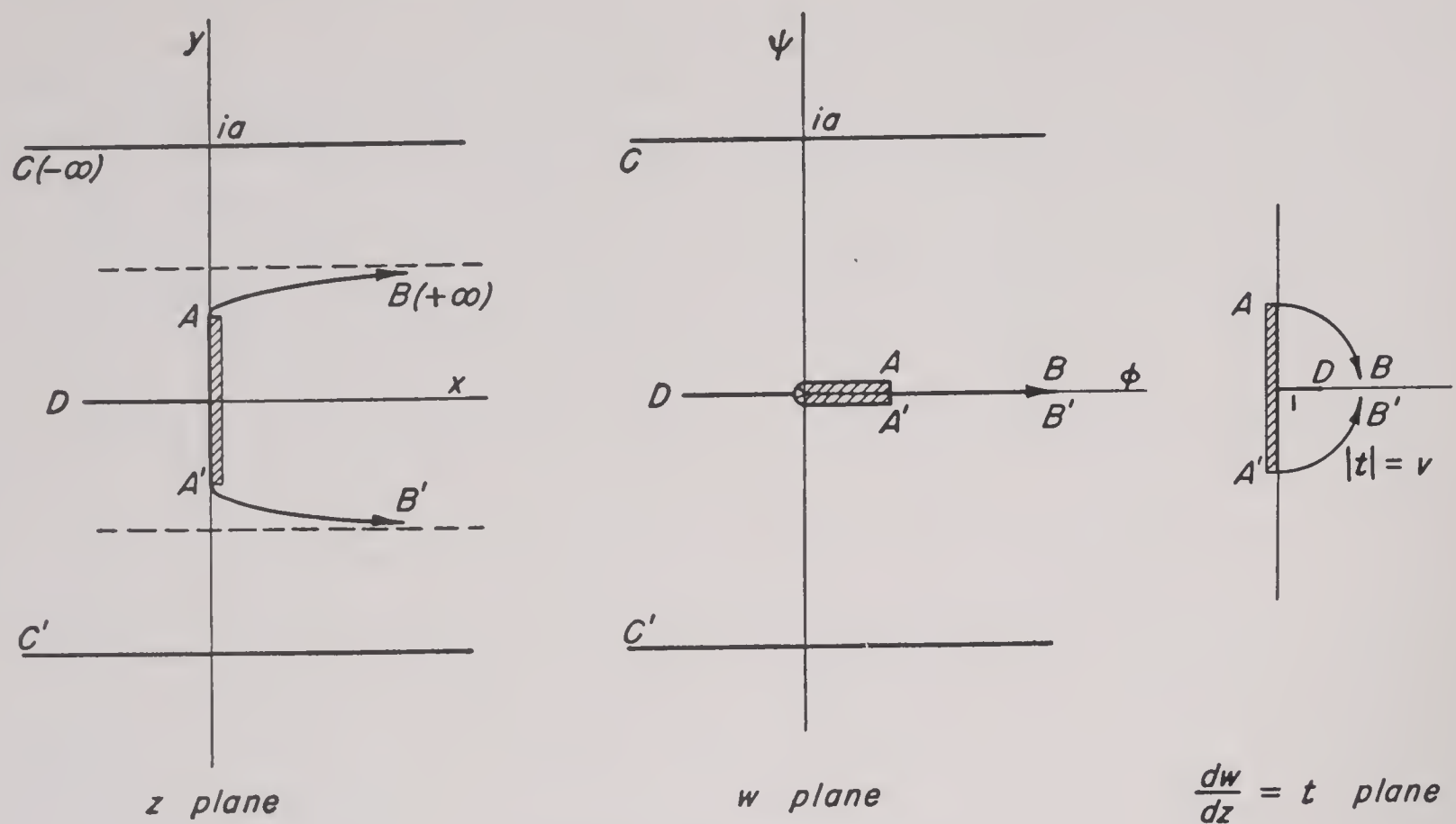


FIGURE 1. Potential diagrams.

change the drag D , but we shall see later that for the cases of interest D remains positive. With $p = 0$ and $q = 0$ at infinity, we have $C = v_0^2/2$ for all streamlines. Thus

$$p = \frac{\rho}{2} [|v_0|^2 - |q - v_0|^2] = \frac{\rho}{2} [2(q \cdot v_0) - (q \cdot q)]. \quad (9)$$

Since $|q| < 1$ outside $S(r)$ for r greater than some r_0 , implying by (9) that $|p| < C'|q|$, and since $D(r) \rightarrow D$ as $r \rightarrow \infty$, we have from (8) that

$$D < C'' \iint_{S(r)} \frac{\rho |q|^2}{2} dS \quad (10)$$

for r greater than a suitable r_1 . The conclusion that the kinetic energy inside $S(R) + \beta(R)$ grows linearly with R follows upon integrating (10) with respect to r from r_1 to R .

If B is a finite body, the drag integral over B of the constant pressure $-p_\infty$ is zero and D remains unchanged. Our theorem is thus applicable and can be regarded as a rigorous proof of a form of the d'Alembert paradox. In particular, if the fluid motion is irrotational, the hypothesis that $q = 0$ at infinity implies that the total kinetic energy of the fluid is finite^{27d} so that $D = 0$, which is the usual form of the paradox.

Now suppose that B is a projectile plus a semi-infinite cavity. In the steady-state motion (with velocity $q - v_0$), the velocity is zero at the stagnation point on the nose and increases along the projectile

profile to its maximum magnitude on the wall of the cavity. The pressure is conversely maximum at the stagnation point and minimum on the cavity wall. Consequently, if a constant pressure is subtracted so that $p = 0$ on the cavity wall and at infinity, then the pressure remains positive on the projectile surface and D is accordingly positive. We can thus infer that steady cavity motion is necessarily accompanied by infinite kinetic energy of the fluid.

5. *Wall Effect in Two Dimensions.* We consider the two-dimensional cavity flow about a flat plate of width 2 placed symmetrically in a channel of width $2a$. The velocity at $-\infty$ is taken to be 1, and the force on the plate is determined parametrically as a function of the channel semiwidth a , the parameter being the velocity v at $+\infty$. The following table illustrates the dependence.

v	$2a$	F	F/v
1.00		0.88	0.88
1.05	773	0.966	
1.10	213	1.07	
1.15	1.0	1.15	
1.20	63.2	1.26	
1.25	44.2	1.38	
1.5	15.8	1.99	0.89
2.0	7.18	3.59	0.90
3.0	4.12	8.24	0.915
4.0	3.32	14.96	0.93
5.0	2.94	23.5	0.94
7.0	2.60	46.8	0.955
10.0	2.39	96.6	0.965
15.0	2.24	221.2	0.98

The asymptotic value of F as $v \rightarrow 1$ ($a \rightarrow \infty$) is, of course, the well-known value of the drag coefficient

for the plate in a uniform unbounded stream, $C_D = 2\pi(4 + \pi) = 0.88$. It is remarkable how rapidly the drag increases as a decreases; notice for instance that if the channel width is about eight times the plate width the drag is already more than twice the asymptotic value. As $a \rightarrow 1$ we find from (12) that $v \sim (2 + \pi)/\pi(a - 1)$, so that

$$F \sim \frac{(2 + \pi)^2}{\pi^2(a - 1)^2}.$$

The region of flow (z plane) and the corresponding regions in the potential and velocity planes (w plane and t plane) are shown in Figure 1 with corresponding points labeled with the same letters. We use the negative of the ordinary potential, i.e., the components of velocity are ϕ_x, ϕ_y . The plate width is taken as 2, the approach velocity (at $x = -\infty$) as 1, and the channel width as $2a$. Then (since $v_\infty = 1$) the strip width in the w plane is also $2a$. The velocity at $+\infty$, v is, of course, greater than 1.

The function dz/dw maps the w region one to one and conformally upon the reciprocal of the t region, and, by symmetry, the upper half-strip in the w

plane upon the reciprocal of the lower quarter circle in the t plane. This function can be calculated from a sequence of elementary maps and is

$$\frac{dz}{dw} = \frac{1}{v} \left\{ \frac{[c^2 - (c^2 - 1)e^{\pi w/a}]^{\frac{1}{2}} - 1}{[c^2 - (c^2 - 1)e^{\pi w/a}]^{\frac{1}{2}} + 1} \right\}^{\frac{1}{2}} \quad c = \frac{v^2 + 1}{v^2 - 1}.$$

Given v , the positions of O , B , and C are fixed in the two planes, and therefore the ϕ coordinate of A is determined. It is $\phi_A = (a/\pi) \log(c^2/c^2 - 1)$. Since the semiplate width is 1, we have

$$\left| \int_0^\phi \frac{dz}{dw} dw \right| = 1. \quad (11)$$

The indefinite integral of dz/dw can be explicitly calculated by elementary methods, and (11) becomes

$$\frac{a}{v} \left[\frac{2}{\pi} \left(v - \frac{1}{v} \right) \arctan v - \left(1 - \frac{1}{v} \right) \right] = 1. \quad (12)$$

The force on the plate can easily be calculated by momentum considerations^{29d} and is

$$F = a(v - 1)^2. \quad (13)$$

Equations (12) and (13) are the required parametric equations for F .

APPENDIX V

TRANSIENT CAVITY THEORY

Very few attempts have been made to formulate aspects of the behavior of the transient cavity into quantitative laws, and even less has been accomplished in the development of quantitative theories. The exact mathematical problem is so difficult that only crude approximations at elementary mathematical levels have been attempted.

Perhaps the simplest quantitative observation which has been made is that if a projectile enters water vertically the maximum cross-section area at different levels is roughly proportional to the space rate at which the projectile loses energy as it crosses the level. This law was explicitly formulated in Section 10.2 for small ($\frac{1}{16}$ - to $\frac{1}{4}$ -in.) steel spheres entering at high speed (3,000 fps), but as long ago as 1865 Hélie observed that the total volume of the crater formed by a projectile fired into dirt is proportional to the initial energy of the projectile. The constant of proportionality is of great interest. McMillen^{15c} found the value 8.92×10^{-7} cm³/erg and observes that if the energy lost were used in expansion against atmospheric pressure^a the constant would be 9.88×10^{-7} cm³/erg ($= 1/1.013 \times 10^{-6}$), a 10 per cent variation which he attributes to loss of energy to the shock wave.

The simple concept that the energy lost by a projectile goes into the work of pushing out the cavity wall *at that level* against a pressure difference is natural and should be examined.

Let r be the cavity width, R the maximum cavity width, and r_0 the cavity width at the point of separation on the projectile. Let y be the depth of the level in question, p_a and p_c the air pressure and the cavity pressure respectively, and Δp the pressure difference $\Delta p = p_w - p_c = \rho gy + (p_a - p_c) = \rho gy + p_u$. Then this assumption states that

$$\begin{aligned} E_0 &= \int_{r_0}^R \Delta p (2\pi r) dr = \pi \rho gy (R^2 - r_0^2) + 2\pi \int_{r_0}^R p_u r dr \\ &= \pi (\rho gy + \bar{p}_u) (R^2 - r_0^2), \end{aligned} \quad (1)$$

where \bar{p} is the average underpressure

$$\bar{p}_u = (2 \int_{r_0}^R p_u r dr) / (R^2 - r_0^2).$$

^a Reference 15c refers to hydrostatic pressures when atmospheric pressure is meant.

If p_c is constant $\bar{p}_u = p_u$, so that, knowing E_0 from the drag coefficient, each of R and p_c can be calculated from the other.

At sufficiently low entrance velocities, where the surface seal occurs after deep seal or does not occur at all, the pressure in the cavity is presumably atmospheric ($p_u = 0$), so that the above hypothesis can be checked with $\Delta p = \rho gh$. Table 1 shows the computed and measured maximum widths of the cavity in centimeters for Plate IVb of reference 13, where a $\frac{5}{8}$ -in. diameter steel sphere is dropped into nitrobenzene with an initial velocity of 19.4 fps in a tank in which the pressure has been reduced to $\frac{1}{76}$ atmosphere. In each case the computed width is

TABLE 1

Depth (cm)	Measured radius (cm)	Computed radius (cm)	Computed Measured
5.85	1.92	2.36	1.23
7.63	1.64	2.03	1.23
9.40	1.49	1.80	1.21
11.26	1.36	1.62	1.19
13.10	1.26	1.49	1.18

close to 20 per cent greater than the measured width. Moving pictures, taken at the David Taylor Model Basin, of aluminum spheres dropped into water with an entrance velocity of 45 fps were also measured for maximum cavity width at a depth of 18.5 in. in the case of a 3.9-in. sphere, and at depths of 5.3, 10.6, and 15.9 in. for a 3-in. sphere. Here again the ratios of predicted to observed width were close to 1.2. According to our assumption, this means that the pressure in the cavity must be below atmospheric pressure, but it seems more reasonable to take this difference as a measure of the error in the assumption, representing perhaps the residual kinetic energy in the water when maximum cavity width has been reached. Since the predicted area is about 1.5 times the measured area, we would say that two-thirds of the energy lost by the sphere goes into pushing out the cavity walls, while one-third is dissipated as residual kinetic energy in the water.

If this principle is assumed to be correct, equation (1) permits the calculation of the average under-

pressure \bar{p}_u in the cavity. If this is done from maximum width measurements at different levels and if we assume that the underpressure at any instant is approximately constant throughout the cavity, then the calculated average underpressures should not vary too much. This fact constitutes another check of the validity of the principle, including the factor of approximately $\frac{2}{3}$, for the amount of the energy lost by the sphere which is effective in creating the cavity. In Table 2, the results are listed for a 1.5-in. steel sphere entering water vertically at 300 fps.

TABLE 2

Depth of measure- ment (ft)	Max. cavity width (ft)	\bar{p} [from (1)] (dynes/cm ²)	ρgh (dynes/cm ²)	$\bar{p}_u (= \bar{p} - \rho gh)$ (dynes/cm ²)
0.4	0.78	17.66×10^4	1.2×10^4	16.5×10^4
1.4	0.62	17.9	4.2	13.7
2.4	0.41	26.2	7.2	19.0
3.4	0.32	27.1	10.2	16.9

Measurements from a second film under the same circumstances yielded for \bar{p}_u at the various levels the values 17.1, 15.1, 22.8, and 19.4 ($\times 10^4$ dynes/cm²).

Considering the difficulties in making accurate measurements and that the values of \bar{p}_u are averages over somewhat different ranges of \bar{p}_u , these results are good. The average underpressures in these circumstances are $\frac{1}{16}$ to $\frac{1}{5}$ atmospheres.

As a further check, two films of a 1.5-in. steel sphere entering water vertically at velocities of 260 and 102 fps were measured carefully for the cavity volumes at surface pressure to be atmospheric at the time of surface seal. By using the formula for adiabatic expansion of air, it was found that 51 per cent and 58 per cent respectively of the energies of the two spheres went into expansion of the cavity. These figures are too low for two reasons. First, since the maximum diameters at the various levels are not assumed simultaneously, the maximum volume calculated from maximum diameters is greater than that actually measured. Second, the cavity pressure at the time of surface seal is probably less than atmospheric. These two effects are hard to evaluate, but in any case they will raise the effective energy per cent to good agreement with our earlier figure of 67 per cent.

The preceding discussion has been concerned entirely with the maximum cavity radius and its connection with the energy lost by the projectile. The more complicated and difficult subject of the kinematics of the motion of the cavity wall has received

some attention in the literature,^{10, 98} and again there is a separation into observed, empirical laws and attempts at simple mechanical explanations of these laws.

The most ambitious descriptive theory is that due to Blackwell.¹⁰ From observations on moving pictures of cavity development, he was led to formulate the following postulates: "the cavity is formed by the projectile giving the walls of the cavity an initial velocity sideways," the wall at this section then moving "under a constant deceleration acting normal to the trajectory" such that

1. . . . The cavity deceleration at any section is directly proportional to the depth of the center of the section and inversely proportional to the calibre of the projectile. . . .

2. The cavity wall initial velocity is related to the velocity of the projectile in a constant ratio *independent* of depth.

In applying these postulates, no cavity is to be considered beyond the time of surface seal, since the subsequent variations in cavity pressure invalidate the postulate of constant deceleration.

If $r(x, t)$ is the cavity radius at the time t and depth x , these postulates imply that

$$r = r(x, t) = a + \lambda v_0 e^{-kx} \left[t - \frac{1}{kv_0} (e^{kx} - 1) \right] - \frac{\mu x}{2a} \left[t - \frac{1}{kv_0} (e^{kx} - 1) \right]^2, \quad (2)$$

where λ and μ are the constants of proportionality for initial cavity wall velocity and cavity wall deceleration respectively and a is the radius of the projectile.

The constant λ is taken to be the tangent of the cone semiangle of the cavity, but the constant μ has no direct geometrical significance and is chosen empirically to give the best fit.

The solution of this equation leads Blackwell to the tabulation of two functions from which the time and depth of deep seal can easily be computed in any given situation. The agreement with experiment is good. Applied to the question of maximum cavity radius, equation (2) gives results running about 20 per cent too low.

There are two objections to Blackwell's theory which are of interest here. First, it is a descriptive account of the motion of the cavity wall instead of a deduction of that motion from reasonable assumptions as to the nature of the flow of the water. For this reason, the constant μ has no significance except as a curve-fitting parameter. Second, equation (2) implies that the graphs of cavity width vs time are

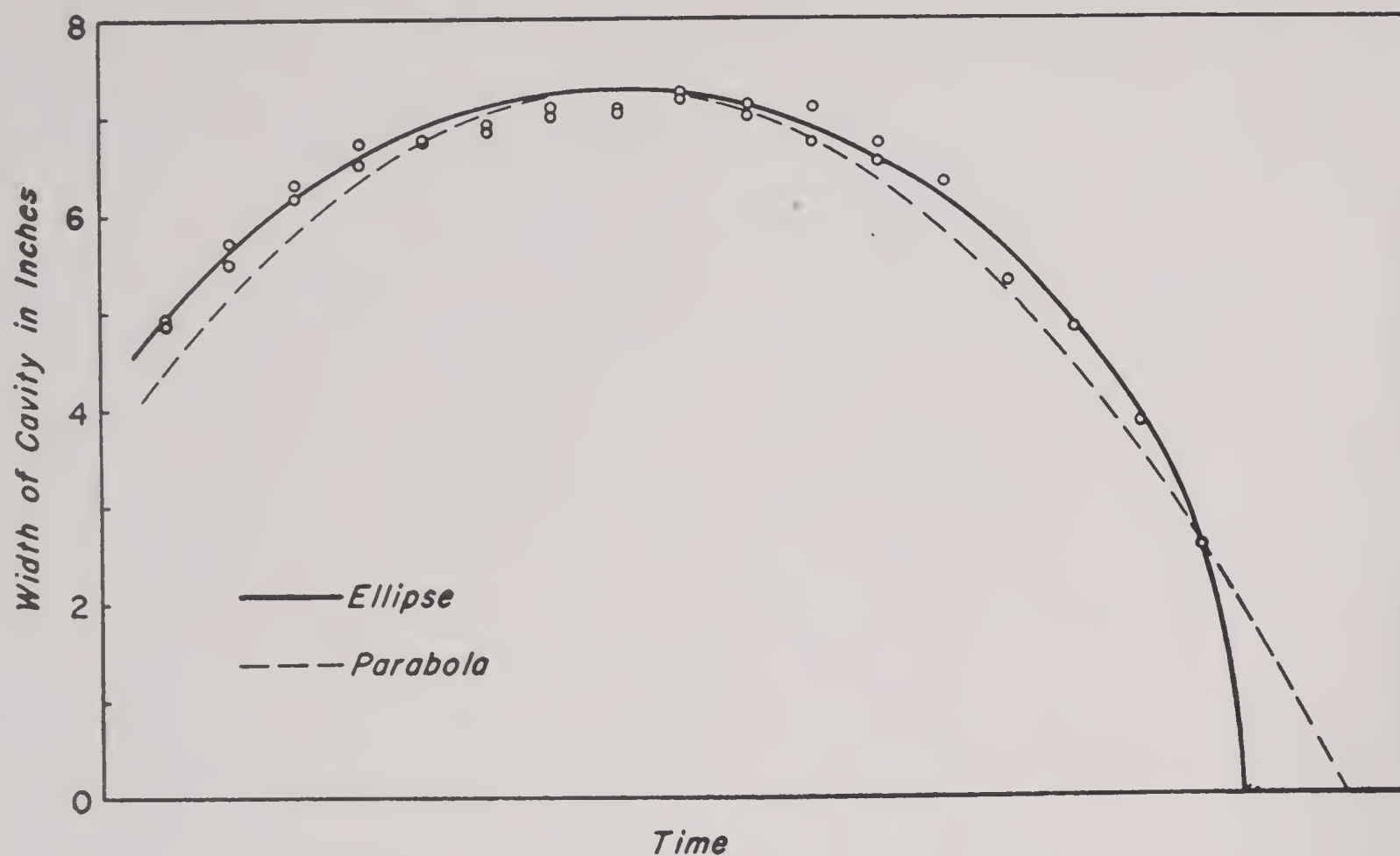


FIGURE 1. Cavity width as function of time, before surface seal.

(roughly) parabolic, whereas *before surface seal* they are often much better fitted by ellipses. (See Figure 1, where the width of the cavity at a depth of 21 in. is plotted against time for a 3.9-in. aluminum sphere having an entry velocity of 45 fps and is compared with the best parabolic and elliptic approximations.)

In an attempt to *derive* the motion of the cavity wall (in the steady-state case) from a simple mechanical model, Bowen¹¹ supposed that the water moved radially outward from the cavity axis. Other authors have more or less explicitly made the same assumption. Actually the motion of the water is far from radial (see Figure 2 of Chapter 10). And even without this evidence there is the mathematical difficulty that in an unbounded fluid the projectile would have to impart infinite kinetic energy to each slab of water it passed. However, some consequences of the radial motion assumption do seem to hold approximately. Thus the pattern of the radial component of the velocity in a plane perpendicular to the trajectory seems to remain nearly similar to itself as the cavity expands.

Taking this as an assumption, the energy E_t (actually, the energy density) is easily found to be $Cr^2 (dr/dt)^2$, where r is the cavity radius, C is the constant of proportionality $E_0/(rdr/dt)_0^2$, and E_0 is the energy given to the slab of water by the passing projectile. One can compute C from the drag coefficient. For $E_0 = -d(1/2mv^2)/ds = -mvdv/ds = D = 1/2\pi\rho r^2v^2C_D$; r_0 can be measured directly (it is, in the case of

spheres, slightly less than r); and $(dr/dt)_0 = v \sin \psi$, where the separation angle ψ is measured from photographs. Thus for spheres, $\psi = 22^\circ$. By substitution,

$$C = \frac{\pi\rho C_D}{2(r_0/r)^2 \sin^2 \psi},$$

where C_D and ψ are known from other measurements.

We shall also neglect variations in the upward component of the velocity over such a plane and shall assume that no energy is transferred into or from the slab of water bounded by two such planes. Then,

$$E_0 = Cr^2 \left(\frac{dr}{dt} \right)^2 + 2\pi \int_0^t p(t) r dr.$$

Differentiating once with respect to t , we obtain

$$p = -\frac{C}{2\pi} \frac{d^2}{dt^2}(r^2), \quad r^2 = -\frac{2\pi}{C} \int dt \int p dt.$$

In particular, if p is constant

$$br^2 + b^2(t + K)^2 = a,$$

where $b = (\pi/C)p$, $a = (E_0/C) + br_0^2$, and K is a constant of integration. The graph of r against t thus has the desired elliptical shape, the r and t semiaxes being $\sqrt{a/b}$ and $\sqrt{a/b}$ respectively.

In the preceding theory, there are no empirical parameters such as Blackwell's μ . Before deep seal, we shall assume zero underpressure in the cavity, so that $p = \rho gx$. Using $C_D^0 = 0.335$, $(r_0/r) = \cos \psi = 0.93$, we are able to predict mathematically the time

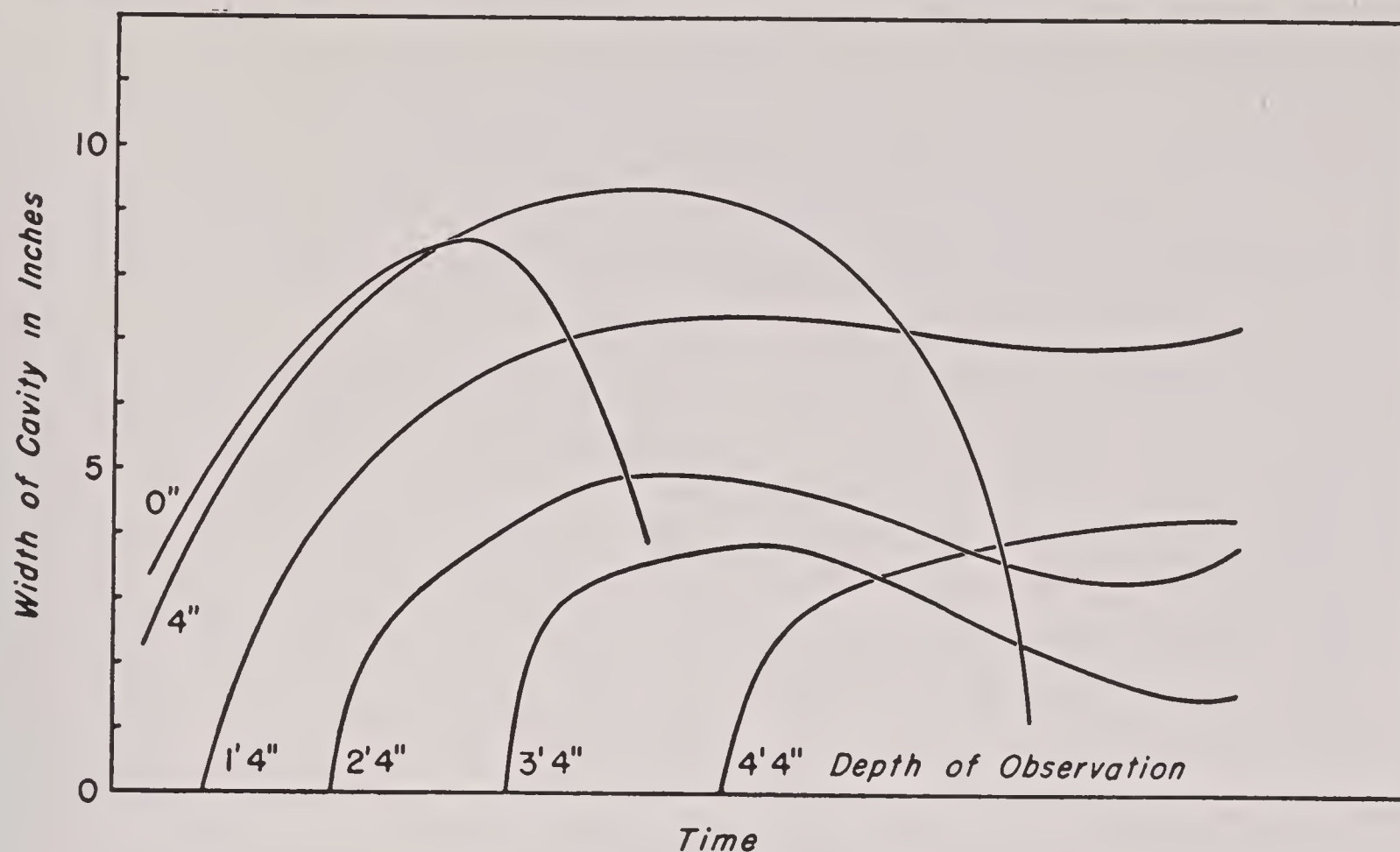


FIGURE 2. Cavity width as a function of time, before and after surface seal.

of deep seal. Table 3 compares the times of deep seal predicted by Blackwell's theory and the present theory, using Blackwell's tables. The first two cases were considered by Blackwell^{9b} and the third case is from a film taken at the David Taylor Model Basin.

TABLE 3

	v_0 (fps)	k (ft ⁻¹)	a (ft)	Pre- dicted t	Observed t	Predicted by Blackwell
Hollow brass sphere	20	0.55	0.8	0.094	0.099	0.094
Magnesium sphere	20	1.4	0.04	0.064	0.066	0.070
Aluminum sphere	44	0.254	0.162	0.126	0.135	0.139

The graphs of cavity width against time after surface seal sometimes tend toward a parabolic shape, in the sense that they are fitted as well or better by parabolas as by ellipses. Thus Figure 2 shows the cavity width at levels 0, 0.33, 1.33, 2.33, 3.33, and 4.33 ft below the surface for a 1½-in. steel sphere with an entrance velocity of about 250 fps. The relative sharpening of the curve (increase in curvature)

at the maximum width and decrease in curvature near zero width, which is equivalent to increase and decrease respectively in deceleration of the cavity wall, can be explained simply as consequences of underpressure at maximum cavity volume and overpressure later when the volume has decreased beyond its size at the time of surface seal.

One can try to interpret the present theory so as to correlate separation angle with the drag coefficient $C'_D = 2D/\pi\rho r_0^2 v^2$ based on wetted area,

$$C = \frac{\pi\rho C'_D}{2 \sin^2 \psi}.$$

A hypothetical slab of water extending τ cavity radii would have an energy corresponding to $C = 2\pi\rho \ln \tau$. This implies

$$C'_D = 4 \ln \tau \sin^2 \psi.$$

But in the case of a disk, where $\psi = 90^\circ$, $C' = 0.77$, $\ln \tau = 0.19$; in the case of a hemisphere, $C'_D = 0.34$, $\psi = 22^\circ$, $\ln \tau = 0.55$. Hence $\ln \tau$ depends greatly on head shape, and we only get a *qualitative* correlation between the separation angle and the drag coefficient C'_D based on wetted area.

APPENDIX VI

MATHEMATICAL CLASSIFICATION OF TYPES OF MOTION

Recall the differential equations (15) of Chapter 11,

$$\frac{d\phi}{ds} = \chi, \quad \frac{d\chi}{ds} = F(\phi, \chi), \quad (1)$$

where $F(\phi, \chi)$ is *single-valued*, provided we can neglect free surface forces, gravity forces, and the dissipation of the cavity (change in the cavitation parameter K along the trajectory). Furthermore, for an axially symmetric projectile, we will have

$$F(-\phi, -\chi) = -F(\phi, \chi). \quad (2)$$

We shall now show that the solutions of (1) can be represented by a family of curves on a circular cylinder. We take as coordinates in the cylinder, ϕ and χ , ϕ being the angular coordinate and χ being the axial coordinate. Through any point (ϕ, χ) on the cylinder for which both right members of (2) are not simultaneously zero, there passes exactly one solution of (1) with slope $d\chi/d\phi = F(\phi, \chi)/\chi$. We also observe that $F(\phi, \chi)$ is periodic of period 2π in ϕ , that is, $F(\phi + 2\pi, \chi) = F(\phi, \chi)$. Thus the solution through the point $(\phi + 2\pi, \chi)$ is the same as through (ϕ, χ) , which justifies the use of a cylinder for the phase space of this problem.

It is very useful to know the qualitative nature of the solutions of (2), regarded as curves on the phase cylinder. This is determined by the number and nature of the singular points of (1) and of the limit cycles of (1). A singular point is defined as a point for which both right members of (1) vanish. A limit cycle is a closed curve on the cylinder which is a solution of (1).

The singular points of (1) must lie in the line $\chi = 0$ and may be readily located by solving $F(0, \phi_0) = 0$. They are of the form $(\phi_0, 0)$. Since by (2) $F(-\phi, 0) = -F(\phi, 0)$, we see that $F(0, 0) = 0$ and also $F(\pm\pi, 0) = 0$. Thus $(0, 0)$ and $(\pi, 0)$ are always singular points of (1). The limit cycles are much less easily located than the singular points, but a knowledge of the singular points may give considerable information about the limit cycles.

The singular point $(\phi_0, 0)$ is said to be stable if all the solutions of (1) which are near the point $(\phi_0, 0)$ on the phase cylinder tend to $(\phi_0, 0)$ as $s \rightarrow +\infty$.

Otherwise the singular point is said to be unstable. The study of stability is of great practical importance and also leads to useful information about the topological nature of the singular point invaluable for our general qualitative study of the solutions of (1). Liapounoff has shown that the singular point $(\phi_0, 0)$ of (1) is stable or unstable according as the linear differential equation (3) is stable or unstable,²⁸

$$\frac{d\phi}{ds} = \chi, \quad \frac{d\chi}{ds} = A(\phi - \phi_0) + B\chi, \quad (3)$$

where

$$A = \frac{\partial F(\phi_0, 0)}{\partial \phi} \quad \text{and} \quad B = \frac{\partial F(\phi_0, 0)}{\partial \chi}.$$

The system (3) is linear with constant coefficients. Thus the solutions of (3) are of the form $\phi - \phi_0 = e^{\lambda s}$, where λ is a solution of the characteristic equation

$$\lambda^2 - B\lambda - A = 0. \quad (4)$$

The roots of (4) are

$$\lambda_1 = \frac{B + \sqrt{B^2 + 4A}}{2}, \quad (5)$$

$$\lambda_2 = \frac{B - \sqrt{B^2 + 4A}}{2}.$$

The solutions of (3) are of the form

$$\begin{aligned} \phi - \phi_0 &= C_1 e^{\lambda_1 s} + C_2 e^{\lambda_2 s}, \\ &= C_1 \lambda_1 e^{\lambda_1 s} + C_2 \lambda_2 e^{\lambda_2 s}, \end{aligned} \quad (6)$$

where C_1 and C_2 are arbitrary constants. (We omit the cases $\lambda_1 = \lambda_2$ and $|\lambda_1| = |\lambda_2| = 1$ which are not of importance here although the latter is of great interest in the case of conservative systems.)

If $R\lambda_1 < 0$ and $R\lambda_2 < 0$, where R denotes the real part, then clearly as s increases $\phi \rightarrow \phi_0$ and $\chi \rightarrow 0$ in (6). Thus, here $\phi = \phi_0$ is a stable solution of (3) and $(\phi_0, 0)$ is a stable singular point. On the other hand, if either $R\lambda_1 > 0$ or if $R\lambda_2 > 0$ then $\phi = \phi_0$ is not a stable solution of (3). We shall now classify the types of singular points.²⁸ The various singular points are sketched in Figure 1.

We return now to equations (1). The singular points of these equations we have seen may be classified

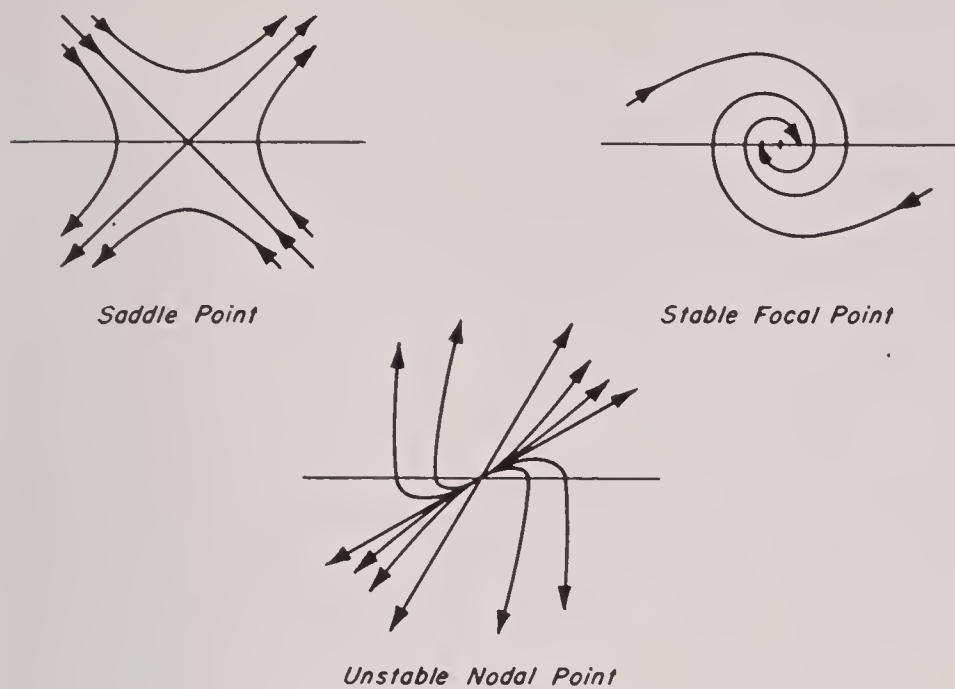


FIGURE 1. Phase plane.

as saddle point, nodal point, or focal point. The saddle point is always unstable. The latter two may be either stable or unstable. The solutions of (1) we have observed may be regarded as curves on a circular cylinder. Through each point of the cylinder except the singular points, there passes one and only one curve of the family of solutions of (1). The closed curves of this family are called limit cycles. They are, as we have already observed, very important.

TABLE 1

Case	Values of λ	Type of Singular Point
C 1. $A > 0$	$\lambda_1 > 0, \lambda_2 < 0$	Saddle point
C 2. $A < 0, B > 0$ $B^2 + 4A > 0$	$\lambda_1 > \lambda_2 > 0$	Unstable nodal point
C 3. $A < 0, B > 0$ $B^2 + 4A < 0$	$\lambda_1 = \bar{\lambda}_2$ $R\lambda_1 = R\lambda_2 > 0$	Unstable focal point
C 4. $A < 0, B < 0$ $B^2 + 4A > 0$	$\lambda_2 < \lambda_1 < 0$	Stable nodal point
C 5. $A < 0, B < 0$ $B^2 + 4A < 0$	$\lambda_1 = \bar{\lambda}_2$ $R\lambda_1 = R\lambda_2 < 0$	Stable focal point

On the cylinder there are two kinds of limit cycles. A limit cycle of the first kind is a closed curve C_2 which bounds an area on the surface of the cylinder. A limit cycle of the second kind makes a circuit of the cylinder in the same way as the circle of cross section.

The motion associated with the latter solution C_2 is one where the projectile tumbles over and over as its center of gravity moves along its trajectory. This is a consequence of the fact that around every circuit of the cylinder the pitch angle ϕ increases by 2π . The occurrence of this phenomenon is excluded if the damping torque is sizable. Experimental evidence indicates that with usual designs this type of motion does not occur. We shall therefore assume that *limit cycles of the second kind do not occur*. The case of a curve on the

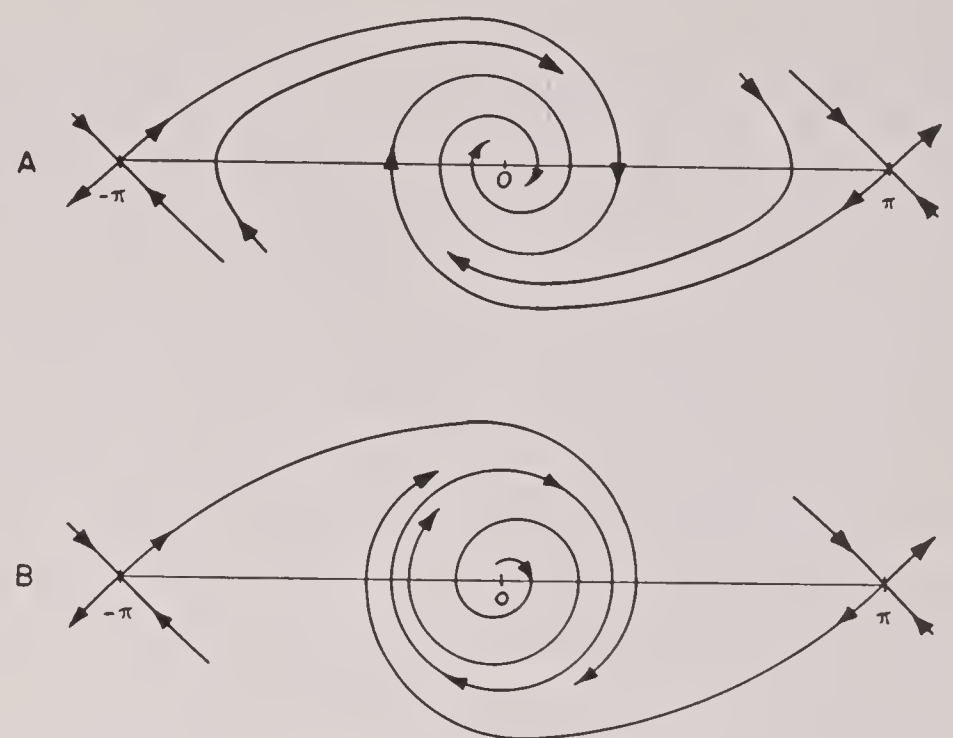


FIGURE 2. Phase plane.

cylinder on which $|\chi| \rightarrow \infty$ is even more strongly precluded than the case of a limit cycle of the second kind.

The focal and nodal points arise, we have seen, when A or $[\partial F(\phi, 0)]/\partial \phi < 0$ and the saddle points when $[\partial F(\phi, 0)]/\partial \phi > 0$. Now, since singular points occur on the line $\chi = 0$ wherever $F(\phi, 0) = 0$ we see that the sign of $[\partial F(\phi, 0)]/\partial \phi$ alternates at successive singular points and therefore that *each saddle point is preceded and followed by a focal or nodal point and each focal or nodal point preceded and followed by saddle points*.

It is also a fact²⁸ that each limit cycle of the first kind must enclose an odd number $2n + 1$ of singular points of which $n + 1$ are focal or nodal points and n are saddle points.

Under certain conditions, it is known²⁸ that concentric limit cycles cannot occur. While these conditions are not entirely fulfilled here, *we shall assume that there are no concentric limit cycles*.

The totality of solutions of (1) may be regarded as a family of curves on the cylinder. The family of curves on the cylinder may include limit cycles of the first kind. *Any curve of the family, other than a limit cycle, must tend to a limit cycle as $s \rightarrow +\infty$ or it must tend to a singular point as $s \rightarrow +\infty$. Any such curve must do the same as $s \rightarrow -\infty$, or it may in this case tend to the extremities of the cylinder, $|\chi| = \infty$. All steady-state motions are then associated with limit cycles or singular points and all other motions tend to these.* We shall now consider the nature and location of singular points and limit cycles of the first kind that may arise for the system (1).

We have seen that the points $(0, 0)$ and $(0, \pi)$ are singular points. We shall now consider the possible

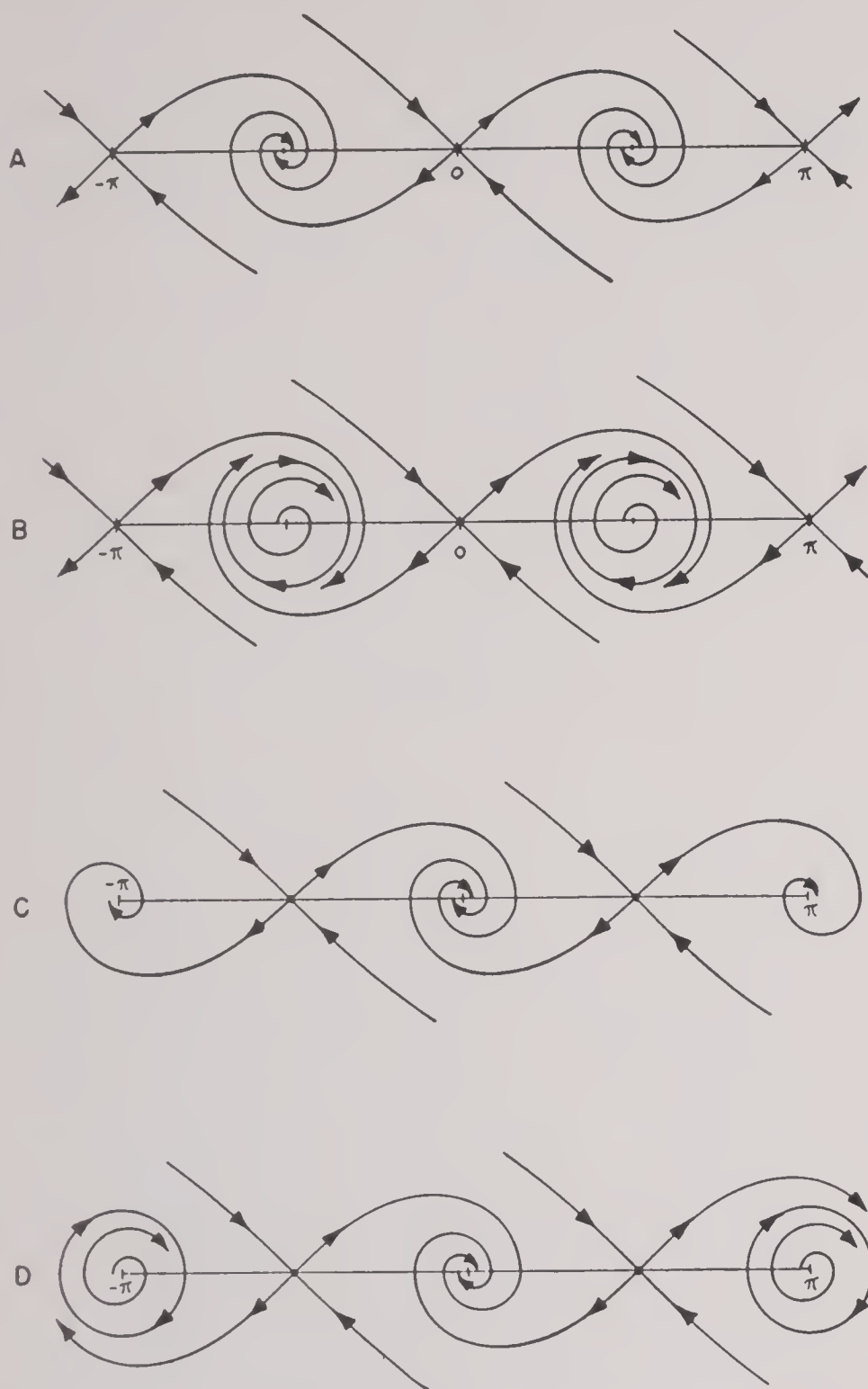


FIGURE 3. Phase plane.

cases that may arise when there are no singular points in the interval $0 < \phi < \pi$ and when there is one singular point in this interval. We shall also consider some typical cases when there are two singular points in the interval.

Case I. Here we consider the possibilities when there is no singular point in the interval $0 < \phi < \pi$.

Case Ia. The singular point $(0,0)$ is a stable focal point (or a stable nodal point). Here the curves are shown on a slit, flattened cylinder in Figure 2. In this case the only stable steady-state motion is head-on motion and all other motions tend to this one. An alternative, essentially similar case arises when the origin is a stable nodal point rather than focal point. Because the singular points alternate in character between focal or nodal and saddle, the point $(0, \pm\pi)$ must be a saddle point as shown.

Case Ib. The origin is an unstable focal or an unstable nodal point. In this case the curves are as shown in Figure 2.

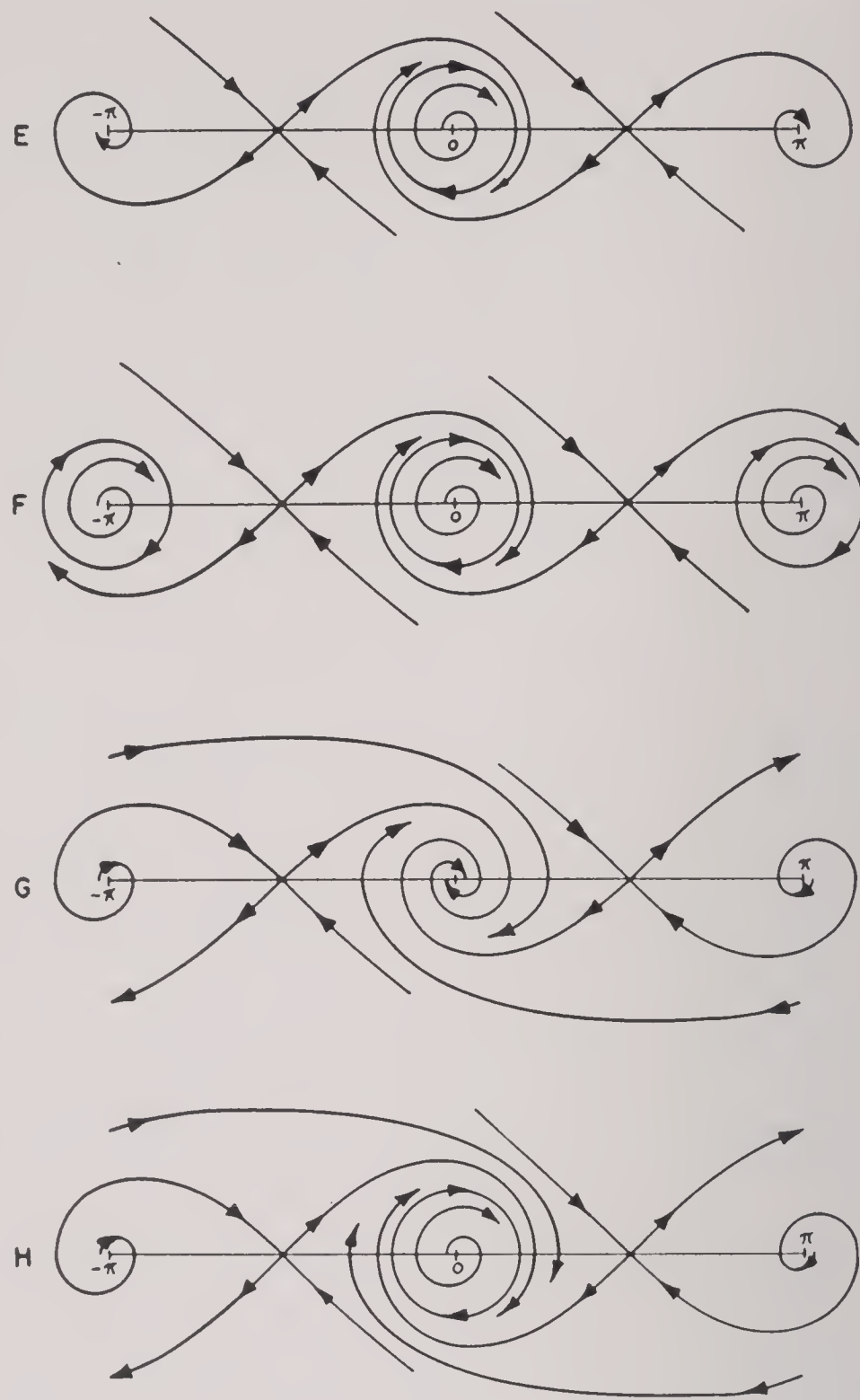


FIGURE 4. Phase plane.

There must be a limit cycle enclosing the origin in this case because otherwise there would have to be limit cycles of the second kind or else curves moving out to the extremities of the cylinder.

In this case the motion is oscillatory.

Cases Ic and Id. These cases are the same as Ia and Ib respectively except that the points $(0,0)$ and $(0,\pi)$ are interchanged.

Physically this means the model performs as in Cases Ia and Ib, but that it moves tail first rather than nose first.

Case II. Here we consider the possibilities when there is one singular point between $(0,0)$ and $(0,\pi)$.

Rather than discuss these cases here, we simply show the various possibilities diagrammatically in Figures 3, 4, and 5. Nodal points and focal points are interchangeable.

Case III. Here several typical possibilities are shown in Figure 6.

The case of stable head-on motion is not possible

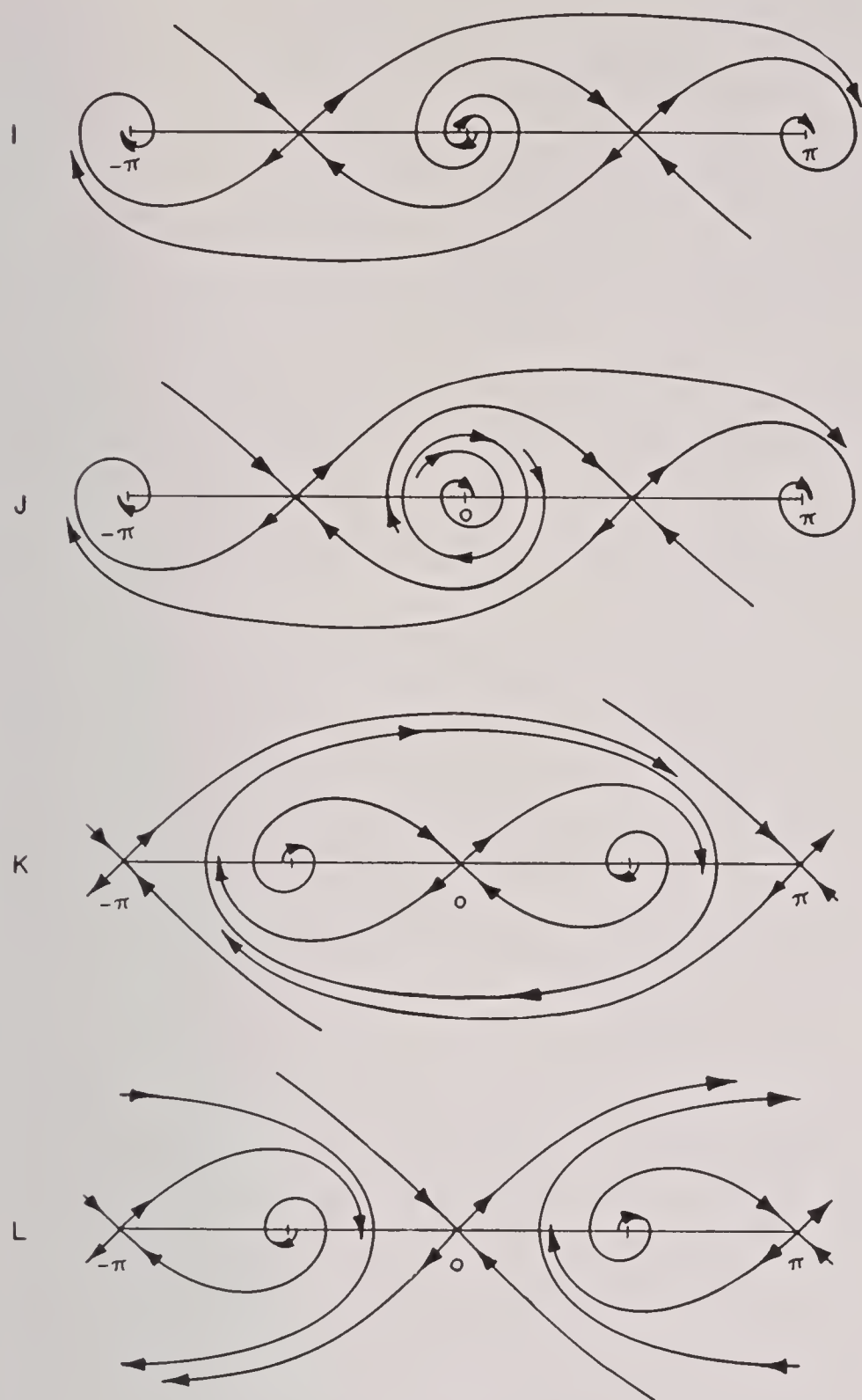


FIGURE 5. Phase plane.

in the case of cavity motion but is of course possible in the noncavity case. Looking at the figures, we see that the possible stable steady-state motions are:

a. Head-on motion given by $\phi = 0$. In this case the focal or nodal singular point at the origin is stable. Examples: Ia, IIc, IId, IIg.

b. Oscillatory motion about the mean position $\phi = 0$. In this case, there is a limit cycle enclosing the singular point $(0,0)$. Examples: Ib, IIc, IIe, IIh, IIk, IIId.

c. Motion given by $\phi = \phi_0$ where ϕ_0 is small (less than 30°). In this case $(\phi_0, 0)$ is a stable focal or nodal singular point and the path is a circular arc. Examples: IIa, IIIa.

d. Oscillatory motion about a mean position $\phi = \phi_0$, where ϕ_0 is not large. In this case, there is a limit cycle enclosing the singular point $(\phi_0, 0)$. The

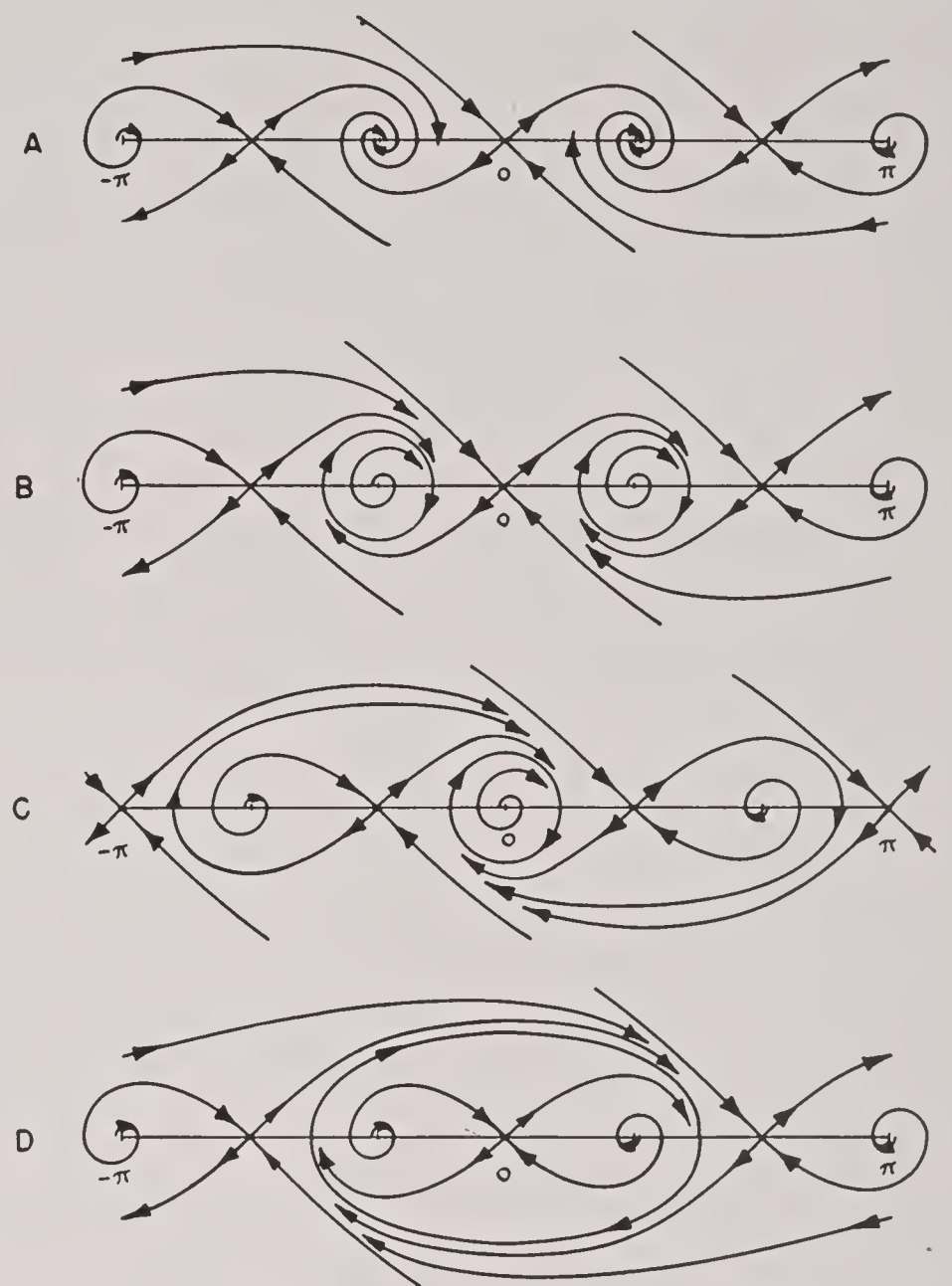


FIGURE 6. Phase plane.

motion is a circular arc with superimposed small oscillations which do not change its basic circular arc appearance. Examples: IIb, IIIb.

e. Same as c but with ϕ_0 large. Here we have broadside motion.

f. Same as d but with ϕ_0 large. In this case we have the broadside type of motion.

g. Stable motions at or near the point $(\pi, 0)$. This means tail-first motion of the projectile, *which is precluded in most practical designs*. Except for the tail-first character, the motion may be classified further as a, b, c, or d above. Examples: IIc, IId, IIe, IIh, IIi, IIj.

The above enumeration of the location of singular points and limit cycles of the first kind is exhaustive under the assumptions that there are no concentric limit cycles and that limit cycles of the second kind do not occur. Hence there are no other types of underwater motion possible than those covered by the names oscillatory (about mean pitch zero), circular arc, broadside, and head-on. The latter is the motion $\phi = 0$ and does not occur as a stable motion in case there is a cavity.

APPENDIX VII

DIFFERENTIAL EQUATION THEORY OF VIRTUAL MASS

In general, induced mass effects may be defined as forces due to the inertia opposed by a fluid to changes in its flow pattern. Strictly, they can only be computed for potential flow without cavitation, but it seems reasonable to suppose that similar forces act generally.

We shall show below that one can explain by induced mass the observed variation in drag coefficient with projectile density and the observed tendency for the trajectory to curve in the direction in which the pitch is turning with small pitch angles. On the other hand, it appears incorrect to attribute the observed^{6,125} increased stability of light (buoyant) projectiles to induced mass; moreover, little light is thrown on increase in stability with L/D ratio.

We turn now to detailed mathematics. From the formulas $\gamma = \theta + \phi$, $x = v \cos \theta$, $y = v \sin \theta$, we get easily

$$\begin{aligned} v \cos \phi &= x \cos \gamma + y \sin \gamma, \\ v \sin \phi &= x \sin \gamma - y \cos \gamma. \end{aligned} \quad (1)$$

Again, the kinetic energy K of induced mass will be homogeneous quadratic in the transverse, axial, and rotational components of velocity, so that

$$\begin{aligned} 2K &= m'(v \sin \phi)^2 + m''(v \cos \phi)^2 + I'\omega^2 + 2m_1v^2 \\ &\quad \sin \phi \cos \phi + 2m_2v\omega \sin \phi + 2m_3v\omega \cos \phi. \end{aligned} \quad (2)$$

The assumed form for K is oversimplified but is tractable. Using this form for K , geometric and kinematic considerations throw more light on m_1 , m_2 , and m_3 . By axial symmetry, if we replace ϕ , γ , ω by $-\phi$, $-\gamma$, $-\omega$, $2K$ will be unchanged. Substituting in (1), we see $m_1 = -m_1$, $m_3 = -m_3$, whence $m_1 = m_3 = 0$. Moreover, as we move the center at which v is measured along the projectile axis, we do not change K , and yet we change $v \sin \phi$. On the other hand, $v \cos \phi$ does not change since the projectile is regarded as a rigid body. Also, ω does not change. If the center from which the v is measured is b units in front of the CG, then the new value of $v \sin \phi$ is given by the old value $+ \omega b$. The invariance of K means that the terms involving $v \sin \phi$ in $m'(v \sin \phi)^2 + 2m_2v\omega \sin \phi$ must be equal to those in $\bar{m}'(v \sin \phi + b\omega)^2 + 2\bar{m}_2v\omega$

$(v \sin \phi + b\omega)$, where \bar{m}_1 and \bar{m}_2 are the new values of m_1 and m_2 . Checking the coefficients of the term $x^2 \sin^2 \phi$ in the two expressions shows that $\bar{m}' = m'$. The coefficients of $v \sin \phi$ show that $2m_2 = 2m'b + 2\bar{m}_2$ or

$$\bar{m}_2 = m_2 - m'b.$$

Thus \bar{m}_2 is a linear function of b . Therefore, for some point which we shall call the *center of virtual mass*, \bar{m}_2 must vanish. If the CG is a units *forward* of this center of virtual mass, we see that $m_2 = am'$. Moreover, because of the tail, the center of virtual mass is usually to the rear of the center of gravity,⁶ so that $a > 0$. In summary,

$$m_1 = m_3 = 0, \quad m_2 = am' \quad (a > 0). \quad (3)$$

We now compute the induced mass forces, from

$$F_x = \frac{\partial K}{\partial x} - \frac{d}{dt} \left(\frac{\partial K}{\partial \dot{x}} \right), \quad F_y = \frac{\partial K}{\partial y} - \frac{d}{dt} \left(\frac{\partial K}{\partial \dot{y}} \right) \quad (4)$$

$$M = F_\gamma = \frac{\partial K}{\partial \gamma} - \frac{d}{dt} \left(\frac{\partial K}{\partial \dot{\gamma}} \right).$$

We first compute the transverse and axial forces due to m' and m'' ; the total forces are additive in the terms of (1). We regard am' as a distinct variable independent of m' here. Substituting (1) in the m' , m'' terms of (2), we get, after differentiating according to (4) and simplifying,

$$\begin{aligned} \frac{\partial F_x}{\partial m'} &= -\frac{d}{dt}(v \sin \phi \sin \gamma), \\ \frac{\partial F_y}{\partial m'} &= \frac{d}{dt}(v \sin \phi \cos \gamma), \\ \frac{\partial M}{\partial m'} &= v^2 \sin \phi \cos \phi, \\ \frac{\partial F_x}{\partial m''} &= -\frac{d}{dt}(v \cos \phi \cos \gamma), \\ \frac{\partial F_y}{\partial m''} &= -\frac{d}{dt}(v \cos \phi \sin \gamma), \\ \frac{\partial M}{\partial m''} &= -v^2 \cos \phi \sin \phi. \end{aligned} \quad (5)$$

The tangential backward and normal downward components D and L of force due to m' and m'' can then be computed from

$$\begin{aligned} D &= -F_x \cos \theta - F_y \sin \theta, \\ L &= -F_x \sin \theta + F_y \cos \theta. \end{aligned} \quad (6)$$

Substituting in (6) from (5), we get after adding and subtracting the term in $\dot{\theta}$,

$$\begin{aligned} \frac{\partial L}{\partial m'} &= \frac{d}{dt} [v \sin \phi (\sin \gamma \sin \theta + \cos \gamma \cos \theta)] \\ &\quad - v \sin \phi (\sin \gamma \cos \theta - \cos \gamma \sin \theta) \dot{\theta} \\ &= \frac{d}{dt} (v \sin \phi \cos \phi) - v \sin^2 \phi \cdot \dot{\theta}. \end{aligned}$$

Similar differentiation by parts gives

$$\frac{\partial L}{\partial m''} = \frac{d}{dt} (-v \cos \phi \sin \phi) - v \cos^2 \phi \cdot \dot{\theta}.$$

Combining, we find the increment due to m' and m'' to be

$$\begin{aligned} \Delta L &= (m' - m'') \left[\frac{d}{dt} \left(\frac{1}{2} v \sin 2\phi \right) + \frac{1}{2} v \cos 2\phi \cdot \dot{\theta} \right] \\ &\quad - \frac{1}{2} (m' + m'') v \dot{\theta}. \end{aligned} \quad (7)$$

The last term amounts simply to increasing the inertial mass by $\frac{1}{2}(m' + m'')$. The first term can also be written as

$$\frac{1}{2} (m' - m'') [\dot{v} \sin 2\phi + v \cos 2\phi (2\dot{\phi} + \dot{\theta})].$$

Similar computations for D give

$$\begin{aligned} \frac{\partial D}{\partial m'} &= \frac{d}{dt} (v \sin^2 \phi) + v \cos \phi \sin \phi \dot{\theta} \\ \frac{\partial D}{\partial m''} &= \frac{d}{dt} (v \cos^2 \phi) - v \dot{\theta} \sin \phi \cos \phi. \end{aligned}$$

Combining, we find the increment in D due to m' and m'' to be

$$\begin{aligned} \Delta D &= \frac{1}{2} (m'' - m') \left[\frac{d}{dt} (v \cos 2\phi) - v \dot{\theta} \sin 2\phi \right] \\ &\quad + \frac{1}{2} (m'' + m') v \dot{\theta}. \end{aligned} \quad (8)$$

From (4), we see that $I'\omega^2$ contributes nothing to the translation forces. From the term $am'\omega v \sin \phi$, we get as with (5)

$$\frac{\partial F_x}{\partial (am')} = -\frac{d}{dt} (\omega \sin \gamma), \quad \frac{\partial F_y}{\partial (am')} = \frac{d}{dt} (\omega \cos \gamma).$$

Substituting in (6), we get as before

$$\begin{aligned} \frac{\partial L}{\partial (am')} &= \frac{d}{dt} (\omega \cos \phi) - \omega \dot{\theta} \sin \phi, \\ \frac{\partial D}{\partial (am')} &= \frac{d}{dt} (\omega \sin \phi) + \omega \dot{\theta} \cos \phi. \end{aligned}$$

Adding to (7) and (8), we see that *the lift due to induced mass is*

$$\begin{aligned} L &= \frac{1}{2} (m' - m'') \left[\frac{d}{dt} (v \sin 2\phi) \right] + am' \frac{d}{dt} (\omega \cos \phi) \\ &\quad + \dot{\theta} \left[\frac{1}{2} (m' - m'') v \cos 2\phi - \frac{1}{2} (m' + m'') v \right. \\ &\quad \left. - am' \omega \sin \phi \right], \end{aligned} \quad (9)$$

while the *drag due to induced mass is*

$$\begin{aligned} D &= \frac{1}{2} (m' + m'') \dot{v} + \frac{d}{dt} \left[\frac{1}{2} (m'' - m') (v \cos 2\phi) \right. \\ &\quad \left. + am' \omega \sin \phi \right] + \dot{\theta} [am' \omega \cos \phi - \frac{1}{2} (m'' - m') v \sin 2\phi]. \end{aligned} \quad (10)$$

For a sphere, $\dot{\theta} = \phi = 0$ in (10), hence only the first term is left; this gives a *decrease in deceleration due to induced mass*. Experimentally, this induced mass $m' = m''$ is about 0.45 the mass of displaced water.

We have already computed in (5) the contributions to M due to the first two terms of (2). From (2) and (4) we compute similarly

$$\frac{\partial M}{\partial I'} = -\frac{d}{dt(\omega)} = -\dot{\omega}; \quad \frac{\partial M}{\partial (am')} = \omega v \cos \phi$$

$$-\frac{d}{dt(v \sin \phi)} = v \dot{\theta} \cos \phi - \dot{v} \sin \phi.$$

Combining with (5), we get

$$\begin{aligned} M &= am' (v \dot{\theta} \cos \phi - \dot{v} \sin \phi) - I' \dot{\omega} \\ &\quad + \frac{1}{2} (m' - m'') v^2 \sin 2\phi. \end{aligned} \quad (11)$$

The term $-I'\dot{\omega}$ can be regarded as simply adding I' to the projectile's moment of inertia and the last term as part of the moment force under steady-state motion (the part predicted by hydrodynamic theory). Thus only the term in am' has any novelty; $am'v\dot{\theta}\cos\phi$ is the component important for stability. Its effect is to replace the static center of mass of the projectile by a *dynamic center* of inertia (see also Biot), which may be defined as the point p on the axis such that a cross force acting through p will have no tendency to make the projectile rotate. It is the centroid of the center of projectile mass and the *center of virtual mass*; hence it moves *back* as the fluid density is increased. Since the first stability condition is that the center of pressure should lie back of the dynamic center, it would appear that *increasing fluid density decreases the dynamic stability of the projectile*. An opposite conclusion is reached by Biot, and appears to be the case experimentally; his reasoning is based on a concept of "tail center."

Applying Newton's laws to the projectile, we have

$$m\dot{v} = -\frac{1}{2}\rho Av^2 C_D - D, \quad (12)$$

$$mv^2 \frac{d\theta}{ds} = \frac{1}{2}\rho Av^2 C_L + L, \quad (13)$$

$$I\dot{\omega} = -\frac{1}{2}\rho Av^2 l_a C_M - \frac{1}{2}\rho Al_a^2 \omega v C_H + M, \quad (14)$$

where L and D are given by (9) and (10).

In the case of motions where ϕ is small, we find on discarding terms involving ϕ^2 , $\phi\dot{\theta}$, and $\phi\dot{\phi}$ that

$$L = (m' - m'')(v\dot{\phi} + \phi\dot{v}) + am' \frac{d\omega}{dt} - m'\dot{\theta}v,$$

$$D = m''\dot{v} + am'\omega^2.$$

By using (13) to appraise $\dot{\theta}$, (14) to appraise $\dot{\omega}$, and neglecting terms in ϕ , we find further that

$$L = (m' - m'')v^2 \frac{d\phi}{ds}.$$

Or if $\lambda' = m'\sigma/m$ and $\lambda'' = m''\sigma/m$, then (13) becomes

$$\frac{d\theta}{dt} = \frac{C_L(\phi)}{2\sigma l_a} + \frac{\lambda' - \lambda''}{\sigma} \frac{d\phi}{ds}.$$

In case of cavity motion, when the lateral surface of the projectile is only partially wetted, it seems reasonable to modify the equation to

$$\frac{d\theta}{ds} = \frac{C_L(\phi)}{2\sigma l_a} + \frac{j\lambda' - \lambda''}{\sigma} \frac{d\phi}{ds}, \quad (15)$$

where j is between 0 and 1, depending on the degree of wetting.

APPENDIX VIII

REMARKS ON MODELING

All theoretical justifications of the use of models require the neglect of various types of forces (viscosity, surface tension, adhesion, water compressibility). In this appendix the validity of the hypothesis that these forces are negligible is discussed.

1. *Viscosity.* As viscosity effects are correlated primarily with the Reynolds' number R , we first compute R in some typical cases. With a 3-in. diameter sphere, moving through water at $v = 25$ fps, $R = vd/\nu = 5 \times 10^5$; if $v = 250$ fps, $R = 5 \times 10^6$; in both cases, R is above the critical Reynolds'⁹⁹ number R_c . Whereas if $d = 0.25$ in. and $v = 40$ fps, $R = 80,000 < R_c$. In flow *without* cavitation, $C_D(8 \times 10^4) = 0.5$, while $C_D(10^6) = 0.2$ to 0.3 ; hence we must preserve R to model noncavity flow through this range of Reynolds' numbers. In flow *with* cavitation, on the other hand, the C_D of spheres does not vary greatly with R .^{7a}

The explanation is simple enough, and in fact the result was conjectured before the experimental facts were available. In the case of flow without cavity, near (in the region of *increasing* pressure) where the boundary layer separates from the sphere, the wake gets much smaller. Whereas with cavity flow, separation occurs just forward of the equator in the region of *decreasing* pressure, where the hydrodynamic pressure falls to the cavity pressure; thus it is not influenced by turbulence or other conditions in the water boundary layer, which alone is affected by viscosity.

Again, the skin friction drag (also due to viscosity) does not greatly alter the C_D of spheres, or presumably of other projectiles,^a if $R > 10^3$; hence it is presumably either negligible or well modeled by models 1-in. or more in diameter in *cavity* motion.

Finally,¹⁰⁰ the cone angles of the cavities formed by

^a Around 10 per cent of the drag of bullets in air, and more of that of bomb shapes, is attributable to skin friction. However, in cavity flow, the wetted area is much less and the wake is large; hence the proportion should be smaller. For spheres, $C_D = 0.5$ was measured in pure glycerin at $R = 200$.¹⁰⁰ The noncavity C_D at $R = 200$ is about 0.75. In 20 per cent gelatin at 21 C, Harvey found $C_D = 0.35$. The effect of R has also been discussed.¹⁰¹

spheres dropped into various liquids differed little (13° to 17°) with the viscosity of the liquid. Similarly, Worthington^{35d} found that a solution of $\frac{6}{51}$ of glycerin in water did not sensibly affect cavity formation. He attributed^{35c} the fluting of the cavity wall to viscosity, but this fluting seems to have no dynamical significance. In summary, *the viscosity of water seems to be unimportant in model tests.*

2. *Surface Tension.* The force of surface tension (capillarity) of water, which is only 70 to 75 dynes per cm^2 at ordinary temperatures, augments imperceptibly the tendency of the cavity to close. However, as Worthington has shown,^b in the case of a 1-in. diameter sphere entering at 20 fps, surface tension is the main force preventing the splash from rising. But the surface tension force is proportional to r ; the gravitational force to r^3 ; hence the importance of surface tension is negligible with larger models. This explains why the splash from small models rises so much less high than would be expected from observations of large missiles on the basis of Froude scaling. By preventing the surface seal from dissipating into spray, surface tension may also cause a quicker surface seal with small models (say, 0.25-in. diameter spheres) than with larger ones, using Froude scaling.

The unimportance of surface tension for shrinking the cavity is shown by the following rough calculation. The energy E_{st} of surface tension of a spherical cavity of radius r cm is $910r^2$ dyne cm. The energy E_p due to work against pressure is $4.2 \times 10^6 r^3$ dyne cm. Hence $E_p/E_{st} = 4,130r(p/p_{\text{atm}})$. The two are comparable for a cavity 5 cm deep ($p/p_{\text{atm}} = 0.01$) only if $r < 0.05$ cm. The same argument appears to show that a spherical cavity is unstable at a pressure of -1 atmosphere, if its diameter is of the order of $1/4,000$ cm or less.

A possible effect of surface tension or viscosity might come from the rate of "pumping" of air out

^b References 35a and 35b. On page 87, the splash has $v = 4$ fps, $v^2/2g = 3$ in., yet the splash rises to a height of less than 1 in. The surface tension force is 600 dynes, or the gravitational force on about 0.6 cc of water.

of the cavity bubble; the physical explanation of this is not known. This would affect the cavitation parameter K , hence cavity size, hence $C_L(\phi)$, and hence the trajectory.

3. *Adhesion.* The force of adhesion was estimated by Worthington³⁵ to be 10,000 times that of surface tension, but we have been unable to confirm this opinion.

Under ideally controlled laboratory conditions, it is true that water can support a large tension and that this force can be transmitted to a solid boundary.^c But this depends on (a) the absence of gas bubbles in the fluid and (b) the absence of gas nuclei on the solid hydrophilic surface. Under normal conditions neither of these occurs, and so it may be doubted that a large tension is supported, except possibly over very short periods of time.

On the other hand, Worthington discovered that cavitation on vertical entry at low speeds (below 20 fps) is much affected by the condition of the surface (hydrophilic or hydrophobic) and may also be affected by heating the solid surface (elimination of gas nuclei). Recent experiments by Knapp on water tunnel cavitation induced by polished steel models gives cavitation at speeds (30 to 60 fps) slightly in excess of those for which the vapor pressure is theoretically reached. A similar effect, more pronounced at low speeds (0 per cent at 100 fps, 3 per cent at 75 fps, 5 per cent at 60 fps) is reported by J. W. Maccoll.¹²

4. *Air Viscosity; Water Compressibility.* The preceding effect seems related to the results on down-nosing and "ventilation" described in Section 12.4 and ascribed by Slichter to *air* viscosity.

These results indicate that air viscosity may have an important influence on lift and especially on overturn moment, if not on drag. In the case of 1-in. diameter models with spherical heads, the critical Reynolds' number for this phenomenon, based on the kinematic viscosity of *air* seems to be about $R = 50,000$. As air viscosity is independent of density (temperature being fixed), this would be multiplied by $\lambda^{2.5}$ under reduced-pressure Froude scaling. Hence *it seems doubtful whether reduced pressure Froude scaling will avoid down-nosing*, any more than ordinary Froude scaling.

^c See "The Tension Which Water Can Exert on a Steel Surface," to be published by R. M. Davies, working in conjunction with Sir Geoffrey Taylor, where steel is made to support a tension of 9 to 10 atm. References are given there to other experiments; see also reference 119.

Finally, it should be noted that experiments by Slichter, using highly aerated (i.e., compressible) water, revealed no indication of effects due to the compressibility of water.¹²⁰

5. *Preservations of Equations of Continuity and State.* It is interesting to determine the most general transformations under which the equations of state and continuity of a fluid are preserved.

As regards the equation of continuity, it is convenient to use Lagrangian coordinates and write it in the form^{102a}

$$\rho(a,b,c;t) \frac{\partial(x,y,z)}{\partial(a,b,c)} = \rho(a,b,c;0). \quad (1)$$

Under any point transformation which multiplies all volumes by the same factor, the Jacobian determinant of (1) satisfies

$$\frac{\partial(x',y',z')}{\partial(a',b',c')} = \frac{\rho(x,y,z)}{\rho(a,b,c)};$$

we can have $t' = f(t)$ arbitrary. Hence

$$\frac{\rho'(a',b',c';t')}{\rho'(a',b',c';0')} = \frac{\rho(a,b,c;t)}{\rho(a,b,c;0)},$$

and if we define

$$\alpha(a,b,c) = \frac{\rho'(a',b',c';0')}{\rho(a,b,c;0)},$$

then

$$\rho'(a',b',c';t') = \alpha(a,b,c)\rho(a,b,c;t). \quad (2)$$

Conversely, if ρ' is defined by (2) from ρ , then the equation of continuity (1) is clearly preserved.

We shall not attempt to discuss the transformations which preserve the most general equation of state $\rho = f(p)$, as it is hard to correlate the general rule $p' = f^{-1}(\alpha[f(p)])$ with the scaling of the equations of motion. Instead, we shall discuss only *polytropic* equations of state $\rho = Cp^\tau$, which includes the incompressible cases ($\tau = 0$) as well as air ($\tau = 0.71$). We then will have $D\rho/Dp = \tau\rho/p$, and $D\rho'/Dp' = \tau\rho'/p'$ is a necessary and sufficient condition that the equation of state be preserved, i.e., that $\rho' = Cp'^\tau$. If $\rho' = \alpha\rho$, where $\alpha = \alpha(a,b,c)$ so that $D\alpha = 0$, this is equivalent to

$$\frac{\tau\alpha\rho}{p'} = \frac{\tau\rho'}{p'} = \frac{D\rho'}{Dp'} = \frac{\alpha D\rho}{Dp'} = \frac{\alpha Dp}{Dp'} \frac{D\rho}{Dp} = \frac{\alpha Dp}{Dp'} \frac{\tau\rho}{p}.$$

This is satisfied if $\tau = 0$ (the incompressible case) for all α and transformations $p' = f(p)$ of pressure. If $\tau \neq 0$, since $\alpha \neq 0$, it is satisfied if and only if (canceling) $Dp/pDp' = 1/p'$, or $D(\ln p) = D(\ln p')$, $\ln p' = \ln p + \ln \beta(a,b,c)$, or

$$p' = \beta(a,b,c)p. \quad (3)$$

It is also interesting to find out under what special circumstances (if any), the equation of state of a fluid is preserved under Froude scaling. The result, which may be viewed as an amplification and partial converse of theorem (6), is the following.

The only equation of state $\rho = f(p)$ preserved by Froude scaling ($\lambda \neq 1$) is:

$$\rho = \rho_1 \quad \text{if} \quad p < \frac{p_0}{1 - \lambda},$$

while

$$\rho = \rho_2 \quad \text{if} \quad p > \frac{p_0}{1 - \lambda}.$$

(4)

This would be the equation of state for water, if $p_0/(1 - \lambda)$ were the vapor pressure and water were incompressible in the liquid state. It is very unlike the equation of state for air.

Proof. We assume that $f(p)$ is a *nondecreasing* function. If $f(p)$ is actually preserved, then by hypothesis

$$f(p) = f(p_0 + \lambda p) = f[p_0 + \lambda(p_0 + \lambda p)] = \dots, \quad (5)$$

for all p . If $\lambda \neq 1$, then (5) is automatically satisfied at $p_c = p_0/(1 - \lambda)$. If $p > p_c$, then $p < p_0 + \lambda p < p_0 + \lambda(p_0 + \lambda p) < \dots$ tends to $+\infty$. Since $f(p)$ is nondecreasing, by (5) $\rho = \rho_2$ is constant in the semi-infinite interval $p > p_c$. An identical argument shows that $\rho = \rho_1$ is constant in the interval $p < p_c$.

GLOSSARY

Part I

$C_+, C_-, \Gamma_+, \Gamma_-$	Characteristics of differential equations in Chapter 1.	p	Pressure.
C_p	Impact drag coefficient.	q, \vec{q}, \mathbf{q}	Velocity; velocity vector.
\bar{F}_s	Average thrust.	q_* or c_*	Critical speed.
I	Impulse.	\hat{q}	Limit or ultimate speed.
M, M_g, M_w	Mass; mass of gas; mass of water.	t, t_s	Time; time of stroke.
R	Rarefaction wave.	(u, v, w)	Velocity components.
R, R	Forward, backward rarefaction wave.	(x, y, z)	Rectangular space coordinates (except in Section 1.2.2).
\vec{S}	Shock wave.	$\Gamma_+, \Gamma_-, C_+, C_-$	Characteristics of differential equations in Chapter 1.
S, S	Forward, backward shock wave.	Γ_l, Γ_r	Left, right transition curve.
\vec{T}	Contact surface (sometimes temperature).	α, β	Characteristic parameters.
TT	Contact zone.	γ	Adiabatic constant.
U	A velocity.	η	Entropy.
W	Weight of explosive.	μ	$\sqrt{\frac{\gamma - 1}{\gamma + 1}}$
c	Speed of sound.	ρ	Density.
c_* or q_*	Critical speed.	τ	1
e	Internal energy per unit mass.	$\phi(x, y, z, t)$	Velocity potential.
i	Enthalpy or heat content.		
l, r	Indices denoting left, right.		
m	Virtual mass.		

Part II

a	Radius of a sphere.	P_n	Legendre functions (polynomials).
c, c_0, c_1	Velocity of sound in various media.	P	Complex amplitude of a wave; in Chapter 4, a "penumbra."
e	A charge.	Q_s	Scattering cross section.
h	Thickness of dome shell.	R	A region of space; sometimes (especially in Chapter 4) a distance.
h_n, j_n	Bessel functions (spherical).	Re	Real part of.
i	The imaginary unit, $\sqrt{-1}$.	S	A surface; in Chapter 4, a shadow region.
$n, \frac{\delta}{\delta_n}$	Normal to a surface, normal derivative. In Chapter 4, n is an enumerative index, referring to n poles.	S_R^*	Radial component of complex Poynting vector.
p, P	Pressure. In Chapter 4, $p = r/R$, the ratio of two distances.	\vec{W}	A displacement vector.
p_n	A multipole component of charge.	η	Characteristic impedance of free space.
r	Distance from origin.	θ	An angle.
s	An index suggestive of shadow or scattering.	∇^2	The operator $(\partial^2/\partial x^2) + (\partial^2/\partial y^2) + (\partial^2/\partial z^2)$.
x, y, z	Rectangular Cartesian coordinates.	λ	A wavelength.
E, E_i, E_r	Electric fields; incident and secondary (or reflected).	μ	The bulk modulus.
H, H_i, H_r	Magnetic fields, incident and reflected.	π	An acoustic pressure.
J	A Bessel function.	ρ	Density; in Chapter 4, $\rho = 2\pi R/\lambda$.
		Φ	A potential.
		ψ	A flux.

Part III

CHAPTER 6

m_0, m_1	Dimensionless masses = $M_0/(M_0 + M_1)$, $M_1/(M_0 + M_1)$.	E	Energy.
p	Pressure.	J	A moment of inertia.
t	Time.	M_0, M_1	Mass of hammer, of diaphragm.
v	A velocity.	M_δ, M_ϕ	Maximum values of $ Q_\delta , Q_\phi $ on ship.
x_0, x_1	Dimensionless displacements $X_0/D, X_1/D$.	P, P_1, P_2	Power expenditures for chains in mine exploders.
A	Amplitude of simple harmonic motion of driven end of hammer.	Q_δ, Q_ϕ	Couples delivered to gun by gear trains controlling elevation and train.
D	Clearance between masses at equilibrium.	T	Period of the periodic motion.

X_0, X_1	Displacement of hammer, of diaphragm.	σ	Coefficient of viscous damping.
W	Work.	ω_p, ω_r	Angular frequencies of pitch, roll.
δ	A phase angle.	ω_0, ω_1	Dimensionless frequencies = $\Omega_0/\omega, \Omega_1/\omega$.
ϵ	Coefficient of restitution.	$\Omega_0, \Omega_1, \omega$	Circular frequencies of hammer, diaphragm, driven end of spring.
ϵ_c	A "critical error."		
ρ	Density.		

CHAPTER 7

e_1, e_2, e_3	Principal values of strain deviation tensor.	L, L_0	Final, original length.
l	Length of bar or powder grain.	M	Bending moment.
p_0, \bar{p}_0, p_1	Pressure on grain.	P	Load or a pull.
s_1, s_2, s_3	Principal values of stress deviation tensor.	S	Area of burning surface or a shear.
A_0	Cross-sectional area (original).	W	Work.
E	Young's modulus of bar.	G, ϵ_1	Strain; true strain.
δ	Polar moment of inertia.	σ, σ_1	Stress; true stress.

Part IV

a	Acceleration.	$q = \frac{1}{2}\rho v^2$	Dynamic pressure at stagnation point.
A	Maximum area of cross section.	r	Radius.
C_D	Drag coefficient.	R	Radius of curvature.
C_D^*	Steady-state drag coefficient.	s	Distance along path.
C_H	Damping coefficient.	t	Travel time.
C_L	Lift coefficient.	u	x component of velocity.
C_M	Moment coefficient.	v	Velocity (also y component dy/dt of velocity).
d	Diameter.	v_1	Entry velocity.
D	Hydrodynamic drag; diameter (when used in L/D).	v_2	Exit velocity.
\bar{D}	Overall drag.	v_t	Terminal velocity.
E	Energy.	V	Volume.
$F = v^2/gr$	Froude number.	V_h	Volume of head.
$g = 32 \text{ f/s}^2$	Acceleration of gravity.	w	z component of velocity.
H	Damping force.	x	Horizontal distance.
I	Moment of inertia.	\dot{x}	dx/dt .
I_L	Lift of entry impulse.	\ddot{x}	d^2x/dt^2 .
I_M	Moment of entry impulse.	X	Length of plough.
I_{MD}	Moment of entry drag impulse.	y	Depth below surface.
K	Cavitation parameter (also kinetic energy).	\dot{y}	dy/dt .
K_c	Critical value of cavitation parameter.	\ddot{y}	d^2y/dt^2 .
la	Average length, V/A .	z	Coordinate perpendicular to trajectory plane.
\bar{L}	Lift, >0 (also length in L/D).	α	Deceleration coefficient (another meaning in Section 11.5).
L	Overall lift.	ϕ	Pitch angle.
L_1	Lift of head.	$-\phi$	Up pitch.
L_2	Lift of tail.	$\bar{\phi}$	Mean pitch.
m	Mass.	ϕ_c	Critical pitch angle.
m'	Induced mass.	ϕ_s	Stable pitch angle.
m_t	Theoretical induced mass (of head plus its mirror image).	ρ	Fluid density.
M	Moment.	σ	Specific gravity.
\bar{M}	Overall moment.	θ_1	Impact angle.
p	Pressure.	θ_2	Exit angle.
\bar{p}	Average pressure.	θ_c	Critical entry angle.
p_a	Static air pressure.	ω	Angular velocity.
\bar{p}_0	Pressure in a free stream.	U	Velocity potential.
\bar{p}_u	Average underpressure.	ψ	Angle between outward normal and direction of motion (also stream-function).
p_v	Vapor pressure.		

Abbreviations — General

AP	Armor piercing.	DTMB	David Taylor Model Basin.
CG	Center of gravity.	EBD	External Ballistics Department, Ordnance Board (British).
CP	Center of pressure.	FCR	Fire Control Research, Princeton University.
GP	General purpose.	H/ARM/RES	Helensburgh Armament Research, Eng.
HE	High explosive.	JPL-GALCIT	Jet Propulsion Laboratory-Guggenheim Aeronautical Laboratory, California Institute of Technology.
NPB	Navy practice bomb.	LHL	Lukas-Harold Laboratory.
AAF	Army Air Forces.	MAEE	Marine Aircraft Experimental Establishment.
AAFPGC	Army Air Force Proving Ground Command.	MIT	Massachusetts Institute of Technology.
AHL	Alden Hydraulic Laboratory.	NACA	National Advisory Committee on Aeronautics.
AMG-B	Applied Mathematics Group-Brown.	NDRC	National Defense Research Committee.
AMG-C	Applied Mathematics Group-Columbia.	NOL	Naval Ordnance Laboratory.
AMG-H	Applied Mathematics Group-Harvard.	OBP	Ordnance Board Proceedings.
AMG-N	Applied Mathematics Group-Northwestern.	OSRD	Office of Scientific Research and Development.
AMG-NYU	Applied Mathematics Group-New York University.	RAF	Royal Air Force.
AMG-P	Applied Mathematics Group-Princeton.	RAE, FC	Royal Aircraft Establishment, Farnborough, Eng.
AMP	Applied Mathematics Panel.	SRG-C	Statistical Research Group-Columbia.
APG	Aberdeen Proving Ground.	STR	Summary Technical Report.
ARD	Aircraft Research Development.	STR	Scientific and Technical Report.
ARL	Admiralty Research Laboratory, Teddington, Eng.	TDBS	Technical Division, Ballistic Section.
ATDU	Aircraft Torpedo Development Unit, Gosport, Eng.	TDU	Torpedo Development Unit, Gosport, Eng.
BRG	Bombing Research Group.	UBRC	Underwater Ballistics Research Committee.
BRG-C	Bombing Research Group-Columbia.	UNM	University of New Mexico.
BRL	Ballistics Research Laboratory.	USN	U. S. Navy.
CIT	California Institute of Technology.		
CUDWR-NLL	Columbia University Division of War Research Underwater Sound Laboratories.		

BIBLIOGRAPHY

Numbers such as AMP-21.1-M4 indicate that the document listed has been microfilmed and that its title appears in the microfilm index printed in a separate volume. For access to the index volume and to the microfilm, consult the Army or Navy agency listed on the reverse of the half-title page.

SUMMARY

1. "Sequential Tests of Statistical Hypotheses," Abraham Wald, *The Annals of Mathematical Statistics*, Vol. XVI, No. 2, June 1945, pp. 117-186.
2. *Sequential Analysis of Statistical Data: Applications*, H. A. Freeman and Abraham Wald, prepared for AMP, Columbia University Press, Revised Report 30.2R [OEMsr-618], SRG-C, Sept. 15, 1945. AMP-21.1-M4

PART I

Chapter 1

1. *Supersonic Flow and Shock Waves: A Manual on the Mathematical Theory of Non-Linear Wave Motion*, Richard Courant and K. O. Friedrichs, AMP Report 38.2R, OEMsr-945, OSRD 4266, AMG-NYU, August 1944. AMP-101.1-M9
2. *Remarks on the Mathematical Theory of Detonation and Deflagration Waves in Gases, Supplement to the Manual on Supersonic Flow and Shock Waves*, Richard Courant and K. O. Friedrichs, AMP Report 38.3R, OEMsr-945, OSRD 5469, AMG-NYU, July 1945. AMP-101.1-M17
3. *Interaction of Shock and Rarefaction Waves in One-Dimensional Motion (Progress Report), Prepared Jointly with Division 8*, Richard Courant and K. O. Friedrichs, AMP Report 38.1R, OEMsr-944, Service Projects OD-03 and NO-144, OSRD 1567, AMG-NYU, July 5, 1943. AMP-101.1-M4
4. *Repeated Reflection of a Shock Against a Rigid Wall*, Harvey Cohn, AMP Memorandum 38.2M [OEMsr-945], AMG-NYU, April 1943. AMP-101.1-M2
5. *Theory of Shock Waves (Progress Report to Aug. 31, 1942)*, John von Neumann, Division 8, OEMsr-218, Service Projects OD-02 and OD-03, OSRD 1140, Jan. 29, 1943. AMP-101.1-M1
6. *On Busemann's Diagrams for Steady (Stationary) Shocks*, K. O. Friedrichs, AMP Memorandum 38.3M14, NYU, May 1943.
7. *Shock Waves in Arbitrary Fluids*, Hermann Weyl, AMP Note 12 [OEMsr-945], AMG-NYU Paper 46, March 1944. AMP-101.1-M8
8. *A Scheme for the Computation of Shock Waves in Gases and Fluids*, Hermann Weyl, AMP Memo 38.7M [OEMsr-945], AMG-NYU, July 4, 1943. AMP-101.1-M3
9. *Proposal and Analysis of a New Numerical Method for the Treatment of Hydrodynamical Shock Problems*, John von Neumann, AMP Report 108.1R [OEMsr-1111], OSRD 3617, AMG-Institute for Advanced Study, Mar. 20, 1944. AMP-102-M3
10. *On Configurations Involving Three Shocks Through One Point Modified by Meyer Waves*, K. O. Friedrichs, AMP Memo 38.9M, OEMsr-945, AMG-NYU, September 1943. AMP-101.1-M7
11. *On Nearly Glancing Reflection of Shocks*, Valentine Bargmann, AMP Report 108.2R, OEMsr-1111, OSRD 5171, AMG-Institute for Advanced Study, March 1945. AMP-101.1-M13
12. *Remarks on the Reflection of Conical Shocks*, K. O. Friedrichs, AMP Memo 38.8M, OEMsr-945, AMG-NYU, September 1943. AMP-101.1-M6
13. *Theoretical Studies on the Flow Through Nozzles and Related Problems*, K. O. Friedrichs, AMP Report 82.1R [OEMsr-945], Service Project NA-167, OSRD 3591, AMG-NYU, April 1944. AMP-101.2-M3
14. *Remarks on the Theory of Exhaust Nozzles*, K. O. Friedrichs, AMP Memorandum 82.1M, NYU, October 1943.
15. *Remarks about R. P. Fraser's Reports on Jet Research*, K. O. Friedrichs, AMP Memo 82.3M [OEMsr-945], AMG-NYU, March 1944. AMP-101.2-M2
16. *On Supersonic Compressors and Nozzles (Supplement to AMP Report 82.1R)*, K. O. Friedrichs, AMP Report 82.2R, OEMsr-945, OSRD 4416, AMG-NYU, October 1944. AMP-101.2-M4
17. *Heat Flow Problems for Rockets Considered by AMG-NYU (Preliminary Report)*, AMP Study 136 [OEMsr-945], AMG-NYU Paper 63, August 1944. AMP-602-M1
18. *On the Estimation of Perturbations Due to Flow around Blast Gauges*, J. K. L. MacDonald, AMP Note 22, OEMsr-945, OSRD 5639, AMG-NYU Paper 136, September 1945. AMP-101.1-M18
19. *Theoretical Remarks on the Performance of a Supersonic Kinetic Air Compressor*, AMP Study 82 [OEMsr-945], [AMG]-NYU Paper 37. AMP-101.2-M5
20. *A Mathematical Analysis of Nozzle Design with Particular Consideration of the Nozzle of the Annapolis Project*, Letter to J. S. Warfel dated January 12, 1944, K. O. Friedrichs, AMP Study 82 [OEMsr-945], AMG-NYU Paper 39, Jan. 12, 1944. AMP-101.2-M1
21. *Shock Conditions and Detonation Conditions*, AMP Study 38 [OEMsr-945], AMG-NYU Paper 68. AMP-101.1-M19
22. *The Problem of the Momentum and Energy Balance in the Wave Produced by a Flying Bullet*, Letter to Jesse W. M. DuMond, dated October 9, 1944, K. O. Friedrichs, AMP Study 38 [OEMsr-945], AMG-NYU Paper 71, Oct. 9, 1944. AMP-101.1-M10

23. First results concerning the problem of an airfoil of minimum drag in supersonic flow; letter to Dr. Hsue-Sheu-Tsien dated December 7, 1944, K. O. Friedrichs, AMP Study 183 [OEMsr-945], AMG-NYU Paper 82, Dec. 7, 1944. AMP-101.1-M11
24. *Methods for Calculating Thermal Stresses and Heat Flow in Rockets, with Estimates*, J. K. L. MacDonald, AMP Study 136 [OEMsr-945], AMG-NYU Paper 104, Feb. 22, 1945. AMP-602-M3
25. *Temperature Perturbations due to Thermocouple Structures Inserted into Walls of Rockets*, AMP Study 136 [OEMsr-945], AMG-NYU Paper 113, Apr. 7, 1945. AMP-602-M4
26. Calculations for the Airfoil in a Flow with a Mach Number 1.6, Letter to Dr. Theodore von Kármán dated April 13, 1945, K. O. Friedrichs, AMP Study 183 [OEMsr-945], AAF Scientific Advisory Board, AMG-NYU Paper 114, Apr. 13, 1945. AMP-101.1-M16
27. *Heat and Gas Flow in Rockets*, J. K. L. MacDonald, AMP Study 136 [OEMsr-945], AMG-NYU Paper 132, July 27, 1945. AMP-602-M5
28. *On Heat Flow in Walls of Rockets, Mathematical Treatment*, AMP Study 136, OEMsr-945, AMG-NYU Paper 1, October 1944. AMP-602-M2
- 29a. *Gesammelte Mathematische Werke, und Wissenschaftluhen Nachlass*, [Georg Friedrich] Bernard Riemann, B. G. Teubner, Leipzig, Chap. VIII, "Ueber die Fortpflanzung Ebener Luftwellen von Endlicher Schwingungsweite," 1876, pp. 145-164.
- 29b. "Ein Beitrag zu den Untersuchungen über die Bewegung Eines Flüssigen Gleichartigen Elliposoides," [Georg Friedrich] Bernard Riemann, *Abhandlungen den Königlichen Gesellschaft der Wissenschaften*, Göttingen, Vol. 9, December 1860, pp. 1-36.
30. "On the Flow of Gases," O. Reynolds, *Proceedings of the Manchester Literary and Philosophical Society*, Vol. XXV, 1885, p. 55.

Chapter 2

1. *Studies on the Gas Bubble Resulting from Underwater Explosions: On the Best Location of a Mine Near the Sea Bed*, Richard Courant, Max Shiffman, and Bernard Friedman, AMP Report 37.1R [OEMsr-945], OSRD 3841, AMG-NYU, May 1944. AMP-407-M1
2. *The Effect of a Rigid Wall on the Motion of an Underwater Gas Bubble*, Max Shiffman, AMP Memorandum 37.1M, AMG-NYU, July 1943.
3. *Theory of the Pulsations of the Gas Bubble Produced by an Underwater Explosion*, C. Herring, OSRD 236, NDRC Division C, October 1941.
4. *The Effect of Non-Spherical Shape on the Motion of a Rising Underwater Gas Bubble*, Max Shiffman, AMP Memorandum 37.5M [OEMsr-945], AMG-NYU, September 1943. AMP-102-M2
5. *Note on Optimum Size of Charges for Blasting Objects Submerged in Shallow Water*, Richard Courant, AMP Study 37 [OEMsr-945], AMG-NYU Paper 36, Dec. 20, 1943. AMP-403-M1
6. *Bubble Periods*, AMP Study 37 [OEMsr-945], AMG-NYU Paper 88, January 1945. AMP-102-M4
7. *The Force of Impact on a Sphere Striking a Water Surface (Approximation by the Flow about a Lens)*, Max Shiffman and Donald C. Spencer, AMP Report 42.1R, OEMsr-945, OSRD 4921, AMG-NYU, February 1945. AMP-404-M3
8. *The Force of Impact on a Sphere Striking a Water Surface (Second Approximation)*, Max Shiffman and Donald C. Spencer, AMP Report 42.2R, OEMsr-945, OSRD 5485, AMG-NYU, July 1945. AMP-404-M5
9. *Theoretical Studies Concerning the Hydropulse, Ideal Mechanical Performance Characteristics*, AMP Report 137.1R, OEMsr-945, Service Project NA-195, OSRD 5738, AMG-NYU, July 1945. AMP-103-M2
10. *Speed of Ships from Aerial Photographs*, J. J. Stoker, AMP Report 98.1R [OEMsr-1007, OEMsr-618, and OEMsr-945], OSRD 3938, AMG-C, SRG-C and AMG-NYU, July 1944. AMP-204-M4
11. *Ship Speeds from Aerial Photographs*, Report No. 44, Photographic Interpretation Center, Office of Naval Intelligence, September 1944.
12. *Diary of Visit to Woods Hole August 14 to 15, 1944* [The cavity formed by the charge entering the water], Max Shiffman and Donald C. Spencer, AMP Study 37, OEMsr-945, AMG-NYU Paper 65, Aug. 15, 1944. AMP-401.2-M7
13. Brief explanation of methods used in cascading problem; AMP Study 137 [OEMsr-945], AMG-NYU Paper 87, January 1945. AMP-101.1-M12
14. *Suggestions for Measurements in Resojets*, J. K. L. MacDonald, AMP Study 137 [OEMsr-945], AMG-NYU Paper 108, Mar. 21, 1945. AMP-101.1-M14
15. *Comparison of Pressure and Impulse Resulting from Detonation Processes Progressing in Different Ways*, AMP Study 137 [OEMsr-945], AMG-NYU Paper 111, Mar. 27, 1945. AMP-101.1-M15
16. *Remarks on the Problem of Contact Explosions*, B. Friedman, AMP Study 37, AMG-NYU Paper 124, June 1945. AMP-101-M1
17. *Note on Methods of Measuring Depth of Functioning of Depth Bombs*, AMP Study 110 [OEMsr-618], SRG-C Paper 384, Dec. 16, 1944. AMP-400-M2
18. "Resistance of Impact on Water Surface, Part V — Sphere," Shumpei Watanabe, *Scientific Papers of the Institute of Physical and Chemical Research*, Tokyo, Vol. 23, No. 484, February 1934, pp. 202-209.

PART II

Chapter 3

1. *Mathematical Theory of the Influence of a Dome on the Directivity Pattern of Sound Beams*, Parts I-IV, E. Bromberg, Richard Courant, K. O. Friedrichs, and James J. Stoker, AMP Memoranda 20.1M, 20.4M, and 20.7M [OEMsr-1007 and OEMsr-945], OSRD 20, AMG-C, and AMG-NYU, July to September 1943.
AMP-201-M1-M3
2. *A Theory of Acoustic Scattering, and Application to Grids, Rods, and Shields under Water*, J. K. L. MacDonald, AMP Memorandum 20.6M [OEMsr-945], AMG-NYU, September 1943.
AMP-201-M5
3. *Preliminary Investigation of Beam Distortion Due to Close Proximity of Sound Projector to a "Dome Nose,"* J. K. L. MacDonald, AMP Memorandum 20.8M [OEMsr-945], AMG-NYU, September 1943.
AMP-201-M4
4. *On Acoustic Reflections and Images in Domes*, J. K. L. MacDonald, AMP Memorandum 20.10M [OEMsr-945], AMG-NYU, October 1943.
AMP-201-M7
5. *Radiation Patterns from a Vibrating Plate*, E. Bromberg and Harvey Cohn, AMP Memorandum 20.9M [OEMsr-1007 and OEMsr-945], AMG-C and AMG-NYU, October 1943.
AMP-201-M6
6. *On Acoustic Shielding by Circular Discs*, AMP Memorandum 20.11M, [OEMsr-945] AMG-NYU, April 1944.
AMP-201-M9
7. *A Mathematical Study of Acoustic Shielding by Some Narrow Cylinders*, J. K. L. MacDonald, AMP Memorandum 115.1M [OEMsr-945], AMG-NYU, October 1944.
AMP-201-M11
8. *Reduction of Interference by Modulated Pulses*, AMP Study 123 [OEMsr-945], AMG-NYU Paper 56, July 1944.
AMP-201-M10

Chapter 4

1. *Optik*, Max Born, Julius Springer, Berlin, 1933, p. 160.
 - 1a. *Ibid.*, p. 153.
 - 1b. *Ibid.*, p. 154, equation 10.
2. *Electromagnetic Theory*, Julius Adams Stratton, McGraw-Hill Book Company, Inc., New York, N. Y., and London, Eng., 1941, p. 568.
 - 2a. *Ibid.*, p. 563.
 - 2b. *Ibid.*, p. 568, equations 17 and 18.
 - 2c. *Ibid.*, p. 284, equation 86.
 - 2d. *Ibid.*, p. 568, equations 20 and 21.
 - 2e. *Ibid.*, p. 572.
 - 2f. *Ibid.*, p. 409.
 - 2g. *Ibid.*, pp. 564-572.
 - 2h. *Ibid.*, p. 564.
 - 2i. *Ibid.*, p. 568, 569, equation 22.
 - 2j. *Ibid.*, p. 569, equation 28.
 - 2k. *Ibid.*, p. 565, equation 13.
 - 2l. *Ibid.*, p. 565, equation 14.
 - 2m. *Ibid.*, p. 569, equation 23.
 - 2n. *Ibid.*, p. 409, equation 56.
 - 2o. *Ibid.*, p. 406, equation 34.
3. *Tables of Functions with Formulae and Curves*, Eugen Jahnke and Fritz Emde, B. G. Teubner, Leipzig and Berlin [G. E. Stechert & Co., New York, N. Y.], 1938, p. 115.
 - 3a. *Ibid.*, p. 111, equation 2.
 - 3b. *Ibid.*, p. 117, equation 6.
4. "Zur Farbentheorie Kolloidaler Metallsuspensionen," G. Jobst, *Annalen der Physik*, Vierte Folge, Vol. 76, No. 8, 1925, pp. 863-888.
5. "Zur Berechnung der Reellen Nullstellen der Besselschen Zylinderfunktion," Fritz Emde, *Archiv der Mathematik und Physik*, Ser. 3, Vol. 24, 1916, pp. 239-250.
6. "Diffuse Strahlung Dielektrischer Kugeln im Grenzfalle, das Kugelmateriale und Umgebendes Medium Fast Fleiche Brechungsindices Haben," G. Jobst, *Annalen der Physik*, Vierte Folge, Vol. 78, No. 18, 1925, p. 158.
7. "Der Lichtdruck auf Kugeln von Beliebigen Material," P. Debye, *Annalen der Physik*, Vierte Folge, Vol. 30, 1909, pp. 57-136.
8. "A Theoretical Investigation of the Transmission of Light Through Fog," J. A. Stratton and H. G. Houghton, *Physical Review*, Ser. 2, Vol. 38, No. 1, July 1, 1931, pp. 159-165.
9. *Verification of Mie Theory, Calculations and Measurements of Light Scattering by Dielectric Spherical Particles* [Progress Report], Victor K. LaMer, Division 10, OEMsr-148, Service Project CWS-1, OSRD 1857, Sept. 29, 1943.
AMP-202-M1
10. *On Light Scattering by Spheres* [Part] II, Leon Brillouin, AMP Report 87.2R, [OEMsr-1007], OSRD 3464, AMG-C, April 1944.
AMP-202-M3
11. *The Problem of a Plane Wave Incident on a Circular Cylinder Parallel to the Electric Vector*, E. B. Moullin and L. G. Reynolds, Report M.397, OSRD WA-933-1, Admiralty Signal Establishment [Great Britain], December 1941.
AMP-203-M1
12. *Expression for the Echoing Power of Cylinder*, E. B. Moullin and L. G. Reynolds, Appendix to Report M.397 (attached to Report M.397), OSRD WA-933-2, Admiralty Signal Establishment [Great Britain], December 1941.
AMP-203-M1
13. "On the Intensity of the Scattered Light from an Unpolarized Beam," W. S. Stiles, *The London, Edinburgh and Dublin Philosophical Magazine and Journal of Science*, London, Eng., Vol. 7, No. 41, Sec. XXIII, January 1929, pp. 204-205.

Chapter 5

1. *The Electromagnetic Field*, Max Mason and Warren Weaver, University of Chicago Press, 1929, p. 15.
2. *Lehrbuch der Elektrodynamik*, Yakov I. Frenkel, Julius Springer, Berlin, Vol. 1, 1926, pp. 93-104.
3. *Electromagnetic Theory*, Julius Adams Stratton, McGraw-Hill Book Company, Inc., New York, N. Y., 1941 [Note that equation 48, p. 179, is incorrect; it refers to "electric moment" but not to "multipole"] pp. 172-183.
 - 3a. *Ibid.*, p. 408, equation 46.
 - 3b. *Ibid.*, p. 174, equation 23.
 - 3c. *Ibid.*, p. 182, equations 67 and 68.
4. *Electromagnetic Waves*, Sergei Alexander Schelkunoff, D. Van Nostrand Company, Inc., New York, N. Y., 1943.
 - 4a. *Ibid.*, p. 70, line 8, p. 162.
5. *Tables of Functions with Formulae and Curves*, Eugen Jahnke and Fritz Emde, Dover Publications, New York City, N. Y., 1943, pp. 107-125.
6. *The Mutual Inductance between Two Spherical Coils*, S. A. Schelkunoff, Report MM-44-110-51, BTL, Aug. 25, 1944. AMP-203.2-M2
7. *A Coil Yielding a Single Dipole Moment*, Leon Brillouin, AMP Report 120.1R [OEMsr-1007], OSRD 4020, AMG-C, July 1944. AMP-203.2-M1
8. *On Spherical Coils*, Leon Brillouin, AMP Memorandum 120.1M, OEMsr-1007, OSRD 4351, AMG-C, October 1944. AMP-203.2-M3

PART III

Chapter 6

1. *On a Problem of Colliding Oscillators*, H. J. Greenberg, George H. Handelman, Witold Hurewicz, W. R. Heller, and W. Prager, AMP Report 36.3R [OEMsr-1066], AMG-B, Oct. 6, 1943. AMP-302.1-M1
2. *The Stability of Periodic Dynamical Processes Subject to Discontinuous Impulses*, H. J. Greenberg and Witold Hurewicz, AMP Report 36.5R [OEMsr-1066], OSRD 4093, AMG-B, Aug. 25, 1944. AMP-302.1-M3
3. *Interfering Linear Systems*, R. F. Specht, Technical Report 542, DTMB, July 1945.
4. *Forced Vibrations of a Simple Oscillator with Limited Displacement*, George H. Handelman, W. R. Heller, and W. Prager, AMP Report 36.4R [OEMsr-1066], OSRD 3031, AMG-B, Dec. 17, 1943. AMP-302.1-M2
5. "Ueber Eine Nicht-Harmonische Schwingung," Ernst Meissner, *Schweizerische Bauzeitung*, Vol. 104, No. 4, July 1934, pp. 35-36.
6. *On Some Computations Determining Stable Periodic Motions of the Spring Hammer Box*, H. J. Greenberg and Witold Hurewicz, AMP Memorandum 36.1M [OEMsr-1066], AMG-B, Oct. 17, 1944. AMP-302.1-M4
7. *The Amplitude of Displacement of the Diaphragm of a Spring Hammer Box in Certain Cases*, H. J. Greenberg, AMP Memorandum 36.2M [OEMsr-1066], AMG-B, Jan. 15, 1945. AMP-302.1-M5
8. *An Electrical Analogue to the Spring Hammer Box*, W. R. Heller, AMP Report 36.6R, OEMsr-1066, Service Project NS-165, OSRD 4926, AMG-B, March 1945. AMP-302.1-M6
9. *Servos with Torque Saturation*, N. B. Nichols and Witold Hurewicz, AMP Report 73.1R [Radiation Laboratory Report 555], [OEMsr-1066], AMG-B, May 1944. AMP-302.2-M1
10. *Guns on Pitching and Rolling Ships*, G. E. Hay, AMP Memorandum 70.1M [OEMsr-1066], AMG-B, May 3, 1944. AMP-904-M1
11. *Gun Equilibrators [Part] I*, G. E. Hay, AMP Report 70.1R [OEMsr-1066], OSRD 4472, AMG-B, Dec. 12, 1944. AMP-302.3-M1
12. *Gun Equilibrators [Part] II*, H. J. Greenberg, AMP Report 70.2R, OEMsr-1066, OSRD 5098, AMG-B, May 1945. AMP-302.3-M2
13. *On Two Types of Mechanical Mine Exploders*, L. J. Savage and W. Prager, AMP Memorandum 69.1M [OEMsr-1066], AMG-B, Oct. 9, 1943. AMP-902-M1
14. *On the Pressure inside the Williams Gage*, H. J. Greenberg and W. Prager, AMP Report 36.2R [OEMsr-1066], OSRD 1738, AMG-B, Aug. 2, 1943. AMP-101.1-M5
15. *On the Application of Dimensional Analysis to the Experimental Study of the Centrifugal Casting of Metals*, W. Prager, AMP Memo 13.1M [OEMsr-1066], AMG-B, Mar. 12, 1943. AMP-301-M1
16. *On the Mechanical Design of the Optical Bars of Range Finders*, W. Prager, AMP Memorandum 84.1M [OEMsr-1066], AMG-B, Jan. 20, 1944. AMP-503.2-M2
17. *The Mathematics Underlying the Centrifugal Casting of Metals (OD-108)*, A. F. MacConochie, W. Prager, and G. Handelman, War Metallurgy Committee [Div. 18], Sept. 10, 1943.
18. *The Stability of Periodic Dynamical Processes Subject to Discontinuous Impulses*, H. J. Greenberg and Witold Hurewicz, AMP Report 36.5R [OEMsr-1066], OSRD 4093, AMG-B, Aug. 25, 1944. AMP-302.1-M3
19. *An Electrical Analogue to the Spring Hammer Box*, W. R. Heller, AMP Report 36.6R, OEMsr-1066, Service Project NS-165, OSRD 4926, AMG-B, March 1945. AMP-302.1-M6
20. *On Some Computations Determining Stable Periodic Motions of the Spring Hammer Box*, H. J. Greenberg and Witold Hurewicz, AMP Memorandum 36.1M, OEMsr-1066, AMG-B, Oct. 17, 1944. AMP-302.1-M4
21. *The Amplitude of Displacement of the Diaphragm of a Spring Hammer Box in Certain Cases*, H. J. Greenberg, AMP Memorandum 36.2M, OEMsr-1066, AMG-B, Jan. 15, 1945. AMP-302.1-M5

Chapter 7

1. *On the Determination of the Energy of Plastic Deformation Absorbed in a Diaphragm*, George H. Handelman and W. Prager, AMP Report 36.1R [OEMsr-1066], OSRD 1698, AMG-B, July 12, 1943. AMP-302.4-M1
2. *Elemente der Technologischen Mechanik*, P. Ludwig, Julius Springer, Berlin, 1909.
3. "Über die Form des Elastizitätsgesetzes bei Ideal Elastischen Stoffen," H. Hencky, *Zeitschrift für Technische Physik*, Vol. 9, No. 6, 1928, pp. 215-220.
4. "Über den Zusammenhang von Spannungen und Formänderungen im Verfestigungsgebiet," R. Schmidt, *Ingenieur-Archiv*, Vol. 3, June 1932, p. 222.
5. "Beitrag zur Mechanik des Bildsamen Verhaltens von Flusstahl," K. Hohenemser and W. Prager, *Zeitschrift für Angewandte Mathematik und Mechanik*, Vol. 12, February 1932, pp. 1-14.
6. *Plasticity*, A. Nadai, McGraw-Hill Book Company, Inc., New York, N. Y., and London, Eng., 1931, p. 75.
7. "The Tension Test," C. W. MacGregor, *American Society for Testing Materials*, Proceedings of the Forty-Third Annual Meeting, held at Atlantic City, N. J., Vol. 40, June 24-28, 1940, p. 526.
8. *Possible Causes of Failure in Powder Grains of H-4.5 Rockets*, George H. Handelman, AMP Report 182.1R, OEMsr-1066, OSRD 5755, AMG-B, September 1945. AMP-606-M4
9. *Theory of Elastic Stability*, S. Timoshenko, McGraw-Hill Book Company, Inc., New York, N. Y., and London, Eng., 1936, p. 122.
10. *Trap Force Measurements, Table I* [Memorandum] from Engineering Department-Experimental 115 MM Group to Dr. Kossiakoff, G. W. Engstrom, OEMsr-273, Allegany Ballistics Laboratory, Feb. 3, 1945. AMP-900-M10
11. *Plasticity*, A. Nadai, McGraw-Hill Book Company, Inc., New York, N. Y., and London, Eng., 1931, p. 73.
12. *A Treatise on the Mathematical Theory of Elasticity*, Augustus Edward Hough Love, Cambridge at the University Press [Eng.], 4th Edition, 1927, p. 144.
13. *The Shell Design Problem*, James J. Stoker, AMP Report 75.1R [OEMsr-1007], OSRD 3244, AMG-C, February 1944. AMP-903.1-M3
14. *Strength and Compressibility of Pads of Tubular Fibres to be Used in Clothing*, James J. Stoker, AMP Report 81.1R [OEMsr-1007], OSRD 2024, AMG-C, December 1943. AMP-900-M3

PART IV

Chapters 8-12

1. *Proceedings of the Second Conference on Underwater Ballistics*, held January 29 to 31, 1945, at DTMB and NOL [OEMsr-1384], AMG-Harvard University [January 1945]. AMP-400-M3
 - 1a. *Ibid.*, pp. 19-29.
 - 1b. *Ibid.*, pp. 105-108.
 - 1c. *Ibid.*, p. 16.
 - 1d. *Ibid.*, p. 110.
 - 1e. *Ibid.*, p. 20.
 - 1f. *Ibid.*, p. 118.
 - 1g. *Ibid.*, p. 17.
 - 1h. *Ibid.*, p. 115.
 - 1i. *Ibid.*, p. 14.
 - 1j. *Ibid.*, pp. 18, 43.
 - 1k. *Ibid.*, p. 33.
 - 1l. *Ibid.*, p. 13.
2. *An Elementary Consideration of Bomb Ricochet*, Technical Armament Department Note 219, UBRC 3, OSRD WA-2526-17b, RAE, Farnborough [Eng.], Sept. 2, 1943. AMP-401.1-M3
3. *An Analytical Consideration of Bomb Ricochet*, OSRD WA-2919-4b, UBRC Report 4, Technical Armament Department Note 238, RAE, Farnborough [England], November 1943. AMP-401.1-M4
4. *The Underwater Behavior of the Mine A, Mark VIII, as Deduced from Model Scale Results*, A. D. Brown, OSRD WA-4296-10, SS Informal Report 1323, Mine Design Department [Great Britain], Apr. 7, 1945. AMP-407-M2
 - 4a. *Ibid.*, p. 3.
5. *Traité de L'Equilibre et du Mouvement des Fluides, pour Servir de Suite au Traité de Dynamique*, Jean-le-Rond d'Alembert, Briasson, Paris, 1770.
 - 5a. *Ibid.*, pp. 216-302.
 - 5b. *Ibid.*, Chap. II.
6. *Dynamic Stability of Bombs and Projectiles*, M. A. Biot, JPC Report 10, OEMsr-418, CIT, Sept. 6, 1943. AMP-401-M1
7. *Modeling of Entry into Water*, Garrett Birkhoff, AMP Memorandum 42.10M, OEMsr-1384, AMG-H, May 1945. AMP-401-M9
8. *Ricochet Off Water*, Garrett Birkhoff, George D. Birkhoff, Willard E. Bleick and others, AMP Memorandum 42.4M [OEMsr-1007], AMG-C, May 1944. AMP-401.1-M5
 - 8a. *Ibid.*, p. 88.
 - 8b. *Ibid.*, Appendix.
 - 8c. *Ibid.*, p. 46.
 - 8d. *Ibid.*, pp. 18-19.
 - 8e. *Ibid.*, p. 47, Appendix III.
9. *A Method of Prediction of the Upturning Underwater Trajectories of Rockets in Two Dimensions*, B. D. Blackwell, OSRD WA-4504-2a, UBRC Report 31, Report UT/8, Department of Scientific Research and Experiment, Admiralty [Great Britain]. AMP-406-M7
 - 9a. *Ibid.*, p. 15.
 - 9b. *Ibid.*, p. 6.

10. *Preliminary Remarks on the Cavity Made by a Projectile Entering Water*, B. D. Blackwell, OSRD WA-1927-3d, UBRC 2, Report UT/4, Department of Scientific Research and Experiment [Great Britain], February 1944. AMP-401.2-M4
11. *Underwater Behavior of 3.5" Aircraft Rockets*, I. S. Bowen, JBC Report 23, OEMsr-418, CIT, Dec. 6, 1943. AMP-406-M1
 - 11a. *Ibid.*, p. 24.
12. *Handbook of Ballistics*, C. J. Cranz, H. M. Stationery Office, London, 1921.
 - 12a. *Ibid.*, Secs. 74-75.
 - 12b. *Ibid.*, p. 452.
 - 12c. *Ibid.*, Vol. 3.
 - 12d. *Ibid.*, pp. 60 ff.
13. *The Influence of Atmospheric Pressure on the Phenomena Accompanying the Fall of Small Scale Projectiles into a Liquid*, R. M. Davis, OSRD WA-2919-4g, Report 21, UBRC, Engineering Laboratory, Cambridge, Eng., September 1944. AMP-401.5-M3
14. *Aerodynamic Theory*, William Frederick Durand, Julius Springer, Berlin, 1934-1936, Vols. 1-6.
 - 14a. *Ibid.*, Vol. 6, p. 10.
 - 14b. *Ibid.*, Vol. 6, p. 110.
15. *The Mechanism of Wounding by High Velocity Missiles* [Part] I, *Quantitative Data*, E. Newton Harvey, E. G. Butler, J. H. McMillen, and W. O. Puckett, Missile Casualties Report 2, RS/B22-301 and Report 6, RS/B36/49, OEMcmr-395, Committee on Medical Research, Princeton University, Dec. 15, 1944. AMP-900-M8
 - 15a. *Ibid.*, p. 24.
 - 15b. *Ibid.*, pp. 28-31.
 - 15c. *Ibid.*, p. 31.
16. *Elements of Ordnance*, Thomas J. Hayes, John Wiley and Sons, Inc., New York, N. Y., 1938.
 - 16a. *Ibid.*, p. 421.
 - 16b. *Ibid.*, Chaps. X-XI.
17. *Structural Damage Associated with Water Entry of Projectiles*, D. E. Hudson, Division 3, IOC Report 3, OEMsr-418, Service Project NO-176, OSRD 2381, CIT, Feb. 15, 1945. AMP-405.3-M5
 - 17a. *Ibid.*, p. 11.
18. *Impact on Seaplane Floats during Landing*, Theodore von Kármán, Technical Note 321, NACA, October 1929.
19. *A 3.5" Rotating Rocket with Various After-Bodies*, H. L. Doolittle and R. T. Knapp, Division 6, Report ND-27.1, NDRC 6.1-sr207-1903, OSRD 4747, CIT, Jan. 4, 1945. AMP-406-M5
 - 19a. *Ibid.*, Fig. 14.
20. *Experiments on Projectile Models and Spheres*, Norman Levinson, AMP Memorandum 42.7M, OEMsr-1384, AMG-H, April 1945. AMP-401-M8
21. *Experiments on Tailless Models of U. S. Army Bombs*, Norman Levinson, AMP Memorandum 42.5M [OEMsr-1384], AMG-H, September 1944. AMP-401.1-M6
22. *On the Asymptotic Shape of the Cavity Behind an Axially Symmetric Nose, and a Relationship between the Asymptotic Cavity Diameter and the Drag Coefficient*, Norman Levinson, AMP Memorandum 42.9M, OEMsr-1384, AMG-H, May 1945. AMP-401.2-M8
23. *Types of Underwater Motion*, Norman Levinson, AMP Study 42, OEMsr-1384, AMG-H, Paper 6, December 1944. AMP-401.4-M1
24. *Investigations on the Inception of Cavitation in Water*, J. W. Maccoll, OSRD WA-2919-4E, Report 12, UBRC, Great Britain, June 1944. AMP-401.5-M2
25. *The Ricochet of Bombs, Targets on Water*, M. Morse and R. Baldwin, Report 2, Technical Division Ballistic Section, Report of Service Branch, Office of Chief of Ordnance, War Department, Dec. 23, 1942.
26. *The Plane Yawing of Bombs Released from Horizontal Suspension*, E. J. McShane, Report 325, BRL, Aberdeen Proving Ground, Md., February 1943.
27. *Theoretical Hydrodynamics*, L. M. Milne-Thomson, Macmillan & Company, Ltd., London, Eng., 1938.
 - 27a. *Ibid.*, pp. 235, 419.
 - 27b. *Ibid.*, pp. 305-310.
 - 27c. *Ibid.*, p. 74.
 - 27d. *Ibid.*, p. 88.
28. *Non-Linear Mechanics*, Parts I and II, N. Minorsky, Reports 534 and 546, DTMB, Navy Department, Part I: December 1944; Part II: September 1945.
29. *Applied Hydro- and Aeromechanics Based on Lectures of Ludwig Prandtl*, Oskar G. Tietjens, McGraw-Hill Book Company, Inc., New York, N. Y., 1934.
 - 29a. *Ibid.*, p. 90.
 - 29b. *Ibid.*, p. 108.
 - 29c. *Ibid.*, Chapter 1.
 - 29d. *Ibid.*, pp. 119-120.
30. *Ueber den Richochetschuss, Inaugural-Dissertation zur Erlangung der Doktorwürde der Hohen Philosophischen Fakultät der Königl. Christian Albrechts'* (Doctoral Thesis), Carl Ramsauer, Universität zu Kiel, Kiel, Ger., 1903. AMP-401.1-M1
31. *The Impact of Bombs on Water and Their Drag in the Cavity Stage*, R. A. Shaw, OSRD WA-2526-17d, Theoretical Research Report 9, Marine Aircraft Experimental Establishment, Helensburgh [Eng.], Report 7, UBRC, Feb. 17, 1943. AMP-401.3-M1
32. *Modeling of Water Entry of Bombs and Projectiles*, L. B. Slichter, OEMsr-418, CIT, Mar. 31, 1944. AMP-401-M4
 - 32a. *Ibid.*, pp. 18 ff.
33. *Resistance of Projectiles Followed by a Cavity in Water*, G. I. Taylor, OSRD WA-2526-17c, Report 6, UBRC, [Great Britain]. AMP 401.2-M9
34. *Mechanism of Pitch Sensitivity for Aircraft Torpedoes*, Harold Wayland, NOC Report 47.1, CIT, February 1945.
35. *A Study of Splash*, A. R. Worthington, Longmans, Green & Company, London, Eng., 1908.
 - 35a. *Ibid.*, pp. 36-38.
 - 35b. *Ibid.*, pp. 77-89, 121-129.
 - 35c. *Ibid.*, p. 116.
 - 35d. *Ibid.*, p. 102.
36. *Ricochet Off Land Surfaces*, Garrett Birkhoff, Report 535, BRL, Aberdeen Proving Ground, Md.
37. *Principles of Mechanics*, Part I, Plane Mechanics, John Lighton Synge and Byron Alexander Griffith, McGraw-Hill Book Company, Inc., New York, N. Y., and London, Eng., 1942.
 - 37a. *Ibid.*, Sec. 7.3.

38. *Underwater Trajectory of a Spinning Projectile*, H. P. Hitchcock, Report 261, BRL, Aberdeen Proving Ground, Md., October 1941.
39. *Underwater Trajectories of the 3.5" Aircraft Rocket Model 5*, R. V. Adams, Division 3, JPC Report 21, OEMsr-418, OSRD 2161, CIT, June 10, 1944. AMP-406-M2
40. *Further Investigations of the Underwater Behavior of Aircraft Rockets*, I. S. Bowen, Division 3, JBC Report 27, OEMsr-418, Service Projects OD-162 and NO-170, OSRD 2152, CIT, June 26, 1944. AMP-406-M3
41. *Underwater Behavior of the 11.75" Aircraft Rocket*, I. S. Bowen, Division 3, IPC Report 65, OEMsr-418, CIT, Oct. 25, 1944. AMP-406-M4
42. *Comparison of Model and Full Scale Results of Aircraft Torpedo Drops*, OSRD WA-647-8, Report N.11/H.24, ARL, Teddington [Eng.], May 8, 1943. AMP-405.1-M2
43. *A Study of the Depth of Initial Dive of the Mark 13 Torpedo with Shroud Ring*, Marvin Gimprich, NDRC 6.1-sr1131-1889, CUDWR, June 9, 1945. AMP-405.3-M8
44. *A Summary of Experimental Observations on the Deceleration of Torpedoes Dropped from Aircraft*, G. Grime, OSRD WA-3582-1c, STR Report 376, Torpedo Experimental Establishment, Greenock, Eng., September 1944. AMP-405.1-M7
45. *Underwater Explosives and Explosions* [for the period] *October 15 to November 15, 1944*, P. C. Cross, OSRD 4406, Division 2 Interim Report UE-27, Service Projects NO-223, NO-224, NO-237, and others, November 1944, pp. 10-16. AMP-403-M2
46. *Use of the Hydropressure Plug for Water Impact Studies*, R. R. Stokes, IOC Report 35, CIT, Sept. 15, 1944. AMP-404-M2
47. *Water Impact Tests on 5.0" HVAR*, P. Metzelaar, Report 975, NOL, May 5, 1945, Table 2.
48. *The Force of Impact on a Sphere Striking a Water Surface, (Approximation by the Flow about a Lens)*, M. Shiffman and D. Spencer, AMP Report 42.1R, OEMsr-945, OSRD 4921, AMG-NYU, February 1945. AMP-404-M3
49. *Added Mass of Projectiles Entering Water*, F. P. Mayo and E. G. Richardson, OSRD WA-3613-1b, Bomb Firing Tank Note 10, Report HB/TE/6013/S, MAEE, Helensburgh, [Eng.], Dec. 28, 1944. AMP-401-M7
50. *Experimental Investigation of Impact in Landing on Water*, R. L. Kreps, Technical Memorandum 1046, NACA, August 1943 (translated from Russian CAHI Report 438, 1939).
51. *Shearing Stress on a Projectile at Water Impact*, Max Mason and L. B. Slichter, IPC Report 74, OEMsr-418, Service Projects NO-141 and NO-146, OSRD 2483, CIT, Apr. 14, 1945. AMP-404-M4
52. *Model Tests of Proposed Designs of the Case for the Mark 25 Mine*, R. D. Bennett, Report 697, NOL, November 1942.
53. *Forces on a Long Cylinder Planing on Water*, H. Hogg and A. G. Smith, OSRD WA-3024-16c, Report Aero 1999, RAE, Farnborough [Eng.], December 1944.
54. *Water Entry of 8" Model of Aircraft Torpedoes with Special Noses and Ring Tail*, B. H. Rule and W. P. Huntley, IOC Report 24, OEMsr-418, OSRD 2255, CIT, Nov. 1, 1944, Fig. 10, p. 24. AMP-405.3-M4
55. *The Effect of Pitch and Entry Angle on the Underwater Orbit of Mark 13-2 Torpedo as Determined by Tests with 1.0" Model*, Max Mason and L. B. Slichter, IOC Report 32, OEMsr-418, OSRD 2198, CIT, Aug. 28, 1944. AMP-405.3-M3
56. *A Note on the Deceleration after Entry of an Aircraft Launched Torpedo*, L. W. Parkin and J. L. Hudson, OSRD WA-1378-14, Report 3, TDE, Gosport, England, March 1943. AMP-405.3-M2
57. *Underwater Behavior of the Torpedo Mk. XII when Fitted with Nose Extensions Suggested by Dr. H. C. H. Townend*, OSRD WA-647-12, Report N.16/H.36, ARL, Teddington [Eng.], Sept. 15, 1942. AMP-405.3-M1
58. "Sounds Produced by Drops Falling on Water," A. Mallock, *Proceedings of the Royal Society*, Vol. 95, Ser. A, London, Nov. 7, 1918, pp. 138-143.
59. "The Line of Action of the Resultant Pressure in Discontinuous Fluid Motion," S. Brodetsky, *Proceedings of the Royal Society*, Vol. 102, Ser. A, London, Dec. 1, 1922, pp. 361-372.
60. *Drag Coefficients of Spherical and Conical Bomb Nose Forms in Cavitated Motion in Water*, R. W. Duncan and F. E. Bradley, OSRD WA-3519-2, Technical Armament Department Note Arm. 301, RAE, Farnborough [Eng.], November 1944. AMP-401.3-M4
61. *Underwater Performance of 1-inch Diameter Models of a Family of Cone Head Rockets*, R. A. Shaw and P. E. Naylor, OSRD WA-3996-9, Report 25, Armament Research Department, MAEE, Helensburgh [Eng.], Feb. 7, 1945, Fig. 4. AMP-406-M6
62. *The Shape of the Cavity behind a Sphere in Steady Motion Through Water*, J. Codd, OSRD WA-2526-17f, Theoretical Research Report 21/44, UBRC 11, Armament Research Department, Fort Halstead, Kent [Eng.], May 1944. AMP-401.2-M5
63. "Bemerkungen zu Meiner Arbeit: Über das Widerstandsgesetz Schnell Bewegter Kugeln in Wasser," W. Bauer, *Annalen der Physik*, Vierte Folge, Vol. 82, No. 7, 1927, pp. 1014-1016.
64. *The Estimation of Underwater Drag Coefficients for Projectiles in the Cavity Stage*, M. W. Melton and A. W. Babister, OSRD WA-4540-2b, Report 32, UBRC, [Great Britain]. AMP-401.3-M5
65. *Control of the Underwater Trajectory of Projectiles in Cavity Flow*, N. Simmons, OSRD WA-3746-3a, Report 29, UBRC, Fort Halstead, [Eng.], December 1944, pp. 38-39. AMP-402-M2
66. "Discontinuous Fluid Motion Past Circular and Elliptic Cylinders," S. Brodetsky, *Proceedings of the Royal Society*, Vol. 102, Ser. A, London, Eng., Feb. 1, 1923, pp. 542-553.
67. *Measurements of the High Frequency Noise Produced by Cavitation Projectiles in the High Speed Water Tunnel*, Robert T. Knapp, HML Report ND-8.2, NDRC 6.1-sr207-924, CIT, Aug. 31, 1943. AMP-401.5-M1
68. *Tables for the Computation of Drag Coefficients*, Norman Levinson, AMG Memorandum 42.7W, AMP Study 42 [OEMsr-1384], AMG-H, October 1944. AMP-401.3-M3

69. *An Analytical Approximation for the Underwater Trajectory of a Nonrotating Projectile*, Norman A. Haskell, IPC Report 77, OEMsr-418, CIT, June 1, 1945.
AMP-402-M4
70. *Torpedo Launching Tests at CIT Torpedo Launching Range Through April 1, 1944*, F. C. Lindvall, JOC Report 2, OEMsr-418, Service Projects NO-148 and NO-177, OSRD 2105, CIT, May 17, 1944. AMP-405.1-M4
71. *Hydrodynamic Forces Resulting from Cavitation on Underwater Bodies*, James W. Dailey and Robert T. Knapp, Report ND-31.2, NDRC 6.1-sr207-2242, OSRD 5756, CIT, June 21, 1945. AMP-401.5-M4
72. *Occurrence of Ricochet from Calibre .30 Springfield Rifle*, R. H. Kent, Memorandum Report 243, BRL, Aberdeen Proving Ground, Md., Nov. 9, 1943.
73. *Torpedo Studies*, Marvin Gimprich, Summary Technical Report, NDRC Div. 6, Vol. 21.
74. *Report on Visit to Germany in 1945*, Leslie Simon, BRL, Aberdeen Proving Ground, Md., Part XI, Sec. 2.
75. *Aircraft Torpedo Drops, Comparison of Model and Full Scale Results*, OSRD WA-647-8, Report N.11/H.24, ARL, Teddington [Eng.], May 8, 1943.
AMP-405.1-M2
76. *Correlation between 1-inch Diameter Model and Prototype Mark 13-2 Dummy Torpedo and the Prototype (1st Revision)*, F. C. Lindvall, Max Mason, and L. B. Slichter, IOC Report 37, OEMsr-418, Service Project NO-176, OSRD 2320, CIT, Dec. 15, 1944. AMP-405.1-M8
77. *The Vertical Motion of a Spherical Bubble and the Pressure Surrounding It*, G. I. Taylor, reprinted in DTMB Report 510.
78. Letter to Ordnance Department, AAF 471.6, AAF Proving Ground Command, Eglin Field, Fla.
79. *Test of Anti-Ricochet Devices for Use on Water Targets*, AAF Board Report on Project 3788C4N.8, Eglin Field, Fla., Feb. 10, 1945.
80. *Test of Minimum Altitudes for Safe Bomb Release*, AAF Board Report 2772, Eglin Field, Fla.
81. *Minimum Safe Altitude for Low Level Bombing*, R. G. Sachs, Report 431, BRL, Aberdeen Proving Ground, Md., Nov. 26, 1943.
82. *Errors of Depth and Roll Recordings of 18" Heads*, COM 12th Fleet X269-45, U. S. Navy, Feb. 8, 1945.
83. *First Report on Anti-Ricochet Tests of Bombs*, D. D. Johnston, Report 3605, Aberdeen Proving Ground, Md.
84. *Underwater Trajectory of Mark 17 and Mark 29 Depth Bombs (Final Report)*, Report NA8/F41-61, F1-5(4)/AAU, AAU Project 10-42, Dec. 12, 1942.
85. *Ricochet of Mark VII Depth Charges*, R. A. Shaw, OSRD WA-4008-1d, Report 7, MAEE, Helensburgh Armament Research, Eng., Jan. 13, 1943.
AMP-401.1-M2
86. *Proceedings of the Ordnance Board, Q 3,256* [includes Q 3,250 to Q 3,257], OSRD WA-4250-14, Ordnance Board [Great Britain], Apr. 11, 1945. AMP-903-M3
87. *German BT and Jet Propulsion Equipment for Bomb, Abandoned Development for German BT 1000*, U. S. Army ALSOS Report 57, Jan. 16, 1945.
88. *Full Scale Trials of 18" Torpedoes Fitted with Nose Spigot*, OSRD WA-4320-3, Report 3, ATDU, Gosport [Eng.], March 1945. AMP-405.3-M6
89. *Proceedings of the Ordnance Board, Q 27,520* [includes Reports Q 27,506 to Q 27,528], OSRD WA-2071-5, Ordnance Board [Great Britain], May 3, 1944. AMP-903-M2
90. *Proceedings of the Ordnance Board, Q 28,494* [includes Reports Q 27,481 to Q 27,505], OSRD WA-2071-10, Ordnance Board, Great Britain, May 1, 1944. AMP-903-M1
91. *Underwater Behavior of the 11.75-in. Aircraft Rocket*, I. S. Bowen, Division 3, IPC Report 65, OEMsr-418, CIT, Oct. 25, 1944. AMP-406-M4
92. *Finnart Trials of $\frac{1}{3}$ Scale Uncle Tom*, Squadron Leader N. Simmons, OSRD WA-4328-5, Report 26, MAEE, Helensburgh Armament Research, Eng. Mar. 3, 1945. AMP-405.3-M7
93. *An Investigation of the Hydrodynamics of Underwater Projectile Forms, and Separate Folder of Drawings*, Clifford P. Kittredge, Calvin A. Gongwer, and John F. Ripkin, OSRD 3023, NDRC C4-sr20-343, CUDWR-NLL Report P16. AMP-102-M1
94. *The Force of Impact on a Sphere Striking a Water Surface, (Second Approximation)*, AMP Report 42.2R, OEMsr-945, OSRD 5485, AMG-NYU, July 1945. AMP-404-M5
95. *Preliminary Tests of 1" Diameter Model Anti-Submarine Bombs and Projectiles with Bubble Eliminating Devices*, B. H. Rule and W. P. Huntley, Morris Dam Report 69, IPC Report 47, CIT.
96. *A Discussion on the Modification of Standard Bombs to Improve Ship-Bombing Technique*, Theodore von Kármán, Louis G. Dunn, Joseph Charyk, JPL Memorandum 2-1, Guggenheim Aeronautical Laboratory-CIT, Apr. 7, 1944. (Available through Armament Laboratory, Air Matériel Command, Wright Field, Dayton, Ohio.) AMP-401-M5
97. "Impulse and Momentum in an Infinite Fluid," Theodore Theodorson, *Theodore von Kármán Anniversary Volume, Contributions to Applied Mechanics and Related Subjects by the Friends of Theodore von Kármán on his 60th Birthday*, Pasadena, Calif., May 11, 1941, pp. 49-58.
98. *Scale Effect on Air Cavities Formed When Spheres Enter Water*, E. G. Richardson, OSRD WA-1475-14, Armament Note 116, Armament S 322/LGC/E.G.I./99, RAE, Farnborough, [Eng.], Sept. 2, 1942. AMP-401.2-M1
99. *Modern Developments in Fluid Dynamics*, S. Goldstein, Clarendon Press, Oxford, Eng., Vol. II, 1938, pp. 495 ff.
100. *Further Experiments on Air Cavities Formed when Spheres Enter Liquids*, E. G. Richardson, OSRD WA-2900-6a, Armament Department Technical Note 289, RAE Farnborough [Eng.], Report 12, UBRC, July 1944. AMP-401.2-M6
101. *Comparison of the Performance of 8.0", 1.0" and 0.5" Models of the 250 lb. Redesigned AS Bomb*, Armament Department Note 140, Technical Research Staff, Farnborough [Eng.], enclosure A to ONI Report 261, Navy Department, November 1942. AMP-400-M1
102. *Hydrodynamics*, Sir Horace Lamb, Cambridge at the University Press [Eng.], 6th Edition, 1932, p. 174.
102a. *Ibid.*, p. 14.

103. *New Methods in Exterior Ballistics*, F. R. Moulton, University of Chicago, 1926, Chap. V.
104. *Mathematics for Exterior Ballistics*, Gilbert Ames Bliss, J. Wiley and Sons, Inc., New York, N. Y., 1944, Sec. 12.
105. "Differential Equations from the Group Standpoint," L. E. Dickson, *Annals of Mathematics*, Vol. 25, Ser. 2, 1923-24, pp. 287-378.
106. *Treatise on Analytical Dynamics*, E. T. Whittaker, Dover Publications, New York, N. Y., 4th Edition, 1944.
107. *An Introduction to Kinetic Theory of Gases*, Sir James Jeans, Cambridge at the University Press [Eng.], 4th Edition, 1940, p. 173.
108. *Underwater Trajectory of AN-MK 41 Depth Bombs*, NA8/F1-5(4), AAU Project 53-42, May 10, 1943.
109. *Water Entry Bibliography*, AMP Memorandum 42.8M, OEMsr-1384, AMG-H, June 1945.
AMP-401-M10
110. *Large Bomb for B-17 Plane*, Report IOC 30x, OSRD 123, Morris Dam Group, CIT, July 29, 1944.
111. "Sur le Ricochet des Projectiles Sphériques à la Surface de L'Eau," E. de Jonquières, *Comptes Rendus*, Académie de Science, Institut of France, Vol. 97, 1883, pp. 1278-1281.
112. "Die Bewegungserscheinungen des Wassers beim Durchgang Schnell Bewegter Kugeln," Carl Ramsauer, *Annalen der Physik*, Vierte Folge, Vol. 84, No. 22, 1927, Fig. 10, p. 731.
113. *Underwater Trajectories*, Naval Ordnance Pamphlet 348, July 1912.
114. "Ricochets in Target Practice," letter to Editor dated June 27, 1910, LeRoy Bartlett, Coast Artillery Corps, *Journal of the U. S. Artillery*, Ft. Monroe, Va., Vol. 34, No. 1, July to August 1910, p. 116.
115. *Underwater Ballistics and Scale Models of Projectiles*, OEMsr-418, OSRD 2551, CIT, 1946.
116. *Impact Forces*, Garrett Birkhoff, AMP Memorandum 42.6M [OEMsr-1384], AMG-H, September 1944.
AMP-404-M1
117. "An Example of Potential Theory," O. D. Kellogg, *American Academy of Arts and Sciences*, Boston, 1923, p. 203.
118. *Fundamentals of Hydro- and Aeromechanics Based on Lectures of Ludwig Prandtl*, Oskar G. Tietjens, McGraw-Hill Book Company, Inc., New York, N. Y. and London, Eng., 1934, Sec. 100, p. 233, "The Momentum Theorem for Steady Motion."
119. *Properties of Ordinary Water Substance in All Its Phases, Water Vapor, Water, and All the Ices*, N. Ernest Dorsey, American Chemical Society Monograph Series 81, J. Reinhold, New York, N. Y., 1940.
120. *Underwater Ballistics, Bi-Weekly Progress Report*, PMC 2.79 Part VI, OSRD 2439, CIT, Apr. 15, 1945.
121. Cavitation Tests on a Systematic Series of Torpedo Heads, Hunter Rouse and others, a series of reports, prepared for DTMB.
122. *Underwater Trajectories of G. P. Bombs and Bombs T14 and T10*, T. L. Smith, Report 616, BRL, Aberdeen Proving Ground, Md.
123. "Shock Wave Pressures," J. H. McMillen, *Journal of Applied Physics*, Vol. 68, 1945, pp. 198-209.
124. *Yahrbuch der Deutschen Luftfahrtforschung*, R. Madelung, Vol. 40, 1939-40, p. 82. (Available through Air Matériel Command, Intelligence T-2, Area B, Air Documents Division, Wright Field, Dayton, Ohio.)
125. *An Experimental Basis for the Development of a Method of Calibration of the Underwater Ballistic Properties of Projectile Forms*, R. W. Duncan and F. E. Bradley, Technical Armament Department Note 328, RAE, Farnborough [Eng.], July 1945.

OSRD APPOINTEES
APPLIED MATHEMATICS PANEL

Chief
WARREN WEAVER

Deputy Chief
THORNTON C. FRY

Acting Chief, May 29, 1945 to April 5, 1946

Technical Aides

B. H. COLVIN
H. H. GERMOND
CECIL HASTINGS, JR.
MYRTLE R. KELLINGTON
MARGARET S. PIEDER

MINA S. REES
I. S. SOKOLNIKOFF
D. C. SPENCER
S. S. WILKS
J. D. WILLIAMS

Members

L. J. BRIGGS
R. COURANT
J. H. DELLINGER
G. C. EVANS
L. M. GRAVES

R. F. MEHL
H. M. MORSE
P. M. MORSE
H. P. ROBERTSON
A. H. TAUB

O. VEBLER

CONTRACT NUMBERS, CONTRACTORS, AND SUBJECTS OF CONTRACTS FOR THE
APPLIED MATHEMATICS PANEL

<i>Contract Number</i>	<i>Name and Address of Contractor</i>	<i>Subject</i>
OEMsr-444	The Franklin Institute Philadelphia, Pa. Technical Representative, H. B. Allen	Computations.
OEMsr-618	Columbia University New York, N. Y. Official Investigator, H. Hotelling Director: W. Allen Wallis	Statistical methods applied to air combat analysis, torpedo tactics, acceptance inspection, research and development, and related problems.
OEMsr-817	University of California Berkeley, California Technical Representative, J. Neyman	Statistical analysis applied to bombing research concerned with problems of land mine clearance, the theory of pattern bombing and the bombing of maneuvering ships, and the theory of bomb damage.
OEMsr-818	Columbia University New York, N. Y. Technical Representative, J. Schilt	Mathematical and statistical studies of bombing problems; the application of IBM computing techniques to statistical problems in warfare analysis.
OEMsr-860	Princeton University Princeton, N. J. Technical Representative, S. S. Wilks	Statistical methods applied to miscellaneous problems in warfare analysis and to (1) verification of various long-range weather forecasting systems; (2) a study of fire effect tables and diagrams for warships; (3) bombing accuracy studies, analysis of guided missiles, and the performance of certain heat-homing devices; and (4) the clearance of mine fields by explosive devices.
OEMsr-944	New York University New York, N. Y. Technical Representative, R. Courant	Investigations in shock wave theory.
OEMsr-945	New York University New York, N. Y. Technical Representative, R. Courant	Research in problems of the dynamics of compressible gases, hydrodynamics, thermodynamics, acoustics, and related problems.
OEMsr-1007	Columbia University New York, N. Y. Technical Representatives, E. J. Moulton S. MacLane A. Sard	Miscellaneous studies in mathematics applied to warfare analysis with emphasis upon aerial gunnery, studies of fire control equipment, and rocketry and toss bombing.
OEMsr-1066	Brown University Providence, R. I. Technical Representative, R. G. D. Richardson	Problems in classical dynamics and the mechanics of deformable media.
OEMsr-1111	Institute for Advanced Study Princeton, N. J. Technical Representative, John von Neumann	Studies of the potentialities of general-purpose computing equipment, and research in shock wave theory, with emphasis upon the use of machine computation.
OEMsr-1365	Princeton University Princeton, N. J. Technical Representative, Merrill M. Flood	Coordination of activities under Project AC-92 at the University of New Mexico, Carnegie Institution of Washington at Pasadena, Columbia University, and Brown University.
OEMsr-1379	Northwestern University Evanston, Ill. Technical Representatives, E. J. Moulton Walter Leighton	Studies in aerial gunnery, particularly the camera assessment of the performance of sights and of airplanes.

CONTRACT NUMBERS, CONTRACTORS AND SUBJECTS OF CONTRACTS (*Continued*)

<i>Contract Number</i>	<i>Name and Address of Contractor</i>	<i>Subject</i>
OEMsr-1381	Carnegie Institution of Washington Pasadena, Calif. Technical Representative, Walter S. Adams	Studies and experimental investigations in connection with the defensive fire power of various bomber formations by means of model planes with their guns replaced by suitable light sources, the total fire power being estimates of the light intensity.
OEMsr-1384	Harvard University Cambridge, Mass. Technical Representative, Garrett Birkhoff	Studies of the principles which determine the dynamic behavior of a projectile entering water and the application of these principles quantitatively to the prediction of underwater trajectories and ricochet.
OEMsr-1390	The University of New Mexico Albuquerque, N. M. Technical Representative, E. J. Workman	Studies and experimental investigations in collaboration with the Army Air Forces of the most effective formations and flight procedures for the B-29 airplane. Emphasis, originally upon the tactical use of the B-29, was later changed to a study of the defense of the B-29.
Transfer of Funds	National Bureau of Standards	Computations by the Mathematical Tables Project for various agencies concerned with war research.

SERVICE PROJECT NUMBERS

The projects listed below were transmitted to the Office of the Executive Secretary, OSRD, from the War or Navy Department through either the War Department Liaison Officer for NDRC or the Office of Research and Inventions (formerly the Coordinator of Research and Development), Navy Department.

<i>Service Project Number</i>	<i>Subject</i>
<i>ARMY PROJECTS</i>	
AC-27	Design data for bombardier's calculator.
AC-91	Statistical problems of combat bombing accuracy.
AC-92	Collaboration of the NDRC with the AAF in determining the most effective tactical application of the B-29 airplane (continuing under AAF Proving Ground Command, Fire Power Analysis Project).
AC-95	Analysis of Waller trainer film.
AC-109	Textbook on flexible gunnery.
AC-115	Study of data accumulated in sight evaluation tests.
AC-122	Study of gun camera film scoring in order to devise a scoring computer.
AN-23	Studies of HE-IB attack on precision target.
CE-33	Checking of hydraulic tables.
OD-143	Study of fuze dead-time correction in AA director.
OD-179	Statistical assistance in rocket propellant tests and specifications.
OD-181	Study of relative destructive effect of machine gun fire against airplane structures.
QMC-35	Food storage data statistics.
QMC-38	Studies of various statistical problems encountered at the Climatic Research Laboratory.
QMC-43	Statistical consultation for Quartermaster Corps inspection service.
SC-81	Rapid solution of linear equations with up to twenty-six unknowns.
SC-100	Binomial distribution calculations.
SOS-2	Probability theory of balloon barrages.
<i>NAVY PROJECTS</i>	
N-110	Mathematical studies of lead-computing sights for use with gunnery training.
N-112	Study and evaluation of sighting methods of instruction used in U. S. Naval Aviation free gunnery training.
N-120	Preparation of instruction course for quality control and statistically based sampling procedures.
NA-167	Study of nozzle design for jet motors.
NA-177	An analytical method of determining ships' speeds in turns from photographs of ships' wakes.
NA-195	Study of jet propulsion devices operating at subsonic and supersonic velocities [continuing under Contract NOa(s)-7370].
ND-2	Assistance to the Air Technical Division — studies of aircraft weapon effectiveness.
NO-108	Probability and statistical study of plane-to-plane fire.
NO-130	Air testing of Mark 15 bombsight.
NO-131	Probability studies desired in connection with estimating hits made by close-range AA gun fire at head-on airplane targets.
NO-136	Mathematical studies of dive-bomber and bomb trajectories in connection with Alkan dive-bombsight.
NO-145	Mathematical studies of bombing.
NO-145 Ext.	Train probability calculations for bombing, November 1944.
NO-145 Ext.	Probability curves for use in connection with gunnery salvo fire, June 1945.
NO-158	Antitorpedo-harbor defense nets.
NO-161	Theoretical studies of water entry phenomena [continuing under Contract NOa(s)-7370 with New York University and under Navy Contract with Harvard University].
NO-188	Study of torpedo spreads and their use against maneuvering targets.
NO-206	Studies of acceptance tests on ordnance material.
NO-237	Determination of depth of underwater explosions from surface observations [continuing under Contract NOa(s)-7370].
NO-261	Statistical analysis of the data on thermal characteristics of targets and the relative performance of candidate heat-homing equipment.

SERVICE PROJECT NUMBERS (*Continued*)

<i>Service Project Number</i>	<i>Subject</i>
NO-264	Gun equilibrators.
NO-269	B-scan radar plotting device.
NO-270	Computation services (continuing under a transfer of funds from the Office of Research and Inventions to the Bureau of Standards).
NO-272	Computation of dynamic performance of AA computer (continuing under Contract NOrd-9153).
NO-280	Statistical assistance in rocket propellant tests and specifications.
NO-294	Study of tactical utilization of offset guns in fighter aircraft.
NR-101	Probability study of a proposed type of antiaircraft projectile.
NR-105	Fire effect tables (continuing under Contract NOrd-9240).
NS-165	Nonlinear mechanics.
NS-166	Gas globe phenomena in underwater explosions.
NS-302	High-temperature metals.
NS-364	Investigation of wave patterns created by surface vessels (continuing under Contract NOa(s)-7370).

INDEX

The subject indexes of all STR volumes are combined in a master index printed in a separate volume. For access to the index volume consult the Army or Navy Agency listed on the reverse of the half-title page.

- Accelerometers, 159, 162
- Acoustic destruction of mines, 109
- Acoustic scattering, 75–79
 - by grids, 77
 - by spheres, 77
 - by thin rings and rods, 77
 - plane waves from cylinders, 79
 - projector close to dome, 77
 - shielding of domes, 77
 - spherical sounds and shells, 77
- Acoustic shadowing, 77
- Acoustic shielding, 77
- Adiabatic exponent of gases, 10, 29
- “Ager head” pressure plugs, 161
- Air-water entry of solids, 59–63
 - impact force, 59
 - impact-drag coefficient, 59
 - oblique entry, 61
 - projectile with a spherical nose, 59
- Alden Hydraulic Laboratory, 170
- AMP, NDRC, summary of research, 1–6
- Anti-broach devices, 203–207
 - beveling and rounding edges, 204
 - bubble shedding devices, 206
 - conical drag on tail, 206
 - fin stabilized, 206
 - flat head on projectiles, 203
 - Kopfring, 204
 - large length/diameter ratio, 205
 - nose extensions, 204
 - pagoda head, 205
 - recessed heads, 205
 - slotted projectile, 207
 - spiral tails, 206
 - tail stabilization, 206
 - vertical wedge, 206
- Applied Mathematics Panel, NDRC, summary of research, 1–6
- Axial multipole, 98

- Babinet’s principle, light scattering, 81
- Baffle, JP, 79
- Ballistic Research Laboratory at Aberdeen, 39
- Bernoulli constant, 33, 34
- Bernoulli’s equation, 10, 62
- Blackwell’s theory of cavity formation, 219
- Blast waves, spherical, 24
- Blasting submerged objects, 58
- Bomb entering water
 - see* Projectile entering water
- Boundary conditions for shock waves, 41
- British
 - anti-broach device, 204
 - shell design, 135
 - torpedo, 191
- Broach of a projectile entering water, 143, 149, 194
 - see also* Anti-broach devices
- Broadside motion of projectiles, 149, 150, 181, 189
- Brown University, 116
- Bubble-shedding devices for anti-broach, 206
- Burning modes, intermittent jet motor, 43

- California Institute of Technology, 193
- Catholic University, 134
- Cavitation, 182–183, 213–217
- Cavity drag coefficients
 - experimental calculations, 180
 - general discussion, 178
 - of cones, 180
 - theoretical estimates, 179
- Cavity formed by projectile entering water, 142, 168–183, 213–221
 - asymptotic cavity shape, 213
 - Blackwell’s theory, 219
 - cavity deceleration, 219
 - cavity drag coefficients, 178–180
 - cavity lift coefficients, 180
 - cavity moment coefficients, 181
 - cavity widths, 218, 221
 - cross sectional area, 176
 - difference from cavitation, 168–183
 - energy lost by projectile, 218
 - jet formation, 176
 - Kinetic energy, 215
 - liquid fire cavity, 214
 - maximum cavity radius, 218
 - model experiments, 229
 - scaling effect, 199
 - steady state theory, 182–183, 213–217
 - transient cavity, 176, 218
 - two dimensional flow above plate, 216
 - underpressure, 219
 - wall motion, 219, 220
- Cavity lift coefficients, 180–181
 - cone headed projectiles, 181
 - flat headed scatter bomb, 181
- Cavity moment coefficients, 181
- Cavity sealing of model underwater projectiles, 195
- Center of gravity, underwater projectiles, 192
- Centrifugal casting, mathematical analysis, 125–126
- Chapman-Jouguet condition for detonation and deflagration of gases, 26
- Characteristic parameters of differential equations, 11, 17, 25, 113
- Charge dropped from an airplane into the sea, explosion depth, 58
- Circular arc underwater motion, 149, 150, 188
- Coils having a sine law mutual inductance, 102, 105
- Coils having a single dipole moment, 96–106
 - theory, 96–101
 - spherical coil, 98, 102
 - thin coils on a sphere, 103, 104
- Colliding linear oscillators, theory, 109–117
- Compression waves in flow around a bend or corner, 18
- Compressive flow of gases
 - see* Compressors in supersonic missiles
- Compressors in supersonic missiles
 - design, 51
 - effect of heat, 50
 - effect of viscosity, 50
 - shock front, 43, 50
 - stability, 50
 - velocity of flow, 50, 51
- Conical flow of gases, 24, 44
- Conical shock, 24, 42
- Contact discontinuity (shock waves), 30, 31
- Contact lines, 14, 16
- Contact surfaces of shock waves, 14, 29, 36, 38
- Contact zone (shock waves), 28
- Continuum, mechanics of, 128–131
- Contraction wave, 14
- Crater from projectile fired into dirt, 176, 218
- Critical angle of underwater projectile, 194
- Critical speed in gas flow, definition, 10

- Crosswind impact coefficient, under-
 water projectile, 211
 Cubic dilatation (definition), 129
 Cusp locus of turning ships, 67
- Damping moment, underwater projec-
 tile, 187
 Dams, underwater attacks against, 53
 Deceleration coefficient of a projectile
 entering water, 143, 185
 Decelerometers, 200
 Deflagration waves, 25, 26, 43
 de Laval nozzle, 43, 44
 De Lavaud process, centrifugal casting,
 125
 Density of air, 196
 Descartes, folium of, 34
 Detonation wave, 25, 26, 43
 Direction finder, coils for, 96
 Directivity patterns
 effect of baffle construction, 79
 effect of dome filling, 75
 from a vibrating plate, 78
 intensity, 73
 side lobes, 72
 Discontinuity conditions of shock-
 waves, 15
 Discontinuity line of shock waves, 23
 Discontinuity surface of shock waves,
 15
 "Dive" of projectiles entering water,
 149
 Dome of a pressure surface, 34, 170
 Domes (sonar)
 see also Acoustic scattering; Direc-
 tivity patterns
 acoustic reflections from, 78
 filling, effect on sound intensity, 74
 general description, 71
 materials, 73
 shape, effect on sound intensity, 74
 shielding of, 77
 specifications, 73
 spherical, 74
 Down-nosing avoidance in Froude
 scaling, 230
 Drag coefficient of a projectile entering
 water, 143, 178, 185
 Dynamic center of inertia, 227
 Dynamically similar motions, mathe-
 matical theory, 195
- Eastman Kodak Co., 105
 Echo ranging, 71
 see also Acoustic scattering; Direc-
 tivity patterns; Domes (sonar)
 Egg, CIT 10C 30x, 189
 Elasticity, mathematical theories of,
 128-131
- Electric charge distribution, multipole
 formulas, 96-98
 cylindrically symmetrical struc-
 tures, 97
 spherically shaped structures, 98
 Electric dipole formulas, 98
 Electric multipole formulas, 96
 Electromagnetic theory of light diffrac-
 tion, 82-84
 11.75" U. S. rockets, 189
 Enthalpy of a gas, definition, 10
 Entropy, constancy in gas flow, 10
 Entropy changes across a shock, dis-
 continuous, 15
 Entry pitch angle of underwater projec-
 tiles, 194
 Entry speed of an underwater projec-
 tile, 198
 Entry whip of an underwater projec-
 tile, 198, 211-212
 cross wind impact coefficient, 211
 overturn impulse moment, 212
 Equation of state, polytropic gas, 10,
 231
 Equations of continuity and state of an
 incompressible fluid, 196, 230
 Equilibrators for guns, 118-122
 Exhaust flow of a fluid, 50
 Exhaust nozzles, perfect, 49
 Expansion waves
 see Rarefaction waves
 Exploding land mines, devices for, 122-
 123
 Explosion intensity measurement, 128-
 131
 Explosions underwater, 53-59
- Fin stabilized projectiles, 206
 Fins for projectiles, 149
 Flat head projectile for anti-broach
 properties, 203
 Fluid dynamics, 9-50
 see also Projectile entering water
 air-water entry of solids, 59-63
 computational methods, 38-40
 gas dynamics of nozzles and jets, 43-
 52
 jet propulsion in water, 63-66
 interactions in one dimension, 27-32
 non-linear wave motion, 9-27
 regular and Mach reflections, 40-43
 shock waves, 9-50
 shock waves in arbitrary fluids, 36-38
 stationary shock transitions, geo-
 metric analysis, 32-35
 underwater explosions, 53-59
 wave patterns from surface vessels,
 66-68
 Fluid flow around a rigid body, 195
 4R ogive, 194
- Freon used in place of water for under-
 water model experiments, 202
 Froude model, reduced pressure, 200,
 201
 Froude modeling, 198-199, 200-202
 Froude number, 199
 Froude scaling, 199, 200, 231
 Fuel injection for hydropulse motor, 65
- Gas bubble motion, 53-59
 effect of gravity, 57
 effect of rigid wall, 56
 interaction with surface and bottom,
 58
 migration, 56
 non-spherical shape, 57
 pressure pulse, 55
 pulsation, 53
 stabilization by gravity, 56
 stabilization by sea bed, 56
 Gas flow
 see also Shock waves
 around bends, 19
 deflagration and detonation waves, 25
 discontinuities, 15, 27
 in a cone, 44
 inside rockets, 43
 limit speed along a streamline, 10, 15
 oblique shock, 21
 one-dimensional motion, 13
 shock fronts, 14
 streamline, definition, 10
 three dimensional flow, 23
 through a nozzle, 43-52
 Gases
 adiabatic exponent, 10, 29
 equation of motion, 11
 equation of state, 10, 231
 for underwater ballistics model ex-
 periments, 202
 heat content, 10
 German bomb-torpedo design, 164
 German work on spinning bombs, 194
 Glass fiber tubes as thermal insulation,
 136
 Glycerin, effect on cavity motion, 229
 G. P. bombs, 149
 Gun equilibrators, 118-122
 Gun mounting methods, 118
 Guns
 factory tests, for stability on ship,
 118
 mountings on board ships, 118-122
 on pitching and rolling ships, 118
 position aboard ship, 120
 strains during firing, 135
- Heat flow in rockets, 51
 Helmholtz-Kelvin theorem, 196
 H-4.5 rocket, powder grain failures,
 131-134

- Hugoniot line, 15, 37
 Huygens' principle, 81
 Hydraulic theory of gas flow through a nozzle, 43-52
 Hydrodynamic modeling, 196
 Hydropulse
 duct, 63, 64
 effect of gas bubbles, 66
 elastic storage of fuel, 65
 fuel injection, 65
 motor, 63
 scavenging operation, 65
 stroke, 64
 tube, 64, 65
 valveless type, 65

 Ideal flow of a gas, 50
 Impact forces of projectiles entering water, 59, 159, 208-210
 Impact phase of underwater ballistics
 see Air-water entry of solids; Projectiles entering water
 Impact-drag coefficient, 59
 Incident shock wave, 23, 93
 Incompressible fluid, equation of continuity and state, 196, 230
 Incompressible material, stress-strain, 129
 Induced mass effects (definition), 226
 Induced mass effects in underwater projectiles, 193
 Induced mass of a fluid, 159, 162, 179
 Induction flux through a collecting coil, 100
 Inertial modeling of underwater projectiles, 197
 Insulating materials, thermal, 135
 Isentropic flow of gases
 see Shock waves
 Isham projectile, 205

 Jet detachment, 47
 Jet formation, 43
 Jet propulsion in water, 63-64
 Jet research, 43
 Jouguet's hypothesis (gas flow), 25
 JP baffle, 79

 Karman theory (impact forces), 208
 Kelvin theory (wave patterns), 66
 Kopfring (projectile head), 204
 Kronecker delta, 114

 LaMer's theory of light scattering, 80
 Land mines clearance, 122-123
 Legendre functions, 92
 Light diffraction
 see Light scattering and diffraction
 Light scattering and diffraction, 80-95
 by spherical obstacles, 80, 86, 88
 energy loss, 80
 fringe patterns, 81
 Mie theory, 85
 Mie-Stratton theory, 82
 polarized light, 80
 scattered radiation, 83
 scattering cross section, 82
 secondary field, 82
 shadow, 81-83
 Stratton's work, 85
 Linear oscillators, collision theory, 109-117

 M30 projectile, 181, 184, 189
 Mach effect, 41
 Mach front, 42
 Mach lines, 11, 17, 19, 35, 49
 Mach modeling, 199
 Mach number, 17, 39, 41, 49
 Mach reflection, 23, 35, 40
 Mach shock, 42
 Mach waves, 40
 Magnetic dipole formulas, 99
 Magnetic pole distribution, multipole formulas, 99
 Magnus effect, 185
 Mark XII torpedo, 198
 Mark 13 torpedo, 204
 broaching, 192
 cavitation, 183
 cavity closure, 201
 circular arc motion, 149, 191
 effect of pitch on water entry, 184
 effect of yaw on torpedo roll, 381
 entry whip, 197, 211
 impact force entering water, 159
 left impulse entering water, 165
 peak pressure reduction, 161
 Mark 13.2 torpedo, 193, 199
 Mark XV torpedo, 198
 Mark 17 depth charge, 184
 Mechanical mine exploders, 122-123
 Mechanics of particles and rigid bodies, 109-127
 colliding linear oscillators, 109-117
 centrifugal casting, mathematical analysis, 125-126
 gun equilibrators, 118-122
 land mines clearance devices, 122-123
 optical bars of range finders, thermal deflection reduction, 126-127
 pressure inside the Williams gauge, 123-125
 servos with torque saturation, 117-118
 Meissner method for determining regions of stability for a motion, 115
 Mie theory of light scattering, 85
 Mine exploders, 122-123
 comparison of two types, 123
 flails, 123
 power expenditure, 122
 Mines, Froude scaling of, 199
 Minesweeping by acoustic methods, 109
 Missiles with compressors, 50
 Model experiments with underwater projectiles
 cavitation, 200
 cavity sealing, 195
 effect of reduced density, 201
 effect of surface tension, 229
 effect of water compressibility, 230
 effect of water-entry speed, 195
 Froude modeling, 198
 inertial modeling, 197
 Mach modeling, 199
 modeling by equal velocities, 199
 reduced pressure differential Froude model with heavy gases, 201
 reduced pressure Froude model, 200
 stress modeling, 199
 theory of dynamic similarity, 195
 ventilating model noses, 195
 viscosity effects, 229, 230
 Momentum virtual mass, 209
 Multipole, axial, 98
 Mutual inductance of two axially symmetric spherical coils, 101

 Navy Ordnance Laboratory, 53, 170
 Navy practice bomb (NPB.), 189, 193
 Navy 3.0" Mk III projectile, 194
 Navy 6.0" Mk XX projectile, 194
 NDRC, Division 6; 53
 New York University, 67
 Non-isentropic flow of gases, 25
 Nonlinear wave motion
 see Shock waves
 Normal shock (wave), 34
 Nose extensions for projectiles, 204
 Nozzles
 for jet motors, 43
 for rocket motors, 43
 perfect nozzles, 49
 reverse nozzle, 43
 thrust of, 43

 Oblique shock, 19, 34, 35
 Oils for dome fillings, 74
 One-dimensional motion, 13
 Optical bars of range finders, design for reduction of thermal deflections, 126-127
 Oscillator theory, linear colliding, 109-117
 Oscillation of an underwater projectile, 150, 191
 Overturn impulse moment, underwater projectile, 212

- Pagoda head (projectile), 205
- Particles, mechanics of
 see Mechanics of particles and rigid bodies
- Peak pressure of gas bubble pulsation, 53
- Penetration (shock waves), 28
- Periodic motion, simple, 112
- Photo Interpretation Center, 66
- Photographs of jets issuing from exhaust nozzles, 48
- Photographs of projectile cavities, 175
- Piston moving in a cylinder, maximum displacement of, 125
- Pitch and yaw effect on projectile path, 141
- Pitch-whip of a projectile, 166
- Plastic diaphragm deformation due to a distant explosion, 128–131
 circular diaphragm, 130
 energy absorbed, 128
 incompressible materials, 129
 strain deviation, 129
 true stress-strain, 128
 work of deformation, 129
- Plasticity, mathematical theories of, 128–131
- Plough of a projectile entering water, 143, 149
- Plumes formed by underwater explosions, 53, 58
- Poincaré phase cylinder, 188
- Polar shock, 34
- Polarized light scattering, 80
- Polytropic gases
 behavior in shock fronts, 16–17
 equations of state, 10, 231
- Powder grain failures in H-4.5 rockets, 131–134
- Powder grains for rockets, buckling of, 131
- Poynting's flux theorems, 80
- Prandtl's relation (shock waves), 16, 20
- Precompression wave, 26
- Pressure plugs, 161
- Pressure pulse of underwater explosion, 53
- Pressure surface of shock waves, 34
- Principle of Babinet (light scattering), 81
- Projectile entering water
 anti-broach devices, 203
 broaching, 194
 broadside motion, 149
 bubbles formed, 143
 cavity, 168–183
 cavity lift coefficients, 181
 circular arc motion, 149
 critical entry angle, 143
 deceleration coefficient, 143
 dome formation, 170
 drag coefficient, 143
 elastic shock force, 159, 208
 entry speeds and ranges, 141
 impact forces, 159–167, 208–210
 induced mass velocity loss, 159, 164
 kinetic energy, 208, 209
 lucite sphere experiments, 165
 oblique impact, 161
 oscillatory and spiral motion, 150
 path through air and in water, 141
 peak pressure, 159, 161
 phases of motion, 142
 pitch-whip, 166
 ricochet, 143, 150
 shape of projectile, 164–166
 speed, 143
 splash, 179
 stability coefficient, 150
 surface seal, 179
 time-deceleration curve for vertical entry, 162
 types of underwater motion, 143
 vibration, 159
 virtual mass, 209
 whip, 159, 166, 211
 yaw and roll, 167
- Projectile fins for preventing broadside motion, 149
- Projectile lengths, radius of curvature, 149
- Projectile shell design, 134–135
- Projectile trajectory underwater
 see Trajectory of an underwater projectile
- Projectile with a spherical shaped nose, 59
- Radius of gyration of a projectile, 192
- Range finders, optical bars for, 126–127
- Rankine-Hugoniot discontinuity condition, 15, 37
- Rankine-Hugoniot equations, 36, 38
- Rarefaction waves, 13, 18, 19, 26, 32
 backward and forward, 29
 centered rarefaction wave, 13
 collision of two waves, 32
 general discussion, 13
 overtaken by shock or rarefaction waves, 32
 penetration, 28, 30
 Riemann wave, 27, 39
- Rayleigh scattering of light, 85
- Reaction front of shock waves, 25
- Reactive thrust of gas flowing through a nozzle, 48
- Recessed heads for projectiles, 205
- Recommendations for future research
 mechanical mine exploders, 123
 underwater explosions, 58
- Reflections of shock waves
 conical waves, 42, 43
 glancing reflections, 40
 Mach reflections, 40
 plane waves, 40
 regular reflections, 21, 35, 40
- Reindeer fur as an insulator, 135
- Reverse nozzle, 43
- Reynolds number, 229
- Ricochet of projectiles
 critical angle for, 165
 definition, 143
 prevention of; *see* Anti-broach devices
 rifle bullets fired into shallow water, 194
 spheres, 143
 spinning effect, 194
 tail up ricochet, 150, 191
- Riemann rarefaction wave, 27, 39
- Rifle bullets fired into shallow water, ricochet, 194
- Rigid bodies, mechanics of
 see Mechanics of particles and rigid bodies
- Rigid body entering water
 see Projectile entering water
- Rigid body moving through a fluid
 see Trajectory of an underwater projectile
- Rocket nozzles
 see also Compressors in supersonic missiles
 contour types, 48
 de Laval nozzle, 44
 hydraulic nozzle theory, 44
 perfect nozzles, 49
 pressure measurements, 49
 requirements, 48
 shock fronts, 49
 theory of gas flow through a nozzle, 43
 thrust, 43, 47, 48
- Rocket propellants, failures of, 131–134
- Rockets
 damage to firing airplanes, 51
 heat flow, 51
 powder burning, 52
 steel casings, 52
- Rule optical whip recorder, 162
- Scaling systems for underwater projectiles
 Froude, 199, 200–202
 inertial modeling, 197
 Mach, 199
 reduced pressure Froude model, 200
- Scatter bomb, flat headed, cavity lift coefficients, 181
- Scatter bomb, oscillatory motion, 191

- Scattering, acoustic
 see Acoustic scattering
- Scattering of light by a sphere, 80–95
- Scattering of sound
 see Acoustic scattering
- Sea mines, location for maximum damage, 54
- Servos with torque saturation, 117–118
- Shell for projectiles, 134–135
 band pressure, 134
 forces acting on shell, 134
 stress analysis, 134
- Shell stresses, 134–135
- Shielding methods, acoustic, 77
- Shielding of domes, 77
- Ship motion, effect on gun mountings, 118, 119
- Ship speed computed from wave pattern data, 67
- Ship speed determined from aerial photographs, 66
- Shock conditions, 14, 20
- Shock fronts
 see Shock waves
- Shock polar, 34
- Shock waves
 adiabatic compression, 36–37
 boundary conditions, 41
 collision of two shocks, 17, 32
 conical shocks, 24, 42
 contraction wave, 13
 definition, 9
 deflagration and detonation waves, 25
 discontinuities, 13, 18–20, 26
 effect of heat conduction, 14
 effect of viscosity, 14, 50
 entropy, 16
 flow around corners, 18
 flow pattern, 22
 forward and backward shocks, 28, 29
 geometric analysis, 32
 heat effect, 14, 36
 in arbitrary fluids, 36
 in nozzles, 48
 incident shock wave, 23, 93
 interactions, 17, 22, 27, 32
 isentropic irrotational steady plane, 17
 numerical computation methods, 38
 oblique, 17, 18
 one-dimensional, 13
 overtaken by shock waves, 32
 plane waves, 40
 precompression wave, 26
 pressure behind and in front, 30
 reflection, 16, 21–22, 35, 37, 40
 set up by a moving piston, 124
 shock layer, 38
 shock lines, 14, 16
 spherical waves, 24
 stationary shock, 20
 strength measurement, 16
 three dimensional, 23
 three shock configuration, 23
 two dimensional, 19
 velocity, 30, 32
- Sinclair's work on light diffraction, 85
- 6.0" Mk. XX projectile, 194
- "Skin effect" of projectiles entering water, 164, 185
- Skin friction drag, 229
- Skip-bombing, broaching, 189, 203
- Slip stream, 36, 38, 41
- Solids entering water
 see Air-water entry of solids
- Sound propagation, effect of dome, 71
- Sound speed, formula, 10
- Sphere entering water, 162, 170, 209, 219, 229
- Spherical blast waves, 25
- Spherical coil system yielding a single dipole, 102
- Spherical domes, 74
- Spherical wave motion, 24
- Spherically symmetric motion, 40
- Spin effect on underwater trajectories, 194
- Spiral motion of underwater projectiles, 150
- Splash of projectile entering water, 179
- Spray dome formed by underwater explosions, 53, 58
- Spring hammer box (SHB), 109–117
 electrical analogue, 115–117
 general description, 109
 motion of system between impacts, 110
 non-interpenetration conditions, 110–112
 simple periodic motion, 112
 stability, 110, 112, 114, 115
 system parameters, 110
- Stability coefficient of a projectile, 150
- Stability conditions for systems in motion
 definition, 113
 general motion, 115
 periodic motions, 112
 theories of Liapunoff and Poincaré, 113
- Stabilization principle for underwater explosions, 54
- Stationary shock waves, 20, 21, 32
- Strains in guns during firing, 135
- Stratton's theories of light diffraction and scattering, 82, 85
- Streamline, definition, 10
- Streamline, ultimate speed along, 10
- Stress-strain of permanently deformed plastic diaphragms, 128
- Stress-strain relationships for incompressible materials, 129–131
- Stroke of a hydropulse, 64
- Suction phase of explosive waves, 25
- Supersonic flow of gases, definition, 10
- "Surface seal" of projectile entering water, 176, 179, 198, 201
- "Tail slap" of projectile entering water, 142, 159
- Tail stabilization of underwater projectiles, 206
- Tail-up ricochet, 150, 191
- "Tallboy" rocket model, 188
- Taylor Model Basin, 109, 115, 181
- Thermal deformation in optical bars, reduction of, 126–127
- Thermal insulating materials, 135
- Thermal stresses in rockets, 51
- Three dimensional flow of gases, 23
- 3 inch 50 mount guns, 120, 118
- 3.5" U.S. rockets, 189
- Three-shock configuration (shock waves), 23
- Thrust of a nozzle, 43
- Time-deceleration curve of projectiles entering water, 162
- Torpedo motions
 see Mark 13 torpedo
- Torpedo roll, 194
- Trajectory of an underwater projectile, 143–150, 184–194, 199, 222–228
 broaching, 194
 broadside motion, 149, 189
 buoyancy force, 184
 circular arc trajectories, 149, 188
 curvature, 188
 damping force and moment, 185, 187
 determination from differential equations of motion, 185, 187
 effect of density and radius of gyration, 192
 effect of entry speed, 190
 effect of nose shape, 189
 effect of shape of head and tail and length, 191
 effect of variations of center of gravity position, 192
 entry pitch angle, 194
 free surface force, 185
 hydrodynamic forces, 186
 induced mass effects, 193
 mathematical analysis of types of motion, 222–225
 oscillatory and spiral motion, 150, 190
 Poincaré phase cylinder, 188
 prediction, 188
 ricocheting, 143, 150, 191, 194
 scale model studies, 190, 199

spin effect, 194
 stability, 188, 189, 192, 225, 227
 tail first motion, 225
 tailless models, 193
 up-pitch, 193
 virtual mass, 185
 yaw effect, 194
 Transducer domes, wave transmission,
 71
 Transient cavity theory, 218
 Transition curves of shock waves, 31

Underwater ballistics
 anti-broach devices, 203-207
 cavity, 168-183
 impact force of projectiles entering
 water, 159-167
 modelling, 195-202
 phases of motion, 141-143
 scale effects, 195-202
 trajectories, 143-150, 184-194
 Underwater bubble
 see Gas bubble motion
 Underwater explosions, 53-59
 blasting through obstacles, 58
 damage to reservoir dams, 53

damage to warships, 53
 maximizing the damage, 54
 peak pressure, 56
 secondary pulse, 56
 stabilization principle, 56
 surface phenomena, 53
 Underwater mine laying, 54
 Underwater motion, types
 see Trajectory of an underwater pro-
 jectile
 Underwater projectile modeling
 see Model experiments with under-
 water projectiles; Scaling sys-
 tems for underwater projectiles
 Underwater projectile trajectories
 see Trajectory of an underwater pro-
 jectile
 Valveless hydropulse, 65
 Velocity potential for gas flow, defini-
 tion, 10
 Ventilation of projectile nose, 195
 Vibrating plate, directivity pattern,
 78
 Virtual mass, differential equation
 theory of, 226-228

Virtual mass effect on underwater pro-
 jectiles, 179, 185, 209
 Virtual mass of a fluid, 60, 61, 63
 Von Kármán, 162
 Wall effect in two dimensional cavity
 flow, 216
 Water, induced mass, 159, 162
 Watertown Arsenal, 135
 Wave, simple, 12, 13
 Wave motion
 see Rarefaction waves; Shock waves
 Wave patterns from surface vessels, 66-
 68
 Wave transmission through metal
 shells, 71
 Whip of a projectile entering water,
 159, 166
 Whip recorder, optical, 164
 Whip recorder, rule type, 162
 Williams gauge, pressure studies of,
 123
 Woods Hole Underwater Laboratory,
 53, 58
 Yaw effect on projectiles entering
 water, 167

DECLASSIFIED

By authority Secretary of

OCT 13 1960

Defense memo 2 August 1960

LIBRARY OF CONGRESS

Return To
SCIENCE AND TECHNOLOGY DIVISION
Library of Congress

